

**EFFECT OF ADVERTISED WINDOW SIZE ON RTT AND RTO IN
D2D COMMUNICATION**

A PROJECT REPORT

Submitted by

ANANYA BISWAS

Supervised by

Mr. Ritwik Mondal

Asst. Professor,

*Department of Information Technology,
Govt. College of Engineering and Ceramic Technology*

In partial fulfillment for the award of the degree

of

M.TECH

IN

INFORMATION TECHNOLOGY

2016-2018



GOVT. COLLEGE OF ENGINEERING & CERAMIC TECHNOLOGY

73, Abinash Chandra Banerjee Lane, Kolkata-10

**EFFECT OF ADVERTISED WINDOW SIZE ON RTT AND RTO IN
D2D COMMUNICATION**

A PROJECT REPORT

Submitted by

ANANYA BISWAS

Supervised by

Mr. Ritwik Mondal

Asst. Professor,
Department of Information Technology,
Govt. College of Engineering and Ceramic Technology

In partial fulfillment for the award of the degree

of

M.TECH

IN

**INFORMATION TECHNOLOGY
2016-2018**



**GOVT. COLLEGE OF ENGINEERING & CERAMIC TECHNOLOGY
73, Abinash Chandra Banerjee Lane, Kolkata-10**

BONAFIDE CERTIFICATE

Certified that this project report "EFFECT OF ADVERTISED WINDOW SIZE ON RTT AND RTO IN D2D COMMUNICATION" is the bonafide work of "ANANYA BISWAS" who carried out the project work under my supervision.

M. Maitra. 5.6.18.

SIGNATURE

Dr. Mausumi Maitra
HEAD OF THE DEPARTMENT

Associate Professor
Information Technology

Govt. College of Engineering &
Ceramic Technology, Kolkata-10

Rll 05/06/2018

SIGNATURE

Mr. Ritwik Mondal
SUPERVISOR

Assistant Professor
Information Technology

Govt. College of Engineering &
Ceramic Technology, Kolkata-10

SIGNATURE

Anandam

External Examiner

ACKNOWLEDGEMENT

I would like to express my sincere gratitude to Govt. College of Engineering & Ceramic Technology for giving me the opportunity to work on this project and partially complete the project during my post-graduation studies.

I am privileged to express my sense of gratitude to my supervisor Mr. Ritwik Mondal, Assistant Professor, Department of Information Technology, Govt. College of Engineering & Ceramic Technology for the immense help with his valuable advice, resourceful guidance, inspiring instructions and constant encouragement, which always insisted me to do work hard in this difficult field.

I am also grateful to Dr. Mausumi Maitra, Head of the Department, Department of Information Technology, Govt. College of Engineering & Ceramic Technology, for her uninterrupted support and encouragement which helped me a lot in fulfilling the project.

Ananya Biswas

ANANYA BISWAS

(Roll No- GCECTM-R16-2003)

(Reg. No-161130410004 of 2016-17)

TABLE OF CONTENTS

CHAPTER NO	TITLE	PAGE NO
	LIST OF TABLE	i
	LIST OF FIGURES	ii
	LIST OF ABRIVIATIONS	iii
	ABSTRACT	iv
1.	Introduction	1
	1.1. Motivations and Objectives	5
	1.2. Projects Overview	6
2.	LTE /LTE-A System overview	7
	2.1. SimuLTE Layer	8
	2.2. SimuLTE Architecture	12
3.	Description of Softwares	15
	3.1. Omnet++	15
	3.2. Inet Framework	16
	3.3. SimuLTE	16
4.	Device to Device Communication	17
	4.1. Taxonomy of D2D Communication	18
	4.1.1. Inband D2D	18
	4.1.2. Outband D2D	19
5.	TCP Overview	22
	5.1. Relation among RTT, RTO and Window Size	23
6.	Side Link Establishment in D2D Communication	24
	6.1. Side Link Transmission	24
	6.2. Side Link Channels	25
7.	Project Implementation and Analysis	26
	7.1. Prior Work on Previous Semester	26
	7.1.1. D2D Modelling	26

	7.1.2. Implementation of Constant Speed and Tractor Mobility in D2d	28
8.	Analysis of the Result	30
	8.1. Measurement of RTT and RTO of IM and DM	33
9.	Conclusion	39
10.	Future Scope in Direct Communication	40
11.	References	41

LIST OF TABLES

TABLE NO.	TABLE NAME	PAGE NO.
Table.1	D2D simulation parameters (Figure 13)	33
Table.2	Values of RTT and RTO at stationary (graph in figure.16 and 17)	37
Table.3	Values of RTT and RTO at linear (graph in figure.18 and 19)	38
Table.4	Values of RTT and RTO at random (graph in figure.20 and 21)	38

LIST OF FIGURES

FIGURE NO.	FIGURE NAME	PAGE NO.
Fig.1	Relaying devices with controlled link establishment from the operator.....	2
Fig.2	Direct communication between devices with operator controlled link establishment.....	3
Fig.3	Relaying devices with device controlled link establishment	3
Fig.4	Direct communication between devices with devices controlled link establishment.....	4
Fig.5	Logical high-level architecture for the evolved system.....	8
Fig.6	LTE protocol Layers.....	9
Fig.7	RLC module representation.....	10
Fig.8	MAC packet flow.....	11
Fig.9	Overview of simuLTE.....	13
Fig10	Uplink Scheduling	17
Fig.11	Classification of D2D communication.....	18
Fig.12	Visualization of side link.....	24
Fig13	A scenario of D2D communication.....	31
Fig14	D2D communication from source to destination.....	31
Fig15	A sequence chart for D2D communication.....	32

LIST OF ABBREVIATIONS

SL. NO.	ABBREVIATIONS	MEANING
1.	UE	User Equipment
2.	eNB	evolved Node Base Station
3.	RLC	Radio Link Control
4.	PDCP	Packet Data Convergence Protocol
5.	RRC	Radio Resource Control
6.	MAC	Medium Access Control
7.	UMTS	Universal Mobile Telephone System
8.	AMC	Adaptive Modulation Coding scheme
9.	PDU	Protocol Data Unit
10.	SDU	Service Data Unit
11.	PGW	Packet Data Network Gateway
12.	SGW	Service Gateway
13.	RTT	Round Trip Time
14.	RTO	Retransmission Time Out
15.	LTE	Long Term Evolution
16.	EPC	Evolved Packet Core
17.	RAN	Radio Access Network

ABSTRACT

A constant need to increase the network capacity for meeting the growing demands of the subscribers has led to the evaluation of cellular communication networks from the first generation to fifth generation. There will be billions of connected devices in the near future. Such a large number of connections are expected to be heterogeneous in nature, demanding higher data rates, lesser delays. The available spectrum resources are limited and need to be flexibly used by the mobile network operators to cope with rising demand. An emerging facilitator of the upcoming high data rate demanding next generation networks is device-to-device communication.

In this project, various types of mobilities are assigned to the users devices under a common constant parameters. The user equipments are positioned at large distance from eNB where the signal of eNB is weak. A comparative study is made between the conventional cellular system and direct communication cellular system. The user devices are working on TCP connection oriented protocol. A real life file is being transferred from source to destination through side link in D2D communication. The sending window size is limited with advertised window size. The Round Trip time and the Retransmission Time Out is measured under various window size for both conventional and direct communication. The results are noticed.

A brief description on TCP protocol of transport layer is discussed. The relation of round trip time, retransmission time out and window size is marked. D2D communication exploited as a new communication opportunity in several fields, like vehicular networks, IoT and machine-to-machine applications.

Chapter 1

INTRODUCTION

The number of hand-held devices is drastically increasing with rising for higher data rate for application. The demand for wireless mobile data continues to explode and increasing in the number of smart phones in usage throughout the world. Dense deployments and heterogeneous topologies with small cells (micro/pico/femto) deployed in conjunction with macro cells have been used. Indoor coverage improvements through the use of remote radio-heads and distributed antennas have proliferated. These approaches using small cells have certain drawbacks, such as a huge mobility increase in mobility events, complex interferences management issues, the cost and effort involved in installing and maintaining large amounts of additional infrastructure, such as high capacity internet backhaul, power sources.

The Long Term Evolution (LTE) of the UMTS is the standard for next generation network that is device to device communication, which is expected to play an indispensable role in the approaching era of wireless communication. The introduction of device to device communication (D2D), direct transmission between mobile devices is expected to improve the reliability of the link between devices, enhance spectral efficiency and system capacity with reduced latency within the network. Device to device communication allows to communicate between devices in two ways that is either partial involvement of base station or without involvement of base station. The devices nearer to each other can directly communicate with each other by establishing direct links (side links). Due to small distance between the D2D devices, it supports power saving within the network which is not possible in conventional cellular communication. It is certain in improvement of energy efficiency, throughout and reduce delay. It has the potential to effectively offload traffic from the network core. Hence, it is very flexible technique of communication within the cellular network.

In a conventional cellular network, every communication is between User Equipments (UEs) through evolved base station (eNB). Even though the UEs are within hearing range of each other, they have to communicate via two-hop path, which becomes delay in communication,

less reliability if the UEs are at the edge of the region of eNB. With the introduction of device to device direct communication, these drawbacks of conventional cellular network can be overcome.

Thus direct communication between UEs is categorized into four different types. They are as follow:

- (1) Device relaying with controlled link establishment from the operator. Devices at the cell edges or in poor coverage areas are capable of communicating with the base station (BS) by relaying information through other devices. All tasks of establishing the communication between the devices are handled by the base station (BS). The battery life of the devices is enhanced this way. The architecture is as shown below:

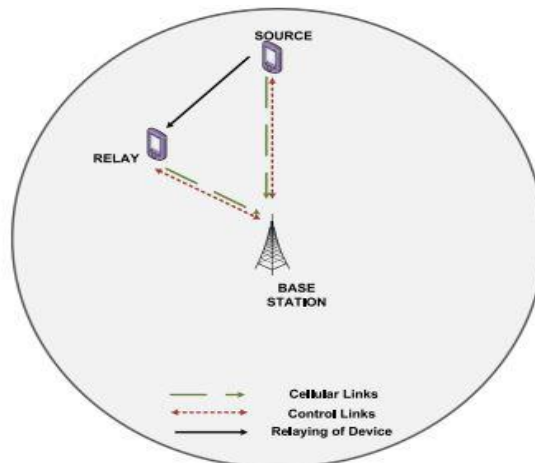


Fig:1 Relaying Devices with controlled link established from the operator

- (2) Direct communication between devices with controlled link establishment by the operator. Two devices communicate directly with each other, with control links provided by the base station. Though direct, the communication is entirely managed by the base station. Since in (1) and (2), a central controlling entity, i.e. the base station(BS) is present, interference management is possible. The architecture is as shown below:

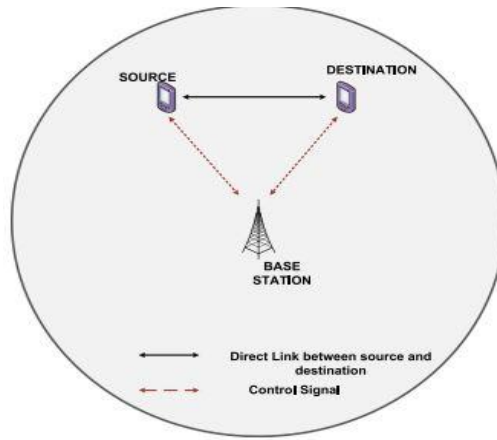


Fig:2 Direct Communication between devices with operator controlled link establishment

(3) Device relaying with controlled link establishment from the device. Two devices communicate via relays, within the cellular networks. Resource allocation, setting up of call, interference management, all is managed by the devices themselves, in a distributive fashion. Control of the base station is missing. is as shown below:

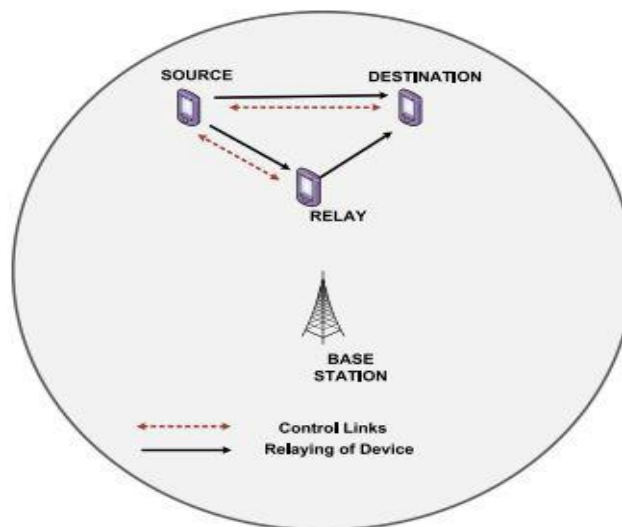


Fig:3 Relaying device with device controlled link establishment

(4) Direct communication between devices (Direct d2d) with controlled link establishment by the device. Devices communicate directly, without aid from the base station(BS). The architecture is as shown below:

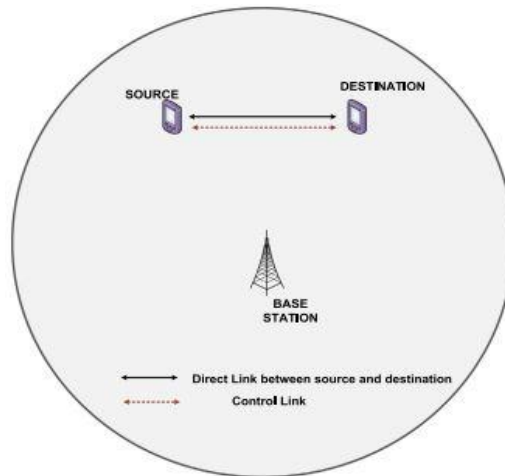


Fig:4 Direct communication between devices with device controlled link established

The benefits offered by direct or D2D communication are as follows:

1. One hop communication: the devices can communicate with each other through a single hop. Lesser resources are then required for the communication, resulting in an efficient utilization of the spectrum. Since proximity users directly communicate with each other in D2D communication, latency is greatly reduced. These are desirable aspects in a cellular network. The mobile network operators are also benefitted by these aspects of D2D communication.
2. Spectrum Reusability: with D2D communication in cellular networks, same spectrum is shared by the D2D users as well as the cellular users. This supports spectrum reusability, thereby improving the spectrum reuse ratio.
3. Optimization of Power Levels: since D2D links exist between proximate devices, over a small distance, transmission power is less. This enhances the battery life of the devices. As a result, higher energy efficiency can be achieved with D2D communication in cellular networks.

4. Improved Coverage Area: as discussed in (1) and (3), D2D communication is possible with relays. This supports communication over greater ranges, thus increasing the overall coverage area.

1.1. MOTIVATIONS AND OBJECTIVE

The evolution of cellular wireless communications has involved the introduction of technologies such as multiple antennas, higher spectral efficiency through better modulation, denser deployments and carrier aggregation. A different approach to enhancing the cellular network by using direct communication D2D (Device to Device) between UEs (User Equipment) is presented in this paper. The direct communication can be used for several purposes including network traffic offloading, public safety, and social applications such as gaming. The objective for D2D communication is mainly used here for traffic offloading and minimizing the load of base station or eNodeB (evolved Node Base station). The steps involved in establishing and maintaining a D2D call and procedures for efficient mobility between a traditional cellular mode and a D2D mode of operation is represented in this paper.

In this paper, how the Round Trip Time (RTT) of Transmission Control Protocol (TCP) in transport layer of TCP/IP suite connection affected by D2D communication is shown. Here the performance obtained by TCP Reno. Our simulation is carried out using SimuLTE, c++ system-level simulation developed for omnet++ which simulates the data plane of the LTE/LTE-A radio access network. A static and some pedestrian mobility scenarios have been evaluated, where flows are sent through either Side Link (SL) D2D or upload/downlink conventional path for some UEs messages transmission from source to destination. In this experiment, one pair of UEs (one to one) and one eNB (evolved Node Base station) with omni direction are considered for simplicity.

1.2. PROJECT OVERVIEW

The wireless communications for having d2d mode of operation is designed by 3GPP LTE-Advanced system as baseline for d2d communications. In telecommunications, LTE (Long-Term Evolution) is a standard for high speed wireless communication for mobile devices and data terminals, based on GSM/EDGE and UTRAN/HSPA technologies. It increases the capacity and speed using a different radio interface together with core network improvements. The standard is developed by 3GPP (3rd Generation Partnership Project). The LTE wireless interface is incompatible with 2G and 3G networks, so that it must be operated on a separate radio spectrum. The further LTE is developed towards LTE-Advanced to provide higher bitrates in a cost efficient way. The main functionalities introduced in LTE-Advanced is Carrier Aggregation(CA). The way to increase the capacity is to add more bandwidth. Since it is important to keep backward compatibility with R8 and R9 mobiles (specified in 3GPP LTE Release 8 and Release 9) the increase in bandwidth in LTE-Advanced is provided through aggregation of R8/R9 carriers.

The implementation and work for wireless d2d communication requires some software platform which include OMNET++5.0, INET Framework and SimuLTE. INET Framework and SimuLTE are the softwares that have been used on the OMNET++5.0 platform.

Chapter 2

LTE/LTE-A SYSTEM OVERVIEW

The term LTE is a project of the Third Generation Partnership Project (3GPP). The goal of the project was to determine the long-term evolution of 3GPP's Universal Mobile Telephone System (UMTS)[10]. The project LTE is inextricably linked with the underlying technology, which is an evolution of UMTS. The UMTS Radio Access Network (RAN) has two major components:(1) the Universal Terrestrial Radio Access (UTRA), which is the air interface including the user equipment (UE) or mobile phone, and (2) the Universal Terrestrial Radio Access Network (UTRAN), which includes the Radio Network Controller (RNC) and the base station known as eNB.

As the LTE is the evolution of UMTS, components along LTE are named as evolved UTRA (E-UTRA) and evolved UTRAN (E-UTRAN). The system is more than just the RAN since the parallel 3GPP project called System Architecture Evolution (SAE) defines a new Internet Protocol (IP)packet only core network known as the Evolved Packet Core (EPC). The combination of the EPC and the evolved RAN (E-UTR aand E-UTRAN) is the evolved packet system (EPS). The EPC provides seamless interworking with existing 3GPP and non-3GPP radio access technologies.

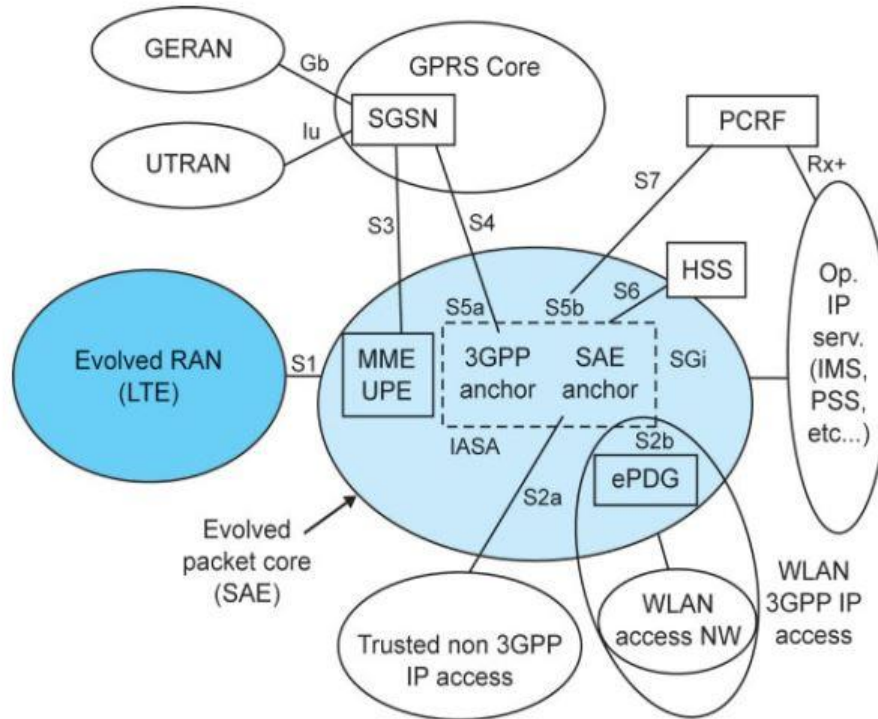


Fig.5 Logical high level architecture for the evolved system

2.1. SIMULTE LAYER

The simulTE is the main platform based on the omnet++ and inet for performing device to device communication. SimulTE simulates the data plane of the LTE/LTE-A Radio Access Network and Evolved Packet Core (EPC). It allows simulation in Frequency Division Duplexing (FDD) mode, with heterogeneous eNBs (macro, micro, pico, etc.), using omni directional and anisotropic antennas, possibly communicating via X2 interface.

The LTE-A protocol stack consists of four layers shown in figure 6 [1], described top to bottom: an IP packet entering an LTE interface first traverses the Packet Data Convergence Protocol (PDCP), where it is cyphered and assigned a sequence number. It is then sent down to the Radio Link Control (RLC) layer, in the form of an RLC SDU, and it is buffered there. It performs segmentation/concatenation of RLC SDUs on transmission, and reassembly, duplicate detection and reordering of RLC PDUs on reception. The MAC sits below the RLC and requests to it an RLC

PDU of a given size. The RLC complies by dequeuing from its buffer one or more RLC SDUs and combining them as necessary into RLC PDUs. The MAC adds its own header and forms a MAC PDU, also called Transmission Block (TB). SimuLTE comes with models of real life applications (e.g., VoIP, Video on demand, Gaming) but any other TCP/UDP based omnet++ application can also be used. In the UE it connects the Network Interface Card (NIC) to applications that use TCP or UDP. In the eNB, it connects eNB itself to other IP peers (e.g., a web server), via Point-to-Point Protocol (PPP). The NIC module structure is shown below implements the LTE protocol layers.

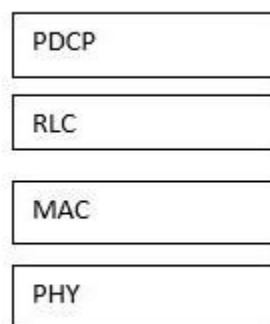


Fig. 6 LTE protocol Layers

The working of the layers of LTE protocol are as follows:

(1) PDCP-RRC module

The PDCP-RRC module is the connection point between the NIC and LTE-IP modules. It receives data from upper layers in the downlink direction from RLC layer in the uplink direction. It performs Robust Header Compression (ROHC) and assigns/ creates the Connection Identifier (CID) along with UE ID that uniquely identifies connection in the whole network. A Logical Connection Identifier (LCID) is established for each 4-tuple in the form of < sourceAddr, destAddr, sourcePort, destPort >. When a packet arrives at PDCP-RRC, the correct LCID is attached to it, otherwise a new LCID is created storing new 4-tuple. Then the packet is encapsulated in a PDCP PDU (Protocol Data Unit) and forwarded to the RLC port depending on the selected RLC mode. A packet coming from

the RLC in the uplink direction, the packet is decapsulated, its header is decomposed and the resulting PDCP PDU is sent to upper layer.

(2) RLC module

The RLC module performs multiplexing and demultiplexing of MAC SDUs (Service Data Unit) to/from the Mac layer. It implements the three RLC modes Transparent Mode(TM), Unacknowledged Mode (UM), Acknowledged Mode (AM) as defined in 3GPP-TS 36.322) [6]. It forward the packet from/to the PDCP-RRC to/from the proper RLC mode entity. RLC operation is same for both eNB and UE. There are three different gates connected with the PDCP-RRC module one for each RLC mode. The TM submodule has no buffer it forwards packet transparently. On the otherhand AM and UM have their own set of transmission/reception buffers, one for each CID associated to that RLC mode. The structure of the RLC module is shown below:

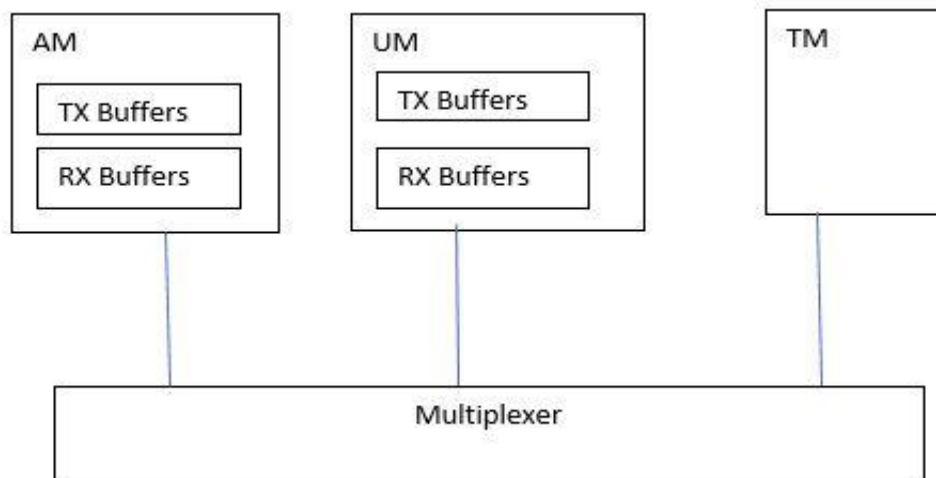


Fig. 7 RLC module representation

(3) MAC module

The MAC module is where most of the intelligence of each node resides. It performs buffering the packets from upper (RLC) and lower (PHY) layers, encapsulating MAC SDUs into MAC PDUs and vice-versa. It manages channel feedback, adaptive modulation and coding (AMC) and scheduling. In the downlink direction, MAC SDUs coming from RLC layer are stored in MAC buffers, one for each CID. One each Transmission Time Interval (TTI) some connections are scheduled for transmissions, according to the schedule list composed by scheduler. MAC SDUs from the scheduled connections are then encapsulated into MAC PDUs, which are then stored in H-ARQ buffers and forwarded to the physical layer. IN the uplink direction, MAC PDUs coming from the physical layer are stored into H-ARQ buffers. They are checked for correctness, decapsulated and forwarded to RLC. Resource scheduling is performed at the eNB for both the uplink and downlink. For the uplink, decisions are notified to the UEs via grant message, that is the current release the Physical Control Channel (PDCCH) is not directly simulated. Each UE reads the grants and decides which local connection will be able to use the granted resources, if any. UEs in turn request uplink resources via Random Access (RAC) Procedure, which is implemented through message generated at the MAC module. The structure of packet flow in MAC module is shown below:

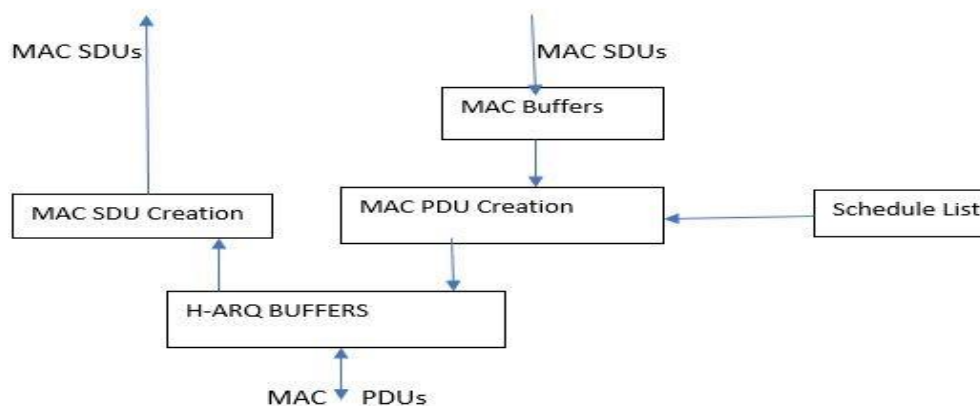


Fig. 8 MAC packet flow

(3) PHY module

The PHY module implements functions related to physical layer. Such as channel feedback computation and reporting, data transmission and reception, air channel emulation and control message handling. It stores the physical parameters of the nodes such as transmission power and antenna profile. Each physical module on eNB and UE has an associated Channel Model which represents physical channel as perceived by the node itself. The Channel Model is an interface that defines two main functions: `getSINR()`, which returns the Signal to Interference and Noise Ratio (SINR), and `error()`, which checks if a packet has been corrupted. At the UE side, tasks related to physical layer procedures are performed by an independent Feedback Generator module, which generates channel feedback (i.e. CQI) [6]. The physical LTE channels, such as Physical Downlink Control Channel (PDCCH), Physical Uplink Control Channel (PUCCH), and Physical Random Access Channel (PRACH) are not modeled down to the level of OFDM symbols, to keep both memory and CPU usage limited.

In downlink direction, MAC PDUs are received from the MAC layer and encapsulated in an Air Frame packet. Packets are marked with a type with either data or control. Then they are directly sent to their destination module, selected according to the controlled information attached to the packet.

In the uplink direction, a received Air Frame packet is selectively processed depending on its type, control packets are directly forwarded to the upper layer whereas data packets are tested against the `error()` function of the Channel Model before being marked and sent to the upper layer.

2.2. SIMULTE ARCHITECTURE

The core SimuLTE module is the LTE NIC card, based on which can instantiate nodes with LTE capabilities, specifically UEs and eNBs. These nodes exploit the LTE NIC as an interface, and add as upper layers modules from INET, i.e. a set of OMNeT++ based modules to simulate standard

Internet entities. A representation of the nodes is given in figure 8 below. The NIC card implementation allows to develop nodes with multiple connectivity capabilities (e.g. LTE and/or Wi-Fi).

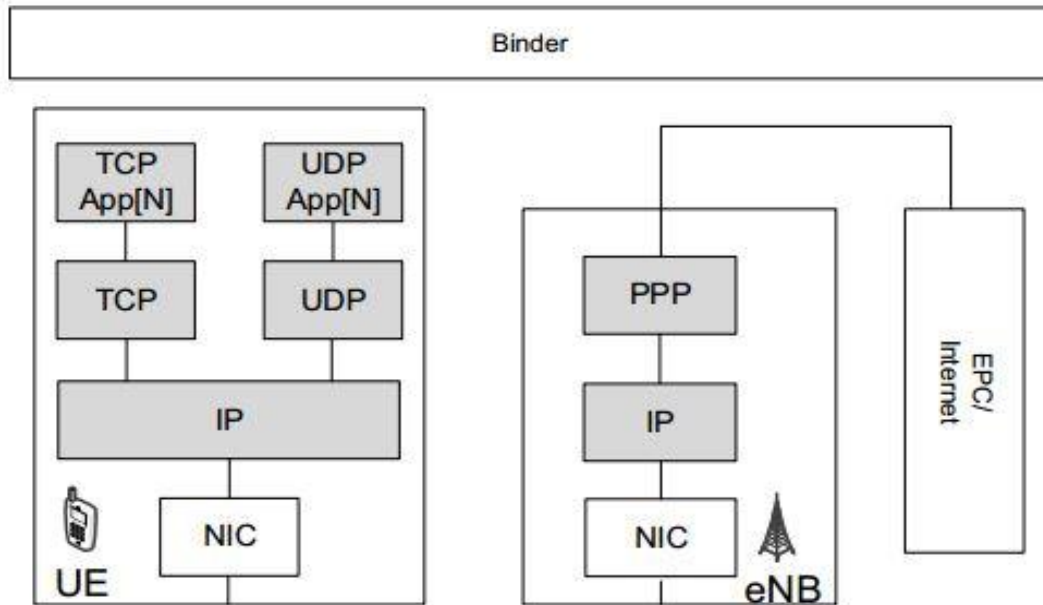


Fig. 9 Overview of simuLTE

The NIC cards in the UE and eNB nodes are organized by layers, namely PDCP, RLC, MAC and PHY, with a one-to-one correspondence with the LTE protocol stack. In fact, OMNeT++ allows inheritance of both the structure and the behavior of modules. Considering the MAC layer as an example, we have the MacUeand, MacEnbclasses, both extending the MacBase class with node-specific functions, such as the resource scheduler on the eNB side [8]. In SimuLTE, data transmission and resource accounting are done separately. Resource accounting is done by a central module, the Binder, which monitors the resource blocks (RBs) in the system on a TTI basis. The Binder has the full visibility of all the nodes in the system, and can be called by every node to obtain shared information. It keeps track of which RBs are used by which node (eNBs in DL and UEs in UL), which still allows a correct interference management. The dataflow is instead modeled via message exchanges between modules. The correspondence between

messages and resources is maintained by the Binder, which associates a certain amount of RBs to each message, based on the length of the MAC PDU and on the modulation and coding scheme employed by the transmitter. Control channels, such as the Physical Downlink Control Channel (PDCCH) is used to carry scheduling assignments, are not directly implemented, rather they are modeled using separated messages and the associated resources are again kept consistent by the Binder. This allows to simulate and evaluate their behavior from a resource perspective, without paying for the added complexity of a full emulation. Finally, each NIC card has a ChannelModel class, which cooperates with the PHY layer and that models the status of the air channel as is perceived by the NIC card itself. It is mainly used to compute the SINR of a signal received by the node, which in turn is used by the PHY layer to compute the CQIs and evaluate transmission errors. Each Channel Model interacts also with the Binder to know exactly which resources are actually used by every node in the system.

Chapter 3

DESCRIPTION OF SOFTWARES

3.1. OMNET++

It is an object-oriented modular discrete event network simulation framework. It is not a simulator of anything concrete, but rather provides infrastructure and tools for writing simulations. One of the fundamental ingredients of this infrastructure is a component architecture for simulation models. Models are assembled from reusable components termed modules. Modules can be connected with each other via gates (other systems would call them ports), and combined to form compound modules. The depth of module nesting is not limited. Modules communicate through message passing, where messages may carry arbitrary data structures. Modules can pass messages along predefined paths via gates and connections, or directly to their destination; the latter is useful for wireless simulations. Modules may have parameters that can be used to customize module behavior and/or to parameterize the model's topology. The lowest level of the module hierarchy are called simple modules, and they encapsulate model behavior. Simple modules are programmed in C++, and make use of the simulation library. OMNeT++ simulations can be run under various user interfaces. Graphical, animating user interfaces are highly useful for demonstration and debugging purposes, and command-line user interfaces are best for batch execution. The simulator as well as user interfaces and tools are highly portable. They are tested on the most common operating systems (Linux, Mac OS/X, Windows), and they can be compiled out of the box or after trivial modifications on most Unix-like operating systems. OMNeT++ also supports parallel distributed simulation. It can use several mechanisms for communication between partitions of a parallel distributed simulation, for example MPI or named pipes. OMNEST is the commercially supported version of OMNeT++.

3.2. INET FRAMEWORK

INET Framework contains IPv4, IPv6, TCP, SCTP, UDP protocol implementations, and several application models. Link layer models are PPP, Ethernet and 802.11. Static routing can be set up using network auto configurators, or one can use routing protocol implementations. The INET Framework supports wireless and mobile simulations as well. The INET version 3.4 is used for omnet++5.0. The INET Framework builds upon omnet++, and uses the same concept: modules that communicate by message passing. Hosts, routers, switches and other network devices are represented by omnet++ compound modules. These compound modules are assembled from simple modules that represent protocols, applications, and other functional units. The INET Framework gives us a platform where we don't have to code with C++ programme. The code is written in a file called omnetpp.ini configuration file which is the main file to change the parameters. The external interfaces of modules are described in NED files. NED files describe the parameters and gates (i.e. ports or connectors) of modules. The packages in INET are organized roughly according to OSI layers.

3.3. SIMULTE

SimuLTE is an innovative simulation tool enabling complex system level performance evaluation of LTE and LTE-Advanced (3GPP Release 8 and beyond) for the omnet++ framework. SimuLTE is written in C++ and is fully customizable with a simple pluggable interface [9]. One can also develop new modules implementing new algorithms and protocols. SimuLTE is an open source project building on top of omnet++ and INET Framework. It borrows the concept of modularity from omnet++ thus it is easy to extend. Moreover it can be integrated with other modules from the INET Framework. SimuLTE requires omnet++v5.0 and INET Framework v3.4. It is designed such that it can be plugged within network elements as an additional Network Interface Card (NIC) to those already provided by the INET framework (e.g. Wi-Fi). Recently, device-to-device(D2D) technology has been widely studied by the research community, as a mechanism to allow direct communications between devices of a LTE cellular network.

Chapter 4

DEVICE TO DEVICE COMMUNICATION

The direct or D2D communication between devices or UEs is performed on the simuLTE platform based on Inet and omnet++. In this section, the procedure on how the user messages or data flows between the devices with the help of side link or with partial involvement of eNB are described. In LTE cell, a base station or eNB allocates radio resources to a number UEs that is handheld devices, laptops or home gateways, using Orthogonal Frequency Division Multiplexing Access (OFDMA) in the downlink, and Single-Carrier Frequency Division Multiplexing (SC-FDMA) in the uplink [8,5]. At each TTI of 1ms, a time/frequency frame of Resource Blocks (RBs) is allocated to the UEs, in both directions. Each RB carries a variable amount of bytes to/from an UE depending on the selected modulation and coding scheme. The UEs requests for uplink resources through RAC request. The RAC requests collisions are resolved through backoff. The requests are being responded by scheduling the UEs in a future TTI, and are re-iterated if unanswered after a timeout. The handshake for UL transmissions takes five messages is shown in figure 9. Before sending data from source to destination, the UE first communicates the sending/receiving control information with the eNB. The UE sends a RAC request to eNB which in turn responds with a small grant message size of Buffer Status Report (BSR). The UE sends its own BSR. The eNB sends a larger grant according to its scheduling policy, and the UE transmits its data.

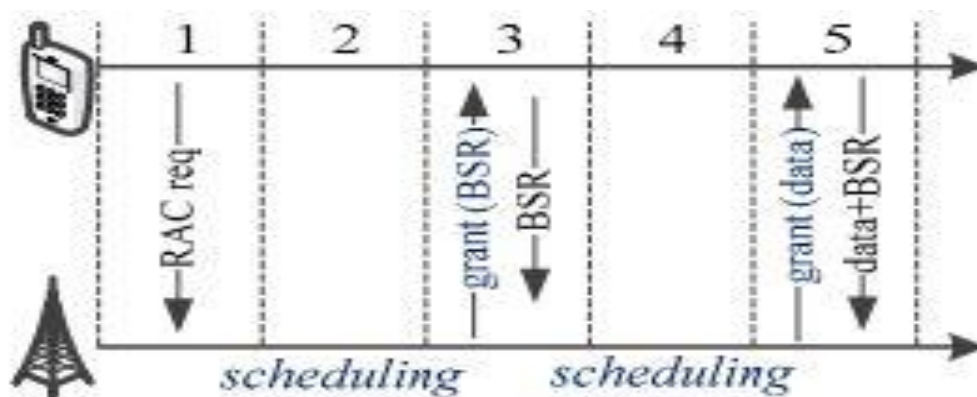


Fig. 10 Uplink Scheduling

4.1. TAXONOMY OF D2D COMMUNICATION

Device to device (D2D) communication use the licensed spectrum (inband) or the unlicensed spectrum (outband) for direct link formation. Inband D2D communication is categorized as underlay and overlay. Underlay D2D communication allows set up of direct links and cellular links in the cellular spectrum. In overlay D2D a dedicated portion of the available spectrum is used for Device-to-Device(D2D) communication, with rest of the spectrum used for cellular communication. As outband D2D communication exploits the unlicensed spectrum for the formation of direct links, it is categorized as autonomous and controlled. The device to device communication classification is shown below:

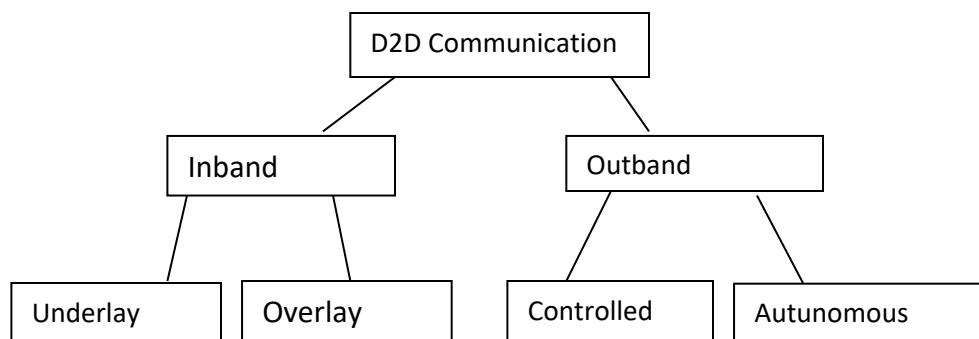


Fig. 11 Classification of D2D communication

4.1.1. Inband D2D

The direct communication under this category contains the majority of the available work, proposes to use the cellular spectrum for both D2D and cellular links. The choosing of inband communication is usually because of the high control over cellular (i.e., licensed) spectrum [8]. Inband communication can be further divided into underlay and overlay categories. In underlay D2D communication, cellular and D2D communications share the same radio resources. In contrast to D2D links in overlay communication are given dedicated cellular resources. Inband D2D can improve the spectrum efficiency of cellular networks by reusing spectrum resources (i.e., underlay) or allocating dedicated cellular resources to D2D users that

accommodates direct connection between the transmitter and the receiver (i.e., overlay). The key disadvantage of inband D2D is the interference caused by D2D users to cellular communications and vice versa. This interference can be mitigated by introducing high complexity resource allocation methods which in turn increase the computational overhead of the Base Station or D2D users.

4.1.2. Outband D2D

The D2D links exploit unlicensed spectrum. The outband D2D communication is used to eliminate the interference issue between D2D and cellular link. The unlicensed spectrum requires an extra interface and usually adopts other wireless technologies such as WiFi Direct, ZigBee or bluetooth. The work on outband D2D suggests to give the control of the second interface/technology to the cellular network (i.e., controlled) [11]. Whereas some propose to keep cellular communications controlled and leave the D2D communications to the users (i.e., autonomous) [12]. Outband D2D uses unlicensed spectrum which makes the interference issue between D2D and cellular users irrelevant. On the other hand, outband D2D may suffer from the uncontrolled nature of unlicensed spectrum. It should be noted that only cellular devices with two wireless interfaces (e.g., LTE and WiFi) can use outband D2D, and thus users can have simultaneous D2D and cellular communications.

When controlled, the radio interfaces in D2D are managed by the eNB, while in autonomous, these are coordinated by the UEs themselves. Interference between D2D users and cellular users is no issue in out band D2D, but coordination of the communication in the unlicensed band requires a second radio interface (like, Wi-Fi Direct, Bluetooth, ZigBee). To utilize the limited available spectrum in the most efficient manner, one must know where to use which category of D2D communication. For implementing D2D communication in cellular networks, a number of key issues need to be marked. For gaining the advantages of direct communication, overcoming these issues efficiently is important.

Some of these are listed below.

(i) PEER DISCOVERY

Since direct communication is gaining popularity, locating the user devices means discovering proximate users has become necessary. The process of peer discovery should be efficient, so that D2D links are discovered and established quickly. It is also important for ensuring optimum throughput, efficiency and resource allocation within the system. Once the users devices are discovered each other, that is establishing the direct links between the devices, the transmission of data over those links occurs. Researchers are working on different approaches for device discovery.

(ii) RESOURCE ALLOCATION

After device discovery, availability of resources is important for enabling communication over the direct links. Radio resource allocation is needed for enhancing the spectral efficiency of D2D communication [8]. Resource allocation strategies in D2D communication can be centralized or distributed. Centralized techniques cause complexity in case of large networks while distributed technique tend to decrease the device complexity. The distributed techniques improve the scalability of the D2D links. For obtaining maximum throughput, D2D communication can operate in a number of modes. These are as follow:

Silent Mode:

In this mode, the D2D devices stay silent and cannot transmit because of lack of resources. Spectrum reuse, as a result, is not possible.

Dedicated Mode:

In this mode, some of the available resources are dedicated for the D2D users, to be used for direct transmission.

Reuse Mode:

In this mode, uplink or downlink resources of the cellular users are reused by the D2D users.

Cellular Mode:

In this, conventional communication occurs, through the eNBs and D2D data is transmitted.

The improvement in the spectrum efficiency can be achieved by the use of reuse mode. The interference management is better with the dedicated and cellular modes. However, these two modes maybe inefficient to maximize the overall network throughput. The decision for resource sharing is made by the base station. When the D2D links and cellular links reuse the same resources, it is referred to as non orthogonal sharing and when they do not share the same resources, it is referred to as orthogonal sharing. The resource utilization efficiency is better achieved through non orthogonal sharing.

(iii) POWER CONTROL

The optimum transmission power for reusing the frequency is an area of interests.

It is particularly important in case of uplink transmissions because of the near-far effect and co channel interference. Once a maximum power level is allocated to the D2D users, the Quality of Service (QoS) of the cellular users is maintained in the network. Controlling power effectively mitigates interference in cellular networks. For D2D under laid cellular networks, there has been a considerable interest in power control methods. A limit is set upon the power level of the D2D transmitter and its reuse partner (the cellular user), in order to maximize the overall system throughput.

(iv) INTERFERENCE MANAGEMENT

The D2D links within a cellular network pose a big threat of interference to the cellular links in the network. The D2D links can cause interference between cellular users and D2D users, resulting in an increase in intra-cell interference. Inter- cell interference is also possible with D2D communication underlying cellular communication. Interference can be mitigated through mode selection, optimum resource allocation, power control. Setting the maximum transmit power limits of the D2D transmitter is an effective technique of limiting the interference between device UEs and cellular UEs.

Chapter 5

TCP OVERVIEW

The Transmission Control Protocol (TCP) is a process-to-process (program-to-program) protocol. TCP is a connection oriented protocol. It creates a virtual connection between two TCPs to send data. In brief, it is called a connection-oriented and adds reliability services of IP. The connection establishment in TCP is called three-way-handshaking. At the application layer, the services offered by TCP are:

- (1) Process-to-Process Communication using port numbers.
- (2) Stream Delivery Services allows the sending process to deliver data as a stream of bytes and allows the receiving process to obtain data as a stream of bytes.
- (3) Sending and receiving buffers because the sending and receiving processes may not write or read data at the same speed, TCP needs buffers for storage.
- (4) The IP layer, as a service provider for TCP, needs to send data in packets, not as a stream of bytes. At the transport layer, TCP groups a number of bytes together into a packet called a segment.
- (5) TCP offers full-duplex services, in which data can flow in both directions at the same time.
- (6) TCP uses an acknowledgement mechanism to check the safe and sound arrival of data providing reliability services.

The TCP at the transport layer of TCP/IP protocol suite provides ordered delivery of application data. Once end to end connection is established, the application streams of bytes are divided into a set of TCP segments, each one identified by the sequence number of the last byte in it. After receiving a segment, the receiver sends back an Acknowledgement (ACK) which contains the sequence number of the next expected segment. The receiver confirms that all the previous bytes are been received. A duplicate ACK (dupACK) is sent by the receiver when out-of-sequence bytes arrive, that is one or more segments are missing. The segment is retransmitted

if the ACK is not received before a retransmission timer expires. The number of segments that can be sent simultaneously is limited by the flow control and congestion control mechanisms. Both use a sliding window to avoid sending more data than those the receiver and the network can handle. The effective sending window is the minimum of the two. When the size of the receive window is specified by the receiver itself, the status of the network must be inferred from the (lack of) reception of ACKs. Most congestion control algorithms begin with a slow-start phase, where the congestion window (cwnd) is increased exponentially. When a threshold is reached, the algorithm enters a congestion-avoidance phase, where the cwnd is increased linearly. If a retransmission timer expires, TCP assumes the network is congested, hence reduces the cwnd.

5.1. RELATION AMONG RTT, RTO AND WINDOW SIZE

The TCP defines the size of the window in bytes that the other party must maintain. The length of the window size is 16 bits, which means the maximum size of the window is 65,535 bytes. This value is referred to as the receiving window (rwnd) and is determined by the receiver. The sender must obey the dictation of the receiver. TCP takes into account the congestion in the network [13]. The amount of data sent by a sender is not only controlled by the receiver, but is also determined by the level of congestion in the network.

For ping and trace route is measured by Round Trip Time (RTT) between sending the ping packet and getting the Internet Control Message Protocol (ICMP) packet back. The TCP connection measures the time sending a packet to getting the acknowledgement packet from the target host.

In modern implementation, a segment is retransmitted on two occasions, when a retransmission timer expires or when the sender receives three duplicate ACKs. TCP maintains one Retransmission Time Out (RTO) timer for all outstanding (sent, but no acknowledged) segments. When the timer comes to end, the earliest outstanding segment is retransmitted even though lack of a received ACK can be due to a delayed segment, a delayed ACK, or a lost ACK. The value of RTO is dynamic in TCP and is updated based on the RTT of segments. An RTT is the time needed for a segment to reach a destination and for an ACK to be received.

Chapter 6

SIDELINK ESTABLISHMENT IN D2D COMMUNICATION

In this project, within the cellular system the one pair of UEs are sending messages through D2D communication without the involvement of eNB. Though, the eNB is present in our cellular system for the transfer of control flow information between eNB and the two UEs. For the direct communication, a link between the two UEs are established which is called Side Link (SL).

6.1. SIDE LINK TRANSMISSION

In conventional cellular system, for both signalling and data transmission the eNB communicates with UEs through uplink and downlink. This concept is extended with the introduction of side link is shown below:

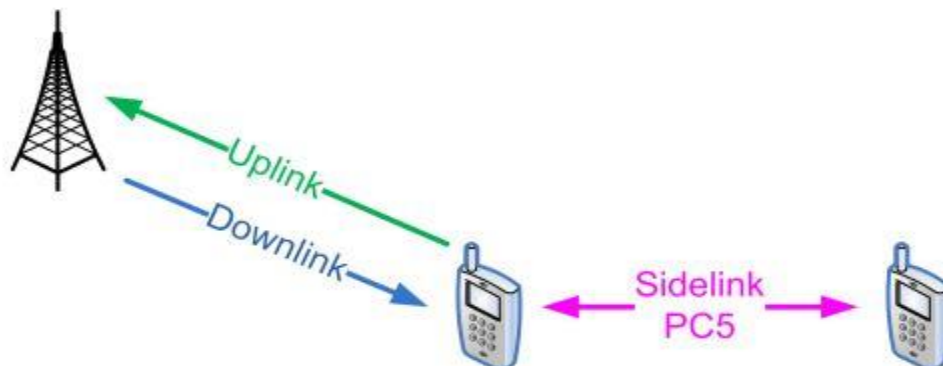


Fig. 12 Visualization of Side Link

The resources are assigned to the SL taken from the uplink, that is from the subframes on the uplink frequency in FDD or from the subframes assigned to uplink in TDD. There are two reasons for this selection. First, the uplink subframes are usually less occupied than those on the downlink. Second, most downlink subframes are never really empty, there are always at least the cell specific reference signals (CRS) transmitted. The side link describes the channel

structure, that is logical channels, transport channels, and physical channels which are used in the air-interface to realize the ProSe application [4].

6.2. SIDELINK CHANNELS

The side link channels are defined for communication between D2D user devices. There are two SL logical channels, SL Traffic Channel (STCH) and the SL Broadcast Control Channel (SBCCH). The STCH is used for the data transmission which carries the user information from the ProSe application. It is a point-to-multipoint channel, reflecting the group call property of the ProSe communication. It is connected with the SL Shared Channel (SL-SCH), a transport channel which may bear a collision risk, depending on the resource assignment from the eNB. It interfaces to the Physical SL Shared Channel (PSSCH), which transports the data over the air.

The SBCCH carries signaling information used for synchronization in the out-of-coverage or partial coverage scenario, or for synchronization between UEs located in different cells. It is connected with the SL Broadcast Channel (SL-BCH), a transport channel with a predefined transport format, which is possible because the blocks from the SBCCH are all of the same size. The SL-BCH interfaces with the Physical SL Broadcast Channel, the PSBCH. The Physical SL Control Channel (PSCCH) is the equivalent to the PDCCH in cellular traffic. It contains the Side link Control Information (SCI), which carries the information the receiving UE requires in order to be able to receive and demodulate the PSSCH. So, the SCI is always sent in advance to an STCH data block.

Chapter 7

PROJECT IMPLEMENTATION AND ANALYSIS

7.1. PRIOR WORK ON PREVIOUS SEMESTER

Some simulations are performed within a cellular network containing one eNB and two UEs. The UEs are nearer to each other at a distance of 20m. The eNB is at a distance of 50m from the UEs. The UEs are sending data through direct communication and giving some mobility to the UEs like constant speed and tractor mobility with varying the speeds.

7.1.1. D2D MODELLING

SimuLTE provides models of UEs and eNBs. Hence it is possible to simulate D2D communications within cellular networks with other Internet devices taken from INET Framework. The direct or D2D communication simulation parameters can be configured in the *.ini* configuration file which is supported by omnet++. The parameters are as follow:

It is necessary to use the D2D specific Adaptive Modulation and Coding (AMC) module for eNB to communicate between users through direct communication. The *d2dPeerAddresses* parameter is a blank spaces-separated list of IP addresses. The peering is unidirectional, it needs to explicitly define the reverse one for bidirectional flows for TCP connections. The Channel Quality Indicator (CQI) is

defined as `**d2dCqi=7`. The position or coordinates of the eNodeB (eNB) has been kept fixed.

The different parameters can be employed for evaluating different scenarios with respect to D2D communication and mobility of sender and receiver are discussed below:

UNICAST ONE TO ONE D2D

A snippet of theomnetpp.ini file is given below:

```
# enable D2D capabilities
*.eNodeB.d2dCapable = true
*.ueD2D*[*].d2dCapable = true
# select the AMC mode
*.eNodeB.nic.mac.amcMode = "D2D"
# set peering relationship
*.ueD2DTx[0].nic.d2dPeerAddresses="ueD2DRx[0]"
# select the CQI for D2D transmissions
*.eNodeB.nic.phy.enableD2DCqiReporting = false
**.usePreconfiguredTxParams = true
**.d2dCqi = 7
# set Tx Power
*.ueD2DTx[0].nic.phy.ueTxPower = 26 # in dB
*.ueD2DTx[0].nic.phy.d2dTxPower = 26 # in dB

# TCP connections
# Traffic Configuration
*.ueD2D*[0].numTcpApps=1
*.ueD2DTx[0].tcpApp[*].typename = "TCPSessionApp"
*.ueD2DTx[0].tcpApp[0].connectionPort = 1000
*.ueD2DTx[0].tcpApp[*].localPort = 1000
```

```

*.ueD2DTx[0].tcpApp[*].sendBytes = 1MiB
*.ueD2DTx[0].tcpApp[0].active = true
*.ueD2DTx[0].tcpApp[0].tOpen = uniform(0.010s,0.1s)
*.ueD2DTx[0].tcpApp[*].tSend = uniform(0.15s,0.5s)
*.ueD2DTx[0].tcpApp[0].connectAddress = "ueD2DRx[0]"
*.ueD2DTx[0].tcpApp[*].localAddress = "ueD2DTx[0]"
# at the receiver side
*.ueD2DRx[0].tcpApp[*].typename = "TCPSink"
*.ueD2DRx[0].tcpApp[*].localPort = 1000
**.tcpApp[*].tClose = -1s

# enabling D2D communication
*.eNodeB.d2dCapable = true
*.ueD2D*[*].d2dCapable = true
**.amcMode = "D2D"

# peering two UEs
*.ueD2DTx[0].nic.d2dPeerAddresses = "ueD2DRx[0]"
*.ueD2DRx[0].nic.d2dPeerAddresses = "ueD2DTx[0]"
*.eNodeB.nic.phy.enableD2DCqiReporting = true

```

7.1.2. IMPLEMENTATION OF CONSTANT SPEED AND TRACTOR MOBILITY IN D2D

The sender ueD2DTx and receiver ueD2DRx mobility are not fixed. The sender and receiver can move anywhere in the constraint given area as a real life user move, but with fixed speed. A cellular network with only one eNB is taken and one pair of UEs are considered for simplicity. The eNB transmission power is 10w maintained. For different eNB transmission power, there is

certain region to catch the signal by UEs. The default transmission power of both the UEs are 26w are taken. When the CQI (Channel Quality Indicator) is better the data transmitted whereas it is terminated when CQI is weak. The simulation for this mobility is taken about 40s. We need to configure the receiver as a possible D2D peer for the sender. To this aim, the `d2dPeerAddresses` parameter is a blank spaces-separated list of IP addresses is written in another demo xml file where the netmask is 255.255.255.0.

A snippet for constant speed mobility is given below:

```
# constant speed mobility for both UEs
*.ue*[0].mobilityType = "ConstantSpeedMobility"
*.ue*[0].mobility.speed = 2mps
**.updateInterval = 0.1s
```

A snippet for tractor mobility is given below:

```
# tractor mobility for both UEs
*.ue*[0].mobilityType = "TractorMobility"
*.ue*[0].mobility.row = 3
*.ue*[0].mobility.column = 1
```

Chapter 8

ANALYSIS OF THE RESULTS

The main purpose of this paper is to observe the Round Trip Time (RTT) with different size of advertised window. The direct communication between one pair of UEs with one eNB are taken within a infrastructure based cellular system. Although, it is infrastructure based, for D2D communication control information and resource allocation is through eNB but data is transferred through side link. This above scenario is being compared with the conventional cellular system. In conventional system the data, control information and resource allocation is through eNB. The comparisons are made with some mobility in UEs. The UEs are placed approximately at the edge of region of the eNB. Thus, analyzing the data transmission in D2D at the edge is far more better than in conventional and reliable. In conventional the signal is weak for data transfer. In D2D communication, there is also less load on eNB. The simulation for conventional cellular system takes almost three minutes to transfer a file of 1 MB whereas in direct communication it takes 50 seconds. The sending rate is made of different sizes by TCP receive window sizes, which is 8KB, 16KB, 32KB and 64KB. The RTT is about 42ms (on average) for conventional infrastructure mode communication whereas direct communication reduces to 30ms, but not less.

Some simulation parameters are given in table 1 which are kept fixed throughout both the comparisons of direct and conventional communication. The scenario for the D2D or direct communication is shown in figure 13.

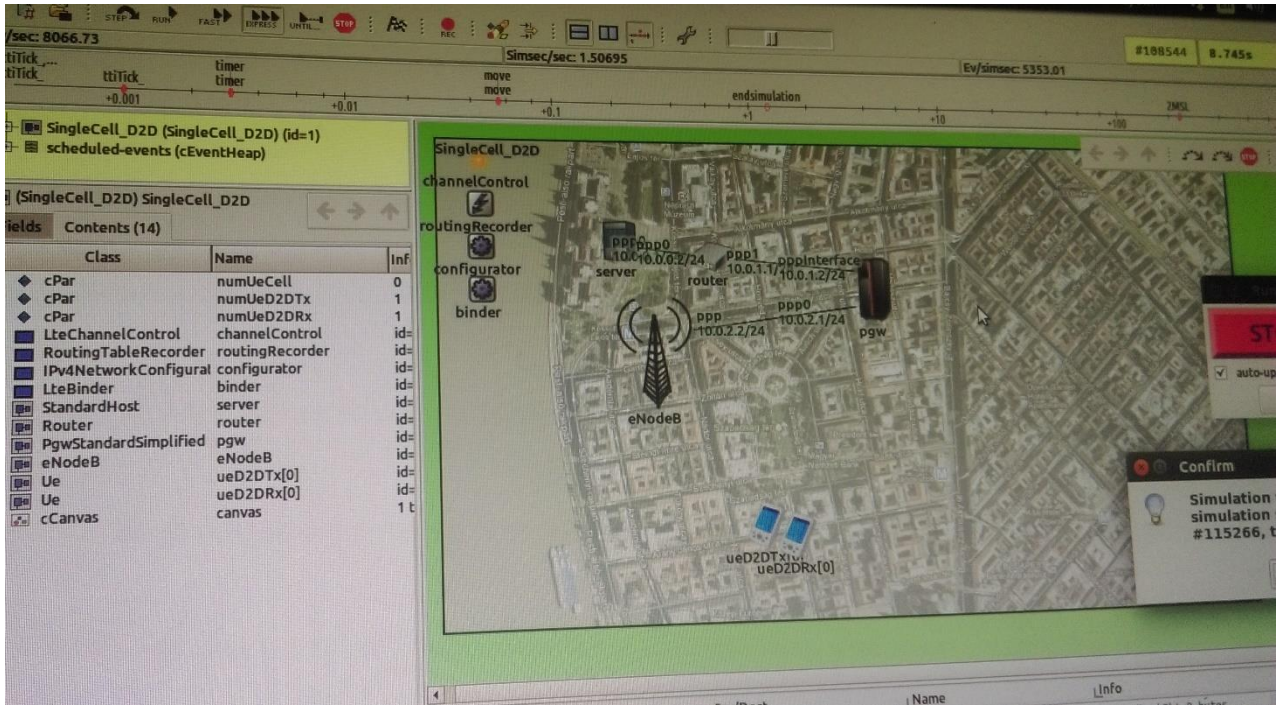


Fig. 13 A scenario for D2D communication

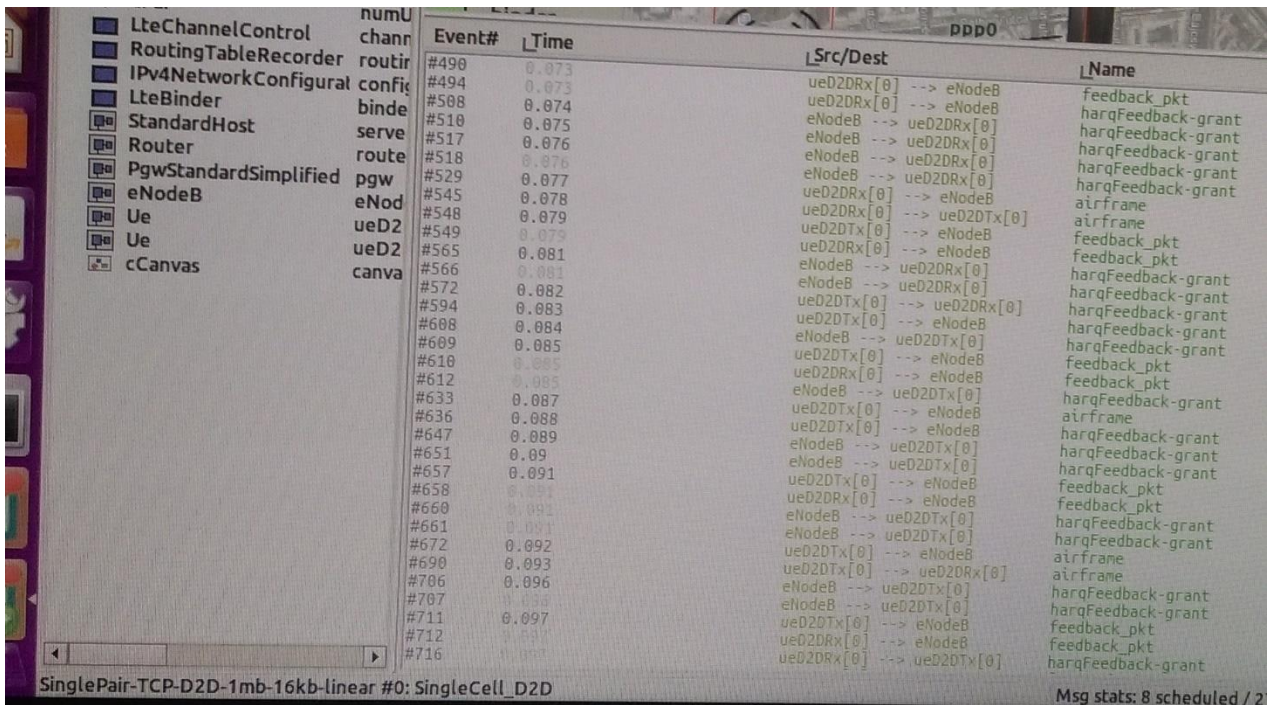


Fig. 14 D2D communication from source to destination

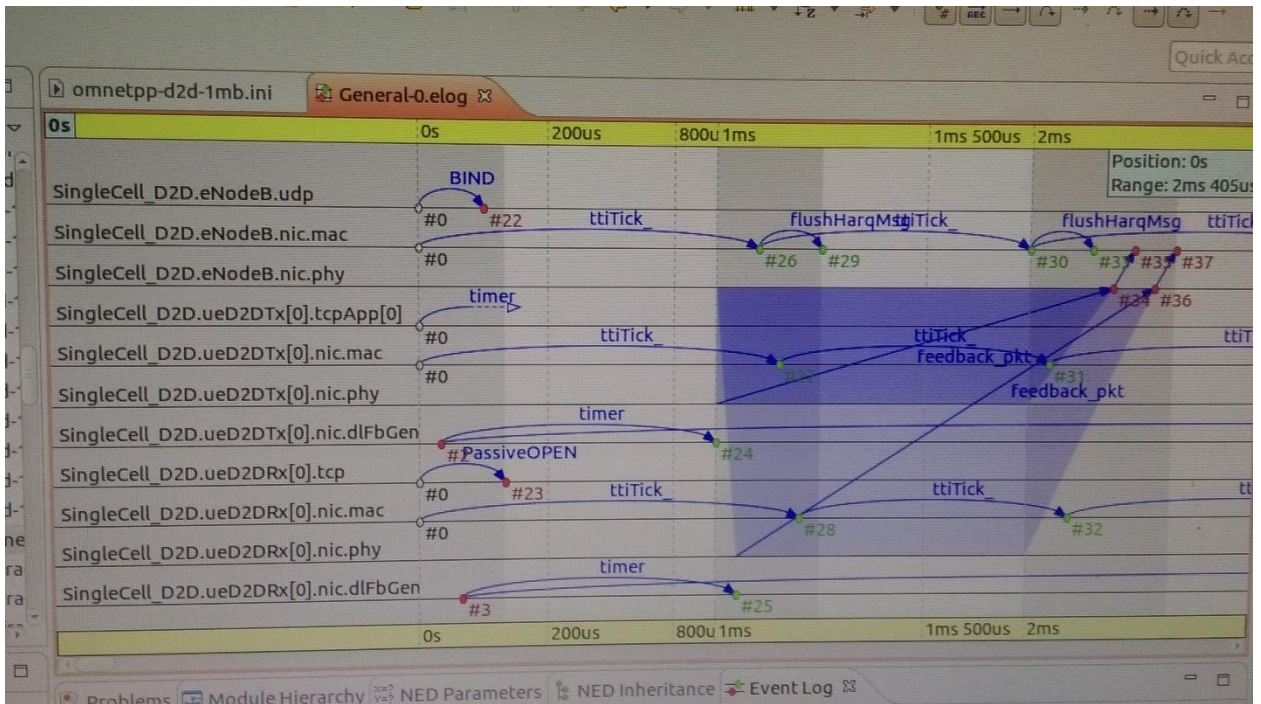


Fig. 15 A sequence chart for D2D communication

The Table 1 parameters maintained through the simulations for both D2D and conventional communication. A comparison is noticed between the two communications. The communication is better in D2D by observing the result and the graph shown below. The two UEs are given different mobility like linear and random with pedestrian speed of real life.

TABLE 1 SIMULATION PARAMETERS

Parameters	Value
Carrier Frequency	2.1 GHz
Bandwidth	50 RBs
Path Loss Model	URBAN MACRO Cell
eNB Transmitter Power	10W
UE Transmitter Power	26 dBm
eNB Antenna Gain	18
Noise Figure	5
Cable Loss	2
Mobility Speed	2 mps
Simulation Time	3 mins

8.1. MEASUREMENT OF RTT and RTO OF Infrastructure Mode (IM) and Direct Mode (DM)

(i) When the UEs are stationary

The distance between UEs are constant and they are at fixed position. In the conventional cellular system the data is transferred through eNB . The control flow is also through eNB. The resource allocation between eNB and UEs for uplink and downlink is done by eNB. Thus the eNB is being over loaded. The variation of RTT and RTO in IM is approximately linearly increasing. But in direct communication the data is transferred through side link. The RTT and RTO in D2D cellular system is in the same range, shown in figure 16 and figure 17.

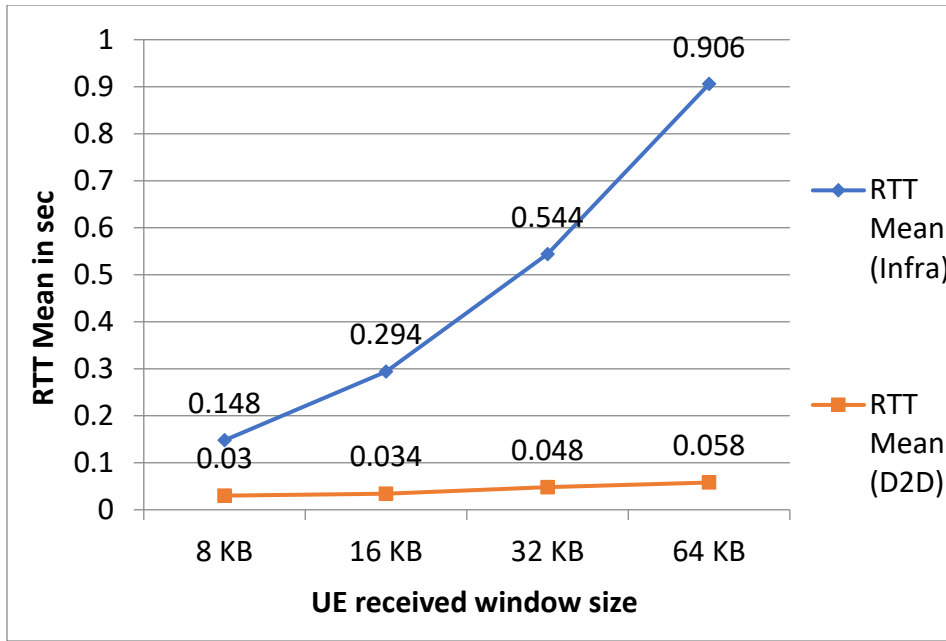


Fig. 16 Variation of RTT (mean) of IM and DM when UEs are stationary

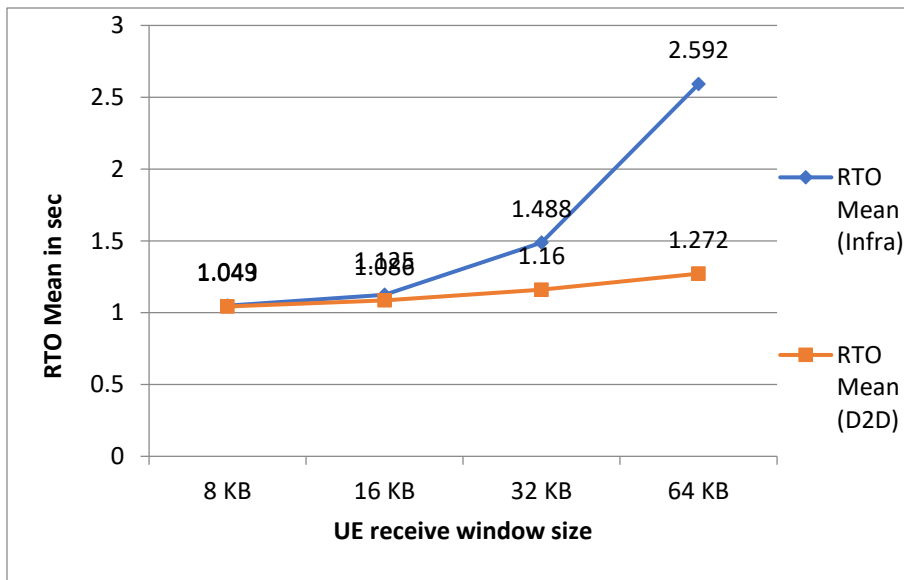


Fig.17 Variation of RTO(mean) of IM and DM when UEs are stationary

(ii) When the UEs are linear

Initially the UEs are nearer to each other. After some time, the receiver UE is fixed at its position that is at the edge of the eNB region but the sender UE comes near to the eNB due to linear movement of the user. Before the completion of the

simulation time, there is about 30m distance between the two UE. In IM, the RTT value should be linear. As the sender UE is nearer to the eNB the RTT drops when the advertised window size is 64 KB. So is the RTO has also dropped as the RTO gets affected by the RTT. In DM RTT remains approximately same as the previous one and also the RTO. The result is shown in the graph in figure 18 and figure 19.

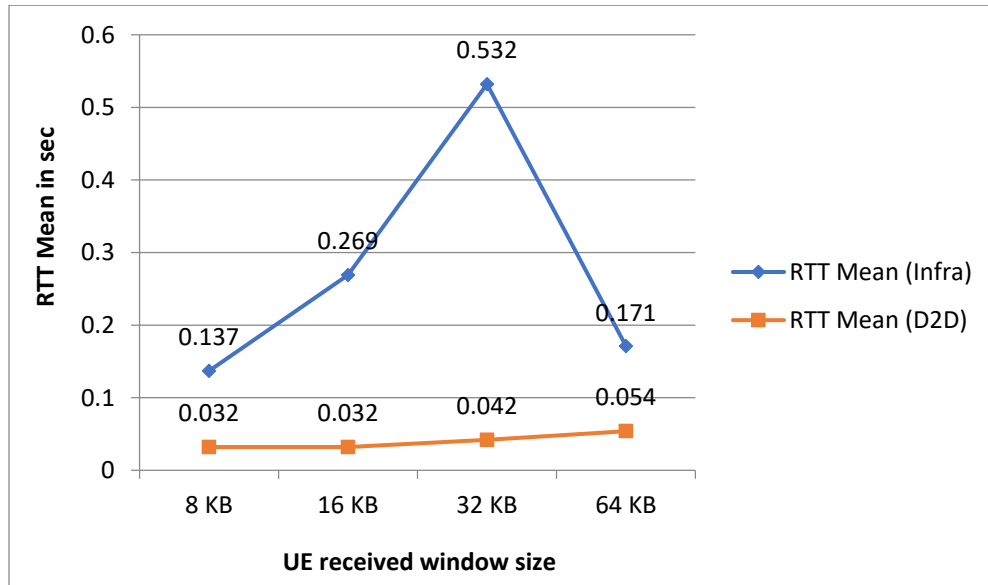


Fig. 18 Variation of RTT(mean) of IM and DM when UEs are linear

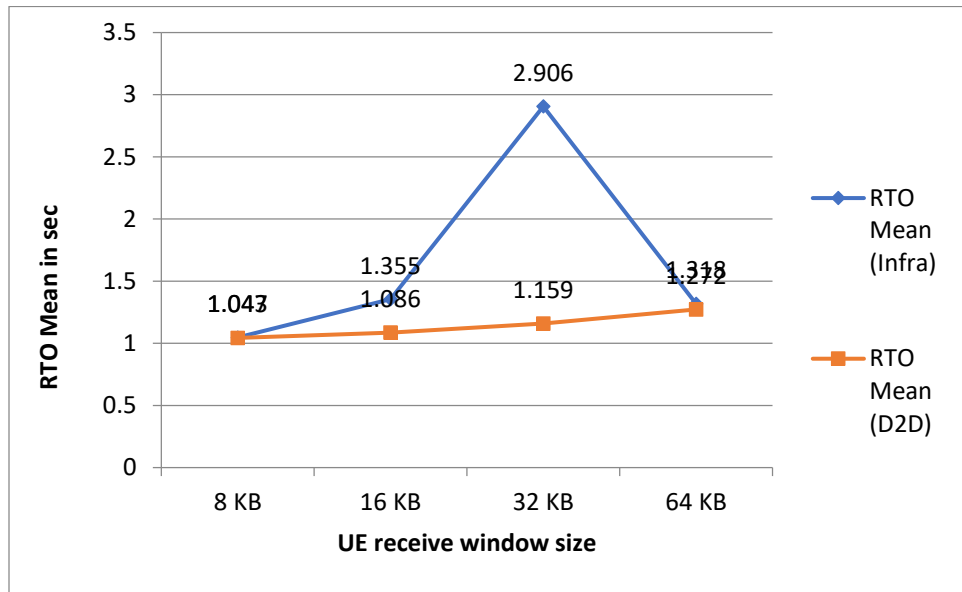


Fig.19 Variation or RTO(mean) of IM and DM when UEs are linear

(iii) When the UEs are random

Both the UEs are at the extreme edge of the region of eNB where the communication through eNB is weak. For a given small constraint area at the extreme edge, the UEs are considered to have random mobility at pedestrian speed of 2m/s. The movement of the receiver UE is far beyond the extreme edge and the sender UE is moving either near or far from eNB. Therefore, there is a variation in RTT and RTO. When the advertised window size is 32 KB the value of RTT and RTO for both IM and DM is almost same. The result is shown in the following graph in figure 20 and figure 21.

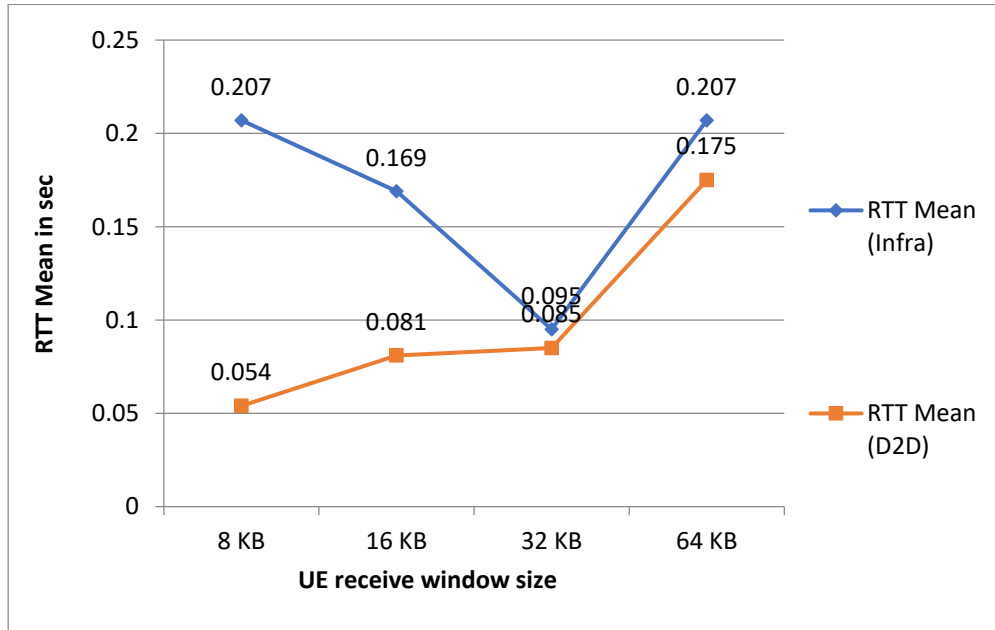


Fig: 20 Variation of RTT(mean) of IM and DM when UEs are random

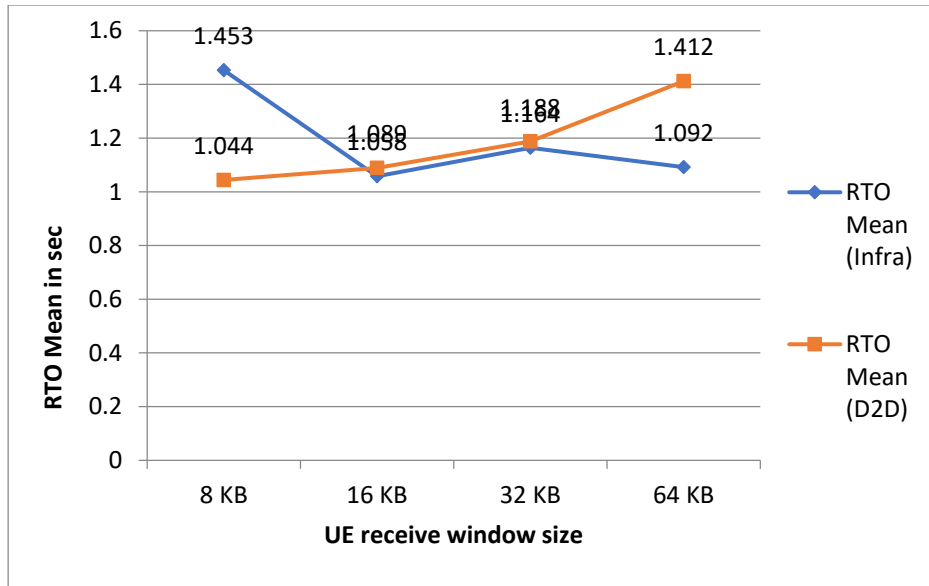


Fig: 21 Variation of RTO(mean) of IM and DM when UEs are random

The Tables below is the values of RTT and RTO at different window size on different UEs mobility.

(i) When UEs are at fixed position

TABLE: 2 RTT AND RTO AT STATIONARY

Window Size	Round Trip Time (RTT)		Retransmission Time Out(RTO)	
	Infrastructure Mode	D2D Mode	Infrastructure Mode	D2D Mode
8 KB	0.148	0.030	1.049	1.043
16 KB	0.294	0.034	1.125	1.086
32 KB	0.544	0.048	1.488	1.160
64 KB	0.906	0.058	2.592	1.274

(ii) When UEs are moving linearly

TABLE: 3 RTT AND RTO AT LINEAR

Window Size	Round Trip Time (RTT)		Retransmission Time Out(RTO)	
	Infrastructure Mode	D2D Mode	Infrastructure Mode	D2D Mode
8 KB	0.137	0.032	1.043	1.049
16 KB	0.269	0.031	1.086	1.125
32 KB	0.532	0.042	1.159	1.488
64 KB	0.171	0.053	1.272	2.592

(iii) When UES are moving in random

TABLE: 4 RTT AND RTO AT RANDOM

Window Size	Round Trip Time (RTT)		Retransmission Time Out(RTO)	
	Infrastructure Mode	D2D Mode	Infrastructure Mode	D2D Mode
8 KB	0.207	0.053	1.453	1.044
16 KB	0.169	0.080	1.058	1.089
32 KB	0.095	0.084	1.164	1.188
64 KB	0.207	0.175	1.092	1.412

Chapter 9

CONCLUSION

In this project, two modes of communication are observed that is conventional or infrastructure communication and direct or D2D communication. In conventional cellular system, there is a lot of overhead over the eNB. Such as the resource allocation, data transfer, location of the devices either in the range or out of the range.

The main purpose of this project is how fast the data is transferred to the destination and ordered reliability of data either in conventional or direct communication. From the above drawn results, it can be concluded that most of the cases direct communication is better. Most of the cases like when the UEs are at the extreme border of the region of eNB the data transfer is same as when the UEs are nearer to the eNB.

In direct the data is transferred between the UEs without the knowledge of eNB. The eNB is only storing the record of the resource allocation. Thus the overhead the eNB is reduced. Earlier days, when a hand over occurs there was a disrupt in the voice communication. After the introduction of the direct communication, if a handover of devices occurs, the users smoothly can communicate with each other, unknowingly that he/she has entered into a different cellular system.

Chapter 10

FUTURE SCOPE IN DIRECT COMMUNICATION

The more days are passed, the users are demanding for fast network means fast delivery of messages through email, getting information they want quickly, booking for travels, etc. For faster network, conventional system is not possible to overcome the demands of the users.

The introduction of direct communication between the handheld devices nearly fulfilling the demands. Thus direct communication has proven to be a better communication than the conventional communication. Further scope for developing in direct communication is the maintaining of resource allocation.

The places where the infrastructure for network is not possible like in the forests or mountain areas, D2D communication can be useful. The developing of the battery power in handheld devices will be helpful for D2D communication. The better protocol for the proximity services of the devices. The implementation of D2D in Internet Of Things (IOT). It is important for providing security to the data that is to be transferred from source to destination.

Chapter 11

REFERENCES

- [1] Varga, A. and Hornig, R. (2008), "An overview of the OMNeT++ simulation environment", in Proc. SIMUTools '08, Marseille, France, March 2008.
- [2] A. Virdis, G. Stea, G. Nardini, "Simulating LTE/LTE-Advanced Networks with SimuLTE", DOI 10.1007/978-3-319-26470-7_5, in: Advances in Intelligent Systems and Computing, Vol 402, pp. 83-105, Springer, 15 January 2016.
- [3] G. Nardini, G. Stea, A. Virdis, D. Sabella, M. Caretti, "Resource allocation for network controlled device-to-device communications in LTE-Advanced", Wireless Networks, 2017
- [4] 3GPP - TS 36.843 v12.0.1, "Study on LTE Device-to-device Proximity Services: Radio aspects (Release 12)", March 2014.
- [5] A. Asadi, Q. Wang, V. Mancuso, "A survey on device-to-device communication in cellular networks," IEEE Comm. Surveys and Tutorials, vol.16, no.4, pp.1801-1819, Fourth quarter 2014.
- [6] Virdis, A., Stea, G. and Nardini, G, "SimuLTE- A modular system-level simulator for LTE/LTE-A networks based on OMNeT++", In Simulation and Modeling Methodologies, Technologies and Applications (SIMULTECH), August, 2014 International Conference on (pp. 59-70), IEEE.
- [7] Rohde & Shwarz, "Device to Device Communication in LTE- White Paper", 2015.
- [8] Gandotra, P. and Jha, R.K., "Device-to-device communication in cellular networks: A survey", Journal of Network and Computer Applications, 71, pp.99-117, 2016.
- [9] SimuLTE – LTE User Plane Simulator for OMNeT++ and INET (<http://simulte.com>).
- [10] Moray Rumney, "LTE and the Evolution to 4G Wireless- Design and Measurement Challenges", Second Edition, WILEY, 2013.
- [11] N. Golrezaei, A. F. Molisch, and A. G. Dimakis, "Base-station assisted device-to-device communications for high-throughput wireless video networks," in Proceedings of IEEE ICC, 2012, pp. 7077–7081.
- [12] Q. Wang and B. Rengarajan, "Recouping opportunistic gain in dense base station layouts through energy-aware user cooperation," in Pro-ceedings of IEEE WoWMoM, 2013, pp. 1–9.
- [13] Forouzan, "Data Communication and Networking", Fourth Edition, 2006

**TRAVELLING TOURNAMENT PROBLEM USING
QUANTUM ALGORITHM**

A PROJECT REPORT

Submitted by

PRATIK CHOWDHURY

Under Supervision of

Prof. SHYAMA MONDAL

*in fulfillment for the award of the degree
of*

**MASTER OF TECHNOLOGY
IN
INFORMATION TECHNOLOGY**

Year : 2022



GOVERNMENT COLLEGE OF ENGINEERING AND CERAMIC TECHNOLOGY

73, ABINASH CHANDRA BANERJEE LANE

KOLKATA-700010

TRAVELLING TOURNAMENT PROBLEM USING
QUANTUM ALGORITHM

A PROJECT REPORT

Submitted by

PRATIK CHOWDHURY

Under Supervision of

Prof. SHYAMA MONDAL

in fulfillment for the award of the degree

of

MASTER OF TECHNOLOGY
IN

INFORMATION TECHNOLOGY

Year:2022



GOVERNMENT COLLEGE OF ENGINEERING AND CERAMIC
TECHNOLOGY

73,ABINASH CHANDRA BANERJEE LANE,KOLKATA-700010

BONAFIDE CERTIFICATE

Certified that this project report “**TRAVELLING TOURNAMENT PROBLEM USING QUANTUM ALGORITHM**” is the bonafide work of “**PRATIK CHOWDHURY**” who carried out the project work under my supervision.

M. Maitra

SIGNATURE

Dr.Mausumi Maitra

HEAD OF THE DEPARTMENT

Professor

Information Technology

73,Abinash Chandra Banerjee Lane
Kolkata-700010

Shyama Mondal

SIGNATURE

Shyama Mondal

SUPERVISOR

Assistant Professor

Information Technology

73,Abinash Chandra Banerjee Lane
Kolkata-700010

Indrajit Bhattacharya


SIGNATURE

24.05.22

External Examiner:

ACKNOWLEDGEMENT

This project would not have been possible without the support of many people. Many thanks to my supervisor Professor Shyama Mondal for guiding me throughout the project, Head of the Department Professor Dr.Mausumi Maitra, and Principal Professor Dr. Krishnendu Chakrabarty for providing the infrastructure and allotting me this project. And finally thanks to my friends and family members for giving me mental support.


PRATIK CHOWDHURY
GCECTM-R20-2009

ABSTRACT

In this thesis, we have worked with a timetable scheduling problem related to sports tournaments. Which is NP-Hard; namely, Travelling Tournament Problem. We have taken a known quantum Algorithm to solve the Travelling Salesman Problem which is Quantum Approximation Optimization Algorithm(QAOA). Briefly had a much better approximation magnitude relation than any glorious polynomial-time classical algorithm till a simpler classical algorithm was proposed. It was presently recognized that a generalization of the QAOA method is actually AN alternating application of a continuous-time quantum walk on an underlying graph followed by a quality-dependent part shift applied to every resolution state. This generalized QAOA was termed as QWOA (Quantum Walk-based improvement Algorithm). I have converted the TTP problem into the TSP problem, since I have already solved TSP problem using QAOA therefore to show that TTP is an instance of TSP we have adopted this method.

TABLE OF CONTENTS

CHAPTER NO	TITLE	PAGE NO.
	ABSTRACT	05
1.	INTRODUCTION	07-08
2.	PROBLEM STATEMENT	09
3.	LITERATURE REVIEW	10-31
4.	METHODOLOGY	32-33
5.	RESULTS AND DISCUSSIONS	34-35
6.	CONCLUSION	36
7.	REFERENCE	37-40

INTRODUCTION

The Traveling Tournament Problem (TTP) is a timetable scheduling problem related to sports tournaments. Professional sports leagues are a part of almost every country. Apart from the entertainment, it provides to the people of the country, as well as of the whole world by the means of television and the internet, these tournaments often possess a vital share of a country's economic scenario. These leagues, most often, generate enormous revenues by selling the stadium tickets, as well as, using the broadcasting rights for the games. Hence, developing the match fixtures, like making timetables for the tournaments and fixation of the order in which the participating teams play with each other and the venue of each of the matches is a very vital part of conducting a successful tournament [1]. This growing importance of TTP has made it an integral part of research in theoretical computer science, especially due to its hardness in reaching an optimal solution. TTP is intended to reduce the distance traveled in a double round-robin tournament (DRRT) where n teams are playing as a part of it. TTP is a kind of combinatorial optimization problem that combines features of two major problems related to theoretical computer science: the traveling salesman problem and the tournament scheduling problem or the vehicle routing problem; although, TTP is many folds harder than the traveling salesman problem. Even a tournament schedule containing a very small number of participating teams becomes extremely difficult to solve TTP is extremely important in the field of the tournament schedule. TTP is primarily intended to design a tournament schedule in order to minimize the total traveling distance. This is more important in order to reduce the distance traveled by the players, as well as for reducing the associated time of travel and minimizing additional fatigue among the players. Hence, TTP holds the position of the most fundamental issues involved in developing a tournament schedule in a sports league, especially where the travel duration is an issue. The design of an

optimal TTP is more important especially in such a host country where the land topology contains major diversities including hilly regions, large water bodies, deserts, or other diverse geographic terrains since the traveling to different points becomes extremely tiresome for the players, as well as costly for the organizing bodies. Apart from this issue of preventing too much travel of the participating teams, another major issue holds a major hindrance to the design of the problem. This is interpreted as the feasibility issue considering the home and away pattern. This order of home and away has to be varied sufficiently in order to avoid a long sequence of home matches or away matches. Both of these issues have been addressed mostly by integer programming or constraint programming communities and their combination. Constraint programming is instrumental mainly in solving complex sets of patterns related to home and away constraints; whereas, integer programming is used to solve primarily the problems related to large traveling salesman problems, as well as vehicle routing problems in order to minimize travel distance [2]. Thus, TTP has emerged as a major problem involving research with a combined approach. Hence, an optimal solution with minimum travel duration is extremely important in order to maintain a better fitness level among the players, which in turn, helps in retaining the quality of the tournament.

In this thesis, we have made an attempt to discuss about Traveling Tournament Problem (TTP) and the different methods developed by researchers to make a way through the analysis of this one of the most important problems linked to a very practical field of sports tournaments.

Problem Statement- Travelling Tournament Problem(TTP) states that the teams that are participating should play among themselves in a Double Round Robin(DRR) manner i.e. if a team A is playing with team B in B's home ground then B should also play with team A in A's homeground.It also has certain constraints stated in [1] are as follows:

- (i)**No repeat-** one team cannot play with the same opponent twice in a row.

- (ii)**At most-** one team cannot play more than $(n-1)$ consecutive home or away games where 'n' is the number of teams.(This 'n-1' has been relaxed to value 3 in mat.tapper site)

LITERATURE REVIEW

TTP was introduced as a major benchmark problem, as mentioned earlier, by Easton, Nemhauser and Trick [4] in the year 2001, where the authors showed a way for scheduling a double round-robin tournament and way for minimizing the total distance of travel, simultaneously satisfying a set of constraints [5]. A DRRT is a set of matches where each of the teams plays each other once at home and once away. A DRRT schedule is developed by mapping matches in slots in order that each team plays exactly once in each slot. Such a schedule contains exactly $2(n - 1)$ slots and an n by n matrix is formed using the mutual distances the home venues of each team. Another constraint is that for computing the total distance traversed by any particular team, each team must start and finish the whole tournament at its home ground [4]. The authors of [4] further describe the results for some basic formulations. More so, they describe a method in which they actually show a way of combining integer and constraint programming methods. This enables solving large problems in less time. Most importantly, this shows the different possibilities which are inherent for other complicated combinatorial problems. TTP is computationally much harder; although there exists a strong similarity of analysis to the traveling salesman problem (TSP), which is a NP-hard problem. The extreme importance of TTP, especially in a practical field like sports tournament scheduling, has become one of the most vital benchmark problems, especially related to computer science. The first NP-completeness proof for a variant of TTP is already given by Bhattacharyya [6]; although, the solution does not consider any bounds on either the number of consecutive home matches or the away matches for any team considered. In this work, the author has used mathematical optimization techniques to reduce the unconstrained TTP problem

to the known NP-complete problem i.e. a Travelling Salesman Problem. The author has further shown that even an unconstrained TTP is an NP-Hard problem. This allows a reduction from the TSP [3]. But the true picture of TTP lies in imposing limits on the upper and lower thresholds on the number of consecutive home matches or away matches. In practical design of the fixtures, it is not encouraged, or even allowed in most of the cases for a team to have only away games or only home games at a stretch for a long duration. This is mostly derived from the economic point of view as the revenue generated due to the sale of match ticket fades away gradually for a consecutive sequence of matches at a particular venue. Further, a better uniform distribution of the home and away matches lead to more equitable team-rankings in a tournament during the long season [3]. Hence, development of a feasible fixture synchronizing these factors becomes a major task of TTP. For these reasons, the reduction from TSP used in [6] is inadequate to some extent, considering the true complexity of the original TTP [3]. It is noted in practice that the usual restriction of an upper bound of consecutive home or away matches is 3; in some cases this number drops to 2 as well. The authors of [3] have shown that variant of this problem is strongly NP-complete when the upper bound on the maximal number of consecutive away games is set to 3. The authors further show that the decision problem TTP(3) is a strongly NP-complete analysis. The authors are further optimistic to predict that the proposed techniques may be carried forward to show that the generalized structure of TTP(k) is NP-complete for fixed $k > 3$. Several authors have proposed numerous methods for the solution of this problem. These include different techniques such as integer programming, tabu search, genetic algorithms, and simulated annealing [7]. A mirrored TTP was proposed by the authors [7], where, they have designed a fast and effective constructive algorithm. Besides, the

authors have further proposed a new heuristic, which is based on the combination of the GRASP and Iterated Local Search metaheuristics. The authors have further proposed a strong neighborhood based on ejection chains which have been shown to lead to major improvement in solution. The authors have proposed a new and effective heuristics for solving mirrored versions of TTP. The authors have achieved two fold contributions in their work: a new and fast constructive heuristic to achieve good initial solutions; and hybrid model of the GRASP and ILS metaheuristics which is found to compute good solutions. The authors of [8] used another hybrid heuristic algorithm by utilizing tabu search and simulating annealing method to solve the Traveling Tournament Problem. A hybrid algorithm is a combined version two or more other algorithms that work on same problem where tabu search and simulating annealing method function on random searching; hence is slow in process. Hybrid heuristic algorithm by utilizing tabu search and simulating methods has evolved as another major way of analyzing this problem and this is used by authors of [8], which showed that it could substantially improve quality and time of consumption. The authors of [9] proposed a Quantum AI solution for the Traveling Tournament Problem the authors have vanquished the drawback of the simulated annealing method. The authors aspire to adapt the selection criteria for the moves of the number of teams by restoring the randomness with a probability factor generated by the quantum circuits, the authors also initialize the execution of existing algorithms with the same probability factor. However the authors find that when the number of teams increases the time taken to solve the problem also increases but the author's restoration of the simulated annealing method gives a considerable solution to the TTP. Constraint programming has evolved as another major way of analyzing this problem and this is used by the authors of [10], which showed considerable

improvement of computation time. These results of [10] were further improved in another constraint programming research conducted by the authors of [11]. The authors of [12] have referred to different advances in the field of constraint programming for different scheduling problems. TTP has combined features of the traveling salesman problem [13] and the tournament scheduling problem [10, 14]. Solution to TTP should exhibit strong feasibility concerns, majorly due to the tournament structure; as well as should comprise of a complex optimization part in order to shorten the distance of travel among the venues where the matches of the tournament are to be played [5]. The authors here have proposed a number of solvers of TTP, developed using tabu search topology, and using the complex combination of several neighborhood structures. The authors have further analyzed different neighborhoods, as well as compared these experimentally using three sets of publicly available benchmarks. Since TTP was proposed by Easton et al. [1], several works were intended towards the development of approximation algorithms and heuristics [3]. TTP, being a combinatorial optimization problem and approximation algorithms are the efficient algorithms to find solution for this kind of problems (NP-Hard), different authors [15, 16] have proposed different approximation algorithms. Another approximation algorithm for TTP was proposed by Imahoriet al. [15], where the authors did the analysis without considering bounds on the number of consecutive home as well as away games. In [16] authors have proposed a random algorithm which is based on Modified Circle Method (MCM) and using the same they have found a feasible solution whose approximation ratio is less than $2 + (9/4)/(n-1)$ here 'n' denotes the number of teams, also they have proposed a lower bound for optimal value of TTP, although they have not considered any bounds i.e. unconstrained TTP. Yamaguchi et al. [16] proposed approximation algorithm for TTP(k) where value of 'k' is

always greater than equals to 3 i.e. $k \geq 3$. The authors of [17, 18] also presented surveys on round robin scheduling and TTP.

Another heuristic approach for TTP problem can be found in [19]. Here authors have a combination of IDA* algorithm and DFS branch-and-bound method to solve this problem. So, in this journal they have first used A* algorithm, followed by IDA* and finally DFS branch and bound. For the pairing of teams they have used this DFS method; and this DFS* algorithm has been formed in several steps such as memory & heuristic Estimates, Sub-trees, new upper bounds, symmetry, parallelization; and after removing the symmetry from the time-table and introducing the new concept i.e. parallelization they have found a better result than all the previous results till date. Another meta-heuristic approach can be found in [20] where authors have used an ant colony optimization (ACO) technique to solve the problem. They have integrated ACO with forward checking and conflicted-directed backward jumping and renamed this as AFC. The authors have further suggested that this method of AFC is better applicable compared to ACO only if the solution space is large and feasible. So, in this new method of AFC, if ants are not able to find any feasible solution, the ant restarts finding the solution from the beginning after back jumping for a certain number of times. This is denoted by 'b.n' where, b is any scalar quantity and n is the number of teams. They have outnumbered all the previous solutions that have been done for this TTP problem using this approach. In this paper [21] authors approach the TTP problem with fixed venues (TTPFV) as a single round robin altar of the Traveling Tournament Problem, the authors have further come up with iterated local search method (ILS) heuristic to clear up the real size instances of TTPFV. ILS heuristic performs better than heuristic based integer programming. The Iterated local search (ILS) meta-heuristic proposes the use of perturbations to

escape from locally optimal problems, where, the method starts by contracting a initial solution and applying a local search procedure on the TTP problem. The authors of [22] have presented new models for Mirrored Traveling Tournament Problem (mTTP), which is another very challenging combinatorial optimization problem. It is related to the generation of a match schedule in a tournaments with two half series. This is rather equivalent to a double round-robin scheduling problem. Apart from minimizing the travel distance, the method also aims at minimizing the longest travel distance as well. This is denoted by MinMaxTTP. Another mirrored TTP was proposed by [7]. The authors have designed a fast and effective constructive algorithm. Besides, the authors have further proposed new heuristic, which is based on the combination of the GRASP and Iterated Local Search meta-heuristics. The authors have further proposed a strong neighborhood based on ejection chains which have been shown to lead to major improvement in solution. The authors have proposed a new and effective heuristics for solving mirrored version of TTP. The authors have achieved twofold contribution in their work: a new and fast constructive heuristic to achieve good initial solutions; and hybrid model of the GRASP and ILS meta-heuristics which is found to compute good solutions. The authors of [23] have proposed a novel encoding scheme for representing a solution instance. The authors have implemented and tested the method for various instances of TTP such as NL-4, NL-6, NL-8, CIRC-4 (Constrained), CIRC-6 (Constrained), CIRC-8 (Constrained), Galaxi-4, Galaxi-6, Galaxi-8, Super-4 , Super-6 and 7 Super-8 from of double round robin TTP. The authors have been inspired by the work carried out for North American Major League Baseball (MLB). Several researches have been carried out keeping in mind different major tournaments, like the college basketball, Australian basketball, Dutch professional football etc. The authors of [24] have divided the

search space and adopted two different methods for serving two purposes. They have used the method of simulated annealing (SA) to search a timetable space, as well as used hill-climbing to explore a team assignment space. The authors of [25] used a combined approach including Lagrangian relaxation and constraint programming which is found to improve some of the contemporary results. The authors were motivated from the three-phased approach discussed by Nemhauser and Trick where team assignments have been handled after the tournament schedule has been finalized. The authors further parallelized components, instead of going for the serial analysis, for developing a better schedule, as well as developing better team assignments. Some researchers have shown that most of the best upper bounds of TTP instances have been achieved by meta-heuristic algorithms. The authors of [26] have considered a TTP, as described by the authors of [1], which is designed to abstract key features of Major League Baseball (MLB) in the US. It rather proposed another simulated annealing algorithm (TTSA) approach to identify both practicable as well as non-practicable schedules. TTSA is found to perform well with small instances of TTP; as well as yields good improvement on the larger instances. The method considers both the constraints of minimizing distance travel, and maintaining feasibility constraints of restricted number of consecutive home or away matches. The authors of [4] used parallelized implementation of the branch -and-price method. This is found to solve NL8 problem in just over 4 days with 20 processors; although the method did not consider the constraint of no repeaters. The authors of [27] showed an important method of reducing the search space by a factor approximating as high as $4n$. The method used problem symmetry to perform the task. The authors of [28] proposed lower bounds for circular instances. The authors of [29] improved the constraint of independent lower bound by considering a few specific

constraints. The authors of [30] presented a two stage method for mTTP to solve the NL8 instance, with a single computer and without using the method of parallelization. The solution required 3.7 days of execution. The authors of [31] proposed a new packing three vertex paths for travelling tournament problem, the authors approached the TTP problem from a graph theory's perspective where each team on a single road trip will play three games for the underlying graph minimum-weight P3-packing the authors have taken initial inputs form hybrid algorithm , they develop the tournament schedule for five benchmark. The authors are shown in this paper the result is beaten the upper bound for previously known five hard benchmark instances. The authors of [32] have analyzed a different aspect of TTP. They have carried out research to identify the relation between breaks and distances; which, in turn, lead to problems relating distance minimization and breaks maximization. A Clustering Search approach has been proposed by the authors of [33] to use hybrid heuristic for solving another mirrored TTP (mTTP). The benchmark problems and a practical 8 tournament schedule of the Brazilian Soccer Championship has been used to validate the same. The Clustering Search approach, used here, has been derived in this work as a generalization of the Evolutionary Clustering Search (ECS). A new hyper-heuristic has been proposed by the authors of [34]. The method is composed of a simple learning automaton based selection mechanism, as well as a new acceptance mechanism, which is actually denoted as the Iteration Limited Threshold Accepting criterion. This hyper-heuristic model is investigated to obtain feasible solution to the challenging TTP. The authors have also displayed the superiority achieved by the new hyper-heuristic method to outperform the Simple Random hyperheuristic, even using a small number of low-level heuristics. The benchmark problems on TTP have also been investigated using the

proposed method, and the results obtained are very much optimistic. Besides, the authors propose a new learning based selection mechanism and a new acceptance mechanism in addition. The authors also introduce a new move acceptance method which is denoted by Iteration Limited Threshold Accepting (ILTA). Another Iterated Local Search (ILS) heuristic has been proposed by the authors of [35]. The outcomes of the model show that the proposed method performs better than the integer programming heuristics. The authors further produce a vital feature. It shows that commonly used neighborhoods in case of developing the sport fixtures, are disconnected for the single round robin tournaments. The papers reviewed are discussed in Table 1.

REFERENCE	METHOD USED	VARIANT OF TTP USED	RESULT
[2]	Integer programming	TTP with Predefined Venues(TTPPV)	Able to solve for team size less than equal to 8 in order of minutes
[3]	Mathematical reduction	Unconstrained TTP	Proved NP-completeness of TTP(3)
[4]	Combination of integer programming and constraint programming	General form of TTP without <i>no-back-to-back</i> constraint	Able to solve for team size less than equal to 6 in order of minutes
[5]	Tabu Search	General form of TTP without <i>mirror</i> constraint	Able to find the then best results for CON instances except CON16,while they were very close to the optimal results of NL and CIRC instances
[6]	Mathematical reduction	Unconstrained TTP	Proved that even unconstrained TTP remains NP-Hard
[7]	Heuristic	Mirrored TTP	Authors had executed the randomized version of their variant for 1000 times and found that on average it was about 17.1% difference with

			the general form of TTP.They have also executed GRILS-mTTP heuristic and found a maximum gap of 9.1%
[8]	Tabu search and simulated annealing	General form of TTP	Authors have executed their hybrid algorithm on NL and NFL instances and for many of the instances their algorithm was giving same time as the optimal one and for the remainings they were very close to the optimal time.They have also compared the algorithm with the algorithm provided by Anagnostopoulos <i>et al.</i> (2006) and Lee <i>et al</i> (2006) and showed that their average time complexity is better than them.
[9]	Simulated annealing and quantum AI	General form of TTP	Authors were able to solve in linear time till team size of 4 but after that time increases exponentially
[10]	Constrained programming	The ACC 1997/1998 tournament scheduling problem	Author was able to solve in less than a minute for all 179 solutions to the ACC 1997/1998 tournament scheduling algorithm
[11]	SAT solver	The ACC 1997/1998 tournament scheduling problem	Author was able to generate all 179 solutions of ACC within two seconds of CPU time
[12]	Constraint programming	Constraints for round-robin tournament problems	Authors have implemented propagation algorithms namely all-different and one factor.In case of unconstrained SRRT they was able to find solution for team size ≤ 26 ,for tightly constrained RRT it results in search tree size reduction by 10,in case of intramural

			<p>dense DRRT(DDRR) they have found feasible solution for team size ≤ 16 and for 18 they proved infeasibility of 17 patterns and without the use of arc-consistent propagation this number reaches 101.</p>
[14]	Constraint logic programming	Scheduling sports tournaments problems	<p>Authors have proposed a constrained branch-and-bound algorithm method to solve these kind of sports scheduling problems. And they had executed their method on Sun SPARC4 and found that for team size ≤ 20 the program runs very fast. They had also discussed that their method in worst case leads to exponential time complexity and along with it they also discussed a local search method that complements branch-and-bound algorithm and which in return could be an useful tool</p>
[15]	Approximation algorithm	Unconstrained TTP	<p>Authors have proposed an 3-approximation algorithm that constructs a short Hamiltonian cycle over the venues of the teams and have done permutations among the teams. And they had also proved their algorithm using mathematical derivations</p>

[16]	Approximation algorithm	General form of TTP	<p>Authors have proposed an approximation algorithm that uses the concept of Kirkman schedule and shortest Hamiltonian cycle and using the same they have found lower bounds as: $(2k - 1)/k + O(k/n)$ when $k \leq 5$ and $(5k - 7)/(2k) + O(k/n)$ when $k > 5$, where k is the team size. And they have also concluded that the approximation ratio can always be found in polynomial time</p>
[19]	IDA* and DFS branch-and-bound	General form of TTP with restriction of <i>at-most</i> limited to 3	<p>They have solved NL4 and NL6 instance in 0.0 secs and 0.98 secs respectively but for NL8 instance they have made a huge difference from the then optimal solution and their algorithm takes only about 400 secs. And for CIRC4 and CIRC6 it takes 0.0 secs and 2.05 secs respectively, for CIRC8 it takes 337 seconds using 4 processors. They have also found new lower bounds for NL10, NL12 and CIRC10 instances and also introduced SUPER and GALAXY instances.</p>
[20]	Ant Colony Optimization	General form of TTP	<p>Authors have used their method i.e. AFC and compared it with all the previous results of ACO and found that from NL4 through NL16 their method is providing the best result than all the previous ones. Also they have compared with CNTS and TTSA methods specially in CNTS authors made AFC method is giving best result to most them and to the remaining CNTS and</p>

			in all of TTSA instances they were very close to the optimal result.
[21]	Iterated Local Search(ILS) heuristic	TTP with fixed venues(TTPFV)	Authors results have provided optimal solution compared to the other heuristic methods of that time, and their solution provides at least 8.48% less time for every benchmark problems after running for at least 30 seconds, and on an average their solution has taken at least 13.62% less time than compared to the known best solutions.
[22]	Integer programming	mTTP	<p>Without applying any strategy for NL4: model 1 takes 8276 and model 2 takes 8429</p> <p>When interrupting the CPLEX when first feasible solution found: for NL4 both model takes 8413, for NL6 both model takes 30555, for NL8 both model takes 56599 and for NL10 model 1 results 88556, model 2 results 91219. When CPLEX execution interrupting results taken w.r.t to gap, for gap=95% model 1 results are NL4=8569, NL6=31068, NL8=55955, NL10=88556 model 2 results are NL4=8413, NL6=30555, NL8=56599, NL10=91219, for gap=90% model 1 results are NL4=8569, NL6=28514 model 2 results are NL4=8413, NL6=30555, NL8=56599, NL10=91219, for gap=50% model 1 result NL4=8276 model 2 result NL4=8596</p>

[23]	Genetic Algorithm(GA)	General form of TTP with <i>non-mirrored and no-repeater</i> as added constraints	Authors have worked on only small instances, and they have found optimal solution for NL4, CIRC4, CIRC6 and GALAXY4 through GALAXY8 also SUPER4 through SUPER8 instances whereas for NL6, NL8, CIRC8 they got sub-optimal solutions.
[24]	Simulated Annealing(SA) and Hill climbing algorithm	General form of TTP	The Authors Approach TTP by using hybrid technique which is a combination of simulated annealing and Hill climbing Algorithm. and they found tere hybrid Approach was given result that is better than best solutions for benchmark sets.
[25]	Hybrid Algorithm	TTP with multiple variants	The authors found the lower bound $w(\lambda^*)$ or $w(\lambda + \max_i \text{pairing}(i, \lambda))$ according to the authors strategy and the upper bound is the best solution after 10. and the authors approach reach and prove paradigmatic NL4 and NL6 But can not reach the best known solution for NL8. And the authors' result did not beat the best known solution for the LP-based approach of Trick, Nemhauser and Easton.
[26]	Simulated Annealing(TTSA)	Classic TTP	The Authors explore both feasible and infeasible schedules in their work. TTSA shows the best known solution on the small instances. and the worst known solution is equal or smaller to the best known solution. However the Authors found its critical for large neighborhood problems for high quality solutions and

			with fast cooling schedules are encouraging.
[27]	Symmetry Reduction	Circular TTP	The authors epitomize the benefit of modifying the DFS* Algorithm and show the speed up can approximate the factor $4n$. they shown that speedups approximate $2n$. with the accelerated branch-and-bound they are able to solve two unconstrained instances circ 8 to proven optimality for the first time.

REFERENCE	METHOD USED	VARIANT OF TTP USED	RESULT
[2]	Integer programming	TTP with Predefined Venues(TTPPV)	Able to solve for team size less than equal to 8 in order of minutes
[3]	Mathematical reduction	Unconstrained TTP	Proved NP-completeness of TTP(3)
[4]	Combination of integer programming and constraint programming	General form of TTP without <i>no-back-to-back</i> constraint	Able to solve for team size less than equal to 6 in order of minutes
[5]	Tabu Search	General form of TTP without <i>mirror</i> constraint	Able to find the then best results for CON instances except CON16, while they were very close to the optimal results of NL and CIRC instances
[6]	Mathematical reduction	Unconstrained TTP	Proved that even unconstrained TTP remains NP-Hard
[7]	Heuristic	Mirrored TTP	Authors had executed the randomized version of their variant for 1000 times and found that on average it was about 17.1% difference with the general form of

			TTP.They have also executed GRILS-mTTP heuristic and found a maximum gap of 9.1%
[8]	Tabu search and simulated annealing	General form of TTP	Authors have executed their hybrid algorithm on NL and NFL instances and for many of the instances their algorithm was giving same time as the optimal one and for the remainings they were very close to the optimal time.They have also compared the algorithm with the algorithm provided by Anagnostopoulos <i>et al.</i> (2006) and Lee <i>et al</i> (2006) and showed that their average time complexity is better than them.
[9]	Simulated annealing and quantum AI	General form of TTP	Authors were able to solve in linear time till team size of 4 but after that time increases exponentially
[10]	Constrained programming	The ACC 1997/1998 tournament scheduling problem	Author was able to solve in less than a minute for all 179 solutions to the ACC 1997/1998 tournament scheduling algorithm
[11]	SAT solver	The ACC 1997/1998 tournament scheduling problem	Author was able to generate all 179 solutions of ACC within two seconds of CPU time
[12]	Constraint programming	Constraints for round-robin tournament problems	Authors have implemented propagation algorithms namely all-different and one factor.In case of unconstrained SRRT they was able to find solution for team size ≤ 26 ,for tightly constrained RRT it results in search tree size reduction by 10,in case of intramural dense DRRT(DDRR) they

			have found feasible solution for team size ≤ 16 and for 18 they proved infeasibility of 17 patterns and without the use of arc-consistent propagation this number reaches 101.
[14]	Constraint logic programming	Scheduling sports tournaments problems	Authors have proposed a constrained branch-and-bound algorithm method to solve these kind of sports scheduling problems. And they had executed their method on Sun SPARC4 and found that for team size ≤ 20 the program runs very fast. They had also discussed that their method in worst case leads to exponential time complexity and along with it they also discussed a local search method that complements branch-and-bound algorithm and which in return could be an useful tool
[15]	Approximation algorithm	Unconstrained TTP	Authors have proposed an 3-approximation algorithm that constructs a short Hamiltonian cycle over the venues of the teams and have done permutations among the teams. And they had also proved their algorithm using mathematical derivations

[16]	Approximation algorithm	General form of TTP	<p>Authors have proposed an approximation algorithm that uses the concept of Kirkman schedule and shortest Hamiltonian cycle and using the same they have found lower bounds as: $(2k - 1)/k + O(k/n)$ when $k \leq 5$ and $(5k - 7)/(2k) + O(k/n)$ when $k > 5$, where k is the team size. And they have also concluded that the approximation ratio can always be found in polynomial time</p>
[19]	IDA* and DFS branch-and-bound	General form of TTP with restriction of <i>at-most</i> limited to 3	<p>They have solved NL4 and NL6 instance in 0.0 secs and 0.98 secs respectively but for NL8 instance they have made a huge difference from the then optimal solution and their algorithm takes only about 400 secs. And for CIRC4 and CIRC6 it takes 0.0 secs and 2.05 secs respectively, for CIRC8 it takes 337 seconds using 4 processors. They have also found new lower bounds for NL10, NL12 and CIRC10 instances and also introduced SUPER and GALAXY instances.</p>
[20]	Ant Colony Optimization	General form of TTP	<p>Authors have used their method i.e. AFC and compared it with all the previous results of ACO and found that from NL4 through NL16 their method is providing the best result than all the previous ones. Also they have compared with CNTS and TTSA methods specially in CNTS authors made AFC method is giving best result to most them and to the remaining CNTS and</p>

			in all of TTSA instances they were very close to the optimal result.
[21]	Iterated Local Search(ILS) heuristic	TTP with fixed venues(TTPFV)	Authors results have provided optimal solution compared to the other heuristic methods of that time,and their solution provides at least 8.48% less time for every benchmark problems after running for at least 30 seconds,and on an average their solution has taken at least 13.62% less time than compared to the known best solutions.
[22]	Integer programming	mTTP	<p>Without applying any strategy for NL4:model1 takes 8276 and model2 takes 8429</p> <p>When interrupting the CPLEX when first feasible solution found:for NL4 both model takes 8413,for NL6 both model takes 30555,for NL8 both model takes 56599 and for NL10 model 1 results 88556,model 2 results 91219.When CPLEX execution interrupting results taken w.r.t to gap,for gap=95% model 1 results are NL4=8569,NL6=31068,NL8=55955,NL10=88556 model 2 results are NL4=8413,NL6=30555,NL8=56599,NL10=91219,for gap=90% model 1 results are NL4=8569,NL628514 model 2 results are NL4=8413,NL6=30555,NL8=56599,NL10=91219,for gap=50% model 1 result NL4=8276 model 2 result NL4=8596</p>

[23]	Genetic Algorithm(GA)	General form of TTP with <i>non-mirrored and no-repeater</i> as added constraints	Authors have worked on only small instances, and they have found optimal solution for NL4, CIRC4, CIRC6 and GALAXY4 through GALAXY8 also SUPER4 through SUPER8 instances whereas for NL6, NL8, CIRC8 they got sub-optimal solutions.
[24]	Simulated Annealing(SA) and Hill climbing algorithm	General form of TTP	The Authors Approach TTP by using hybrid technique which is a combination of simulated annealing and Hill climbing Algorithm. and they found tere hybrid Approach was given result that is better than best solutions for benchmark sets.
[25]	Hybrid Algorithm	TTP with multiple variants	The authors found the lower bound $w(\lambda^*)$ or $w(\lambda + \max_i \text{pairing}(i, \lambda))$ according to the authors strategy and the upper bound is the best solution after 10. and the authors approach reach and prove paradigmatic NL4 and NL6 But can not reach the best known solution for NL8. And the authors' result did not beat the best known solution for the LP-based approach of Trick, Nemhauser and Easton.
[26]	Simulated Annealing(TTSA)	Classic TTP	The Authors explore both feasible and infeasible schedules in their work. TTSA shows the best known solution on the small instances. and the worst known solution is equal or smaller to the best known solution. However the Authors found its critical for large neighborhood problems for high quality solutions and

			with fast cooling schedules are encouraging.
[27]	Symmetry Reduction	Circular TTP	The authors epitomize the benefit of modifying the DFS* Algorithm and show the speed up can approximate the factor $4n$. they shown that speedups approximate $2n$.with the accelerated branch-and-bound they are able to solve two unconstrained instances circ 8 to proven optimality for the first time.
[28]	Constructive Algorithms	Constant Distance TTP (CDTTP)	The Authors Proposed a lower bound of the optimal value of CDTTP. And there minimum Break feasible solution up to $n \leq 50$.In addition for all instances of $n \equiv 1 \text{ For Mod } 3$ teams,the minimum break method generates an optimal solution if they obtain single round-robin tournaments satisfying some conditions.
[29]	Combinatorial Optimization	Classic TTP	The Authors introduce a new method for a lower bound to this problem.and authors technique shows the larger reduction as 38.6% gap between upper and lower bound.
[30]	One factorizations	Mirrored TTP (mTTP)	Author showed the best result for mTTP benchmark instance NL8 And CIRC8 is optimal.and the cpu time required to solve for each instance was less than 3.7 days.

[31]	Hybrid Algorithm Combination of Local search and Integer Programing	General form of TTP	Authors tackled the TTP from a graph perspective. Where they have shown that the result is beaten by the upper bound for previously known five hard benchmark instances.
[33]	Clustering Search	Mirrored TTP	Authors Executed their variant and they observed 51.09% reduction in total distance traveled by 24 teams which is 1.048.134 km and their schedule found by their work is 512.545 km only.
[34]	Hyper heuristic	Unconstrained TTP	The authors compared different variants of TTP and their result was better than existing results. even though they tested for small instances. as a whole result they found hyper Heuristic has a potential to solve TTP.

METHODOLOGY

Section I(solving TSP problem using QAOA):

We have executed a classical traveling salesman problem using QAOA. At first, we have mapped TSP to the Ising Problem so that we can minimize the hamiltonian Ising Problem to solve the same. Then we have applied hamiltonian to this problem to find the write cost, by finding the lowest eigenvalue and eigenvector. The graph we have found after applying Ising hamiltonian is given in figure 1. After finding this we have executed our model on a quantum computer (IBM Quantum Lab). Where the optimization routine uses a feedback loop with a quantum computer that uses trial functions built with Y single-qubit rotations takes place.

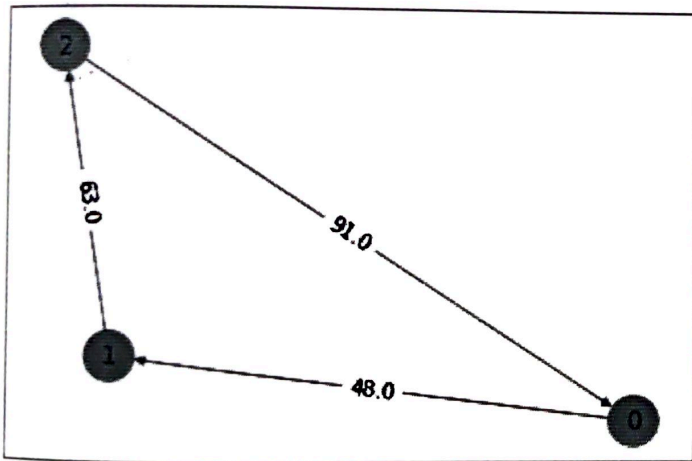


figure 1.

Section II(TTP to TSP conversion):

we have converted TTP to TSP problem as we want to show that TTP is an instance of TSP, hence according to the law of reduction if anyone solves TSP then actually its possible to convert the total scenario into TTP problem. Here first we have solved TSP using QAOA algorithm which is one of the many quantum algorithms that are present and thereby indirectly we have solved the TTP problem using quantum algorithm. And other reason for not approaching TTP directly by this quantum algorithm is that because this match schedule takes lots of time. So, we have used this method. First we have taken the number of matches from user and after that we have presented all applicable combinations of the matches which are possible and followed this three methods:

- i) If the current match is (i,j) and the next match is (z,i) then in the total distance matrix it will be 2*maximum of the distance for reaching point z*
- ii) Else if the current match is (i,j) and the next match is (i,z) then in the total distance matrix it will be maximum of the distance for reaching point i*
- iii) Else if the current match is (i,j) and the next match is (y,z) then in the total distance matrix it will be 2*maximum of the distance for reaching point y*

(Here i, j, y, z are independent of one another)

And after this formation of the *total_distance* matrix we have used CONCORDE TSP solver for giving the possible efficient solution available from our datas.

RESULTS AND DISCUSSIONS

We have executed TSP using a quantum algorithm that QAOA. And found distance Matrix and distance graph in figure 2.

Distance matrix of TSP:

[[0. 8. 21. 54. 75.]

[8. 0. 13. 55. 72.]

[21. 13. 0. 63. 74.]

[54. 55. 63. 0. 37.]

[75. 72. 74. 37. 0.]

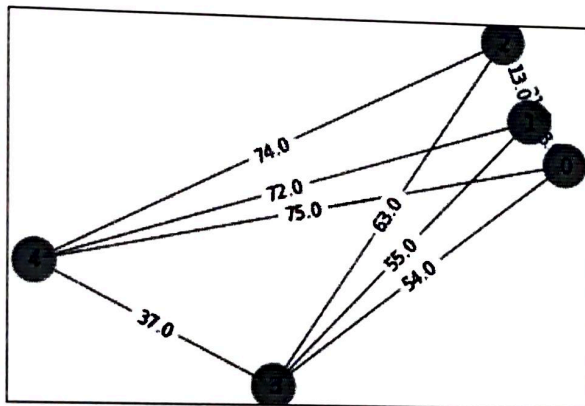


figure 2

Shortest distance of our graph is 176

Table-2

Instance Name with Team Size	Best Value(Using Conversion)	Unconstrained Feasible Solution	Percentage error ((Best soln-Feasible soln)/Feasible soln)
NL6	23497	19990	≈ 0.1754
NL10	57711	44762	≈ 0.2892
NL12	105049	79312	≈ 0.3245
NL14	199977	125416	≈ 0.5945
NL16	287461	154566	≈ 0.8597

CONCLUSION

For this thesis, we have solved travelling salesman problem by mapping it to the Ising problem, and then we have found the hamiltonian cost by getting the Eigenvalue and eigenvector, and then we have executed our model on a quantum computer and found distance matrix and distance graph for TSP. After this we have converted TTP into TSP thereby we have solved the TSP problem based on the certain rules that we have assumed, thereby indirectly solved TTP problem using quantum algorithm. In future we will try to directly fit this QAOA algorithm to solve TTP problem.

REFERENCES

- [1] Easton, K., Nemhauser, G. & Trick, M. "The Traveling Tournament Problem Description and Benchmarks", In Principles and Practice of Constraint Programming -- - CP 2001, pages 580-584, Springer, 2001.
- [2] Melo, R.A., Urrutia, S. & Ribeiro, C.C. "The traveling tournament problem with predefined venues". J. Sched., 12:607, Springer, 2009.
- [3] Thielen, C., & Westphal, S. (2011). Complexity of the traveling tournament problem. Theoretical Computer Science, 412(4-5), 345-351.
- [4] Easton, K., Nemhauser, G., & Trick, M. (2002, August). Solving the travelling tournament problem: A combined integer programming and constraint programming approach. In International Conference on the Practice and Theory of Automated Timetabling (pp. 100-109). Springer, Berlin, Heidelberg.
- [5] Di Gaspero, L., & Schaerf, A. (2007). A composite-neighborhood tabu search approach to the traveling tournament problem. Journal of Heuristics, 13(2), 189-207.
- [6] Bhattacharyya, R. (2009). A note on complexity of traveling tournament problem. Optimization Online, 2480.
- [7] Ribeiro, C. C., & Urrutia, S. (2007). Heuristics for the mirrored traveling tournament problem. European Journal of Operational Research, 179(3), 775-787.
- [8] Kim, J., Han, J. & Jeong, S., "Solving the traveling tournament problem based on the simulated annealing and Tabu search algorithm", Journal of Engineering and Applied Sciences, 13(21):9204-9212
- [9] C. Fernandes, D. Lobo, S. Gawane and K. Wagaskar, "Proposed Quantum AI solution for the Travelling Tournament Problem," 2020 International Conference for Emerging Technology (INCET), 2020, pp.1-5, doi:10.1109/INCET49848.2020.9154037.

- [10] Henz, M. (2001). Scheduling a major college basketball conference— revisited. *Operations research*, 49(1), 163-168.
- [11] Zhang, H. (2002, February). Generating college conference basketball schedules by a SAT solver. In *Proceedings Of The Fifth International Symposium on the Theory and Applications of Satisfiability Testing, Cincinnati* (pp. 281-291).
- [12] Henz, M., Müller, T., & Thiel, S. (2004). Global constraints for round robin tournament scheduling. *European Journal of Operational Research*, 153(1), 92-101.
- [13] Jünger, M., Reinelt, G., & Rinaldi, G. (1995). The traveling salesman problem. *Handbooks in operations research and management science*, 7, 225-330.
- [14] Schaerf, A. (1999). Scheduling sport tournaments using constraint logic programming. *Constraints*, 4(1), 43-65.
- [15] S. Imahori, T. Matsui, R. Miyashiro, "An approximation algorithm for the unconstrained traveling tournament problem," in: *Proceedings of the 8 th International Conference on the Practice and Theory of Automated Timetabling, PATAT, 2010*.
- [16] Yamaguchi, D., Imahori, S., Miyashiro, R., & Matsui, T. (2009), "An improved approximation algorithm for the traveling tournament problem." In *International Symposium on Algorithms and Computation* (pp.679-688). Springer, Berlin, Heidelberg
- [17] G. Kendall, S. Knust, C. Ribeiro, S. Urrutia, Scheduling in sports: an annotated bibliography, *Computers and Operations Research* 37 (1) (2010) 1–19.
- [18] R. Rasmussen, M. Trick, Round robin scheduling — a survey, *European Journal of Operations Research* 188 (2008) 617–636.
- [19] Uthus D.C., Riddle P.J., Guesgen H.W. (2009) "DFS* and the Traveling Tournament Problem." ,In: van Hoeve WJ., Hooker J.N. (eds) *Integration of AI and OR Techniques in Constraint Programming for Combinatorial Optimization Problems*. CPAIOR 2009.

- [20] David C. Uthus, Patricia J. Riddle, and Hans W. Guesgen. 2009. "An ant colony optimization approach to the traveling tournament problem." In Proceedings of the 11th Annual conference on Genetic and evolutionary computation (GECCO '09).
- [21] Fabrício N. Cost, Sebastián Urrutia, Celso C. Ribeiro, "An ILS heuristic for the travelling tournament problem with fixed venues", *Annals of Operations Research*, (Apr 2002). 194(1), 137-150.
- [22] deCarvalho, M. A. M., & Lorena, L. A. N. (2012). New models for the mirrored traveling tournament problem. *Computers & Industrial Engineering*, 63(4), 1089-1095
- [23] Choubey, N. S. (2010). A novel encoding scheme for traveling tournament problem using genetic algorithm. *IJCA Special Issue on Evolutionary Computation*, 2(7), 79- 82
- [24] Lim, A., Rodrigues, B., & Zhang, X. (2006). A simulated annealing and hill-climbing algorithm for the traveling tournament problem. *European Journal of Operational Research*, 174(3), 1459-1478.
- [25] Benoist, T., Laburthe, F., & Rottembourg, B. (2001, April). Lagrange relaxation and constraint programming collaborative schemes for travelling tournament problems. In *Proceedings CPAIOR* (Vol. 1, pp. 15-26).
- [26] Anagnostopoulos, A., Michel, L., Van Hentenryck, P., & Vergados, Y. (2006). A simulated annealing approach to the traveling tournament problem. *Journal of Scheduling*, 9(2), 177-193.
- [27] Gschwind, T., & Irnich, S. (2011). A note on symmetry reduction for circular traveling tournament problems. *European Journal of Operational Research*, 210(2), 452- 456
- [28] Fujiwara, N., Imahori, S., Matsui, T., & Miyashiro, R. (2006, August). Constructive algorithms for the constant distance traveling tournament problem. In

- International Conference on the Practice and Theory of Automated Timetabling (pp. 135-146). Springer, Berlin, Heidelberg
- [29] Urrutia, S., Ribeiro, C. C., & Melo, R. A. (2007, April). A new lower bound to the traveling tournament problem. In 2007 IEEE Symposium on Computational Intelligence in Scheduling (pp.15-18). IEEE
- [30] Cheung, K. K. (2008). Solving mirrored traveling tournament problem benchmark instances with eight teams. *Discrete Optimization*, 5(1), 138-143
- [31] Goerigk, M., Hoshino, R., Kawarabayashi, K.-ichi, & Westphal, S. (2014). Solving the Traveling Tournament Problem by Packing Three-Vertex Paths. *Proceedings of the AAAI Conference on Artificial Intelligence*, 28(1)
- [32] Urrutia, S., & Ribeiro, C. C. (2006). Maximizing breaks and bounding solutions to the mirrored traveling tournament problem. *Discrete Applied Mathematics*, 154(13), 1932-1938.
- [33] Biajoli, F. L., & Lorena, L. A. N. (2007, November). Clustering search approach for the traveling tournament problem. In Mexican international conference on artificial intelligence (pp.83-93). Springer, Berlin, Heidelberg.
- [34] Misir, M., Wauters, T., Verbeeck, K., & VandenBerghe, G. (2009). A new learning hyper-heuristic for the traveling tournament problem. In the 8th Metaheuristic International Conference (MIC'09), Date: 2009/07/13-2009/07/16, Location: Hamburg, Germany
- [35] Costa, F. N., Urrutia, S., & Ribeiro, C. C. (2012). An ILS heuristic for the traveling tournament problem with predefined venues. *Annals of Operations Research*, 194(1), 137-150
- [36] "Max-Cut and Traveling Salesman Problem" <https://qiskit.org>
- [37] "Quantum approximate optimization algorithm" <https://en.wikipedia.org>
- [38] "IBM Quantum Lab" <https://lab.quantum-computing.ibm.com>

IMAGE ENCRYPTION BASED ON CHAOTIC MAP CRYPTOSYSTEM

A PROJECT REPORT

Submitted by

SIMRAN PARVEEN

in partial fulfillment for the award of the degree

of

MASTER IN TECHNOLOGY

IN

INFORMATION TECHNOLOGY

Year:2020-2021



GOVT. COLLEGE OF ENGINEERING AND CERAMIC TECHNOLOGY

73, Abinash Banerjee Lane, KOLKATA-700010

BONAFIDE CERTIFICATE

Certified that this project report "IMAGE ENCRYPTION BASED ON CHAOTIC MAP CRYPTOSYSTEM" is the bonafide work of "SIMRAN PARVEEN" who carried out the project work under my supervision.

M. Maitra - 24/06/21

SIGNATURE

PROF. MAUSUMI MAITRA

HEAD OF THE DEPARTMENT

INFORMATION TECHNOLOGY

Govt. College of Engineering and Ceramic
Technology

73, Abinash Banerjee Lane, Kolkata-700010

AKP - 24/06/2021

SIGNATURE

ATANU KUMAR PAL

SUPERVISOR

Asst. PROFESSOR

INFORMATION TECHNOLOGY

Govt. College of Engineering and Ceramic
Technology

73, Abinash Banerjee Lane, KOLKATA-700010

Ishita Chandra

SIGNATURE

External Examiner:

2

ACKNOWLEDGMENTS

I am expending this chance to express my appreciation to the only who supported me all through the thesis project of this Masters of Technology. It gives me great pleasure in acknowledging my Professor ATANU KUMAR PAL for the non-stop guide and supervision for the achievement of this project. I am genuinely thankful to him for sharing his sincere and enlightening opinions on some of concerns associated with the project.

I would also like to thank my parents and my family for being a great model and encouraging me all through my studies, and making this project viable.

SIMRAN PARVEEN

ABSTRACT

Transmission of essential information like textual content, images, video, and many other over the internet has been growing hastily these days as a result it's far essential to apply a few stable strategies for multimedia data. So, to offer such security and privateness to the user, image encryption may be very essential to guard from any unauthorized user's access. It has emerged as one of the maximum vital data providers which can be useful for biometric authentication, scientific science, military, online private photo album, etc.

Image encryption differs from any other multimedia additives encryption because of a few intrinsic features, which include bulk data capacity and excessive correlation amongst pixels. The traditional cipher algorithm encryption method consists of AES, DES, and many others are actually now no longer appropriate for realistic application. The combination of chaotic standards and cryptography forms an essential area of information security. The latest trend in image encryption is chaos-based totally on a few specific traits which include sensitivity to preliminary conditions, non-periodicity, non-convergence, and control parameters. There are a variety of image encryption algorithms based totally on chaotic maps that had been proposed, a number of them are time-consuming and complicated, a few have little keyspace. In this, a non-linear 3-D chaos-based 3D logistic map and 2D Henon map have been proposed.

TABLE OF CONTENTS

CHAPTER NO.	TITLE	PAGE NO.
	<i>ABSTRACT</i>	<i>4</i>
	<i>LIST OF TABLES</i>	<i>7</i>
	<i>LIST OF FIGURES</i>	<i>8-9</i>
	<i>LIST OF ABBREVIATIONS</i>	<i>10</i>
1.	INTRODUCTION	11
2.	CRYPTOLOGY	12
	2.1 CRYPTOGRAPHY	13-16
	2.1.1 CRYPTOGRAPHY.	13
	2.1.2 PURPOSE OF CRYPTOGRAPHY	14
	2.1.3 TYPES	15-16
	2.2 CRYPTANALYSIS	17
	2.2.1 General INTRODUCTION	17
	2.2.2 TYPES OF CRYPTANALYSIS ATTACK	17
3.	CHAOS BASED CRYPTOSYSTEM	18-25
	3.1 Concept of Chaos theory	18-19
	3.2 Introduction to Chaos-based Cryptosystem	20
	3.2.1 Types of chaos-based cryptosystem.	21-22
	3.2.2 CHARACTERISTICS OF CHAOS.	23
	3.2.3 HOW CHAOS RELATES TO CRYPTOGRAPHY	24
	3.2.4 REASONS FOR SELECTING CHAOS-BASED CRYPTOSYSTEM.	25

3.3	LOGISTIC MAP.	26-37
3.3.1	1-D LOGISTIC MAP	26-29
3.3.2	2-D LOGISTIC MAP.	30-33
3.3.3	3-D LOGISTIC MAP	34-37
3.4	HENON MAP	38-40
4.	IMPLEMENTATION AND RESULTS	41-47
5.	SECURITY ANALYSIS	48-53
6.	CONCLUSION	54
	<i>REFERENCES</i>	55

LIST OF TABLES

<i>Table 1: Lyapunov Exponents.</i>	<u>19</u>
<i>Table 2: Types of Analog Chaos-Based Cryptosystems.</i>	<u>21</u>
<i>Table 3: Types of Digital Chaos-Based Cryptosystems.</i>	<u>22</u>
<i>Table 4: Comparison of Properties of Chaos and Cryptography.</i>	<u>25</u>
<i>Table 5: Correlation coefficient between two adjacent pixels.</i>	<u>50</u>

LIST OF FIGURES

<i>Figure 2.1.1: Cryptosystem</i>	13
<i>Figure 2.1.2: Symmetric key Cryptographic</i>	15
<i>Figure 2.1.3: Asymmetric key Cryptographic</i>	16
<i>Figure 3.1: Typical Architecture of Chaos Based Image Cryptosystems</i>	20
<i>Figure 3.2: The bifurcation diagram of the 1D logistic map</i>	27
<i>Figure 3.3: Shows the value of x after predefining the initial condition and parameter</i>	28
<i>Figure 3.4: Plot of x values in y-axis and range of iterations, n in x-axis</i>	29
<i>Figure 3.5: shows the value of x after predefining the initial conditions and control parameter</i>	31
<i>Figure 3.6: display the value of y after predefining the initial conditions and control parameter</i>	32
<i>Figure 3.7: Plot of x and y values that shows a chaotic behaviour of Two-D Logistic map</i>	33
<i>Figure 3.8: display the value of x after predefining the initial conditions and parameters</i>	35
<i>Figure 3.9: display the value of y after predefining the initial conditions and parameters</i>	35
<i>Figure 3.10: display the value of z after predefining the initial conditions and parameters</i>	36
<i>Figure 3.11: Plot of x, y, and z values that shows a chaotic behaviour of Three-D Logistic map</i>	37
<i>Fig.3.12: shows the value of X after predefining the initial conditions and control parameter</i>	38
<i>Fig.3.13: shows the value of Y after predefining the initial conditions and control parameter</i>	39
<i>Fig.3.14: Plot of X and Y after predefining the initial conditions and control parameter</i>	40
<i>Figure 4.1: Flow-chart of an image encryption</i>	43
<i>Figure 4.2: Output of an image encryption</i>	44
<i>Figure 4.3: Output of an image decryption</i>	46
<i>Figure 4.4: Flow-chart of an image decryption</i>	47
<i>Figure 5.1: (a) Lena (gray-scale image) and (b) Histogram of gray-scale image</i>	48

Figure 5.2: (c) Lena (cipher-image) and (d) Histogram of cipher-image _____ 49

Figure 5.3: Shows the correlation between the two adjacent pixels along horizontal, vertical and diagonal direction of a gray-scale image. _____ 51

Figure 5.4: Shows the correlation between the two adjacent pixels along horizontal, vertical and diagonal direction of a cipher-image. _____ 51

LIST OF ABBREVIATIONS

DES- DATA ENCRYPTION STANDARD

AES- ADVANCED ENCRYPTION STANDARD

3DES- TRIPLE DATA ENCRYPTION STANDARD

IDEA- INTERNATIONAL DATA ENCRYPTION ALGORITHM

RSA- RON **R**IVEST, ADI **S**HAMIR, and LEONARD **A**DLEMAN

DSA- DIGITAL SIGNATURE ALGORITHM

INTRODUCTION

The digital image ends up one of the most vital data providers that are beneficial for biometric authentication, scientific science, military, online private photo album, etc. Image encryption is different from textual encryption. Conventional cipher algorithms which include DES, IDEA, AES, 3DES, and many others are actually now no longer considered appropriate for multimedia documents because of data capacity, sturdy pixel correlation, and excessive redundancy which reduces the encryption performance. The suited cryptographic properties of chaotic maps such as initial conditions and random-like conduct may be used to develop new encryption algorithms. Chaos-based cryptographic algorithms have counseled new methods to expand image encryption schemes. For an image encryption scheme to be steady, it needs to have a clear understanding of the confusion and diffusion stage.

The confusion stage is the pixel permutation in which the positions of the pixels are shuffled over the entire image without value transformation of pixels. This property of confusion generally hides the connection among the ciphertext and the key. With this mechanism image become unrecognizable.

The diffusion stage refers to converting the individual value of the pixels of an image which leads to the reduction of excessive correlation among the pixels.

CRYPTOLOGY

Cryptology is the study of cryptography and cryptanalysis. Cryptography is the study and practice of securing communications among parties, the encrypter, and decrypter, withinside the presence of a third party, the eavesdropper. The cause of cryptanalysis is to locate a weakness in a cryptosystem with the intention to permit the eavesdropper to benefit information about secure communication.

Cryptography

The goal of cryptography is to permit people, the encrypter and decrypter, to communicate over a non-secure channel using a cryptosystem without permitting their opponent, the eavesdropper, to benefit information about their communication. There are five components to any cryptosystem: plaintext, ciphertext, keyspace, encryption rule, and decryption rule.

A cryptosystem is a 5-tuple (P, C, K, E, D) , wherein the subsequent situations are satisfied:

1. P is a finite set of viable plaintexts;
2. C is a finite set of viable ciphertexts;
3. K , the keyspace, is a finite set of viable keys;
4. For every $K \in K$, there's an encryption rule $e_K \in E$ and a corresponding decryption rule $d_K \in D$. Each $e_K : P \rightarrow C$ and $d_K : C \rightarrow P$ are functions such that $d_K(e_K(x)) = x$ for each plaintext element $x \in P$.

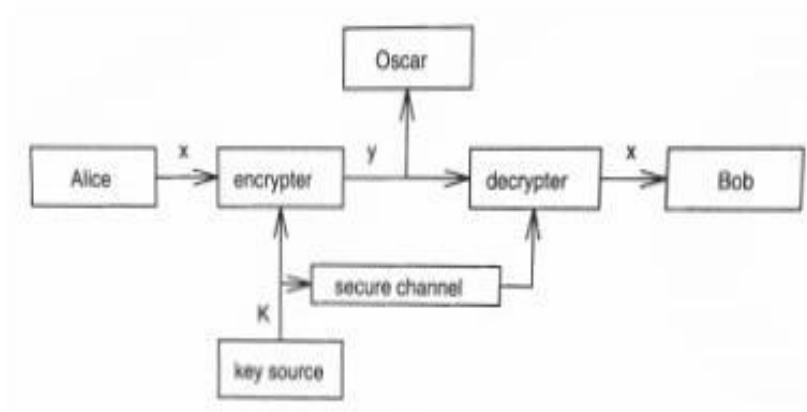


Figure 2.1.1: Cryptosystems

PURPOSE OF CRYPTOGRAPHY

- Authentication: The system of proving one's identity. (The primary forms of host-to-host authentication on the Internet nowadays are name-based or address-based, each of which might be notoriously weak.)
- Privacy/confidentiality: Ensuring that no person can access the message besides the meant receiver.
- Integrity: Assuring the receiver that the acquired message has not been altered in any manner from the original.
- Non-repudiation: A mechanism to show that the sender actually despatched this message.

Types of Cryptography Method

Symmetric Key Cryptography:

It is an encryption system wherein the sender and receiver of a message use a shared key to encrypt and decrypt messages. Symmetric Key Systems are quicker and easier but the hassle is that sender and receiver should by some means exchange keys in a steady manner. The most popular symmetric-key cryptography system is DES, AES, 3DES, IDEA, and many others.

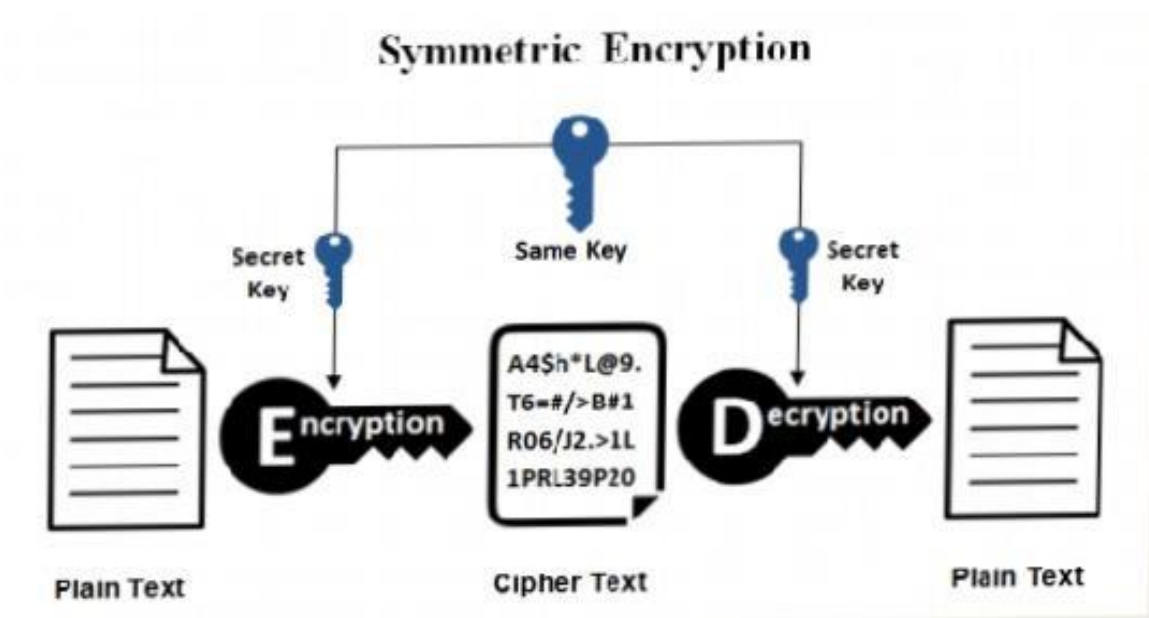


Figure 2.1.2: Symmetric key Cryptographic

Asymmetric Key Cryptography:

The problems of key dissemination are deciphered by asymmetric key cryptography. Asymmetric key cryptography is also termed as public key cryptography. Under this system, a pair of keys is used to encrypt and decrypt the data. A public key is used for encryption and a private key is used for decryption for security purposes. A public key and a Private Key are unique. Even if the public key is known by everyone the meant receiver can only decode it due to the fact, he alone is aware of the private key. An example is RSA, DSA, Diffie-Hellman.

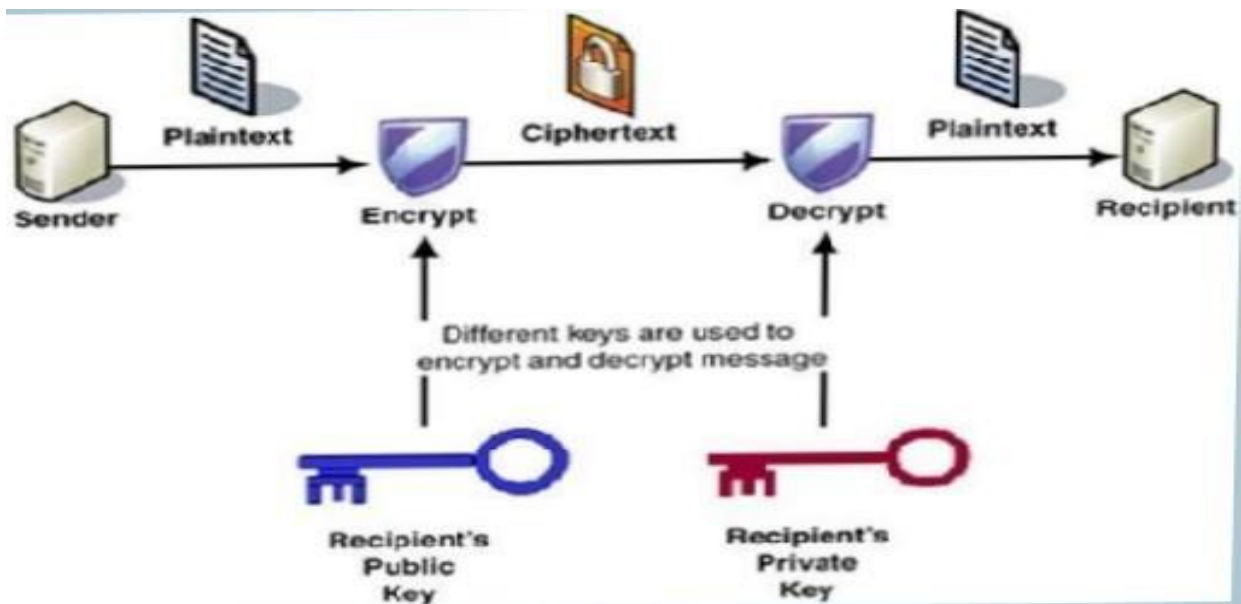


Figure 2.1.3: Asymmetric key Cryptographic

CRYPTANALYSIS

Cryptanalysis is the study of analyzing a cryptosystem to benefit information about the secret key. Gaining information about the secret key permits an eavesdropper to "break a Cryptosystem." Generally, the term "break a cryptosystem" refers to the ability of the eavesdropper to decide the secret key or a part of it.

CRYPTANALYSIS ATTACK

- Ciphertext Only

Has get right of entry to the ciphertext only.

- Known Plaintext

It has a string of plaintext and the corresponding ciphertext.

- Chosen Plaintext

It has got right of entry to the encryption system and may choose a plaintext to create the corresponding ciphertext.

- Chosen Ciphertext

It has access to the decryption machine and can choose ciphertext to create the corresponding plaintext.

- Brute Force

It does an exhaustive search of each viable key.

CHAOS THEORY

- Chaos refers to the complex, difficult-to-predict behavior observed in nonlinear systems.
- Chaos is the state of randomness or confusion and Chaos theory is the field of study in mathematic.

Chaos speculation is the research of nonlinear dynamical frameworks that could show compelling affectability to starting conditions and have arbitrary-like practices, founded by Edward Lorenz in 1963. There are standard methods to use a chaos map in a very cipher system:

- Using chaotic systems for generation of pseudo-random keystream which corresponds to stream ciphers.
- Using the plaintext or the secret key(s) as the preliminary conditions and control parameters then apply some iterations on chaotic systems to get cipher-text equivalent to the block ciphers.

This behavior is named deterministic chaos, or essentially chaos. Irregular like behavior, non-anticipating and affectability to preliminary value are three features that make it an adequate option to relate it with cryptography. The foremost difference is that encryption operations are characterized on limited sets of numbers whilst chaos maps are characterized on actual numbers. Chaotic behaviors are displays by chaotic maps. These maps are grouped by non-stop maps and discrete maps. Discrete maps typically take the manifestation of iterated functions. Iterates are like rounds in cryptosystems, so discrete chaotic dynamic systems are utilized as a part of cryptography. Every map includes parameters that are correspondent to the encryption key in cryptography.

Chaotic behavior is characterized by a Lyapunov exponent greater than zero. Again, the Lyapunov exponent λ is defined as a degree of the stretching of an orbit. If that orbit is stable, then the largest Lyapunov exponent is negative and stretching is minimal. A positive Lyapunov exponent shows exponential stretching of the orbit. Table 1 summarizes what the values of λ explain about the orbit of the system.

Table 1: Lyapunov Exponents

Lyapunov Exponent	Type of Orbit Map Exhibits
$\lambda < 0$	The orbit attracts to a stable fixed point or stable periodic orbit The more negative λ is, the more stable the system
$\lambda = 0$	The orbit is a neutral fixed point or eventually fixed point The system is in a steady state mode
$\lambda > 0$	The orbit is unstable or chaotic All intervals of the phase space will eventually be visited

It is essential to note down that the chaotic behavior exists for precise parameter values. The chaotic orbit is set by the initial condition used along with the parameter value. The existence of a chaotic orbit does not mean the rest of the orbits also will be chaotic.

CHAOS-BASED CRYPTOGRAPHY

Chaos-based cryptography, attracting many researchers in the past decade, had been considered as research field across two fields, i.e., chaos (nonlinear dynamic system) and cryptography (computer and data security). It Chaos' properties, like randomness and ergodicity together with sensitive dependence towards preliminary conditions, have been proved to be suitable for designing the means for data protection. Chaos-based cryptography is the application of chaos theory in cryptographic systems.

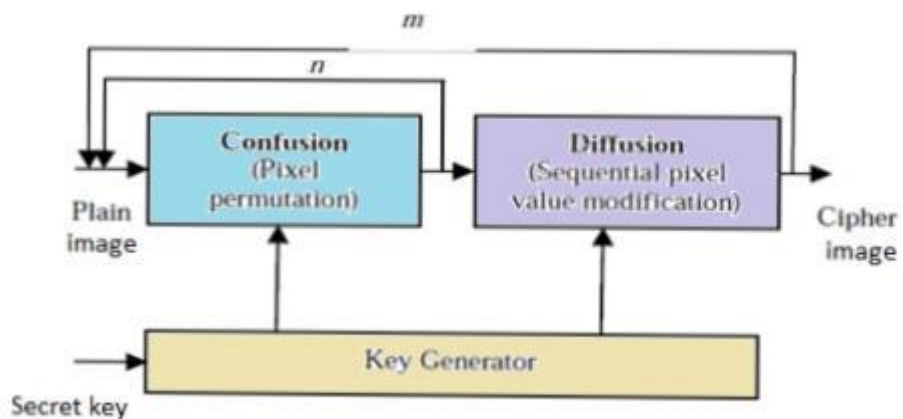


Figure 3.1: Typical Architecture of Chaos Based Image Cryptosystems

TYPES OF CHAOS-BASED CRYPTOSYSTEMS

Just as in classical cryptography, chaos-based cryptography has both public-key and Private-key cryptosystems. However, the design difference of chaotic cryptosystems lies elsewhere. There are two different types of chaos-based cryptosystems: analog and digital. The Research supplied on this report focuses on the digital chaotic cryptography.

The motive of analog chaos-based cryptosystems is to provide secure communication over a noisy channel. The technique utilized in these forms of cryptosystems is chaos synchronization.

Table 2: Types of Analog Chaos-Based Cryptosystems

Method	Description
Additive chaos masking	A chaotic signal is added to the message.
Chaotic shift keying	A digital message signal switches among different chaotic systems space of the chaotic transmitter
Chaotic modulation	A message signal is used to change the parameters of the phase space of the chaotic transmitter
Chaotic control	A message signal is ciphered in a classical way and used to perturbate the chaotic system

The focus of this paper is on digital chaos-based cryptosystems. These varieties of cryptosystems are designed to be used with digital computers. One or more chaotic maps together with an initial condition and control parameter are implemented in computer programs or digital circuits using finite computing precision to encrypt a plaintext message.

Table 3: Types of Digital Chaos-Based Cryptosystems

Digital cryptosystems	Stream ciphers	Chaotic PRNG	A chaotic signal generates a pseudorandom sequence (keystream) to XORed the message
		Chaotic Inverse System approach	A message signal is added to the output of the chaotic signal, which has been feeded by the ciphered message signal in previous instants
	Block ciphers	Backwards iterative	A block of a clear message is ciphered using of inverse chaotic systems
		Forwards iterative	A block of ciphered message is obtained by pseudorandom permutations obtained from a chaotic system
		S-Boxes	An S-Box is created from the chaotic system. There can be dynamic or static S-Boxes
	Miscellaneous	Searching based chaotic ciphers	A table of characters is generated from a chaotic system. The table is used to cipher the characters of the message text
		Cell. Automata	The chaotic system is a Cellular Automata

CHARACTERISTICS OF CHAOS

- The avalanche effect, or dynamical instability, of a chaotic system is the concept of sensitivity to preliminary conditions and control parameters.
- Topological mixing refers to what the orbit of an initial condition appears like.
- Given a chaotic system, the orbit of any initial condition will in no way repeat itself, consequently it is aperiodic.
- Chaotic orbits are considered dense once they have a disorderly-looking orbit within which any initial condition will expand over the entire region of the state space. While a chaotic system isn't periodic, it'll have a dense phase-space. This implies that any orbit will "arbitrarily closely approach every viable asymptotic state".
- Ergodicity is a statistical measurement which offers the identical end result of the behavior averaged over time and over the space of the attractor.
- They are ruled by one or more control parameters, a small change in that could result a chaos to appear or disappear.
- Their governing equations are nonlinear.
- Chaotic system will produce the identical outcome if, given the identical inputs, it's a long way unpredictable in a way that you just cannot predict in what manner the system's behaviour will change for any change within the input to that system. A random system will produce different outcomes when given the identical inputs.

HOW CHAOS RELATES TO CRYPTOGRAPHY

An accurate cryptographic system has pseudo-random behavior. The main components that create the pseudo-random behavior are confusion and diffusion. Confusion is a property which makes it tough to see a connection among the plaintext and the ciphertext. For chaotic cryptosystems, confusion occurs when the encryption rule and the secret key combine in a way that makes finding a function that maps the two together a complex and involved process. Diffusion makes it tougher to process statistical data. Diffusion is inherently related with sensitivity to preliminary conditions and control parameters. With proper diffusion, a chaos-based cryptosystem will have the avalanche effect.

The main characteristics of a chaotic system relate directly to what makes a cryptographic system good or secure. Table 2.2 summarizes the connection between chaos and cryptography. This strong connection between chaotic and cryptographic property is what drew researchers to the study of chaos-based cryptosystems.

Table 4: Comparison of Properties of Chaos and Cryptography

Chaotic Property	Cryptographic Property	Description
Ergodicity	Confusion	The output has the same distribution for any input
Sensitivity to Initial Conditions/Parameter	Diffusion with small changes in plaintext/secret key	Small deviation in the input causes a large change in the output
Topological Mixing	Diffusion with small changes in one plain-block of the whole plaintext	Small deviation in the local area causes a large change in the whole space
Deterministic Dynamics	Deterministic Pseudo-Randomness	A deterministic process can cause random-like (pseudo-random) behavior
Structure Complexity	Algorithmic (Attack) Complexity	A simple process has a very high complexity

Reasons for selecting chaos-based cryptosystem over traditional cryptosystem

- Traditional symmetric ciphers which include Advanced Encryption Standard (AES) are designed with accurate confusion and diffusion properties.
- These two properties also can be observed in chaotic systems that have desirable properties of pseudo-randomness, ergodicity, excessive sensitivity to preliminary conditions and parameters.
- Chaotic maps have demonstrated great potential for data security, specifically image encryption, whilst the standard encryption strategies like AES algorithm seems now not to be appropriate to cipher such kind of data.

1D LOGISTIC MAP

Recently, one quite simple chaotic map has been studied for cryptography applications is a logistic map. Mathematically, the logistic map is written as:

$$x(n + 1) = rxn(1 - xn) \dots (1)$$

Where x_n is a number between zero and one. The parameter r is a positive number in the range of 0 to 4. Depending on the value of r the eq. (1) has different properties which has been pointed below:

- When r between 0 and 1 the value of $x(n)=0$ which is independent of the preliminary conditions $x(0)$.
- When r is in between interval 1 and 3 the value of $x(n)$ stabilizes on the value $[(r-1)/r]$ independent of the preliminary conditions $x(0)$.
- When r is in between 3 and 3.45 the value of $x(n)$ oscillates between two values forever depending on r .
- When r is in between 3.45. and 3.54. (approximately) the value of $x(n)$ oscillates between four values forever. with r slightly bigger than r the value of $x(n)$ oscillates between 8 values, then 16, 32, etc. This behavior exhibits a period-doubling cascade.
- At r approximately 3.57 is the onset of chaos, and the cease of the period-doubling cascade. In this region slight variations in the initial condition yield dramatically distinctive outcomes over time, a prime characteristic of chaos.

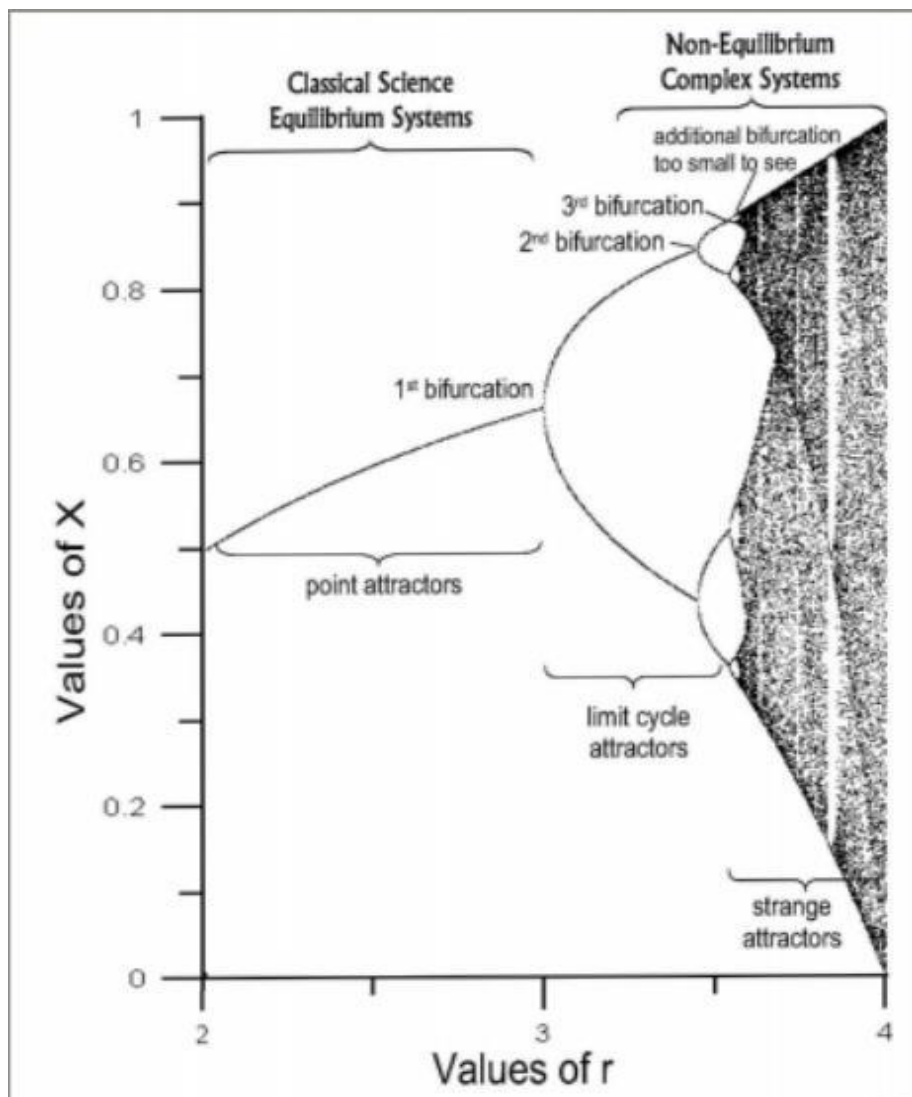


Figure 3.2: The bifurcation diagram of the 1D logistic map.

The logistic map suggests quite a few behaviors and it has transitions among those behaviors as we change the parameter r . Such transitions in dynamical systems are known as bifurcations. Bifurcation is a systematic manner to say something splits in two—branches. If patterns bifurcate quick enough, they could become complex very fast, leading to bifurcation cascade and chaos.

After assigning value to govern parameter and initial condition i.e., $r=3.6$, and $x(1)=0.8907$ for 25 iterations, it shows the chaos phenomena of the one-d logistic map. The output is given below:

```
>> disp(x)
Columns 1 through 7
    0.8907    0.3505    0.8195    0.5325
0.8962    0.3349    0.8019
Columns 8 through 14
    0.5720    0.8814    0.3764    0.8450
0.4714    0.8971    0.3324
Columns 15 through 21
    0.7989    0.5783    0.8779    0.3858
0.8530    0.4513    0.8915
Columns 22 through 25
    0.3483    0.8172    0.5378    0.8949
```

Figure 3.3: Shows the value of x after predefining the initial condition and parameter

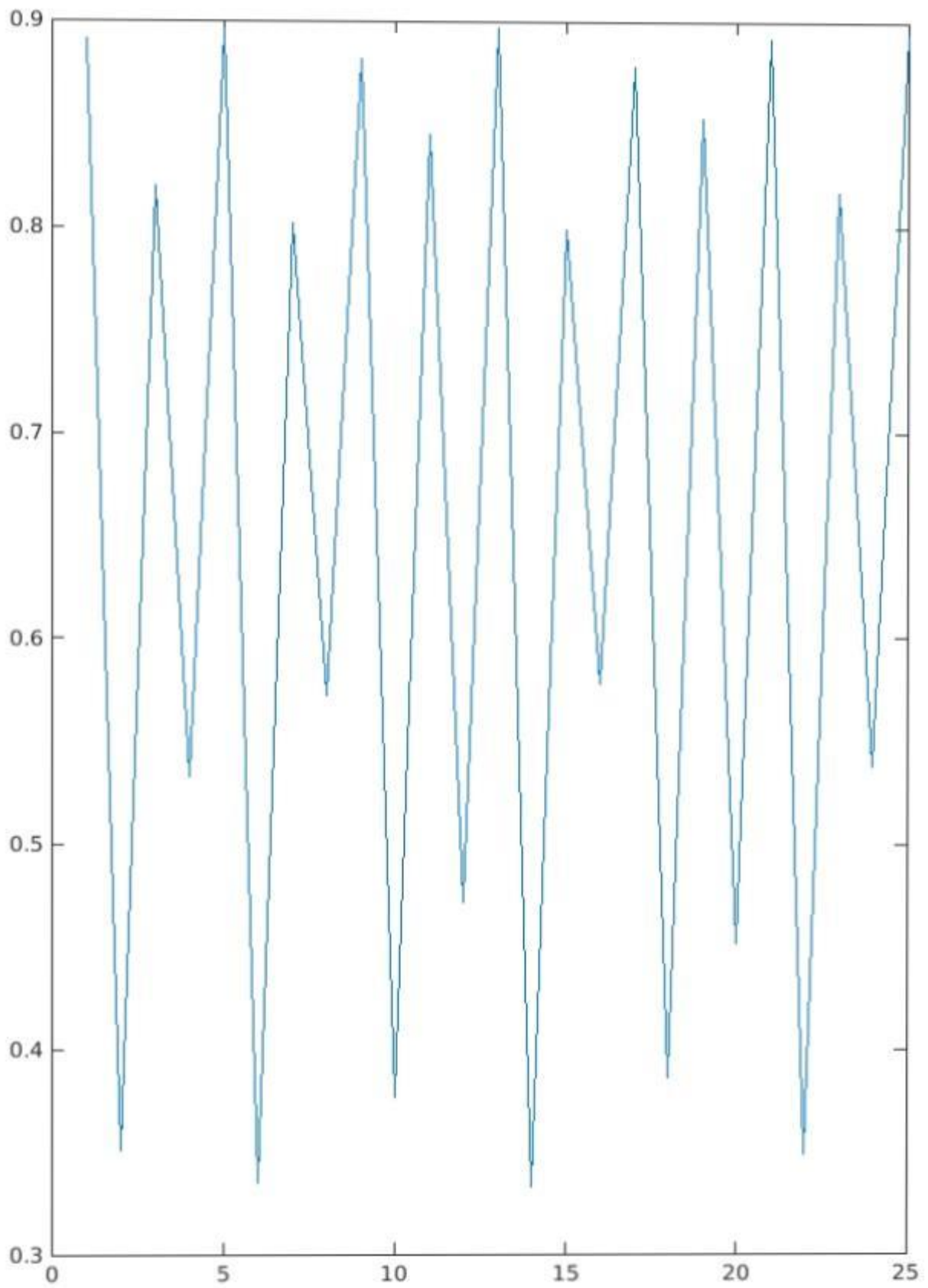


Figure 3.4: Plot of x values in y -axis and range of iterations, n in x -axis

Two-D LOGISTIC MAP

2D logistic map has more complex chaotic behaviors than one-dimensional Logistic map. This 2D logistic map can be discretely defined as below equation: in which r is the system parameter and (x_i, y_i) is the pair-wise point at the i th iteration.

$$x_{i+1} = r(3y_i + 1)x_i(1 - x_i) \text{ and}$$

$$y_{i+1} = r(3x_i + 1 + 1)y_i(1 - y_i)$$

2D logistic map using the parameter $r = 1.19$ and the initial value $(x_0; y_0)$ at $(0.8909; 0.3342)$, the i th point on the trajectory can be determined by knowing $(x_0; y_0; r; i)$ as Eq. (1) shows.

$$X_i = Lx_{2D}(x_0; y_0; r; i), y_i = Ly_{2D}(x_0; y_0; r; i) \dots (1)$$

When $r \in (-1, 1)$, the system has one attractive node and two saddle points, and makes both x and y axes being unstable manifolds.

After predetermining the value to control parameter and initial conditions i.e. $r=1.18$, $x(1)=0.8909$, and $y(1)=0.3349$ for 25 iterations, it shows the chaos phenomena of the one-d logistic map. The output is given below:

```
>> disp(x)
```

```
Columns 1 through 7
```

```
    0.8909    0.2299    0.4873    0.9291  
0.2890    0.3784    0.5963
```

```
Columns 8 through 14
```

```
    0.9466    0.1998    0.3696    0.7214  
0.8968    0.2057    0.4221
```

```
Columns 15 through 21
```

```
    0.8404    0.6130    0.3945    0.5386  
0.8674    0.5282    0.3884
```

```
Columns 22 through 25
```

```
    0.4855    0.7676    0.8229    0.2342
```

Figure 3.5: shows the value of x after predefining the initial conditions and control parameter

```
>> disp(y)
Columns 1 through 7
    0.3349    0.4441    0.7172    0.9064
0.1868    0.3828    0.7775
Columns 8 through 14
    0.7839    0.3197    0.5413    0.9271
0.2944    0.3964    0.6398
Columns 15 through 21
    0.9575    0.1365    0.3036    0.6526
0.9636    0.1069    0.2440
Columns 22 through 25
    0.5347    0.9696    0.1206    0.2131
```

Figure 3.6: display the value of y after predefining the initial conditions and control parameter

3D LOGISTIC MAP

Recently, a 3D logistic map with a higher chaotic property than a 1D logistic map was studied. It may be described by the following equation:

$$x(i + 1) = axi(1 - xi) + byi^2 xi + cxi^3.....(1)$$

$$y(i + 1) = ayi(1 - y(i)) + bzi^2yi + cxi^3.....(2)$$

$$z(i + 1) = az(i)(1 - z(i)) + bxi^2zi + cyi^2.....(3)$$

Here the above equations showcase the chaotic behaviour for $3.53 < a < 3.81$, $0 < b < 0.022$, $0 < c < 0.015$ and (x, y, z) can take the value between $[0, 1]$.

After assigning value to initial condition i.e. $a=3.7800$, $b=0.0139$, $c=0.0121$ and $x(1)=0.5250$, $y(1)=0.8300$, $z(1)=0.4600$ for 25 iterations, it shows the chaos phenomena of the 3d logistic map.

The result is given below:

```

>> disp(x)
Columns 1 through 7
    0.5250    0.9494    0.1958    0.5982
0.9120    0.3156    0.8215
Columns 8 through 14
    0.5624    0.9338    0.2556    0.7199
0.7698    0.6869    0.8157
Columns 15 through 21
    0.5873    0.9181    0.2995    0.7987
0.6228    0.8934    0.3755
Columns 22 through 25
    0.8908    0.3885    0.8991    0.3538

```

Figure 3.8: display the value of x after predefining the initial conditions and parameters

```

>> disp(y)
Columns 1 through 7
    0.8300    0.5379    0.9572    0.1554
0.4998    0.9604    0.1456
Columns 8 through 14
    0.4788    0.9475    0.2099    0.6276
0.8921    0.3791    0.8952
Columns 15 through 21
    0.3722    0.8866    0.3967    0.9084
0.3284    0.8393    0.5265
Columns 22 through 25
    0.9461    0.2128    0.6345    0.8913

```

Figure 3.9: display the value of y after predefining the initial conditions and parameters

```
>> disp(z)
Columns 1 through 7
    0.4600    0.9496    0.1963    0.6080
0.9048    0.3394    0.8597
Columns 8 through 14
    0.4647    0.9457    0.2167    0.6427
0.8780    0.4221    0.9271
Columns 15 through 21
    0.2739    0.7552    0.7176    0.7693
0.6881    0.8167    0.5837
Columns 22 through 25
    0.9236    0.2880    0.7767    0.6697
```

Figure 3.10: display the value of z after predefining the initial conditions and parameters

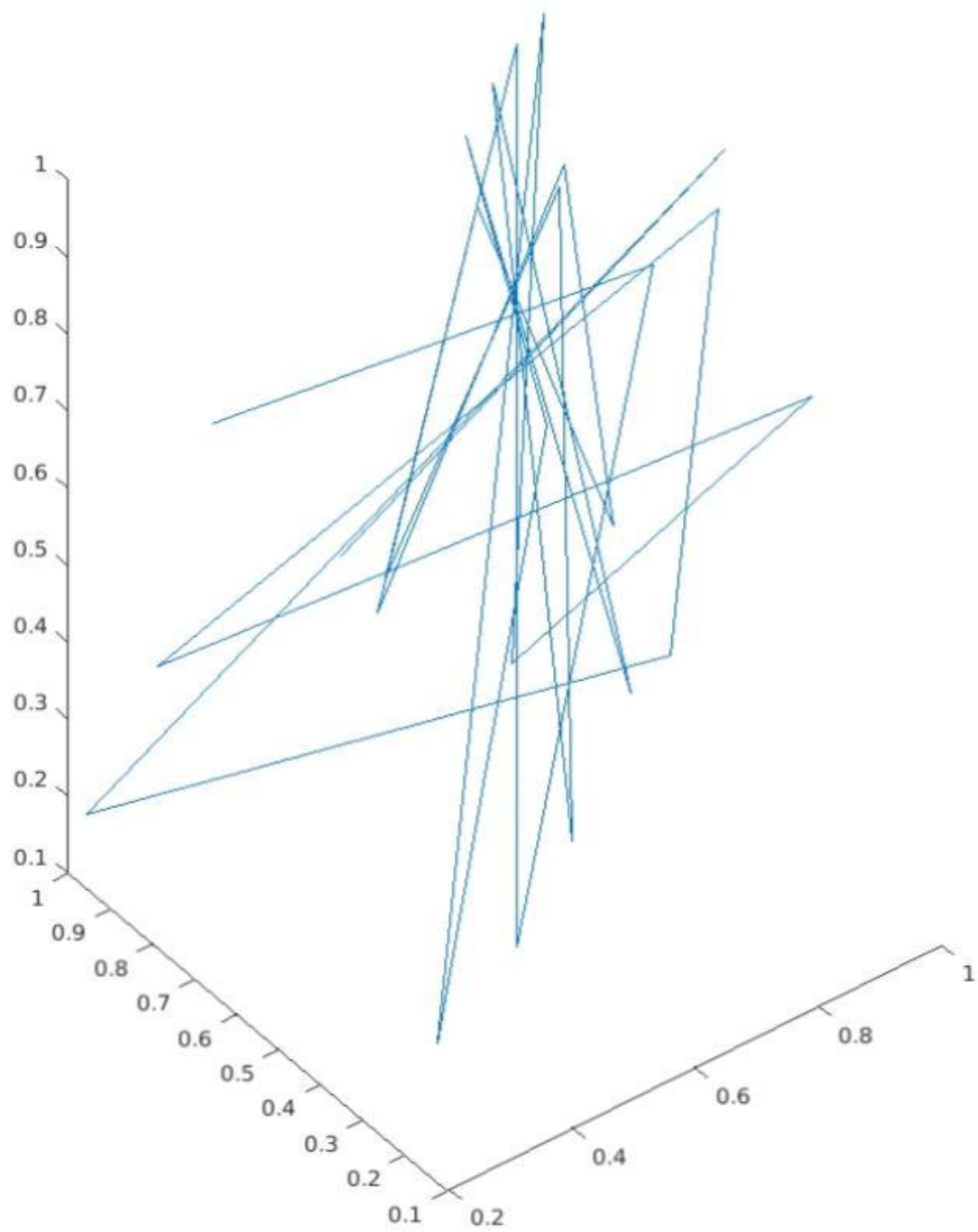


Figure 3.11: Plot of x, y, and z values that shows a chaotic behaviour of Three-D Logistic map

2D HENON MAP

2D Henon is proposed by French astronomer Michel Henon (1976). 2D Henon map is a 2D non-linear map; which can be mathematically represented as follows: -

$$X(n)=1-a*X(n-1)^2-Y(n-1).....(I)$$

$$Y(n)=B*X(n-1).....(ii)$$

where parameters a and b are the variables of bifurcation, when $1.4 < |a| < 2$, $0 < |b| < 1$, and $n= 0, 2, 3, \dots$, it's shows a chaotic behaviour.

After assigning value to control parameters i.e. $a=1.4$, $b=0.03$ and initial conditions $X(1)=0$, $Y(1)=1$ for 25 iterations, it shows the chaos phenomena of the 2D Henon map.

```
>> disp(X)
Columns 1 through 7
-0.7409      0      1.0000      -0.4000      1.0760
      0.5543      0.3476
Columns 8 through 14
      0.9972      -0.2879      1.1831      -1.0461
-0.1771      0.6422      0.3694
Columns 15 through 21
      1.0016      -0.2938      1.1797      -1.0364
-0.1498      0.6577      0.3495
Columns 22 through 25
      1.0263      -0.3697      1.1165      -0.8563
```

Figure 3.12: shows the value of X after predefining the initial conditions and control parameter

```

>> disp(Y)
  Columns 1 through 7
    0          0          0.3000          -0.1200
0.3228  -0.2223  0.1663
  Columns 8 through 14
    0.1043    0.2992   -0.0864    0.3549
-0.3138   -0.0531    0.1927
  Columns 15 through 21
    0.1108    0.3005   -0.0881    0.3539
-0.3109   -0.0449    0.1973
  Columns 22 through 25
    0.1049    0.3079   -0.1109    0.3350

```

Fig.3.13: shows the value of Y after predefining the initial conditions and control para

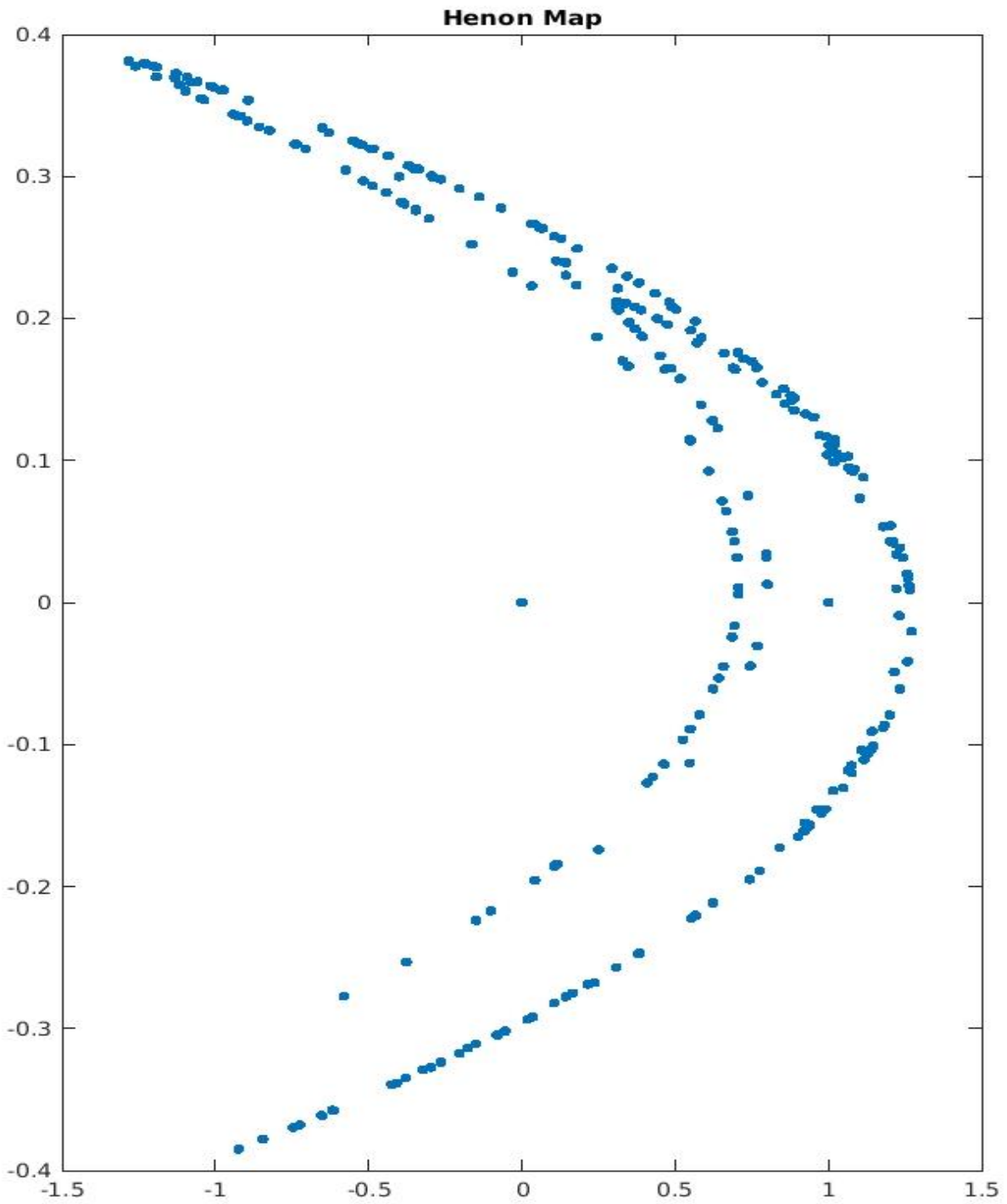


Figure 3.14: Plot of X and Y value after predefining the initial conditions and control parameter

ALGORITHM FOR IMAGE ENCRYPTION

STEP1: Generate a 3D chaotic key sequence using 3D Logistics map:

$$X(i+1) = ax_i(1-x_i) + by_i^2 + cx_i^3 \dots (1)$$

$$Y(i+1) = ay_i(1-y_i) + bz_i^2 + cx_i^3 \dots (2)$$

$$Z(i+1) = az_i(1-z_i) + bx_i^2 + cy_i^2 \dots (3)$$

Partition x and z into two equal halves i.e., x_1, x_2, z_1 , and z_2 of size $(1*128)$.

Therefore Key1(x_1, x_2), Key2(z_1, z_2) and key3(i.e., y of size $(1*256)$) are generated using 3D Logistic map.

STEP2: Generate a chaotic key sequence using 2D Henon map:

$$X(n+1) = 1 - a * X(n)^2 + Y(n) \dots (4)$$

$$Y(n+1) = b * X(n) \dots (5)$$

Key4($\text{mod}(X, 256)$) and Key5(Y) of size $(1*256)$ are generated using 2D Henon map.

STEP 3: Read the color plain-image and resize the color plain-image as matrix and acquire its size $256*256$ and store the R,G,B color information in channel 1, channel 2, and channel 3 respectively.

STEP4: Convert the color plain- image to a gray-scale image.

STEP5: Partitioned gray-scale image horizontally into two equal halves of images i.e. A(top) and B (bottom) of size $128*128$.

STEP6: Partitioned the same gray-scale image vertically into two equal halves of images i.e. C(left) and D(right) of size $128*128$.

STEP7: Perform the circular shift operation on image A to shift the location of pixel row-wise as well as column-wise and acquire a Circular Shifted Image(confused process). Add key1 to Circular Shifted Images to change the value of pixels(diffused process).

STEP8: Perform the same operation as performed on STEP7 on image C.

STEP9: Perform the fliplr (flip left and right) operation on image B and acquired a flipped Image. Add key2 to flipped images.

STEP10: Perform the same operation as performed on STEP9 on image D.

STEP11: Take a new image (i.e., A,B,C, and D after performing operations on it) as a whole of size $256*256$,E (say) and then perform flipud (flip up and down) on it and then amplified it by multiplying with factor $(1/128)$. Add key3 to amplified image of size $256*256$ which is a final fusion of confusion and diffusion stage of image, T.

STEP12: Perform the permutation operation on image T, and acquired a Permuted image which is the confused stage of an image.

STEP13: Add (key4 +key5) to the permuted image and perform modulo function on it to acquired a main diffused image which is a final cipher-image of size $(256*256)$

FLOW-CHART OF AN IMAGE ENCRYPTION

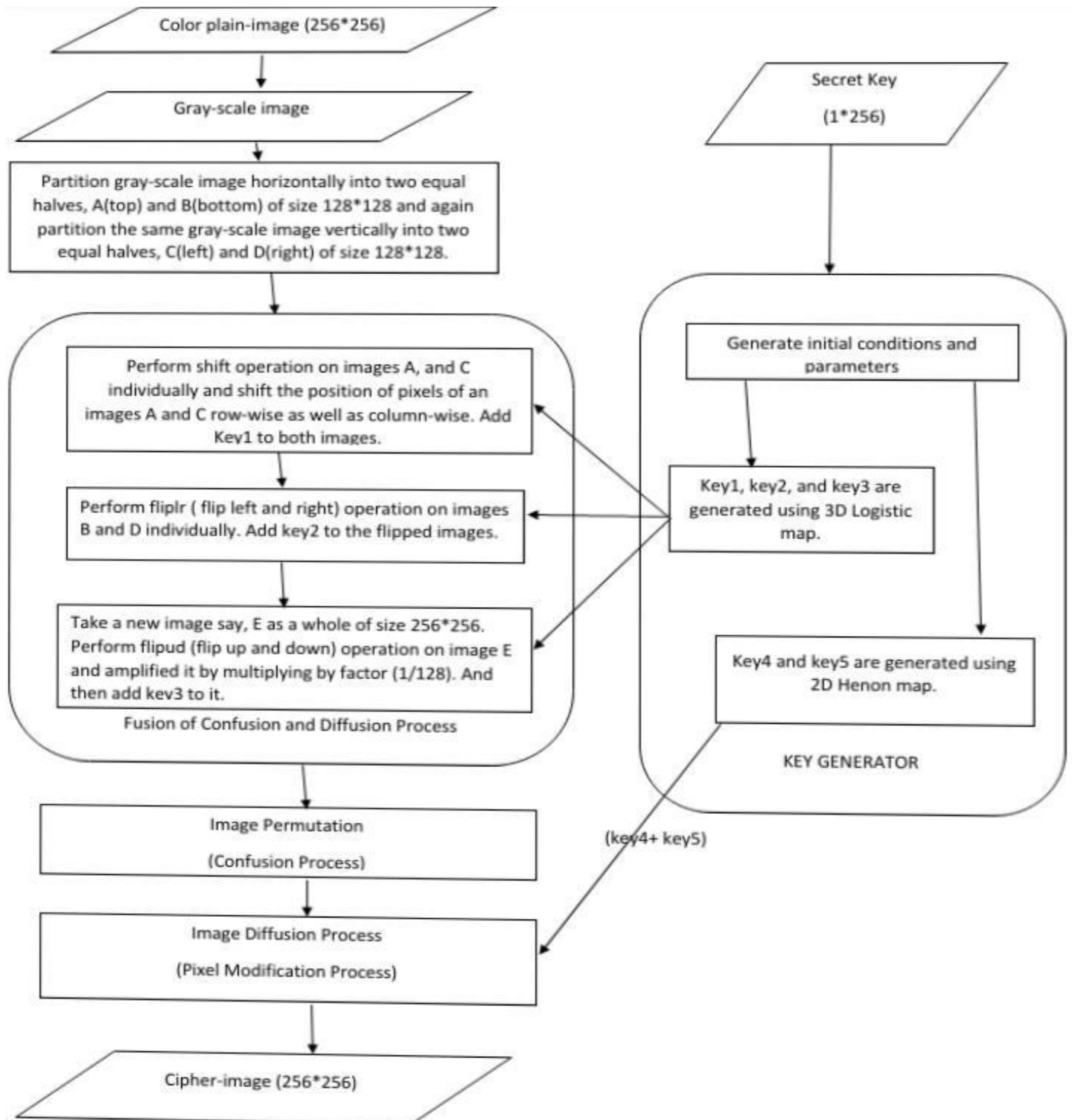


Figure 4.1: Flow-chart of an image encryption

OUTPUTS:



Color plain-image



gray-scale image.



Image E

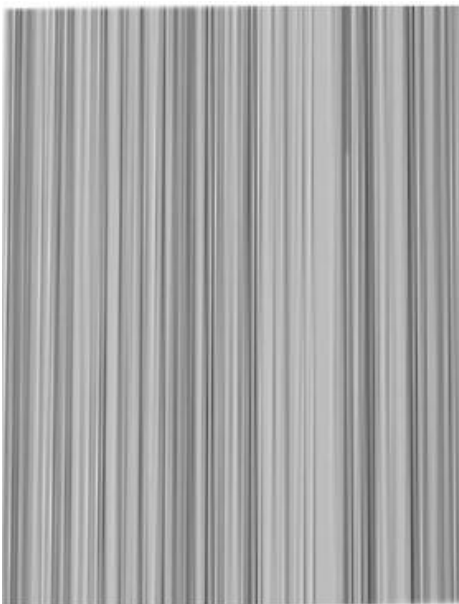
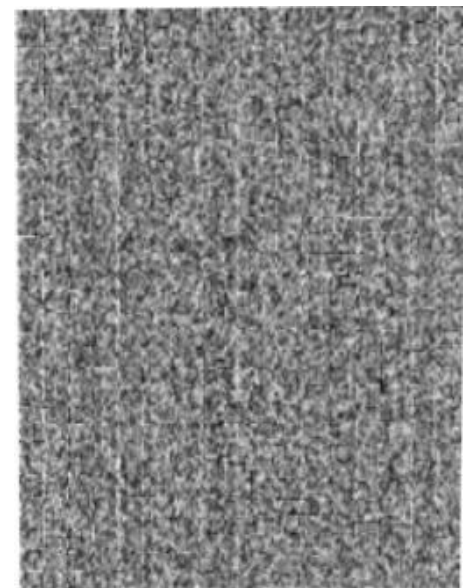


Image T.



Permuted image.



Diffused image

Figure 4.2: Output of an image encryption

ALGORITHM FOR IMAGE DECRYPTION

STEP1: Read a cipher-image of size $256*256$.

STEP2: Subtract (key4+key5) from cipher-image to acquired permuted image.

STEP3: Perform permutation operation on permuted image to acquired an image, T.

STEP4: Subtract key3 from an image, T and amplified by dividing with factor (1/128) and perform flipud (flip up and down) operation to acquired E image.

STEP5: Partitioned image E horizontally into two equal halves of images i.e., P(top) and Q (bottom) of size $128*128$.

STEP6: Partitioned the same image E vertically into two equal halves of images i.e., R (left)and S (right) of size $128*128$.

STEP7: Subtract Key2 from image S and then perform the fliplr (flip left and right) operation on it to acquired a flipped Image.

STEP8: Perform the same operation as performed on STEP7 on image Q.

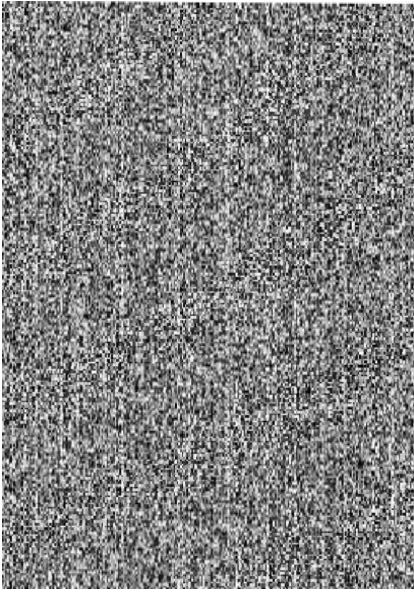
STEP9: Subtract Key1 from image R and then perform the circular shift operation on it to shift the location of pixel row-wise as well as column-wise and acquire a Circular Shifted Image.

STEP10: Perform the same operation as performed on STEP9 on image P.

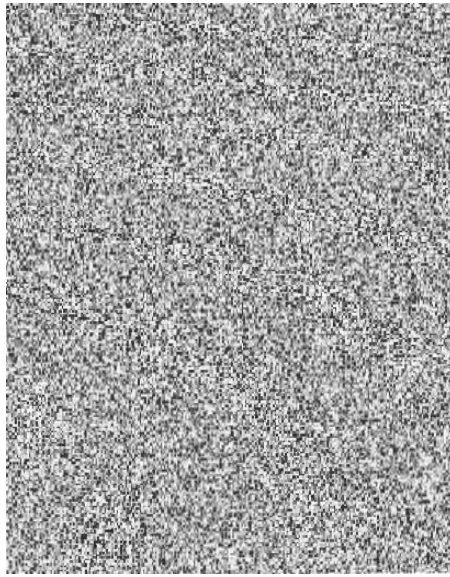
STEP11: Obtained a new image which is a gray-scale image of size $256*256$.

STEP12: Convert gray-scale image to color plain-image by concatenating the information of channel 1, channel 2, and channel 3.

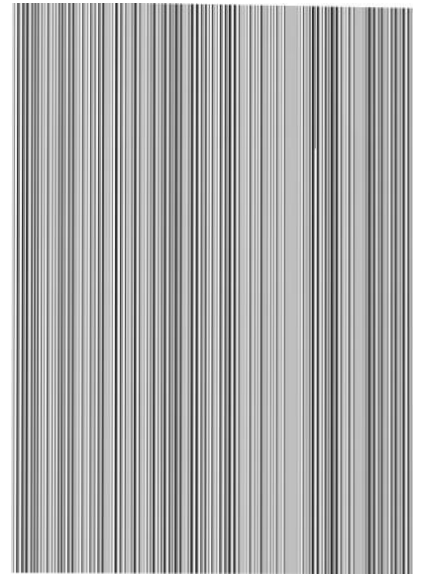
OUTPUT



Cipher-image



Permuted image.



Image, T



Image, E.



Gray-scale image.



Color plain-image

Figure 4.3: Output of an image decryption

Flow-chart of an image decryption

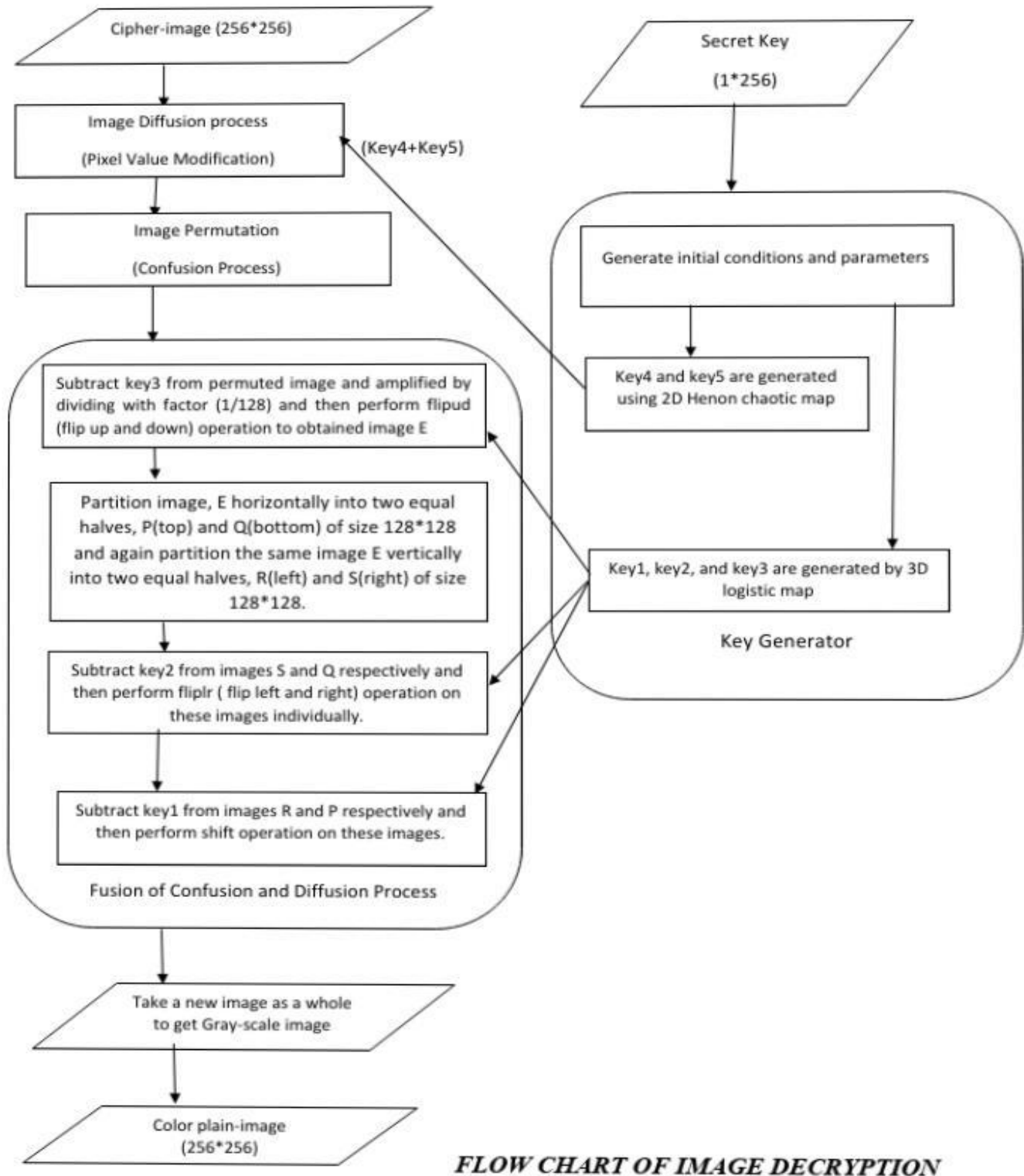


Figure 4.4: Flow-chart of an image decryption

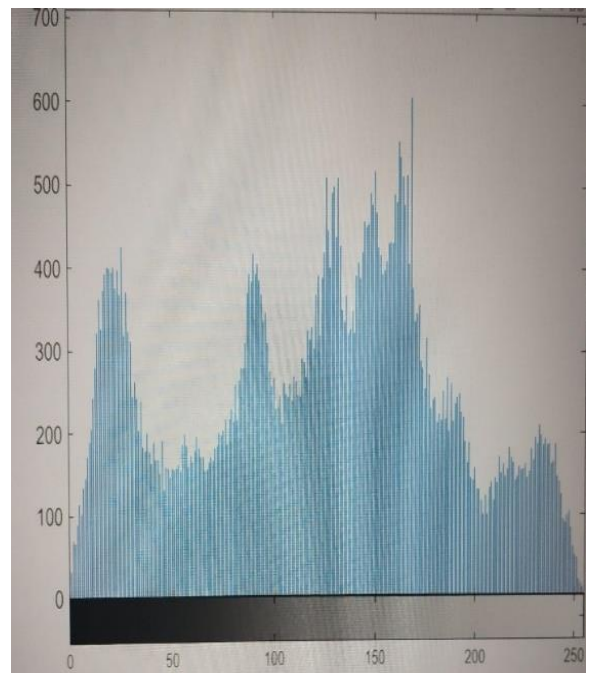
SECURITY ANALYSIS

a) Histogram Analysis:

Histogram is a graphical representation of an image. The histogram of gray-scale image and its ciphered image that are obtained by the proposed image encryption algorithm are shown in below fig.(b) and (d) respectively. From the figure it is clear that the number of pixels in a cipher image is distributed uniformly which implies that cipher image does not provide any clue to employ any statistical attack which makes it statistical attack difficult.

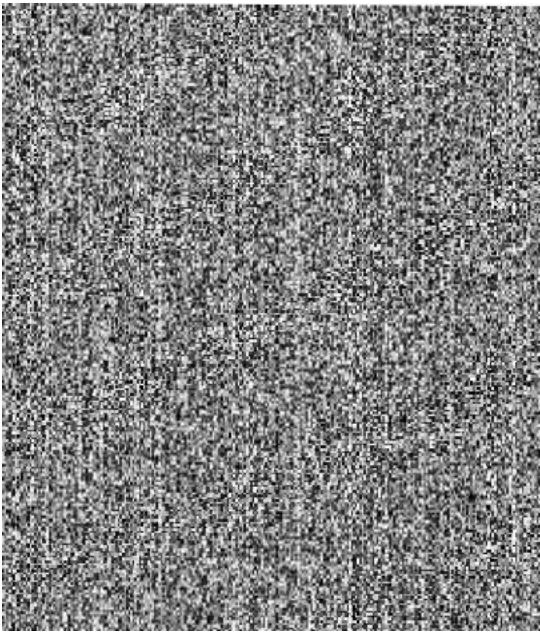


(a)

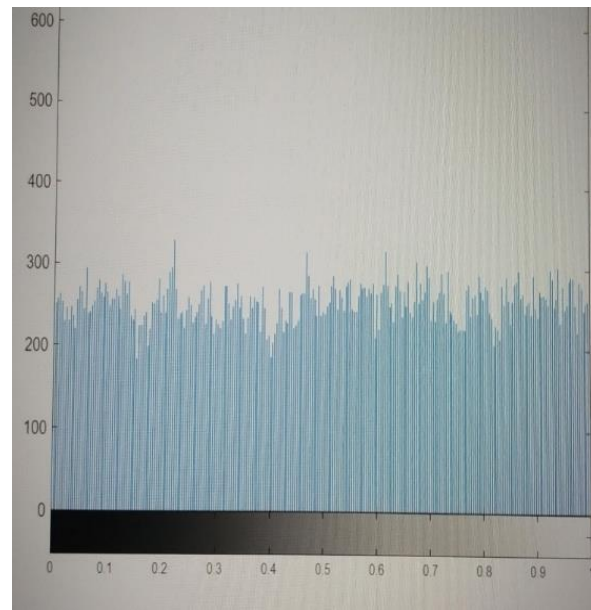


(b)

Figure 5.1: (a) Lena (gray-scale image) and (b) Histogram of gray-scale image



(c)



(d)

Figure 5.2: (c) Lena (cipher-image) and (d) Histogram of cipher-image

b) Correlation Coefficient Analysis

It is used for to measure the relationship among neighbouring pixels in an image. For any plain-image the correlation between any two adjacent pixels is high either in horizontal, vertical or diagonal directions which can be calculated by following equations,

$$E(x) = \frac{1}{N} \sum_{i=0}^N x(i)$$

$$D(x) = \frac{1}{N} \sum_{i=0}^N (x(i) - E(x(i)))^2$$

$$\text{cov}(x, y) = \frac{1}{N} \sum_{i=0}^N (x(i) - E(x_i))(y(i) - E(y_i))$$

$$r_{xy} = \frac{\text{cov}(x,y)}{\text{square root of}(D(x)*D(y))}$$

where x and y are gray-scale value of two adjacent pixels of an image and $E(x)$ is the mean and $D(x)$ is the variance intensity of an image. Theoretically, the value of any adjacent pixels of an image is usually near to 1 and that of an encrypted image near to 0 which implies weak correlation between the adjacent pixels and hence the better encryption algorithm. Below table and figures 5.3 and 5.4 shows the result of two adjacent pixels in horizontal, vertical and diagonal direction of standard Lena (gray-scale image) and encrypted images respectively.

Table 5: correlation coefficient between two adjacent pixels

	Lena (gray-scale image)	Cipher-image
Horizontal	0.9518	-0.0282
Vertical	0.9789	0.0483
Diagonal	0.9492	0.0085

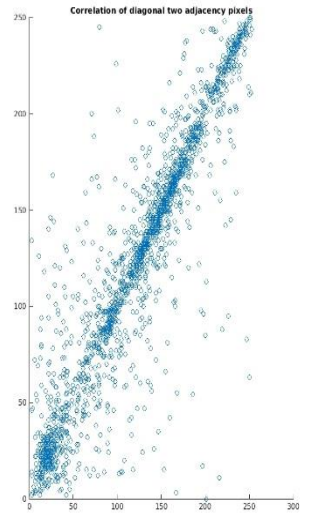
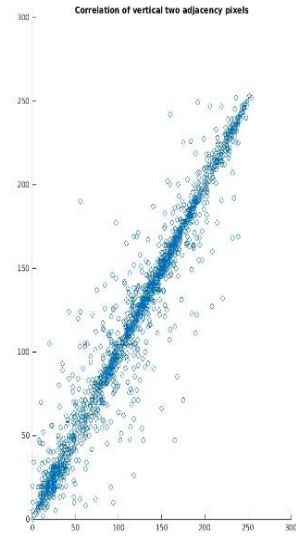
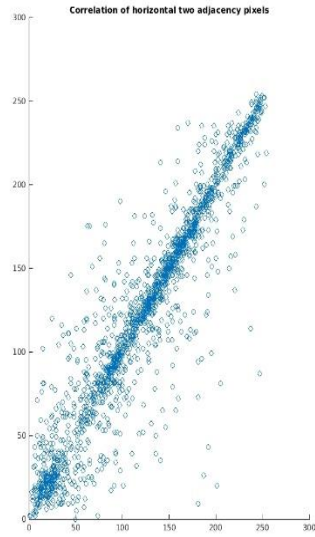


Figure 5.3: Shows the correlation between the two adjacent pixels along horizontal, vertical and diagonal direction of a gray-scale image.

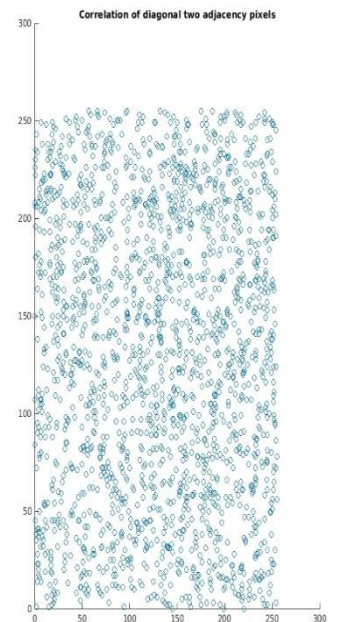
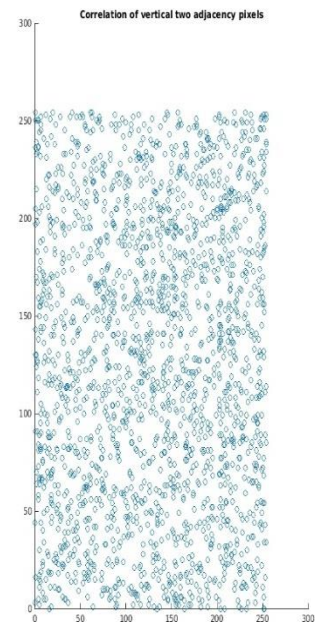
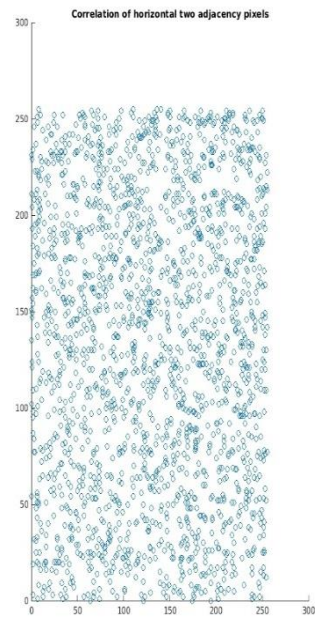
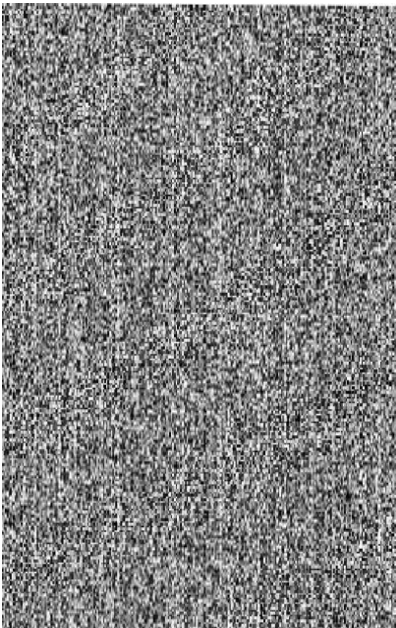


Figure 5.4: Shows the correlation between the two adjacent pixels along horizontal, vertical and diagonal direction of a cipher-image.

c) *Differential Attack Analysis*: -

For the implementation of differential attack, the intruder creates a plain-image that slightly differs from original plain-image and tries to perceives the variations of cipher-image to figure out some expressive association existing amongst the plain-image and cipher-image, which supplementary simplifies in defining the secret key. If an intruder predicts cipher-image from slight variation in the plain-image, then such type of differential analysis would turn out to be practically inadequate. There are two types of criteria that are practically active to measures the diffusion capacity of an image chaos-based cryptosystem. They are: -

- i) NPCR is the number of pixel change rate. It is used for the purpose of measuring the percentage of different pixel numbers among two images. Suppose $S1(i, j)$ and $S2(i, j)$ be the (i, j) th pixel of two images $S1$ and $S2$ where the size of both images is same and are of same data type, then the NPCR is defined as:

$$NPCR = \frac{1}{W \times H} \sum(i,j) D(i, j) \times 100\%$$

where $D(i, j)$ represents the difference between $S1(i, j)$ and $S2(i, j)$. If $S1(i, j) = S2(i, j)$, then $D(i, j) = 0$; otherwise, $D(i, j) = 1$. W is the width of an image and H is the height of an image.

- ii) The second criterion is, UACI which is a unified average changing intensity that can be utilized to measure the intensity of dissimilarities among two images. It is defined as: -

$$UACI = \frac{1}{W \times H} (\sum(i,j) | S1(i,j) - S2(i,j) |) / 255 \times 100\%$$

For an 8-bit gray-scale image, the expected estimates are NPCR = 99.98% and UACI = 33.141%.

d) Information Entropy: -

Entropy is a self-information which plays an important role for analysing security of an encrypted image. Information entropy is a measure of the uncertainty associated with random event and used to tell how much information there is in an event. The more uncertain or random an event is, the more information entropy it will contain. The entropy of a message x can be defined as $H(x)$. If there are N symbols and $p(x_i)$ is the probability of occurrence of symbol x_i , then the equation of an entropy can be mathematically represented as: -

$$H(x) = \sum_{i=0}^{N-1} p(x_i) \log(1/p(x_i))$$

After computing the entropy using above equation, the entropy of a Lena (gray-scale image) image is 7.8 and cipher image is 7.9. For a gray-scale having 256 level theoretical value of entropy is 8 bits. However, practically achieving this ideal value is not possible. So, encryption algorithm which reach nearest to ideal value are considered.

CONCLUSION

The proposed algorithm discusses the method for image encryption using 2D Henon map and 3D Logistic chaotic map for generation of secret key sequences. The method consists of fusion of confusion and diffusion process, confusion process and diffusion which makes it secure and provide confidentiality to an image. Use of 2D Henon map and 3D Logistic chaotic map for generation of secret key sequences provide the higher key sensitivity which results in providing an additional security to the proposed system.

The proposed system is basically analysed based on technique, histogram analysis and correlation of two adjacent pixel along with resistance against entropy attack and differential attack, which are very essential requirement for real time application. So, we can conclude that the chaotic based proposed system is suitable for real time applications.

REFERENCES

- I. D. ARROYO, G. ALVAREZ, AND S. LI, some hints for the design of digital Chaos-based Cryptography: Lessons learned from cryptanalysis, *Analysis and Control of Chaotic Systems*, 2 (2008).
- II. Ercan Solak, Rhouma, and Safya Belghith (2010), Cryptanalysis of a multi-chaotic systems Based image cryptosystem, *Optics Communications* 283 (2010) 232–236.
- III. G. ALVAREZ AND S. LI, Some basic cryptographic requirements for chaos-based Cryptosystems, *International Journal of Bifurcation and Chaos*, 16 (2006), pp. 2129–2151.
- IV. G.A.Sathishkumar, Dr.K.Bhoopathy bagan and Dr.N.Sriraam(2011), Image Encryption Based on Diffusion and Multiple Chaotic Maps, *International Journal of Network Security & Its Applications (IJNSA)*, Vol.3, No.2, March 2011.
- V. Komal D Patel, Sonal Belani (2011), Image Encryption Using Different Techniques: A Review, *International Journal of Emerging Technology and Advanced Engineering* Website: www.ijetae.com (ISSN 2250-2459, Volume 1, Issue 1, November 2011).
- VI. LEI Li-hong, BAI Feng-ming, HAN Xue-hui (2013), New Image Encryption Algorithm Based on Logistic Map and Hyper-chaos, *International Conference on Computational and Information Sciences*.
- VII. Rajinder Kaur, Er.Kanwalprit Singh (2013).Image Encryption Techniques: A Selected Review, *IOSR Journal of Computer Engineering (IOSR-JCE)* e- ISSN: 2278-0661, p- ISSN: 2278-8727Volume 9, Issue 6 (Mar. – Apr. 2013), PP 80-83.
- VIII. Rashidah Kadir, Rosdiana Shahril, Mohd Aizaini Maarof (2010), a modified image encryption Scheme based on 2D Chaotic map, *International Conference on Computer and Communication Engineering (ICCCE 2010)*, 11-13 May 2010, Kuala Lumpur, Malaysia.
- IX. Shubo Liu, Jing Sun¹, Zhengyuan Xu (2009), An Improved Image Encryption Algorithm based on Chaotic System, *Journal of Computers*, Vol. 4, No. 11.

**SYNTHESIS & CHARACTERISATION OF ALUMINA & FLUORIDE
CONTAINING S₅₃P₄-BASED ANTI-BACTERIAL BIOACTIVE GLASS FOR
DENTAL & OTHER BIOMEDICAL APPLICATIONS**



A Thesis

Presented to the Department of Ceramic Technology,
Government College of Engineering & Ceramic Technology,
73, Abinash Chandra Banerjee Lane Kolkata-700010

**In partial fulfilment of the Requirements
For the Degree of Master of Technology in Ceramic Technology**

Submitted by

NABONITA CHAKRABORTY

Department of Ceramic Technology,
Government College of Engineering and Ceramic Technology (GCECT)

Roll No. : GCECTM-R20-1001

Registration No. : 201130410710004 of 2020-21

Under the guidance of

Dr. Kaberi Das,

Associate Professor,

Department of Ceramic Technology, GCECT

June 2022

**SYNTHESIS & CHARACTERISATION OF ALUMINA & FLUORIDE-
CONTAINING S₅₃P₄-BASED ANTI-BACTERIAL BIOACTIVE GLASS FOR
DENTAL & OTHER BIOMEDICAL APPLICATIONS**



A Thesis

Presented to the Department of Ceramic Technology,
Government College of Engineering & Ceramic Technology,
73, Abinash Chandra Banerjee Lane Kolkata-700010

**In partial fulfilment of the Requirements
For the Degree of Master of Technology in Ceramic Technology**

Submitted by

NABONITA CHAKRABORTY

Department of Ceramic Technology,
Government College of Engineering and Ceramic Technology (GCECT)

Roll No. : GCECTM-R20-1001

Registration No. : 201130410710004 of 2020-21

Under the guidance of

Dr. Kaberi Das,

Associate Professor,

Department of Ceramic Technology, GCECT

June 2022

Copyright © 2022 Nabonita Chakraborty
All Rights Reserved

Dedicated to my beloved Parents

I, the undersigned **Nabonita Chakraborty**, hereby declare that my thesis titled "*Synthesis & Characterisation of Alumina & Fluoride-containing S53P4-based Anti-bacterial Bioactive Glass for Dental & other Biomedical Applications*" submitted in partial fulfilment of requirements for the award of the degree of Master of Technology in Ceramic Technology at the Government College of Engineering & Ceramic Technology, Kolkata, West Bengal, comprises of only my original research work. No part of this thesis has been previously presented by me for the obtainment of another degree or diploma at this or any other institution.

I affirm that I have conscientiously acknowledged and given credit and referred to the researchers wherever their works have been cited in the body of the thesis. I further declare that I have not copied anyone else's data/ work/ results etc. published in any journal, magazine, books, report, dissertation, thesis, internet etc. and claimed as my own work. All the data and diagrams/ graphs/ figures documented in this thesis are results of my own *bona fide* research carried out at the Department of Ceramic Technology of the Government College of Engineering & Ceramic Technology (GCECT), Kolkata under the supervision of Dr. Kaberi Das, Associate professor, Department of Ceramic Technology, GCECT.

Name: **NABONITA CHAKRABORTY**

Signature: *Nabonita Chakraborty*

Date: 06/06/2022

Place: Kolkata

Approved by Dr. Kaberi Das,
Associate Professor,
GCECT, Kolkata.



Government of West Bengal

Government College of Engineering & Ceramic Technology

(An Autonomous Institute under MAKAUT, NAAC accredited A grade)



73, Abinash Chandra Banerjee Lane, Kolkata-700010, India

Telephone number - 091 033 2370 1264, 091 033 2363 3675

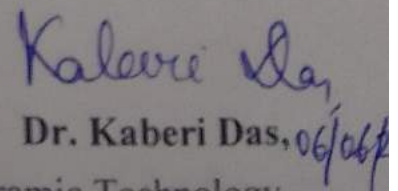
E-mail - gcectwb@gmail.com

Date: 06/06/2022

TO WHOM IT MAY CONCERN

This is to certify that the thesis titled, "**Synthesis & Characterisation of Alumina & Fluoride-containing S53P4-based Anti-bacterial Bioactive Glass for Dental & other Biomedical Applications**" submitted by **Nabonita Chakraborty** in partial fulfilment of the requirements for the award of Master of Technology Degree in Ceramic Technology at Government College of Engineering & Ceramic Technology (GCECT), Kolkata, West Bengal, an autonomous College under MAKAUT, is an authentic documentation of *bona fide* research work carried out by her under my supervision and guidance.

To the best of my knowledge, the matter embodied in the thesis has not been submitted to any other University / Institute for the award of another Degree or Diploma.


Dr. Kaberi Das, 06/06/22

Associate Professor, Department of Ceramic Technology,
Government College of Engineering & Ceramic Technology, Kolkata.

Acknowledgement

Foremost, with deep regards and profound respect, I avail this opportunity to earnestly thank my project supervisor & guide, **Dr. Kaberi Das** (Associate Professor, Department of Ceramic Technology, GCECT, Kolkata) for her inspiring guidance, constructive criticisms and valuable mentorship through and through, due to which I was always motivated and was able to smoothly work on my M.Tech project titled "*Synthesis & Characterisation of Alumina & Fluoride-containing S53P4-based anti-bacterial bioactive glass for dental and other biomedical applications*".

I express my heartfelt gratitude to **Dr. Rituparno Sen** (Professor and HOD, Department of Ceramic Technology, GCECT, Kolkata,) and **Dr. Krishnendu Chakrabarty** (Principal, GCECT, Kolkata), for providing me with the golden opportunity to work on this project.

I am sincerely thankful and indebted to **Mrs. Pamei Pal** (Research Fellow, GCECT) who has supported me and guided me every step of the way, without whose constant support, continued encouragement, kind advices, invaluable suggestions and expeditious helping hand, I wouldn't have been able to accomplish this project.

I am grateful to **Dr. T.K. Bhattacharya** (Asst. Professor, GCECT) for lending me some important instruments and allowing me to use his lab from time to time. I am also thankful to **Mr. Jibon Dey** (Lab attendant, GCECT) and to all non teaching staffs in GCECT for providing me all possible help throughout the duration of the project. I express my appreciation for **Ms. Shreya Barua** (B.Tech student, GCECT) for assisting me on this project.

I convey my wholehearted gratefulness for my parents **Mrs. Babita Chakraborty & Mr. Sandip Chakrabarti**, my extended family and friends who have always been my pillars of strength in every situation.

Lastly, I would like to thank everyone who helped me out during my project but whose name I might have, although inadvertently, forgotten to mention above.

Nabonita Chakraborty

Nabonita Chakraborty

Abstract

The present work deals with the synthesis of melt-derived Fluoride & Alumina-modified S53P4-based bioactive glasses with anti-bacterial attributes and evaluates their properties pertaining to dental applications. CaF_2 was introduced, substituting CaO (10, 9 & 8 wt%), as Fluoride promotes tooth remineralization & restricts its demineralization, and also effectively suppresses bacterial activity. Al_2O_3 was added, replacing CaO (1, 2 & 3 wt%), to enhance the mechanical properties of the glass. The structural characteristics of the synthesised glasses were studied by means of X-ray diffraction (XRD), Fourier-transform Infra-red spectroscopy (FTIR), and Raman Spectroscopy. The dissolution characteristics and Bioactivity of the synthesized glasses were examined by measuring changes in pH, Fluoride ion (F^-) concentration, weight loss and by subjecting the samples to FTIR & Raman Spectroscopy after immersion in Simulated Body Fluid (SBF) as well as in Artificial Saliva (AS) over the course of 28 days. Scanning Electron Microscopy (SEM) and Energy-dispersive X-ray spectroscopy (EDX) were used to investigate the microstructure and elemental composition of the glass samples before and after immersion in SBF. The anti-bacterial properties of the prepared glass samples were tested in vitro against *Escherichia coli*. The inhibition of bacterial growth was measured using the standard agar-plate count technique. The analysis revealed evidence of bactericidal action, which increased with Fluoride content. The produced glasses exhibited strong bioactivity, as evidenced by the formation of Hydroxyapatite and Fluorapatite on their surfaces, following immersion in SBF and AS at 37°C , demonstrated by the FTIR, Raman Spectroscopy, and SEM results. The Bioactivity of the glasses was found to decrease with increase in Al_2O_3 content. The pH and the F^- concentration were both observed to escalate higher in the Artificial Saliva than in the SBF. The addition of Al_2O_3 & CaF_2 significantly elevated the brilliance and fluidity of the glass at the melting temperature respectively.

Keywords: Bioactive Glasses, Fluorapatite, In-vitro bioactivity, Anti-bacterial glass, Dental glass, Glasses for biomedical applications

INDEX

Serial No.	Topic	Page No.
	Acknowledgement	v
	Abstract	vi
1.	Introduction	1
1.1.	Biomaterials	1
1.2.	Bioceramics	1
1.3.	Bioactive glasses	1
1.3.1.	Bioactive glass S53P4	6
1.3.2.	Advantages of bioactive glasses	7
1.3.3.	Disadvantages of bioactive glasses	7
1.4.	Role of Fluoride in dental & other biomedical applications	8
1.4.1.	Role of Fluoride in prevention of dental caries	8
1.4.2.	Role of Fluoride in bone graft materials	10
1.4.3.	Fluorapatite vs. Hydroxyapatite	11
1.5.	Dental materials	12
1.6.	Scope & Application of the presented research work	17
2.	Literature Review	18
3.	Objectives of the project	35
4.	Plan of the work	36
5.	Process Flow Chart	37
6.	Materials & Methods	38
6.1.	Preparation of Bioactive glass	38
6.1.1.	Batch mixing	39
6.1.2.	Melting	39
6.1.3.	Casting	39
6.1.4.	Annealing	40
6.1.5.	Making glass powder and glass blocks	40
6.2.	Characterisation of bioactive glass	40
6.2.1.	Differential Thermal Analysis (DTA)	40
6.2.2.	X-ray Diffraction (XRD)	41

1. Introduction

1.1. Biomaterials

A biomaterial is described as a substance (apart from drugs) or a mixture of substances of synthetic or natural origin that can be utilised for any length of time, as a whole or as part of a system that treats, augments, or replaces any tissue, organ, or function of the body. Metals, polymers, ceramics, and even composite materials can be used to design biomaterials.

1.2. Bioceramics

Bioceramics are ceramic materials which exhibit biocompatibility. Biocompatibility allows the surrounding tissue and the human body to accept and retain the synthetic materials or implants without eliciting any negative immune reactions, allergic responses, or any inflammatory or chronic disorders, and also does not induce carcinogenicity. Bioceramics are a major class of biomaterials. Bioceramics range in biocompatibility from ceramic oxides, which are inert in the body, to resorbable materials, which are gradually replaced by the body after assisting restoration. Many medical interventions make use of bioceramics.

1.3. Bioactive Glasses

Bioactive glasses refer to a group of hard surface-reactive amorphous bio-compatible materials which are used as implants in the human body for repair, replacement and/or regeneration of diseased and/or damaged tissues in body. The majority of bioactive glasses are silicate-based glasses that degrade in physiological fluids and can act as a transport for administering therapeutic ions. Bioactive glass is distinguished from other synthetic ceramic biomaterials (e.g., calcium sulphate, biphasic calcium phosphate, hydroxyapatite,) by its anti-infective and angiogenic capabilities not found in others. Bioactive glasses possess the attributes of osteointegration,

osteinduction, and osteoconductivity. The bond strength at the interface between the material and the biological tissues is around 15 to 25 MPa.

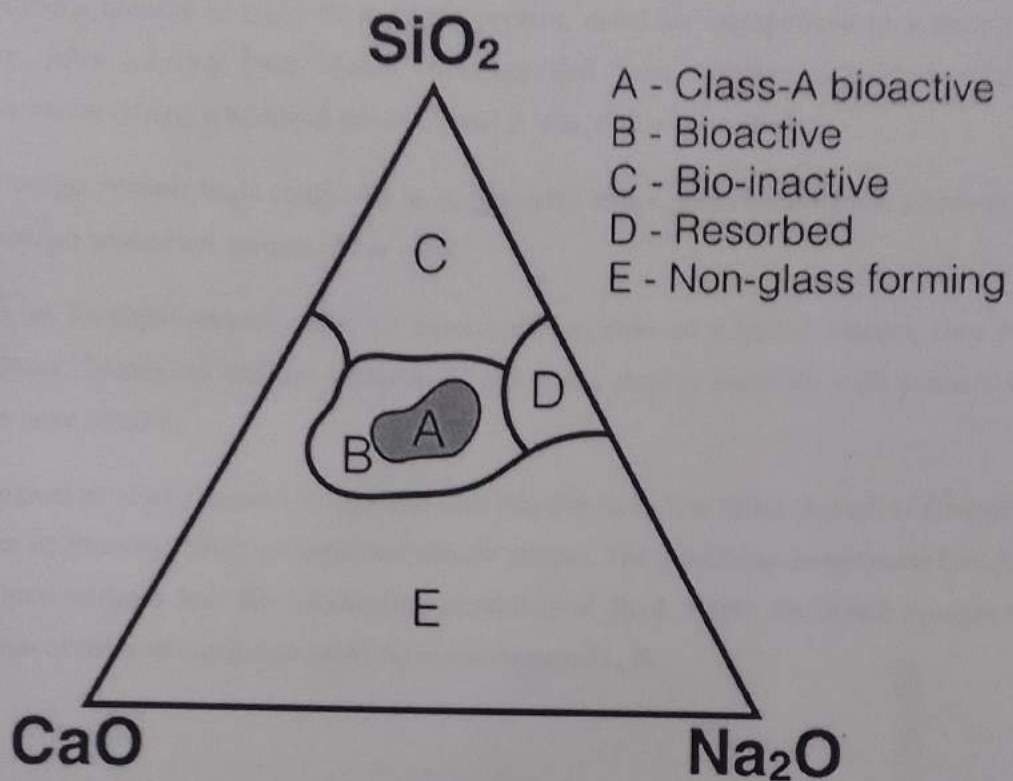


Figure 1. Ternary phase diagram of SiO₂-Na₂O-CaO

Larry L. Hench invented the first bioactive glass, Bioglass[®] (45S5), in the 1970s. Hench intended to develop a substance that was biocompatible and capable of developing a long-lasting bond with the host tissue during the process of wound-healing [1]. Hench intentionally chose the original 45S5 composition, which comprises of 45 weight percent SiO₂, 24.5 weight percent CaO, 24.5 weight percent Na₂O, and 6.0 weight percent P₂O₅, so as to enable bone synthesis while retaining glass properties [1].

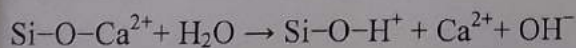
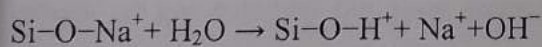
Dr. Hench selected 45 weight % SiO₂ as the network former for the following four reasons:

- 1) The composition was close to a ternary eutectic with low melting temperature, making the glass easier to melt in a regular furnace equipped with SiC heating elements.
- 2) A sizeable content of CaO, 24.5 weight percent, could be incorporated as a glass network modifier, after learning from Hamis Histology that bone contains significant amounts of Hydroxyapatite (HAp), a hydrated salt of Ca and P ions, as the bone mineral.
- 3) 24.5 weight percent Na₂O could well be employed as a flux, upon learning that all physiological fluids contain substantial amount of Na⁺ ions.
- 4) P₂O₅ at 6 weight percent could be introduced not only as a mixed valence flux but also as a network former, as well as a source of phosphate ions to associate with calcium ions to produce bone mineral.

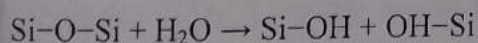
The Bioglass network degrades in aqueous solutions due to its low Silica content in comparison to the more structurally robust conventional silicate glasses. The modifying components (Na, Ca, and P) are then released into the surrounding physiological fluid, where the 5-step process for the generation of the hydroxyapatite (HA) layer commences [1, 2].

When a bioactive glass is submerged in a physiological environment, the following five inorganic reaction steps are usually believed to occur:

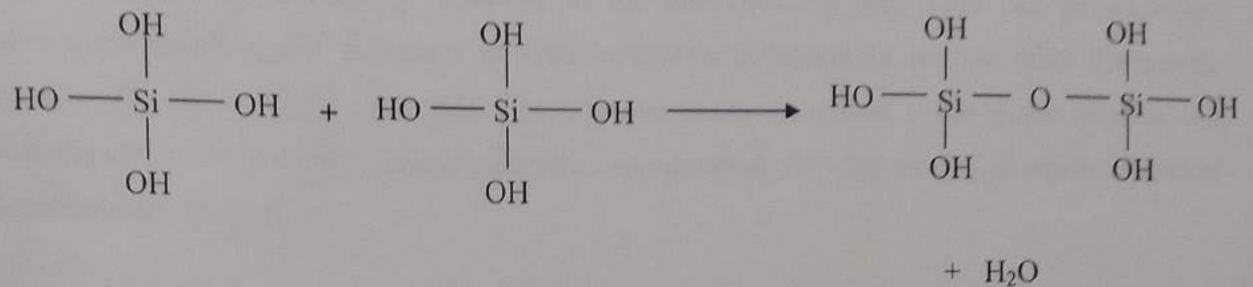
1. **Ion exchange** in which the mobile modifier cations in the glass (such as Na⁺) swap with the hydronium ions (H₃O⁺/ H⁺) in the circumambient solution.



2. **Hydrolysis**, in which Si-O-Si bridges are ruptured, simultaneously creating Si-OH silanol groups and disrupting the glass network.



3. **Condensation of silanols**, whereby the morphology of the disintegrated glass metamorphoses to yield a gel-like surface layer deficient in sodium and calcium ions.



4. **Migration of Ca^{2+} and $(\text{PO}_4)^{3-}$ groups** available in the glass to the glass surface through the SiO_2 -rich layer forming a $\text{CaO-P}_2\text{O}_5$ -rich film over the Silica gel layer, followed by the growth of this amorphous calcium phosphate (ACP) layer by incorporating calcium and phosphate ions from the ambient solution.

5. **Crystallization** of the $\text{CaO-P}_2\text{O}_5$ film to Hydroxycarbonate Apatite (HCA) by incorporation of Hydroxyl ions (OH^-) and Carbonate ions ($(\text{CO}_3)^{2-}$) from the circumambient solution. Mineralization occurs, eventually converting the calcium phosphate layer into crystalline hydroxyapatite, which mirrors the mineral phase found naturally in vertebrate bones. [30]

Extensive investigation in bioactive glass has contributed to the development of diverse set of formulations with varying elemental compositions. Regardless of the bioactive glass composition, the mechanism for producing Hydroxyapatite remains essentially unchanged. Silanol (Si-OH) groups are generated on the glass surface when Na^+ and Ca^{2+} react with H^+ from the ambient physiological fluid, raising the pH.

The increased pH disrupts the Silica network and facilitates the release of silicic acid $\text{Si}(\text{OH})_4$, resulting in enhanced silanol production. The silanols re-polymerize to develop an amorphous silica gel layer. The calcium (Ca^{2+}) and phosphate ($(\text{PO}_4)^{3-}$) groups react with hydroxyl (OH^-) and carbonates ($(\text{CO}_3)^{2-}$), leading to the formation of a crystalline Hydroxycarbonate Apatite (HCA) layer on the surface of the glass. [1, 2]

The rate at which bioactive glasses degrade in solution dictates their ion release patterns. Although difficult to predict, monitoring variations in ion concentration over time can point towards conclusions regarding the efficiency of Hydroxyapatite formation as well as other therapeutic potential. [3] The inclusion of certain ions with therapeutic value can result in the creation of a bioactive glass with enhanced osteoconductive, antimicrobial, or other biological and/or structural characteristics. [4, 5, 6]

Essential features of Bioactive glasses are:

- Biocompatibility
- Non-toxicity
- Non-inflammatory
- Non-carcinogenic
- Non-immunogenic
- Non-allergenic
- Non-corrosive
- Biofunctionality
- Resistance to Mechanical Failure

There have been many variations on the original composition of bioactive glass Bioglass 45S5. The two most popular bioactive glass compositions are:

• **45S5**: 45 wt% SiO₂, 24.5 wt% CaO, 24.5 wt% Na₂O and 6.0 wt% P₂O₅. Bioglass®

• **S53P4**: 53 wt% SiO₂, 23 wt% Na₂O, 20 wt% CaO and 4 wt% P₂O₅.

(S53P4 is the only bioactive glass composition which inhibits bacterial growth).

Various compositions of bioactive glasses are listed in Table 1.

Table 1. Different Bioactive Glass compositions

Composition (wt%)	45S5	S53P4	58S	70S30C	P50C35N15	6P53B	13-93
SiO ₂	45	53	58	70	-	-	53
Na ₂ O	24.5	23	-	-	15	10	6
CaO	24.5	20	33	30	35	18	20
K ₂ O	-	-	-	-	-	3	12
P ₂ O ₅	6	4	9	-	50	6	4
MgO	-	-	-	-	-	10	5
B ₂ O ₃	-	-	-	-	-	53	-

1.3.1. Bioactive glass S53P4

S53P4 bioactive glass (BAG-S53P4) is a biomaterial composed of silica, soda, lime, and phosphate. [31]. S53P4 is both osteoconductive and osteopductive in the stimulation, migration, proliferation, and differentiation of osteogenic cells, and the production of the matrix. [32]. To put it more simply, S53P4 bioactive glass promotes bone synthesis and regeneration (osteostimulation). S53P4 has also been shown to effectively inhibit the growth of up to 50 clinically relevant strains of bacteria. [33, 34, 35, 36]. S53P4 bioactive glass was invented in Turku, Finland, in the 1980s. S53P4 was discovered to be osteostimulative, but it also had one new property: its composition of 53% silica and smaller percentages of sodium, calcium, and phosphorus induced surface reactions in vitro which happened to inhibit bacterial growth, resulting in the discovery of a material that could not be infected by bacteria.

S53P4's anti-bacterial effect stems from two simultaneous physical & chemical reactions that occur when the bioactive glass comes in contact with the physiological fluids. Sodium ions (Na⁺) are released from the bioactive glass surface, elevating the pH and creating an alkaline environment which is unfavourable for bacteria, thus suppressing their growth and multiplication. The released Na, Ca, Si, and P ions lead to an increase in the osmotic pressure owing to an

increase in salt concentration, resulting in a hostile environment in which bacteria cannot thrive. [37]

The Si-O matrix is the basic framework of the S53P4 bioactive glass. In addition to acting as a flux during melting, sodium ions (Na^+) impair network connectivity of the glass, amplifying its bioactivity. The primary components of the Hydroxyapatite (HAp) layer are Calcium (Ca) and Phosphorus (P), which play an important role in odontoblast replication and maturation. [7, 8].

1.3.2. Advantages of Bioactive Glasses

- Compared to conventional glasses, bioactive glasses are relatively soft. Consequently, they can be machined quite easily, notably with diamond tools, or ground to powder.
- High Biocompatibility, as evidenced by their ability to resist negative immune responses and fibrous encapsulation when placed in vivo.
- Offer good osteoconductivity and bioactivity, it can deliver to cells and is biodegradable.
- Durable and High Compressive Strength
- Lightweight but high hardness
- Wear & corrosion resistance
- Good aesthetic appearance

1.3.3. Disadvantages of Bioactive Glass

- Bioglass has to be stored in a dry environment, as it readily absorbs moisture and reacts with it since it is hygroscopic.
- Brittle
- Low fracture toughness due to amorphous 2-dimensional glass network.
- Low tensile strength.
- The bending strength of most Bioactive glasses is in the range of 40–60 MPa, which is not enough for load-bearing applications

1.4. Role of Fluoride in dental & other biomedical applications

1.4.1. Role of Fluoride in prevention of dental caries

Dental caries is a multifactorial disease caused by the interaction of dietary sugars, dental biofilm and the host's dental tissue within the oral environment [9]. It is the cumulative result of consecutive cycles of demineralization and remineralization at the interface between the biofilm and the tooth surface. Oral bacteria excrete acid after consuming sugar, leading to demineralization [10]. Upon this acid challenge, the hydroxyapatite crystals are dissolved from the subsurface. Remineralization is the natural repair process for non-cavitated lesions. It relies on calcium and phosphate ions, assisted by fluoride, to rebuild a new surface on the existing crystal remnants in the subsurface. The remineralized crystals are less acid soluble than the original ones [11].

Under normal physiological conditions (pH 7), saliva is supersaturated with calcium and phosphate ions, making caries progress slow. However, as the bacteria in the biofilm continue to produce acid with sugar consumption, plaque pH falls to 4.5-5.5; This shifts the driving force within the tooth to mineral dissolution [9]. As the pH is lowered, the saturation point of the minerals in the surrounding fluid is changed. The lower the pH, the higher the concentrations of calcium and phosphate required to reach saturation with respect to hydroxyapatite. This is called the "critical pH", the point where equilibrium exists. There is no mineral dissolution and no mineral precipitation. The critical pH of hydroxyapatite is around 5.5 and that of fluorapatite is around 4.5. This varies with individual patients. Below critical pH, demineralization occurs while above critical pH, remineralization occurs.

The critical pH is significantly higher for children than adults. Children have a greater driving force for demineralization in a more acidic oral environment and a decreased driving force for remineralization at normal oral pH. This puts children at greater risk for demineralization than adults [12].

1. Fluoride inhibits demineralization.

If fluoride is present in the plaque fluid when bacteria produce acids, it will penetrate along with the acids at the subsurface, adsorb to the apatite crystal surface and protect the crystals from dissolution [13]. This coating makes the crystals similar to fluorapatite (critical pH of 4.5) ensuring that no demineralization takes place until the pH reaches this point. Fluoride present in solution at low levels among the enamel crystals can markedly inhibit dissolution of the tooth mineral by acid [14, 15]. This fluoride comes from topical sources such as drinking water, and fluoride products like toothpastes and varnishes. The fluoride, which is incorporated systemically into the tooth, is insufficient to have a measurable effect on its acid solubility [15, 16].

2. Fluoride enhances remineralization.

When the pH returns to pH 5.5 or above, the saliva which is supersaturated with calcium and phosphate, forces mineral back into the tooth [15]. Fluoride adsorbs to the surface of the partially demineralized crystals and attracts calcium ions. This new surface veneer takes up fluoride preferentially from the solution around the crystals and excludes carbonate [15].

Fluoride speeds up the growth of the new surface by bringing calcium and phosphate ions together and is also preferentially incorporated into the remineralized surface. This produces a surface which is now more acid resistant.

3. Fluoride may inhibit essential bacterial activity.

Fluoride cannot cross the bacterial cell wall in its ionized form (F). However in an acid environment, F combines with H to form HF which easily diffuses into the bacterial cell [17, 18]. Inside the cell HF breaks up and releases fluoride ions that interfere with the essential enzyme activity of the bacterium.

4. Fluoride is retained in intraoral reservoirs after the application of a fluoride treatment such as toothpaste, varnish or restorative material and is then released into the saliva over time [19, 20]. Fluoride can remain on dental hard tissue, the oral mucosa or within the dental plaque. Fluoride retention, especially in dental plaque, is clinically beneficial since it can be released during cariogenic challenges to decrease demineralization and enhance remineralization [9].

1.4.2. Role of Fluoride in bone graft materials

Physicochemical studies of Fluorapatite (FAp) versus Hydroxyapatite (HAp) samples demonstrate an increase in density as Fluoride ions increase [38, 39]. Fluoride has the ability to accelerate the process of crystallisation of calcium phosphate as well as that of mineralization during bone formation [40, 41, 42]. In addition, there is substantial evidence that F^- utilised for osteoporosis treatment can effectively accelerate bone formation while also increasing bone mass [43, 44]. In vitro, the F^- furnished by F^- -containing bone substitutes enhanced osteogenic cell proliferation and differentiation [45, 46, 47, 48]. It has also been observed that the activity of the enzyme Alkaline phosphatase (ALP) improves mildly in the presence of fluoride. [49]. ALP is the most well-known biochemical indicator of osteoblast activity, as it promotes mineralization of the bone extracellular matrix (ECM) by phosphate hydrolysis [50]. Hence, Fluoride-containing bioactive glasses can be successfully employed in bone graft applications.

1.4.3. Fluorapatite vs. Hydroxyapatite

Dental caries is an infectious disease caused by the complex interaction of cariogenic (caries-causing) bacteria with carbohydrates (i.e., sugars) on the tooth surface over time. Cariogenic bacteria metabolize carbohydrates for energy and produce organic acids as byproducts. The acids lower the pH in the plaque biofilm. [27]

The hydroxyapatite of tooth enamel is primarily composed of phosphate ions (PO_4^{3-}) and calcium ions (Ca^{2+}). Under normal conditions, there is a stable equilibrium between the calcium and phosphate ions in saliva and the crystalline hydroxyapatite that comprises 96% of tooth enamel. When the pH drops below a critical level (approximately 5.5 for enamel, and 6.2 for dentin), it causes the dissolution of tooth mineral (hydroxyapatite) in a process called demineralization. When the natural buffer capacity of saliva elevates pH, minerals are reincorporated into the tooth through the process of remineralization. [27, 28, 29]

When the pH on the tooth surface becomes acidic, phosphate in oral fluids combines with hydrogen ions (H^+) to form hydrogen phosphate species. Under these conditions, phosphate is “pulled” from tooth enamel to restore phosphate levels in the saliva, and the hydroxyapatite dissolves. As pH returns to normal, the calcium and phosphate in saliva can recrystallize into the hydroxyapatite, remineralizing the enamel.

Caries is simply the result of a series of demineralization/remineralization cycles where, over time, demineralization conditions prevail. The caries process can be affected in several ways. One of the most effective methods to prevent caries is by promoting remineralization and slowing down demineralization. This can be accomplished with fluoride therapy. [23, 24, 25]

When fluoride is present in oral fluids (i.e., saliva), fluorapatite, rather than hydroxyapatite, forms during the remineralization process. Fluoride ions (F^-) replace hydroxyl groups (OH^-) in the formation of the apatite crystal lattice. In fact, the presence of fluoride increases the rate of remineralization.

Fluorapatite is inherently less soluble than hydroxyapatite, even under acidic conditions. When hydroxyapatite dissolves under cariogenic (acidic) conditions, if fluoride is present, then

fluorapatite will form. Because fluorapatite is less soluble than hydroxyapatite, it is also more resistant to subsequent demineralization when acid challenged.

Caries is a sub-surface phenomenon. With fluoride treatment, a non-cavitated lesion can be remineralized with fluorapatite and have greater resistance to subsequent demineralization than hydroxyapatite. Even when available at very low concentrations, fluoride is effective as an anti-caries agent. [23, 25, 26].

Also, Fluorapatite was found to boost osteoprogenitor cell proliferation and differentiation, accelerate bone formation and increase bone mass at much higher levels than that done by Hydroxyapatite.

1.5. Dental Materials

Dental products are specially fabricated materials, designed for use in dentistry. There are many different types of dental products, and their characteristics vary according to their intended purpose:

A. Dental Cements : Dental Cements are the materials that set intraorally and are commonly used to join a tooth and a prosthesis or restoration of the decayed tooth. Dental Cements have been used in dentistry for a very long time now. They are used in restorative, endodontic, orthodontic, periodontic as well as surgical procedures. The last few decades have seen a host of changes in dental cement composition and the introduction of newer, advanced biocompatible materials.

- i. **Zinc Phosphate Cements:** Zinc Phosphate is the oldest dental cement. Zinc Phosphate cements have good compressive strength, excellent thermal insulation ability, and they don't dissolve in oral fluids. However, they don't offer chemical adhesion, and can even cause pulp irritation and lead to poor aesthetics.

- ii. **Zinc Polycarboxylate Cements** : Zinc Polycarboxylate cements were devised by Dennis Smith in 1968. This is the first cementing system that arose as a result of the effort to obtain an adhesive cemented agent that could be firmly attached to the tooth structure and it is also known as polyacrylate cement. Polycarboxylate cements can be easily manipulated, and cause significantly less pulpal irritation due to the larger size of polyacrylic acid molecules. Although these cements cannot be used for restorative purposes because the cement is opaque.

- iii. **Glass Ionomer Dental Cements** : Glass Ionomer cements are tooth coloured materials, introduced by Wilson & Kent, soon after Zinc Polycarboxylate cements in 1972. It combines the properties of silicate cements and polycarboxylate cements. Glass ionomers have excellent translucency and very low film thickness. They are used primarily for metallic and porcelain-fused-to-metal restorations, as they can chemically bond to stainless steel, tin-plated noble metals, and base metals. Pulpal response to glass ionomer is favourable due to high buffering capacity of hydroxy apatite and the large molecular weight of polyacrylic acid, which prevents entry into dentinal tubules. Glass ionomer can act as a good marginal seal and offer biocompatibility, but it's also less sensitive compared to composites. They offer low resistance to fractures and wearing. Glass-ionomer cements are based on the acid-base reaction of silicate glass-powder (calciumaluminofluorosilicate glass) [21] and polyacrylic acid, an ionomer. This reaction produces a powdered cement of glass particles surrounded by matrix of fluoride elements and is known chemically as glass polyalkenoate [22]. It is on the World Health Organization's List of Essential Medicines.

B. Dental Lining Materials : Dental lining materials are used during restorations of large cavities, and are placed between the remaining tooth structure and the restoration material. The purpose of this is to protect the dentinal tubules and the sensitive pulp, forming a barrier-like structure. Various materials used for dental linings are:

- i. **Calcium Hydroxide**: The alkaline nature promotes anti-bacterial atmosphere in the oral cavity. Its low thermal conductivity can provide thermal insulation [22]. Additionally, it is

radiopaque and shows good restorative material compatibility [22]. But $\text{Ca}(\text{OH})_2$ has a lot of disadvantages too, as in its viscous consistency makes it difficult to apply to cavities in thick sections. Also, it is soluble in oral fluids [22] and has low compressive strength.

- ii. **Polycarboxylate Cement:** Polycarboxylate Cements have decent compressive and tensile strength [22]. It is radiopaque and compatible with most restorative materials. It shows good adhesive and insulation properties. But it is mildly acidic and can thus irritate the pulp. It is hard to handle due to strong bond with stainless steel instruments and since it turns rubbery during setting reaction thus hard to manipulate in deep cavities.
- iii. **Zinc oxide eugenol :** Zinc oxide eugenol has the lowest compressive and tensile strength in relative to the rest of the liners that are clinically used. Zinc oxide eugenol can be used as linings in deep cavities without causing harm to the pulp, due to its obtunding effect on the pulp as well as its bactericidal properties due to Zinc. However eugenol may have an effect on resin based filling materials as it interferes with the polymerization and occasionally causes discoloration.
- iv. **Glass Ionomer Cements :** GIC has the strongest compressive and tensile strength out of all the linings. GI is used as a lining material as it is very compatible with most restorative materials, insulates thermally and electrically and adheres to enamel and dentine. Lining GI contains glass of smaller particle sizes in comparison to its adhesive restorative mix to allow formation of a thinner film. Some variations are also radiopaque which makes it good for X ray cavity detection. In addition, GI is bacteriostatic due to its fluoride release from un-reacted glass cores [22].

C. Dental Fillings: Dental restorative materials or fillings are used to replace tooth structure loss, usually due to dental caries (dental cavities), but also tooth wear and dental trauma. On other occasions, such materials may be used for cosmetic purposes to alter the appearance of an individual's teeth.

The ideal restorative material would be identical to natural tooth structure in strength, adherence, and appearance. The properties of an ideal filling material can be divided into four categories: physical properties, biocompatibility, aesthetics and application.

- Requisite physical properties include low thermal conductivity and expansion, resistance to different categories of forces and wear such as attrition and abrasion, and resistance to chemical erosion. There must also be good bonding strength to the tooth. Everyday masticatory forces and conditions must be withstood without material fatigue.
- Biocompatibility refers to how well the material coexists with the biological equilibrium of the tooth and body systems. Since fillings are in close contact with mucosa, tooth, and pulp, biocompatibility is very important. Common problems with some of the current dental materials include chemical leakage from the material, pulpal irritation and less commonly allergy. Some of the byproducts of the chemical reactions during different stages of material hardening need to be considered.
- Radiopacity in dental materials is an important property that allows for distinguishing restorations from teeth and surrounding structures, assessing the absorption of materials into bone structure, and detecting cement dissolution or other failures that could cause harm to the patient.
- Ideally, filling materials should match the surrounding tooth structure in shade, translucency, and texture.
- Dental operators require materials that are easy to manipulate and shape, where the chemistry of any reactions that need to occur are predictable or controllable.

People have been using dental fillings for nearly 10,000 years. According to a recent discovery, beeswax was used to make a filling for a young man in Italy around 6,500 years ago.

- i. **Amalgams:** Various metals were used to fill dental cavities during the nineteenth century (1801-1900). Silver, gold and tin were among the early dental filling materials. The use of dental amalgams became more popular as the century progressed. The amalgams, are by definition, a mixture, composed of tin, copper, silver, and mercury. Within 20 years, there was widespread concern about the use of mercury, owing to both its ineffectiveness as a

filling material and its negative health effects on the human body. Mercury poisoning, cancer, and multiple sclerosis were among the most serious side effects of mercury on human body.

- ii. **Gold fillings:** Gold fillings are composed of an alloy of gold with copper etc. Gold dental fillings are very durable, lasting 20 years or more, but it is also the most costly. Gold fillings also necessitate more than one visit to the dentist because impressions must be created at a dental laboratory. Furthermore, since gold fillings don't match the natural colour of the teeth, many people find it visually unappealing.
- iii. **Porcelain:** Porcelain fillings resemble real teeth and are a good option for keeping the natural appearance of a tooth. They are, however, more fragile than other materials. They are classified as indirect fillings because they are not applied directly to the tooth. Instead, a mould of the tooth that needs to be repaired is made and sent to a lab. The lab will then craft an inlay or a replacement tooth. Indirect fillings necessitate more than one visit to the dentist due to the need to send the mould away.
- iv. **Dental Composites:** A composite filling is typically composed of acrylic resin and powdered glass. When placed in a visible location, it can be colour matched to existing teeth, allowing it to blend in with the smile. As a result, white filling is an appealing option for a natural appearance. After preparing the tooth, the composite material is applied in layers and hardened with a special light. When all of the layers are finished, the resin is ground to fit the tooth and polished to prevent stains and wear. But composite fillings are not as strong as metal fillings and are not the most appropriate for load-bearing applications.
- v. **GIC:** Glass Ionomer Cements are also popular for dental filling applications. They are biocompatible with the dental pulp and are tooth-coloured. One of the major advantages of GI compared to other restorative materials is that they can be placed in cavities without any need for bonding agents. They are not subject to shrinkage and micro-leakage, as the

bonding mechanism is an acid-base reaction and not a polymerization reaction. Glass ionomers contain and release fluoride, which is important to preventing carious lesions. The most important disadvantage of GI is lack of adequate strength and toughness.

1.6. Scope & Application of the presented research work

In the presented research work carried out on Bioactive glasses, Fluoride (F^-) has been incorporated into the S53P4-based bioactive glass formulations to carry out specific therapeutic functions such as facilitating remineralization of teeth and bones, preventing demineralization of teeth and bones, increasing the anti-bacterial efficacy etc. Alumina (Al_2O_3) has been incorporated into the bioactive glasses in order to enhance the overall mechanical strength of the glass, so that it can be considered for load-bearing applications. Bioactivity and other properties of thus synthesised glasses were measured by appropriate means.

The synthesised bioactive glasses could play pivotal roles in dentistry as the major component of Glass Ionomer Cements (GIC) and Composite Dental fillings employed as dental cements, dental linings and dental restorations. They could also serve as key constituents of bone grafts and bone fillers.

2. Literature Review

M. Jokinen et al. used AFM to analyse the nanoscale surface structure of bioactive glass S53P4 as a function of immersion time in simulated bodily fluid. Prior to the formation of calcium phosphate, changes in the glass surface occurred, which were investigated further using FTIR to determine the chemical composition of the surface. Local super-saturation sites created by nanoscale modifications for calcium phosphate nucleation. The nanoscale dimensions are similar to those of sol-gel generated SiO₂ and TiO₂ surfaces, which have been shown to aid calcium phosphate production in vitro. The surface has a lot of nanoscale roughness, usually in the form of 5-50 nm "surface holes." The peak heights range from 2 to 25 nanometers. The characteristic peak for Si-OH at 830-910 cm⁻¹ becomes stronger with time, according to the DRIFT FT-IR data, and it is strongest for samples immersed in SBF for 8 and 24 hours. The P-O-P vibration at 900-970 cm⁻¹ is significant before immersion and weakens as the Si-OH peak becomes stronger, similar to the Si-OH results. [51]

Helena Yli-Urpo et al. examined the antibacterial effects of glass ionomer cements incorporating bioactive glass S53P4 on oral microbes in vitro. On *Streptococcus mutans* and *Candida albicans*, the antimicrobial effects of two glass ionomer cements (GICs), GC Fuji II and Fuji II LC, mixed with varying percentages (0 wt. %, 10 wt. %, and 30 wt. % of the total powder weight) of bioactive glass S53P4. Only GICs containing 30 wt. % BAG reduced *S. mutans* growth in the agar diffusion test. The ingredients had no effect on the pH of the *S. mutans* culture at the end. Within 10 minutes, the number of viable *S. mutans* numbers had dropped dramatically. All GICs containing BAG in water suspension had a pH that was 0.6-2.8 pH units higher than equivalent GICs without BAG. When compared to GICs, adding 30wt percent BAG to the material enhanced Fluoride release, but GICs with 10 wt. % BAG released the same amount of Fluoride. Commercially available GICs, as well as a GIC disc containing 30% BAG, have antibacterial activity against *S. mutans*. Both *S. mutans* and *C. albicans* were susceptible to BAG's antibacterial properties. [52]

Matthias Zehnder et. al. carried out an in vitro evaluation of bioactive glass S53P4 as an endodontic medication. Aqueous calcium hydroxide or a bioactive glass S53P4 (Bioactive Glass) powder suspension were used to treat standardized bovine dentin blocks contaminated with *Enterococcus faecalis*. After 5 days, the Bioactive glass suspension had completely cleared the infection in the sampled dentin layers. The pH of root dentin did not change when bioactive glass was put in the root canals of removed teeth. Facultative bacteria may dominate the flora in teeth following failed root canal operations. BAG's efficiency in the root canal system may be hampered by blood, tissue remains, clogged dentinal tubules, and a variety of other confounding variables. Because of its great tolerance for an alkaline environment, which is due to the proton pump in this species, calcium hydroxide cannot eradicate *E. faecalis* from dentinal tubules. With increasing distance from the hydroxide ion source, i.e. the calcium hydroxide medicine, the pH of root dentin drops due to its high buffering capacity. Because bioactive glass's ability to create an alkaline environment has been linked to its antibacterial properties, pH variations in root dentin were measured in removed teeth treated with a bioactive glass or calcium hydroxide suspension. In the BAG dentin samples, the percent \log_{10} CFU value of *E. faecalis* was approximately 60% lower than the control, indicating a reduction in absolute CFU counts of more than 99%. No live bacteria were found in dentin BAG suspensions with the other microbes examined. [53]

Ari-Pekka Forsback et. al. examined the mineralization of dentin induced by treatment with bioactive glass S53P4 in vitro. Dentin tubules can be blocked with a calcium phosphate layer identical to the primary inorganic component of dentin using a calcium phosphate precipitation process. Mineralization happens in physiologically neutral solutions such as simulated body fluid and re-mineralization solution after treatment with bioactive glass S53P4 or standard commercial glass. The dentin is totally coated by the CaP layer after 14 days of mineralization, while the dentin decalcifies after 14 days of immersion in RMS. Pretreatment with BAG reduces the degree of dentin decalcification during the mineralization process. After 15 minutes and 24 hours of immersion, the relative amount of silicon grew from 0.5 to 9.5 percent. When the discs were incubated in RMS without BAG pretreatment, the weight loss was significantly higher than when they were incubated in RMS with BAG pretreatment. Dentin mineralization with BAG pretreatment in SBF resulted in a dense and homogenous coating of CaP on the dentin surface,

covering all of the tubules. For CaP precipitation, silica on dentin acts as a heterogenic nucleation centre. Ca^{2+} released from the BAG enhances apatite's ionic activity product, which promotes CaP nucleation. Once created, apatite nuclei consume calcium and phosphate ions from the surrounding SBF, as well as possibly from saliva. [54]

Toshiyuki Itota *et. al.* investigated how much total and free fluoride ions were released from four fluoride-containing resin-based composites (Heliomolar (HE), UniFil S (UF), Beautifil (BE), and Reactmer paste (RP)) and one glass ionomer cement (Ketac-Fil Plus Aplicap (KF)). Five disc specimens of each material were made and the fluoride release was measured at 1, 2, 4, 7, 14, 21 and 28 days. Using an ion-selective electrode (ISE) and ion chromatography, the amounts of total and free fluoride ions liberated from materials were determined (IC). A ttest was used to statistically assess the data at a significance level of 0.05. The ISE method failed to identify fluoride release in HE, whereas the IC method did. The amount of free and total fluoride ions released by UF and BEp did not differ significantly. 0:05P: After 4 days, free fluoride ions in RP were considerably lower than total fluoride ions p, 0:05: At 7 and 28 days, KF indicated a significant difference between total and free fluoride ions p, 0:05. The amount of free and total fluoride ions released from dental materials was affected by the type of fluoride used in the materials. [55]

Helena-Yli Urpo *et. al.* examined compound alterations and tooth mineralization effects of glass ionomer cements by an *in vivo* study including bioactive glass (S53P4). Bioactive restorative materials were created by combining bioactive glass with glass ionomer cement. The materials were created by combining 10–30 wt percent BAG powder with GIC particles to create powder and liquid. To test the materials' bioactivity and ability to mineralize dentin, SEM, EDS, and visual examination were used. We used both traditional cure and resin-modified light-curing GIC. The restorations formed homogenous CaP surfaces when in contact with Saliva Resin-modified GIC containing BAG. Resin-modified GICs incorporating BAG show promise as base and liner materials in deep cavities, as well as in the treatment of hypersensitive dentin. It can be inferred that BAG-containing resin-modified GICs have the ability to mineralize dentin *in vivo*. [56]

Matthias Zehnder *et. al.* explored whether dentin boosts the efficacy of bioactive glass S53P4 against an *Enterococcus faecalis* strain. BAG was suspended (pre-incubated) in saline at 37°C with or without human dentin powder, hydroxylapatite, or decalcified dentin at various time periods. After that, *Enterococcus faecalis* ATCC 29212 cells were introduced to the suspensions, and bacterial recovery was assessed using gentle sonication and without. Bacteria survival in test and control suspensions was monitored throughout time. The element composition of suspension supernatants was determined using atomic absorption spectrophotometry. Using specially produced solutions, the effects of pH, silica, and osmolarity on *E. faecalis* viability were investigated. In comparison to pure BAG solutions, BAG pre-incubated with dentin powder resulted in a substantial (P.05) reduction in viability. BAG killing efficacy was not increased by hydroxyl apatite or decalcified dentin. BAG 1 dentin powder had an additive action that was dose dependent, only occurred with solids in suspension, and increased with suspension time. In comparison to pure BAG suspensions or analogues incorporating hydroxyl apatite or decalcified dentin, BAG 1 dentin powder showed increased dissolution of glass components, particularly silicon. The observed behaviour was linked to enhanced BAG dissolution produced by dentin powder, resulting in higher pH and silica levels in the immediate area. [57]

Tuomas Waltimo *et. al.* observed the efficacy of bioactive glass S53P4 against *Porphyromonas gingivalis* and *Actinobacillus actinomycetemcomitans* in suspension with bone powder. The antibacterial activity of an inert borosilicate powder with the same particle size as the bioactive glass was taken as control. The ionic breakdown of bioactive glass S53P4 caused by dentin powder in suspension resulted in elevated local pH and silica levels, interfering with bacterial survival. The observations implied that the complex organic/inorganic dentin surface would operate as a recipient for ions in solution and hence as a catalyst for the bioactive glass disintegration. Controls were counts of bacteria suspended in a pure unbuffered saline solution. S53P4 Bioactive glass effectively suppressed multiplication of bacteria and exhibited antibacterial property on the bone powder. [58]

Tadashi Kokubo *et. al.* investigated the capacity of a material to generate apatite on its surface in a simulated body fluid (SBF) with ion concentrations almost equivalent to that of human blood plasma is typically used to assess its bone-bonding ability. The validity of this method for testing bone-bonding ability, however, has not been thoroughly investigated. The history of SBF is discussed, as well as the relationship between the ability of apatite to form on various materials in SBF and their in vivo bone bioactivities, as well as some examples of the development of novel bioactive materials based on apatite production in SBF. It was determined that examining apatite formation on a material in SBF is effective for predicting a substance's in vivo bone bioactivity, and that employing this method can significantly minimise the number of animals employed in animal investigations and their time. [59]

Ulrich Lohbauer *et. al.* examined dental glass ionomer cements as permanent filling materials: properties, limitations, and future trends. Because of their unique qualities, glass ionomer cements (GICs) are therapeutically appealing dental materials. They can be used as restorative and luting materials. This includes qualities such as adherence to moist tooth structures and base metals, anticariogenic properties from fluoride release, thermal compatibility with tooth enamel, biocompatibility, and low toxicity. Because of their ease of usage and exceptional biocompatibility among direct restoratives, GIC are preferred restorative materials. Their extensive usage in dentistry as a filler material in stress-bearing applications is limited due to poor mechanical qualities such as low fracture strength, toughness, and wear. Glass ionomer cements are commonly utilised as a temporary filling material in the posterior dental region. Several attempts to improve their mechanical properties are still underway, and some experts predict that GIC will have a bright future as a dental filling material with a wide range of applications. The need to reinforce those cements has prompted an increase in research on reinforcing and strengthening approaches. [60]

AR Prabhakar *et. al.* carried out an in vitro study to compare the remineralizing effects and surface microhardness of glass ionomer cements including S53P4 bioactive glass. Bioactive restorative materials were created by modifying glass ionomer cements (GICs) by adding

bioactive glass (BAG) to GIC. The re-mineralization effects of the study materials on dentin were investigated using polarised light microscopy (PLM). The Vickers micro-hardness of the experimental materials was also assessed. Glass ionomer cement (GIC)-BAG composites were created by combining 10% BAG particles with conventional cure and resin-modified GIC powders. Eighty removed mandibular teeth were restored with Class V restorations, divided into four groups of 20 teeth each. After pH cycling, 100 μ m slices of the teeth were studied under a polarised light microscope. Before mechanical tests, the materials were formed into 80 cylindrical specimens and immersed in water for 7 and 30 days. On the restoration-dentin interface, resin-modified GIC containing BAG showed a thick homogeneous layer of mineralization. Surface microhardness was higher in the traditional cure GIC-based materials than in the resin-modified materials. Following cavity replacement with experimental materials, the teeth were treated to a pH cycling model, which involved exposing the specimen to alternate remineralizing and demineralizing solutions. Because dental caries is a process of alternating demineralization and re-mineralization phenomena that is a direct function of settings that maintain a critical pH in the mouth, it recreates a dynamic situation. Bioactive glass has the ability to remineralize artificially carious enamel and dentin, according to Raman spectroscopy. The addition of BAG to GIC affects the materials' mechanical characteristics to some degree. As a result, their clinical use should be limited to applications where their bioactivity is helpful, such as root surface fillings, deep cavity base and liner materials, and the treatment of hypersensitive dentin. [61]

Jonathan Massera et. al. investigated the crystallization mechanism of the bioactive glasses 45S5 and S53P4. Differential thermal analysis (DTA), optical microscopy, and scanning electron microscopy were used to investigate the crystallisation kinetics of two marketed bioactive glasses, 45S5 and S53P4 (SEM). For two glass fractions, fine powder (45 μ m) and coarse powder (300–500 μ m), thermal characteristics, crystallisation activation energy, and the Johnson-Mehl-Avrami (JMA) exponent were calculated. The crystallisation behaviour of 45S5 differed significantly between the two fractions, whereas the crystallisation behaviour of S53P4 was unaffected by particle size. For both size fractions, the JMA exponent of S53P4 showed surface crystallisation. The coarse powders of S53P4 had the highest nucleation rate at 608 $^{\circ}$ C. The increased SiO₂ concentration of S53P4 was blamed for the higher maximum nucleation temperature. Together

with DTA data, the nucleation temperature range of these two glasses allows for the development of guidelines for modifying thermal treatment parameters to obtain acceptable glass-to-crystal ratios. With a controlled glass-to-crystal ratio, both glasses can be treated into glass-ceramics. [62]

S. Fagerlund *et al.* investigated porous implants fabricated of bioactive glass S53P4 for phase composition and in vitro bioactivity. The implants had a modest mechanical strength that rose with sintering temperature, from 0.7 MPa at 635 °C to 10 MPa at 1000 °C. pH measurements and ion analysis with inductively coupled plasma optical emission spectrometry were used to assess changes in the composition of simulated body fluid (SBF), the immersion solution. The implants were sintered at temperatures ranging from 600 - 1000 °C. Even while there was minor surface crystallisation, consolidation took place mostly by viscous flow sintering over the entire temperature range investigated. Scanning electron microscopy–electron-dispersive X-ray analysis was used to confirm the formation of a calcium phosphate layer on the implant surfaces. All of the samples developed a calcium phosphate layer when immersed in SBF, although the shape of this layer was influenced by the surface crystalline phases. On amorphous and semi crystalline implants comprising both primary and secondary $\text{Na}_2\text{O} \cdot \text{CaO} \cdot 2\text{SiO}_2$ crystals, hydroxyapatite developed more rapidly than on implants containing only primary crystals. Only a few narrow necks between undeformed particles were formed when the implants were sintered at 600 °C, resulting in very brittle particle compacts. At 635 °C, there was significant neck expansion but no visible crystal formation. The viscosity of S53P4 drops from roughly 109 dPas at 600 °C to 108.4 dPas at 634 °C, resulting in a melt viscosity acceptable for the sintering of porous structures made of glasses. Consolidation of partially crystallised particles proceeded primarily via viscous movement of the remnant glassy phase, as evidenced by the deformation of initially irregular particles into particles with rounded edges and convex surfaces, as well as simultaneous neck development. The layer structure and thickness varied depending on the heat treatment temperature. Surface crystallisation of S53P4, which forms $\text{Na}_2\text{O} \cdot \text{CaO} \cdot 2\text{SiO}_2$, began at 650 °C, and secondary crystals of $\text{Na}_2\text{Ca}_4(\text{PO}_4)_2 \cdot 2\text{SiO}_4$ were found at temperatures ranging from 850 to 1000 °C. The viscous movement of the remnant glassy phase was primarily responsible for sintering. [63]

Lukasz Pajchel *et. al.* carried out solid-State NMR and Raman Spectroscopic Investigation of Fluoride-substituted apatites. Heating causes loss of OH⁻ groups in both HAp and fluoridated samples. On the other hand, the crystallinity increased for HAp and decreased for Fluoride-substituted apatite with heating temperature. Raman spectroscopy and NMR studies established that the powders substituted with fluoride ions were not pure fluorapatite (FAP) but do contain some OH⁻ groups in the crystal structure. Both the synthetically prepared Hap and FAP had crystals with a shape similar to that of biological apatite, as revealed by SEM. [64]

J. McAndrew *et. al.* examined the use of bioactive glass S53P4 (BonAlive) in the treatment of chronic osteomyelitis. In recent years, the use of bioactive glass in conjunction with antimicrobial therapy has emerged as a promising new treatment option. In three patients, bioactive glass S53P4 was used in combination with intravenous and oral antibiotics to treat persistent osteomyelitis (two male, one female). The time between initial diagnosis and therapy ranged from 16 months to 16 years, and all three patients had previously had repeated debridements and antibiotic regimens with little success. All haematological and biochemical markers have returned to normal, and discomfort and function in the affected limbs have disappeared. All antibiotics have been withdrawn, and there is no sign of osteomyelitis on radiography. The bioactive glass has become a part of the surrounding bone. Between the glass surface and the surrounding bodily fluid, ions (H⁺, Na⁺, Ca²⁺) exchange. This results in the formation of silanol groups, which are followed by a layer of silicon dioxide. Over this, an amorphous calcium phosphate (ACP) layer forms, which eventually crystallises into hydroxyapatite (HAp). After the HAp layer is created, growth factors are absorbed, and osteoprogenitor cells migrate inward, triggering the synthesis of extracellular matrix and new bone formation. Antibacterial qualities are likely complex, involving the establishment of a local alkaline environment as well as the material's resistance to bacterial adherence and biofilm formation. The combination of mesenchymal stem cells and growth factors like vascular endothelial growth factor (VEGF) improves the materials' ability to heal tissue defects and drive neovascularization. [65]

Rayees Ahmad Shiekh *et. al.* created a nanohydroxyapatite-silica powder using an ethanol-based sol-gel method. FTIR, ^{29}Si CP/MAS NMR, EDX, and XRD spectroscopy were used to analyse the produced powder in commercial glass ionomer powder (Fuji II GC). The ^{29}Si CP/MAS NMR data revealed a higher degree of silyl species cross-linking between silica and GIC, making the Nano-HA-Silica-GIC composite more stronger. The morphology of the produced powder was investigated using high-resolution transmission electron microscopy (TEM) and scanning electron microscopy (SEM). The results demonstrated that a larger nanosilica content resulted in a denser and stronger GIC. As a result, the use of nanohydroxyapatite-silica-GIC with improved characteristics is expected to have a significant clinical impact, particularly in stress-bearing areas. [66]

Istvan Gergely *et. al.* examined S53P4 bioactive glass and gentamicin impregnated polymethylmethacrylate beads in vitro for antibacterial activity. During the 24 hours of incubation, the number of colony forming units (CFU) of *Staphylococcus aureus*, *Staphylococcus epidermidis*, *Escherichia coli*, and *Klebsiella pneumoniae* was determined hourly by Standard Plate Count. BAG granules were nearly as efficient as gentamicin-impregnated PMMA beads against *S. aureus*, with no statistically significant differences. PMMA beads, on the other hand, had a better antibacterial activity against *S. epidermidis* and *K. pneumoniae*. Granule size and contact time had a big impact on BAG's antibacterial efficacy. In the case of S53P4 BAG granules, there was a statistically significant association between pH values and the quantity of CFU. S53P4 bioactive glass can be a good alternative in the local therapy of osteomyelitis because it is biocompatible and biodegradable. We demonstrated statistically significant changes in bacterial viability under the influence of S53P4 BAG granules versus PMMA beads in the cases of *S. epidermidis* and *K. pneumoniae*, where PMMA beads had a superior antibacterial effect. The antibacterial action of S53P4 BAG appears to be highly dependent on particle size: when compared to the granular form, the powdered form's enhanced surface area allows for a faster and quantitatively superior release of alkali ions. The BAG releases ions like as sodium, calcium, phosphate, and silicate into its environment, which could explain the rise in pH and osmotic pressure that appears to be responsible for the compound's bactericidal activity. A minor increase in the quantity of *S. aureus* CFUs between 3 and 6 hours after contact with the S53P4 BAG

granules, followed by a sharp drop; this could be explained by a partial suppression of certain germs that remained viable for a few hours before being destroyed by the BAG. Several methods, including proton collection and retention inside the bacterial cell (changes in cell surface layers, or enzymatic or carrier means) and increased acid production, can lead to bacterial adaptation to alkaline pH. [67]

Lorenzo Drago et. al. investigated different bioglass S53P4 formulations for antimicrobial efficacy and resistance selection against multidrug resistant bacteria. The capacity of bioglass to select for resistance and the antibacterial efficacy of two different formulations of bioglass BAG-S53P4 against multiresistant pathogens involved in bone infections. After being exposed to bioglass, scanning electron microscopy revealed cell shrinkage and membrane degradation. For *S. epidermidis* and *A. baumannii*, MIC values before exposure were comparable to MIC values after selective pressure with bioglass, whereas for *K. pneumoniae*, there was a twofold rise. Both formulations were able to kill all of the tested bacterial strains after 48 hours of incubation, with no change in MICs. Untreated cells, on the other hand, had a smooth and undamaged surface. *A. baumannii* cells had a mean diameter of 0.85 0.04 μ m in control samples and 0.56 0.01 μ m following treatment ($p < 0.01$). Similarly, the mean diameter of *S. epidermidis* cells in control samples was 0.74 0.09 μ m, while it was 0.63 0.02 μ m in treated samples ($p < 0.01$). The diameters of *K. pneumoniae* cells were also significantly different: 1.95 0.05 0.53 0.06 μ m in controls and 1.60 0.06 0.72 0.01 μ m in tests ($p < 0.01$). The alkaline ions released by the bioglass create a rapid rise in the pH and osmolarity of the surrounding environment, rendering it unsuitable for bacterial growth. The pH change is dependent on the bioglass composition, surface area to volume ratio, and system agitation rate, and is critical for bioglasses' antibacterial characteristics, as neutralisation of a strongly alkaline solution with bioactive glass has been found to abolish the antibacterial effect. Putty is made up of granules of the same size embedded in a polymeric gel that takes time to lose its consistency and resemble granules. Antibiotic use is one of the factors that leads to the selection of bacteria that can develop resistance, posing a severe threat to our ability to treat bacterial diseases. The bacterial cytoplasm has a larger concentration of solutes than the surrounding environment, resulting in a positive pressure on the cell membrane. Both the granules and the putty formulation have significant antibacterial activity and do not appear to select for resistance in the

microbiological strains studied, making them ideal bone substitutes for the treatment of bone infections, even when multiresistant strains are present. [68]

Shariq Najeeb *et. al.* examined nano-Sized fillers and bioactive nano-ceramics as modifications to glass ionomer cements. Nanotechnology is the utilisation of systems, changes, or materials with a size between 1 and 100 nanometers. By incorporating nano-sized fillers into RMGICs, lowering the size of the glass particles, and introducing nano-sized bioceramics to the glass powder, traditional GICs and resin modified GICs (RMGICs) can be nano-modified. Incorporating nano-sized apatite crystals, on the other hand, improves the mechanical characteristics of traditional GICs while simultaneously increasing fluoride release and bioactivity. Apatites can make the set cement chemically more stable, insoluble, and improve the binding strength with tooth structure by enhancing the crystallinity of the set matrix. Fluoride release can also help to prevent and treat secondary caries. The use of nano-modified glass ionomers in daily clinical dentistry is still limited due to a lack of long-term clinical research. In terms of flexural and tensile strength, commercially available nano-filled RMGIC (Ketac Nano) has no noticeable benefit over micro-filled RMGICs. Nano-filled RMGIC's bonding properties are still a source of concern. To determine the status of nano-modified GICs in clinical practise, mechanical, biological, and eventually clinical experiments are required. [69]

T. De Caluwé *et. al.* examined the effect of adding bioactive glass to glass ionomer cements on physico-chemical characteristics and biocompatibility. The melt process was used to make conventional aluminosilicate glass (ASG) and (modified) BAG. Setting time, compressive strength, and bioactivity of BAG-GIC were examined. Fourier transform infrared (FT-IR), scanning electron microscopy (SEM), EDS, and $(\text{PO}_4)^{3-}$ and Ca^{2+} uptake in SBF were used to assess surface alterations. A direct toxicity experiment was used to determine the biocompatibility of various BAG-GICs. BAG increases the bioactivity of the GIC, as evidenced by the production of an apatite (Ap) layer, particularly in CF9-containing GICs. More BAG increases bioactivity but reduces strength. The inclusion of Al^{3+} to the BAG composition boosts strength while lowering

bioactivity. Bioactivity is unaffected by decreasing particle sizes, although strength is reduced. The creation of an Ap layer appears to help the BAG-GICs' biocompatibility. Bioactive GICs may have various advantages over traditional GICs, including remineralization of demineralized tissue, bone and dental cell adhesion and proliferation, and tissue integration. When added in 20 wt% to a GIC, CF9 BAG-GIC combinations with a maximum of 10 mol% Al^{3+} are the most promising. [70]

Wan Nurshamimi Wan Jusoh *et. al.* examined the impact of sintering temperature on the physical and structural properties of Alumino-Silicate-Fluoride glass ceramics made from clam shell and soda lime silicate glass. Energy X-ray (EDX), density, linear shrinkage, X-ray Diffraction (XRD), Fourier Transforms Infrared (FTIR), and Field Emission Scanning Electron Microscopy (FE-SEM) were used to examine the composition of ASF glass ceramics with 25 wt. % SiO_2 - 20 wt. % CaO - 20 wt. % P_2O_5 - 20 wt. % Al_2O_3 - 15 wt. % CaF_2 . The sintering temperature affects the density and linear shrinkage of the samples. Furthermore, XRD data revealed that fluorapatite ($Ca_5(PO_4)_3F$) was a major phase in all samples, while FTIR corroborated the presence of silica and the creation of the CaP phase. The high Ca and Si concentration of CS and SLS glass, respectively, encourages the utilisation of waste materials in ASF composition manufacturing. When the sintering temperature was raised, FESEM examination revealed that grain size increased and a needle-like microstructure known as fluorapatite formed. The effect of various sintering temperatures on ASF glass ceramics was studied, and it was discovered that ASF glass ceramic samples sintered at 1000 °C produced the best results. e. The presence of an apatite phase in the composition of ASF glass ceramics is advantageous for dental applications. [71]

Hans Erling Skallevoid *et. al.* reviewed bioactive glass applications in dentistry. The chemistry of BAG is mimicking the natural hard tissues composition, and has a bioactive role in the regeneration of bones and teeth. In addition, various elements such as Si, P, Sr, Cu, F, Ag, Zn, and F can be added to the glass to enhance the bioactivity and antimicrobial properties. The structure and content of the glass, manufacturing procedures, and the rate of ionic dissolution all have an impact on bioactivity. The most bioactive glasses have a larger specific surface area and a greater dissolution rate, resulting in more rapid apatite formation. BAG's bioactive qualities make it

suitable for a variety of therapeutic applications in medicine and dentistry involving the regeneration of hard tissues. Dental restorative materials, mineralizing agents, as a coating material for dental implants, pulp capping, root canal therapy, and air-abrasion are some of its applications in dentistry, and it has applications in medicine ranging from orthopaedics to soft-tissue restoration. [72]

Sakthi Prasad *et. al.* elucidated the influence of CaF_2 on the structure, biocompatibility, and antibacterial characteristics of S53P4 glass. Molecular dynamics (MD) simulations were used to interpret and assess the role of integrated fluoride and its distribution inside the glass, and the results were compared to the modified random network (MRN) model. The steady substitution of CaF_2 for CaO in the base glass resulted in an increase in silicate network connection with a decrease in NBOs, as well as an increase in modifier cation interaction with fluoride ions. The antibacterial efficiency of fluoride-containing glasses was tested in an *E.coli* bacterial inoculum at varied doses (5, 10, and 20 mg/ml), and bactericidal action was observed. With the addition of fluoride: (i) the modifier cations are strongly attracted by the fluoride ions; (ii) the average coordination of Na and Ca per F is about 3.9 and 1.2, respectively, indicating that the strong affinity of Na than Ca, (iii) the channel region becomes narrow and the cluster regions enriched with fluoride ions grows, (iv) the association of modifier cations with NBOs gradually decreases with increase in fluoride ions, (v) due to reduced oxygen anions, the silicate network region becomes more cross-linked and leaner and (vi) the orthophosphate units which were initially present within inter-network region for fluoride free glass are shifted towards the interface between the network and inter-network region and leads to the formation of Si-O-P bonds. The use of CaF_2 instead of CaO appears to increase the polymerisation of silicate networks. The T_g of the glass was observed to steadily decrease as the amount of CaF_2 in the foundation glass increased. This decrease in T_g was discovered to be in opposition to the rising trend in NC Si values linked with the progressive increase in CaF_2 incorporation. Furthermore, due to the drop in T_g of glass with CaF_2 incorporation, ΔT of the glass was shown to steadily increase. With the steady incorporation of CaF_2 , a minor shift towards the negative side was detected, indicating a shielding effect linked with a marginal increase in Na^+ association around the fluoride ion. Apatite production was found on BG-2F glass with roughly 10.89 mol percent CaF_2 after 7 days of SBF immersion, but not on

BG-3F glass with higher fluoride content after 14 days of SBF immersion. Up to 7 days of SBF immersion, the release of fluoride ion from each CaF_2 inserted glass was consistently found to rise. The Si-F and P-F bonds were not present in the fluoride-containing bioactive glasses, according to MD simulations. This result demonstrates that CaF_2 does not act as a modifier (no Si-F linkages), but the reduction in CaO (modifier oxide) caused an increase in silicate network polymerisation. The thermal stability of the glasses was increased due to a lower glass transition temperature (T_g) caused by the presence of a bigger inter-network region made up of modifier cations fluoride and phosphates. [73]

Eline G. J. Thijssen et al. investigated injectable S53P4 bioactive glass material formulations for their ability to reduce the growth of five clinical pathogens. By incorporating a synthetic binder to retain glass particles, new injectable S53P4 putty materials have been produced. The researchers wanted to see how well they could get rid of five clinically important pathogens: methicillin-sensitive *Staphylococcus aureus* (MSSA), methicillin-resistant *Staphylococcus aureus* (MRSA), *Enterococcus coli* (*E. coli*), *Enterococcus faecalis* (*E. faecalis*), and *Pseudomonas aeruginosa* (*P. aeruginosa*). S53P4 granules (500–800 μm) and S66 glass (45 μm) were used as controls. The materials were cultivated with pathogens in a Müller-Hinton II broth for a week with daily colony forming unit (CFU) counts to assess antibacterial capabilities. *P. aeruginosa* was completely eradicated and the quantity of CFUs of other pathogens was reduced in the S66 glass, but not in the S53P4 granules. The pH of the broths was initially between 7.14 and 7.35. The pH raised to values of 9 and higher after the biomaterials were added. The S66 powder demonstrated the greatest reduction in CFUs, with a 2 \log_{10} drop compared to the number observed in the growth controls. To ease the handling of S53P4 BAG granules, putty formulations containing S53P4 bioactive glass granules wrapped by a synthetic binder of polyethylene glycol (PEG) and glycerol were created. In vitro experiments, bacteriostatic materials frequently exhibit a minor reduction in growth in the first 18–24 hours, but bactericidal materials reduce more than 3 \log_{10} CFU/mL. The S53P4 granules' low pH could be related to the particle size of 500–80 μm , which was smaller than the other biomaterials evaluated, which had particles smaller than 45 μm . Antimicrobial resistance was elevated, highlighting the need for representative and repeatable in vitro studies that are predictive of the in vivo situation, as well as the development of new antimicrobial biomaterials. [74]

Francesco Baino *et. al.* explored the effect of surface-treatments on bio-inert materials. Some implanted materials are considered "bioactive" if they can develop a tight and chemically stable contact with living bone. This feature, which is inherent in specific glass compositions or can be generated by applying appropriate surface treatments to otherwise bio-inert metals, can be tested in vitro using immersion tests in simulated bodily fluid (SBF), which mimics the composition of human plasma. As a result, an apatite coating may grow on the material surface, and the presence of this "biomimetic skin" that resembles bone is thought to predict bone-bonding ability in vivo. The impact of testing factors (e.g., formulation and circulation of the solution) and material-related parameters on in vitro bioactivity testing procedures utilising SBF is highlighted in this review paper (e.g., composition, geometry, texture). [75]

Sharat Chandra Pani *et. al.* investigated the staining properties of a commercially available restorative glass ionomer cement to a formulation with carbon nanotubes and another with silver nanoparticles added to the powder of the same cement. Methodology. Twenty samples of a control glass ionomer cement (PULPDENT[®] Glass Fill[®], Pulpdent Corp., Watertown, MA, USA), a control cement reinforced with 0.0006 gm (0.03 percent by weight) of carbon nanotubes (Sigma Aldrich, St Louis MO, USA), and a control cement reinforced with 0.2 gm (10 percent by weight) of silver nanoparticles (NanocylTM, Nanocyl SA, Sambre After 1 hour, 24 hours, and 1 week, colour evaluations were conducted. The values of colour change were calculated. When compared to controlled glass ionomer cement specimens, carbon nanotube reinforced specimens showed less colour stability; nevertheless, both samples had much greater colour stability than silver nanoparticle reinforced glass ionomer samples. Conclusion. Within the restrictions of this work, it may be inferred that carbon nanotube reinforced glass ionomer cements are more colour stable than silver nanoparticle reinforced glass ionomer cements. [76]

Maria Cannio et. al. investigated, based on the emerging literature about the potential bioactivity and biocompatibility of these materials, particularly with reference to Bioglass 45S5, BonAlive, and 19-93B3 bioactive glasses, the use of bioactive glasses in dentistry, reconstructive surgery, and infection treatment can be considered broadly beneficial. Several studies have been conducted to (i) obtain bioactive glasses in various forms, such as bulk materials, powders, composites, and porous scaffolds, and (ii) study their potential biomedical uses. Although in vivo animal research provide an early glimpse into the biological performance of these systems and are an unavoidable step before clinical trials, only clinical investigations can illustrate how these materials behave in the complex physiological human milieu. [77]

Burcu Karakuzu-Ikizler et. al. investigated the effect and Alumina (1 wt%) incorporation on the in vitro bioactivity and biodegradation behavior of 45S5 bioactive glasses. The incorporation of Alumina (Al_2O_3) enhanced the Vickers hardness of bioglasses. All the bioglasses showed the hydroxyapatite layer formation after SBF treatment as confirmed by the FTIR, SEM and XRD analysis after dissolution in SBF, however, the bioactivity was impeded with increasing Alumina incorporation. Al_2O_3 inhibits bone-bonding, nonetheless the addition of Al_2O_3 as a part of the aluminosilicate crystal phase may overcome this problem as well as maintain an increment in the mechanical properties of glasses such as compressive strength and elastic modulus of the glass. [78]

Monica Bortolin et. al. assessed the effectiveness of BAG-S53P4 against biofilm produced in vitro by multiresistant bacterial strains. Multiresistant *Staphylococcus epidermidis*, *Acinetobacter baumannii* and *Klebsiella pneumonia* isolated from bone and joint infections were used in their study. Titanium discs covered by bacterial biofilm were incubated with BAG-S53P4 or inert glass as a control. The amount of biofilm on each titanium disc was evaluated after 48 hours of incubation by means of confocal laser scanning microscopy. Significantly lower total biomaterial volumes were observed for all strains after treatment with BAG-S53P4 when compared with controls. Moreover, the percentage of dead cells was significantly higher in treated samples than controls for all the tested strains. Owing to its osteoconductive and antibacterial and properties, t

use of BAG-S53P4 may be a successful strategy for the treatment of bone and prosthetic joint infections. [79]

Konstantinos Dimitriadis *et. al.* worked on developing alumina-containing bioactive glass-ceramics for dental implant applications. They found that the mechanical characteristics of the alumina-infused GCs outperformed those of titanium and zirconia dental implant materials, and their modulus of elasticity (27-34 GPa), microhardness (6.0-6.7 GPa), and fracture toughness (2.1-2.6 MPa m^{0.5}) were comparable to those of human jaw bone and dentine. The bioactivity of the synthesized GCs was perfectly maintained as demonstrated by the production of hydroxyapatite on their surface following immersion in SBF at 37°C. The addition of 1.7 weight% Al₂O₃ increased the temperatures of T_g, T_c, and T_p, widened the sintering window (T_c-T_g) by 10–20 K, and increased the E_a of crystallization, suggesting a retarding effect on the crystallization process. Besides bioactivity, a dental implant material must have the ability to distribute the load to the adjacent bone and, thereby, to maintain its density which means that if the values of the modulus of elasticity of the dental implant material and the adjacent bone are close to one another, then the stress distribution will approach the natural mode of distribution. [80]

3. Objectives of the project:

- To prepare S53P4 bioactive glass following melting-quenching-annealing route
- To prepare S53P4-based bioactive glasses after incorporating varying amounts of Calcium fluoride and Alumina.
- To find out the effect of substitution of CaO by CaF₂ and Al₂O₃ on the bioactive glass properties like glass transition and crystallization temperatures, density, antibacterial property and microstructure.
- To observe the dissolution characteristics of the synthesized bioactive glasses by measuring pH, fluoride ion concentration and weight loss after immersion in Simulated Body Fluid (SBF) and in artificial saliva.
- To study the structural characteristics of the glasses using XRD, FTIR and Raman Spectroscopy and correlate the properties with the structure of the glasses.

3. Objectives of the project:

- To prepare S53P4 bioactive glass following melting-quenching-annealing route
- To prepare S53P4-based bioactive glasses after incorporating varying amounts of Calcium fluoride and Alumina.
- To find out the effect of substitution of CaO by CaF₂ and Al₂O₃ on the bioactive glass properties like glass transition and crystallization temperatures, density, antibacterial property and microstructure.
- To observe the dissolution characteristics of the synthesized bioactive glasses by measuring pH , fluoride ion concentration and weight loss after immersion in Simulated Body Fluid (SBF) and in artificial saliva.
- To study the structural characteristics of the glasses using XRD, FTIR and Raman Spectroscopy and correlate the properties with the structure of the glasses.

4. Plan of the Work:

The present investigation was performed to study the development of Alumina & Fluoride-incorporated S53P4-based bioactive glasses prepared by the melting route. The effects of partial substitution of CaO by CaF₂ and Al₂O₃ on the glass structure and in-vitro dissolution were thoroughly studied followed by characterization of the glass in term of micro-structural analysis.

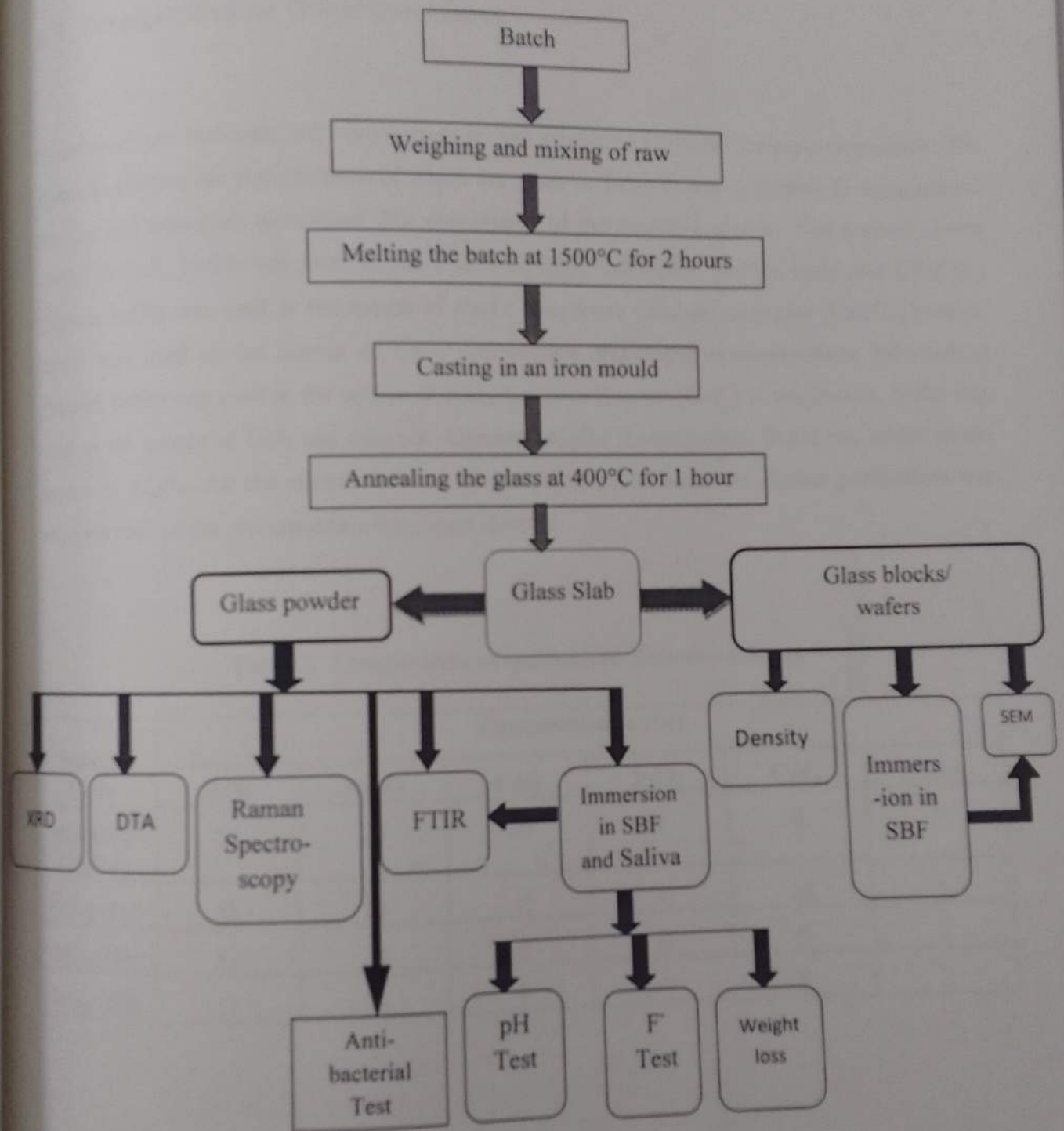
For this purpose, analytical grade reagents were used to prepare the bioactive glass samples. The reference glass composition was S53P4. The effect of partial substitution of CaO by CaF₂ and Al₂O₃ were investigated.

Each batch composition was thoroughly mixed for homogeneous mixing before melting of the batch at temperature where the viscosity of the melt was low enough for it to be bubble free. To minimize contamination from the crucible, Pt/Rh crucible was used for this melting with intermittent stirring with quartz rod. Casting into preheated rectangular mould was performed followed by annealing to prepare internal stress free glass slab. To confirm the amorphous nature, powder X-ray Diffraction Analysis (XRD) of the powdered sample was done. Bonding characteristics of the glass samples were assessed by Fourier-Transform Infra-red Spectroscopy (FTIR) and Raman Spectroscopy of the powdered samples. To identify the glass transition temperature and the crystallization temperature, differential thermal analysis (DTA) of powder sample was conducted.

In-vitro bioactivity evaluation is an important preliminary test of each bioactive glass. This property was assessed by measuring the pH & Fluoride ion concentration after immersion into simulated body fluid (SBF) and in artificial saliva for different immersion times from 1 hour to 28 days. The weight loss of the bioactive glasses were measured after immersion in artificial saliva after time intervals from 1 day to 28 days.

The microstructure of the synthesized glass samples were studied by Scanning Electron Microscopy (SEM) before & after immersion in SBF.

5. Process Flow Chart



6. Materials & Methods

6.1. Preparation of Bioactive Glass

Selection of raw materials and composition is very important for bioactive glass preparation. The bioactive glasses, the compositions of which are given in Table 2, were prepared by using normal melting and annealing techniques. For preparation of the bioactive glasses, fine grained Quartz [SiO_2] (Merck, India) was used as the source of SiO_2 , anhydrous Sodium carbonate [Na_2CO_3] (Merck, India) was used as the source of Na_2O , anhydrous Calcium carbonate [CaCO_3] (Merck, India) was used as the source of CaO , Ammonium dihydrogen orthophosphate [$\text{NH}_4\text{H}_2\text{PO}_4$] (Merck, India) was used as the source of P_2O_5 , Calcium fluoride [CaF_2] (LobaChemie, India) was used as the source of CaF_2 and calcined Alumina [Al_2O_3] (LobaChemie, India) was added as the source of Al_2O_3 . All the chemicals were of analytical grade, hence no further purification was required and all the raw materials were used directly.

Table 2. Composition of synthesised Bioactive Glasses

Sample Code	Composition (wt%)					
	SiO_2	Na_2O	CaO	P_2O_5	CaF_2	Al_2O_3
BG-A0F0 (S53P4)	53	23	20	4	0	0
BG-A1F10	53	23	9	4	10	1
BG-A2F9	53	23	9	4	9	2
BG-A3F8	53	23	9	4	8	3

6.1.1. Step 1 : Batch mixing

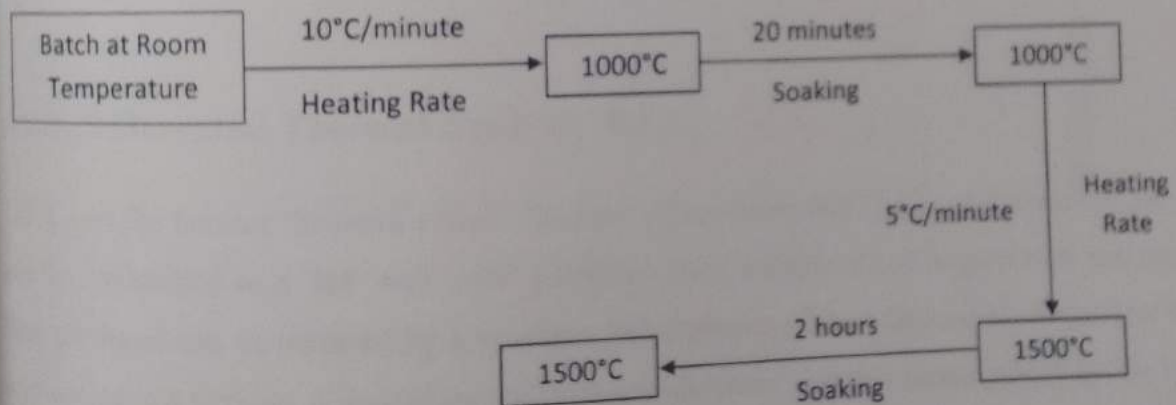
Appropriate proportions of the raw materials were weighed and were mixed homogenously for 40 minutes using an agate mortar and pestle to make the batches.

6.1.2. Step 2 : Melting

The batches were melted in a Platinum crucible inside a moving hearth furnace at 1500°C for 2 hours.

The batches were melted in a Platinum crucible inside a moving hearth furnace at 1500°C for 2 hours.

Melting Schedule :



6.1.3. Step 3 : Casting

The homogeneous melts at 1500°C were cast into a stainless steel mould pre-heated to 500°C.

6.1.4. Step 4 : Annealing

After casting, the glass samples were immediately transferred to a muffle furnace regulated at the temperature of 500°C for annealing in order to obtain thermal stress-free glass slabs. After 1 hour, the muffle furnace was left to cool to room temperature at a rate of 30°C/hour.

6.1.5. Step 5 : Making glass powder & blocks

The glass slabs obtained after annealing were wrapped in clean sheets of paper and hammered to obtain smaller glass blocks which were used to measure the density of the glass samples. The glass blocks were then smashed, crushed and ground to powder of -100 mesh size. These glass powders were used for various other characterisation tests like XRD, DTA, FTIR, Bioactivity tests etc.

6.2. Characterisation of Bioactive Glass

6.2.1. Differential Thermal Analysis (DTA)

DTA uses the famous 'Seebeck effect'. Seebeck effect states that if the junction of a thermocouple can be maintained as a 'hot' and 'cold' junction, then a feeble e.m.f is generated and the current thus produced can be detected by a sensitive galvanometer. When the sample under test is heated and cooled in a furnace, it undergoes physical and chemical changes accompanied by the liberation or absorption of energy (heat). However if an 'inert' sample (previously heated) is heated or cooled under the same standard condition as the active sample, it shows no such changes. Thus, if both the materials are heated together in the same furnace, a difference of temperature between the two occurs, and this can be detected and measured by a galvanometer.

Differential Thermal Analysis (STA449 F3/GD, NETZSCH) was carried out on the powdered bioactive glass samples from room temperature to 1000°C using powdered alumina as a reference material and the heating rate was 10°C / minute. The glass transition temperature as well as the glass nucleation and crystallization temperatures were obtained from the DTA results.

6.2.2. X-ray diffraction (XRD) :

Powder diffraction patterns are typically plotted as the intensity of the diffracted X-rays vs. the scattering angle 2θ . Peaks will appear in the diffraction pattern at 2θ values when constructive interference is at a maximum, that is, when Bragg's Law is satisfied.

$$n\lambda = 2d$$

[d = interplanar distance; λ = wavelength of X-ray; n = order of reflection]

In order to confirm that the glass samples prepared were completely amorphous and contained no crystalline phase, the fine glass powders were subjected to X-ray diffraction analysis (XRD). A DB-ADVANCE BRUKER diffractometer adopted Cu-K α radiation ($\lambda = 1.5405 \text{ \AA}$) with a tube voltage of 40 kV and current of 35 mA in a 2θ range between 10° and 70° . The scanning rate set to $2^\circ/\text{minute}$ was used in the present investigation.

6.2.3. Density measurement :

The densities of the prepared bioactive glasses were measured by Archimedes principle with Xylene as the immersion fluid. The measurements were performed at room temperature. Thin copper wire was used for immersing the samples (prepared bioactive glass blocks) into Xylene.

The density was determined from the following formula:

$$\text{Density} = \frac{M_2}{M_2 - M_1} \times \rho$$

M_2 = Mass of sample in air

M_1 = Mass of immersed sample

ρ = Density of liquid; here, density of Xylene = 0.87

6.2.4. pH & Fluoride ion (F^-) concentration measurement

6.2.4.1. Preparation of Simulated Body Fluid (SBF):

In 1991, Kokubo developed Simulated Body Fluid (SBF), which has become the most widely used solution for in-vitro investigation of bioactivity of bioactive materials. SBF is a metastable solution containing calcium and phosphate ions already supersaturated with respect to the apatite. The ion concentration of the simulated body fluid is nearly equal to that of human blood plasma and is given in Table 3.

Table 3. Ion concentration of Simulated Body Fluid and the human blood plasma

Ion	Ion Concentration (mM)							
	Na^+	K^+	Mg^{2+}	Ca^{2+}	Cl^-	HCO_3^-	HPO_4^{4-}	SO_4^{2-}
SBF	142.0	5.0	1.5	2.5	147.8	4.2	1.0	0.5
Human blood plasma	142.0	5.0	1.5	2.5	103.0	27.0	1.0	0.5

SBF was prepared as follows:

- (i) **Cleaning** : All the required bottles, flasks, beakers, measuring cylinders etc. were cleaned with dilute hydrochloric acid solution, sterilizing agent and deionised double distilled water in this order. Only Polypropylene vessels were used for SBF preparation and storage.
- (ii) **Dissolution of chemicals** : 750 ml of ultrapure deionised double distilled water was taken in a 1000 ml Polypropylene beaker and heated to a temperature of $37^\circ C$ on a magnetic stirrer equipped with heater, all the while stirring it continuously with the help of a cleaned magnetic needle.

Handwritten text, first paragraph, mostly illegible due to blurring.

Handwritten text, second paragraph, mostly illegible due to blurring.

Handwritten text, third paragraph, mostly illegible due to blurring.

Table 4. Reagents for preparation of SBF (pH 7.4, 1 litre)

Order	Reagent	Manufacturer	Amount
#1	NaCl	Merck, India	7.996 g
#2	NaHCO ₃	Merck, India	0.350 g
#3	KCl	Merck, India	0.224 g
#4	K ₂ HPO ₄ •3H ₂ O	Sigma-Alorich	0.228 g
#5	MgCl ₂ •6H ₂ O	Merck, India	0.305 g
#6	1N HCl	Merck, India	39 ml
#7	CaCl ₂	Sigma-Alorich	0.278 g
#8	Na ₂ SO ₄	Merck, India	0.071 g
#9	Tris Buffer [(CH ₂ OH) ₃ CNH ₂]	Merck, India	6.057 (+ as required for pH adjustment)
#10	1N HCl	Merck, India	As required for pH adjustment

6.2.4.2. pH Measurement in SBF:

The prepared bioactive glass powders were soaked in SBF at 36.9°C in the ratio of 1:50 (1 g powder soaked in 50 ml of SBF) and pH of the solution was measured at different time intervals — 0 hour, 1 hour, 2 hours, 4 hours, 6 hours, 8 hours, 12 hours, 18 hours, 24 hours (1 day), 2 days, 3 days, 5 days, 7 days, 10 days, 14 days, 21 days and 28 days— using Orion (Star A214) Thermo Scientific pH meter. Before pH measurement, the pH meter was calibrated each time with standard buffer solutions of pH 4, pH 7 and pH 9.2 at room temperature. pH values were recorded at the aforementioned time intervals.

6.2.4.3. Fluoride ion (F^-) concentration measurement in SBF:

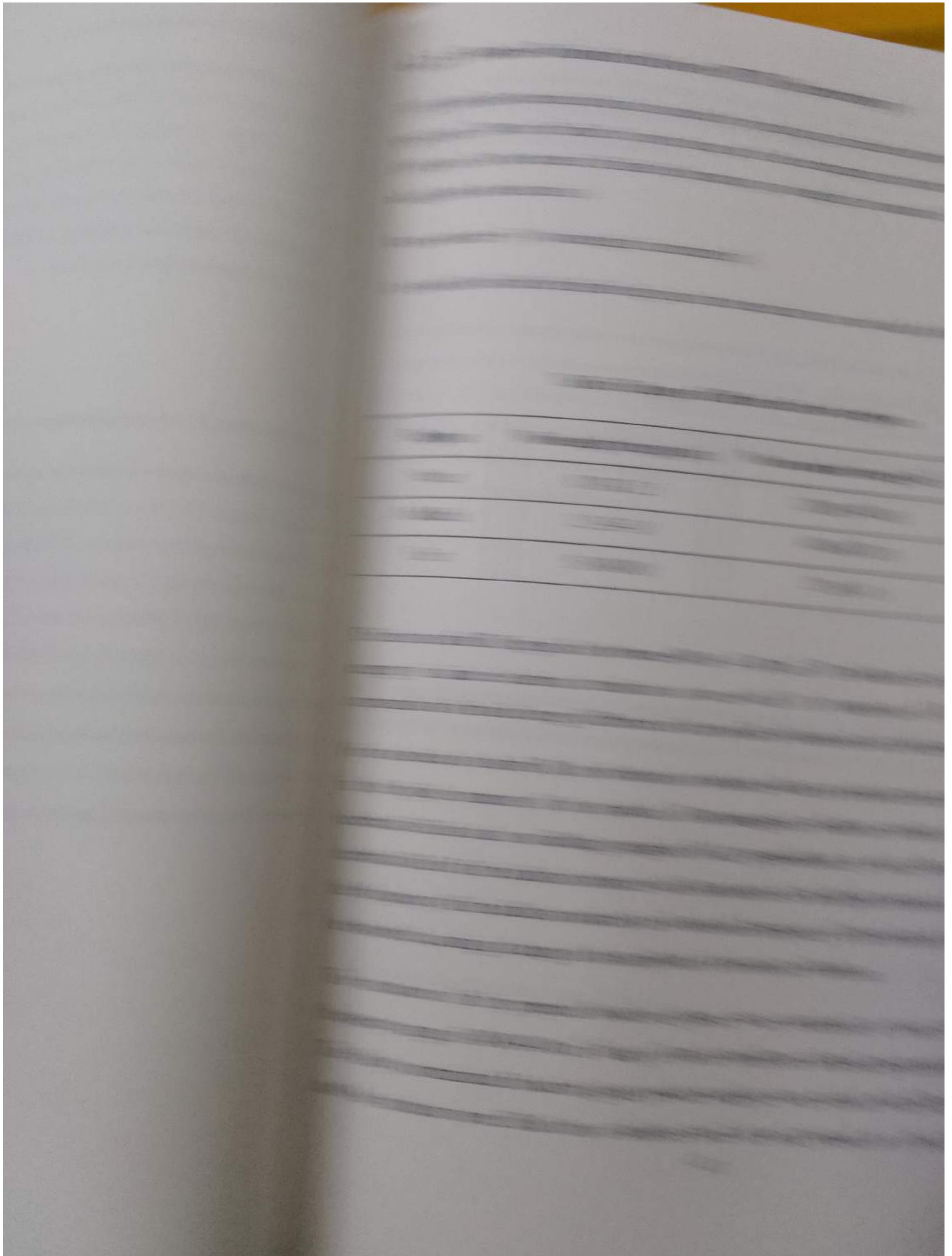
The prepared bioactive glass powders were soaked in SBF at 36.9°C in the ratio of 1:50 (1 g powder soaked in 50 ml of SBF) and the Fluoride ion concentration in the solution was measured at different time intervals — 0 hour, 1 hour, 2 hours, 4 hours, 6 hours, 8 hours, 12 hours, 18 hours, 24 hours (1 day), 2 days, 3 days, 5 days, 7 days, 10 days, 14 days, 21 days and 28 days — using Orion (Star A214) Thermo Scientific ISE meter. An ion-selective electrode (ISE) is a type of sensor used to determine the concentration of specific ions in an aqueous solution by converting the activity of that ion into an electrical potential which can be measured by a voltmeter. TISAB III solution was added to the test solution in the ratio of 1:10 (1 ml of TISAB III with 10 ml of the SBF solution to be tested for Fluoride ion concentration). TISAB III is a concentrated ISA (ion strength adjustment) solution that is used to fix the activity of the fluoride ions in the solution so that a concentration measurement can be made. The Total-Ionic Strength Adjustment Buffer (TISAB) III also reduces interferences from a low pH and from interfering ions that will complex with fluoride, making it not detectable by the ISE. Before every Fluoride ion concentration measurement, the ISE meter was calibrated with standard Fluoride solutions of 1 ppm, 3 ppm and 7 ppm after adding TISAB III to each of those in the ratio of 1:10. F^- concentration values in ppm (parts per million) of the SBF with immersed bioactive glass powders were recorded at the aforementioned time intervals.

6.2.4.4. pH Measurement in artificial saliva :

The prepared bioactive glass powders were soaked in artificial saliva at 36.9°C in the ratio of 1:50 (1 g powder soaked in 50 ml of artificial saliva) and pH of the solution was measured at different time intervals — 0 hour, 1 hour, 2 hours, 4 hours, 6 hours, 8 hours, 12 hours, 18 hours, 24 hours (1 day), 2 days, 3 days, 5 days, 7days, 10 days, 14 days, 21 days and 28 days— using Orion (Star A214) Thermo Scientific pH meter. Before pH measurement, the pH meter was calibrated each time with standard buffer solutions of pH 4, pH 7 and pH 9.2 at room temperature. pH values were recorded at the aforementioned time intervals.

6.2.4.5. Fluoride ion (F⁻) concentration measurement in artificial saliva:

The prepared bioactive glass powders were soaked in artificial saliva at 36.9°C in the ratio of 1:50 (1 g powder soaked in 50 ml of saliva) and the Fluoride ion concentration in the solution was measured at different time intervals — 0 hour, 1 hour, 2 hours, 4 hours, 6 hours, 8 hours, 12 hours, 18 hours, 24 hours (1 day), 2 days, 3 days, 5 days, 7days, 10 days, 14 days, 21 days and 28 days — using Orion (Star A214) Thermo Scientific ISE meter. TISAB III solution was added to the test solution in the ratio of 1:10 (1 ml of TISAB III with 10 ml of the saliva solution to be tested for Fluoride ion concentration). Before every Fluoride ion concentration measurement, the ISE meter was calibrated with standard Fluoride solutions of 1 ppm, 3 ppm and 7 ppm after adding TISAB III to each of those in the ratio of 1:10. F⁻ concentration values of the Saliva with immersed bioactive glass powders were recorded in ppm at the aforementioned time intervals.



produce clear homogeneous discs. The prepared discs were immediately subjected to IR spectrometer to measure the transmittance spectra in order to avoid moisture attack. KBr (Potassium bromide) was taken as the reference material for the background data as it is optically transparent for the light in the IR region.

6.2.6. Raman Spectroscopy :

All bioactive glass samples were examined using Raman spectroscopy. Raman spectra was measured with a Triple Raman spectrometer (Model: T64000, Make: Horiba) equipped 1800 / mm grating, TE cooled Synapse CCD detector and a open stage Olympus microscope with 50x objective. The samples were excited with a 532nm wavelength laser from a DPSS Nd:YAG laser (Make: Spectra Physics). The measurements were performed on powder samples in the range 200–2000 cm^{-1} at room temperature.

6.2.7. In vitro bioactivity study of bioactive glass :

To investigate the formation of Hydroxycarbonate apatite (HCA) layer or Fluorapatite on the surface of the prepared bioactive glass samples, in-vitro bioactivity was done. The bioactive glass powder samples were immersed in SBF (pH 7.4 at $\sim 37^\circ\text{C}$) in the ratio of 1:50 (1 g powder in 50 ml SBF) in small sterile plastic containers which were then placed in an incubator at 36.9°C and left undisturbed for the following time periods — 1 day, 3 days, 5 days, 7days, 10 days, 14 days, 21 days and 28 days. Different samples were prepared for the different time periods. After soaking for the pre-determined time, the samples were filtered, rinsed with double distilled deionised water, and dried overnight in an oven at 110°C . The dried powder samples were then analyzed by FTIR to determine the formation of apatite.

6.2.8. Weight Loss of Bioactive Glass in Saliva:

The prepared glass powders were immersed in artificial saliva (Ph 6.8 at $\sim 37^{\circ}\text{C}$) in the ratio of 1:10 (5g powder in 50 ml of artificial saliva) in small sterile plastic containers which were then placed in an incubator at 36.9°C and left undisturbed for the following time periods — 1 day, 3 days, 7 days, 14 days and 21 days. Different samples were prepared for the different time periods.

6.2.9. Anti-bacterial Test of the Bioactive Glasses :

The anti-bacterial test of the synthesized bioactive glasses were performed using the standard plate count method. The standard plate count method consists of diluting a sample with sterile diluents until the bacteria are dilute enough to count accurately. That is, the final plates in the series should have between 30 and 300 colonies. Fewer than 30 colonies are not acceptable for statistical reasons (too few may not be representative of the sample), and more than 300 colonies on a plate are likely to produce colonies too close to each other to be distinguished as distinct colony-forming units (CFUs). The assumption is that each viable bacterial cell is separate from all others and will develop into a single discrete colony (CFU). Thus, the number of colonies should give the number of bacteria that can grow under the incubation conditions employed.

The initial dilution was made by transferring 1 ml of *E. coli* sample to 9 ml sterile saline blank. This was the 10^{-1} dilution of the original sample. Then, 1 ml of this 10^{-1} dilution was transferred to another 9 ml sterile saline blank, thus producing a 10^{-2} dilution of the original sample. Similarly, by this serial dilution method, 10^{-3} dilution of the original sample was also prepared.

Agar nutrient medium was prepared and maintained at a temperature of $48-50^{\circ}\text{C}$ in a water bath. The agar nutrient medium was carefully poured in a sterilized Petri dish and then 1 ml of the 10^{-3} dilution of the bacterial sample was poured into it. This was labeled as the "Control". The similar process was carried out for 4 more Petri dishes and in each of them, additionally 1 gram of synthesized bioactive glass powders were added and the Petri dish labeled respectively. The agar and samples were immediately mixed gently by moving the plate in a figure-eight motion or a circular motion while it rests on the tabletop. After the pour plates had cooled and the agar had hardened, they were inverted and incubated 37°C for 24 hours. At the end of the incubation period,

bacterial colonies on all the Petri dishes were counted. Plates with more than 300 colonies cannot be counted and are designated too many to count (TMTC). Plates with fewer than 30 colonies are designated too few to count (TFTC). The number of bacterial colonies (CFU) per gram of our glass sample was obtained by dividing the number of colonies by the dilution factor multiplied by the amount of specimen added to the liquefied agar.

$$\text{CFU} = (\text{Number of Colonies} / \text{Dilution factor})$$

6.2.10. Scanning Electron Microscopy (SEM) :

A scanning electron microscope (SEM) is a type of electron microscope that produces images of a sample by scanning the surface with a focused beam of electrons. The electrons interact with atoms in the sample, producing various signals that contain information about the surface topography and composition of the sample. SEM was performed the synthesized solid bioactive glass samples, before and after immersing into the SBF. The glass samples were coated with platinum (Pt) by sputtering(Q150T ES, England) and then the microstructures were observed using a scanning electron microscope (ZEISSEVOR 18 Special Edition, England).

6.2.11. Energy Dispersive X-Ray Analysis (EDX) :

Energy Dispersive X-Ray Analysis (EDX), referred to as EDS or EDAX, is an x-ray technique used to identify the elemental composition of materials. EDX systems are attachments to Electron Microscopy instruments (Scanning Electron Microscopy (SEM) or Transmission Electron Microscopy (TEM)) instruments where the imaging capability of the microscope identifies the specimen of interest. The data generated by EDX analysis consist of spectra showing peaks corresponding to the elements making up the true composition of the sample being analysed. Elemental mapping of a sample and image analysis are also possible.

7. Results & Discussions

The important and basic constituent of bioactive glass is silica, which due to cross-linked structure, provides structural framework to the glass. The bioactive glasses prepared were soda-lime-fluoro-phosphosilicate, which showed response in human physiological environment. These glasses consisted of silica network with other components similar in many aspects to window glass with low silica content and more alkali and CaO content. Another difference is that phosphorus is not found in window glass. The controlling factor for intra-cellular response is the release of soluble Ca^{2+} , Na^{+} ions from the glass structure. As glass is an amorphous material, a large variation in composition is possible to control the physiological activity of the bioactive glass. Index of bioactivity (IB) is the measurement method to determine the rate of producing biological bond between the artificial and the natural material. IB is 100 divided by the time taken to achieve 50% of the bonded interface.

7.1. Differential Thermal Analysis (DTA)

Differential Thermal Analysis (DTA) is an important characterization method where chemical changes and phase changes in the material can be assessed as function of temperature in comparison with an inert material.

Table 6. DTA characteristic temperatures for the different bioactive glasses prepared

Sample	T_g (°C)	T_x (°C)	T_c (°C)	ΔT_{TS} (°C)
BGA0F0	516.4	601.8	688.9	85.4
BGA3F8	496.2	620.4	735	124.2
BGA2F9	489.6	618.2	732.2	128.6
BGA1F10	487.9	616.3	725.7	128.4

DTA of different glass samples prepared were recorded with a heating rate of 10°C/min up to 1000°C and shown in Figure 2.

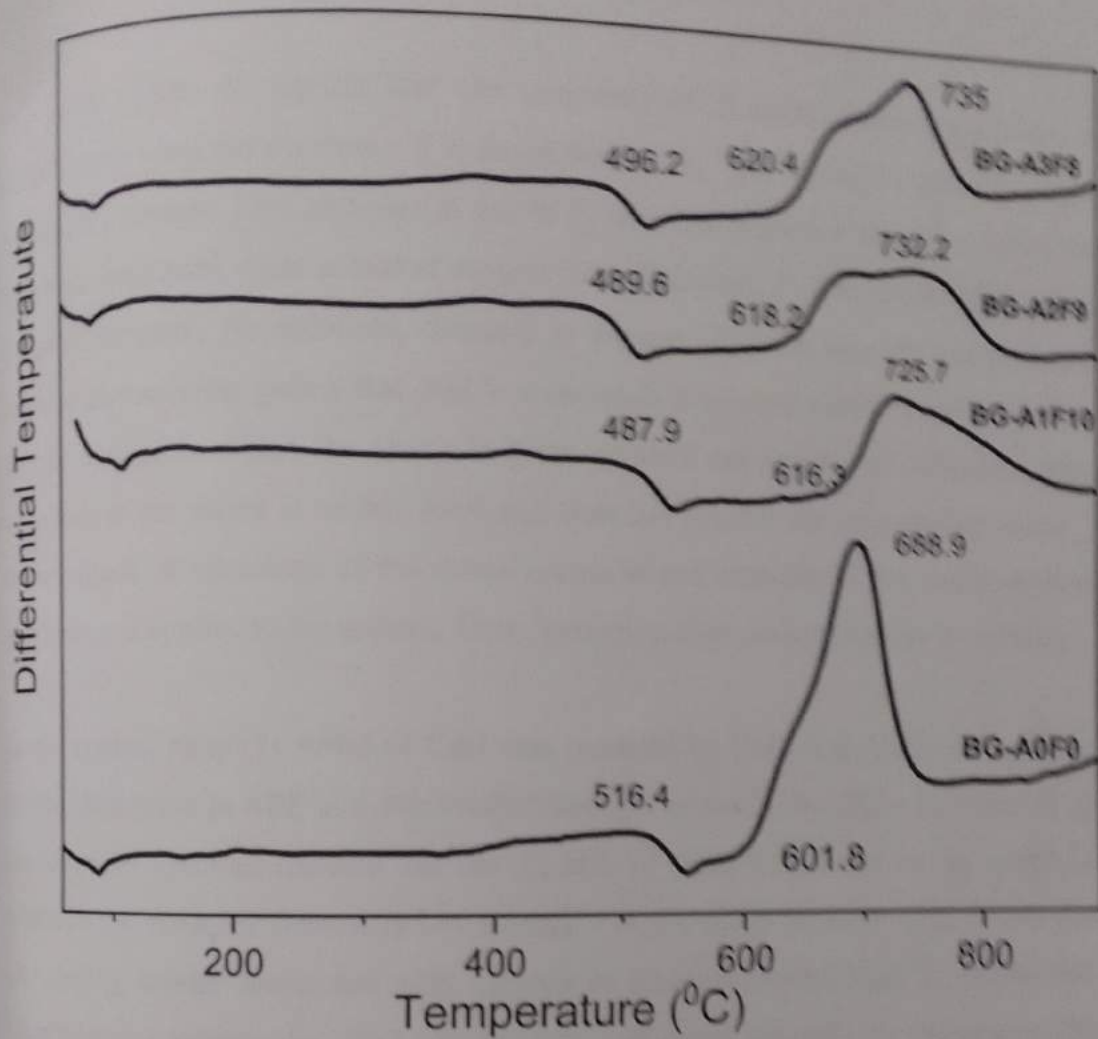


Figure 2. DTA thermograms of the synthesized Bioactive Glasses

The glass transition temperatures (T_g), crystallization onset temperatures (T_x) and crystallization peak temperatures (T_c) were obtained from the DTA plot of all the glass samples and displayed in Table 6. T_g of glass was found to decrease after introduction of CaF_2 & Al_2O_3 in place of CaO in Bioactive glass S53P4 (BG-A0F0). Lowest T_g was observed with BG-A1F10 (Al_2O_3 1 wt% & CaF_2 10 wt%). The characteristic temperatures obtained from DTA curves are glass transition temp (T_g), onset and peak crystallization temp (T_x and T_c respectively). Glass stability (G_s)

denotes the resistance of a glass to crystallization on heating. An evaluation of thermal stability of each glass was achieved by measuring its working range, which is the temperature interval between T_g and the onset of crystallization (T_x), that is, $\Delta T_{TS} = T_x - T_g$. The smaller this temperature interval, the lower is the thermal stability of the glass and more difficult it is to prevent partial crystallization during any working operation.

The table (Table 6) reports that the presence of fluoride causes significant changes in characteristic glass temperatures. It is found that the T_g , T_x & T_c values decrease with an increase in the CaF_2 content. This tendency is due to F^- ions that imparts a fluidizing action in glasses. F^- ions have ionic radii close to that of oxygen ions. Therefore, F^- ions can partially substitute O^{2-} in the glass network. Nevertheless, contrary to oxygen, fluoride ions are monovalent and create reticular discontinuity points that lead to a decrease in viscosity [81]. From a structural point, T_g denotes a stage in which the atoms in glass network are capable of vibration. Below T_g , the vibrations of the atoms is mainly local and does not involve the surrounding atoms. Above T_g , the amplitude of vibrations of the atoms increases and mobility of the atoms improves as more heat energy is applied to the system. Thus, formation of crystalline phases is feasible.

In this system, parts (11 wt%) of CaO was replaced by CaF_2 and Al_2O_3 to improve the fluoro-apatite formation in SBF and mechanical strength respectively. Here, T_g value of glasses were controlled by Calcium fluoride but the T_x and T_c were influenced by the presence of Al_2O_3 . Although the Alumina content is low enough - Al_2O_3 varies between 1, 2, 3 wt% (0.63, 1.27 & 1.84 mol%), it was found that with increase in alumina content T_x & T_c values had increased. Since Alumina reduces the NBO when it enters the glass network, its introduction increases the T_x & T_c . The lowest T_c of 688.9°C was found with S53P4 whereas the highest T_x & T_c were observed with the bioactive glass containing 3wt% Al_2O_3 and 8wt% CaF_2 . Due to the presence of Alumina, devitrification is arrested leading to glass structure stabilization.

7.2. X-Ray Diffraction Analysis (XRD)

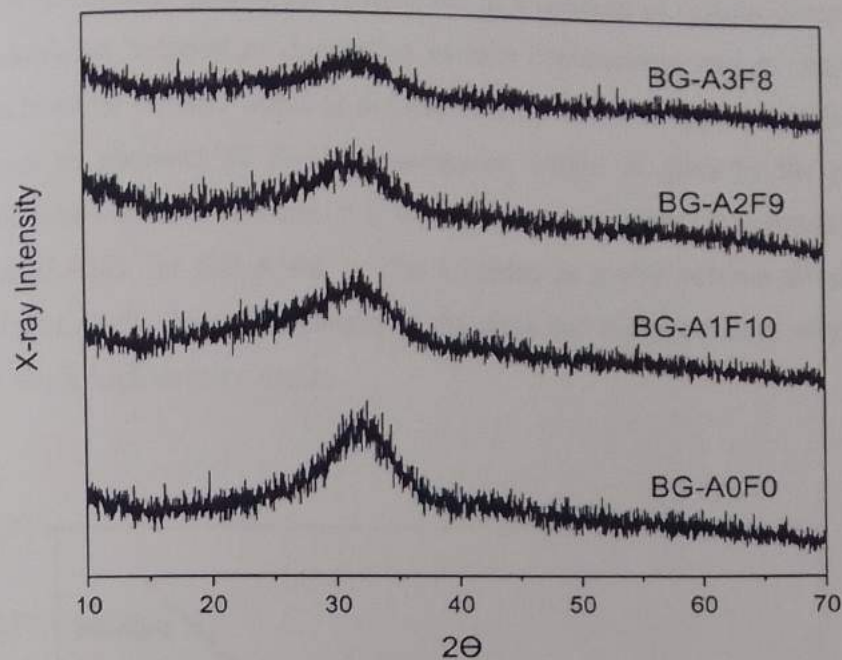


Figure 3. XRD graph of the synthesized bioactive glasses

All the glasses were found to be optically clear glass slabs on casting. The powder X-ray diffraction patterns of the prepared glass samples are displayed in Figure 3. All the glasses were found to be completely amorphous in the X-ray diffractogram and devoid of any significant crystalline phases as manifested by a broad hump in the XRD pattern.

7.3. Density & Molar Volume

Density of the prepared glass samples were measured by Archimedes method using Xylene as the displacement liquid. The density and molar of all four glass samples are reported in Table 7 and showed in Figure 4 & Figure 5. The density was found to decrease from 2.704 g/cc for the reference glass BG-A0F0 (containing neither Fluoride nor Alumina) to 2.642 for BG-A1F10 bioactive glass sample. Density was found to decrease since high density CaO (3.345 g/cc) is

partially replaced by low density CaF_2 (3.18 g/cc). CaO has been partly replaced by high density Al_2O_3 (3.99 g/cc) as well. But the amount of Al_2O_3 substitution is only 3 wt% at most whereas that of CaF_2 is 10 wt% maximum. Since glass is regarded as a solution of various components, density property of glass is an additional function of density of various constituents present. Another important property of glass is molar volume which is defined as the volume occupied by one mole of glass. Molar volume can be obtained by dividing molecular weight of glass by the respective glass density. If we consider the molar volume, it is found that molar volume is increased from 22.5734 for BG-A0F0 to 23.9583 for BG-A3F8. The increase in molar volume dominates over the increase in density of Al_2O_3 . Therefore density of the glass had decreased after substitution of CaO by low density CaF_2 & high density Al_2O_3 .

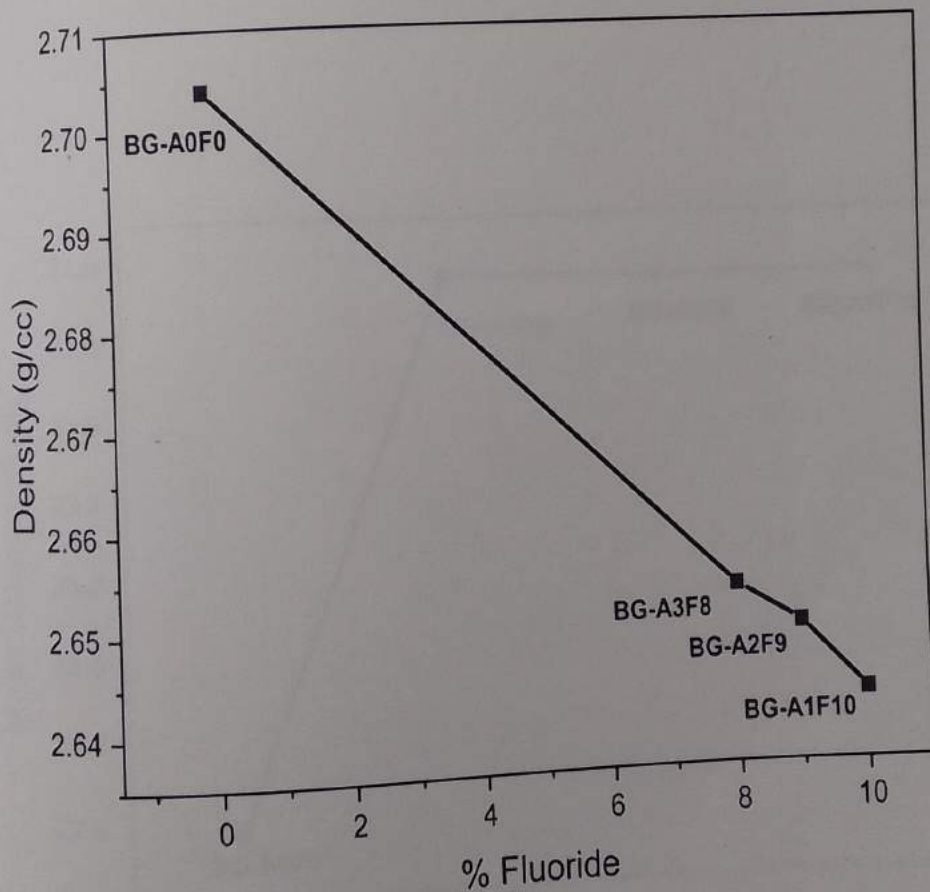


Figure 4. Density plot of the synthesized Bioactive Glasses

Table 7. Density and Molar volume of the different bioactive glass samples prepared

Sample Code	Density (g/cc)	Molar Volume (g/mol)
BG-A0F0	2.704	22.5734
BG-A3F8	2.653	23.9583
BG-A2F9	2.649	23.9409
BG-A1F10	2.642	23.9445

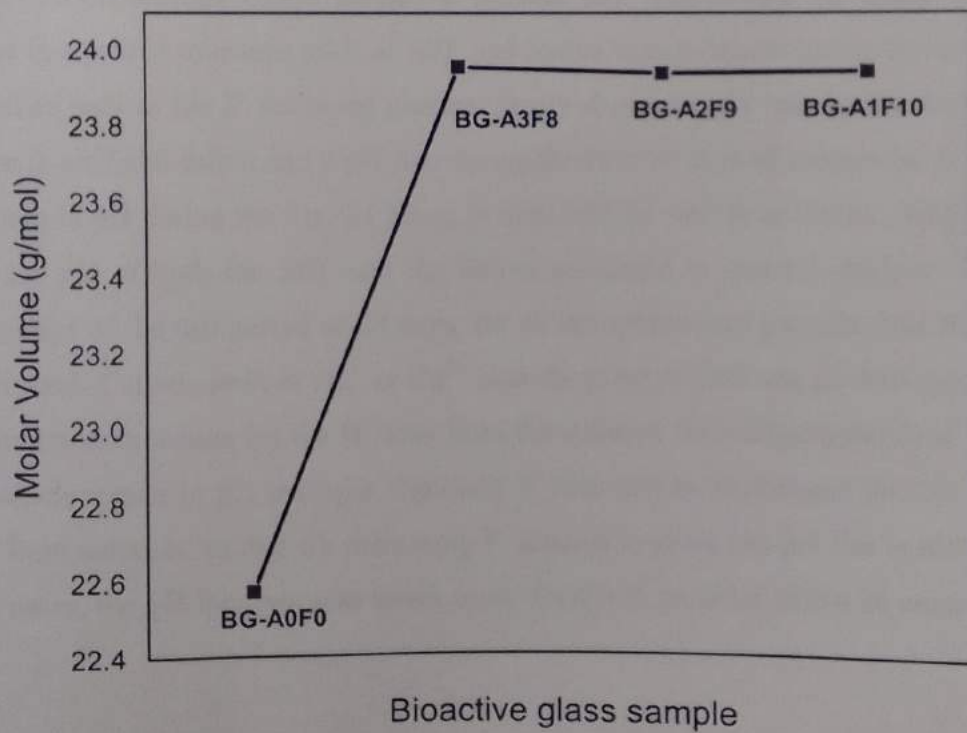


Figure 5. Molar Volume graph of the synthesized Bioactive Glasses

7.4. pH Analysis in Simulated Body Fluid (SBF) & Artificial Saliva

The powdered glass samples were immersed in SBF and in artificial saliva for different time periods – 0 hour, 1 hour, 2 hours, 4 hours, 6 hours, 8 hours, 12 hours, 18 hours, 24 hours (1 day), 2 days, 3 days, 5 days, 7 days, 10 days, 14 days, 21 days and 28 days. For this experiment, the ratio of the mass of glass to the volume of SBF or saliva was kept constant at 1:50. Figure 6 & Figure 7 present the change in pH of SBF solution as a function of immersion time, Figure 6 mapping the pH in the first 24 hours after immersion and Figure 7 showing pH change over the course of 28 days of immersion in SBF. Figure 8 & Figure 9 present the change in pH of artificial saliva as a function of immersion time, Figure 8 mapping the pH in the first 24 hours after immersion and Figure 9 showing pH change over the course of 28 days of immersion in artificial saliva. All the bioactive glass samples showed an increase in pH with increasing time of immersion in both SBF as well as in artificial saliva till 7-10 days and thereafter, a fall in pH was observed.

Soda-lime-phosphosilicate based bioactive glasses are well-known to cause a pH rise on immersion in aqueous solutions such as SBF and Saliva which favour apatite formation. The non-fluorinated as well as the F^- releasing glasses clearly showed a pH rise during the first 7 days of immersion in artificial saliva and a pH rise during the first 10 days of immersion in SBF, with the biggest jump in pH during the first 24 hours in both SBF as well as in Saliva. After this initial pH increase, the pH of both the SBF and the Saliva continued to steadily decline over the course remaining days of the test period of 28 days, for all the synthesised glasses- fluorinated as well as non-fluorinated. Cations such as Na^+ or Ca^{2+} near the glass surface can go into the SBF/ artificial saliva solution in exchange for the H^+ ions from the solution from disintegration of water into (H^+ & OH^-) which results in pH increase. Similarly F^- ions can be exchanged for OH^- ion removing OH^- ions from solution, so that for increasing F^- content in glass, the pH rise is more pronounced. In all the cases, the pH increase was much more drastic in artificial saliva as compared to that in SBF.

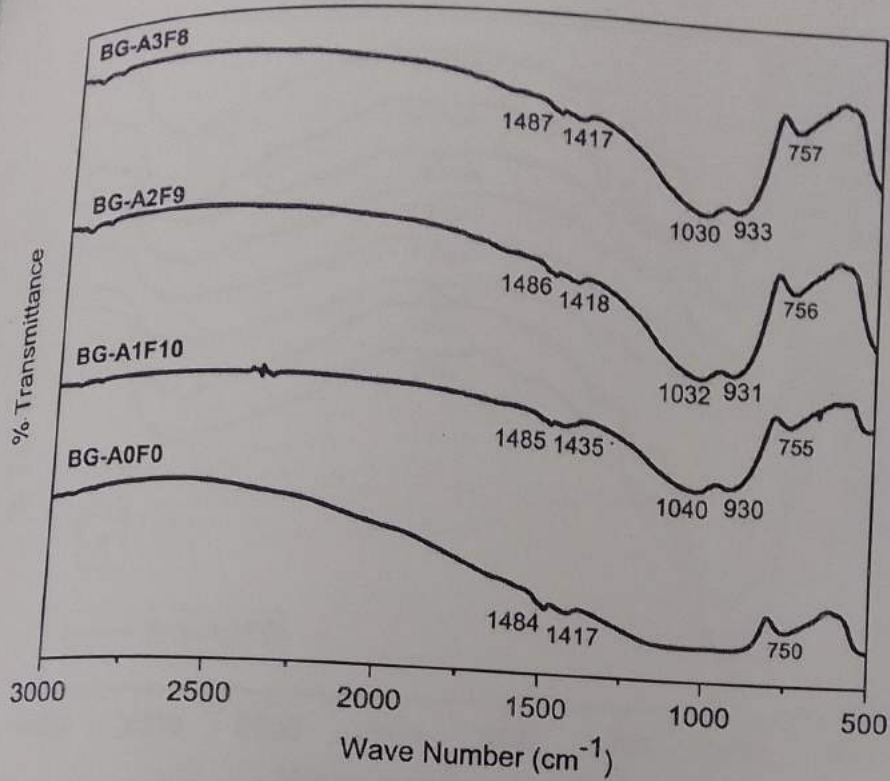


Figure 16. FTIR Spectra of synthesized bioactive glass samples before immersion in SBF

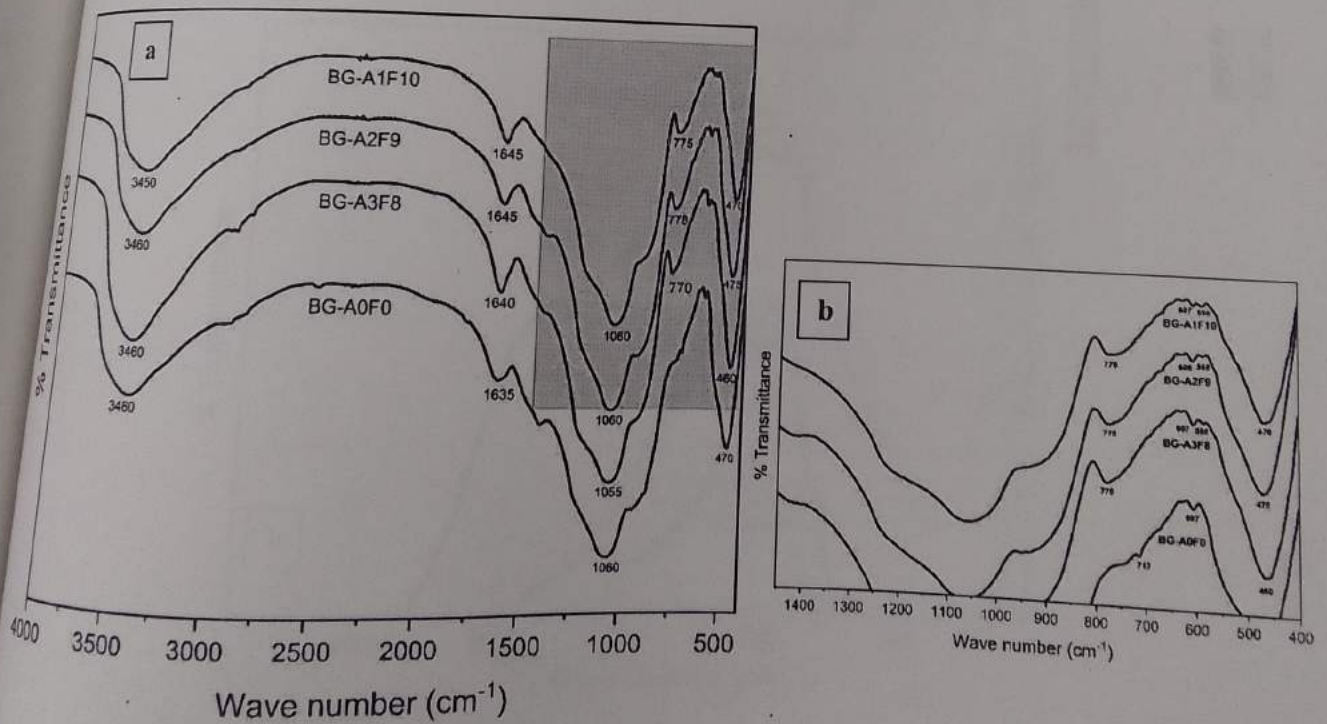


Figure 17. (a) FTIR Spectra of synthesized bioactive glass samples after 28 days of immersion in SBF (b) Enlarged image of the shaded portion in 17 (a)

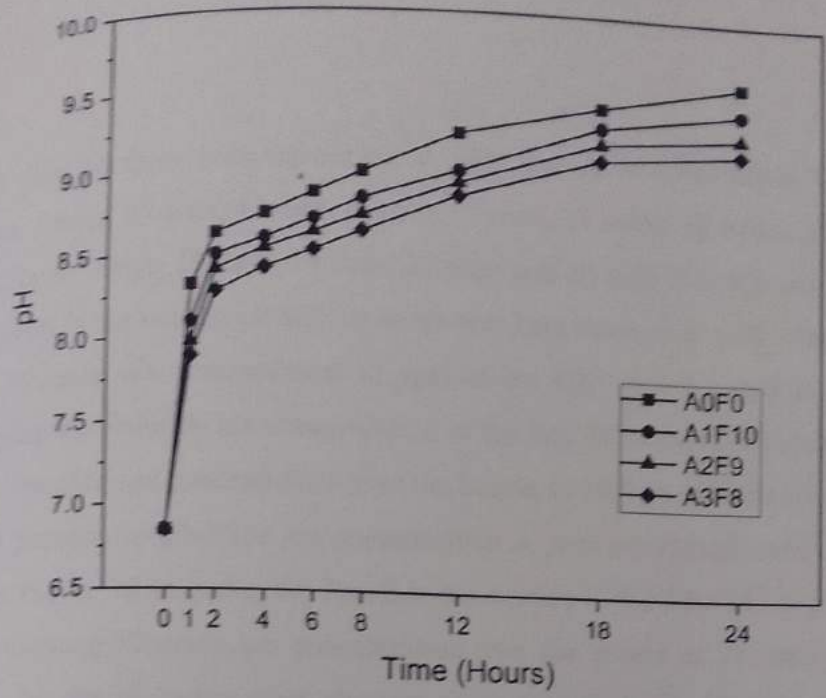


Figure 8. pH of artificial saliva in the first 24 hours after immersion of synthesized bioactive glasses

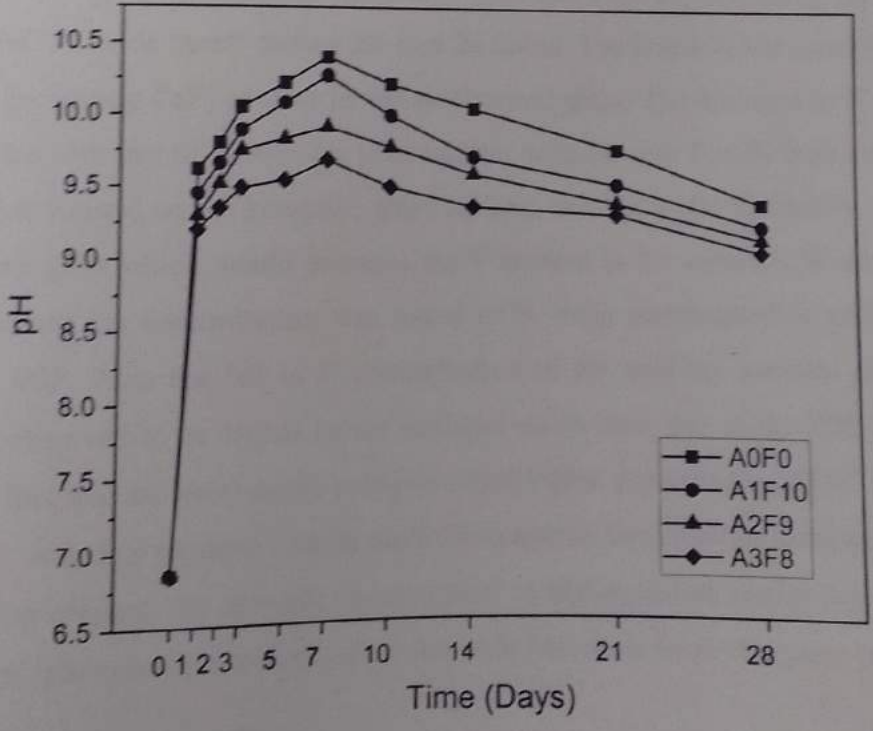


Figure 9. pH of artificial saliva over 28 days after immersion of synthesized bioactive glasses

The powdered glass samples were immersed in SBF and in artificial saliva for different time periods - 0 hour, 1 hour, 2 hours, 4 hours, 6 hours, 8 hours, 12 hours, 18 hours, 24 hours (1 day), 2 days, 3 days, 5 days, 7 days, 10 days, 14 days, 21 days and 28 days. For this experiment, the ratio of the mass of glass to the volume of SBF or saliva was kept constant at 1:50. Figure 10 & Figure 11 present the Fluoride ion concentration in ppm of the SBF as a function of immersion time, Figure 10 mapping the Fluoride ion concentration in the first 24 hours after immersion and Figure 11 showing the Fluoride ion concentration over the course of 28 days of immersion in SBF. Figure 12 & Figure 13 present the Fluoride ion concentration in ppm of artificial saliva as a function of immersion time, Figure 12 mapping the Fluoride ion content in the first 24 hours after immersion and Figure 13 showing Fluoride ion concentration over the course of 28 days of immersion in artificial saliva. All the bioactive glass samples show an increase in Fluoride ion concentration with increasing time of immersion in both SBF as well as in artificial saliva till 7 days, after which the Fluoride ion concentration started to gradually drop and kept on decreasing till the 28th day. There is an initial "Fluoride burst" during the first 24 hours. The Fluoride ion concentration values decreased with decreasing CaF_2 content in the synthesized glass. The decrease in F^- concentration observed from the 10th day of immersion is consistent with the fact that F^- ions migrate towards the silica gel layer formed on the bioactive glass surface, leading to the formation of Fluorapatite over the bioactive glass which would decrease the F^- content in the solution. In all the cases, the elevation in Fluoride ion concentration was found to be more pronounced in artificial saliva as compared to in SBF. Also the fall in F^- concentration of the soaking medium after 1 week of immersion, was observed to be higher in the artificial saliva than that in the SBF. This could be attributed to the fact that artificial saliva contains much higher percentages of Ca^{2+} and Phosphate groups than SBF, and thus promotes much rapid Fluorapatite formation as compared to SBF. For fluoride containing glasses, the network is composed of distinguished zones: one with prevalent covalent character (phosphosilicate) and other one with prevalent ionic character (metal- fluorine) [82].

2.5.1. Fluoride Ion (F⁻) Concentration analysis in Simulated Body Fluid (SBF)

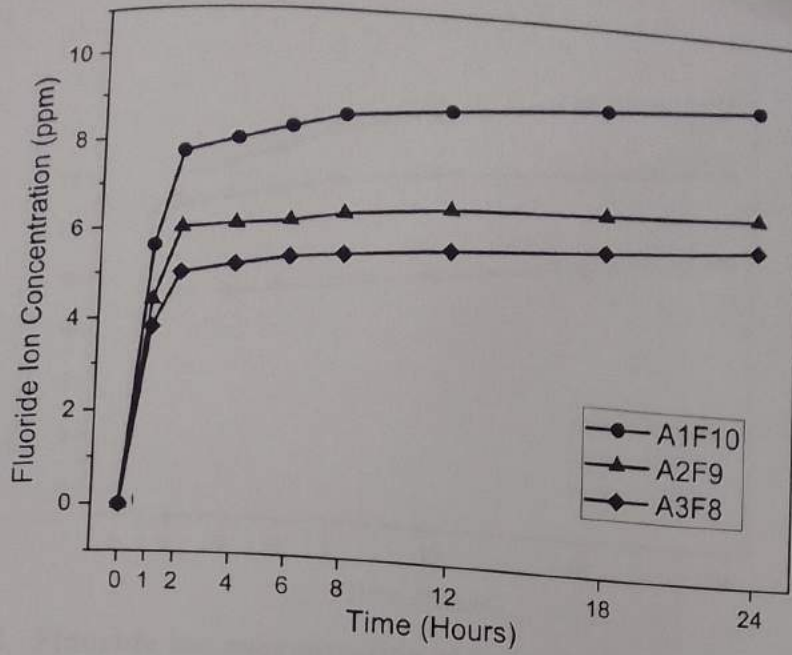


Figure 10. Fluoride ion concentration of SBF in the first 24 hours after immersion of the synthesized bioactive glasses

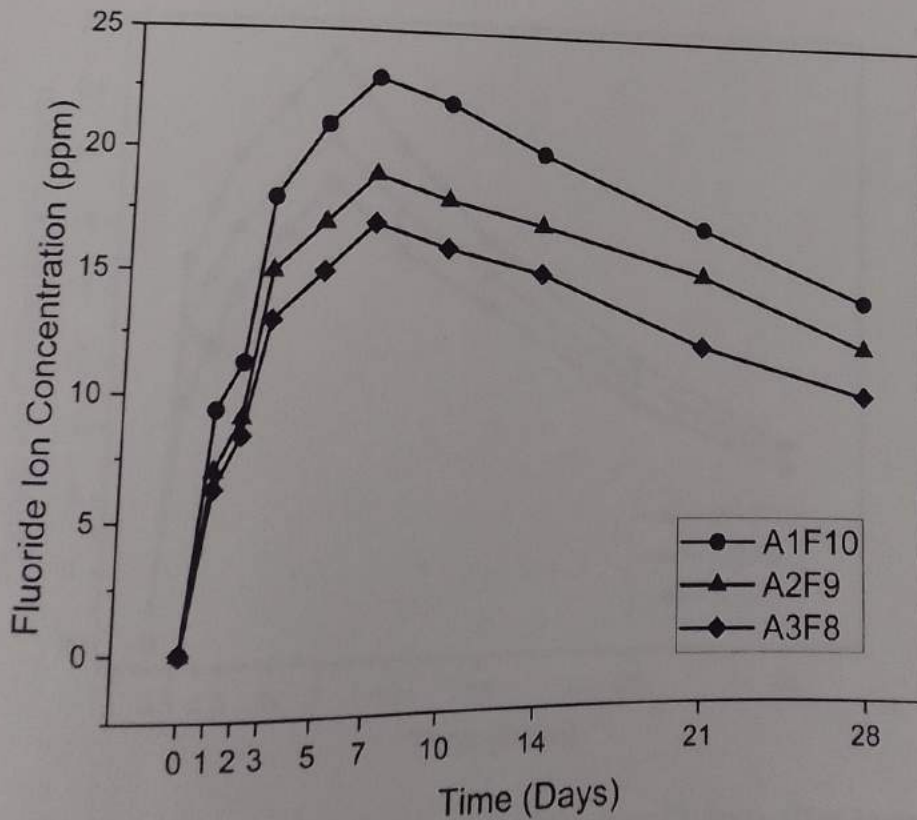


Figure 11. Fluoride ion concentration of SBF over 28 days after immersion of the synthesized bioactive glasses

3.2. Fluoride Ion (F⁻) Concentration analysis in Artificial Saliva (AS)

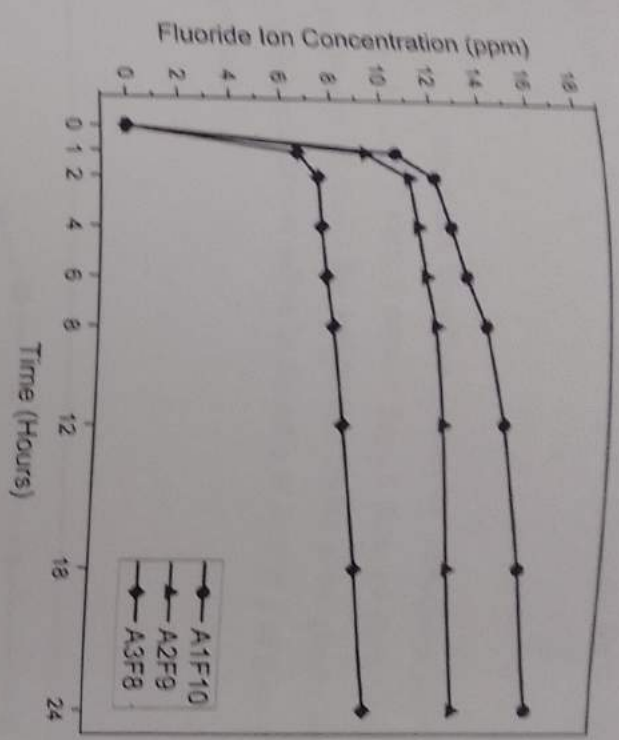


Figure 12. Fluoride ion concentration of Saliva in the first 24 hours after immersion of the synthesized bioactive glasses

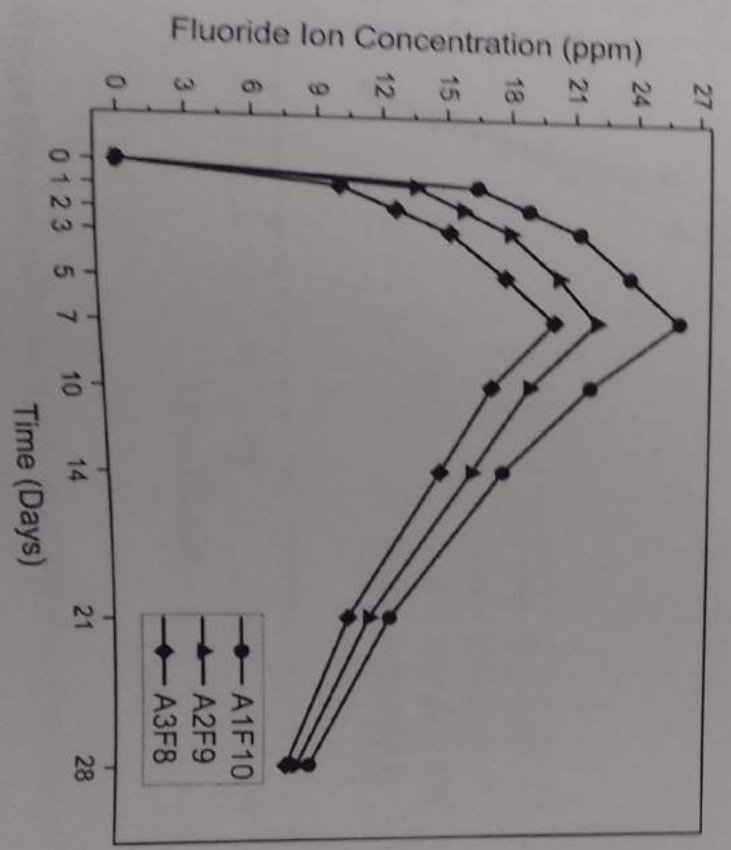


Figure 13. Fluoride ion concentration of Saliva over 28 days after immersion of the synthesized bioactive glasses

7.6. Weight loss of synthesized bioactive glasses in Saliva

The weight loss of the synthesized bioactive glasses on immersion in Artificial Saliva was measured at intervals of 1 day, 2 days, 3 days, 5 days, 7 days, 10 days, 14 days, 21 days and 28 days. Figure 14 and Figure 15 depict the weight loss trends of the glasses throughout the course of 28 days after soaking in artificial saliva in the ratio of 1:10 (5 g of glass powder immersed in 50 ml of saliva solution).

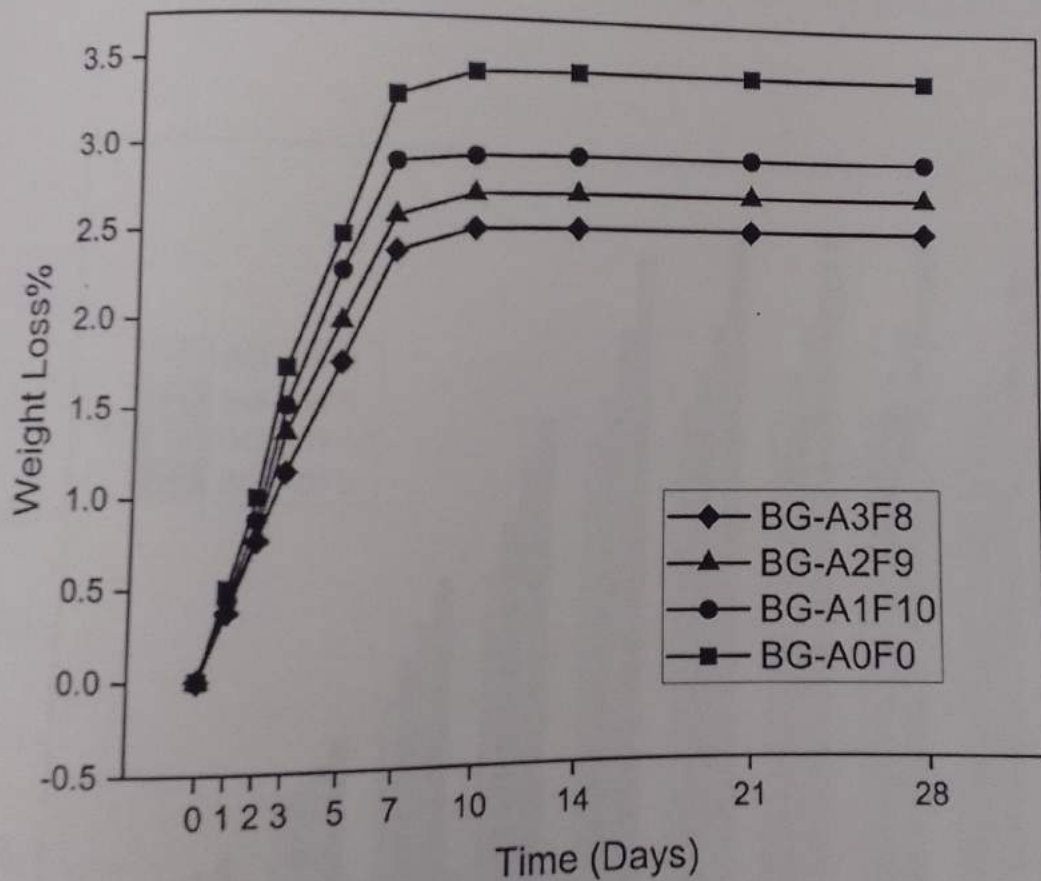


Figure 14. Weight loss showed by the synthesized bioactive glasses in artificial saliva

From the pH graphs, the inference has already been drawn that pH is increasing due to release of Ca^{2+} and Na^+ ions from the glass into SBF solution by exchanging with H_3O^+ or H^+ ion in the SBF solution. At high pH, Si—O—Si network was ruptured to form Si-OH or $Si(OH)_4$. Among fluorinated glasses, the glass with higher content of F showed higher rate of dissolution and consequently, weight loss, due to release of more fluoride ions from the same. The rate of weight loss was almost constant after 7 days due to the formation of Apatite layer on the glass surface which restricted the release of ions from the glass. The weight loss is related to the degradability of the glass network and also supported by the pH value of the SBF solution. The weight loss increased with increased Alumina content in glass, as incorporation of Alumina increases the network connectivity and causes a decrease in leaching out of ions. The parent S53P4 glass (BG-A0F0) with no Alumina content showed the maximum weight loss at any given period of time.

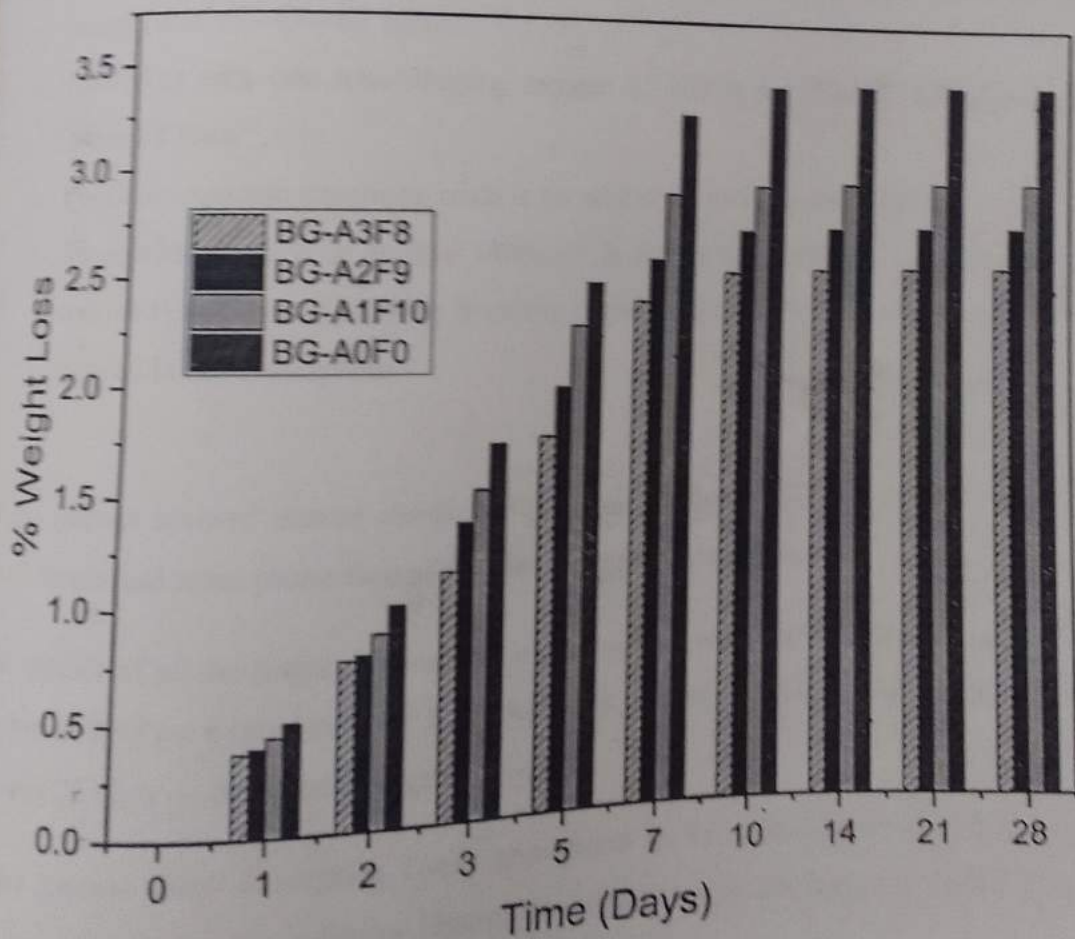


Figure 15. Bar graph representation of weight loss of synthesized bioactive glasses in saliva

7.7. Fourier-Transform Infra-red Spectroscopy (FTIR) :

FTIR spectroscopy is a valuable analytical and descriptive technique which can be applied in many applications of glass science. It can also provide useful information about structural building units in different oxide glasses. It is an important tool for investigating the bone bonding or bioactivity behaviours of silicate, borate or phosphate glasses. Another application includes confirming the degradation/ corrosion mechanism of glass in aqueous/ SBF/Tris solution.

The glass structure was investigated by using FTIR. As demonstrated in Figure 16, important transition nodes of Si-O-Si in FTIR spectroscopy were detected as follows:

1. Band at $450-500\text{ cm}^{-1}$ is associated with Si—O—Si bending node.
2. Spectra shows transmittance band at around 750 cm^{-1} is assigned to symmetric stretching vibration of Si—O—Si bond.
3. The Si-O with one non-bridging oxygen (1 NBO) per $[\text{SiO}_4]^{4-}$ tetrahedron is located around 930 cm^{-1} .
4. P—O asymmetric stretching node is located at $1030-1050\text{ cm}^{-1}$ region.
5. Transmittance band at around 1490 cm^{-1} is due to symmetrically co-ordinated carbonate species (C—O bonds) arising from the slight reaction between bioactive glass and carbon dioxide in the atmosphere.

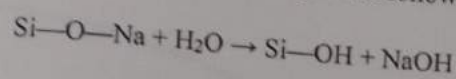
All the glasses showed almost identical FTIR spectroscopy. This suggests that there are same Si—O bonds and same proportion of Q^n species in each glass. [83, 84]

FTIR studies of all the prepared bioactive glass samples were carried out after soaking the glass powders in SBF (at a fixed ratio of 1:50) for 1 day, 3 days, 5 days, 7 days, 10 days, 14 days, 21 days and 28 days — depicted in Figures 17-21.

All the glasses show absorption bands correspond to the vibration of the $(\text{PO}_4)^{3-}$ group and $(\text{CO}_3)^{2-}$ group. This also indicates Hydroxycarbonate apatite formation after the immersion in

SBF solution. The band at around 1600 cm^{-1} is due to molecular water on glass surface. Bands at 1448 and 1414 cm^{-1} are due to the stretching of C—O bonds in $(\text{CO}_3)^{2-}$ group.

Bands at 1055 cm^{-1} and 1106 cm^{-1} are due to asymmetric stretching of P—O bonds in $(\text{PO}_4)^{3-}$ group. The split bending bands associated with bending vibration in O—P—O bond in crystalline phosphate at around 585 cm^{-1} and 610 cm^{-1} coupled with marked decrease of the intensity of absorption band at $920\text{--}940\text{ cm}^{-1}$ is related to Si—O with one or two NBOs and this can be correlated with the ion-exchange process between H^+ or H_3O^+ ions from aqueous solution and Na^+ ions from the surface of the bioglass according to the following reaction:



Confirmation of this ion exchange process is visualized by increase of the near infrared absorption broad band at 3550 cm^{-1} for Si—OH together with the appearance of the band at 1640 cm^{-1} . These two absorption bands are assigned to Si—OH group and molecular H_2O respectively. The formation of Si—OH leads to surface silica gel layer. The observation of the small kink at $1230\text{--}1270\text{ cm}^{-1}$ can be attributed to phosphate chain (either P—O or PO_3) asymmetric stretching. [85]

Significant changes were noticed at around $500\text{--}600\text{ cm}^{-1}$ and at $1000\text{--}1100\text{ cm}^{-1}$. Twin peaks at around $500\text{--}600\text{ cm}^{-1}$ and $560\text{--}611\text{ cm}^{-1}$ were observed due to P—O bonding (crystalline) & P—O bonding (amorphous) vibrations respectively.

The Hydroxycarbonate Apatite (HCA) layer is characterized by P—O bond vibration peaks at around 557 & 600 cm^{-1} and P—O asymmetric stretching vibration bands between $1000\text{--}1150\text{ cm}^{-1}$. The bands due to bonding vibration of P—O bonds are mostly used to discriminate between HCA & bioactive material as P—O stretching bond is superimposed on Si—O stretching ($1030\text{--}1050\text{ cm}^{-1}$) corresponding to glasses. The band corresponds to Si—O bonding between $450\text{--}500\text{ cm}^{-1}$ at lower frequencies compared with P—O bonding in HCA. Transmittance band at $1425\text{--}1491\text{ cm}^{-1}$ are due to stretching vibration of $\text{O}^-\text{—C—O}^-$ bonds in CO_3^{2-} units. Bands at 1620 cm^{-1} and 3400 cm^{-1} are due to the presence of hydroxyl groups. These bands confirm the formation of hydroxycarbonate apatite. The apatite formation was found gradually reduce with Al_2O_3 incorporation. [86, 87]

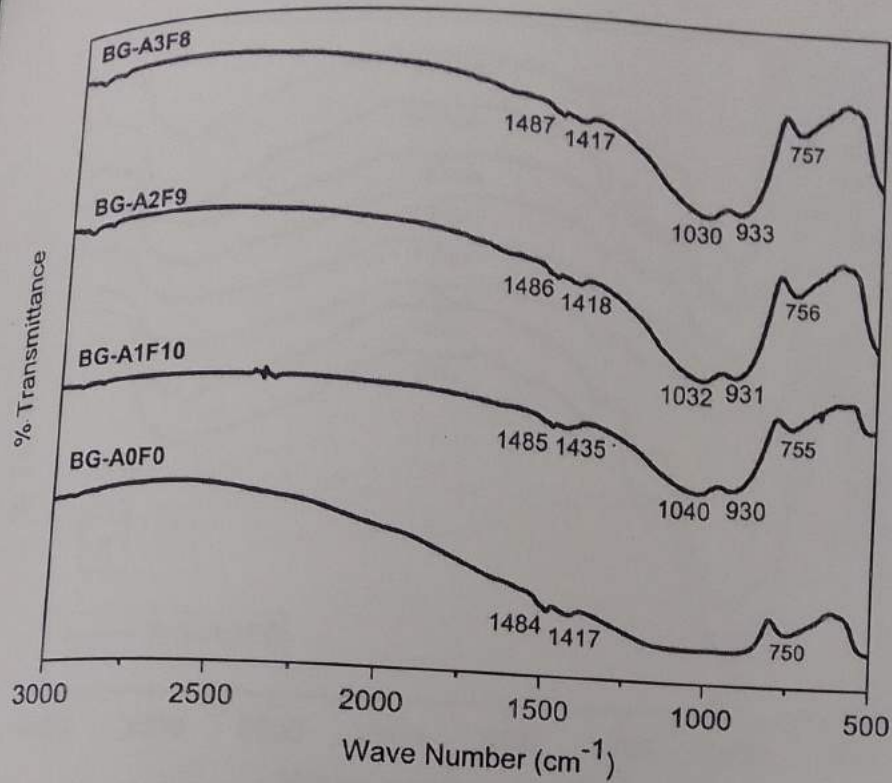


Figure 16. FTIR Spectra of synthesized bioactive glass samples before immersion in SBF

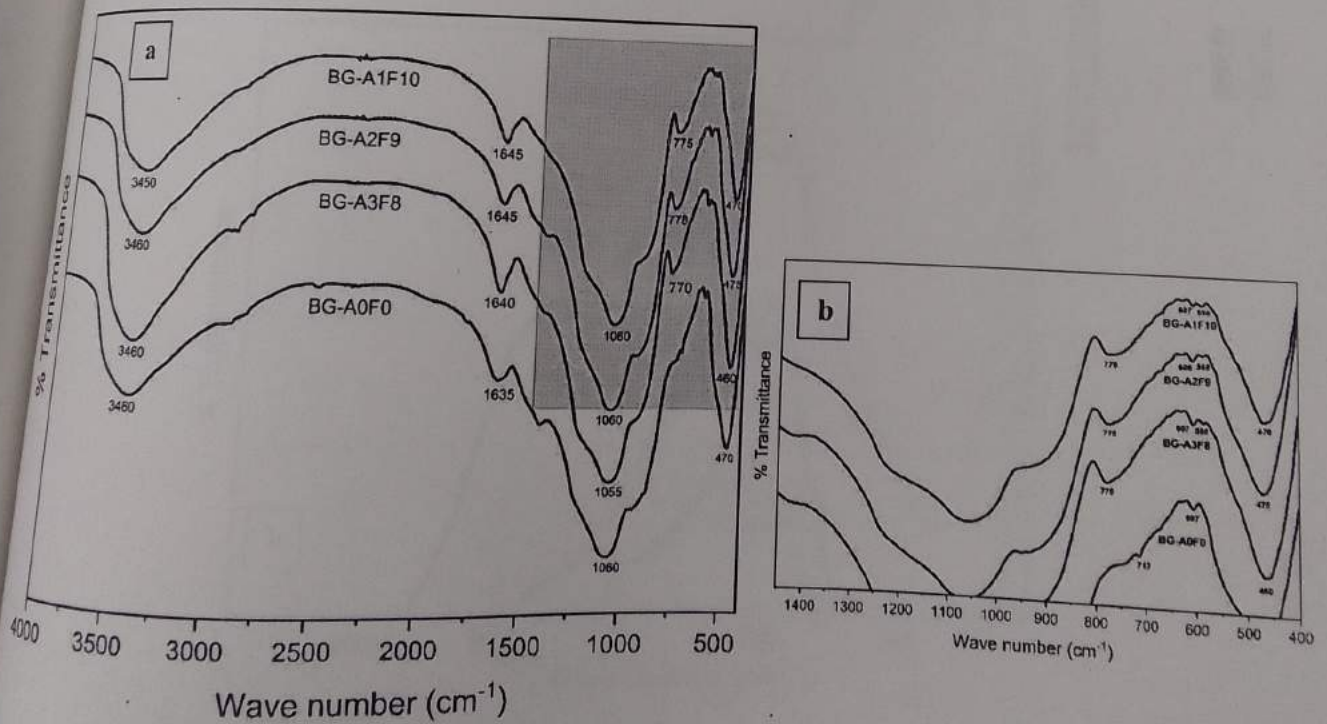


Figure 17. (a) FTIR Spectra of synthesized bioactive glass samples after 28 days of immersion in SBF (b) Enlarged image of the shaded portion in 17 (a)

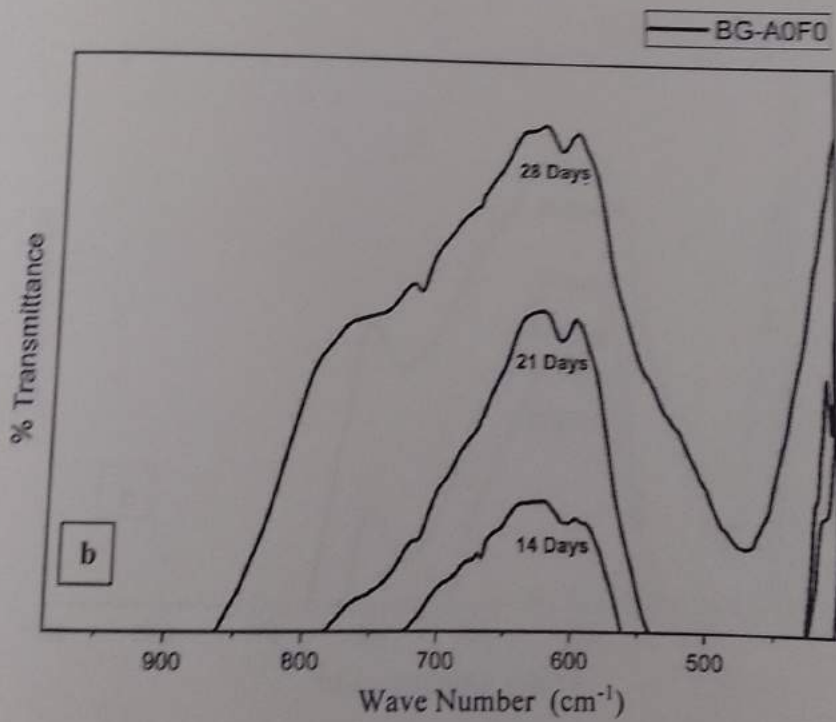
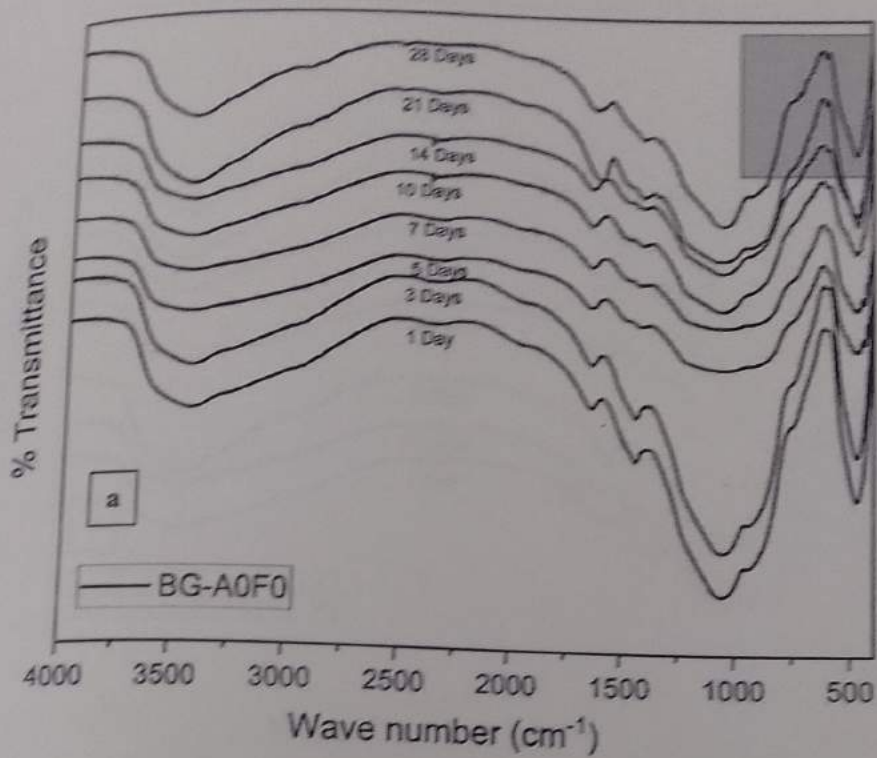


Figure 18. (a) FTIR Spectra of BG-A0F0 after soaking in SBF for different time intervals
 (b) Enlarged image of the shaded portion in 18 (a)

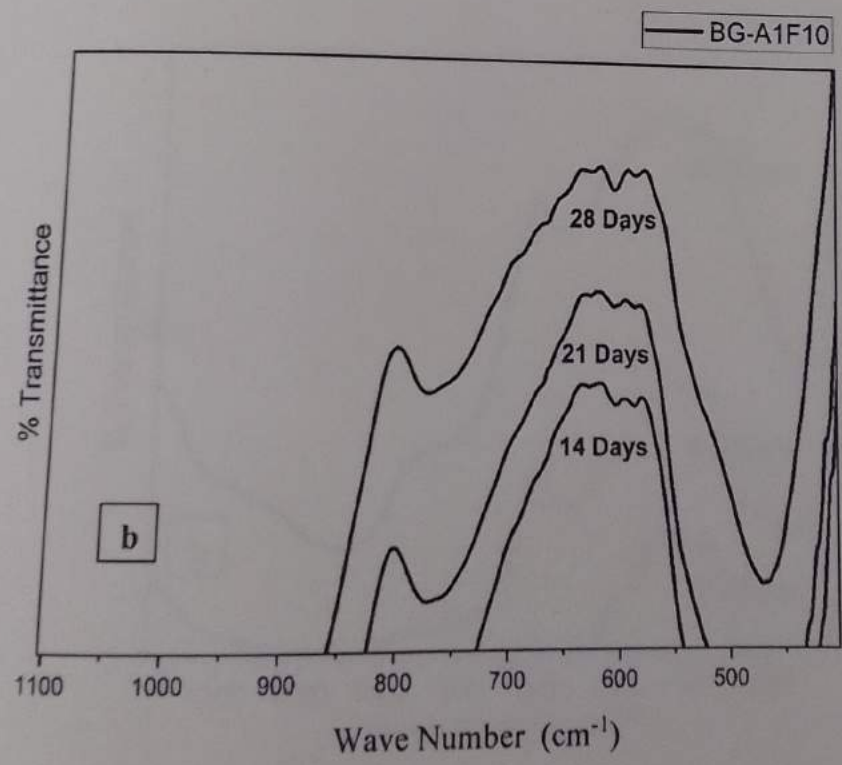
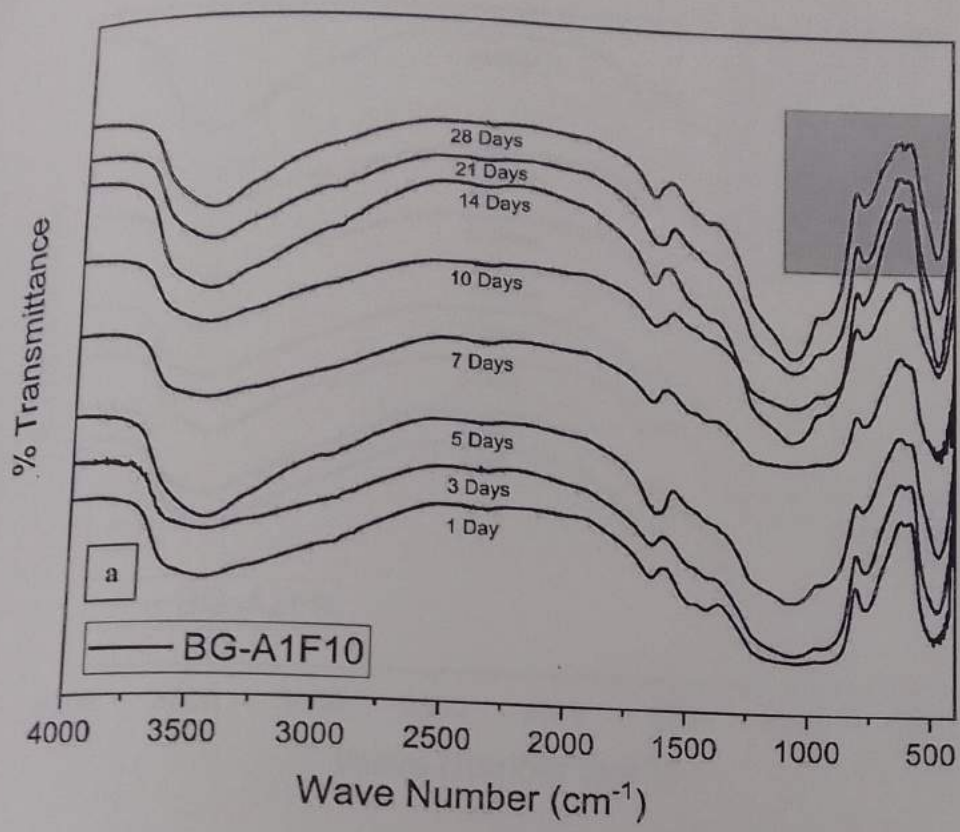


Figure 19. (a) FTIR Spectra of BG-A1F10 after soaking in SBF for different time intervals
 (b) Enlarged image of the shaded portion in 19 (a)

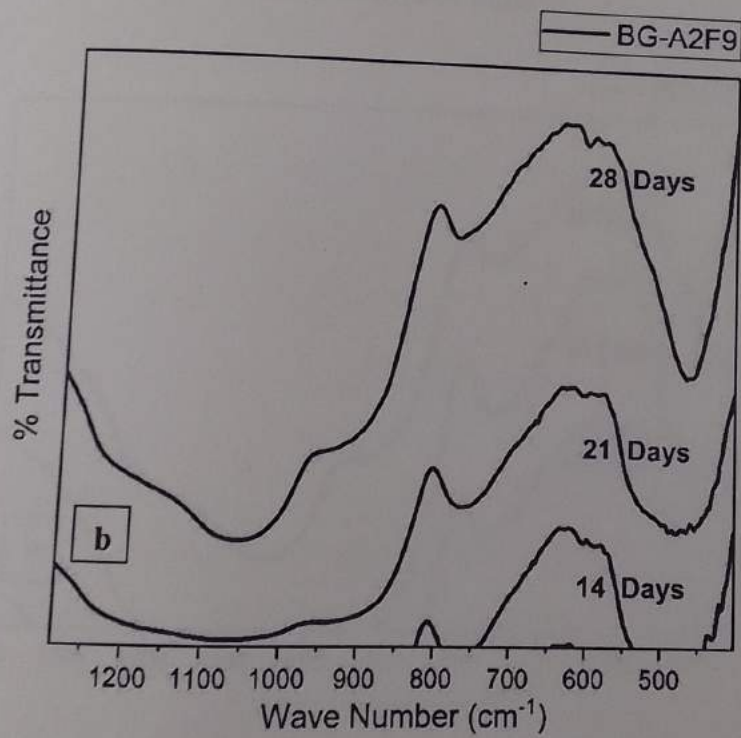
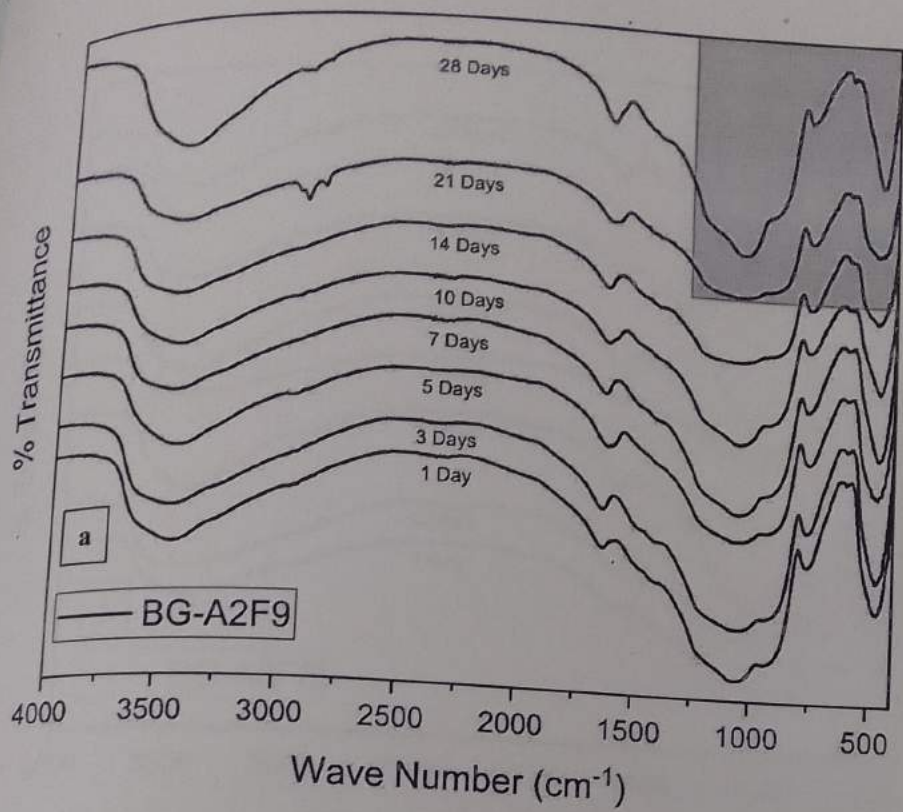


Figure 20. (a) FTIR Spectra of BG-A2F9 after soaking in SBF for different time intervals
 (b) Enlarged image of the shaded portion in 20 (a)

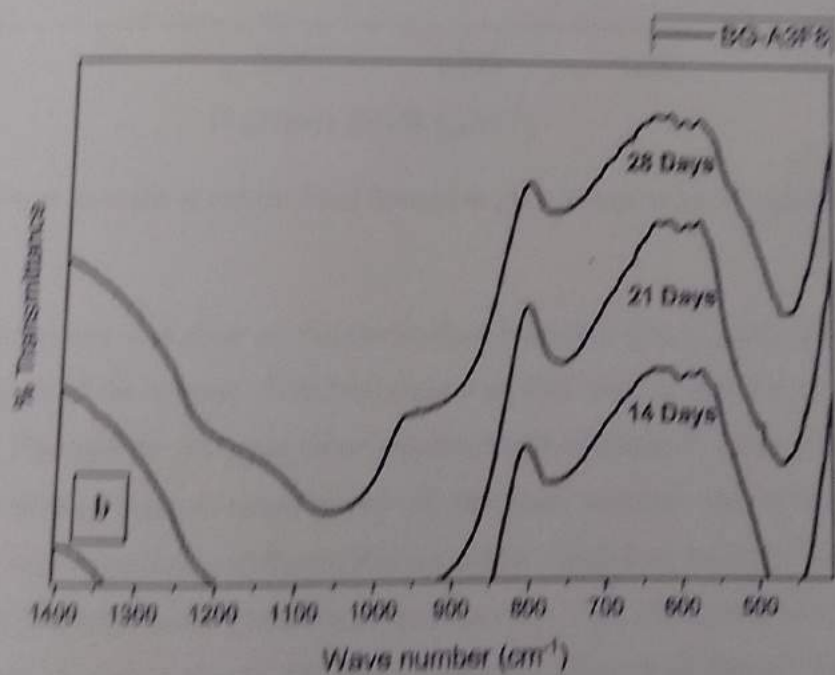
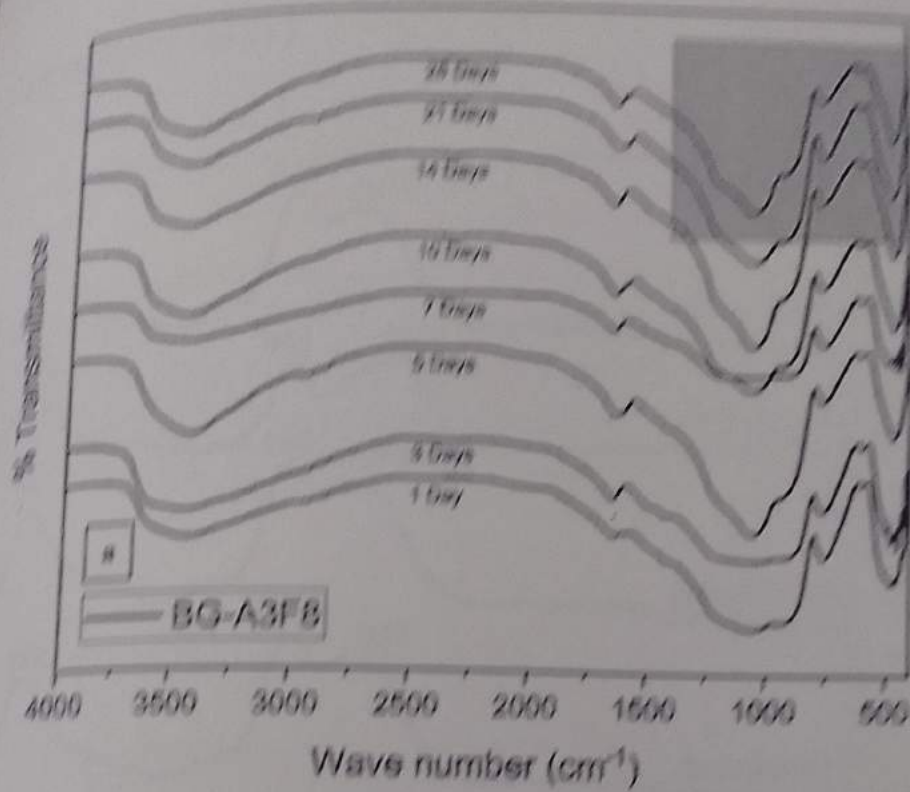


Figure 21. (a) FTIR Spectra of BG-A3F8 after soaking in SBF for different time intervals
 (b) Enlarged image of the shaded portion in 21 (a)

Raman Spectroscopy

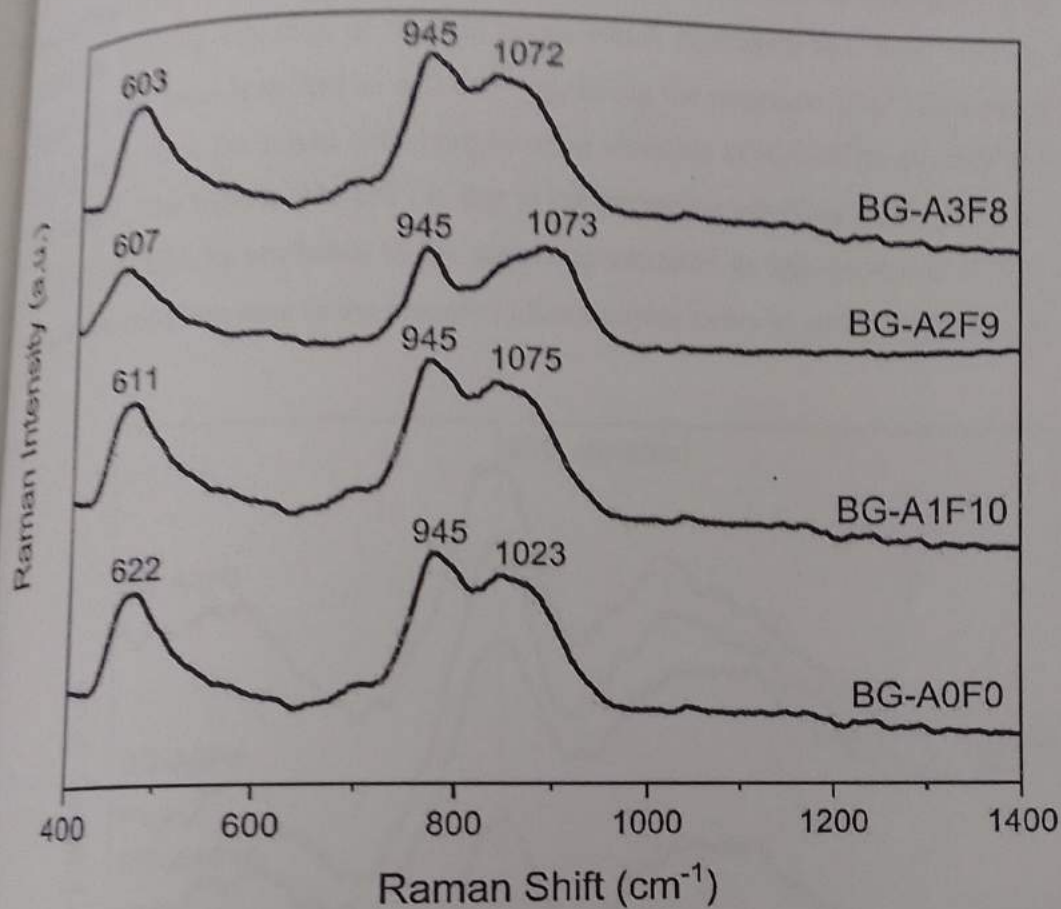


Figure 22. Raman Spectra of synthesized bioactive glass samples before immersion in SBF

The Raman spectroscopy was done on the synthesized bioactive glass powder samples to study the structural aspect of the glasses. This technique was also used to confirm the formation of Hydroxyapatite/ Fluorapatite on glass after immersion in Simulated Body Fluid (SBF) for different time intervals. Raman spectroscopy of the glass samples reports the presence of vibrational bonds corresponding to different Raman-active vibrational modes of various bonds in silicate, phosphate structural units. The Raman spectroscopy of all the synthesized glasses before soaking in SBF are shown in Figure 22. Main important features of Raman spectroscopy of bioactive silicate glasses are the bands associated with asymmetric and symmetric stretching vibration of SiO_2 network in the $850\text{-}1200\text{ cm}^{-1}$ region as it gives the information of glass

network connectivity which is related to its biodegradability. Bands at 945-959 cm^{-1} is due to Si-tetrahedron with 2NBOs & the peaks at 1029 to 1083 cm^{-1} is assigned to vibration involving Si-tetrahedron with 1 NBO. The presence of Q^3 (Si) units can also be confirmed from the mixed stretching bonding vibration of Si-O-Si bonds which contribute to a band at around 570 cm^{-1} . However, this band is shifted to 622 cm^{-1} signifying the presence of Q^2 (Si) units in addition to Q^3 (Si) units, since the mixed stretching-bending vibration of Si-O-Si bonds in Q^2 (Si) units occur at 630 cm^{-1} . The band at 945 cm^{-1} is due to the stretching vibration in Q^2 (Si) unit. The band at 945 cm^{-1} can also be attributed to the stretching vibration in orthophosphate Q^0 (P) units. It can be said that the phosphate in the prepared glass samples exists in orthophosphate state.

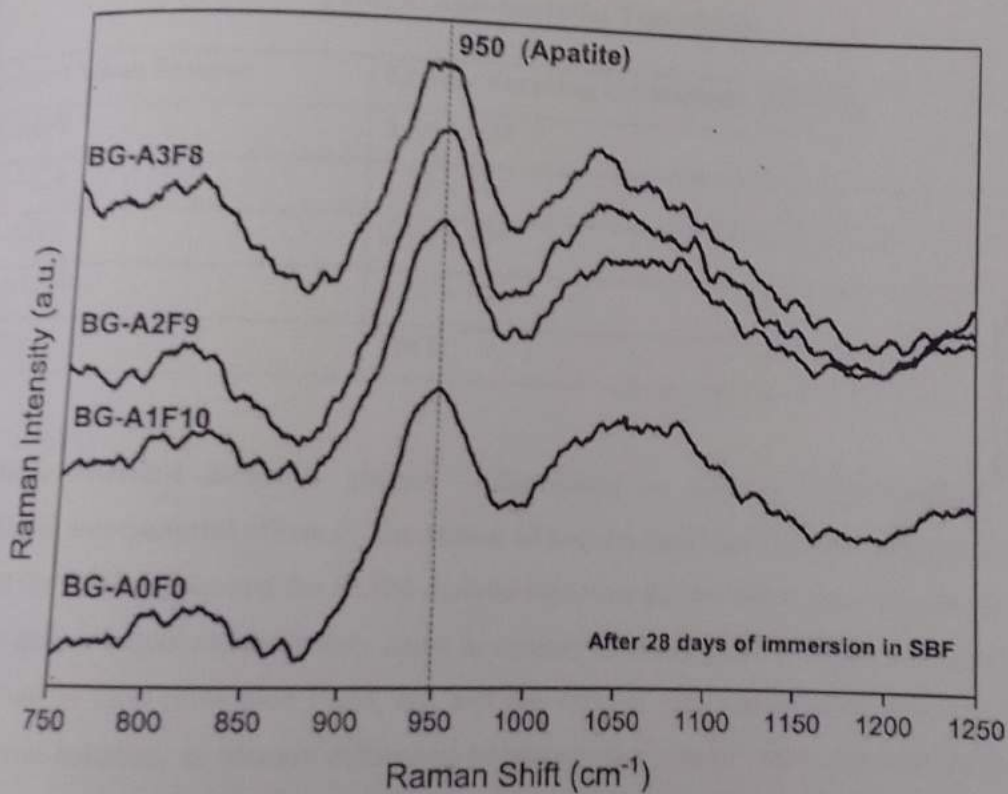


Figure 23. Raman Spectra of synthesized bioactive glass samples after soaking in SBF for 28 days

Figure 23 depicts the Raman spectroscopy of all the synthesized glasses after soaking in SBF for 28 days. The peak obtained at 950 cm^{-1} confirms the formation of apatite on the glasses since the most intensive peak of vibration of $(\text{PO}_4)^{3-}$ tetrahedron has been observed to be in the range of 940 – 980 cm^{-1} [88].

7.9. Anti-bacterial Test

The anti-bacterial test of the synthesized bioactive glasses was performed by the Standard Plate Count Method. The total number of bacterial colony forming units in specimens with and without the prepared bioactive glass powders were counted after the incubation period, as listed in Table 8.

Table 8. Anti-bacterial Test results

Bioactive Glass Sample	Colony Forming Units/gram (CFU /g)
BG-A0F0	2.91×10^5
BG-A3F8	1.79×10^5
BG-A2F9	0.98×10^5
BG-A1F10	0.33×10^5
Control	TMTC

All the synthesized bioactive glasses – fluorinated as well as non-fluorinated, showed exceptional anti-bacterial efficacy. The reason of anti-bacterial activity could be ascribed to the fact that the S53P4 glass and the S53P4-derived bioactive glasses release mobile cations like Na^+ into the ambient medium, once they come in contact with any aqueous fluid, such as Simulated Body Fluid or Oral Simulated Fluid, etc. and the leached ions significantly increase the pH of the ambient solution, as already evidenced by the pH test results. Also, the osmolarity and the osmotic pressure of the ambient solution are considerably elevated consequentially. The environment with high pH and high osmotic pressure is not at all conducive to the growth of bacteria.

The bioactive glass with the maximum Fluoride content showed the highest anti-bacterial effect. The anti-bacterial property markedly decreased with decreasing Fluoride content of glass. This could be attributed to the bacterial growth-inhibiting property of Fluoride.

7.10. Scanning Electron Microscopy (SEM) & Energy-dispersive X-ray (EDX)

Apatite formation on the synthesized glass samples was assessed by the microstructural analysis of the glasses before and after soaking in SBF for 14 days and 28 days and the obtained micrographs, at magnifications of 5k, 10k and 30k, are displayed in Figure 24 and Figure 25.

From Figure 24, the microstructure obtained by Scanning Electron Microscopy (SEM), it was found that the morphology or texture of the BG-A0F0 sample surface had changed from a plain glass surface to a surface fully covered with cotton ball like aggregates, characteristics of Hydroxyl carbonate apatite (HCA). Energy dispersive X-ray analysis of the same sample also confirmed the presence of Silicon, Calcium, Sodium, Phosphorus and Oxygen in the glass prior to soaking in SBF and the content of Silicon and Sodium were observed to be the highest in that order. But after the immersion of the glass in SBF medium for 14 days, the EDX analysis of the glass surface showed a much higher percentage of Calcium and Phosphorus with respect to the concentrations of Silicon and Sodium. This microstructural analysis revealed the visual evidence of formation of HCA layer on the glass surface which was also confirmed by the FTIR analysis.

The SEM images of the modified S53P4 bioactive glass with 1 wt% Alumina and 10 wt% CaF_2 (BG-A1F10) are shown in Figure 25. The glass surface is partially covered by two phases with distinct morphology. Small granular particles in agglomerate form and other white large crystals are found in the microstructure. The granular particles might be Hydroxyapatite (HAp) and the white large crystals could be Fluorapatite (FAP). The EDX analysis showed the presence of Fluorine & Aluminium along with Silicon, Sodium, Calcium and Phosphorus in the glass sample before SBF immersion. Here, the amounts of Silicon and Sodium were found to be the highest in that order. But after the immersion in SBF, the glass surface was observed to be partially covered by the HAp/FAP layer, and moreover, the EDX analysis of the whole surface after soaking in SBF clearly showed that the content of Calcium and Phosphorus were the highest. Fluorine content was also higher than that found on the plain glass surface. The high percent of P and Ca, along with increase in the percentage of F, confirms the formation of HAp and FAP layer on the glass surface. This is also consistent with the findings of the FTIR and pH tests.

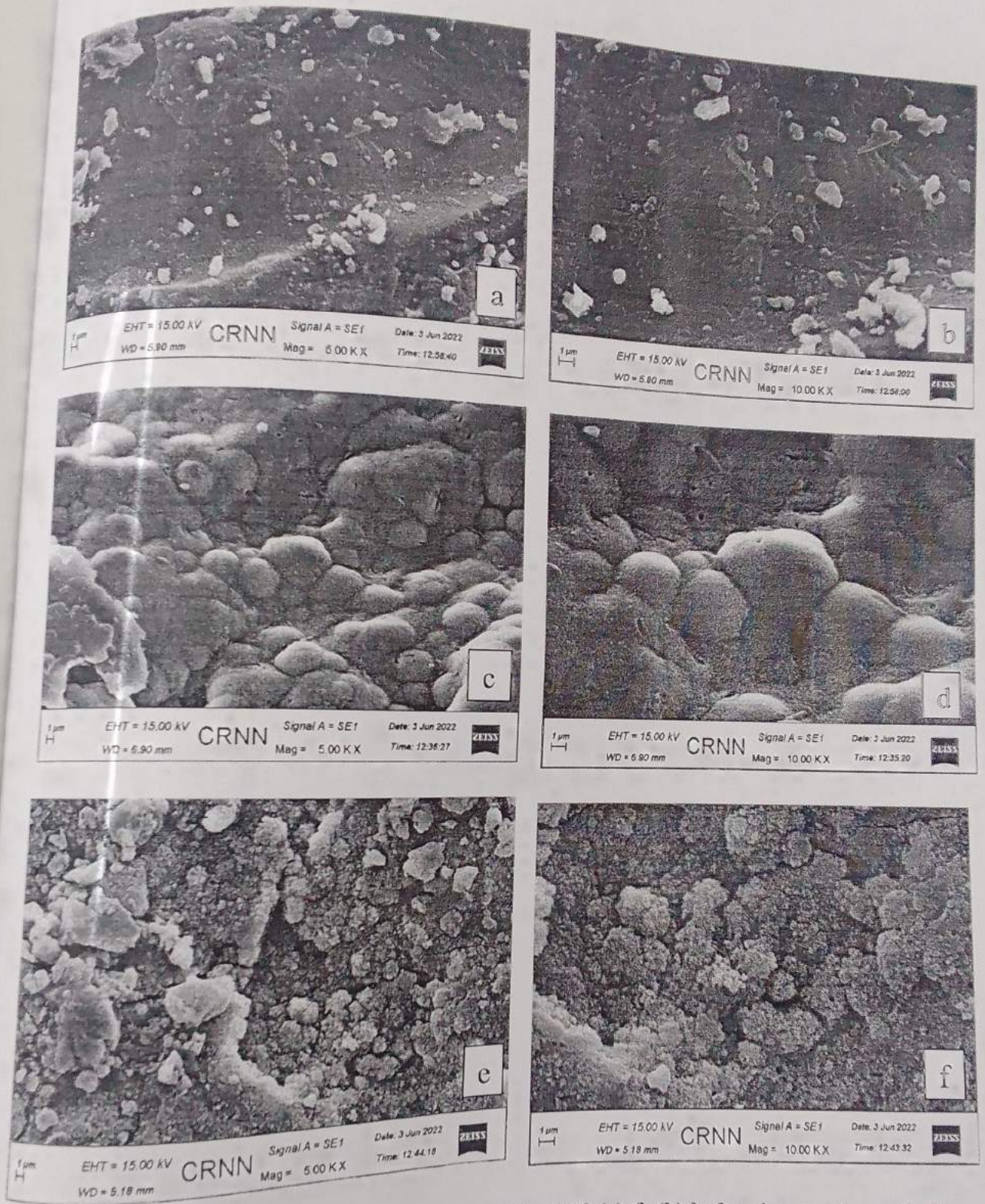
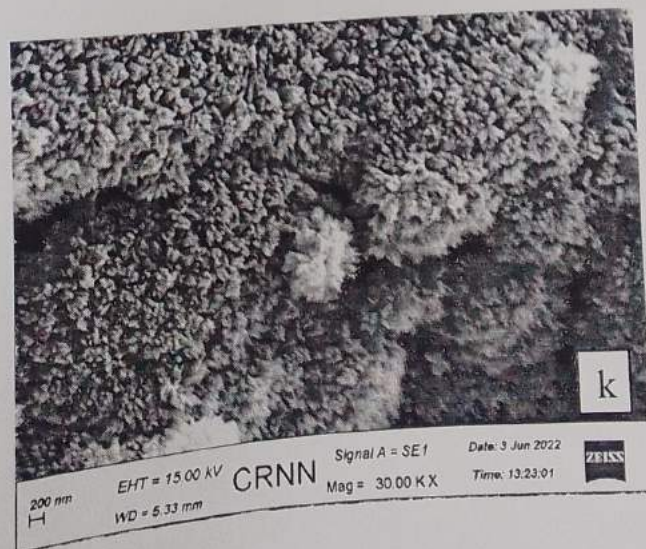
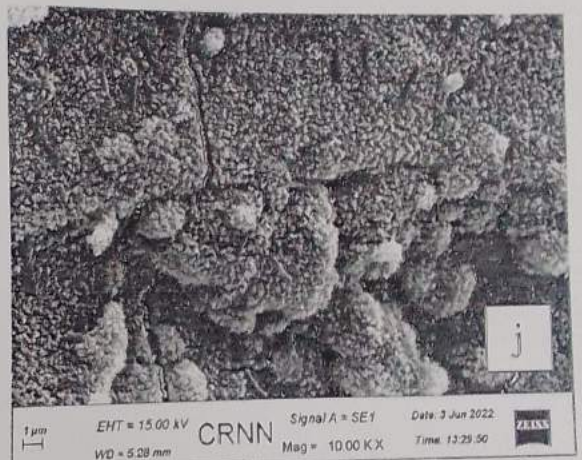
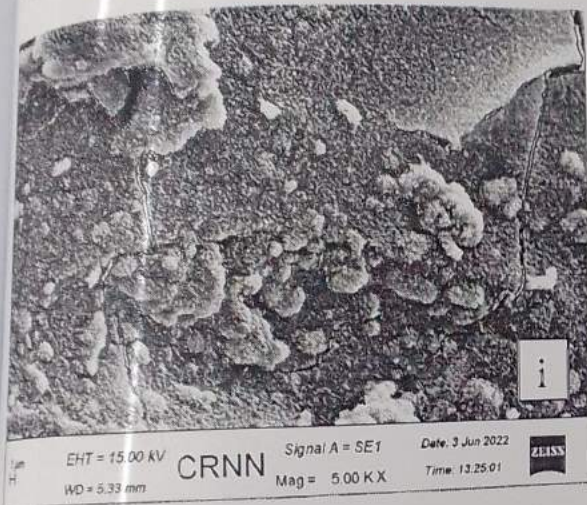


Figure 24. SEM images of bioactive glass BG-A0F0 (a) & (b) before immersion in SBF (c) & (d) after immersion in SBF for 14 days (e) & (f) after immersion in SBF for 28 days



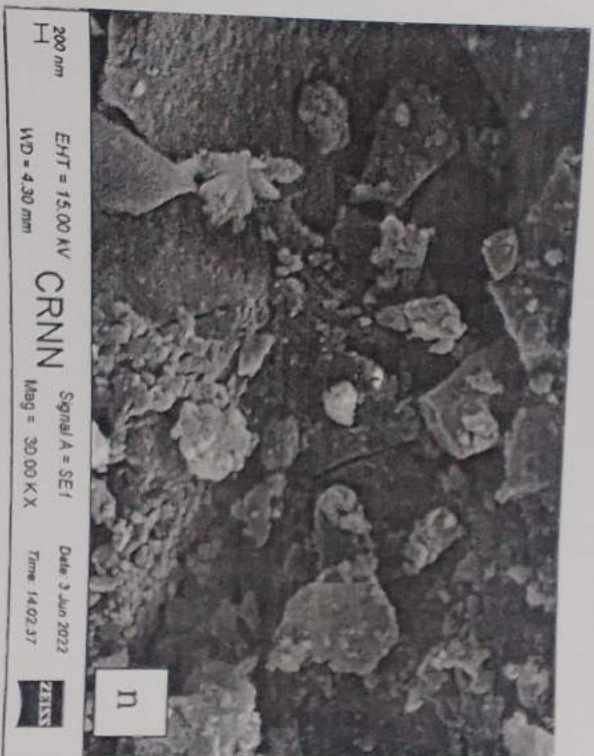


Figure 25. SEM images of bioactive glass BG-AIF10 (g) & (h) before immersion in SBF (i), (j) & (k) after immersion in SBF for 14 days (l), (m) & (n) after immersion in SBF for 28 days

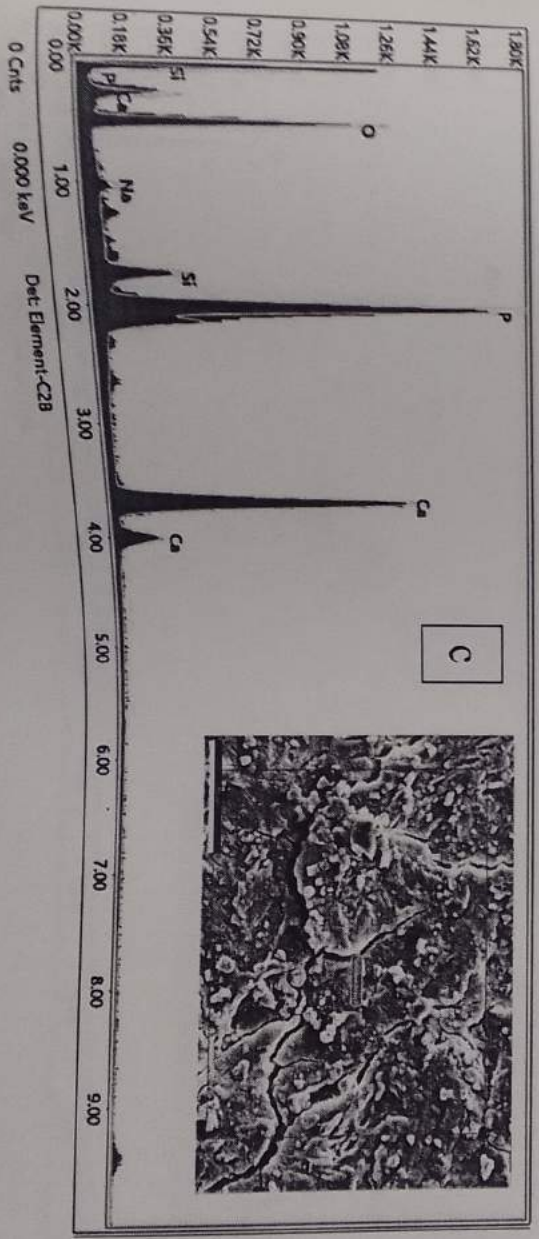
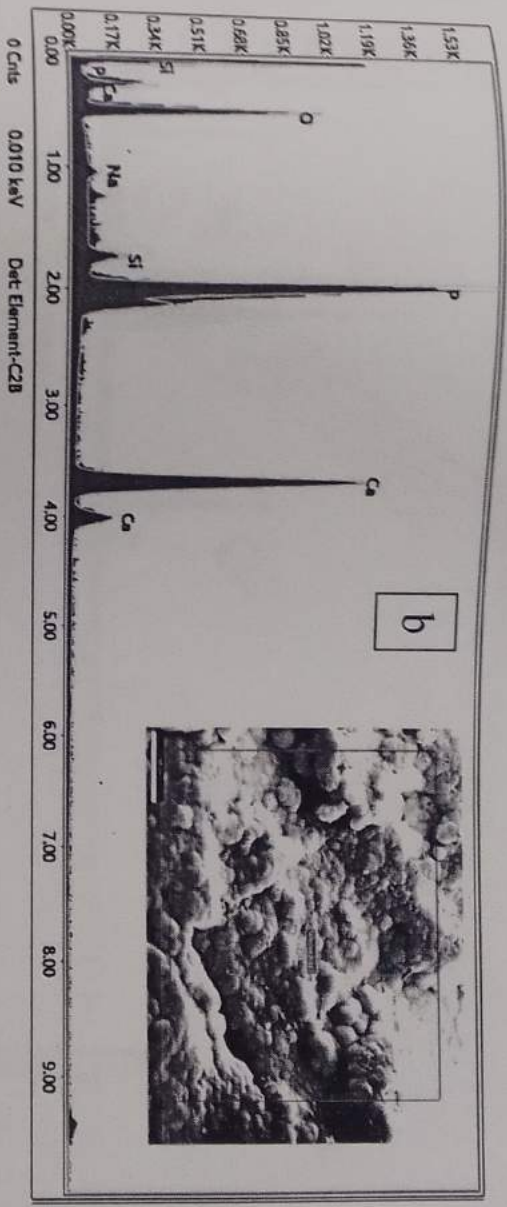
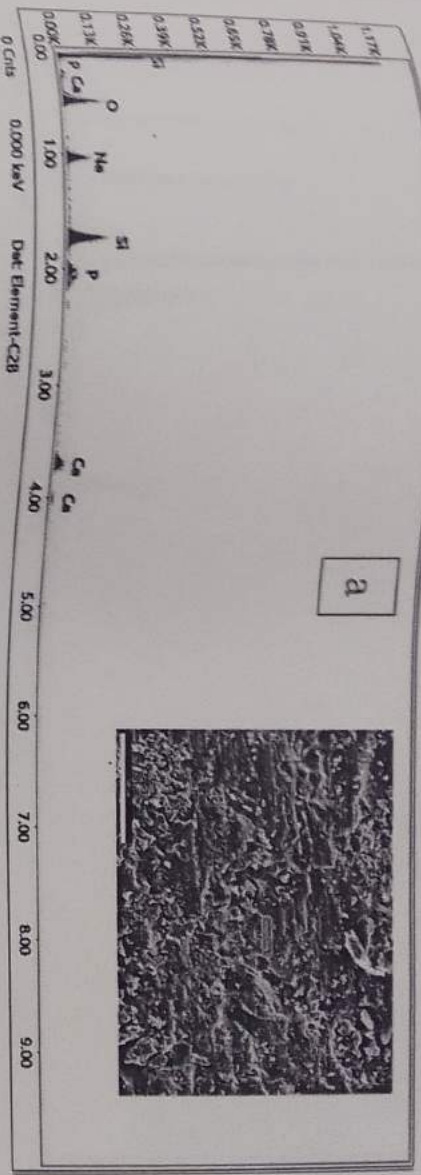


Figure 26. EDX graph of bioactive glass BG-A0F0 (a) before immersion in SBF (b) after immersion in SBF for 14 days (c) after immersion in SBF for 28 days

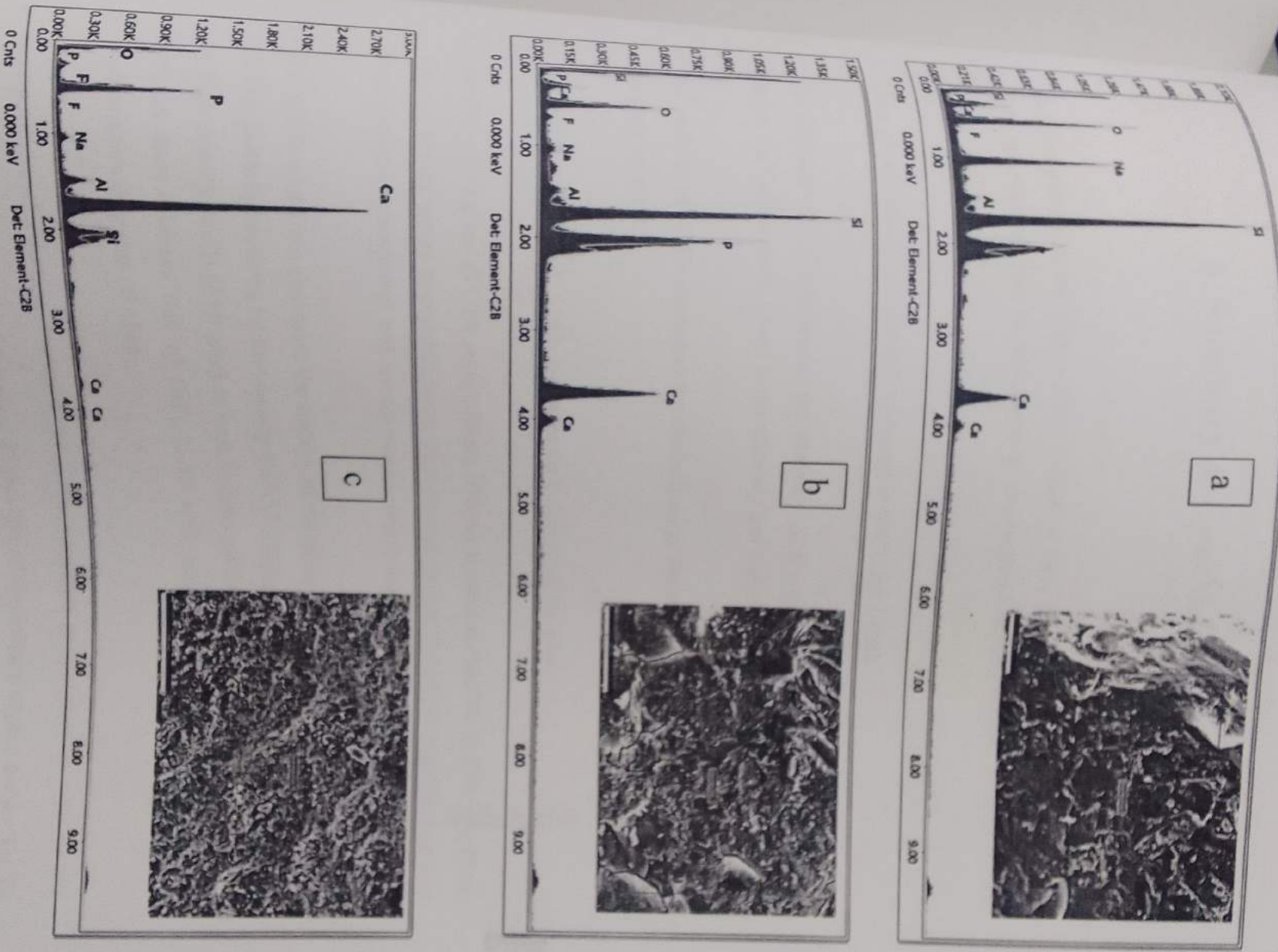


Figure 27. EDX graph of bioactive glass BG-A1F10 (a) before immersion in SBF (b) after immersion in SBF for 14 days (c) after immersion in SBF for 28 days

1. Bioactive glasses in the $\text{SiO}_2 - \text{CaO} - \text{Na}_2\text{O} - \text{P}_2\text{O}_5$ system with and without CaF_2 & Al_2O_3 incorporation can be developed by conventional melting method at 1500°C for 2 hours.
2. These glasses can be successfully annealed at 400°C for 1 hour.
3. The addition of CaF_2 decreases the viscosity of the glass at the melting temperature. Higher the CaF_2 content, lower is the viscosity and higher is the fluidity of the glass.
4. The addition of Al_2O_3 decreases the devitrification tendency of the glass as it strengthens the glass network.
5. The addition of CaF_2 & Al_2O_3 increases the brilliancy of the glass.
6. The BG-A0F0 glass (SS3P4 composition) with no alumina or fluoride exhibits a pinkish tint and is very prone to crystallization whereas alumina and fluoride incorporated glasses are completely transparent and are not much prone to devitrification.
7. The addition of CaF_2 decreases the density of the glass as CaO of higher density (3.345 g/cc) is partially replaced by low density CaF_2 (3.18 g/cc). CaO has been partly replaced by high density Al_2O_3 (3.99 g/cc) as well. But the amount of Al_2O_3 substitution is only 3 wt% at most whereas that of CaF_2 is 10 wt% maximum. So, the effect of CaF_2 predominates over that of Al_2O_3 .
8. Incorporation of Alumina increases the Glass transition temperature as well as the Crystallization temperature of the glass. Higher the Al_2O_3 content, higher are the T_g , T_x

& T_c .

9. The synthesized bioactive glasses showed a pH rise during first 14 days of immersion in SBF, with the biggest rise in the first 24 hours, due to the leaching out of Na^+ , Ca^{2+} and F^- ions in the aqueous medium. After this initial pH increase, the pH remains constant due to formation of apatite layer which restricts further leaching out of ions.
10. The synthesized fluoride containing glasses release F^- ions when the glasses come in contact with any aqueous medium. The glasses showed an increase in fluoride release with increasing fluoride content in glass. After 1 week of immersion in SBF, the fluoride concentration decreases due to the formation of fluorapatite. As fluorapatite has low solubility in water, fluoride release decreases in high immersion time.
11. The pH and F^- concentration were both observed to be higher in saliva than in SBF
12. FTIR of the SBF soaked bioactive glass powder confirmed the formation of apatite.
13. The apatite formation was found gradually reduce with Al_2O_3 incorporation.
14. The weight loss of the synthesized bioactive glasses increased upto 10 days after which it remained almost constant. The weight loss decreased with increase in alumina content, as alumina increases the network connectivity.
15. The synthesized bioactive glasses exhibited sufficiently high anti-bacterial properties. The anti-bacterial efficacy increased with the increase in fluoride content.

9. Scope of Future Work

Further research on the presented topic will harvest more integrated results which will assist us to exploit these S3P4-modified bioactive glasses in several biomedical and scientific areas. There is always scope to improve the property of the biomaterial. Additional investigation that we could perform in the future are as follows:

1. Micro-hardness tests of the bioactive glass samples to evaluate the effect of addition of Alumina to the glass batches.
2. Cytotoxicity tests of the prepared bioactive glasses to assess their biocompatibility through the use of isolated cells in vitro which would aid us in evaluating the toxicity or irritancy potential of the reported biomaterials.
3. Fracture toughness and bending tests of the bioactive glass samples to determine their utility in load-bearing applications.
4. Ca^{2+} and Phosphorus ion analysis of SBF and artificial saliva after immersing the bioactive glass samples in them.
5. XRD analysis of the synthesized bioactive glasses after soaking in SBF and Artificial saliva for fixed time intervals, at a slow scanning rate, so as to ascertain the formation of crystalline Hydroxyapatite or Fluorapatite.
6. FE-SEM of the prepared bioactive glasses before and after immersion in SBF and artificial saliva for obtaining better and conspicuous images of the microstructure.
7. Detailed EDX mapping of several positions on the SBF/Saliva-soaked glass topography in order to get the accurate elemental composition at different points on the glass surface so as to analyze and examine the different morphologies observed on the glass.
8. Incorporation of therapeutic ions like Ag^+ etc. in the glasses in order to increase the biological benefits.
9. In-vivo testing of the reported bioactive glasses for dental and other biomedical applications.

REFERENCES

1. L. Hench, "The Story of Bioglass," *Material Science*, vol. 17, pp. 967-978, 2006.
2. M. N. Rahaman, "Bioactive Glass in Tissue Engineering," *El Sevier*, vol. 7, pp. 2355-2373, 2011.
3. G. Kaur, "A Review of Bioactive Glasses: Their Structure, Properties, Fabrication & Apatite Properties," *Biomedical Materials Research Part A*, vol. 102, no. 1, 2013.
4. A. Coughlan, "Does Elevatin Silver Content in Zinc-Based GPCs Increase Their Antibacterial Efficacy Against Two Common Bacteria?," *Biomaterials Application*, vol. 27, no. 7, 2012.
5. D. Reffitt, "Orthosilicic acid stimulates collagen type I synthesis and osteoblastic differentiation in human osteoblast-like cells in vitro," *Bone*, vol. 32, no. 2, pp. 127-35, 2003.
6. S. Kargozar, "Bioactive Glasses: Sprouting Angiogenesis in Tissue Engineering," *Biotechnology Trends*, vol. 36, no. 4, pp. 430-444, 2018.
7. Y. N. S. Maeno, "The effect of calcium ion concentration on osteoblast viability, proliferation and differentiation in monolayer and 3D culture," *Biomaterials*, vol. 26, no. 23, pp. 4847-4855, 2005.
8. P. Valerio, "Effects of extracellular calcium concentration on the glutamate release by bioactive glass preincubated osteoblasts," *Biomaterials*, 2009.
9. Buzalaf MAR, Fluoride and the Oral Environment, *Monogr Oral Sci*, Basel, Karger, 2011, vol 22, p 97-114.
10. Fejerskov O, Kidd, EA, Nyvad B, Baclum V, Defining the disease: an introduction: in Fejerskov O, KiddE (eds): *Dental Caries- The Disease and its Clinical Magement*, ed 2, Oxford, Blackwell Munksgaard, 2008, p 3-6.
11. Featherstone JD, Dental Caries: a dynamic disease process, *Aust Dent J*, 2008;53(3):286-91.
12. Anderson P, Hector MP, Rampersad MA, Critical pH in resting and simulated whole saliva in groups of children and adults, *Int J Paediatr Dent*, 2001, 11 (4):266-73.
13. Featherstone JDB, Prevention and reversal of dental caries: role of low level fluoride, *community Dent Oral Epidemiol* 1999, 27: 31-40.

14. Featherstone JDB, Glenna r, Shariati M, Shields CP, Dependence of invitro demineralization and remineralization of dental enamel on fluoride concentration, *J Dent Res*, 1990, 69:620-5.
15. Ten Cate JM, featherson JDB, Mechanistic aspects of the interactions between fluoride and dental enamel, *Crit Rev Oral Biol* 1991, 2:283-96.
16. Fejerskov O, Thystrup A, Larsen MJ, Rational use of fluorides in caries prevention, *ACTA Odontol Scand*, 1981:39:241-9.
17. Hamilton IR, Bowden GHW, Fluoride effects on oral bacteria, In Fejerskov O Ekstrand J, Burt BA (eds) *Fluoride in Dentistry*, Copenhagen, Munksgaard, 1996 p 230-51.
18. Van Louveren C, the antimicrobial action of fluoride and its role in caries inhibition, *J Dent Res*1990:69:676-81.
19. Whitford GM, Wadison JL, Schafer TE, Adair SM, Plaque fluoride concentrations are dependent on plaque calcium concentrations, *Caries Res* 2002, 36:256-265.
20. Pessan JP, Alves KM, Ramires I, et al, Effects of regular and low-fluoride, *J Dent Res*, 2010, 89:1106-1110.
21. Sonis, Stephen T. (2003). *Dental Secrets* (3 ed.). Philadelphia: Hanley & Belfus. p. 158.
22. McCabe, John F.; Walls, Angus W.G. (2008). *Applied Dental Materials* (9 ed.). Oxford, United Kingdom: Wiley-Blackwell (an imprint of John Wiley & Sons Ltd). pp. 284–287.
23. Tenuta LM, Cury JA. Fluoride: its role in dentistry. *Braz Oral Res*. 2010;24 Suppl 1:9-17.
24. Tenuta LM, Zamataro CB, Del Bel Cury AA, Tabchoury CP, Cury JA. Mechanism of fluoride dentifrice effect on enamel demineralization. *Caries Res*. 2009;43(4):278-285.
25. Cury JA, Tenuta LM. Enamel remineralization: controlling the caries disease or treating early caries lesions?. *Braz Oral Res*. 2009;23 Suppl 1:23-30.
26. Dijkman A, Huizinga E, Ruben J, Arends J. Remineralization of human enamel in situ after 3 months: the effect of not brushing versus the effect of an F dentifrice and an F-free dentifrice. *Caries Res*. 1990;24(4):263-266.
27. Featherstone JD. The caries balance: the basis for caries management by risk assessment. *Oral Health Prev Dent*. 2004;2 Suppl 1:259-264.
28. Fejerskov O. Concepts of dental caries and their consequences for understanding the disease. *Community Dent Oral Epidemiol*. 1997;25(1):5-12.

29. Silverstone LM. Laboratory studies on the demineralization and remineralization of human enamel in relation to caries mechanisms. *Aust Dent J.* 1980;25(3):163-168.
30. El-Cezeri Journal of Science and Engineering Vol: 4, No: 3, 2017 (436-471)
31. Cunha MT, Murça MA, Nigro S, Klautau GB, Salles MJ (April 2018). "In vitro antibacterial activity of bioactive glass S53P4 on multiresistant pathogens causing osteomyelitis and prosthetic joint infection". *BMC Infectious Diseases. BioMed Central.* 18 (1): 157. doi:10.1186/s12879-018-3069-x. PMC 5883601. PMID 29614973.
32. Virolainen P, Heikkilä J, Yli-Urpo A, Vuorio E, Aro HT (April 1997). "Histomorphometric and molecular biologic comparison of bioactive glass granules and autogenous bone grafts in augmentation of bone defect healing". *Journal of Biomedical Materials Research.* 35 (1): 9–17. doi:10.1002/(SICI)1097-4636(199704)35:1<9::AID-JBM2>3.0.CO;2-S. PMID 9104694.
33. Zhang D, Leppäranta O, Munnukka E, Ylänen H, Viljanen MK, Eerola E, et al. (May 2010). "Antibacterial effects and dissolution behavior of six bioactive glasses". *Journal of Biomedical Materials Research. Part A.* 93 (2): 475–83. doi:10.1002/jbm.a.32564. PMID 19582832.
34. Leppäranta O, Vaahio M, Petola T, Zhang D, Hupa L, Hupa M, et al. (February 2008). "Antibacterial effect of bioactive glasses on clinically important anaerobic bacteria in vitro". *Journal of Materials Science: Materials in Medicine.* 19 (2): 547–51. doi:10.1007/s10856-007-3018-5. PMID 17619981. S2CID 21444777.
35. Drago L, De Vecchi E, Bortolin M, Toscano M, Mattina R, Romano CL (2015). "Antimicrobial activity and resistance selection of different bioglass S53P4 formulations against multidrug resistant strains". *Future Microbiology.* 10 (8): 1293–9. doi:10.2217/FMB.15.57. PMID 26228640.
36. Drago L, Vassena C, Fenu S, De Vecchi E, Signori V, De Francesco R, Romano CL (2014). "In vitro antibiofilm activity of bioactive glass S53P4". *Future Microbiology.* 9 (5): 593–601. doi:10.2217/fmb.14.20. PMID 24957087
37. Bortolin, M., De Vecchi, E., Romano, C. L., Toscano, M., Mattina, R., & Drago, L. (2015). Antibiofilm agents against MDR bacterial strains: is bioactive glass BAG-S53P4 also effective? *Journal of Antimicrobial Chemotherapy*, 71(1), 123–127. doi:10.1093/jac/dkv327
38. Y. Gao, N. Karpukhina, Robert V. Law, Phase segregation in hydroxyfluorapatite solid solution at high temperatures studied by combined XRD/solid state NMR, *RSC Adv.* 6 (105) (2016) 103782–103790.

39. K. Pajor, L. Pajchel, J. Kolmas, Hydroxyapatite and fluorapatite in conservative dentistry and oral implantology — a review, *Materials* 12 (17) (2019) 2683.
40. Z. Lei, F. Li, X. Chen, F.-M. Mo, X. Chen, The in vitro osteogenic and angiogenic effects of sodium-free fluoride-containing bioactive glasses, *Mater. Lett.* 248 (2019) 138–142.
41. F.A. Shah, D.S. Brauer, R.M. Wilson, R.G. Hill, K.A. Hing, Influence of cell culture medium composition on in vitro dissolution behavior of a fluoride-containing bioactive glass, *J. Biomed. Mater. Res. Part A* 102 (3) (2014) 647–654.
42. M. Kleerekoper, R. Vieth, Fluoride and the skeleton, *Crit. Rev. Clin. Lab. Sci.* 33 (2) (1996) 139–161.
43. F. Yao, R.Z. LeGeros, Carbonate and fluoride incorporation in synthetic apatites: comparative effect on physico-chemical properties and in vitro bioactivity in fetal bovine serum, *Mater. Sci. Eng. C* 30 (3) (2010) 423–430.
44. D. Haguenaer, B. Shea, P. Tugwell, G.A. Wells, V. Welch, Fluoride for treating postmenopausal osteoporosis, *Cochrane Database Syst. Rev.* (4) (2000).
45. Z. Li, B. Huang, S. Mai, X. Wu, H. Zhang, W. Qiao, X. Luo, Z. Chen, Effects of fluoridation of porcine hydroxyapatite on osteoblastic activity of human MG63 cells, *Sci. Technol. Adv. Mat.* 16 (3) (2015) 035006.
46. E. Gentleman, M.M. Stevens, R. Hill, D.S. Brauer, Surface properties and ion release from fluoride-containing bioactive glasses promote osteoblast differentiation and mineralization in vitro, *Acta Biomater.* 9 (3) (2013) 5771–5779.
47. H. Qu, M. Wei, The effect of fluoride contents in fluoridated hydroxyapatite on osteoblast behavior, *Acta Biomater.* 2 (1) (2006) 113–119.
48. Leszek Borkowskia, Agata Przekoraa, Anna Belcarza, Krzysztof Palkab, Grzegorz Jozefaciukc, Tomasz Lübekd, Mariusz Jojczukd, Adam Nogalskid, Grazyna Ginalskaa, Fluorapatite ceramics for bone tissue regeneration: Synthesis, characterization and assessment of biomedical potential, *Materials Science & Engineering C* 116 (2020) 111211, <https://doi.org/10.1016/j.msec.2020.111211>
49. M. Mansoorianfar, M. Mansourianfar, M. Fathi, S. Bonakdar, M. Ebrahimi, E.M. Zahrani, A. Hojjati-Najafabadi, D. Li, Surface modification of orthopedic implants by optimized fluorine-substituted hydroxyapatite coating: enhancing corrosion behavior and cell function, *Ceram. Int.* 46 (2) (2020) 2139–2146.

50. Golub, Ellis & Boesze-Battaglia, Kathleen, The role of alkaline phosphatase in mineralization, *Current Opinion in Orthopaedics*, 18, (2007), 444-448.
51. M..Jokinen , T.Peltola , J.Simola ,J.Korventausta and A.Yli-Urpo , Nanoscale surface structure of bioactive glass (S53P4) as a function of immersion time in SBF , *Key Engineering Materials Vols 192-195 (2001) pp 601-604* , Page no:5.
52. Helena Yli-Urpo , Timo Narhi and Eva Soderling , Antimicrobial effects of glass ionomer cement containing bioactive glass (S53P4) on oral micro-organisms in vitro , *Acta Odontol Scand* 61 (2003) , Page no:6.
53. Matthias Zehnder, DMD, Eva Söderling, PhD, Jukka Salonen, DDS, PhD, and Tuomas Waltimo, DDS, PhD , Preliminary evaluation of bioactive glass S53P4 as an endodontic medication in vitro,*Journal of Endodontics* Vol. 30, No. 4, April 2004 , Page no:5.
54. Ari-Pekka Forsback , Sami Areva and Jukka I.Salonen , Mineralization of dentin induced by treatment with bioactive glass (S53P4) in vitro , *Acta Odontol Scand* 62 ,2004 , Page no:7.
55. Toshiyuki Itotaa, Thomas E. Carricka , Sandra Rusbya , Omar Taha Al-Naimia , Masahiro Yoshiyamab , John F. McCabe , Determination of fluoride ions released from resin-based dental materials using ion-selective electrode and ion chromatograph , *Journal of Dentistry* (2004) 32, 117–122 , Page no:6.
56. Helena Yli-Urpo , Matti Na`rhi and Timo Na`rhi , Compound changes and tooth mineralization effects of glass ionomer cements containing bioactive glass (S53P4), an in vivo study , *Biomaterials* 26 (2005) 5934–5941 , Page no:8.
57. Matthias Zehnder, DMD,a Tuomas Waltimo, DMD, PhD,b Beatrice Sener,c and Eva So`derling, PhD,d Zurich and Basel , Dentin enhances the effectiveness of bioactive glass S53P4 against a strain of *Enterococcus faecalis* , *Larz S. W. Spangberg* Vol. 101 No. 4 April 2006 , Page no:6.
58. Tuomas Waltimo , Matthias Zehnder & Eva so` Derling , Bone powder enhances the effectiveness of bioactive glass S53P4 against strains of *Porphyromonas gingivalis* and *Actinobacillus actinomycetemcomitans* in suspension, *Acta Odontologica Scandinavica*, 2006, 64: 183/186 , Page no:4.
59. Tadashi Kokubo, Hiroaki Takadama , How useful is SBF in predicting in vivo bone bioactivity? , *Biomaterials* 27 (2006) 2907–2915 , Page no:9.

60. Ulrich Lohbauer , Dental Glass Ionomer Cements as Permanent Filling Materials? — Properties, Limitations and Future Trends , *Materials* 2010, 3, 76-96, doi:10.3390/ma3010076 , Page no:22
61. AR Prabhakar, Jibi Paul M, N Basappa , Comparative Evaluation of the Remineralizing Effects and Surface Microhardness of Glass Ionomer Cements Containing Bioactive Glass (S53P4): An in vitro Study , 10.5005/jp-journals-10005-1057 ,2010 , Page no:9.
62. Jonathan Massera, Susanne Fagerlund, Leena Hupa, and Mikko Hupa , Crystallization Mechanism of the Bioactive Glasses, 45S5 and S53P4 , *J. Am. Ceram. Soc.*, 95 [2] 607–613 (2012) , Page no:7.
63. S. Fagerlund , J. Massera , N. Moritz , L. Hupa , M. Hupa , Phase composition and in vitro bioactivity of porous implants made of bioactive glass S53P4 , *Acta Biomaterialia* 8 (2012) 2331–2339 , Page no:9.
64. Pajchel, L.; Borkowski, L., Solid-State NMR and Raman Spectroscopic Investigation of Fluoride-Substituted Apatites Obtained in Various Thermal Conditions. *Materials*, (2021), 14, 6936, <https://doi.org/10.3390/ma14226936>
65. J. McAndrew , C. Efrimescu , E. Sheehan , D. Niall , Through the looking glass, bioactive glass S53P4 (BonAlive) in the treatment of chronic osteomyelitis , *Ir J Med Sci* (2013) 182:509–511 ,Page no:3.
66. Rayees Ahmad Shiekh , Ismail Ab Rahman, Sam'an Malik Masudi, Norhayati Luddin , Modification of glass ionomer cement by incorporating hydroxyapatite-silica nano-powder composite: Sol–gel synthesis and characterization , *Ceramics International* 40 (2014) 3165–3170, Page no:8.
67. Istvan Gergely , Ancuta Zazgyva, Adrian Man , Sandor Gyorgy Zuh and Tudor Sorin Pop , The in-vitro antibacterial effect of S53P4 bioactive glass and gentamicin impregnated polymethylmethacrylate beads, *Acta Microbiologica et Immunologica Hungarica*, 61 (2), pp. 145–160 (2014) , Page no:16.
68. Lorenzo Drago , Elena De Vecchi, Monica Bortolin, Marco Toscano , Roberto Mattina & Carlo Luca Romanò , Antimicrobial activity and resistance selection of different bioglass S53P4 formulations against multidrug resistant strains, *Future Microbiol.* (2015) 10(8), 1293–1299 , Page no:7.

69. Shariq Najeeb , Zohaib Khurshid , Muhammad Sohail Zafar , Abdul Samad Khan , Sana Zohaib , Juan Manuel Nuñez Martí , Salvatore Sauro , Jukka Pekka Matinlinna and Ihtesham Ur Rehman , Modifications in Glass Ionomer Cements: Nano-Sized Fillers and Bioactive Nanoceramics , *Int. J. Mol. Sci.* 2016, 17, 1134, doi:10.3390/ijms17071134 , Page no:14.
70. T. De Caluwé a,*, C.W.J. Vercrusse a, I. Ladik a, R. Convents a, H. Declercq b, L.C. Martens c , R.M.H. Verbeeck , Addition of bioactive glass to glass ionomer cements: Effect on the physico-chemical properties and biocompatibility , *dental materials* 33 (2 0 1 7) e186–e203 , Page no:18.
71. Wan Nurshamimi Wan Jusoha , Khamirul Amin Matoria , Mohd Hafiz Mohd Zaida , Norhazlin Zainuddin , Mohammad Zulhasif Ahmad Khirib , Nadia Asyikin Abdul Rahmana , Rohaniah Abdul Jalila , Esra Kuld , Effect of sintering temperature on physical and structural properties of Alumino-Silicate-Fluoride glass ceramics fabricated from clam shell and soda lime silicate glass , *Results in Physics* 12 (2019)1909-1914 , Page no:6.
72. Hans Erling Skallevoid , Dinesh Rokaya , Zohaib Khurshid and Muhammad Sohail Zafar , Bioactive Glass Applications in Dentistry , *Int. J. Mol. Sci.* 2019, 20, 5960, doi:10.3390/ijms20235960 , Page no:24.
73. Sakthi Prasad , Sudheer Ganiseti , Anuradha Jana, Shashi Kant , P.K. Sinha , Sucheta Tripathy , Kavya Illath , T.G. Ajithkumar , K. Annapurna , Amarnath R. Allu , Kaushik Biswas, Elucidating the effect of CaF₂ on structure, biocompatibility and antibacterial properties of S53P4 glass , *Journal of Alloys and Compounds* 831 (2020) 154704 , Page no:14.
74. Eline G. J. Thijssen, Nicole A. P. van Gestel , Raymond Bevers , Sandra Hofmann , Jan Geurts , Inge H. M. van Loo⁴ and J. J. Arts , Assessment of Growth Reduction of Five Clinical Pathogens by Injectable S53P4 Bioactive Glass Material Formulations , ORIGINAL RESEARCH published: 26 June 2020 doi: 10.3389/fbioe.2020.00634 , Page no:9.
75. Francesco Baino and Seiji Yamaguchi , The Use of Simulated Body Fluid (SBF) for Assessing Materials Bioactivity in the Context of Tissue Engineering: Review and Challenges , *Biomimetics* 2020, 5, 57, doi:10.3390/biomimetics5040057 , Page no:19.
76. Sharat Chandra Pani , Moath Tofik Aljammaz, Abdullah Mohammed Alrugi, Abdulaziz Mohammed Aljumaah, Yazeed Minahi Alkahtani, and Abdulaziz AlKhuraif , Color Stability of Glass Ionomer Cement after Reinforced with Two Different Nanoparticles , *Hindawi International Journal of Dentistry* Volume 2020, Article ID 7808535, Page no:5.

77. Maria Cannio , Devis Bellucci , Judith A. Roether , Dino. N. Boccaccini and Valeria Cantillo, Bioactive Glass Applications: A Literature Review of Human Clinical Trials , *Materials* 2021, 14, 5440. <https://doi.org/10.3390/ma14185440> , Page no:25.
78. Bureu Karakuzu-Ikizlera, Pinar Terzioğlu, Yeliz Basaran-Elalmisa, Bilge Sema Tekerek, Sevil Yücel, Role of magnesium and aluminum substitution on the structural properties and bioactivity of bioglasses synthesized from biogenic silica, *Bioactive Materials* 5 (2020) 66–73
79. Monica Bortolin, Elena De Vecchi, Carlo Luca Romano, Marco Toscano, Roberto Mattina, Lorenzo Drago, Antibiofilm agents against MDR bacterial strains: is bioactive glass BAG-SS3P4 also effective, *J. Antimicrob. Chemother.*, 2015, doi:10.1093/jac/dkv327
80. Konstantinos Dimitriadis, Dishat U. Tulyaganov, Simeon Agathopoulos, Development of novel alumina-containing bioactive glass-ceramics in the CaO-MgO-SiO₂ system as candidates for dental implant applications, *Journal of the European Ceramic Society* 41 (2021) 929–940
81. R.Casasola , J.M.Perez,M.Pomero,Effect of fluorine content on glass stability and crystallization mechanism for glasses in SiO₂-CaO-K₂O-F system , *Jr-Non-crys solids* ,378 (2013), 25-33
82. G. Lusvardi et. al., *J. Phy.Chem.B.* Vol 113, No. 30, 2009, 10331-10338
83. Y.C. Fred halm , Natalia Kanpukhina , R. Law & R.G.H-U , Strontium containing bioactive glasses, 'Glass structure and physical properties', *J.non-crys. solids*, 356(2010)2546-2551
84. Ram Karan , Influence of SeO on properties of bioglass in SiO₂-Na₂O-CaO-P₂O₅ system, *J.Aus-Ceram SoC.*56(2020)1135-1145
85. J. Pure, *Appl. Phys* 38, 2000, 741-761
86. Chayris , Bouhazna , Studies on preparation and characterization of SiO₂-CaO-P₂O₅ and SiO₂-CaO-P₂O₅-Na₂O bioglasses substituted with ZnO , *J.Mate. Environ Sci .* 6 (1882-1897) 2015
87. Sakthi Prasad et al. *Ceramic International* 48(2022) 4512-25
88. Ather Farooq Khan, Muhammad Awais, Abdul Samad Khan, Sobia Tabassum, Aqif Anwar Chaudhry, Intesham Ur Rehman, Raman Spectroscopy of Natural Bone and Synthetic Apatites, *Applied Spectroscopy Reviews*, 48 (4), 2013, 329-355

**ROLE OF MWCNT IN LOW CARBON CONTAINING
MAGNESIA CARBON BRICK**

*A thesis submitted in partial fulfillment of the
Requirement for the degree of*

MASTER OF TECHNOLOGY
In Ceramic Technology

By

Somak Basu Mallick

Roll No.- GCECTM-R20-1003

Registration No. - 201130410710003 OF 2020-21



Under the guidance of

Dr. Barun Kumar Saufi

Assistant Professor

Department Of Ceramic Technology

Government College of Engineering & Ceramic Technology

Kolkata-700010

**ROLE OF MWCNT IN LOW CARBON CONTAINING
MAGNESIA CARBON BRICK**

*A thesis submitted in partial fulfilment of the
Requirement for the degree of*

**MASTER OF TECHNOLOGY
In Ceramic Technology**

By

Somak Basu Mallick

Roll No.- GCECTM-R20-1003

Registration No.- 201130410710003 OF 2020-21



Under the guidance of

Dr. Barun Kumar Sanfui

Assistant Professor

Department Of Ceramic Technology

Government College of Engineering & Ceramic Technology

Kolkata-700010

9748765816

PROSENJIT

9433133101

(Bishu)
SUJIT

**DECLARATION OF ORIGINALITY AND COMPLIANCE OF
ACADEMIC ETHICS**

I do hereby declare the thesis contents including literature review are original research work by the undersigned candidate, as part of fulfilment of Master of Technology in Ceramic Technology, undertaken in academic session 2020-2022.

All information in the document has been obtained and presented in accordance with academic rules and ethical conduct.

I also declare that in this thesis, I have fully cited and referred all the material and results related to this original work.

Name- Somak Basu Mallick

Roll No.- GCECTM-R20-1003

Registration No.- 201130410710003 OF 2020-21

Signature: Somak Basu Mallick

Date: 03/06/2022

Somak Basu Mallick
03/06/2022

INDEX

Serial No.	Topic	Page No.
	Acknowledgements	v
	List of figures	vi
	List of tables	viii
Chapter 1	Introduction	1
Chapter 2	Literature Review	6
2.1.1	Carbon Nanotube	6
2.1.2	Types of Carbon Nanotube	7
2.1.3	Different Techniques for Fabrication of Carbon Nanotube	8
2.1.4	Property of Carbon Nanotube	10
2.2	Magnesia Carbon Refractory	12
Chapter 3	Objectives	17
Chapter 4	Plan Of Work	18
Chapter 5	Experimental Procedure	19
5.1	Starting Materials	19
5.2	Procedures	19
5.2.1	Preparation of standard batch composition with flaky graphite	21
5.2.2	Preparation of standard batch composition with flaky graphite & nano carbon black	22
5.2.3	Preparation of standard batch composition with flaky graphite & nano carbon black & MWCNT	24
5.2.3.1	Dispersion of MWCNT in PF Resin	25
5.2.3.2	Viscojet Stirrer	26
5.3	Mixing	26
5.4	Ageing	27
5.5	Pressing	28
5.6	Tempering	28
5.7	Coking	28
5.8	Flow Chart of process of manufacturing of MGC brick with all ingredients	29
5.9	Theory of Testing & Measurement	30
Chapter 6	Results and Discussion	33
6.1	Bulk Density	33

6.2	Apparent Porosity	36
6.3	CCS	39
6.4	Linear Firing Shrinkage	42
6.5	Oxidation resistance	43
Chapter 7	Conclusion	48
Chapter 8	Scope of Future Work	49
Chapter 8	Reference	50

Acknowledgements

This dissertation would not have been possible without the guidance and the help of several individuals who in one way or another contributed and extended their valuable assistance in the preparation and completion of this study.

Foremost, I would like to express my sincere gratitude to my HOD Mr. Rituparno Sen, my guide/advisor Dr. Barun Kumar Sanfui for the continuous support during my M. Tech project, for his patience, motivation, enthusiasm, and continuous knowledge sharing. It is my pleasure and fortune to receive their encouragement and immense effort without which this thesis, too, would not have been completed or written timely.

I express my sincere thanks to Dr. Barun Kumar Sanfui, Assistant professor, Department of Ceramic Technology, Government College of Engineering & Ceramic Technology for providing me all the departmental facilities required for the completion of the thesis. His profound help and guidance helped the thesis to reach a final shape executing the project on time inspite of several odds of Covid. I express vote of thanks to all other teachers of our department & institution.

I am also indebted to Mr. Savan Kumar Sharma SRF, CSIR, Government College of Engineering & Ceramic Technology and Tanmoy Biswas, SRF, IREL for their unconditional support and constant motivation whenever needed. And a big thanks to my classmates Udayan Mukherjee, Santanu Majumdar & Nabonita Chakraborty for giving me a helping hand whenever needed.

Last but not the least, I would like to thank my dear parents, my well wishers for their support.

Somak Basu Mallick

List of Figures

Figure No.	Title	Page No.
1	The conceptual diagram showing the general dimensions of the length and width of single-walled carbon nanotubes (SWCNTs) and multi-walled carbon nanotubes (MWCNTs) (1)	2
2	Structure of Magnesia (MgO).	5
3	Figure 3. a) SWCNT, b) Multiple graphene roll give rise to MWCNT.	6
4	a) The chiral vector C_h determine the tube diameter. b) Three model of atomically perfect SWNT structure.	7
5	(1) Schematic Diagram of Arc-discharge. Two graphite electrodes are used to produce a dc electric arc-discharge in inert gas atmosphere, (2) Schematic Diagram of Laser-ablation. Laser beam vaporizes target of a mixture of graphite and metal catalyst (Co, Ni) in a horizontal tube in a flow of inert gas at controlled pressure and in a tube furnace at 1200 8C. The nanotubes are deposited on a water-cooled collector outside the furnace.	9
6	Mixing batch prepared with fused Magnesia & flaky graphite	21
7	Visco jet stirring arrangement for dispersion of MWCNT in PF Resin	25
8	Viscojet Stirrer (Three cone arrangement)	26
9	Cylinder of Mixer	27
10	Stirrer of Mixer	27
11	Ready Mix After Ageing	27
12	Uniaxial hydraulic press.	28

13	Tempered Samples	29
14	Coked Samples	29
15	Mettler Toledo analytical balance with a density measurement kit.	31
16a&16b	Graph of Tempered BD variation	34
17a&17b	Graph of Coked BD variation	35
18a&18b	Graph of Tempered AP variation	37
19a&19b	Graph of Coked AP variation	38
20a&20b	Graph of Tempered CCS variation	40
21a&21b	Graph of Coked CCS variation	41
22	Graph of Oxidation Resistance Variation	43
23	Tempered sample after Oxidation at 1400° C	44
24a&24b	Sample with 3wt % graphite, no MWCNT & 2.10 wt % graphite with 0.9 wt% nano carbon black after oxidation at 1400° C	44
25	Sample with 0.05 wt % MWCNT after oxidation at 1400° C	45
26	Sample with 0.1 wt % MWCNT after oxidation at 1400° C	45
27	Sample with 0.2 wt % MWCNT after oxidation at 1400° C	45
28	SEM Image of 0.1 wt % MWCNT bearing sample, 2kx	46
29	SEM Image of 0.1 wt % MWCNT bearing sample, 5kx	46
30	XRD Analysis of 0.1 wt % MWCNT bearing sample	47

List of Tables

Table No.	Title	Page No.
1	Summary and comparison of three most common CNT synthesis methods (2)	8
2	Raw Material properties as in literature	14
3	Raw Material Analysis	20
4	Standard Batch Composition with Graphite	21
5	Batch variation of 0.5 wt % Nano carbon & 2.5 wt % graphite	23
6	Batch variation of 0.9 wt % Nano carbon & 2.10 wt % graphite	23
7	Batch variation of 1.5 wt % Nano carbon & 1.5 wt % graphite	23
8	Batch variation of 2.0 wt % Nano carbon & 1.0 wt % graphite	23
9	Batch variation of 3.00 wt % Nano carbon & 0 wt % graphite	23
10	Fused Magnesia Size Fractions	22
11	Batch variation of 0.95 wt % nanocarbon & 0.05 wt % MWCNT	24
12	Batch variation of 0.9 wt % nanocarbon & 0.1 wt % MWCNT	24
13	Batch variation of 0.8 wt % nanocarbon & 0.2 wt % MWCNT	24
14	Fused Magnesia Size Fractions	22
15	B 1 to B 4 BD variation Analysis	33
16	B 5 to B 12 BD variation Analysis	33
17	B 1 to B 4 AP variation Analysis	36
18	B 5 to B 12 AP variation Analysis	36

19	B 1 to B 4 CCS variation Analysis	39
20	B 5 to B 12 CCS variation Analysis	39
21	Linear Shrinkage of MWCNT containing batches	42
22	Oxidation Resistance Test Results	43

Chapter 1

Introduction

Growth in steel sector is one of the key factor indicating the infrastructural development of a country and thereby its economy. To facilitate the making of steel, refractory plays a significant role without which high temperature (say 1000°C above) unit operations can hardly be done. Discussion about steel plant refractory remains incomplete without the mention of magnesia carbon refractory. Almost all essential equipment linked to steel making (primary and secondary) are lined with this magnesia carbon refractory in general. As the name suggests this type of refractory constitutes broadly of magnesia (MgO) from different raw materials and carbon (C) say in the form of flaky graphite etc. Till date all over the world bulk production of the magnesia carbon bricks or refractory is done using flaky graphite (fixed carbon > 90 %) as carbon source in sufficiently high percentage. Several research and attempts have been made to lower the use of graphite in refractory due to different reasons which are to be discussed subsequently. Use of nano sized carbon has been suggested as an alternative (partially) to support further developments and improvements in magnesia carbon refractory making. The use of nanocarbon (say nano carbon black etc.) is relatively new compared to the use of graphite. The nanoparticles are almost in molecular scale [1] and are the smallest unit of materials commercially available. The reactivity of these nanosized materials being much more (due to higher exposed surface area) compared to micron sized carbon particle, improved refractory properties are expected with a significantly reduced carbon quantity. Moreover the rate of occurrence of chemical reactions, formation of compounds, composites, ease of sintering, melting etc. are noteworthy positives of using nanomaterials in refractory matrix. To further enhance the scope of research of nanocarbon inclusion and encash the benefit of tube/rod like structure our study will be based on addition of carbon nano tubes (CNT) in the refractory matrix of magnesia carbon bricks/refractory and thereby to assess the properties vis-a-vis the properties derived by using only graphite (present day practice). The research interest in the field of MWCNT has grown extensively in the past decade. Many numbers of attempts have been made to develop ceramic nanobased refractory with better mechanical & corrosion resistance properties as compared to conventional ceramics with graphite in past decades. Since Niihara introduced the concept of

nanocomposites in 1991, the addition of nanofillers as a reinforcement phase has become one of the most promising methods of improving the mechanical properties of ceramic materials. Carbon nanotubes has emerged as potentially attractive nano materials for ceramic matrix which was only limited to graphite earlier, due to its small size, low density, high aspect ratio, high tensile strength and high electrical and thermal conductivity (3). Carbon nanotubes (CNT) were first discovered by Dr. Ijima of Japan in 1991 (4). It is a rolled-up sheet of graphene or a tube made of graphene sheet. Elemental carbon in the sp^2 hybridization can form a variety of structures, which give rise to variety of material such as graphene, fullerenes. In graphene, carbon atoms are densely organized in a sp^2 bonded atomic scale hexagonal pattern, later known as honeycomb pattern. This pattern is the basic structure of carbon nanotube. Due to this we can see some similarities in properties between graphene and carbon nanotube. Carbon can bond in different ways to construct structures with completely different properties. The sp^2 hybridization of carbon builds a layered construction with weak out of plane bonding of the van der Waals type and strong in plane bonds. Carbon nanotube have diameters ranges of 1-100 nm and lengths up to several centimetres. It has high aspect ratio i.e., length to diameter ratio. CNTs are classified as Single walled Carbon nanotubes or Multi walled Carbon nanotube, depending on the rolling layers of graphene sheets.

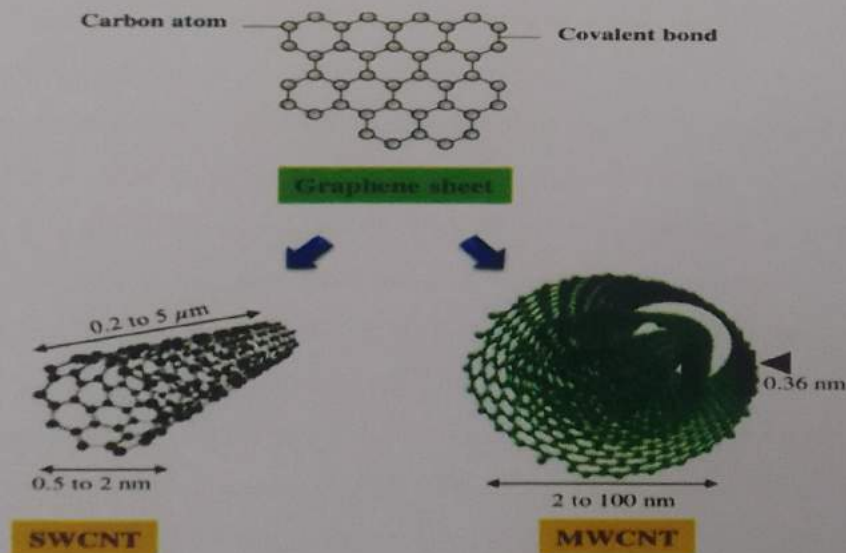


Figure 1. The conceptual diagram showing the general dimensions of the length and width of single-walled carbon nanotubes (SWCNTs) and multi-walled CNTs (MWCNTs) (1).

Despite the excellent properties of CNTs, their reinforcing effects on ceramic matrices have not been fully realized, as they are difficult to disperse and are not compatible with the ceramic matrix because of their bonding nature and hydrophobicity. There are several techniques for the production of CNTs, including arc discharge, laser ablation and chemical vapor deposition. CNTs by their design are chemically unreactive in pristine form, which is typically not desirable for certain applications. To overcome this challenge, it is necessary to functionalize CNTs. The process of functionalization improves their dispersion and consequently their application potential. Commonly, three procedures are being used for producing CNTs: (i) the chemical vapor deposition (CVD) technique, (ii) the laser-ablation technique and (iii) the carbon arc-discharge technique.

Magnesia carbon refractory can be described as a composite material based on MgO and C. It is used either in the form of bricks or castables. The constituents of magnesia carbon bricks are: magnesia grains, which are the main component, graphite, antioxidants to protect the carbon from getting oxidized and high carbon-containing pitch or resin as a binder to keep the different parts of the refractory together. Since the slag in steel-making is predominantly basic in nature, refractories are also basic. They are widely used for steelmaking applications, e.g. the lining of basic oxygen furnaces, steel ladles, LD converters, electric arc furnaces, and applications in secondary steelmaking. These refractories have been dominant along the slag line of ladles for at least a decade due to the properties which are contributed by MgO and carbon. Clean steel can be produced with less refractory consumption by using MgO-C bricks [2]. These refractories enjoy a very significant advantage over Al₂O₃-based and SiO₂-based materials since the melting point of magnesia is 2800 °C. Moreover, a reaction between MgO and C leads to the nascent formation of a dense layer of MgO at the working surface of the MgO-C brick. This layer restricts penetration of slag and metal and promotes corrosion resistance. Unfortunately, MgO has poor thermal shock resistance. In contrast, graphite has high thermal conductivity, low thermal expansion and better spalling resistance. To overcome the shortcomings of MgO, graphite was added to MgO matrix to create a new high temperature material with improved properties. Carbon fills the porous structure of the MgO matrix and, by virtue of its non-wetting character, helps to improve slag and metal corrosion and penetration resistance [3, 4]. Graphite also has lubricating properties due to the presence of weak van der Waals inter-layer bonds. Generally MgO-C refractories contain about 12–18% total carbon and the primary source of carbon is graphite [17–23]. Use of graphite as carbon source offers the following major advantages:

- Higher application temperature due to high melting point and no eutectic formation.
- Improvement in the corrosion resistance against metal and slag due to very low wettability.
- Increase in thermal conductivity, reduction in thermal expansion and elastic modulus, resulting in excellent thermal shock resistance.
- Better packing efficiency due to lubrication property.
- Reduced chances of iron oxide corrosion as iron oxide may reduce to metallic Fe by C.

But carbon suffers from poor oxidation resistance. It may be oxidized to form CO or CO₂, which results in a porous structure having poor strength and reduced corrosion resistance. Adding large amounts of carbon also leads to more heat loss through the refractory and causes higher shell temperatures on steel vessels. Shell deformation then increases, leading to reduction of ladle life. Greater carbon percentage also leads to increased carbon pick-up by steel which is undesirable since steelmaking is normally a decarburization process. Another result is more CO and CO₂ gas by-product, a rising concern for the global environment. These factors have necessitated efforts to reduce the total amount of carbon used in MgO-C materials without sacrificing their major beneficial properties. Use of nano carbon has been found to be an effective solution to this problem. Some of the challenges driving improvement of MgO-C refractories are closely linked with future significant technological advances in the manufacturing of iron and steel, including higher furnace capacities, increases in operating and hot metal temperatures better manufacturing and application environments. These factors have contributed to the launch of extensive research work in the field of MgO-C refractories. Researchers have addressed diverse topics that aim toward better material properties and applications. Use of nanomaterials in refractories has shown following two control technologies [40].

(1) Control of the packing structure by dispersion of nano particles of various shapes, or in pore structure by modification on the surface of coarse grains.

(2) Control of the combination structure in the heat treatment process of binding materials.

In magnesia-carbon refractories, use of nanoadditions has provided a marked increase in the refractory quality and its performances. Use of nano sized antioxidants, namely metallic aluminium and silicon greatly improves oxidation resistances and increases the formation of carbide phases during operation resulting in higher hot strength [41]. A combination of these nano sized anti-oxidants with lamellar type graphite, densely enclosing periclase particles and recompensing their thermal expansion, has made it possible to reduce the carbon content in converter refractories. Apart from protection from oxidation, oxide nano coatings based on silicon oxide or alumino-magnesia-spinel [42], are able to provide hydrophobic from

hydrophilic properties to metal and carbon particles, and to accomplish control of rheological characteristics of repair mass for converters. Nano sized oxide powders are very promising from the point of use in low-cement alumina based unshaped refractories used in ferrous metallurgy [43–45]. In particular, addition of 0.05–0.20 wt % of nano powders makes it possible to increase the ultimate strength in compression for corundum monolithic components by 25–30% [41]. Use of nano boron carbide as anti-oxidant[46] in MgO-C refractory showed higher hot strength and oxidation resistance at an early temperature and better thermal shock properties. Use of nano-sized $MgAl_2O_4$ spinel in the matrix of MgO-C refractory showed improved corrosion, oxidation, and thermal spalling resistances compared to that of conventional MgO-C refractory [47–51]. Nano-spinel particles modify the pore size distribution of MgO-C refractory, restricting the flow of oxygen and slag into the matrix, protect the graphite particles from possible decarburization and results in better performances in the slag lines of ladle metallurgical furnaces.

The structure of magnesium oxide, MgO

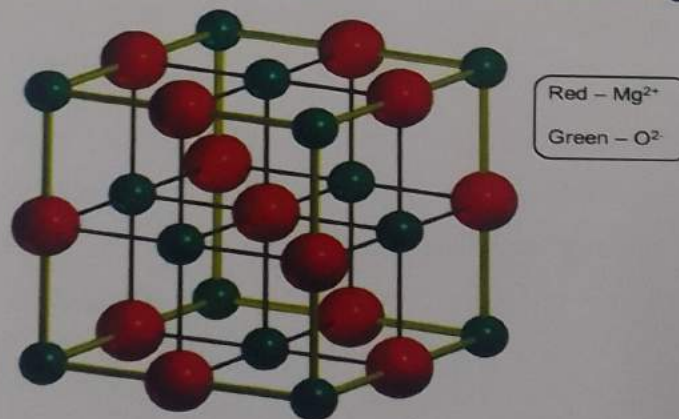


Figure 2. The conceptual diagram showing Magnesia structure

Literature Review

2.1.1 Carbon Nanotube

Carbon is the chemical element with atomic number 6 and has six electrons which occupy $1s^2$, $2s^2$, and $2p^2$ atomic orbital. It can hybridize in sp , sp^2 , or sp^3 forms. The nanometer size sp^2 carbon bonded materials such as graphene, the stunning discovery of fullerenes by Nobel laureates Dr. Richard Smalley, Dr. Harold Kroto and Dr. Robert Curl in the year 1985 which opened a new area of carbon chemistry and carbon nanotubes, first observed in 1991 under an electron microscope by Sumio Iijima and his co-workers, has been the object of intense scientific research ever since (7).

Most of the physical properties of carbon nanotubes derive from graphene. In graphene, carbon atoms are densely organized in a regular sp^2 -bonded atomic-scale honeycomb (hexagonal) pattern, and this pattern is a basic structure for other sp^2 carbon bonded materials (allotropes) such as fullerenes and carbon nanotubes. Carbon nanotube is theoretically distinct as a rolled-up sheet of graphene (2).

Carbon nanotubes can be categorized based on how many of concentric cylinders of carbon nanotubes with the regular periodic interlayer spacing locate around ordinary central hollow and other is depending on which way we fold the same graphene structure (atomic arrangement). Depending on the atomic arrangement, length and diameter, carbon nanotube shows different properties.

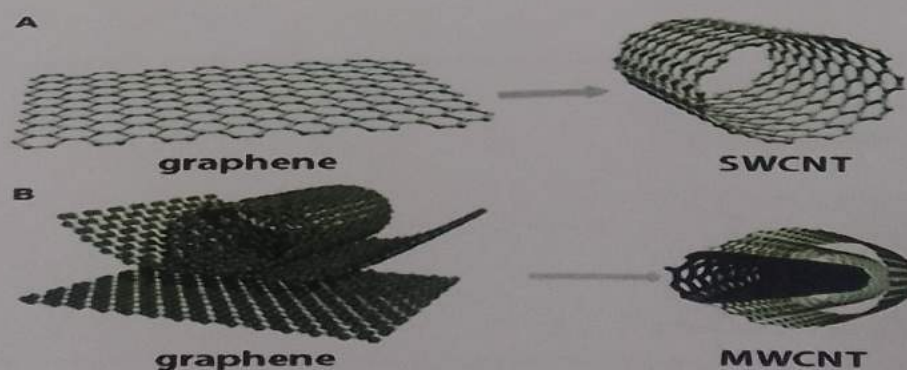


Figure 3. a) SWCNT, b) Multiple graphene roll give rise to MWCNT.

2.1.3 Different Techniques for Fabrication of Carbon Nanotube.

There are several techniques that have been developed for fabricating CNT structures. Commonly, three procedures are being used for producing CNTs: (i) the chemical vapor deposition (CVD) technique, (ii) the laser-ablation technique, and (iii) the carbon arc-discharge technique (Figure 3). High temperature preparation techniques for example arc discharge were first used to synthesize MWCNTs by Iijima in 1991 (4). This method has been used long before that in the production of carbon fibers and fullerenes. It took 2 years to Iijima and Ichihashi (8), and Bethune et al. (9) to synthesize SWCNTs by use of metal catalysts in the arc-discharge method in 1993. And also a significant progress was achieved by another high temperature preparation technique, laser-ablation synthesis of bundles of aligned SWNTs with small diameter distribution by Smalley and co-workers (10). But currently, these techniques have been substituted by low temperature chemical vapor deposition (CVD) methods which was first used by (11) ($<800^{\circ}\text{C}$). Because of the nanotube length, diameter, alignment, purity, density, and orientation of MWCNTs can be accurately controlled in the low temperature chemical vapor deposition (CVD) methods. The industrial application of the carbon nanotubes requires the development of techniques for large-scale production of defect-free nanotubes. In this section, the three main production techniques will be considered separately.

Table 1: Summary and comparison of three most common CNT synthesis methods (2).

Method	Arc discharge	Laser ablation	CVD
Yield rate	>75%	>75%	>75%
SWNT or MWNT	Both	Both	Both
Advantage	Simple, inexpensive, high-quality nanotubes	Relatively high purity, room-temperature synthesis	Simple, low temperature, high purity, large-scale production, aligned growth possible
Disadvantage	High temperature, purification required, tangled nanotubes	Method limited to the lab-scale, crude product purification required	Synthesized CNTs are usually MWNTs, defects

In 1991, Iijima reported the preparation of a new type of finite carbon structures consisting of needle-like tubes (4). The tubes were produced using an arc-discharge evaporation method similar to that used for the fullerene synthesis. The carbon needles, ranging from 4 to 30 nm in diameter and up to 1 mm in length, were grown on the negative end of the carbon electrode used for the direct current (dc) arc-discharge evaporation of carbon in an argon-filled vessel (100 Torr) (Fig 5). Transmission electron microscopy (TEM) revealed that each of the needles comprised coaxial tubes of graphitic sheets, ranging in number from 2 to about 50, later called multi-walled carbon nanotubes. On each of the tubes the carbon-atom hexagons

were arranged in a helical fashion about the needle axis. The helical pitch varied from needle to needle and from tube to tube within a single needle. The tips of the needles were usually closed by curved, polygonal, or cone-shaped caps. A growth model was proposed in which the individual tubes have spiral growth steps at the tube ends.

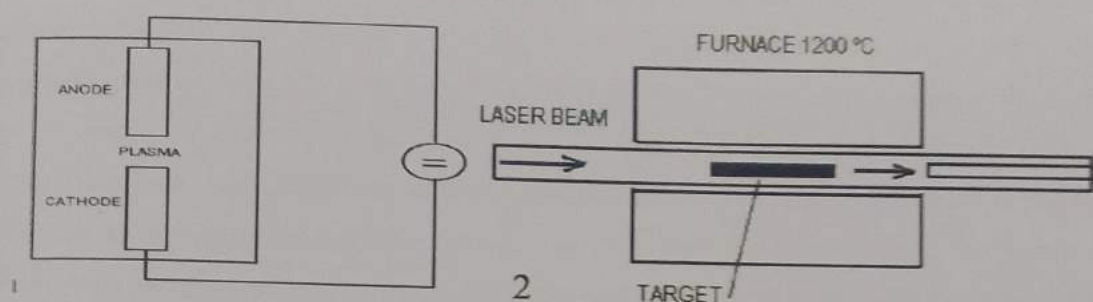


Figure 5. (1) Schematic Diagram of Arc-discharge. Two graphite electrodes are used to produce a dc electric arc-discharge in inert gas atmosphere, (2) Schematic Diagram of Laser-ablation. Laser beam vaporizes target of a mixture of graphite and metal catalyst (Co, Ni) in a horizontal tube in a flow of inert gas at controlled pressure and in a tube furnace at 1200 °C. The nanotubes are deposited on a water-cooled collector outside the furnace.

In 1993, Iijima and Ichihashi (4) and Bethune et al. (9) almost simultaneously reported the arc discharge and catalyst-assisted synthesis of SWNTs. Iijima used arc-discharge chamber filled with a gas mixture of 10 Torr methane and 40 Torr argon. Two vertical thin electrodes were installed in the center of the chamber. The lower electrode, the cathode, had a shallow dip to hold a small piece of iron during the evaporation. The arc-discharge was generated by running a dc current of 200 A at 20 V between the electrodes. The use of the three components—argon, iron and methane, was critical for the synthesis of SWNTs. The TEM analysis of the obtained specimens revealed the presence of SWNT threads, which were curved and tangled together to form bundles. The nanotubes had diameters of 1 nm with a broad diameter distribution between 0.7 and 1.65 nm.

In the arc-discharge synthesis of nanotubes, Bethune et al. (9) used as anodes thin electrodes with bored holes which were filled with a mixture of pure powdered metals (Fe, Ni or Co) and graphite. The electrodes were vaporized with a current of 95–105 A in 100–500 Torr of He. The TEM analysis of the obtained specimens showed that only cobalt-catalyzed nanotubes had single atomic layer walls with uniform diameters of 1.2–0.1 nm.

were arranged in a helical fashion about the needle axis. The helical pitch varied from needle to needle and from tube to tube within a single needle. The tips of the needles were usually closed by curved, polygonal, or cone-shaped caps. A growth model was proposed in which the individual tubes have spiral growth steps at the tube ends.

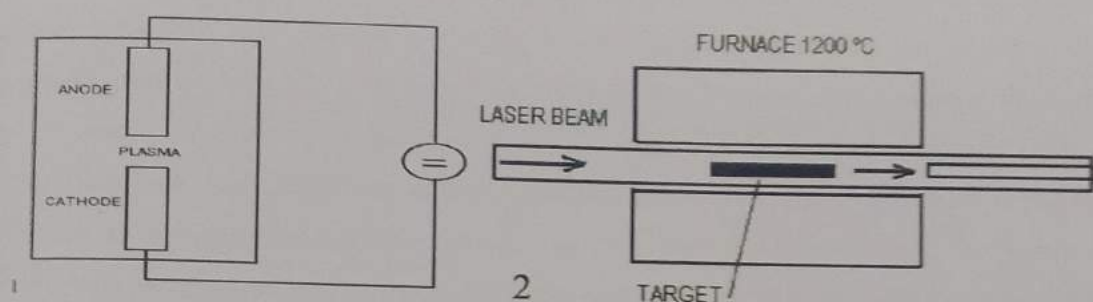


Figure 5. (1) Schematic Diagram of Arc-discharge. Two graphite electrodes are used to produce a dc electric arc-discharge in inert gas atmosphere, (2) Schematic Diagram of Laser-ablation. Laser beam vaporizes target of a mixture of graphite and metal catalyst (Co, Ni) in a horizontal tube in a flow of inert gas at controlled pressure and in a tube furnace at 1200 °C. The nanotubes are deposited on a water-cooled collector outside the furnace.

In 1993, Iijima and Ichihashi (4) and Bethune et al. (9) almost simultaneously reported the arc discharge and catalyst-assisted synthesis of SWNTs. Iijima used arc-discharge chamber filled with a gas mixture of 10 Torr methane and 40 Torr argon. Two vertical thin electrodes were installed in the center of the chamber. The lower electrode, the cathode, had a shallow dip to hold a small piece of iron during the evaporation. The arc-discharge was generated by running a dc current of 200 A at 20 V between the electrodes. The use of the three components—argon, iron and methane, was critical for the synthesis of SWNTs. The TEM analysis of the obtained specimens revealed the presence of SWNT threads, which were curved and tangled together to form bundles. The nanotubes had diameters of 1 nm with a broad diameter distribution between 0.7 and 1.65 nm.

In the arc-discharge synthesis of nanotubes, Bethune et al. (9) used as anodes thin electrodes with bored holes which were filled with a mixture of pure powdered metals (Fe, Ni or Co) and graphite. The electrodes were vaporized with a current of 95–105 A in 100–500 Torr of He. The TEM analysis of the obtained specimens showed that only cobalt-catalyzed nanotubes had single atomic layer walls with uniform diameters of 1.2–0.1 nm.

In 1996, Smalley and co-workers produced high yields (>70%) of SWNTs by laser-ablation (vaporization) of graphite rods with small amounts of Ni and Co at 1200 °C (Fig. 5). The X ray diffraction and TEM showed that the synthesized nanotubes were remarkably uniform in diameters and that they formed ropes (or bundles) 5–20 nm in diameter and tens to hundreds of micrometres long. The ropes formed a two-dimensional (2D) triangular lattice with lattice constant a $\sqrt{3}$ 1:7 nm through van der Waals bonding. The ropes were metallic and it was argued that a particular tube (10, 10), might be the dominant component. The growth of the nanotubes was explained by a “scooter” mechanism (Fig. 5). In this mechanism a single Ni or Co atom chemisorbs onto the open edge of a nanotube. The metal atom must have a sufficiently high electronegativity as to prevent formation of fullerenes and it must be highly effective in catalyzing the nanotube growth. The metal atom circulates around the open-end of the tube and absorbs small carbon molecules and converts them into graphite-like sheet. The tube grows until too many catalyst atoms aggregate on the end of the nanotube. The large particles either detach or become over-coated with sufficient carbon to poison the catalysis. This allows the tube to terminate with a fullerene-like tip or with a catalyst particle. It was argued that the scooter mechanism favours the growth of armchair type nanotubes with of most probable type (10, 10) which corresponds to the experimental observations (10).

During nanotube synthesis, a B of bi-products are also formed which include amorphous carbon, carbon black, non-tubular fullerenes and also excess catalyst particles. This accounts for subsequent purification steps to separate and isolate nanotubes from the rest. Since the discovery of carbon nanotubes (MWCNT) in 1991 and the realization of their unique physical properties, including mechanical, thermal, and electrical, many investigators have endeavoured to fabricate advanced MWCNT composite materials that exhibit one or more of these properties. To explore the full potential of carbon nanotubes for application in ceramic nanocomposites, one must fully understand the fracture and elastic properties of carbon nanotubes as well as the interactions at nanotube-matrix interface (4).

2.1.4 Property of Carbon Nanotube

The multi-walled carbon nanotubes with a diametrical range of 5-40 nm are known for their exceptional mechanical properties. MWCNT whose modulus is comparable to that of diamond (1.2 TPa), are reported to have strengths 10- 100 times higher than the strongest steel at a fraction of the weight (8). This, coupled with approximately 500 times more surface

area per gram (based on equivalent volume fraction of typical carbon fiber) and aspect ratios of around 1000, has created a great deal of interest in using MWCNT as a reinforcing phase for polymer matrices.

In addition to the exceptional mechanical properties, they also possess superior thermal and electrical properties. They have a thermal stability up to 750°C in air and 2800°C in vacuum. Their thermal conductivity is about twice as high as diamond, with electric current transfer capacity 1000 times greater than copper wires. For high-temperature applications, the high thermal conductance of MWCNTs suggests that their incorporation, even at low volume fractions, might provide the thermal transport needed to reduce material operating temperatures and improve thermal shock resistance. Electrical conductance can also be useful in ceramic-based materials, as heating elements and electrical igniters, for instance. For example, as conductive fillers, MWCNT are quite effective compared to traditional carbon black micro particles, primarily due to their high aspect ratios. The electrical percolation threshold was recently reported at 0.0025 wt. % MWCNT and conductivity at 2 S/m at 1.0 wt.% MWCNT in epoxy matrices. Control of electrical resistance through the use of MWCNT as filler is therefore, an attractive alternative to other composite systems (9). These exceptional properties have been investigated for devices such as field emission displays (FED), scanning probe microscopy tips, and microelectronic devices.

Although single walled nanotubes possess better properties than multiwalled nanotubes, but the relative simplicity in preparation of multiwalled nanotubes and ease in its isolation and purification makes it more economical for most applications including dispersing in ceramic matrix. Another property that is getting a B of attention is the nanotubes surface, namely the interface between the carbon nanotubes and surrounding composite matrix. From micromechanics, it is through shear stress build-up at this interface that stress is transferred from the matrix to the nanotubes. Numerous researchers have attributed lower-than predicted carbon nanotube-ceramic and carbon nanotube polymer composite properties to a lack of interfacial bonding. If one considers the surface of a carbon nanotube, essentially an exposed graphene sheet, it is not surprising that interfacial interaction is a concern. It is the weak interplanar interaction of graphite that provides its solid lubricant quality, and resistance to matrix adhesion. If the mechanical properties of multi walled nanotubes can be effectively incorporated into a ceramic's matrix, comparatively lighter weight composites with exceptional strength can be achieved. In ceramic matrix materials, the mechanical property of greatest importance is toughness or resistance to crack growth. Ceramics are already stiff and

strong and so, in analogy to ceramic composites with micron-scale fiber additions, the incorporation of carbon nanotubes is aimed at enhancing toughness. NASA (USA) is focusing on making use of MWCNTs to develop high-strength composite materials for the next generation spacecraft via this revolutionary technology (7).

2.2 Magnesita carbon refractory

Though refractory materials has worldwide applications in different sectors, different industrial segments, the major consumption of it is done in the steel sector followed by Cement, Nonferrous, Glass and other industries (power, petroleum etc.). Approximately 75 % of world refractory is consumed in steel Industry. While steel making essentially means both iron making and steel making yet this is generally restricted to integrated Steel Plants and PSU Steel plants in our country. Other smaller volume and mini steel plants are generally carrying out the process of steel making only utilizing the raw materials like steel scrap, HBI, DRI, ingots etc. The steel making process being conducted through the basic route, use of refractories which are basic in nature like Magnesia based, lime based, dolomite based, etc are commonly lined in the vessels carrying the melting and purification process. However the most commonly used refractory is magnesia based or magnesia carbon to be specific which is lined in vessels like Basic Oxygen Furnace, ladle Furnace, Electric Arc Furnace, Vacuum Arc Degassing, Vacuum oxygen Decarburizer etc. The magnesia carbon based refractory is primarily made from magnesia, graphite, antioxidants and binder like pitch powder and resin. Three different types of magnesia raw materials are used like a) fused magnesia produced by melting magnesia in electric arc furnace b) Sea water magnesia extracted from sea water c) dead burnt natural magnesia i.e. sintered magnesia produced from natural magnesite by sintering [52]. In MgO-C brick, carbon plays a very important role by providing non-wetting nature to the refractory. Graphite is used as the carbon source because among different commercial sources of carbon, graphite shows the highest oxidation resistance. Due to the flaky nature of graphite it imparts higher thermal conductivity and lower thermal expansion, resulting in very high thermal shock resistance. The flaky and non-wetting characteristics of graphite makes it very difficult to produce a dense brick without any strong binder. In the early days pitch was used as binder for MgO-C brick. But during operation pitch releases large amounts of volatile matters, which are very toxic due to their high content of polycrystalline aromatic compound (PAC) like benzoalpa-pyrenes. Also to use pitch hot pressing of the mixture was necessary. So, phenol formaldehyde resin was found to be the best binder for MgO-C refractories. Each type of raw materials has its own merit and

demerits. The magnesia grain or periclase grain provide the excellent refractory properties like a very high melting point of 2800 °C [53], very good slag corrosion resistance against basic slag of steel making route, stable chemical purity and good mechanical strength i.e. good erosion resistance. However the major pitfall of Magnesia refractory is its poor thermal shock resistance due to very high coefficient of linear expansion and tendency to hydrate forming brucite thereby expanding in volume to form crack leading to failure. So carbon in the form of graphite is generally used with magnesia to counter these negative effects. Graphite has high thermal conductivity, low coefficient of thermal expansion, low elastic modulus, better spalling resistance and also imparts a non wetting character to the magnesia carbon refractory brick which hinders the probability of corrosion of them due to chemical attack followed by penetration of slag and/or liquid metal[53]. Development of magnesia carbon bricks has been a revolutionary invention since long which provided much rapid steel handling operation procedure and much less downtime compared to other refractories (like high alumina etc.) prevalent earlier. With passing years, process development, energy, environment, costing etc. studies were done on the overall impact of operating these bricks where it was found that carbon in spite of having such excellent properties, suffers from poor oxidation resistance to release toxic CO and CO₂ gas in our environment leaving a porous refractory structure susceptible for easy mechanical damage and chemical corrosion. Mohammad-Ali Faghihi-Sani et al. (2001) conducted a detailed study on the rate and kinetics of oxidation or disappearance of graphite, such oxidation being a major limitation of the MgO-C refractories since this results in degradation of the brick properties in service [54]. Oxidation of carbon is of two types: direct oxidation or gas-phase oxidation where carbon is consumed by gaseous oxygen. $2C(s) + O_2(g) = 2CO(g)$ is the major mechanism of oxidation for temperatures less than 1400 °C and is mostly used for comparison of oxidation resistance of refractories. Indirect oxidation or solid-phase oxidation where reaction of carbon occurs with oxygen of solid MgO occurs through $C(s) + MgO(s) = CO(g) + Mg(g)$. This reaction is important for temperatures above 1400 °C. This work was carried out in the temperature range 1000 °C to 1200 °C. Therefore the oxidation due to gaseous oxygen of air was explored. As carbon was effectively lost from the brick by oxidation, addition of higher amount of carbon was initially done. With higher carbon in refractory the immediate concern developed was the inclusion of higher amount of carbon in steel from refractory. The primary objective of steel making process was decarburization. Steel with high carbon content becomes more brittle and less weldable due to increased hardness. More carbon resulted in rapid loss of heat through the refractory surface due to high thermal conductivity which hampered the energy conservation

and also made the outer shell temperature too hot to operate, more amount of toxic gases emission occurred. Generally fixed carbon around 18% maximum (12-18%) [55] is commercially found in magnesia carbon bricks which with B of research and findings have come down to as low as 7 % depending on the application purpose or area of use. However the quest was always on based on need of the hour, researchers took the challenge to reduce carbon further on one hand, yet improve the refractory properties on the other. This urge paved the way of using nano carbon materials either partially or completely in place of graphite. The nano sized carbon particles reduces porosity by moving inside finer voids, improves density, thereby strength. The nano carbon containing magnesia carbon bricks improves the refractory Bulk Density, reduces Apparent Porosity, provides good cold crushing strength, reduces carbon pick up in steel as the carbon content found in refractory brick is drastically lower with nanocarbon, thereby also reducing the heat /energy loss. Literature shows Bag et al [56,57]. has used the nanocarbon grade N220 different amounts (0.3, 0.6, 0.9, 1.2 and 1.5 mass %) along with different amount of graphite (1, 3, 5, 7 and 9 mass-%) in the refractory matrix. The most optimum results were obtained at compositions containing 3wt % flaky graphite with 0.9 wt % nanocarbon black. Use of overall carbon while using nano sized materials are generally kept below 5wt% (3wt % and 5 wt%) [58]. The raw materials used in literature of [7] are as per Table 2 below

Table 1
Physico-chemical properties of fused magnesia.

Chemical analysis (oxide content, wt%)							Physical properties		
SiO ₂	Al ₂ O ₃	Fe ₂ O ₃	TiO ₂	CaO	MgO	Alkalis	Bulk density	App. porosity	Crystal size
0.46	0.07	0.50	Traces	1.40	97.35	0.50	3.3 g/cc	3.8%	800 μm

Table 2
Physico-chemical properties of flake graphite, nano carbon black, pitch powder and liquid resin.

Raw materials	Flake graphite	Nano carbon black	Pitch powder	Liquid resin
Fixed carbon (%)	94.1	98.03	52	47.85
Volatile matter (%)	0.80	1.42	47	
Ash (%)	5.08	0.39	1.4	
Surface area (m ² g ⁻¹)	6.37	116.5		
Softening point (°C)			135	
Specific gravity at 25 °C				1.23
Viscosity (CPS) at 25 °C				8500-9000
Moisture				~4.0

Generally nano carbon black is found mostly in literature as the source material where use of effective antioxidant has been indicated to be Boron carbide in place of the conventional Al metal or Si metal powder due to oxidation potential. In case of nano materials the tendency to oxidise is much faster than normal graphite, the surface area being much higher, so Al metal can be replaced by boron carbide. Four different antioxidant effects were studied by A.C.

Gokce, et al. (2004), namely Al, Si, B₂C and SiC in normal magnesia carbon bricks [59]. The oxidation resistance of B₂C was found to be excellent due to the formation of an Mg₂B₂O₆ layer on the brick surface. Similarly the oxidation resistance of Al was due to the formation of the spinel phase MgAl₂O₄, addition of MgAl₂O₄ spinel significantly improves slag corrosion and erosion resistance of MgO-C refractory. A study showed that 10 wt% addition of micron sized stoichiometric spinel improves the resistance against oxidation, thermal shock and slag penetration in MgO-C brick particularly in the slag zone of steel ladles.[60,61]. The oxidation resistance of Si and SiC was due to the formation of the forsterite phase Mg₂SiO₄. With presence of nanocarbon in the matrix both the cold crushing strength (CCS) and bending strength (Modulus Of Rupture) was very good both in the tempered and coked state along with superior oxidation resistance, corrosion resistance and thermal shock resistance. As graphite use had its own pitfalls stated earlier, similarly some major pitfalls were also found while using the nanocarbon, though the positive aspect it imparts in the refractory material is phenomenal. Till now the tremendous potential of nanocarbon has not been utilised fully due to its inferior oxidation resistance and lower thermal conductivity compared to the graphite flakes. [1]. So use of nanocarbon has been restricted to partial amount to be used in combination only, it is unable to completely replace graphite and thus further scope of study developed. Researcher focused on finding any such advanced material which will have properties of nanocarbon and will be able to replace the graphite completely or lower the overall amount of carbon or improve the pitfalls experienced with graphite and nanocarbon. Here lies the objective or scope of our work to use carbon nano tube (CNT) in place of nanocarbon black and investigate the outcome. We have studied literature where the use of CNT has been (0.4, 0.8, 1.2, 1.6) mass % [62]. Very few literature are present with complete study of magnesia carbon brick properties with CNT in matrix. So our line of work will be to use multiwalled industry grade CNT below 1wt% in the refractory matrix. We will initially add ex situ multiwalled CNT along with graphite to prepare samples for our study. Idea of CNT was developed mainly due to the rod/tube like structure in place of sheet like structure in graphite or other nanocarbon bearing materials. The tube like structure is expected to impart better oxidation resistance than sheet structured nanocarbon, better thermal shock resistance and mechanical strength at high temperatures. Carbon nanotubes (CNTs) have attracted extensively interest of scientists and engineers due to their outstanding physical properties such as low density, high aspect ratio, Young's modulus, electrical and thermal conductivities. When single-wall carbon nanotubes (SWCNTs) or multi-wall carbon nanotubes (MWCNTs) are introduced into ceramics, metals

and polymers as matrices, ultra-high strength and/or multifunctional composites can be developed. In Al₂O₃-C refractories for slide gates and carbon blocks for blast furnaces in iron and steel making industry multiwalled carbon nano tubes (MWCNTs) were introduced to improve their mechanical properties and thermal conductivity [63]. Higher cost of CNTs can be compensated by its too low mass percentage and improved life/properties of the refractory material during use as per expectation. As learnt from literature [62] two major challenges that we are going to face is a) Dispersion of CNT during mixing of ingredients as CNT has the tendency to self agglomerate without getting properly dispersed b) Uniform distribution of CNT in the flake like particles of magnesia carbon matrix after the brick has been tempered. The phases present inside the refractory body can be Al₄C₃, spinel, Mg₃B₂O₆, periclase, carbon etc. There is further scope for higher level research of insitu development of CNT inside the matrix by treating of the resin with Co, Ni, Fe catalyst. The in-situ development of materials reinforces the matrix and improves the microstructure. In-situ development of ceramic whiskers (mainly AlN and Al₄C₃ occurs at lowers temperature whereas for SiC requires higher temperature to enhances the performance of Continuous Casting Refractories.

Objectives

From our literature review we have found, to lower the graphite content in MgO-C brick, nanocarbon was introduced in the refractory matrix by researchers, which in spite of showing promising results had some major pitfalls like poor oxidation resistance and lower thermal conductivity. Thereby in this study our objective is to follow a different approach to reduce the carbon content further as well as to increase the thermo-mechanical properties, oxidation resistance. Here multiwalled carbon nano tube (MWCNT) has been chosen to partially substitute graphite in MgO-C refractories. Very small amounts of MWCNT (~0.2 mass%) will be used with graphite phase and carbon black in an overall low carbon containing MgO-C brick formulation and properties will be measured and discussed accordingly. Alongside low carbon MgO-C bricks having only graphite (no CNT & carbon black) will also be developed keeping the base composition same. A comparative study of the properties of these two types of bricks will be investigated and analysed to understand the role of MWCNT addition in low carbon Magnesia carbon brick.

Chapter 4

Plan Of Work

- Raw material collection & proper storage
- Physico-chemical analysis of the raw materials
- Designing compositions
- Sintering of raw materials as per chosen compositions
- Fabrication of magnesia-carbon bricks with & without (MW/CNT)
- Characterizations (XRD & SEM)
- Testing (AI, BH, CCS, Oxidation Resistance, etc.)
- Results & Discussion
- Conclusion

Chapter 5

Experimental Procedure

5.1 Starting Materials

As per the batches mentioned in below tables

5.2 Procedures

The experimental part is presented in the form of flow diagram for the time being

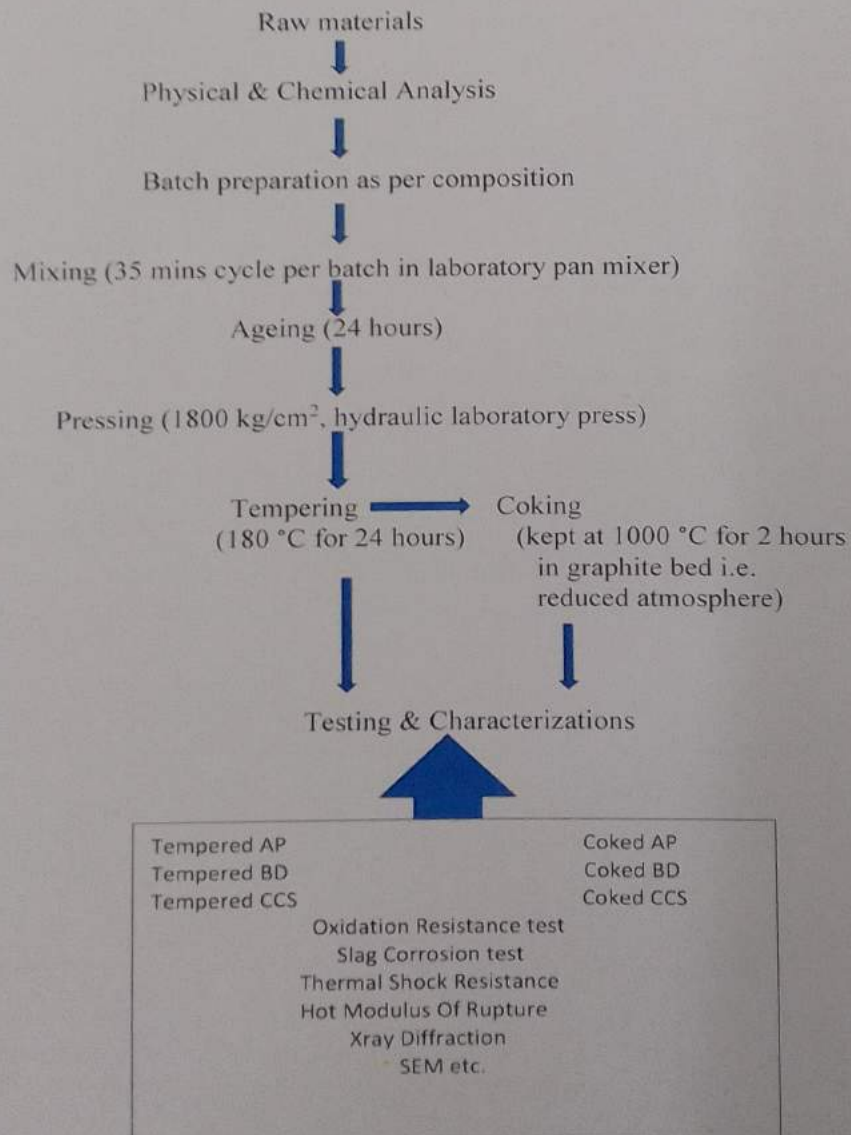


Table 3. Raw Material Analysis

Constituents /Parameters (%)	Fused Magnesia (800 micron crystal size)	Nano Carbon black	Graphite	Liquid Resin	MWCNT (NANOSHELL), Functionalised - COOH
MgO	97.00				
SiO ₂	0.70				
Fe ₂ O ₃	0.50				
Al ₂ O ₃	0.20				
CaO	1.40				
LOI	0.10				
BD	3.3 g/cc				0.05-0.17 g/cc
AP	3.8%				
Fixed Carbon		98.03	94	48-52	
Surface Area		124 m ² /g	6.37 m ² /g		90-350m ² /g
Ash		0.39	4-5		
Volatile Matter		1.42	1		
Viscosity at 25° C				7500 +/- 1000 CPS	
Solid content				78-82%	
pH				6.5 - 7.5	
Moisture				4	
Specific gravity at 25°C				1.23	
Bundle of Tubes length					5-15 micrometer
Diameter					20-30 nanometer
Purity					>95%
Amorphous carbon					<3%
Avg. interlayer distance					0.34 nm
Residue(calcination in air)					<2%
COOH content %					3-5 wt%

5.2.1 Preparation of standard batch composition with flaky graphite.

The desired amount of fused magnesite fraction wise was taken in a zip packets and put inside the lab scale modified Hobert mixer sequentially. Weighted amount of graphite (3 wt %) was added along with phenol formaldehyde resin. The phenol formaldehyde resin normally has a self life of 15 days and stored in air conditioning atmosphere to prevent any setting tendency. Before addition of the resin it is generally warmed to 80-90 deg C for few minutes and finally added to the mixer (4 v/wt%). Addition of antioxidants in the form of Al metal and Si metal is normally done as 1 wt % each. After the mixing is complete the standard batch (B 1) is prepared. Likewise B 2, B 3 & B 4 was prepared with 1 inch and 2 inch diameter cylinders.



Figure 6. Mixing batch prepared with fused MgO and flaky graphite.

Table 6. Standard Batch Composition with Graphite (all batches are of 900 gms)

Batch code	Fused Magnesite (wt. %)	Graphite (wt. %)	Al metal powder (wt. %)	Si metal powder (wt. %)	Liquid Resin (v. wt. %)
B 1 to B 4	85.00	3.00	1.00	1.00	4

Note: B 1 to B 4 analysis was done with cylinder samples to study the property variation with this standard composition.

Table 10

Main component	(3-5) mm size fraction %	(1-3) mm size fraction %	(0-1) mm size fraction %	-325 #
*Fused Magnesia	15.00	30.00	30.00	20.00

5.2.2 Preparation of batch composition with flaky graphite & nano carbon black

The desired amount of fused magnesite fraction wise was taken and put inside the lab scale modified Hobert mixer sequentially. Weighted amount of graphite & nanocarbon black was added along with phenol formaldehyde resin. Five batches were prepared varying the amount of graphite & nano carbon black as per below tables. Addition of antioxidants in the form of Al metal and B_4C is normally done. B_4C has a much better antioxidation property compared to Si metal when used with nano materials. It has been already mentioned in literature review. After the mixing is complete the standard batch B 5, B 6, B 7, B 8 & B 9 were prepared. Mixing sequence was monitored specially so that nano carbon black gets dispersed in resin properly.

Table 11

Main component	(3-5) mm size fraction %	(1-3) mm size fraction %	(0-1) mm size fraction %	-325 #
*Fused Magnesia	15.00	30.00	30.00	20.00

Table 5

Batch code	Fused Magnesia*(wt.%)	Graphite (wt.%)	Carbon black (wt.%)	Al metal powder (wt.%)	B ₄ C powder (wt.%)	Liquid Resin (v/wt.%)
B 5	95.00	2.50	0.50	1.00	1.00	5

Table 6

Batch code	Fused Magnesia*(wt.%)	Graphite (wt.%)	Carbon black (wt.%)	Al metal powder (wt.%)	B ₄ C powder (wt.%)	Liquid Resin (v/wt.%)
B 6	95.00	2.10	0.90	1.00	1.00	5

Table 7

Batch code	Fused Magnesia*(wt.%)	Graphite (wt.%)	Carbon black (wt.%)	Al metal powder (wt.%)	B ₄ C powder (wt.%)	Liquid Resin (v/wt.%)
B 7	95.00	1.50	1.50	1.00	1.00	5

Table 8

Batch code	Fused Magnesia*(wt.%)	Graphite (wt.%)	Carbon black (wt.%)	Al metal powder (wt.%)	B ₄ C powder (wt.%)	Liquid Resin (v/wt.%)
B 8	95.00	1.00	2.00	1.00	1.00	5

Table 9

Batch code	Fused Magnesia*(wt.%)	Graphite (wt.%)	Carbon black (wt.%)	Al metal powder (wt.%)	B ₄ C powder (wt.%)	Liquid Resin (v/wt.%)
B 9	95.00	0.00	3.00	1.00	1.00	5

5.2.3 Preparation of batch composition with flaky graphite, nano carbon black & MWCNT

The desired amount of fused magnesite fraction wise was taken and put inside the lab scale modified Hobert mixer sequentially. Weighted amount of graphite & nanocarbon black was added along with phenol formaldehyde resin. Additionally, here use of MWCNT was done. MWCNT has the problem of agglomeration when mixed with resin. So, dispersion of MWCNT had to be done separately before being used as an ingredient in mixing. Three batches were prepared keeping the amount of graphite fixed at 2.10 wt % but varying the wt % of nano carbon black & CNT. CNT being so expensive was decided to be used as 0.05 wt %, 0.1 wt % & 0.2 wt %. Addition of antioxidants in the form of Al metal and B₄C is normally done here. B₄C has a much better antioxidation property compared to Si metal when used with nano materials. It has been already mentioned in literature review. After the mixing is complete the batches B 10, B 11 & B 12 were prepared. Mixing sequence was monitored specially so that nano carbon black gets dispersed in resin properly as CNT is in already dispersed state.

Table 11

Batch code	Fused Magnesia (wt.%)	Graphite (wt.%)	Carbon black (wt.%)	MWCNT (wt%)	Al metal powder (wt.%)	B ₄ C powder (wt.%)	Liquid Resin (v/wt.%)
B 10	95.00	2.00	0.95	0.05	1.00	1.00	5

Table 12

Batch code	Fused Magnesia (wt.%)	Graphite (wt.%)	Carbon black (wt.%)	MWCNT (wt%)	Al metal powder (wt.%)	B ₄ C powder (wt.%)	Liquid Resin (v/wt.%)
B 11	95.00	2.00	0.90	0.10	1.00	1.00	5

Table 13

Batch code	Fused Magnesia (wt.%)	Graphite (wt.%)	Carbon black (wt.%)	MWCNT (wt%)	Al metal powder (wt.%)	B ₄ C powder (wt.%)	Liquid Resin (v/wt.%)
B 12	95.00	2.00	0.80	0.20	1.00	1.00	5

5.2.3.1 Dispersion of MWCNT in PF Resin

The desired wt.% of MWCNT was mixed along with sodium dodecyl sulphate (SDS) which was taken 0.5 wt. % of MWCNT, Then Ultrasonicated for 35 mins. Carbon nanotube used in our project has the following specification, (i) -COOH functionalized, (ii) Diameter 20-30nm, (iii) Length 5-15 μm , (iv) Impurity 5%, (v) Bulk Density 0.17gm/cm^2 . Due to having high surface area and high van der Waals force of attraction carbon nanotube tends to form agglomerates. For proper dispersion of carbon nanotube in the resin solution a surfactant is needed. If we don't add a surfactant Multiwalled CNT agglomerates and settles in the beaker within minutes after ultrasonication. Dispersion is a system in which distributed particle are dispersed in a continuous phase of another material. To homogenously disperse nanomaterials it is essential to break the bundles into smaller sizes. After separation, it is necessary to stabilize the nanomaterials so that they do not form agglomerates again and instead remain adequately dispersed. Hence, numerous methods have been reported to achieve the optimum dispersion of nanofillers in the host matrix. For our research work, when ultrasonication is done, a separate arrangement of visco jet stirrer was prepared. The visco jet stirrer was inserted inside the plastic beaker and simultaneously the ultrasonication was done. The SDS was initially added in the resin following which the MWCNT was slowly added, the stirring (around 800 RPM) was continued for 31 to 35 mins to find a black viscous solution with no agglomeration seen from outside.



Figure 7. Visco jet stirring is going on with simultaneous ultrasonication

5.2.3.2 Visco jet stirrer

VISCO JET homogenises low and high viscosity liquids in vessels by creating dynamic flow conditions by means of the so-called cone principle. Turbulent flows are created at the taper end by acceleration, displacement and retardation. These flows advance through the stirred medium and result in the new dynamic mixing motion.

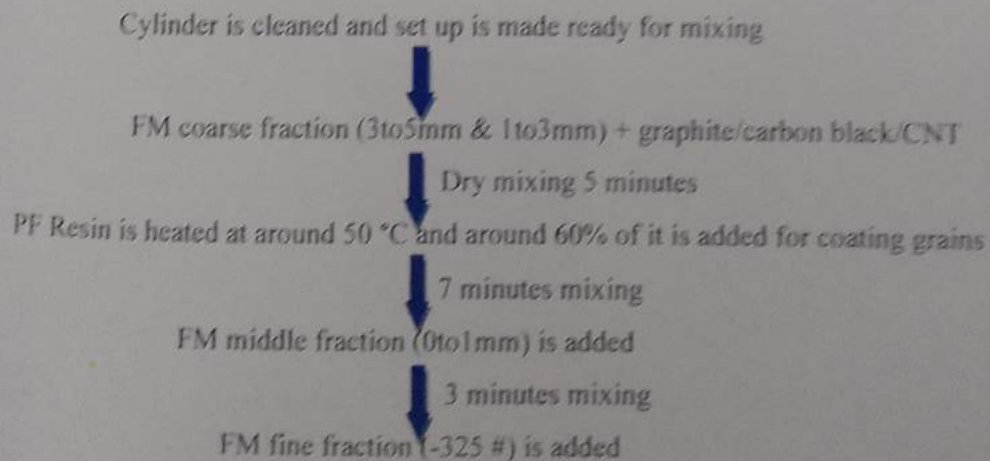


Figure 8. Visco jet stirrer

5.3 Mixing

Mixing is one of the most important step in this procedure. Improper mixing may lead to segregation during pressing, agglomeration during mixing, porous low strength product and can affect other associated properties. So a uniform mixing sequence was followed during mixing of each batch with proper monitoring and RPM lower than 50 in lab mixer. The mixing stirrer and cylinder are presented as figure no 4 & 5. Heating of PF Resin is done for better coating.

Mixing sequence



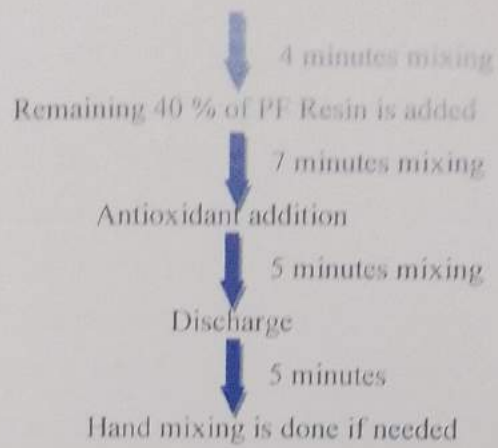


Figure 9. Cylinder of mixer



Figure 10. Stirrer of mixer, rotation clockwise

5.4 Ageing

In order to eliminate all volatile matter from the mix, it is allowed to age under normal room temperature for 24 hours. Care should be taken that no foreign elements or water/fluid should contaminate the mix during ageing.



Figure 11. Ready mix after ageing

5.5 Pressing

From the aged mixture, 300 gms of sample is weighted for sample preparation. Taking the theoretical Bulk density of 3 gm/cc and calculating the volume of a 2 inch diameter cylinder we decided to feed 300 gms in mould for one sample pressing. A 2 inch cylinder mould is taken with pin and pressing is done by the hydraulic press (max. loading capacity is 450KN) at pressures of 1800 kg/cm² which is 360 KN. Two step pressing is done, after 50 KN pressure is achieved then pressure is released for 2 minutes and then it is raised directly to 360 KN. Once 360 KN is achieved, the pressure is allowed to fall back slowly and finally mould release is done to have a pressed green cylinder of 2inch dia and almost 2 inch height.



Figure 12. Uniaxial hydraulic press.

5.6 Tempering

Once the green samples are pressed and ready they are allowed to undergo the tempering process where the resin polymerises and with temperature like 180 °C, the C-C bond develops strength. The whole process of tempering is done in humidity and temperature controlled drier for 24 hours to allow complete polymerisation. Initially the rate of temperature rise in drier is 5° C/min and after attaining 180° C, it is kept at that temperature for 24 hours.

5.7 Coking

Some of the tempered samples are allowed to undergo a coking process to understand the behaviour of the magnesia carbon refractory under complete reducing condition. This process is usually done by putting the tempered samples inside a crucible full of graphite with a lid on. The crucible is allowed to be fired at 1000 °C. The rate of heating is 5°C/min upto 1000° C then soaking at 1000 °C for 2 hours. The idea is, at this temperature the surrounding peripheral graphite in the crucible will be oxidised but the inner zone graphite will protect the

sample from oxidation by maintaining a reducing atmosphere inside. After the coking is done, samples are tested for their coked properties.

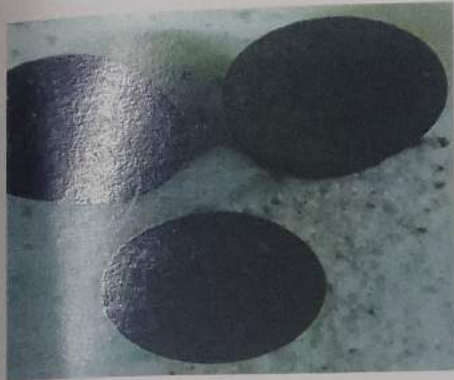
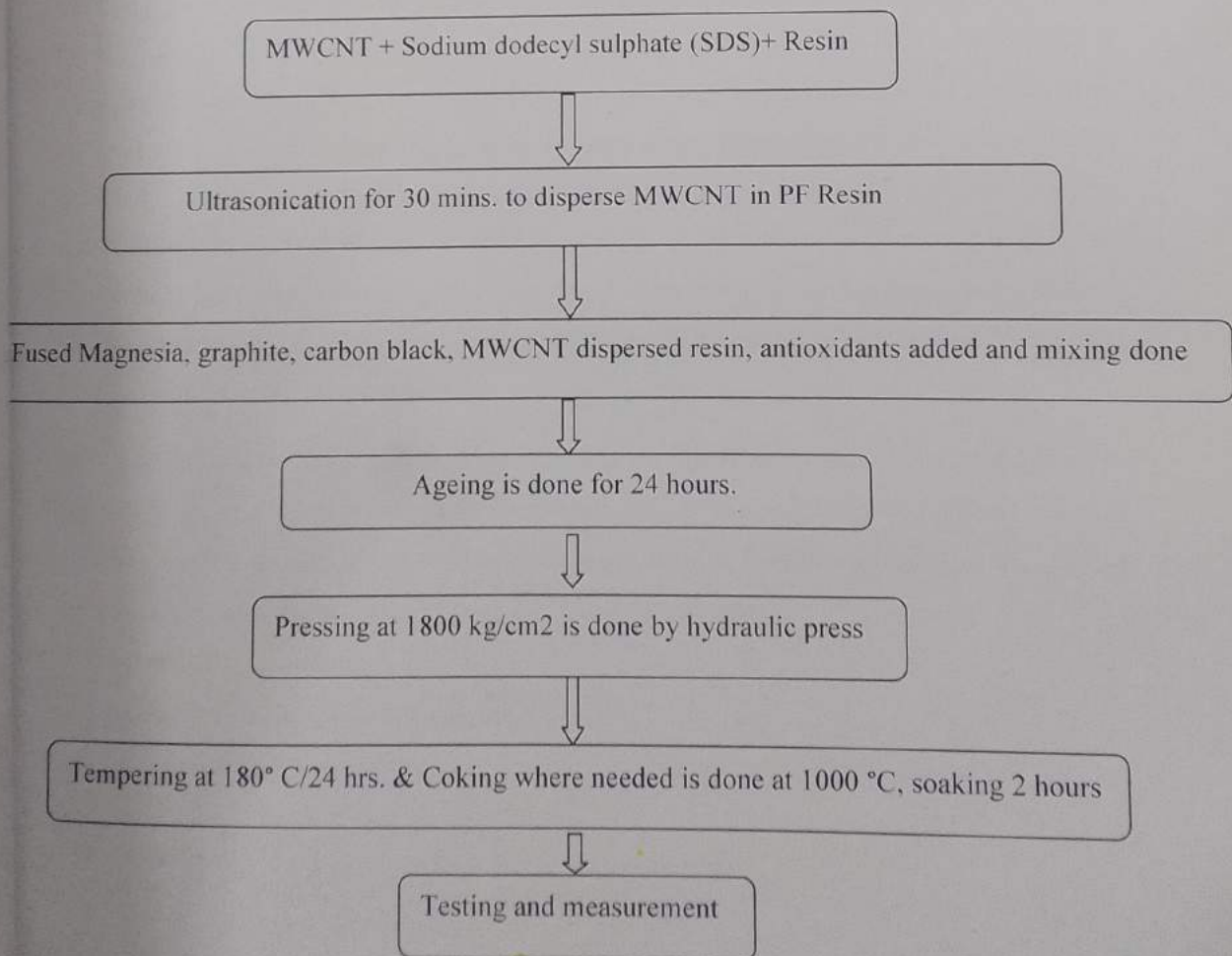


Figure 13. Tempered samples



Figure 14. Coked samples

5.8 Flow chart of entire process for making of MagnesiaCarbon brick with graphite, nano carbon black and MWCNT:



From prepared samples regarding the characterization part, XRD has been done for the different phase analysis in the magnesia carbon brick, SEM has been done to study the microstructure.

5.9 To elaborate about the testing and measurement part;

1) Apparent porosity (AP) and bulk density (BD):

AP is defined as ratio of the total volume of the closed pores to its bulk volume and expressed as a percentage of the bulk volume. Closed porosity is the pores that are not penetrated by the immersion liquid, whereas open porosity are those pores which are penetrated by the immersion liquid. AP needs to be measured both for tempered and coked samples. The vacuum evacuation method generally measures both bulk density and apparent porosity for magnesia carbon samples. After taking dry weight (W1) all the samples needs to be put into a container and kerosene has to be added. Then the container will be placed inside vacuum chamber and vacuum to be made, the samples will remains inside so that all the open pores are filled with kerosene. After that, the suspended weight (W2) and soaked weight (W3) will be taken and AP will be calculated as follows: $\%AP = (W3-W1) / (W3-W2) \times 100 \%$. BD is the ratio of the mass of the dry material of a porous body to its bulk volume expressed in gm/cm³ or kg/m³, where bulk volume is the sum of the volumes of the solid material, the open pores and the closed pores in a porous body. BD will be measured both for tempered and coked samples. True density is the ratio of mass of the material of a porous body to its true volume and true volume is the volume of solid material in a porous body. $B.D = (W1/W3-W2) \times \text{density of liquid at temperature of test (e.g. density of kerosene at 25°C : 0.80 gm/cc)}$. It can also be interpreted as,

The bulk density of the bar was determined by Archimedes method. The samples were weighed in air, and when suspended in kerosene, using an electronic balance of least count of ± 0.0001 g. with a density measurement kit package Mettler Toledo was used for the density measurements. Bulk density (B.D) given by following equation,

$$B.D. = [(W_d)/W_{SO}-W_{sus}] * \rho_k ,$$

And Apparent Porosity (A.P) is given by,

$$\%A.P. = (W_{so}-W_d)/(W_{sus}-W_d),$$

Where W_{so} , W_d and W_{sus} represents soaked weight, dry weight and suspended respectively. ρ_k is the density of kerosene.



Figure 15. Mettler Toledo analytical balance with a density measurement kit.

2) Cold crushing strength (CCS):

Cold crushing strength of refractory bricks and shapes is the gross compressive stress required to cause fracture. The cold crushing strength of the tempered and coked samples will be measured. The test samples were cut from the standard brick samples. Cold crushing strength of the refractories is measured by placing a suitable refractory specimen on flat surface followed by application of uniform load to it through a bearing block in a standard mechanical or hydraulic compression testing machine. The load at which crack appears in the refractory specimen represents the cold crushing strength of the specimen. The load is applied uniformly on the sample in the flat position. It is expressed as kg/cm^2 .

The working formula for calculating CCS is given by,

$$\text{CCS} = \text{Load/Area (kg/cm}^2\text{)}$$

3) Oxidation resistance:

Oxidation resistance of the fabricated bricks is tested on cube shaped samples. The samples were fired in an electrical furnace at 1400°C for 2 hours soaking in normal/air atmosphere. At this temperature all the carbonaceous materials of the brick gets oxidized particularly from the outer surface. The color of the oxidized portion turns pale yellow compared to the black colour of the virgin brick and therefore the boundary between the non-oxidized and the oxidized regions becomes quite evident. After the heat-treatment, the cylindrical samples are

cut and the diameter of black portion is measured at different locations and the average value was taken.

Oxidation index is determined by the formula:

$$\text{Oxidation index} = (\text{Area of oxidized zone} / \text{Total area}) \times 100$$

Lower oxidation index indicates the higher oxidation resistance of the brick

4) Linear Shrinkage:

Linear shrinkage is measured in both the direction of height and diameter of the cylinder sample. Linear Shrinkage % is measured as the dimensional change between the green body and the tempered body. It can also be measured between the green sample and the coked sample.

Let the height of green body is "X" mm

Let the height of tempered body is "Y" mm

Let the height of the coked body is "Z" mm

Therefore liner shrinkage for tempered body = $(X-Y)/X\%$

Therefore liner shrinkage for coked body = $(X-Z)/X\%$

Chapter 6

Results and Discussion

6.1 Bulk Density

B 1 to B 4 Analysis (Batches with Fused Magnesia & graphite)

Table No. 15 Vacuum evacuation with Kerosene method

Batch No.	Sample diameter	Tempered	Coked	BD (g/cc)
1	2 inch	x	yes	2.95
2	2 inch	x	yes	2.94
3	1 inch	yes	x	2.96
3	1 inch	yes	x	2.98
3	1 inch	x	yes	2.92
3	1 inch	x	yes	2.91
3	2 inch	yes	x	3.07
3	2 inch	yes	x	3.07
3	2 inch	x	yes	2.97
2	1 inch	x	yes	2.96
2	1 inch	x	yes	2.95
3	1 inch	yes	x	3.04
3	1 inch	yes	x	3.02
4	2 inch	yes	x	3.06
4	2 inch	x	yes	2.97

B 5 to B12 Analysis(Batches with Fused Magnesia, graphite, carbon black & MWCNT,2inch samples)

Table No. 16 Vacuum evacuation with Kerosene method

Batch No.	Sample diameter	Tempered	Coked	BD (g/cc)
5	2 inch	yes	x	3.01
5	2 inch	x	yes	2.90
6	2 inch	yes	x	3.00
6	2 inch	x	yes	2.91
7	2 inch	yes	x	2.96
7	2 inch	x	yes	2.89
8	2 inch	yes	x	2.98
8	2 inch	x	yes	2.90
9	2 inch	yes	x	2.82
9	2 inch	x	yes	2.77
10	2 inch	yes	x	2.98
10	2 inch	x	yes	2.86
11	2 inch	yes	x	3.03
11	2 inch	x	yes	2.96
12	2 inch	yes	x	2.96
12	2 inch	x	yes	2.86

From table number 15 we can find the Bulk Density values where for 1 inch diameter sample, tempered BD value is seen to lie between 2.96 to 3.04 g/cc, coked BD value is seen to lie between 2.91 to 2.96 g/cc. For 2 inch diameter sample tempered BD value is seen to be around 3.06 to 3.07 g/cc and coked BD is seen to be around 2.94 to 2.97 g/cc.

From table number 16 we can find the Bulk Density values for 2 inch diameter sample. tempered BD value in B 5 to 9 is seen to be between 2.82 g/cc to 3.01 g/cc and coked BD is seen to be between 2.77 to 2.91 g/cc. In B 10 to 12, i.e. Bs with MWCNT, the tempered BD is seen to be between 2.96 to 3.03 g/cc and coked BD is seen to be between 2.86 to 2.96 g/cc. So from the table 16, B no. 6 was a preferred composition, based on which B 10 to B 12 were prepared varying MWCNT %. Now, in-between B 10 to B 12, results shows B 11 as the best composition.

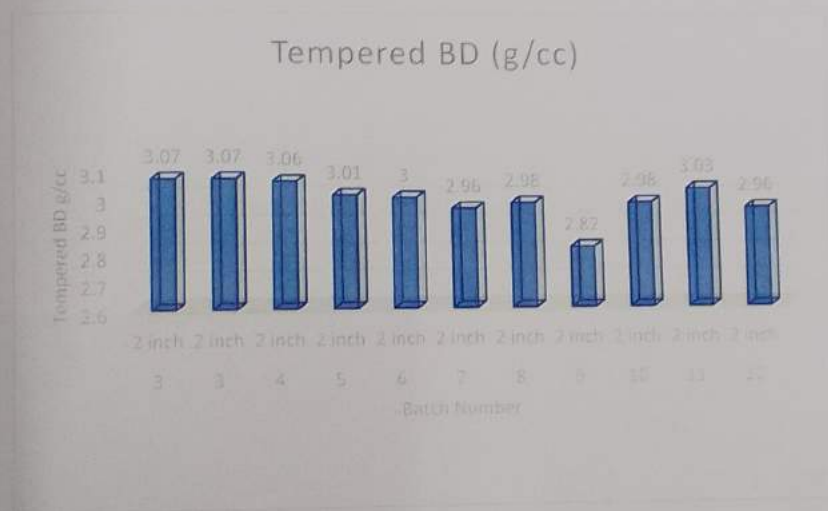


Figure No. 16a of Tempered BD batch wise

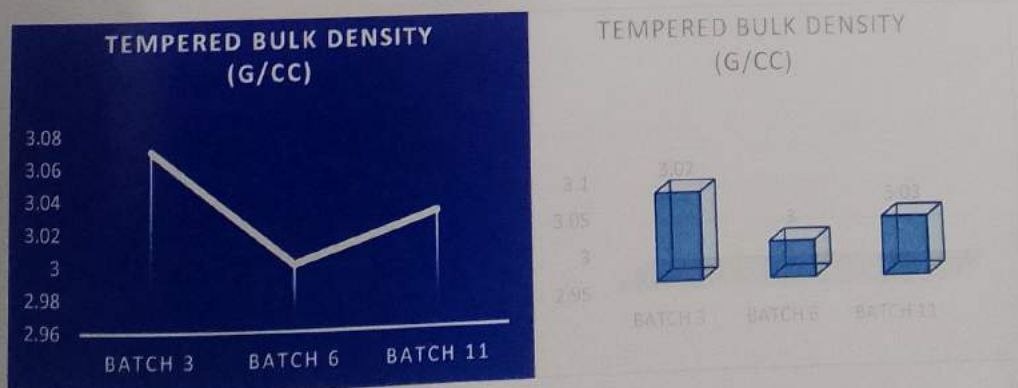


Figure No. 16b of Tempered BD comparative between batches

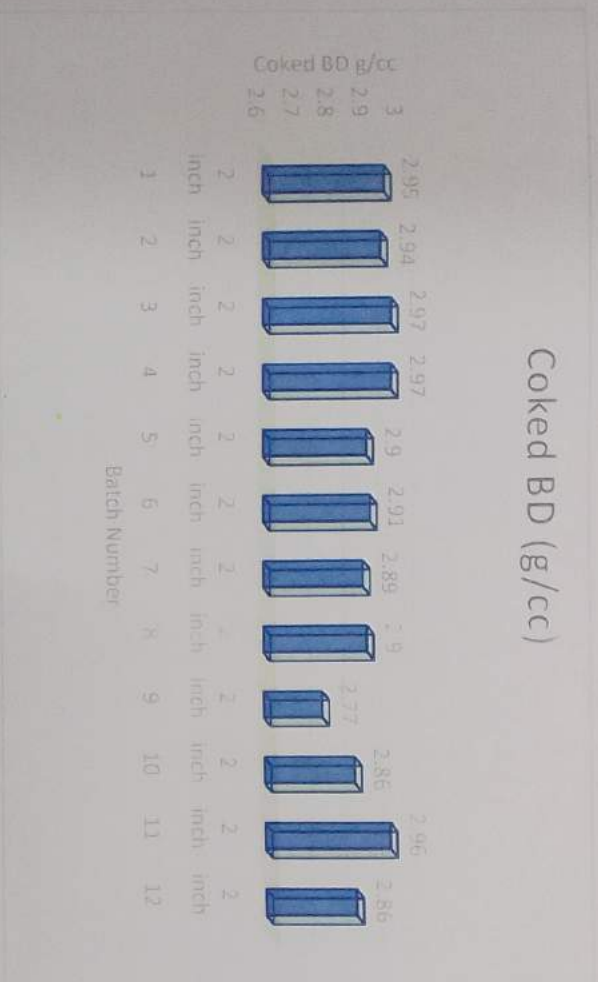


Figure No. 17a of Coked BD batch wise

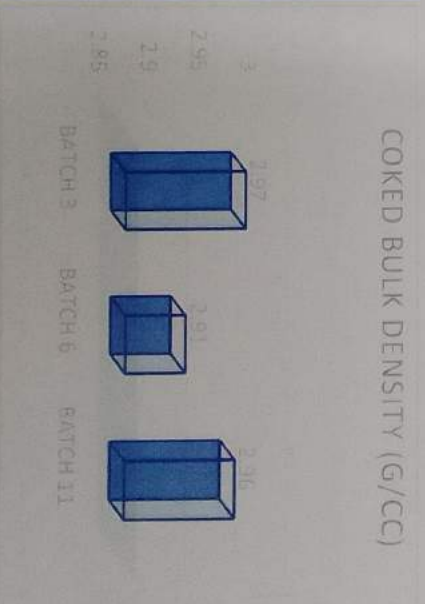


Figure No. 17b of Coked BD comparative between batches

6.2 Apparent Porosity

B1 to B4 Analysis (Batches with Fused Magnesia & graphite)

Table No. 17 Vacuum evacuation with Kerosene method				AP %
Batch No.	Sample diameter	Tempered	Coked	
1	2 inch	x	yes	11.70
2	2 inch	x	yes	11.05
3	1 inch	yes	x	5.58
3	1 inch	yes	x	5.60
3	1 inch	x	yes	12.10
3	1 inch	x	yes	12.20
3	2 inch	yes	x	5.55
3	2 inch	yes	x	5.65
3	2 inch	x	yes	11.35
2	1 inch	x	yes	11.68
2	1 inch	x	yes	11.60
3	1 inch	yes	x	5.55
3	1 inch	yes	x	5.60
4	2 inch	yes	x	5.45
4	2 inch	x	yes	11.40

B5 to B12 Analysis (Batches with Fused Magnesia, graphite, carbon black & MW CNT, 2inch samples)

Table No. 18 Vacuum evacuation with Kerosene method				%AP
Batch No.	Sample diameter	Tempered	Coked	
5	2 inch	yes	x	7.24
5	2 inch	x	yes	12.48
6	2 inch	yes	x	6.51
6	2 inch	x	yes	11.67
7	2 inch	yes	x	7.90
7	2 inch	x	yes	15.56
8	2 inch	yes	x	8.15
8	2 inch	x	yes	15.28
9	2 inch	yes	x	13.20
9	2 inch	x	yes	19.81
10	2 inch	yes	x	7.93
10	2 inch	x	yes	12.93
11	2 inch	yes	x	5.87
11	2 inch	x	yes	12.73
12	2 inch	yes	x	8.90
12	2 inch	x	yes	14.31

From table number 17 we can find the Apparent Porosity values where for 1 inch diameter sample, %AP value is seen to lie between 5.55 to 5.60, coked AP value is seen to lie between 11.60 to 12.10. For 2 inch diameter tempered sample %AP value is seen to be around 5.45 to 5.65 and coked AP is seen to be around 11.60 to 11.80.

From table number 16 we can find the Apparent Porosity values for 2 inch diameter sample, tempered AP value in B 5 to 9 is seen to be between 7.24 to 13.20 and coked AP is seen to be between 12.48 to 19.81. In B 10 to 12, i.e. Bs with MWCNT, the tempered AP is seen to be between 5.87 to 8.90 and coked AP is seen to be between 12.93 to 14.31. So from the table 16, B no. 6 was a preferred composition, based on which B 10 to B 12 were prepared varying MWCNT %. Now, in-between B 10 to B 12, results shows B 11 as the best composition.

Tempered AP %

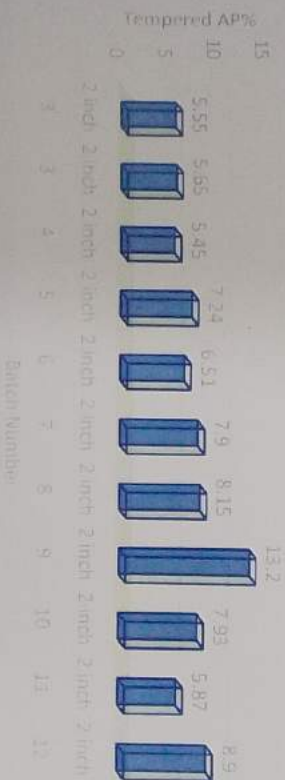
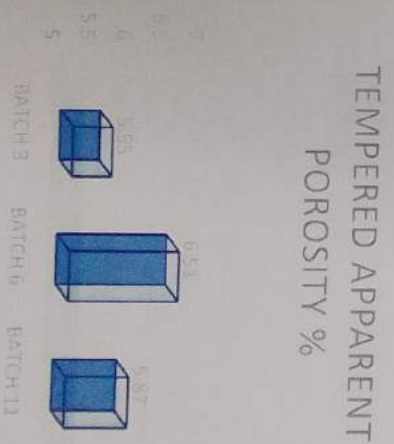


Figure No. 18a of Tempered AP batch wise



Figure No. 18b of Tempered AP comparative between batches



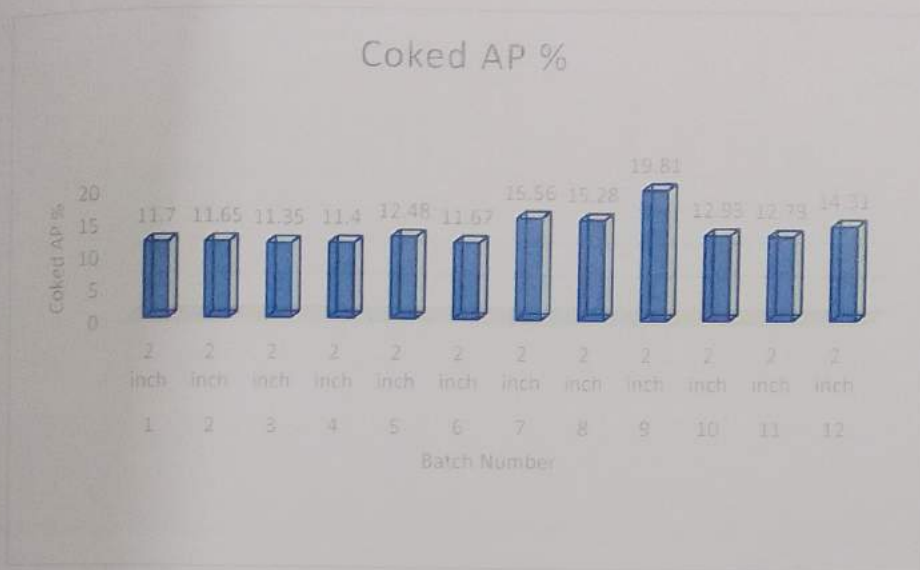


Figure No. 19a of Coked AP batch wise

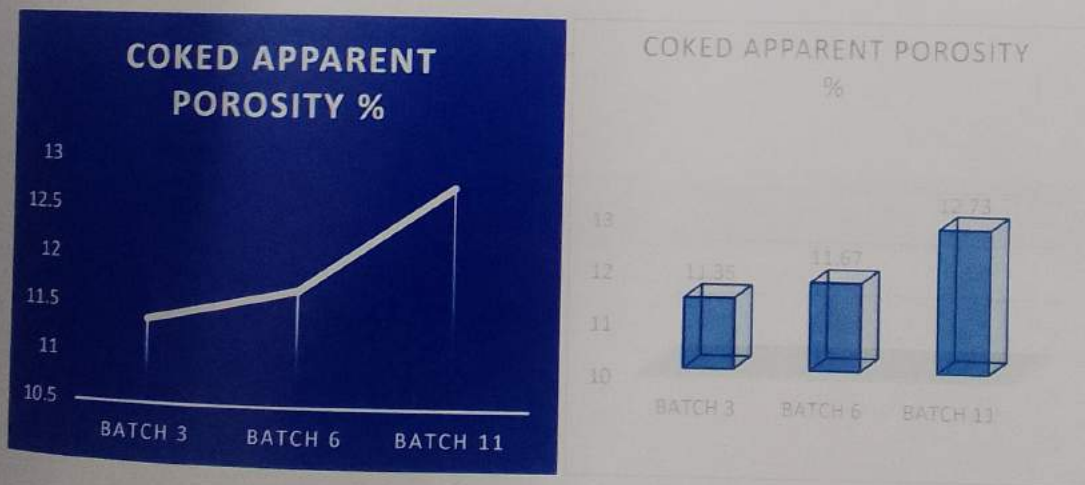


Figure No. 19b of Coked AP comparative between batches

6.3 Cold Crushing Strength

B 1 to B 4 Analysis (Batches with Fused Magnesia & graphite)

Table No. 19

Batch No.	Sample diameter	Tempered	Coked	Actual CCS (kg/cm ²)
1	1 inch	yes	x	594
1	2 inch	x	yes	354
2	1 inch	yes	x	675
2	1 inch	yes	x	735
2	2 inch	x	yes	270
3	2 inch	yes	x	1110
3	2 inch	x	yes	315
4	2 inch	yes	x	950
4	2 inch	x	yes	350

B 5 to 12 Analysis (Batches with Fused Magnesia, graphite, carbon black & MWCNT, 2 inch samples)

Table No. 20

Batch No.	Sample diameter	Tempered	Coked	CCS (kg/cm ²)
5	2 inch	yes	x	640
5	2 inch	x	yes	420
6	2 inch	yes	x	725
6	2 inch	x	yes	380
7	2 inch	yes	x	610
7	2 inch	x	yes	270
8	2 inch	yes	x	605
8	2 inch	x	yes	261
9	2 inch	yes	x	200
9	2 inch	x	yes	100
10	2 inch	yes	x	595
10	2 inch	x	yes	337
11	2 inch	yes	x	910
11	2 inch	x	yes	400
12	2 inch	yes	x	550
12	2 inch	x	yes	363

From table number 19 we can find the CCS values where for 1 inch diameter sample, CCS value is seen to lie between 594 to 675 kg/cm², coked CCS value was not done as other parameters shows it will be lower than our expected values. For 2 inch diameter sample tempered CCS value is seen to be around 950 to 1110 kg/cm² and coked CCS is seen to be around 270 to 354 kg/cm²

From table number 20 we can find the CCS values for 2 inch diameter sample, tempered CCS value in B 5 to 9 is seen to be between 200 to 725 kg/cm² and coked CCS is seen to be between 100 to 420. In B 10 to 12, i.e. Bs with MWCNT, the tempered CCS is seen to be between 550 to 910 kg/cm² and coked CCS is seen to be between 400 to 337 kg/cm². So from the table 16, B no. 6 was a preferred composition, based on which B 10 to B 12 were prepared varying MWCNT %. Now, in-between B 10 to B 12, results shows B 11 as the best composition.

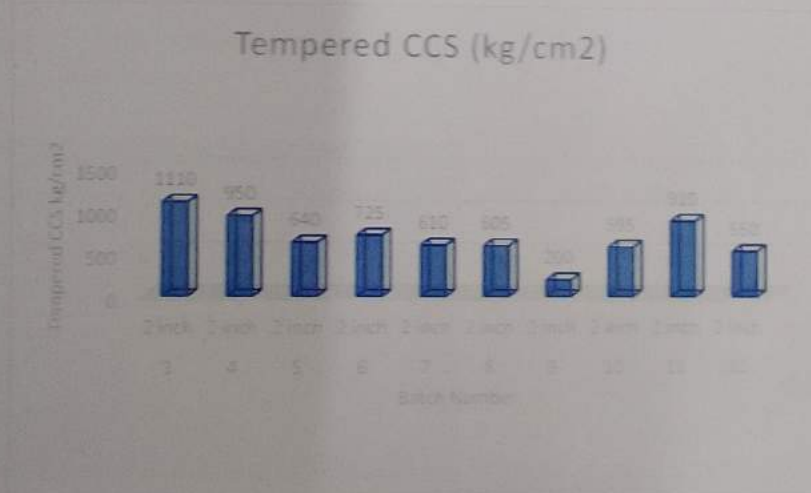


Figure No. 20a of Tempered CCS batch wise



Figure No. 20b of Tempered CCS comparative between batches

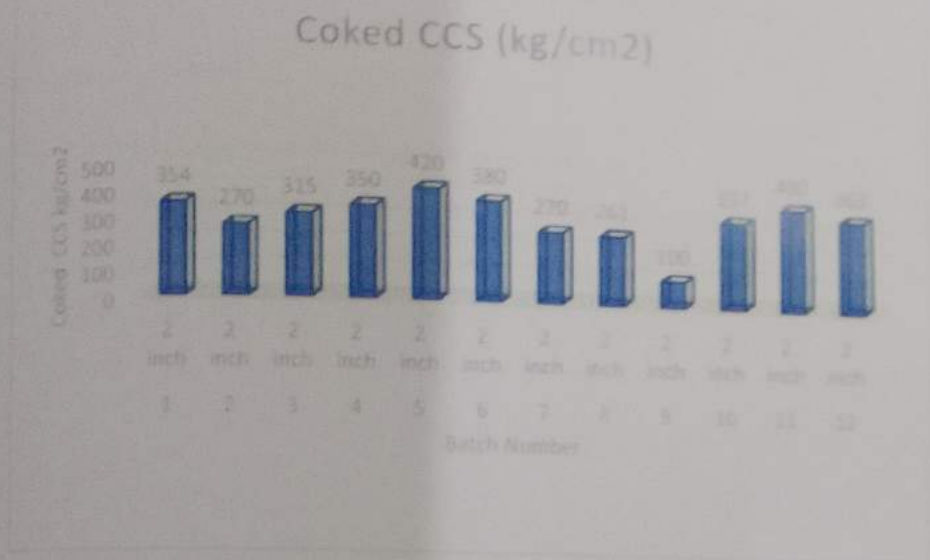


Figure No. 21a of Coked CCS batch wise

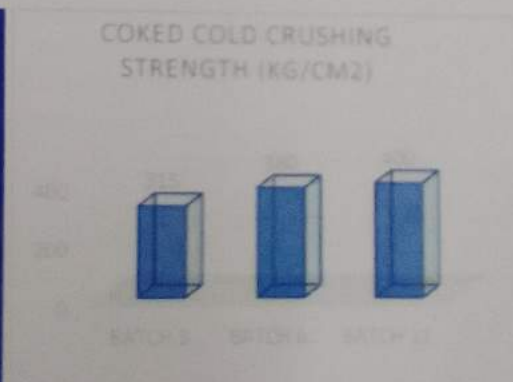
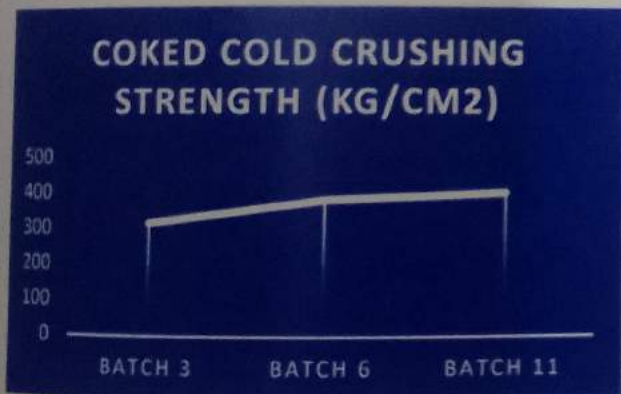


Figure No. 21b of Coked CCS comparative between batches

6.4 Linear Firing shrinkage:

Linear firing shrinkage measurement has been done only with the samples containing MWCNT. The results clearly denote that in place of shrinkage, expansion of the samples has taken place. No expansion or shrinkage is found in samples along the diameter. Expansion only occurred along height. The coked sample has a higher tendency to expand as it has undergone firing at 1000 °C with 2 hours soaking at a reduced atmosphere. Among the three batches, here also B 11 shows more promising figures. All dimensions are measured with vernier caliper.

Batch Code	Green sample		Tempered sample		% Linear Firing shrinkage in tempered compared to green in height	Coked sample		% Linear Firing shrinkage in coked compared to green in height
	Height (mm)	Dia(mm)	Height (mm)	Dia(mm)		Height (mm)	Dia(mm)	
B 10	50	51	50	51	0	52	51	-4
B 11	48.9	51	49.2	51	-0.613	49.3	51	-0.817
B 12	50	51	49.98	51	0.04	51	51	-2

Table 21. Linear Firing Shrinkage of MWCNT containing batches (tempered & coked)

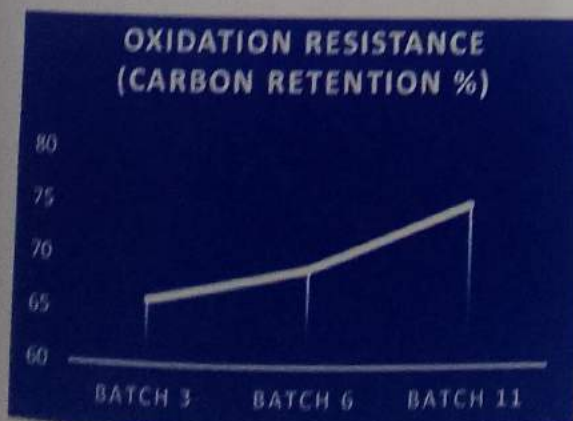
6.5 Oxidation Resistance

Oxidation Resistance test is done inside electrical furnace by direct firing 2 inch diameter samples at normal/air atmosphere at 1400° C (Heating element MoSi₂). Oxidation resistance test is one of the most critical factors in deciding the application of magnesia carbon refractory. Presence of more carbon provides chances of higher oxidation. so in this research work, very low i.e. 3 wt % graphite bearing magnesia carbon brick has been tested for this test, followed by other Bs containing carbon black & MWCNT. From the below table we can find a significant increase in oxidation resistance in B 11.

The rate of heating is as follows :

- Room temperature to 1000° C at the rate 8 °C/minute
- 1000° C to 1400° C at the rate 5 °C/minute
- Soaking at 1400 °C for 2 hours.

Batch Code	Oxidation Resistance Test results	
	% Retention	% Loss
B 1	70	30
B 2	66	34
B 3	66	34
B 5	65	35
B 6	69	31
B 7	66	34
B 8	65	35
B 9	47	53
B 10	69	31
B 11	75	25
B 12	68	32



OXIDATION RESISTANCE (CARBON RETENTION %)

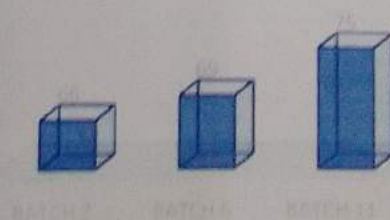


Figure No. 22 of Oxidation Resistance

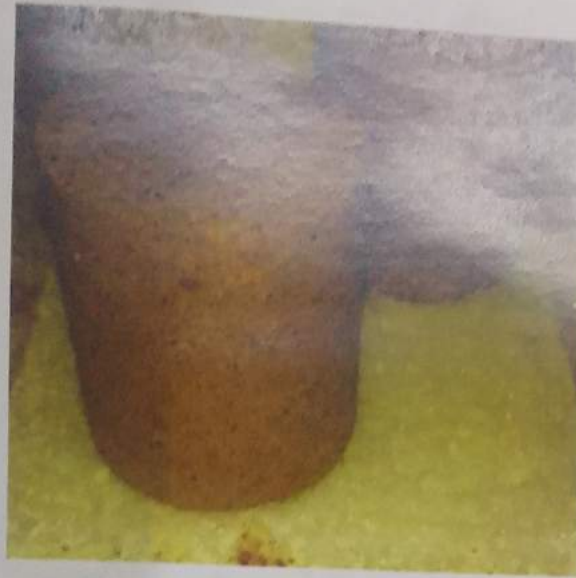


Figure No. 23, Tempered Sample after Oxidation has taken place

B3



Figure No. 24a

3 wt % Graphite, no MWCNT
after oxidation at 1400°C

B6



Figure No. 24b

2.1 wt % Graphite, 0.90 wt
% nano Carbon Black

B 10



Figure No. 25 , 0.05 %MWCNT

B 11



Figure No. 26, 0.1% MWCNT

B 12



Figure No. 27, 0.2% MWCNT

SEM and XRD Analysis

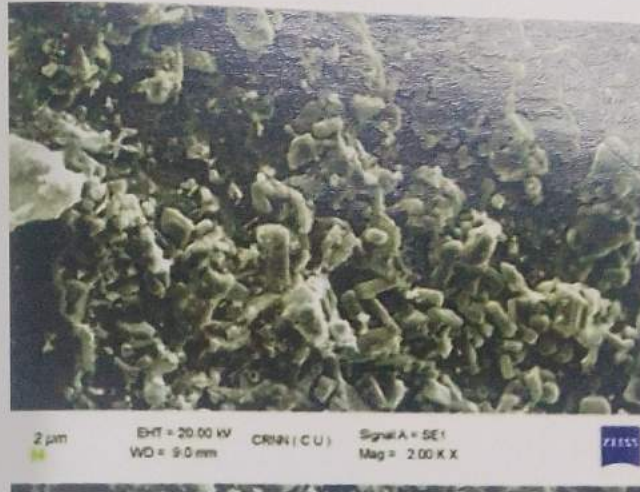


Figure No. 28, 0.1% MWCNT SEM Result



Figure No. 29, 0.1% MWCNT SEM Result

From the SEM picture of sample of B no. 11, we can find the large magnesia grains present, around the magnesia grain connectivity of carbon nano tubes is seen. The amount of MWCNT added being very small and magnification being upto 5 kx, a connective structure of CNT can only be seen, but minute study of the tubes would need much greater magnification which can be done in continuation of this research work. Presence of graphite flakes is also evident from the pictures.

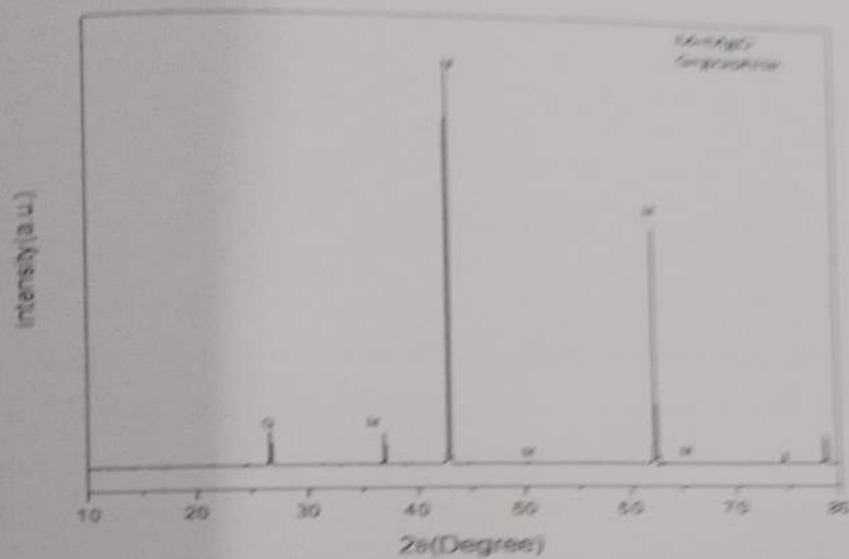


Figure No. 30, 0.1% MWCNT XRD Result

Along with SEM study, X-Ray Diffraction of B 11 was also done, where presence of Magnesia peak and graphite peak is clearly visible, which confirms the phase analysis part. The peaks at 2θ values of 36.9° , 42.9° , and 62.3° in the 2θ range confirm the presence of Magnesia. The graphite shows a sharp and tight peak ($2\theta = 26.5^\circ$) which corresponds to the diffraction line G with the intercellular spacing in the crystal (d) as 3.36 \AA .

Conclusion

1. Development of suitable composition of low carbon bearing Magnesia carbon brick within our lab set up structure. Modification of the old lab mixer to carry on the resin mixing process for mixing of Magnesia carbon bricks. Higher bulk density by using the uniaxial pressing hydraulic press which can impart cost effectiveness rather than inclusion of other expensive processes i.e., Isostatic pressing etc.
2. Use of visco jet stirrer for dispersion of MWCNT in highly viscous PF Resin and controlling the RPM with the help of a variator/resister.
3. Further lowering of graphite from 3 wt % to 2wt % and inclusion of nano carbon black to enhance densification rate and other properties.
4. Encouraging study with 2 wt % graphite and 0.9 wt % nano carbon provided opportunity to incorporate MWCNT with an aim to increase the mechanical strength. Both the tempered CCS and coked CCS of B 11 i.e. having 0.1 % MWCNT showed indication of achieving high CCS value, the coked CCS was the highest among B3, B6 & B11.
5. Surface area of MWCNT being much higher compared to graphite & nano carbon black, chances of very low oxidation resistance was assumed with addition of MWCNT. But interestingly B 11 with MWCNT showed the best oxidation resistance with greater than 75 % carbon retention in actual. This can happen due to the tube like structure of MWCNT where the tube have inner & outer surface leading to lesser effective outer surface area to get oxidised compared to other forms of carbon. Thus both indication of higher mechanical strength and lesser oxidation can be concluded from this work.

Chapter 8

Scope of Future Work

Further research on this topic, will harvest more integrated results which will assists us to exploit this nanocomposite in several industrial and scientific areas. So, there is always scope to Improve the process and property of the material. Further additional investigation that we could perform are as follows:

- Further study is required for slag corrosion (static) analysis with Ladle slag etc to understand the effect of MWCNT addition in corrosion resistance of the MgO-C refractory.
- HMOR & Thermal shock resistance analysis can be done for a complete study, however as per the testing/values we have achieved indication is there Thermal shock resistance will be in line to our expectation atleast greater than 15 cycles.
- Spectroscopic studies can further be done like FTIR & RAMAN.
- Cost analysis needs to be done while using MWCNT in composition. We have used 0.1 wt% which should bring down the cost economics vis a vis the performance to a considerable level for future scope of bulk production if viable.

Reference

1. [Faint reference text]
2. [Faint reference text]
3. [Faint reference text]
4. [Faint reference text]
5. [Faint reference text]
6. [Faint reference text]
7. [Faint reference text]
8. [Faint reference text]
9. [Faint reference text]
10. [Faint reference text]

Metallic Carbon Nanotubes. *Science* (80-) [Internet]. 1996 Jul 26;273(5274):483-7. Available from: <https://www.sciencemag.org/lookup/doi/10.1126/science.273.5274.483>

11. José-Yacamán M, Miki-Yoshida M, Rendón L, Santiesteban JG. Catalytic growth of carbon microtubules with fullerene structure. *Appl Phys Lett*. 1993;62(6):657-9.
12. Baudín C. Processing of Alumina and Corresponding Composites. Vol. 2, *Comprehensive Hard Materials*. 2014. 31-72 p.
13. Meng L, Fu C, Lu Q. Advanced technology for functionalization of carbon nanotubes. *Prog Nat Sci* [Internet]. 2009;19(7):801-10. Available from: <http://dx.doi.org/10.1016/j.pnsc.2008.08.011>
14. Saito T, Matsushige K, Tanaka K. Chemical treatment and modification of multi-walled carbon nanotubes. *Phys B Condens Matter*. 2002;323(1-4):280-3.
15. Rancoule, G. and Debastiani, L.D., WO Patent 9321128A1, 1993.
16. Buchener, G. and Pike, S., Veitsch-Radex Rundsch., 1996, vol. 2, p. 3.
17. Yin, G.X., Pan, B., Gao, X.K., et al., *Taikbastu* (Chinese), 2010, vol. 44, p. 355.
18. Wei, T., Fan, Z.J., Luo, G.L., et al., *Carbon*, 2008, vol. 47, p. 337.
19. Ogata, K. and Litsuka, S., WO Patent 9938818A1, 1999.
20. Buhr, A., *CN Refract.*, 1999, vol. 6, p. 19.
21. Takeshita, S., Hasegawa, S., Aratani, K., and Kawakani, T., *Taikbastu (Refractories)*, 1987, vol. 39,

- p. 345.
22. Mianami, M., Furusato, I., Fukurka, H., et al., *Refractories* (Tokyo), 1994, vol. 6, p. 277.
 23. Engh, T.A., *Principle of Metal Refining*, New York: Oxford Univ. Press, 1992.
 24. Zhang SC, Fahrenholtz WG, Hilmas GE, Yadlowsky EJ. Pressureless sintering of carbon nanotube-Al₂O₃ composites. *J Eur Ceram Soc.* 2010;30(6):1373–80.
 25. Shi SL, Liang J. Effect of multiwall carbon nanotubes on electrical and dielectric properties of yttria-stabilized zirconia ceramic. *J Am Ceram Soc.* 2006;89(11):3533–5.
 26. Zhang HL, Li JF, Yao KF, Chen LD. Spark plasma sintering and thermal conductivity of carbon nanotube bulk materials. *J Appl Phys.* 2005;97(11):11–6.
 27. Yamamoto G, Omori M, Hashida T, Kimura H. A novel structure for carbon nanotube reinforced alumina composites with improved mechanical properties. *Nanotechnology.* 2008;19(31).
 28. Lim DS, You DH, Choi HJ, Lim SH, Jang H. Effect of CNT distribution on tribological behavior of alumina-CNT composites. *Wear.* 2005;259(1–6):539–44.
 29. Liu Y, Ramirez C, Zhang L, Wu W, Padture NP. In situ direct observation of toughening in isotropic nanocomposites of alumina ceramic and multiwall carbon nanotubes. *Acta Mater* [Internet]. 2017;127:203–10. Available from: <http://dx.doi.org/10.1016/j.actamat.2017.01.024>
 30. Sun J, Gao L, Li W. Colloidal processing of carbon nanotube/alumina composites. *Chem Mater.* 2002;14(12):5169–72.
 31. Ghobadi H, Nemati A, Ebadzadeh T, Sadeghian Z, Barzegar-Bafrooei H. Improving CNT distribution and mechanical properties of MWCNT reinforced alumina matrix. *Mater Sci Eng A* [Internet]. 2014;617:110–4. Available from: <http://dx.doi.org/10.1016/j.msea.2014.08.052>

32. Yamamoto G, Shirasu K, Nozaka Y, Wang W, Hashida T. Microstructure-property relationships in pressureless-sintered carbon nanotube/alumina composites. *Mater Sci Eng A* [Internet]. 2014;617:179–86. Available from: <http://dx.doi.org/10.1016/j.msea.2014.08.068>
33. Ahmad I, Cao H, Chen H, Zhao H, Kennedy A, Zhu YQ. Carbon nanotube toughened aluminium oxide nanocomposite. *J Eur Ceram Soc* [Internet]. 2010;30(4):865–73. Available from: <http://dx.doi.org/10.1016/j.jeurceramsoc.2009.09.032>
34. Tanaka, M., Kamioa, H., Yoshitomi, J., et al., in Proc. Unified Int. Tech. Conf. Refract., Bienn. Worldwide Congr., Kyoto, Japan, 2011, p. 976.
35. Yasumitsu, H., Hirashima, M., Matsuura, O., et al., in Proc. Unified Int. Tech. Conf. Refract., Bienn. Worldwide Congr., Kyoto, Japan, 2011, p. 975.
36. Tamura, S., Ochiai, T., Takanaga, S., et al., in Proc. Unified Int. Tech. Conf. Refract., Bienn. Worldwide Congr., Kyoto, Japan, 2011, vol. 2, p. 971.
37. Hattanda, H., Yotabun, T., Tsuda, T., et al., in Proc. Unified Int. Tech. Conf. Refract., Bienn. Worldwide Congr., Dresden, Germany, 2007, p. 204.
38. Tamura, S., Urushibara, Y., Matsuura, O., and Shin, T., in Proc. Unified Int. Tech. Conf. Refract., Bienn. Worldwide Congr., September 18–21, 2007, Dresden, Germany, 2007, p. 627.

39. Hatta, M., Takanaga, S., Matsuura, O., et al., in Proc. Unified Int. Tech. Conf. Refract., Bienn. Worldwide Congr., Dresden, Germany, 2007, p. 614.
40. Tamura, S., Ochiai, T., Mastui, T., and Goto, K., Nippon Steel Technical Report No. 98, 2008, p. 18.
41. Kuznetsov, D.V., Lysov, D.V., Nemtinov, A.A., et al., Refract. Ind. Ceram., 2010, vol. 51, p. 61.
42. Saberi, A., J. Eur. Ceram. Soc., 2008, vol. 28, p. 2011.
43. Mukhopahyay, S., Ceram. Int., 2009, vol. 35, p. 373.
44. Ghosh, S., Ceram. Int., 2003, vol. 29, p. 671.
45. Cardoso, F.A., J. Eur. Ceram. Soc., 2004, vol. 24, p. 2073.
46. Pagliosa, C., Freire, N., and Cholodovskis, G., in Proc. Unified Int. Tech. Conf. Refract., Bienn. Worldwide Congr., British Columbia, Canada, 2013, p. 673.
47. Das, R.R., Nayak, B.B, Adak, S., and Chattopadhyay, A.K., Mater. Manuf. Process., 2012, vol. 27, p. 242.
48. Mukhopadhyay, S. and Pal, T.K., Ceram. Int., 2009, vol. 35, p. 373.
49. Das, R.R., Nayak, B.B, Adak, S., and Chattopadhyay,

- A.K., in Proc. Indian Int. Refractories Congr. (IREFCON), Kolkata, India, 2010, p. 155.
50. Ghosh, S., Lodha, R., Barick, P., and Mukhopadhyay, S., Mater. Manuf. Process., 2007, vol. 22, p. 81.
51. Mukhopadhyay, S. and Poddar Das, P.K., Mater. Manuf. Process., 2006, vol. 21, p. 669.
- [52] **Subham Mahato**: Expanded graphite fortified magnesia-carbon : fabrication and properties, M.Tech Thesis , NIT Rourkela
- [53] **Mukherjee .S , Pramanik. S** : A Comprehensive Review of Recent Advances in Magnesia Carbon Refractories. June 2014 InterCeram: International Ceramic Review 63(3):90-98
- [54] **Sani, M.A.F., Yamaguchi, A.**: Oxidation kinetics of MgO-C refractory bricks. Ceram. Int. 28 (2002) 835–839
- [55] **Pickering, G.D; Batchelor, J.D.** Carbon-MgO reactions in BOF refractories. Amer. Ceram. Soc. Bull. 1971, 50 611–614.
- [56] **Bag, M., Adak, S., Sarkar, R.**: Study on low carbon containing MgO-C refractory: Use of nano carbon. Ceram. Int. 38 (2012) 2339–2346
- [57] **Bag, M., Adak, S., Sarkar, R.**: Nano carbon containing MgO-C refractory: Effect of graphite content. Ceram. Int. 38 (2012) 4909–4914
- [58] **Behera. S, Sarkar. R**: Low-Carbon Magnesia-Carbon Refractory: Use of N220 Nanocarbon Black Int. J. Appl. Ceram. Technol., 11 [6] 968–976 (2014)
- [59] **Gokce, A.S., Gurcan, C., Ozgen, S., Aydin, S.**: The effect of antioxidants on the oxidation behaviour of magnesia-carbon refractory bricks. Ceram. Int. 34 (2008) 323–330
- [60] **R.R. Das, M.Tech(Research) Thesis**, “Effect of micron and nano MgAl₂O₄ spinel addition on the properties of magnesia-carbon refractories”, National Institute of Technology, Rourkela, Oct., 2010
- [61] **R. R. Das, B. B. Nayak, S. Adak, A. K. Chattopadhyay**, “Effect of spinel addition in MgO-C refractory for slag zone of steel ladle”, 8th IREFCON Feb 6-8, Kolkata, page 155 – 59 (2010)

**FABRICATION AND CHARACTERISATION OF
MWCNT- REINFORCED ALUMINA BASED
NANOCOMPOSITE**

*A thesis submitted in partial fulfilment of the
Requirement for the degree of*

MASTER OF TECHNOLOGY
In Ceramic Technology

By

Udayan Mukherjee

Roll No.- GCECTM-R20-1004

Registration No.-

Under the guidance of

Dr. Barun Kumar Sanfui

Assistant Professor

Department Of Ceramic Engineering

Government College of Engineering & Ceramic
Technology

Kolkata-700010



**FABRICATION AND CHARACTERISATION OF
MWCNT- REINFORCED ALUMINA BASED
NANOCOMPOSITE**

*A thesis submitted in partial fulfilment of the
Requirement for the degree of*

MASTER OF TECHNOLOGY
In Ceramic Technology

By

Udayan Mukherjee
Roll No.- GCECTM-R20-1004
Registration No.-

Under the guidance of

Dr. Barun Kumar Sanfui
Assistant Professor
Department Of Ceramic Engineering
Government College of Engineering & Ceramic
Technology
Kolkata-700010



INDEX

Serial No.	Topic	Page No.
	Acknowledgements	i
	List of figures	ii
	List of tables	iv
Chapter 1	Introduction	1
Chapter 2	Literature Review	5
Chapter 3	Objectives	19
Chapter 4	Experimental Procedure	20
4.1	Starting Materials	20
4.2	Procedures	20
4.3	Preparation of precipitation	20
4.4	Calcination	21
4.5	Pressing	22
4.6	Firing	23
4.7	Green Density measure	24
4.8	Bulk Density and Apparent Porosity Measurement	24
4.9	Flexural Strength	25
4.10	Particle size distribution	25
4.11	FTIR	27
Chapter 5	Results and Discussion	28
5.1	Green Density	28
5.2	Linear Firing shrinkage:	29
5.3	Apparent Porosity, Bulk Density and Relative Density:	30
5.4	Flexural strength:	35
5.5	Hardness:	37
Chapter 6	Conclusion	40
Chapter 7	Scope of Future Work	41

ACKNOWLEDGEMENT

First of all I pay zillion obeisance to "The almighty God and Maa Saraswati" and venerable parents with whose grace and blessing I would be able to accomplish this task.

I would like to express my deep sense of gratitude and indebtedness to professor Dr. Barun Kumar Sanfui, Assistant Professor, Department of Ceramic Technology, Govt. College of Engineering and Ceramic Technology, Kolkata, for introducing the present research topic and also for inspiring guidance throughout the project work. Two things that I have learned from him are quantitative approaches of scientific problems and critical evaluation of results. Also thank to SERB-DST Government of India (file no.-EEQ/218) for financial support.

I am also indebted to my senior research scholar, Mr. Savan Kumar Sharma SRF, CSIR, Government College of Engineering & Ceramic Technology for his unconditional support and constant motivation whenever needed. And a big thanks to my senior Tanmoy Biswas for giving me a helping hand whenever needed.

Udayan Mukherjee
3/06/2022
Udayan Mukherjee

DECLARATION OF ORIGINALITY AND COMPLIANCE OF ACADEMIC ETHICS

I do hereby declare the thesis contents literature review and original research work by the undersigned candidate, as part of my Master of Technology in Ceramic Technology, studies during academic session 2021-2022.

All information in the document has been obtained and presented in accordance with academic rules and ethical conduct.

I also declare that I have fully cited and referred all the material and results that are not original to this work.

Name- Udayan Mukherjee

Roll No.- GCECTM-R20-1004

Registration No.- 201130410710002 OF 2020-2021

Signature Udayan Mukherjee.

Date 03/06/2022

Udayan Mukherjee
03/06/2022

Chapter 1

Introduction

Carbon nanotubes (CNTs) have extremely high tensile strength and stiffness, good flexibility [8], and low density. These superior properties make CNTs attractive for many applications and technologies [10]. In order to take advantage of the intrinsic properties of individual CNTs, various CNT forms and composites [7] have been demonstrated to overcome the performance limits of conventional materials. Engineering ceramics have high stiffness, excellent thermostability, and relatively low density, but their brittleness impedes their use as structural materials. Incorporating CNTs into a ceramic matrix might be expected to produce tough as well as highly stiff and thermostable ceramic composites.

It is well known that the two problems exist in CNT/ceramic composite materials research. The first is the inhomogeneous dispersion of CNTs in the matrix. Pristine CNTs are well known for poor solubilization, which leads to phase segregation in the composite owing to the van der Waals attractive force. Severe structural inhomogeneities result in the degradation of the mechanical properties of the CNT composite materials [12]. The second problem is the poor connectivity between CNTs and the ceramic matrix, which leads to a limited stress transfer capability from the matrix to the CNTs. The connectivity with the matrix, and uniform distribution within the matrix are essential structural requirements for the stronger and tougher CNT/ceramic composites.

Carbon nanotubes (CNT) were first discovered by Dr. Iijima of Japan in 1991. It is a rolled-up sheet of graphene or a tube made of graphene sheet. Carbon nanotube have diameters ranges of 1-100 nm and lengths up to several centimetres. CNTs are classified as Single walled Carbon nanotubes Double walled Carbon nanotube and Multi walled Carbon nanotube, depending on the rolling layers of graphene sheets [15].

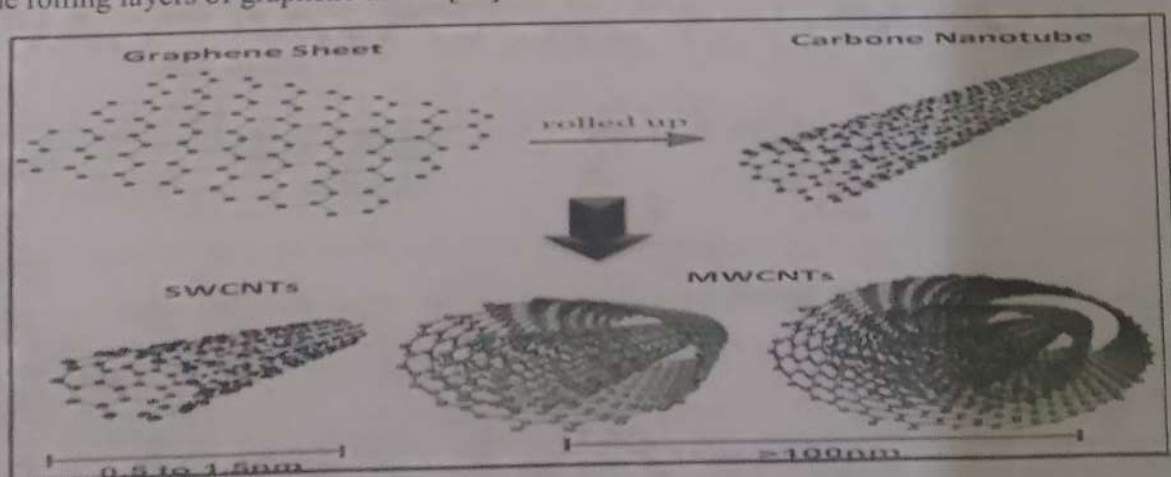


Figure 1. The conceptual diagram showing the general dimensions of the length and width of SWCNTs, DWCNTs and MWCNTs

As the majority of the previous studies, alumina powder are mechanically mixed with CNTs in order to prepare CNT/alumina composites. Engineering ceramics such as Al_2O_3 , Si_3N_4 , SiC and SiC are promising material for microcomposites, due to their high stiffness, excellent impermeability and relatively low density. Among the various engineering ceramics, Al_2O_3 is one of the most cost-effective and environmentally viable materials, due to their good mechanical properties, its inherent brittleness and high melting behavior as other ceramic oxide materials has, which limited its extensive application. Alumina (Al_2O_3) or aluminum oxide is a amphiphilic oxide that exists in nature as the naturally occurring (Al_2O_3) kyanite, ($Al_2O_3 \cdot H_2O$) gibbsite ($Al_2O_3 \cdot 3H_2O$) and includes several hexatic, which is a rare form of gibbsite. The crystal structure of alumina comprises hexagonal and octahedral sites, as shown in Fig 2.

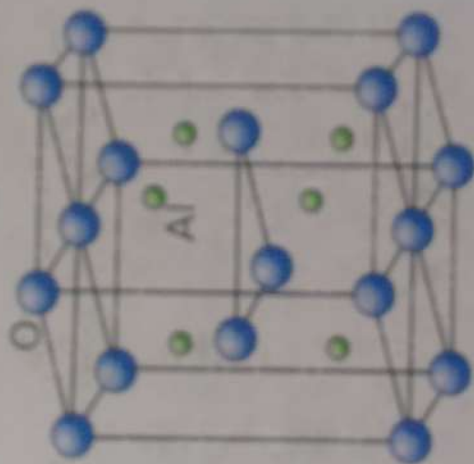


Figure 2. Alumina crystal structure (where green ball suggests Aluminium atoms and blue ball indicates oxygen atoms).

Alumina exists in numerous crystalline structures, such as γ , δ , ϵ , θ , η , ζ , ρ . Al_2O_3 besides the thermodynamically stable α - Al_2O_3 (corundum). Metastable phases, usually called transition alumina phases that are irreversibly transformed to Alpha-alumina by appropriate thermal treatments. Fig 3, shows the pathways of transition Al_2O_3 during the heat treatment. The crystal structure of alumina comprises hexagonal and octahedral sites. Various reports conclude that the average crystalline size of the Al_2O_3 powder increases with increasing calcination temperature. Our objective was to use laboratory fabricated alumina by

precipitation method and carbon nanotube to follow more conventional route to achieve high grade property comparable to high-cost processing method. For our research work, we follow more conventional route to lower down the processing cost.

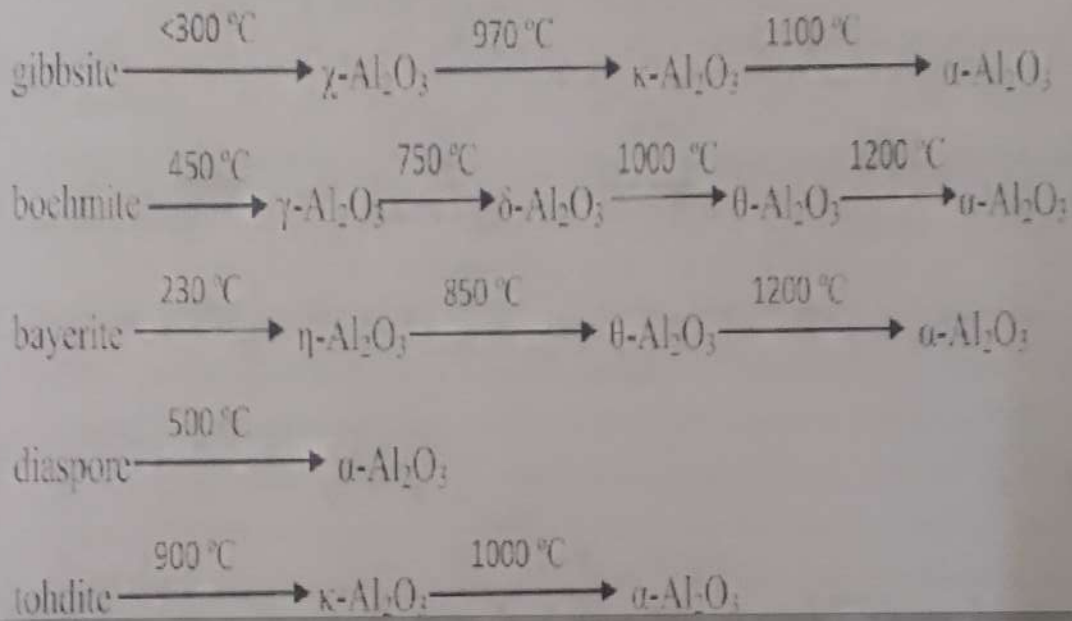


Figure 3. Transformation of alumina and alumina hydroxide structure.

Literature Review

➤ **Jing Wang et al.** published a paper in the year of 2007 and they concluded that In this article Nanoparticles are densely decorated on MWNTs successfully by a simple and effective in-situ synthetic method. The most important advantage for the in-situ composite method is to make MWNTs homogeneously distributed in the matrix. The in-situ precipitation could be a promising method to fabricate CNTs composites of ceramics matrix especially those hard to sinter. In the course of coating MWNTs with precursor of ceramics, the surface modification of MWNTs by SDS for imparting a negative charge is effective. The metal positive ions then can be adsorbed onto the surface of MWNTs due to the electrostatic attraction, and in-situ react with acid radical ions via electrovalent bond to form precipitates of ceramic precursors. The addition of MWNTs in-situ synthesized mullite composites showed advantages in the microstructure and mechanical property compared to the traditionally mixed mullite composites. The simple method presented here may be extended to synthesize other ceramics composites based on coating MWNTs with the precursor particles of ceramics by varying type of dispersant. The coated MWNTs pave the way for the development of nanotubes composites with a stable and dense tube-matrix interfaces and improved performance.

In this paper Firstly, the multiwalled carbon nanotubes were dispersed in a dilute sodium dodecyl sulfate (SDS) aqueous solution by ultra-sonification. Aluminum ammonium sulfate, $\text{AlNH}_4(\text{SO}_4)_2 \cdot 12\text{H}_2\text{O} > 99.5\%$, and Ammonium bicarbonate, NH_4HCO_3 were separately dissolved in dilute $\text{NH}_3 \cdot \text{H}_2\text{O}$ with $\text{p}^{\text{H}} > 10$. The dispersed MWNTs were sonicated in the NH_4HCO_3 solution and the $\text{AlNH}_4(\text{SO}_4)_2$ solution was then added slowly into the above mixture at room temperature with vigorous agitation. The mixture was agitated for 2h and the obtained precipitates were then rinsed with water and alcohol. After further drying grinding, The SDS adsorbed MWNTs- $\text{AlNH}_4(\text{OH})_2\text{CO}_3$ was obtained and then dispersed in dilute $\text{NH}_3 \cdot \text{H}_2\text{O}$ with $\text{p}^{\text{H}} > 10$, and the Ethyl silicate (TEOS), $(\text{C}_2\text{H}_5)_4\text{SiO}_4$ ($\text{SiO}_2 > 28.0\%$) was added slowly into the above

mixture at 50 °C with vigorous agitation. The double coated mixture was agitated for 6h, and the obtain precipitates were rinsed with water and alcohol. Then after drying and grinding, the composite powders of MWNTs $\text{AlNH}_4(\text{OH})_2\text{CO}_3\text{--Si}(\text{OH})_4$ were calcined into the product powders of MWNTs- $\text{Al}_2\text{O}_3\text{--SiO}_2$ at 500 °C in the air. As a contrast to the in-situ synthesized powder, the mixture of MWNTs- $\text{Al}_2\text{O}_3\text{--SiO}_2$ nano powders was produced by the traditional mixing method. The dense compact of single-phased multite powders and the composite powders were sintered by SPS (Spark-plasma-sintering). Densities of the sintered samples were measured using the Archimedes technique. Zeta potential of the MWNTs in dilute aqueous suspensions (0.005wt.%) was measured with a zetaplus and analyzer. The phase composition of the powder and composites was identified by X-ray diffraction (XRD). Transmission electron microscope (TEM) was used to observe the micrograph of the CNTs and the composite powders. Field emission scanning electron microscope (FESEM) was used to observe the fracture surface. Composites with 15vol.%MWNTs were tested for illustration of bending strength (σ_f) that was measured by three-point method with a span of 30 mm and a crosshead speed of 0.5 mm/min (Jing Wang1, 2007)

➤ **G Yamamoto et al.** published a paper in the year of 2008 and they concluded that a homogeneous distribution of MWCNTs in an alumina matrix has been achieved by a novel processing approach based on the precursor method for the synthesis of alumina and acid-treated MWCNTs. Combined with enhanced frictional resistance through the mechanical interlocks induced by the chemically modified MWCNTs, this approach leads to an increase in the strength and toughness of MWCNT/alumina composites. The addition of only 0.9 vol% acid-treated MWCNTs to alumina results in 27% and 25% simultaneous increases in bending strength (689.6 MPa) and fracture toughness (5.90 MPa m^{1/2}), respectively, indicating enhanced stress transfer capability from the alumina to the MWCNTs.

The first instance in this research paper is that the pristine MWCNTs were refluxed in 3:1 (volume ratio) concentrated $\text{H}_2\text{SO}_4\text{:HNO}_3$ mixture at 70°C for 2 h, washed thoroughly with distilled water to be acid-free, and then finally dried in an oven at 60°C. A typical synthesis procedure for the composite preparation is as follows. The 50 mg pristine MWCNTs or acid-treated MWCNTs were dispersed in 300 ml ethanol with aid of ultrasonic agitation. 15.2 g aluminum hydroxide was added to this solution and ultrasonically agitated. 73 mg magnesium hydroxide was added to prevent

excessive crystal growth. Here, the weight loss of the hydroxides caused by the dehydration process was accounted for in the calculation of the composite composition. The weight loss of aluminum hydroxide and magnesium hydroxide was 34.7% and 31.9%, respectively. The resultant suspension was filtered and dried in an oven at 60 °C. Finally, the product obtained in the previous step was put into a half-quartz tube and was dehydrated at 600 °C for 15 min in argon atmosphere. The composites were prepared by spark plasma sintering in a graphite die with an inner diameter of 30 mm at a temperature of 1500 °C under a pressure of 20 MPa in vacuum for 10 min. Bulk densities of the sintered bodies were measured by the Archimedes method using deionized water as an immersion medium. The nanostructures and microstructures were observed using scanning electron microscopy and transmission electron microscopy. The surface roughness was measured by a stylus profilometer. The changes in zeta potentials were measured in 1.0 mM KCl aqueous solution of varying p^H using a zeta potential analyzer. The p^H value of the aqueous solution was adjusted with HCl and NaOH. Zeta potential values were calculated using the Smoluchowski equation (G Yamamoto, 2008).

➤ **Kasperski et al.** published a paper in the year of 2014 and they concluded that MWCNTs with prior covalent functionalization, are not able to provide any crack bridging in the corresponding Al_2O_3 -matrix composites, probably because the chemical treatment was detrimental to their mechanical properties, which is correlated with low fracture toughness. In contrast, the non-covalent functionalization (here performed with preserves the mechanical properties of the MWCNTs, thus allowing for crack bridging on a large scale in the corresponding composites. Moreover, it is shown that, in order for this to provide toughening, long MWCNTs are to be preferred to shorter ones, although they are more difficult to disperse homogeneously because they permit the establishment of sufficiently long mechanical interlocking of the CNTs by the matrix grains.

The first instance in this research paper is that the MWCNT samples were divided into two batches, which were sub-mitted to a covalent or non-covalent functionalization treatment. For covalent functionalization, the MWCNTs were poured into a nitric acid aqueous solution using 1 mg of CNT per ml of solution. After refluxing overnight (130 °C, magnetic stirring), the suspension was neutralized, filtered and redispersed in an NaOH aqueous solution in order to remove any disorganized carbon. After

neutralization and filtration, the covalent functionalized MWCNTs obtained were dispersed again in deionized water, yielding a stable suspension as required for the study. For non-covalent functionalization, the CNTs were dispersed in an aqueous solution of gum arabic (GA), a water soluble polysaccharide, using the same concentration of 1 g/l for both CNT and GA (A. Kasperski, 2014).

➤ **Soumya Sarkar et al.** published a paper in the year of 2011 and they concluded that fabricate MWCNT/Al₂O₃ nanocomposites by simple wet mixing of as-received commercial grade precursors without any purification and/or surface modification steps of the raw materials followed by pressureless sintering without damaging structural integrity of MWCNTs. Further, during sintering at high temperature formation of extensive internal bamboo morphology in reinforcing MWCNTs contributed considerably in improving mechanical properties of present nanocomposites. Nanocomposites containing up to 0.6 vol.% MWCNT extend better reinforcing effects in structural Al₂O₃. Improved mechanical performance of nanocomposites was achieved by homogeneous dispersion of CNTs up to 0.6 vol.%, proper densification of matrix containing grains of lower size than sintered pure Al₂O₃ and better interface performance. The well-distributed MWCNTs aligned both parallel and perpendicular to crack plane helped in successful crack bridging, crack deflection and nanotube pull-out that resulted in improved mechanical properties of these low cost MWCNT/Al₂O₃ nanocomposite. At first, requisite MWCNT was dispersed in isopropyl alcohol using ultrasonic agitation for 1 h in an ultrasonic bath. The dispersed slurry was then mixed with aqueous suspension of Al₂O₃ by magnetic stirring for 1–2h followed by drying at 100 °C to remove volatiles and sieving through 60 mesh (B.S.) screen. Green billets were prepared by cold isostatic pressing at 150 MPa. Samples were finally sintered at 1500, 1600 and 1700 °C for 2 h each in a graphite resistance heating furnace. Density and apparent porosity of sintered samples were evaluated by *Archimedes* water immersion technique (Soumya Sarkar, 2011).

➤ **Zhang et al.** have recently prepared MWCNT/Al₂O₃ nanocomposites by pressureless sintering considering its commercial viability towards manufacturing of complex geometries to near net-shape using typical ceramic powder processing techniques. However, the initial precursor treatment procedure adopted by Zhang et al. [25] was stringent comprising of concentrated acid purification and surface oxidation of as-received MWCNTs for 27 h and ball milling of Al₂O₃ powder for 24 h. Furthermore,

the freeze-drying method used to prevent MWCNT segregation is not a readily available technique in industrial field. In this study an attempt was made to explore opportunities of fabricating structural MWCNT/Al₂O₃ nanocomposites having superior performance than pure Al₂O₃ by a simple and cost-effective process using commercial raw materials. To evade chances of strength limiting nanoscale defect formation on CNT surface by concentrated acid treatment [26], both MWCNT and Al₂O₃ were used directly in their as received state without any pre-treatment. In addition, normal air drying of MWCNT/ Al₂O₃ slurry was employed instead of freeze drying. Nanocomposites containing five different CNT volume fractions from 0.15 vol.% to 2.40 vol.% were fabricated by wet mixing of as received precursors followed by pressureless sintering in Argon atmosphere at three temperatures viz. 1500, 1600 and 1700 °C. Nanocomposites were characterized in terms of density, apparent porosity, Vickers hardness, fracture toughness and four-point bending strength. Microstructure of sintered and polished specimens and fractographic analyses of flexure tested specimens through grain boundary engineering were done to predict structure-property relationship. Properties were compared with pure Al₂O₃ to assess changes in performance of present nanocomposites (Shi C. Zhang et al., 2010).

➤ **Shi C. Zhang et al.** published a paper in the year of 2010 and they concluded that Alumina matrix composites containing 1, 3 and 5 vol.% CNTs were successfully densified using sintering. Commercial MWCNTs were purified, dispersed, and homogeneously mixed with Al₂O₃ powder in water at pH 12. The slurry of CNTs and Al₂O₃ was freeze dried to maintain its homogeneity. Pellets of the Al₂O₃-CNT composite powder were sintered to high density without externally applied pressure. The combination of CNT purification and freeze drying of the Al₂O₃-CNT suspension resulted in a uniform distribution of CNTs in an Al₂O₃ matrix. Al₂O₃-CNT composites were densified using pressureless sintering when the CNT content was kept below 3 vol.%. Reactions between Al₂O₃ and the CNTs, which could lead to CNT loss, were limited by keeping the sintering temperature to 1550 °C or below. The composite containing 1 vol.% CNTs had a higher flexure strength (~540MPa) than nominally pure Al₂O₃(~400MPa). The increase in strength was attributed to the inhibition of grain growth in the Al₂O₃ composite due to the pinning effect of the CNTs at the grain boundaries. Flexure strengths of composites with higher CNT contents were lower (230-240MPa) due to the presence of porosity and clusters of CNTs in the composites

Compared to nominally pure Al_2O_3 , the fracture toughness values for all Al_2O_3 -CNT composites were improved due to the CNT content (Shi C. Zhang a *, W., 2010).

➤ **Paromita Das et al.** published a paper in the year of 2022 and they concluded that fabricate a one-dimensional MgAl-binary-oxide MWCNT-based core-shell nano-hybrid architecture featuring the decent control and stable generation of a thin, continuous, and agglomeration free binary oxide passivation layer over the MWCNT surface. The structural parameters have been optimized expressly to promote a stable integrated bridging network at the interfacial position of the nano-hybrid architecture, combined with effectively tailoring the surface chemistry of the CNT structure. The noticeable colloidal stability of the CNTs in the as-synthesized MgAl-binary-oxide precursor sol, the high degree of structural integrity at the interfacial position of the nanohybrid structure, the conspicuous prevalence of the distinctive oxide protective shell, and the persistence of the well-organized crystallographic orientation of the inner MWCNT walls are well documented, even after harsh oxidation and thermal treatment. The results obtained from XRD, FTIR, Raman, and SEM analysis provide striking evidence for the successful and coherent surface deposition of a nominal 2.5 wt% oxide loading concentration which, after its subsequent thermal treatment at an appropriate temperature. Also documented a suitable mechanism that allowed a quick assessment of the influence of interaction chemistry at the binary oxide-MWCNT interface on altering the oxygen entrapment pathway, thus reducing the rate of progression of the high temperature oxidation reaction in a suitably controlled way. Lastly, this research elucidated the ultimate prospects of the structure-property relationship via recognizing the real-world application potential of the developed nano-hybrid structure as a competent reinforcement candidate for use in ceramic matrix based composite structures; its inclusion resulted in an instant 165% performance enhancement in the load-bearing capacity of a spinel-based ceramic composite structure compared to a pure sintered compact (Paromita Das, 2022)

PROPERTIES OF CNT/ Al_2O_3 NANOCOMPOSITE

The multi-walled carbon nanotubes with a diametrical range of 5-40 nm are known for their exceptional mechanical properties. MWCNT whose modulus is comparable to that of diamond (1.2TPa), are reported to have strengths 10- 100 times higher than the strongest steel at a fraction of the weight. This, coupled with approximately 500 times more surface area per gram

(based on equivalent volume fraction of typical carbon fiber) and aspect ratios of around 1000, has created a great deal of interest in using MWCNT as a reinforcing phase for polymer matrices.

➤ **Mechanical Properties:** In ceramic matrix materials, the mechanical property of greatest importance is toughness or resistance to crack growth. Ceramics are already stiff and strong and so, in analogy to ceramic composites with micron-scale fiber additions, the incorporation of carbon nanotubes is aimed at enhancing toughness.

- Hardness of this particular ceramic matrix nanocomposites depends on various factors e.g. CNT purity, content and extent of dispersion, sintering temperature, extent of densification, nature of interface formed, matrix grain size and applied indentation load. Vickers hardness (HV) of pure Al_2O_3 differed significantly from one report to another ranging from 14-28.4 GPa. Hardness was found to increase with increasing MWCNT content, and maximum hardness was reached when the CNT content was 4 vol%. With further increasing the concentration of MWCNTs, can attributed agglomeration of MWCNTs, leading to poor densification of the composites and ultimately decreasing the hardness value. Ahmed et al. obtained HV of 18 Gpa in 2 wt% of CNT Al_2O_3 composite having matrix grain size 0.4 micrometer. A hardness of 9.98 Gpa was achieved for nanocomposites sintered at 1450°C , while the hardness of pure monolithic alumina was measured at 9.21 Gpa under the same condition.
- Various methods have been adopted to measure fracture toughness(K_{1s}) like direct crack measurement(DCM), indentation strength in bending(ISB), single edge notched beam(SENB) etc. Regardless of measurement technique, CNT/ Al_2O_3 nanocomposites generally offered improved K_{1c} over pure Al_2O_3 , obviously up to a certain CNT loading where less or no CNT agglomeration were present. Researchers shown that mixed gum arabic (GA) and Sodium dodecyl sulphate (SDS) was the most effective dispersant in enhancing K_{1c} Of MWCNT/ Al_2O_3 nanocomposite than GA or SDS alone. Maximum toughness $4.7 \text{ Mpa m}^{1/2}$ was obtained by Momohjimoh et al. at 7.39 wt % of CNT sintered at 1450°C . Lee et at. showed on addition of 2.48 wt% of MWCNT the fracture toughness was increased by 152%. Yamamoto et al. showed on addition of 0.9vol% acid treated MWCNT on alumina increased fracture toughness by 25%.

- Due to wide variation in matrix grain size, the individual flexural strength values differed significantly from one report to another. The highest improvement in strength has been reported by Zhu et al. The authors reported 67% increase in flexural strength over pure Al_2O_3 in a 1.5 wt% nano- ZrO_2 coated MWCNT/ Al_2O_3 . Yamamoto et al. showed on addition of 0.9 vol% acid treated MWCNT on alumina increased bending strength by 27%.

➤ **Electrical Properties:** The pure alumina that has an extremely low electrical conductivity. CNTs existing in the grain boundary will connect and form a conductive network to transport electrons even at very low content. It has been reported that electrical conductivity of CNT/ Al_2O_3 nanocomposite was increase by increasing the grain size when the amount of CNT was fixed, as the density of CNT at the boundaries was increased. In addition the electrical conductivity was increased by increasing the amount of CNT, but by maintaining a fixed grain size.

- The threshold conductivity was attained at 0.18 wt% of CNT reported by Lee et al.
- Yamamoto et al. showed addition of 0.9 vol% acid treated MWCNT to the alumina matrix increased the electrical conductivity of the composite by about 7-9 orders of magnitude compared with pure alumina.
- Zhan et al. obtained an electrical conductivity of 3345 S/m on the 15 vol% SWCNT-alumina nanocomposites, an increase of 13 orders of magnitude over that of pure alumina.

➤ **Thermal Properties:** In addition to the exceptional mechanical properties, they also possess superior thermal and electrical properties. They have a thermal stability up to 750°C in air and 2800°C in vacuum. Their thermal conductivity is about twice as high as diamond, with electric current transfer capacity 1000 times greater than copper wires. For high-temperature applications, the high thermal conductance of MWCNTs suggests that their incorporation, even at low volume fractions, might provide the thermal transport needed to reduce material operating temperatures and improve thermal shock resistance

- Kumari et al. obtained a notable increase in thermal conductivity for a 7.39 wt% MWCNT/ Al_2O_3 nanocomposite over pure Al_2O_3 after sintering at 1550°C.

- Hafiz Muzammil Irshad et al. obtained that the polysulphone–CNT composite with 10 wt% CNTs shows an enhancement in thermal conductivity of 163%, which is approximately 50% increase in comparison to the addition of 10 wt% graphene nano-platelets.
- Sarkar et al. studied the influence of CNT loading and sintering temperature on the thermal conductivity of alumina. The thermal conductivity of pure alumina sintered at 1500 °C by reached 29.39 W/mK, and it increased to 38.63 W/mK as the sintering temperature was increased to 1700 °C.
- Zhang et al. studied the thermal conductivity of Al₂O₃/SWCNT nanocomposites densified by spark plasma sintering with CNT content ranging from 5 to 15 vol% .

CNT CONTENT IN CNT/Al₂O₃ NANOCOMPOSITE

- The reported range of CNT content in CNT/Al₂O₃ nanocomposites varied over a wide span from 0.01 wt% to 35 wt% .
- Yamamoto et al. , Sarkar and Das, cha et al., and Zhang et al. found that MWCNT started to form agglomerates beyond 0.9, 0.6, 1.8, 1, vol% respectively. Agglomeration of nanotubes beyond 2 – 7.39 wt% MWCNT has also been reported in various research paper.
- Sharma et al. showed large number of agglomerates of MWCNT entangled and clustered with Al₂O₃ particles at 5 vol% of MWCNT. CNT agglomeration depends also on CNT type and dimension.

SYNTHESIS AND FABRICATION METHOD OF CNT

There are several techniques that have been developed for fabricating CNT structures. Commonly, three procedures are being used for producing CNTs: (i) the chemical vapor deposition (CVD) technique, (ii) the laser-ablation technique, and (iii) the carbon arc-discharge technique . High temperature preparation techniques for example arc discharge were first used to synthesize MWCNTs by Iijima in 1991. This method has been used long before that in the production of carbon fibers and fullerenes. It took 2 years to Iijima and Ichihashi, and Bethune et al. to synthesize SWCNTs by use of metal catalysts in the arc-discharge method in 1993. And also a significant progress was achieved by another high temperature preparation technique, laser-ablation synthesis of bundles of aligned SWNTs with small diameter distribution by Smalley and co-workers. But currently, these techniques have been substituted

by low temperature chemical vapor deposition (CVD) methods which was first used by (<800°C). Because of the nanotube length, diameter, alignment, purity, density, and orientation of MWCNTs can be accurately controlled in the low temperature chemical vapor deposition (CVD) methods. The industrial application of the carbon nanotubes requires the development of techniques for large-scale production of defect-free nanotubes.

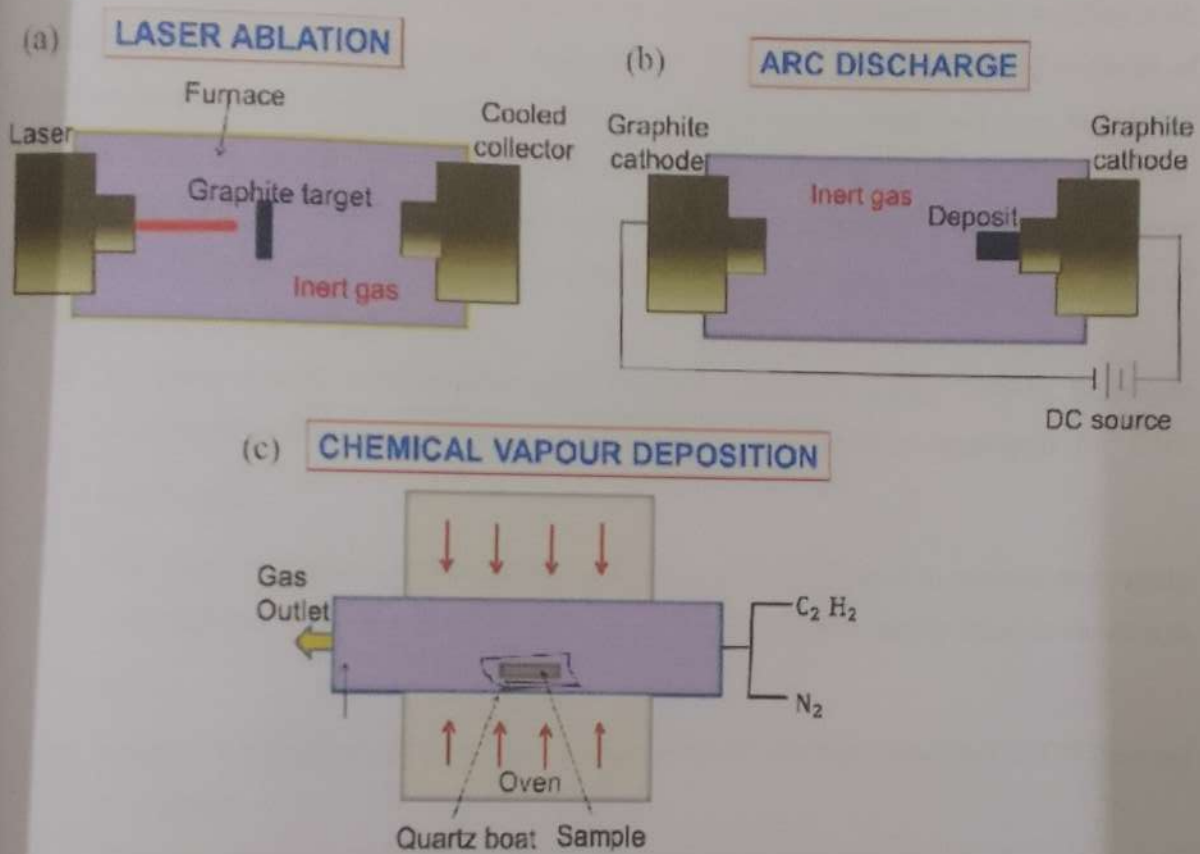


Figure 4. the (A) Diagram of Arc-discharge. Two graphite electrodes are used to produce a dc electric arc-discharge in inert gas atmosphere, (B) Schematic Diagram of Laser-ablation. Laser beam vaporizes target of a mixture of graphite and metal catalyst (Co, Ni) in a horizontal tube in a flow of inert gas at controlled pressure and in a tube furnace at 1200 °C. The nanotubes are deposited on a water-cooled collector outside the furnace. (C) Diagram of Chemical vapour deposition .

PRE-TREATMENT OF CNT (Functionalization)

The addition of oxygen containing species to the surfaces of MWCNTs promotes their solubility in aqueous or organic solvents and decreases van der Waals associations between different MWCNTs, enhancing the dissociation of nanotube bundles into individual tubes.

There are essentially two means of functionalizing MWCNTs: chemical and physical functionalization. Chemical functionalization is typically executed using strong acids, such as HNO_3 , H_2SO_4 or a mixture of them, or using strong oxidants, such as KMnO_4 . The treatment process involves employing a mixture of MWCNTs, nitric acid and sulfuric acid of high concentration (mainly 3:1), followed by 3 h of sonication. The mixture is then stirred for 24 h and rinsed with distilled water until the PH is 7. The MWCNTs are sieved and dried overnight at 100°C . Defects created by the oxidation agents are neutralized through their bonding with carboxylic acid (-COOH) or hydroxyl (-OH) groups. The study on two chemical methods of functionalization that involve using nitric acid and hydrogen peroxide, and they found that hydrogen peroxide-based functionalization is more effective than nitric acid functionalization. The MWCNTs were found to be completely de-roped in hydrogen peroxide, and better dispersion outcomes were observed in the epoxy, resulting in high mechanical properties of MWCNT-epoxy nanocomposites.

- In many reports, concentrated acid treatment, primarily using 3:1(v/v) Sulphuric acid(H_2SO_4):Nitric acid(HNO_3) solution have been widely employed for CNT purification.
- The MWCNTs were refluxed in the acid mixture at 70°C for 2 h, washed thoroughly with distilled water until the PH is 7 to be acid free, and then finally dried in an oven at 60°C .
- Kasperski et al. used only aqueous solution of nitric acid and using 1mg of CNT per ml of solution.
- Presence of such -COOH groups at the open ends of CNT also facilitate nanotube dispersion in liquid medium.
- Some researchers also did hydrogen peroxide based functionalization.
- The physical functionalization of CNT involves the adsorption of surfactant molecules on the surfaces of MWCNT to ensure that agglomeration do not form.(CNT were dispersed in an aqueous solution of GA using the concentration 1mg/lit for both CNT and GA)

Chapter 3

Objectives

The objective of this work is to prepare MWCNT reinforced alumina-based nanocomposite by precipitation technique using conventional pressureless sintering.

Chapter 4

Experimental Procedure

4.1 Starting Materials

1. Aluminium nitrate
2. Ammonia solution
2. Distilled Water (H₂O), Merck.
3. -COOH Functionalised Multi-Walled Carbon Nanotubes (Purity>95%)
4. Sodium Dodecyl Sulphate (SDS) (Purity≥90%), Merck.

4.2 Procedures

Table 1. Batch Composition.

Batch code	Al(NO ₃) ₃ . 9H ₂ O(wt%)	Sodium Dodecyl Sulphate(wt%)	MWCNT (wt.%)
Al-CNT0	100	1.5 wt% of CNT	0
Al-CNT0.25	99.72	1.5 wt% of CNT	0.25
Al-CNT0.50	99.49	1.5 wt% of CNT	0.50
Al-CNT0.75	99.23	1.5 wt% of CNT	0.75

4.3 Preparation of precipitation

To prepare Al-CNT nanocomposite at first we prepare 1:1 ammonia solution. Then a amount of desired water was taken in a beaker along with aluminium nitrate to form precipitation in control way. Then the beaker placed on the magnetic stirrer with a magnetic bead to mix Aluminium nitrate in the water homogeneously. On the other hand the desired amount of water was taken in a beaker to dispersed CNT. Then the desired wt.% of MWCNT was mixed along with sodium dodecyl sulphate (SDS) which was taken 1.5 wt.% of MWCNT, Then Ultrasonicated for 10min. Carbon nanotube used in our project has the following specification,

(i) -COOH functionalized, (ii) Diameter 20-30nm, (iii) Length 5-15 μm , (iv) Impurity 5%, (v) Bulk Density 0.17gm/cm³.



Figure 5. A and B Dispersion of MW-CNT in water before and after addition of SDS and ultrasonication.

Due to having high surface area and high van der Waals force of attraction carbon nanotube tends to form agglomerates. For proper dispersion of carbon nanotube in the aqueous solution a surfactant is needed. If we don't add a surfactant MW-CNT agglomerates and settled in the beaker within minutes after ultrasonication. Dispersion is a system in which distributed particle are dispersed in a continuous phase of another material. In fig5 and 6, we can identify agglomeration and dispersion side by side. For our research work, after ultrasonication is done, then the MW-CNT dispersed water was mixed slowly with that liquid solution which was already spinning by magnetic stirrer with a magnetic bead. After that the rest of the part of

Ammonia Solution ($\text{NH}_3 + \text{H}_2\text{O} - \text{NH}_4\text{OH}$) was added to the mixture dropwise using a burette.

While adding the ammonia solution need to check the pH (should be greater than 9.5) of the alumogel precipitation using pH meter (LABMAA Scientific Instruments, LMPH-10). Then the whole system left overnight to settle down the precipitate. After that we decanted the water 4-5 times so that it takes less time during washing the precipitate.



Figure 6. Dispersion of MW-CNT on ultrasonication bath

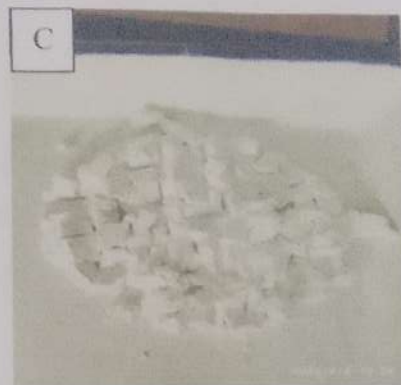


Fig 7.(A) Checking p^H during precipitation process , (B)during filtration, (C) natural air dry after filtration

Then for filtration by suction method we used filter paper and filter cloth in the Buchner funnel. Then the residue was washed using warm water ($70\text{ }^{\circ}\text{C}$ - $80\text{ }^{\circ}\text{C}$) to remove the basic ions. After that it kept in the air oven for overnight (24hr) for drying at $110\text{ }^{\circ}\text{C}$. Solid mixture obtained after drying and then grounded by using agates to make powder.

4.4 Calcination

After drying the agated powder was pressed by hand and then those samples are placed inside an alumina crucible vertically and covered with graphite powder to form a reducing atmosphere around those samples. Putting a cover on the crucible before loading it into the furnace at $600\text{ }^{\circ}\text{C}$. We used Muffle furnace(fig-7) for calcination our samples. During calcination, samples are heated at high temperature below the firing temperature. This is done to mainly remove volatile substances ,water etc.



Figure 8: Picture of Muffle Furnace

4.5 Pressing

after calcination using agates to make powder. Then 10% PVA is added in to the powder as a binder agent. Then the mixer of alumina- MWCNT and PVA, is weighted 4gm each. Which is pressed by the hydraulic press (max. loading capacity is 450KN) at different pressures 100 MPa, and 150 MPa to give the samples a bar like shape. Then those bars are placed inside the air oven before firing.



Figure 9. Uniaxial hydraulic press.

4.6 Firing

Those bar samples are placed inside an alumina crucible vertically and covered with graphite powder to form a reducing atmosphere around those bars. Putting a cover on the crucible before loading it into the furnace. We used a furnace form ANTS Ceramics for firing our samples. During firing, if we do not cover those samples with graphite then carbon nanotubes which was mixed thoroughly in the alumina matrix oxidized in high temperature. Those samples of nanocomposite material which were pressed at different pressures were fired at 1450°C, 1550 °C, and 1600 °C. A constant heating rate was maintained for every firing temperature at 5 °C/minute until temperature reaches to 1000 °C then the firing rate converted to 3°C/minute until target temperature reaches, where it holds for 2 hours. After firing is done, we stick out the crucible from furnace, then removed samples from the crucible and thoroughly



Figure 10. sample loading is done in graphite inside the crucible

cleaned to remove graphite which were sticking to the samples. Samples colour became darker because of moisture present in the sample and due to firing is done inside a graphite bed as shown in fig. 10. And after firing is done, packaging is done for those sample in zip packet with proper marking for further tests.

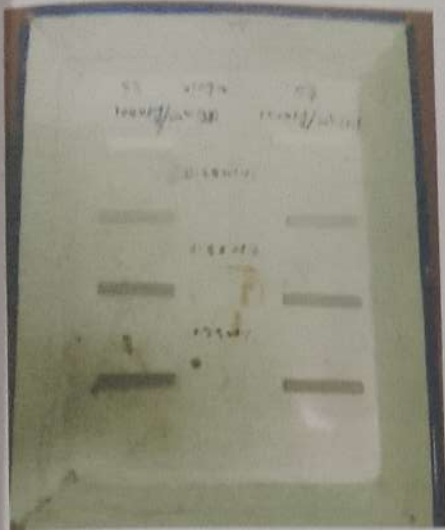


Figure 11. Samples before and after firing.

4.7 Green Density measure

Green density was taken after pressing of powdered sample was done. the dimensions of samples were measured by digital calliper.

$$\text{G.D} = \text{Mass of the compact (M)} / \text{Volume of the compact (V)}$$

4.8 Bulk Density and Apparent Porosity Measurement

The bulk density of the bar was determined by Archimedes method. The samples were weighed in air, and when suspended in distilled water, using an electronic balance of least count of $\pm 0.0001\text{g}$. with a density measurement kit package Mettler Toledo was used for the density measurements. Bulk density (B.D) given by following equation,

$$\text{B.D.} = [(\text{Wsoaked} - \text{Wdry}) / \text{W}_{\text{suspended}}] * \rho_w,$$

And Apparent Porosity (A.P) is given by,

$$\text{A.P.} = (\text{Wsoaked} - \text{Wdry}) / (\text{Wsoaked} - \text{W}_{\text{suspended}}),$$

Where W_{soaked} , W_{dry} and $W_{suspended}$ represents soaked weight, dry weight and suspended respectively. ρ_w is the density of water.



Figure 12. Mettler Toledo analytical balance with a density measurement kit.

4.9 Flexural Strength or Modulus of Rupture

The flexural Strength or MPR of the CNT reinforced fired body was analysed using a MOR testing machine (Aimil Pvt. Ltd.). The span length and crosshead speed for the strength tests were 20.0 mm and 0.50 mm/s.



Figure 13. Modulus of Rupture testing machine.

The Flexural strength (σ_b) is given by the following equations:

$$\sigma_b = 3WL / 2bd^2$$

where W is the maximum load, L is the span length, b is the specimen width, d is the specimen thickness.

4.10 Particle Size Distribution

The particle size distribution analysis of calcination powder was done via DLS measurements (Nanosizer Malvern). At first I disperse Sodium Hexametaphosphate (SHMP) (0.15% of water) into water (approx. 20ml taken). After shaking for some time added the powder sample which was taken 0.2% of water. Then the solution left for Ultrasonication for 10-20 min to make homogeneous mixture.



Figure 14. Particle size analyser machine

4.11 Fourier Transform Infrared Spectroscopy measurement

FTIR spectra were obtained with an FTIR spectrophotometer (Model: PerkinElmer spectrum version 10.03.06) in the wavenumber range of $4000-400 \text{ cm}^{-1}$. A pinch of sample powders were stirred and pressed in a mixture with KBr. The spectra were recalculated into the absorbance spectra.



Fig16: Fourier Transform Infrared Spectroscopy FTIR Machine

4.12 Thermo Gravimetric Analysis (TGA) And Differential Thermal Analyzer test

A TGA and DTA testing machine that works at the temperature range of 0–1000 °C was used to test the thermal characteristics of the samples. Small amount of pure Al_2O_3 powder and 0.75 wt% of MWCNT composite powder was used for this analysis.



Fig17: TGA/DTA Machine

Results and Discussion

5.1 Apparent Porosity, Bulk Density

The apparent Porosity and bulk density of the samples are varying due to the addition of MWCNT as shown in Table.1 and Table.2. The apparent porosity of the pure alumina ceramics decreases with increasing firing temperature from 1450-1550-1600°C as well as with increasing compaction pressure. Bulk density of the respective sample shows a similar trend with the apparent porosity of the respective compact. The density of the respective compacts increases with increasing firing temperature and initial compaction pressure though increasing MWCNT compact results in decreased densification of the compact at all set of temperature range. Significant variation in physical properties of the respective fired compact clearly denotes the decreasing sintering rate and compaction ratio of the compact with increasing MWCNT content, clearly creates hinderance in the sintering rate of the compact.

Batch code	Pressure (MPa)	Apparent Porosity (%)		
		1450 °C	1550 °c	1600 °C
Al-CNT0	100	33.7910	5.0182	4.36
	150	31.1344	4.3526	4.22
Al-CNT0.25	100	34.7916	5.9567	5.81
	150	32.2302	5.8339	5.23
Al-CNT0.50	100	35.9287	6.2439	5.89
	150	32.5254	5.8801	4.40
Al-CNT0.75	100	37.3307	7.5765	6.25
	150	37.5990	7.1901	5.42

Table 1. Apparent Porosity of Alumina-MWCNT nanocomposite for two different pressures and three different firing temperature.

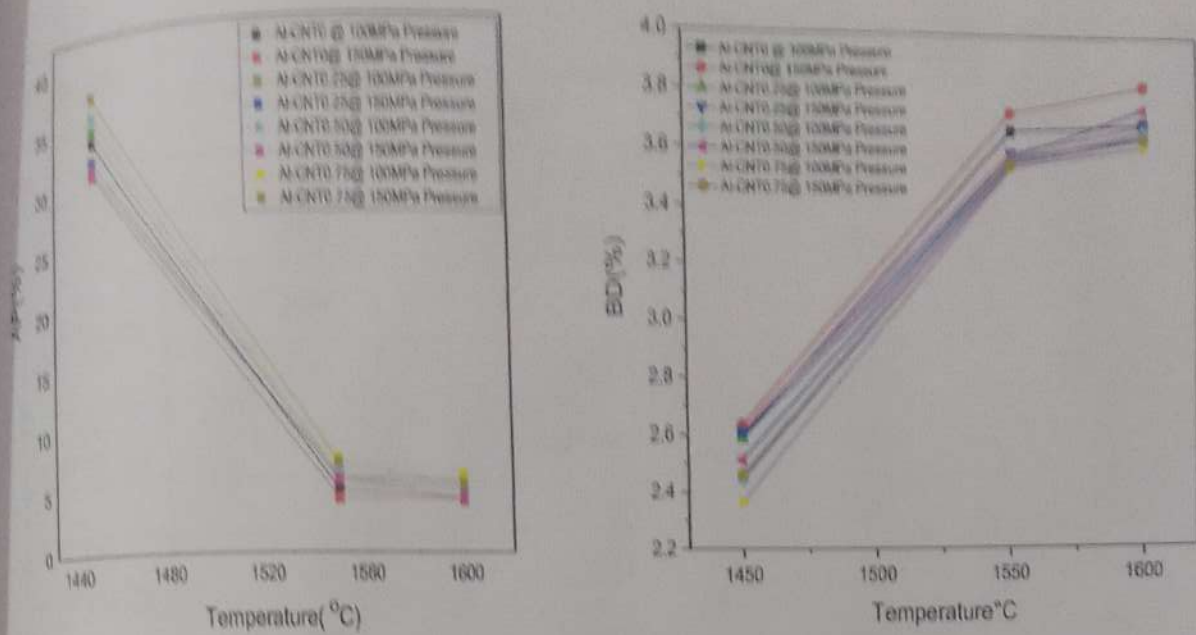


Fig 18. Variation of Apparent Porosity and Bulk Density with different firing temperature.

Soumya Sarkar et al. indicates that up to 0.6 vol.% MWCNT, only temperature played the primarily role in controlling sinterability of samples but beyond that, CNTs also had significant role in lowering consolidation of Al_2O_3 by restraining the process of pore removal and material transport through grain boundary even at high sintering temperatures. In addition, MWCNT aggregates, mainly acted as pores of similar dimensions and played a negative role in densification and resulted in less dense, porous samples [10]. As well as T. Arun kumar et al. says that It is shown that the apparent density values are slightly increasing with the addition of MWCNT (up to 1%) and dropped from thereon, which may have been a result of CNT filling up the voids inside the composite by slipping away during the compaction process while sintering. However, a higher concentration of MWCNTs in the composite could lead to agglomeration that increases the open pores network resulting in density drop.

Batch code	Pressure (MPa)	Bulk Density (gm/cm ³)		
		1450 °C	1550 °C	1600 °C
Al-CNT0	100	2.5953	3.6606	3.6906
	150	2.6351	3.7246	3.8246
Al-CNT0.25	100	2.5886	3.5658	3.648
	150	2.6128	3.5855	3.6855
Al-CNT0.50	100	2.4440	3.5526	3.6626
	150	2.5147	3.5688	3.7421
Al-CNT0.75	100	2.3664	3.5319	3.6123
	150	2.4613	3.5440	3.6420

Table 2. Bulk Density of Alumina-MWCNT nanocomposite for two different pressures and three different firing temperature.

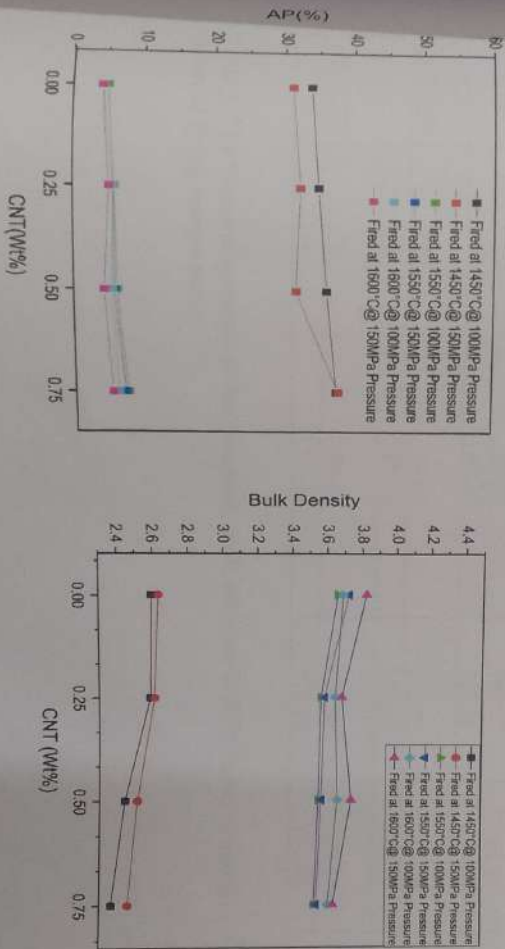


Fig 19. Variation of Apparent Porosity and Bulk Density with Carbon nanotube content.

5.2 Flexural strength:

The comparative study of the Al_2O_3 -MWCNT nanocomposite of the respective fired compact at 100 MPa and 150 MPa has been shown in fig 21. It is clear from the fig. that with increasing pressure the flexural strength of the composite has been found to be increasing at all firing range of temperature. In addition, the flexural strength of the composite improved simultaneously with the increasing the addition of the functionalised MWCNTs sintered at set of temperature. The maximum flexural strength of 195 MPa has been noted for 0.75 wt.% of MWCNT addition in alumina matrix at 1600°C of temperature range. Sarkar and Das [11] also obtained better results for alumina nanocomposite (pressureless sintered at 1600 °C, containing 0.6 vol% CNT) compared to pure alumina; their best results were flexural strength of 265 MPa.

Batch	Pressure (MPa)	Flexural Strength (MPa)		
		1450 °C	1550 °c	1600 °C
Al-CNT0	100	72.67	97.90	108.46
	150	77.23	99.87	115.23
Al-CNT0.25	100	79.93	103.57	118.96
	150	81.24	115.32	123.04
Al-CNT0.50	100	84.61	143.27	131.42
	150	85.32	149.17	156.13
Al-CNT0.75	100	89.43	153.96	163.51
	150	91.27	179.26	195.01

Table 3. The Flexural strength of the composite with different MWCNTs wt.% and in different firing temperature

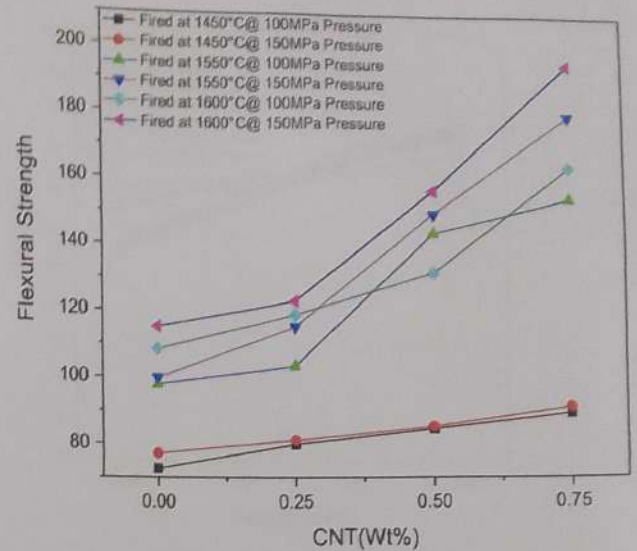
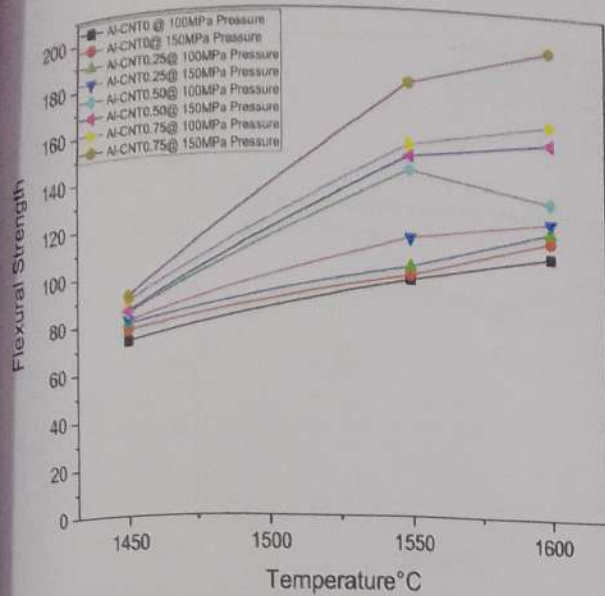


Figure- 20.A Variation of Flexural Strength with different firing temperature.

20.B Variation of Flexural Strength with Carbon nanotube content

5.3 Linear Firing shrinkage:

Linear firing shrinkage of the compacts with increasing MWCNT as well as compaction pressure content has shown in fig 18. The results clearly denote that shrinkage of the compacts clearly decreases with increasing CNT content as well as increasing the initial compaction pressure. High compaction rate and higher green for the compact may induce high amount of strain in compact which results reduction in sintering phenomenon. Increasing temperature causes high sintering of the respective particles which causes higher shrinkage due to pore filling and particle growth mechanism in the relative compacts.

Batch code	Pressure (MPa)	Linear Firing Shrinkage (%)		
		1450°C	1550 °C	1600°C
Al-CNT0	100	22.54	32.58	35.17
	150	21.54	31.42	34,09
Al-CNT0.25	100	26.98	31.56	34.90
	150	26.65	31.36	34.59
Al-CNT0.50	100	22.15	31.05	34.51
	150	23.52	31.35	34.13
Al-CNT0.75	100	28.52	30.90	34.14
	150	26.72	30.02	32.68

Table 4. Linear Firing Shrinkage of Alumina-MWCNT nanocomposite for two different pressures and three different firing temperature.

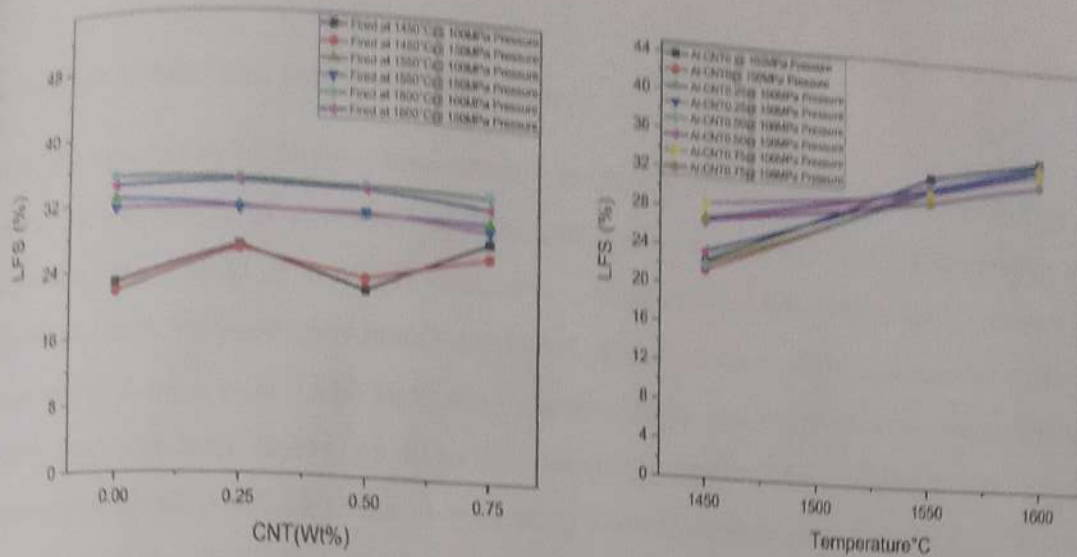


Figure- 21.A Variation of LFS with Carbon nanotube content

21.B Variation of LFS with different firing temperature.

5.4 Particle Size Distribution (PSD)

One of the most important physical properties of particulate samples is particle size distribution (PSD). The PSDs of pure Al_2O_3 and Al_2O_3 -MWCNT powder mixtures were determined by dynamic laser scattering. The particle size distribution of Al_2O_3 -MWCNT powder mixtures was determined in order to find out the average particle size of the various powder mixtures. The particle size distribution of pure in Fig. 15 shows that the average size of the Al_2O_3 particles is ~ 1258.78 nm and the average size of Al-CNT 0.75 wt% is ~ 624.25 nm. Nidhi sharma et al. noted that the pure Al_2O_3 has a particle size in the range of ~ 80 - 140 μm (21). It is evident that the average particle size of the Al_2O_3 -MWCNT powder mixture becomes lower with increase in the volume fraction of MWCNTs in Al_2O_3 mixture. This confirms the uniform particle size distribution in all the powder mixtures.

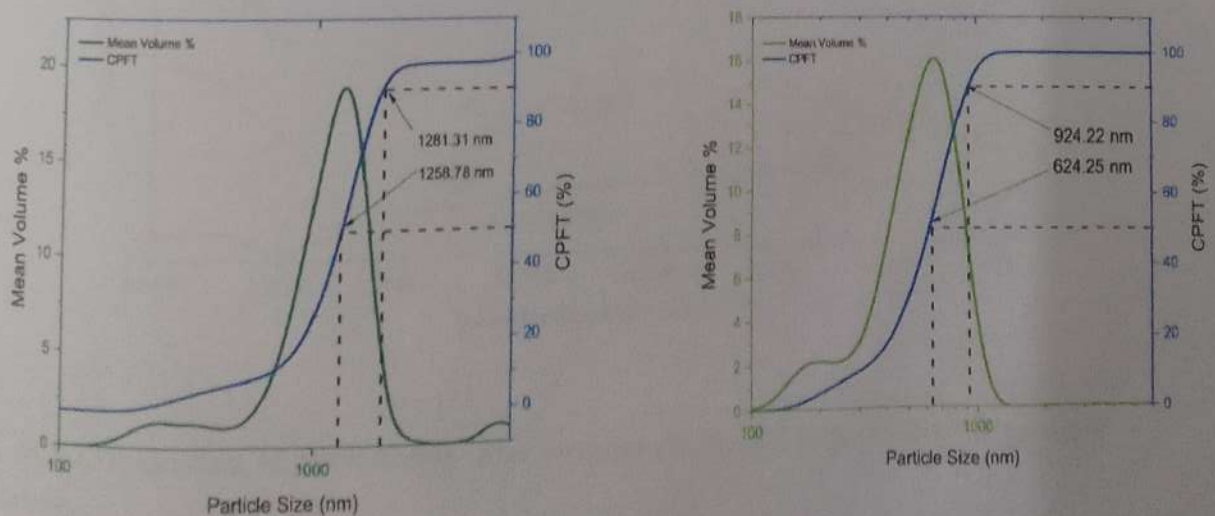


Fig. 9 particle size distribution of (a) pure Al_2O_3 (b) Al_2O_3 -0.75 wt% MWCNT powder mixtures

5.5 Fourier Transform Infrared Spectroscopy

The FTIR spectra provide the characteristic evidence of the structural variability by clearly illustrating the nature of evolved bond formation characteristics. In all the samples water is observed a broad band of the O-H stretching vibrations at $3800\text{--}3400\text{ cm}^{-1}$, which is mainly originated from the hydrogen bonds exhibited at the surface of the dispersed particles. The formation of a peak near $1640\text{--}1660\text{ cm}^{-1}$ (deformation vibration of O-H) is assigned to the several physisorbed layers of loosely interacting water film, whereas, the weak band appearing at about $3100\text{--}2800\text{ cm}^{-1}$ may arise from the symmetric stretching of interlayer -OH groups. A band at 1385 cm^{-1} in the IR spectrum of all the sample is due to stretching vibrations of $\text{-NO}_3\text{-}$ group. At $1550\text{--}1510$ very weak band can be attributed to HCO_3^- and CO_3^- . In addition to the above, the characteristic peaks of boehmite, for e.g., 474 , 621 , and 744 cm^{-1} , which has been prominently observed. Boehmite is mainly composed of octahedral AlO_6 structures with a small amount of AlO_4 in the surface layers and amorphous fragments. The presence of both tetrahedral AlO_4 and octahedral AlO_6 structures in aluminas results in broadening of the Al-O stretching and deformation vibration bands. The broad bands at $1100\text{--}650\text{ cm}^{-1}$ and $650\text{--}300\text{ cm}^{-1}$ can be roughly assigned to tetrahedral and octahedral structures in aluminas.

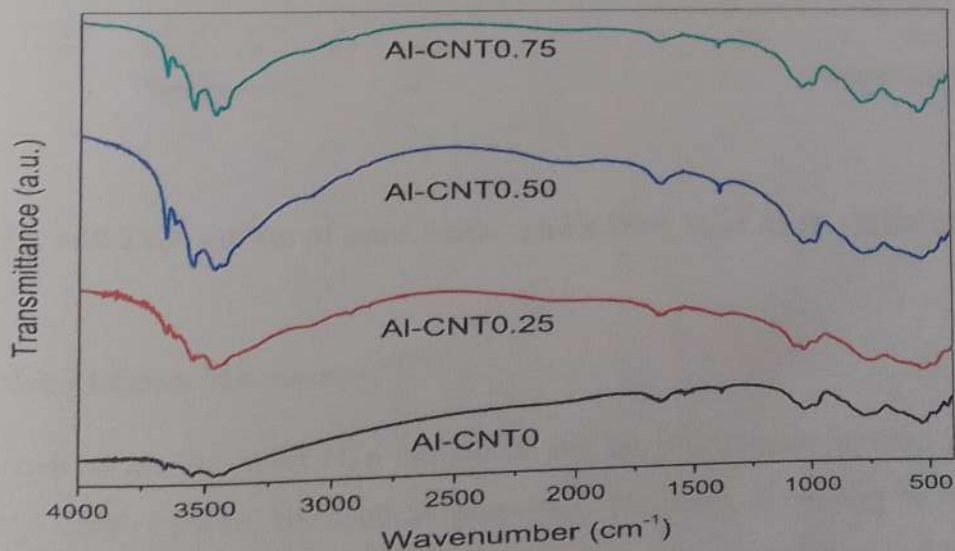


Fig. 10 FTIR spectra of pure Al_2O_3 and various wt.% of Al_2O_3 -MWCNT powder mixtures

DTA and TGA

Thermal analysis (DTA and TGA) can be considered as an effective tool because of its ability to determine the thermal stability and thermal characteristics also the optimal temperature of the treatment or calcination can be specified. Fig. 4 represents the DTA and TGA curves for Al_2O_3 /MWCNTs composite. The DTA and TGA curve shows an endothermic peak at around 250°C , which is accompanied by a small weight loss approx. 21% primarily due to the removal of water. The endothermic peak has disappeared as shown in fig11. The amount of Al_2O_3 nanoparticles on the surface of MWCNTs was estimated from 0.75 wt.% of Al-CNT curve to a small weight loss.

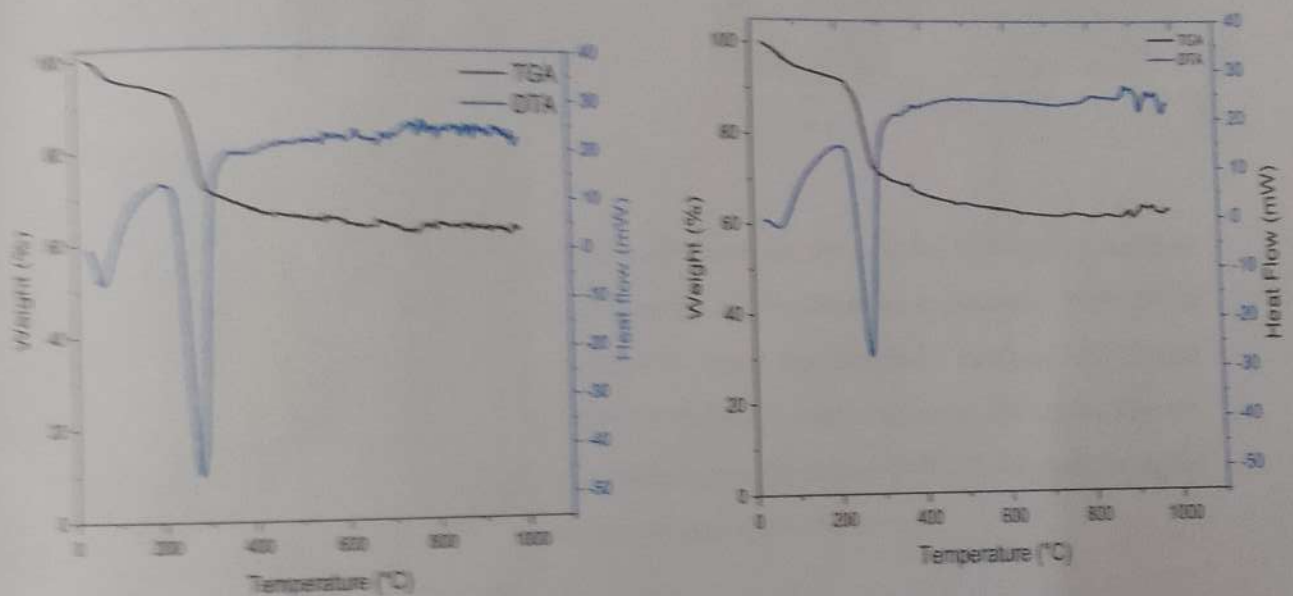


Fig-11 DTA and TGA curves of pure Al_2O_3 and 0.75wt.% of Al_2O_3 -MWCNT powder mixture

5.7 Scanning Electron Microscope

The nano defects on the MWCNTs introduced via the precipitation process might reduce significantly their intrinsic mechanical properties. However, according to the SEM observations, no apparent breakage of MWCNTs was noted in general, except for special cases as illustrated in figure 5(b). We infer that the improvement of the strength and toughness may be due to the crack-bridging effect with the enhanced frictional resistance between acid-treated MWCNTs and the alumina matrix through mechanical interlocks.

**DESIGN OF E-DOCUMENT
VALIDATION TECHNIQUE WITH
MULTI-PHASE AUTHENTICATION
AND DATA SECURITY CONCEPTS**

B.Tech. Project Report

By

APURBA PATRA

KRISHNENDU DASPRADHAN

RASHMI TIRKEY

SUMIT PAUL

Under Supervision of

Dr. SOUMIT CHOWDHURY



**Department of Computer Science & Engineering
Government College of Engineering and
Ceramic Technology**

Kolkata - 700010

May 2022



Government College of Engineering and Ceramic Technology

73, A. C. Banerjee Lane, Kolkata, West Bengal 700010

BONAFIDE CERTIFICATE

Certified that this project report titled **DESIGN OF E-DOCUMENT VALIDATION TECHNIQUE WITH MULTI-PHASE AUTHENTICATION AND DATA SECURITY CONCEPTS** is the authentic work carried out by **APURBA PATRA (GCECTB-L19-3001), KRISHNENDU DASPRADHAN (GCECTB-L19-3003), RASHMI TIRKEY (GCECTB-L19-3006), SUMIT PAUL (GCECTB-L19-3010)** who carried out the project work under my / our supervision. Certified further, that to the best of my knowledge the work reported herein does not form part of any other project report or dissertation on the basis of which a degree or award was conferred on an earlier occasion on this or any other candidate.

S. G. 11/05/22

Dr. Soumit Chowdhury
SUPERVISOR

Assistant Professor

Department of Computer Science and Engineering

Government College of Engineering and Ceramic Technology

Kolkata-700010

K. Saha 11.05.2022

Dr. K. Saha Roy

HEAD OF THE DEPARTMENT

Assistant Professor & Head of Department

Department of Computer Science and Engineering

Government College of Engineering and Ceramic Technology

Kolkata-700010

Maithi Mondal
11/5/2022

External Examiner

DECLARATION

We hereby declare that the project entitled "DESIGN OF E-DOCUMENT VALIDATION TECHNIQUE WITH MULTI-PHASE AUTHENTICATION AND DATA SECURITY CONCEPTS " submitted for the B. Tech. (CSE) degree is our original work and the project has not formed the basis for the award of any other degree, diploma, fellowship or any other similar titles.

Name and Roll No. of the Students

Signature of the Students

1. Apurba Patra (GCECTB-L19-3001)

Apurba Patra

2. Krishnendu Daspradhan (GCECTB-L19-3003)

Krishnendu Daspradhan

3. Rashmi Tirkey (GCECTB-L19-3006)

Rashmi Tirkey

4. Sumit Paul (GCECTB-L19-3010)

Sumit Paul.

Place: Kolkata

Date: 06/05/2022

DESIGN OF E-DOCUMENT VALIDATION TECHNIQUE WITH MULTI-PHASE AUTHENTICATION AND DATA SECURITY CONCEPTS

B.Tech. Project Report

By

APURBA PATRA

KRISHNENDU DASPRADHAN

RASHMI TIRKEY

SUMIT PAUL

Under Supervision of

Dr. SOUMIT CHOWDHURY



**Department of Computer Science & Engineering
Government College of Engineering and
Ceramic Technology**

Kolkata - 700010

May 2022

**DESIGN OF E-DOCUMENT VALIDATION
TECHNIQUE WITH MULTI-PHASE
AUTHENTICATION AND DATA SECURITY
CONCEPTS**

A Project Report

*Submitted in partial fulfilment of the
requirements of the award of the degree*

of

Bachelor of Technology

In

Computer Science and Engineering

By

APURBA PATRA (GCECTB-L19-3001)

KRISHNENDU DASPRADHAN (GCECTB-L19-3003)

RASHMI TIRKEY (GCECTB-L19-3006)

SUMIT PAUL (GCECTB-L19-3010)



**Department of Computer Science and Engineering
Government College of Engineering and
Ceramic Technology**

Kolkata - 700010

May 2022

DECLARATION

We hereby declare that the project entitled “**DESIGN OF E-DOCUMENT VALIDATION TECHNIQUE WITH MULTI-PHASE AUTHENTICATION AND DATA SECURITY CONCEPTS** ” submitted for the B. Tech. (CSE) degree is our original work and the project has not formed the basis for the award of any other degree, diploma, fellowship or any other similar titles.

Name and Roll No. of the Students

Signature of the Students

1. Apurba Patra (GCECTB-L19-3001)
2. Krishnendu Daspradhan (GCECTB-L19-3003)
3. Rashmi Tirkey (GCECTB-L19-3006)
4. Sumit Paul (GCECTB-L19-3010)

Place: Kolkata

Date: 06/05/2022



Government College of Engineering and Ceramic Technology

73, A. C. Banerjee Lane, Kolkata, West Bengal 700010

.....

BONAFIDE CERTIFICATE

Certified that this project report titled **DESIGN OF E-DOCUMENT VALIDATION TECHNIQUE WITH MULTI-PHASE AUTHENTICATION AND DATA SECURITY CONCEPTS** is the authentic work carried out by **APURBA PATRA (GCECTB-L19-3001), KRISHNENDU DASPRADHAN (GCECTB-L19-3003), RASHMI TIRKEY (GCECTB-L19-3006), SUMIT PAUL (GCECTB-L19-3010)** who carried out the project work under **my / our** supervision. Certified further, that to the best of my knowledge the work reported herein does not form part of any other project report or dissertation on the basis of which a degree or award was conferred on an earlier occasion on this or any other candidate.

.....

Dr. Soumit Chowdhury

SUPERVISOR

Assistant Professor

Department of Computer Science and Engineering

Government College of Engineering and Ceramic Technology

Kolkata-700010

.....

Dr. K. Saha Roy

HEAD OF THE DEPARTMENT

Assistant Professor & Head of Department

Department of Computer Science and Engineering

Government College of Engineering and Ceramic Technology

Kolkata-700010

.....
External Examiner

ACKNOWLEDGEMENT

Through this acknowledgement, we express our sincere gratitude to all those people who have been associated with this Project and have helped with it and made it a worthwhile experience. On this great occasion of accomplishment of our project on E-Document validation for health care application. We would also like to expand our deepest gratitude to all those who have directly and indirectly guided us in this project.

Foremost, we would like to express our sincere gratitude to our guide, Professor **Dr. Soumit Choudhury**, for his encouragement, patience, guidance, insightful comments, helpful information, practical advice, endless ideas, support and understanding that have always helped us to accomplish this project. His immense knowledge, in-depth experience and professional expertise has enabled us to complete this project successfully. His suggestions were invaluable, which enabled us to overcome the difficulties we encountered during the project.

We would also be thankful to H.O.D.(CSE) Mrs **Dr. Kalpana Saha(Roy)** and our principal Mr/Mrs Prof. Krishnendu Chakrabarty of Govt. College of Engineering & Ceramic Technology for providing all the required facilities in completion of this project. We are also grateful to our college for giving us the opportunity to work with them and providing us the necessary resources for the project.

Finally, as one of the team members, I would like to appreciate all my group members for their support and coordination, I hope we will achieve more in our future endeavours.

Thanks for all your encouragement!

With Gratitude,

Apurba Patra (GCECTB-L19-3001)

Krishnendu Daspradhan (GCECTB-L19-3003)

Rashmi Tirkey (GCECTB-L19-3006)

Sumit Paul (GCECTB-L19-3010)

ABSTRACT

This propose concept is mainly focus on developing a robust data security protocol for digital validation of medical e-document from the issuing hospital, insurance office and the incumbent. The idea here is to address all data security issues like authentication, confidentiality, integrity and non-repudiation while exchanging critical data between client and server. In this protocol, medical report image is logically divided into four non overlapping regions and each region is further divided into four non overlapping segments. The protocol initiated with fabrication of four signatures on each region of the medical e-document. Here three out of four signatures used for issuing hospital ownership while fourth one used for incumbent authenticity. Each signature is fabricated on each segment based on two hash values derived from self-design hash operation on some important data on e-document. For authentication of hospital, two share images are generated from hospital logo and one share is embedded into the medical report and other share along with original logo made available in public domain. The receiving authority can validate the report by merging the hidden share with the public share and match it with the original hospital logo. For incumbent authentication, fingerprint of the incumbent is embedded in the medical report. The receiving authority can verify the identity of the incumbent by extracting the fingerprint and matching it with fingerprint stored in their server. Validation of the medical report can only be done by issuing hospital. Issuing hospital validate the medical report in two levels. In the first level report data is collected through optical character recognize technology (OCR) and then those data are matched with the data stored in hospital server. In the second level of validation, right hand fingerprint and left hand fingerprint are extracted from medical report and matched with the stored one. If the all the data matches then hospital server conforms the total validation of the medical report. Overall, this propose idea promotes significant improvement over the existing concepts in terms of both security features and data hiding solutions related to the online validation of sensitive e-documents.

TABLE OF CONTENTS

CHAPTER NO.	TITLE	PAGE
	ABSTRACT	vi
	LIST OF FIGURES	viii
	LIST OF EQUATIONS	ix
1.	INTRODUCTION	1
	1.1 Background of Study	1
2.	LITERATURE REVIEW	3
3.	ENHANCEMENT ADDRESS IN PROPOSED WORK	7
4.	PROPOSED E-DOCUMENT AUTHENTICATION PROTOCOL	8
5.	ALGORITHMS	19
	5.1 Bit Insertion Algorithm	20
	5.2 Bit Detection Algorithm	26
	5.3 Signature Share Generation Algorithm	31
6.	OCR IMPLEMENTAION CONCEPTS	33
7.	EXPERIMENTAL RESULTS & DISCUSSION	39
8.	CONCLUSION & FUTURE WORK	46
	REFERENCES	47

LIST OF FIGURES

FIG. NO.	FIGURE DESCRIPTION	PAGE
1	Signature fabrication at hospital server-side	9
2	Signature fabrication at client-side	10
3	Client authentication at hospital server-side	11
4	Signature fabrication at hospital-side and client-side	12
5	Authentication of e-document at client-side	13
6	Signature fabrication at client-side	14
7	Client authentication at insurance server-side	15
8	Authentication of e-document at insurance server-side	16
9	Level 1 authentication of e-document at hospital server-side	17
10	Level 2 authentication of e-document at hospital server-side	18
11	Bit fabrication in host image	20
12	Output of OCR Program	38
13	Comparison between original signature and extracted signatures	41
14	Comparison between original hospital logo and merged logo	42
15	Comparison between left hand fingerprint and extracted right hand fingerprint	42
16	Comparison between right hand fingerprint and extracted left hand fingerprint	42
17	Comparison between someone else fingerprint and extracted right hand fingerprint	43
18	Original cover image and Signature fabricated image	44
19	PSNR, MSE, SSIM, NCC values of signature fabricated image	44
20	Histogram comparison between original and signature fabricated image	45

EQN NO.	EQUATION DESCRIPTION	PAGE
1-10	Hashing Equation	10 - 14
11-13	Matrix Operation Equation	21 - 22
14-19	Share Equation	31 - 32

CHAPTER 1

INTRODUCTION

1.1 Background of Study:

With the rapid growth of internet and multimedia technology in recent years, digital documents such as image, videos and audios, etc. can easily be copied, tampered, altered and distributed over internet without loss of quality. Therefore, the protection of ownership of digital documents has becoming very important issue. In the modern era of digital data transmission, authentication and copyright protection of digital documents can be achieve through digital watermarking. The idea behind digital watermarking technique is to embed secret copyright information such as text or image, called watermark, into the content of the digital document and embedding have to be done in such way that it can be extracted later. In the existing concepts, copyright signatures are fabricated on the digital documents to establish the ownership claims and address major data security issues like authentication, confidentiality, integrity, non-repudiation, etc. Existing concepts give more emphasize on the ownership accepts through various signature fabrication procedures while it is also important to secure and validate the content of the digital documents from intentional or unintentional forgery.

However, in modern era, digital document validation is a bigger issue where the authenticity of the whole document is also important. This purpose concept on the other hand not only provide ownership protection but also validate content of the e-document. To incorporate such critical data security issues, this purposed concept provides a strong data security protocol for online validation of digital e-documents. This protocol is developed for online authentication of medical report, concerned hospital and the owner of the report. Following are the key features of this protocol.

- (1) Certify the ownership of the incumbent and issuing hospital by fabrication of incumbent's fingerprint and copyright signature of hospital on the report based on hash values derived from important data from the report.

- (2) Multi-level validation of sensitive data of the medical report through the optical character recognizing technique and hash based secret signature fabrication.
- (3) Generation private and public share of copyright signatures of the issuing hospital and fabrication of private share on the medical report.
- (4) Addressing data security issues like authentication, confidentiality, integrity and non-repudiations.

CHAPTER 2

LITERATURE REVIEW

In this section we provide a brief literature review on recent water making technique and e-document validation schemes with focus on integrity and authentication of medical documents.

Among the recent approaches in the field of e-document authentications, the idea of biometric watermarking was implemented by Anitha et al [1], in order to verify the relation between the owner and the corresponding details that appears on the document. Regarding this, the Biometric details which is basically the iris image of the user is captured and converted to a live template in order to obtain a bit code image. This bit code image is then periodically duplicated to be of same size of the cover image. Thereafter, both of these images are partitioned into blocks having equal size. After performing an XOR operation of the bit code image blocks, the watermark bits are obtained. The LSBs of the cover image blocks are encoded by a hash value for each block from a set of inputs interconnected to the image particulars. This model can be used to detect largescale tampering of the document but the drawback is that when it comes to distinguish the sensitive tampering from the external noise attacks, it fails, because for noise and small-scale tampering it is not validated.

Another approach in this context, introduced by Kamta et al [2], incorporates a method which use the biometric details of the owner including facial characters, retinal scan, palatal patterns, fingerprints to verify the legitimacy of the document's owner and DNA to be inserted in a smart card which is provided to the owner for identification purpose. Sixteen possible categories are therefore created based on the biometric details of the owner. Each of these sixteen possible categories is a string containing 'y' and 'n', a central database is used to store the biometric identifier string corresponding to each user. An NFA with five possible states and having input symbols for each state, is used to match the recalculated string and the recaptured biometric details during the verification process. The authenticity of the owner is verified if the NFA accepts the string. However, the drawback of this scheme is that it fails to determine the impact of external noise incorporated in the smart card, also it is not focused on how biometric data can be used for template generation.

Among the very recent approaches on e-document authentications, Hasan et al [3] implemented the idea of segmented multi watermarking which divides the cover image into three separate regions of variable intensity namely R, G, B components in order to enhance the security and for better robustness of digital documents. The components namely R, G, B are therefore embedded into the components of the watermark image namely RW, GW, BW by converting the R, G, B components of the cover image into transformation domain using DWT. Therefore, LH1, LL2, LL3 these three levels along with the watermarks are inserted into LL3. Afterwards, in order to obtain the watermarked image of the digital document the RRW, GGW, BBW are combined together.

Gull et al [4] divides the medical cover image into 4x4 non overlapping pixel blocks and each pixel blocks are further sub divided into upper and lower half block. Upper half block pixels are used for fabricate data to ensure temper detection and lower half block pixels contains the watermark information. Arithmetic mean of each block is computed and XORed with the watermark pixels and converts into bits. Converted bits are then embedded with lower half block pixels and arithmetic mean bits are embedded with the upper half block pixels to get the watermark fabricate image.

Swaraja et al [5] purposed a region based medical image watermarking by exploiting visual and edge entropy of the image. Watermark image is compressed by LZW lossless compression technique and concealed into region of non-interest blocks. These blocks are chosen using by the human visual system.

Hanan et al [6] also purposed region based watermarking technique where ROI is compressed and combined with signature. Generated watermark inserted into the RONI of the host image.

Lee et al [7] purposed an adaptive reversible medical image watermarking algorithm. To minimize the quality degradation of the medical image, image is segmented into object and background regions and then watermark is embedded into each region. To minimize quality degradation in object region, low embedding level is set for the object regions and high embedding level is set for the background region

In the view of achieving multipurpose authentication, the multi-signature fabrication accept can be considered for claiming ownership of the e-document. In multi-signature fabrication multiple copy of signature can also be embedded. These multi signature-

based fabrication also known as multi-watermarking and provides much more secure robust authentication. So, this e-document validation and authentication concept is implemented using the segmented type multi-watermarking. Some segmented multi-watermarking ideas are as follows.

Behnia et al [8] proposed a secure watermarking scheme based on the pair-coupled map and showed a map-based technique to hide different binary watermarks into the Red, Green, Blue frames.

Rohit et al [9] purposed multi-level watermarking where multi-purposed DWT is applied on the host fingerprint image and high recurrence values are used for watermarking. One level DWT is used on face and iris image. Data is obtained from DWT values. This data is played the role of a secure watermark, is placed on the host fingerprint for iris and face watermark pictures.

Mohananthini et al [10] developed a multi-watermarking method based on discrete wavelet transmute. The watermarks are inserted into sub bands using genetic algorithm.

Shi-jinn et al [11] purposed a blind copyright protection for government e-document image through combination of Discrete Cosine Transform and Singular Value Decomposition based on Genetic algorithm. Here DCT is applied to the entire image and mapped by zigzag manner to four areas from lowest to highest frequencies. While SVD is applied in each area and then singular value of DCT transformed host image. Host image is modified in each area with the quantizing value using GA to increase the visual quality and robustness.

Another government e-document watermarking is suggested by Ali Al-Haj [12]. Here e-document is watermarked in frequency domain using second order Discrete Wavelet Transformation and then followed by Singular Value matrix Decomposition. Non-reversible fabrication of the well-defined watermark is carried out on the diagonal elements of the DWT-SVD decomposed document.

Here Nasir et al [13] presented a novel multiple watermarking technique for copyright protection. The binary watermark image is divided into four fragments. Each fragment encrypted using a secret key and fabricated in different regions of blue component of the color cover image using spatial encoding mechanism.

Further, more sophisticated work on multi-watermarking is carried out in the frequency domain for better security and robustness. Among these works, Gaurav et al [14]

fabricated multiple signatures on non-overlapping DCT blocks where threshold value is used for secret data encoding. Here Yaxun et al [15] embedded three binary watermarks on non-overlapping blocks of DCT decomposed original gray scale image to improve the quality of watermarked image.

In these existing approaches, it is noticed that most of the watermarking approaches have focused on robust data hiding. In most of these approaches digital validation is achieved through multi-watermarking rather than developing a secure data security protocol. Hence, by considering these issues, this purposed validation and authentication approach aims to develop a client-server-based authentication protocol to validate e-documents.

CHAPTER 3

ENHANCEMENT ADDRESS IN THE PROPOSED WORK

In contrast to the existing concepts, which are mostly focuses on watermarking approach for authentication of copyright data, this proposed concept addresses all the critical data security issues (Authentication, Confidentiality, Integrity, Non-repudiation) along with multi-watermarking approach for trusted validation of digital documents.

This proposed protocol uses OCR technique along with watermarking approach for trusted content authentication, whereas existing approaches only uses watermarking technique for content authentication.

While, existing approaches mostly adopts specific watermarking technique for authentication, this suggested idea introduces variable watermarking approaches for better robustness and also promotes multi-phase authentication concepts for validation of e-documents from different angles.

CHAPTER 4

PROPOSED E-DOCUMENT AUTHENTICATION PROTOCOL

The e-document authentication process starts with the fabrication of three signature by the authorized hospital server and fabrication of fingerprint by the client. Each signature is fabricated using two hash values, derived from one of six most important data present in e-document i.e. medical report. Hospital server fabricate private share of hospital logo, patient right fingerprint and left fingerprint based on the hash value computed from the test id, test date, customer id, customer name, transaction id and amount on the first, second and third segment of each four regions of the cover image respectively. At the client-side incumbent fabricate his/her left/right fingerprint using the hash value computed from secret key which is previously given by the hospital, on the fourth segment of each four regions of the cover image for his/her authenticity. This fabricated e-document is then uploaded to the insurance server. Insurance server check the validity of the received e-document by extracting and merging the private and public share of the hospital logo and match it with the original hospital logo, store in the insurance database. Insurance server transmit the e-document the authorized hospital server if the merged and original hospital logo matches. At the hospital server-side the received e-document is authenticated in two level. In the first level data in the cover image is extracted through the optical character recognizer program and match with the data store in hospital database. In the second level right hand fingerprint and left hand fingerprint is extracted from the two hash values computed from customer id and transaction id, which are extracted from cover image in first level. The stepwise explanation of the protocol is as follows-

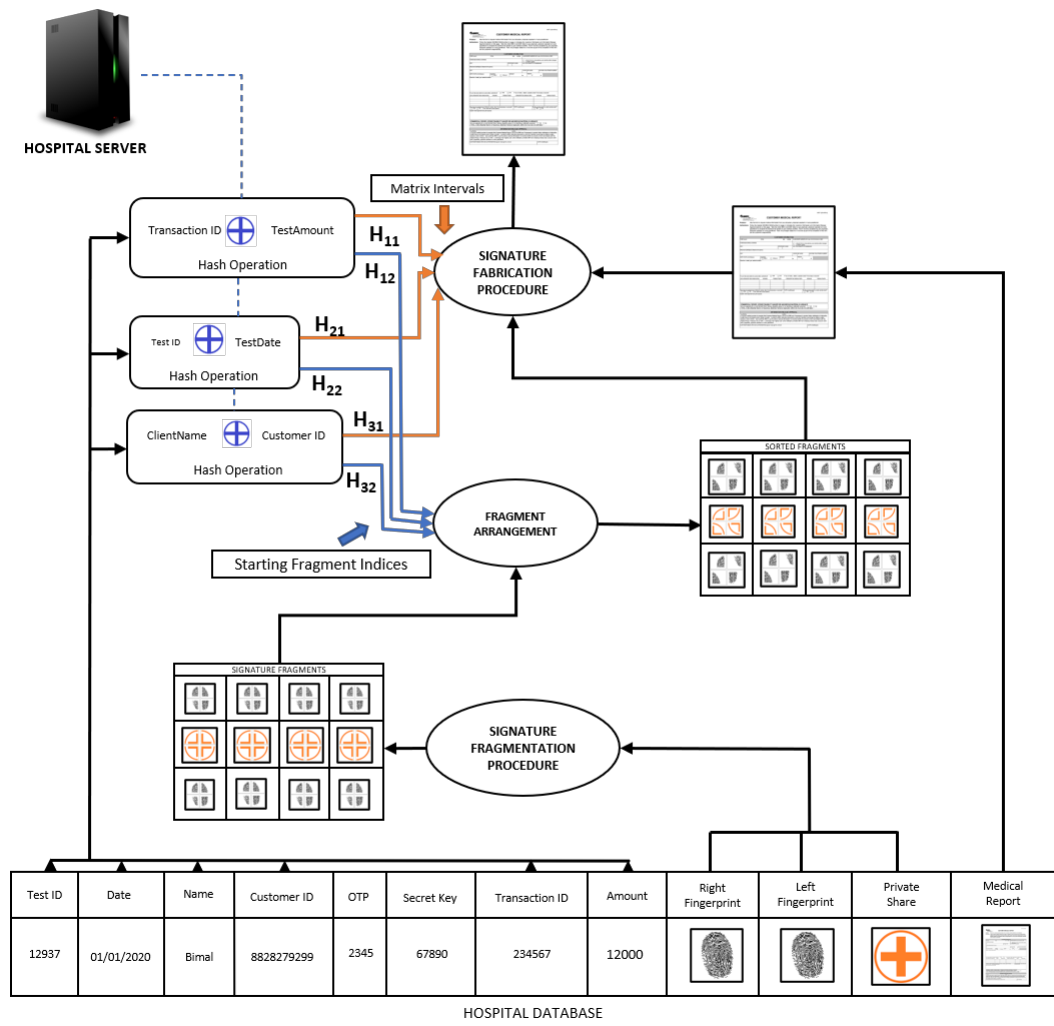


Figure 1: Signature fabrication at hospital server-side

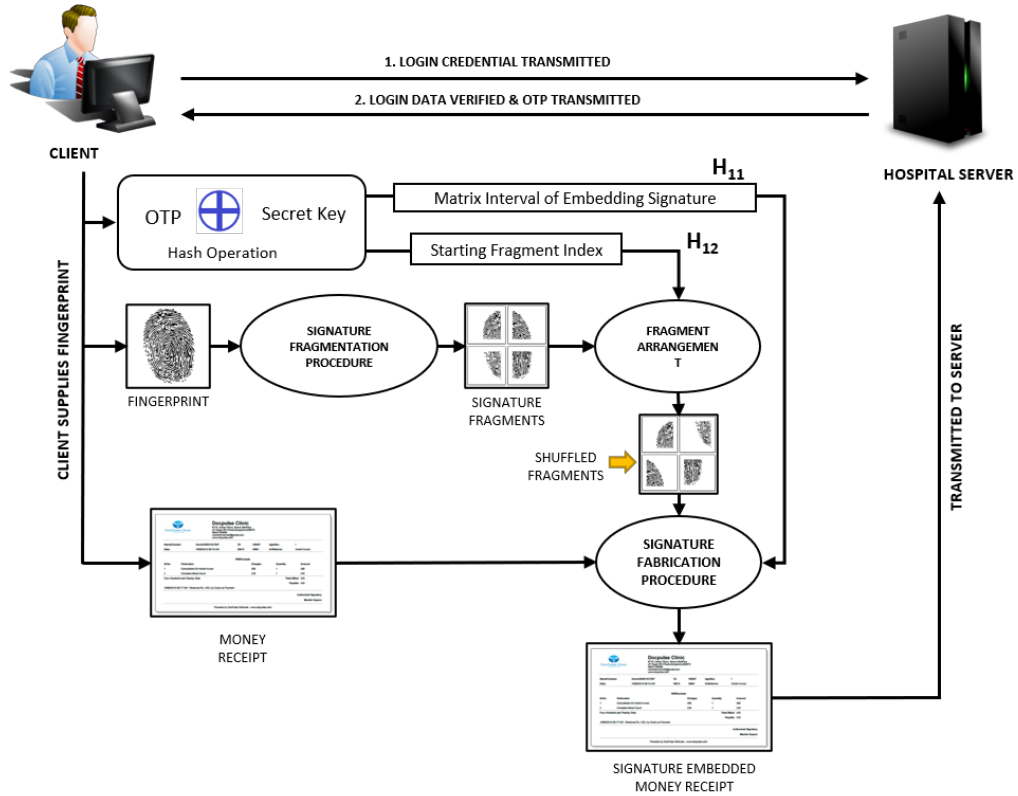


Figure 2: Signature fabrication at client-side

Step 1: User login to the hospital server account by sending username/password.

Step 2: Hospital server recognize the user after verifying those transmitted login credential and sends an One Time Pin (OTP) to the user.

Step 3: User fabricate his/her on spot fingerprint in the digital copy of money receipt using two hash values (H_{11} , H_{12}) computed from the received OTP and the secret key which user received at the first visit of hospital for his/her authenticity. These two hash values (H_{11} , H_{12}) determine the starting fragment index for the circular orientation of the signature fragment and the matrix interval. The fabricated money receipt is then sent to the hospital server.

$$H_{11} = \{(\text{Secret Key} + \text{OTP}) + \text{sum of digits}(\text{Secret Key}) + \text{sum of digit}(\text{OTP})\} \text{ Mod } 4 \quad (1)$$

$$H_{12} = \{\text{Difference}(\text{Secret Key}, \text{OTP}) + (\text{Reverse of Secret Key} + \text{Reverse of OTP}) + \text{sum of digits}(\text{Secret Key}) + \text{sum of digit}(\text{OTP})\} \text{ Mod } 4 \quad (2)$$

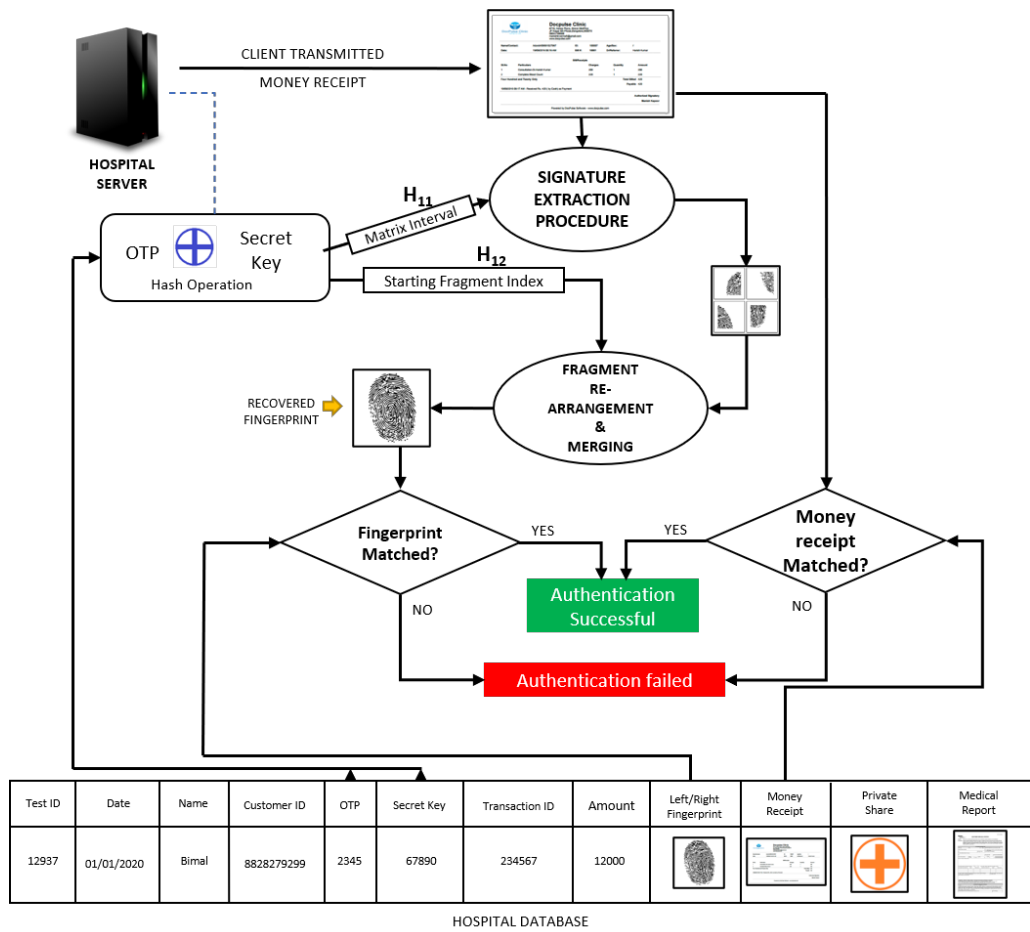


Figure 3: Client authentication at hospital server-side

Step 4: Hospital server verify user identity by extracting the embedded fingerprint and match it with the stored one. If both fingerprint match then hospital server send the e-medical report to the user. Before sending the medical report, three signatures in fabricated in the three segments of each four regions of the medical report. In the segment 1, private share of the hospital logo is fabricated using two hash values (H_{21} , H_{22}) computed from “Test ID” and “Date”. These two hash values (H_{21} , H_{22}) determine the starting fragment index for the circular orientation of the private share fragment and the matrix interval. In segment 2, patient right hand fingerprint is fabricated using two hash values (H_{31} , H_{32}) derived from “Customer ID” and “Name”. These two hash values (H_{31} , H_{32}) determine the starting fragment index for the circular orientation of the fingerprint fragment and the matrix interval. In segment 3, patient left hand fingerprint is fabricated using another two hash values (H_{41} , H_{42}) computed from “Transaction ID”

and “Amount”. These two hash values (H_{41} , H_{42}) determine the starting fragment index for the circular orientation of the money receipt fragment and the matrix interval. After this fabrication process the fabricated medical report is transfer the user.

$$H_{21} = \{(Test\ ID + Date) + \text{sum of digits}(Test\ ID) + \text{sum of digit}(Date)\} \text{ Mod } 4 \quad (3)$$

$$H_{22} = \{\text{Difference}(Test\ ID, Date) + (\text{Reverse of Test ID} + \text{Reverse of Date}) + \text{sum of digits}(Test\ ID) + \text{sum of digit}(Date)\} \text{ Mod } 4 \quad (4)$$

$$H_{31} = \{(Aadhaar\ No + Name) + \text{sum of digits}(customer\ id) + \text{sum of digit}(Name)\} \text{ Mod } 4 \quad (5)$$

$$H_{32} = \{\text{Difference}(customer\ id, Name) + (\text{Reverse of Aadhaar No} + \text{Reverse of Name}) + \text{sum of digits}(Aadhaar\ No) + \text{sum of digit}(Name)\} \text{ Mod } 4 \quad (6)$$

$$H_{41} = \{(Transaction\ ID + Amount) + \text{sum of digits}(Transaction\ ID) + \text{sum of digit}(Amount)\} \text{ Mod } 4 \quad (7)$$

$$H_{42} = \{\text{Difference}(Transaction\ ID, Amount) + (\text{Reverse of Transaction ID} + \text{Reverse of Amount}) + \text{sum of digits}(Transaction\ ID) + \text{sum of digit}(Amount)\} \text{ Mod } 4 \quad (8)$$

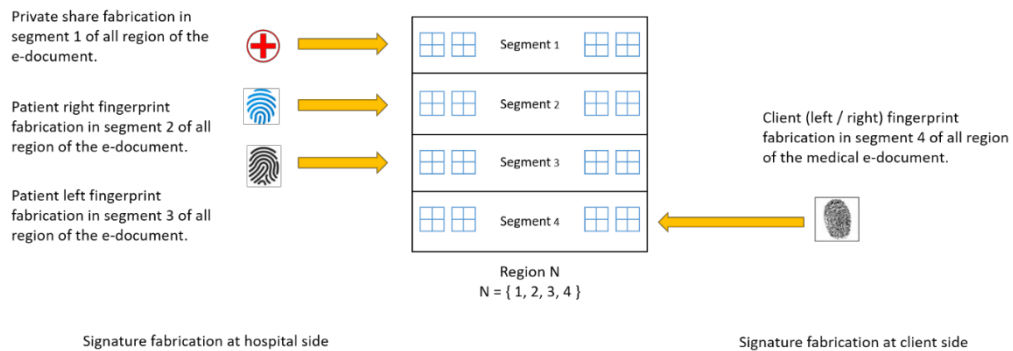


Figure 4: Signature fabrication at hospital-side and client-side

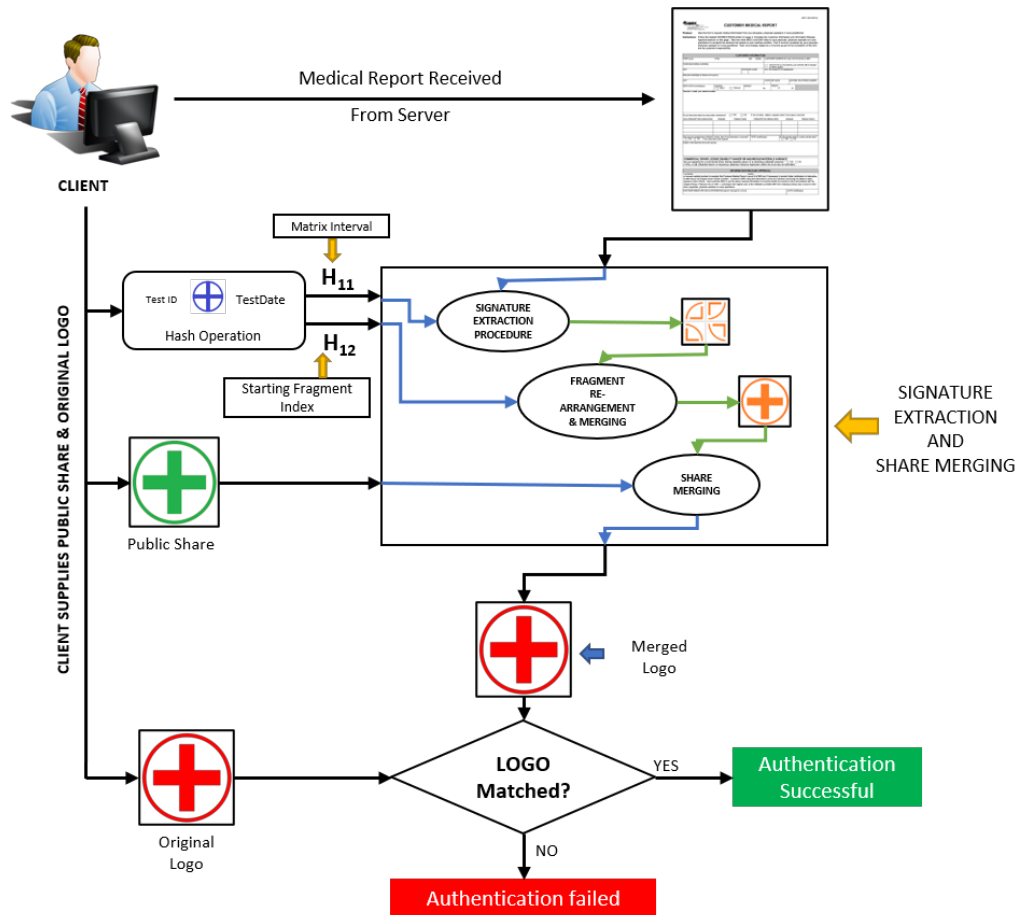


Figure 5: Authentication of e-document at client-side

Step 5: User authenticate the received medical report by extracting and merging the private and public share of the hospital logo and matches it with the original hospital logo, which is available in public domain. By matching the merged logo with original logo, user can conclude whether the medical report is coming from a trusted source or not.

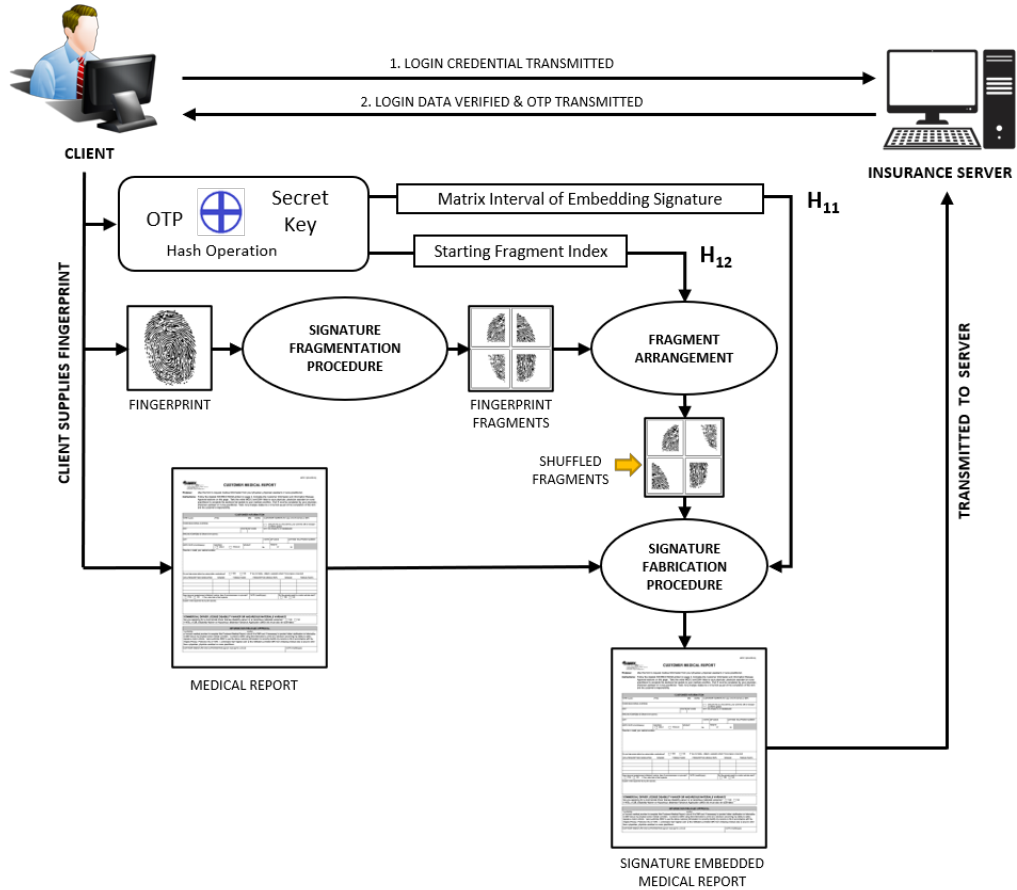


Figure 6: Signature fabrication at client-side

Step 6: User login to the insurance server account by submitting the username/password.

Step 7: Insurance server recognize the user after verifying the received login credential and sends a One Time Pin (OTP).

Step 8: User fabricate his/her on spot fingerprint on the fourth segment of all regions of the medical report using two hash values (H_{51} , H_{52}) derived from received OTP and the secret key, received at first visit of the insurance office, for his/her authenticity. One hash value will determine the starting fragment index and another will determine the interval between two matrices. Fabricated medical report is sent to the insurance server.

$$H_{51} = \{(Secret\ Key + OTP) + sum\ of\ digits(Secret\ Key) + sum\ of\ digit(OTP)\} \text{ Mod } 4 \quad (9)$$

$$H_{52} = \{Difference(Secret\ Key, OTP) + (Reverse\ of\ Secret\ Key + Reverse\ of\ OTP) + sum\ of\ digits(Secret\ Key) + sum\ of\ digit(OTP)\} \text{ Mod } 4 \quad (10)$$

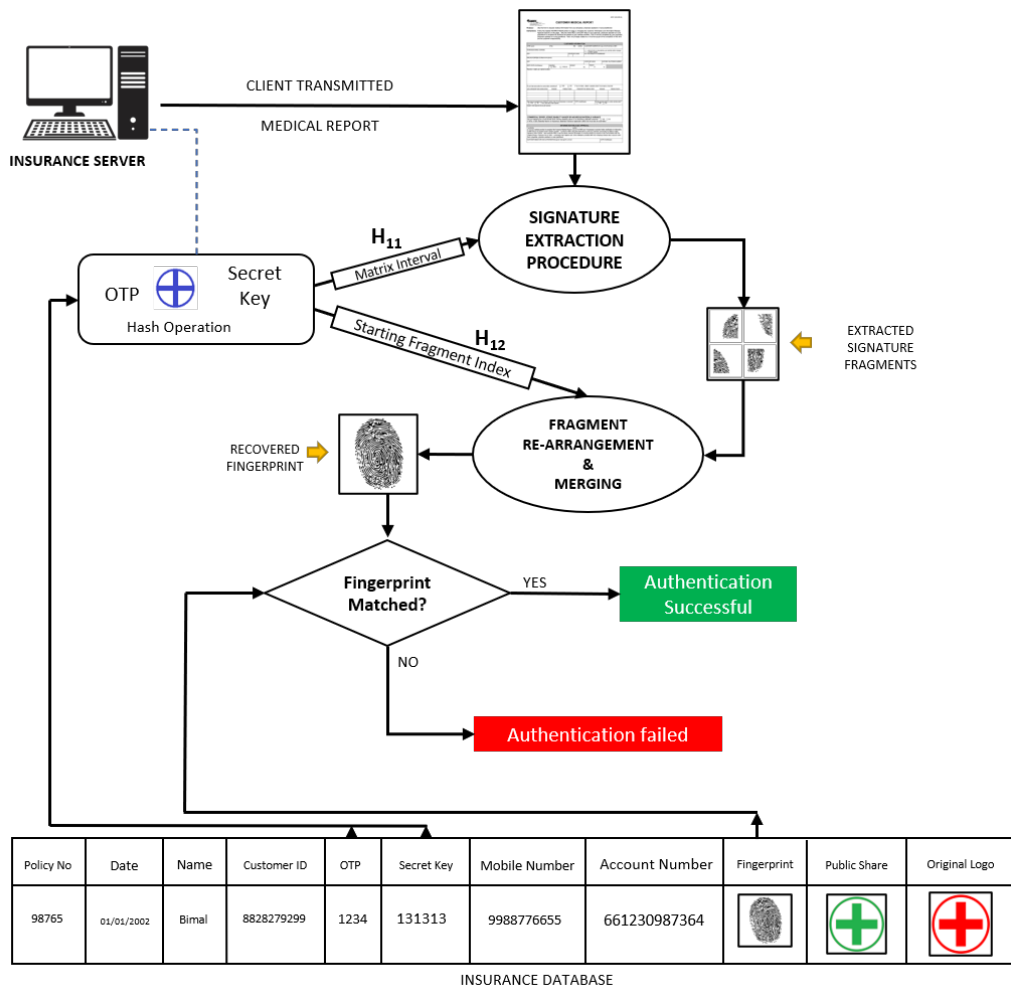


Figure 7: Client authentication at insurance server-side

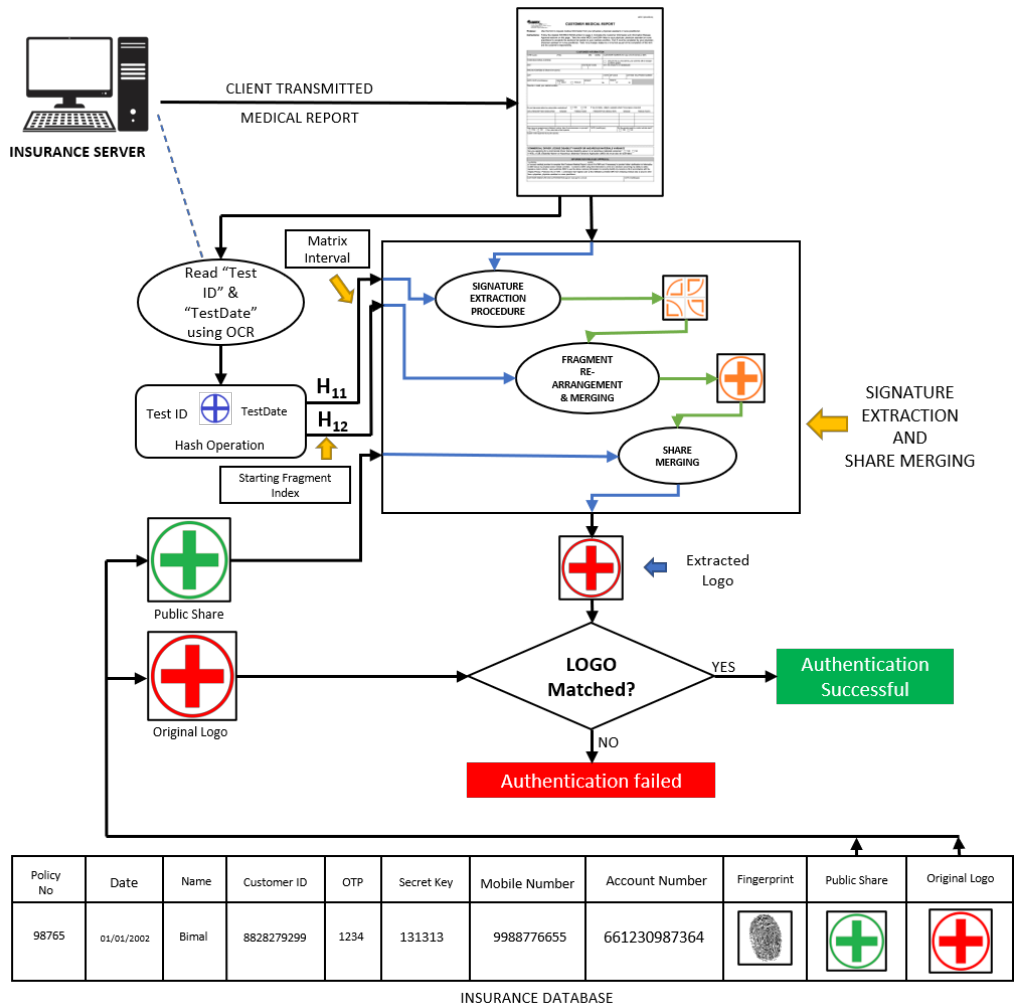


Figure 8: Authentication of e-document at insurance server-side

Step 9: After receiving the medical report, insurance server authenticates two things: (i) authenticity of the user, (ii) authenticity of the medical report. For authenticating the user, insurance server simply extracts the fingerprint from fourth segment of the medical report and matches it with fingerprint store in their database. And for the authentication of medical report, insurance server extract and merge the private and public share of the hospital logo from the first segment of the medical report. Merged logo and original hospital logo are then match with each other. Public share and original hospital logo are available in public domain. If two logos matches, then insurance server send the medical report to the concern hospital server for further verification.

Step 10: After receiving the medical report hospital server authenticate it in two levels. In the first level, hospital server simply read the medical report using optical character recognizer (OCR) and extract its data and then match those data with the data stored in database. If all the data matched then it starts the second level authentication. In second level authentication, server computes these hash values using the extracted “Customer id”, “Name”, “Transaction ID”, “Amount”, and recover the 4 copies of right hand fingerprint from segment 2 and 4 copies of left hand fingerprint from segment 3 from all regions. All these recovered signatures are matched with the original signature copy stored in hospital database to track the best detected copy of each signature. If at least one of the signatures of each segment satisfied a predefined threshold value of matching then hospital server conforms the total validation of the medical report.

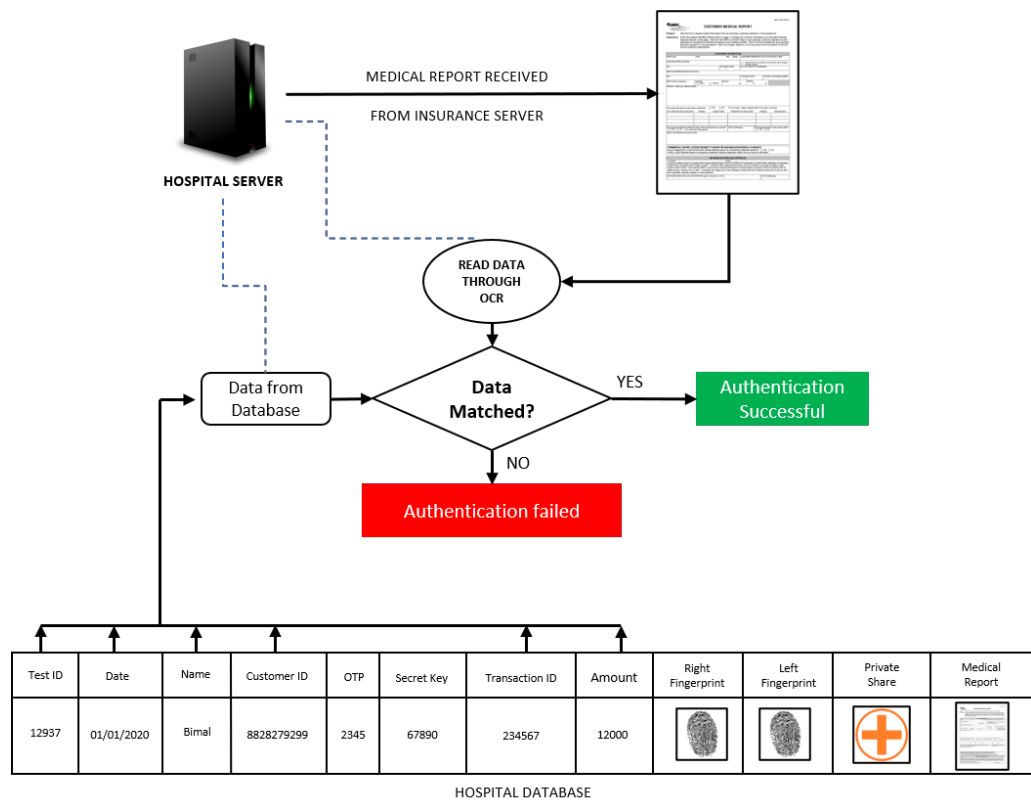


Figure 9: Level 1 authentication of e-document at hospital server-side

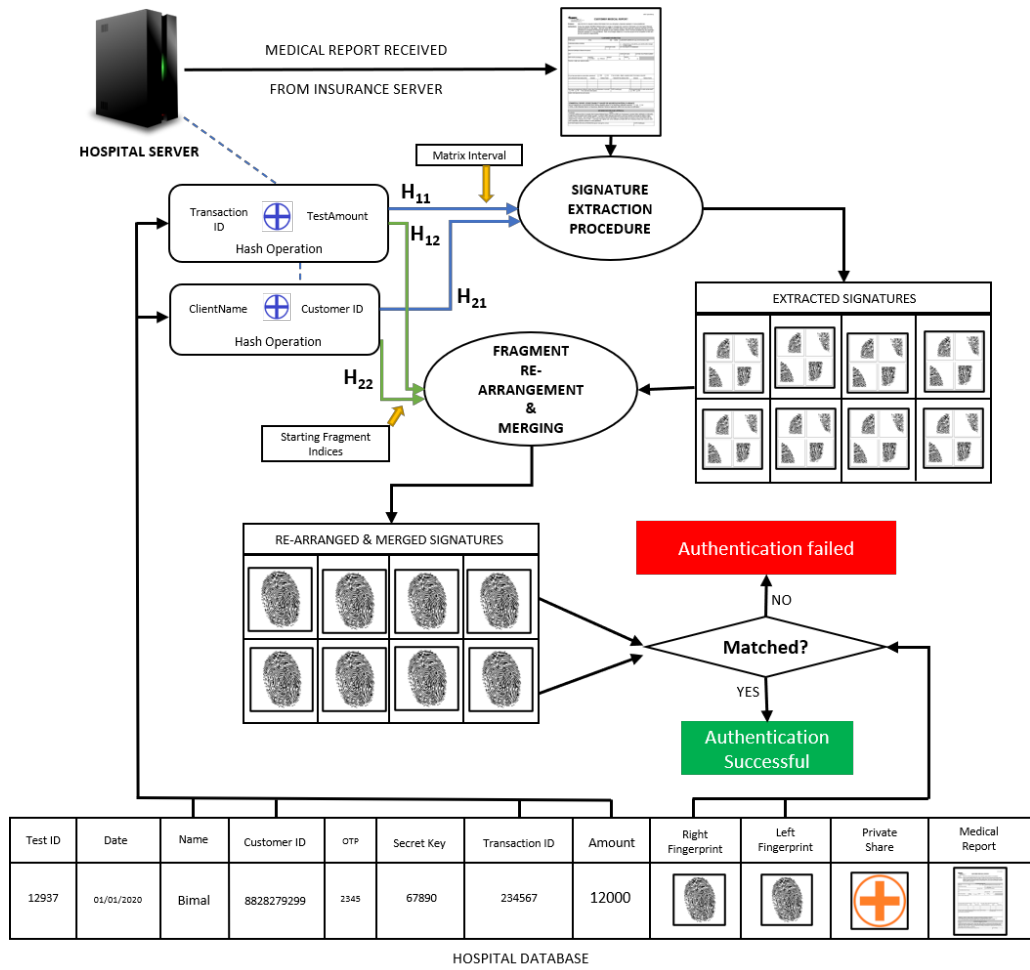


Figure 10: Level 2 authentication of e-document at hospital server-side

CHAPTER 5

ALGORITHMS

Signature bit fabrication and detection

The cover host image is logically divided into four equal regions. Each region is further divided into four equal segments. And each segment is logically filled with consecutive 2x2 pixel byte matrix. Now one single bit is fabricated on each pixel byte of the 2x2 matrix. Signature bits are fabricated in 1st and 3rd segments of 1st and 3rd regions and 1st and 2nd segments of 2nd and 4th regions using Spatial domain digital watermarking technique. And Transform domain digital watermarking technique is used in 2nd and 4th segments of 1st and 3rd regions and 3rd and 4th segments of 2nd and 4th regions of the cover host image. Bit fabrication and detection algorithm is same in both spatial and transform domain technique. In spatial domain technique bit fabrication and detection is done in each elements of the pixel byte matrix. It doesn't need any kind of matrix transformation. But in transform domain technique pixel byte matrix M is transform into M' and signature bits are fabricated in each elements of transform matrix M' which turn it into fabricated transform matrix M'' . Each element in fabricated matrix M'' is then reverse transformed to obtain final signature bit fabricated matrix M''' . This final fabricated matrix M''' is then sent to the receiver. For bit extraction, each elements of pixel byte matrix are forward transformed and hidden bits are then extracted using bit detection algorithm.

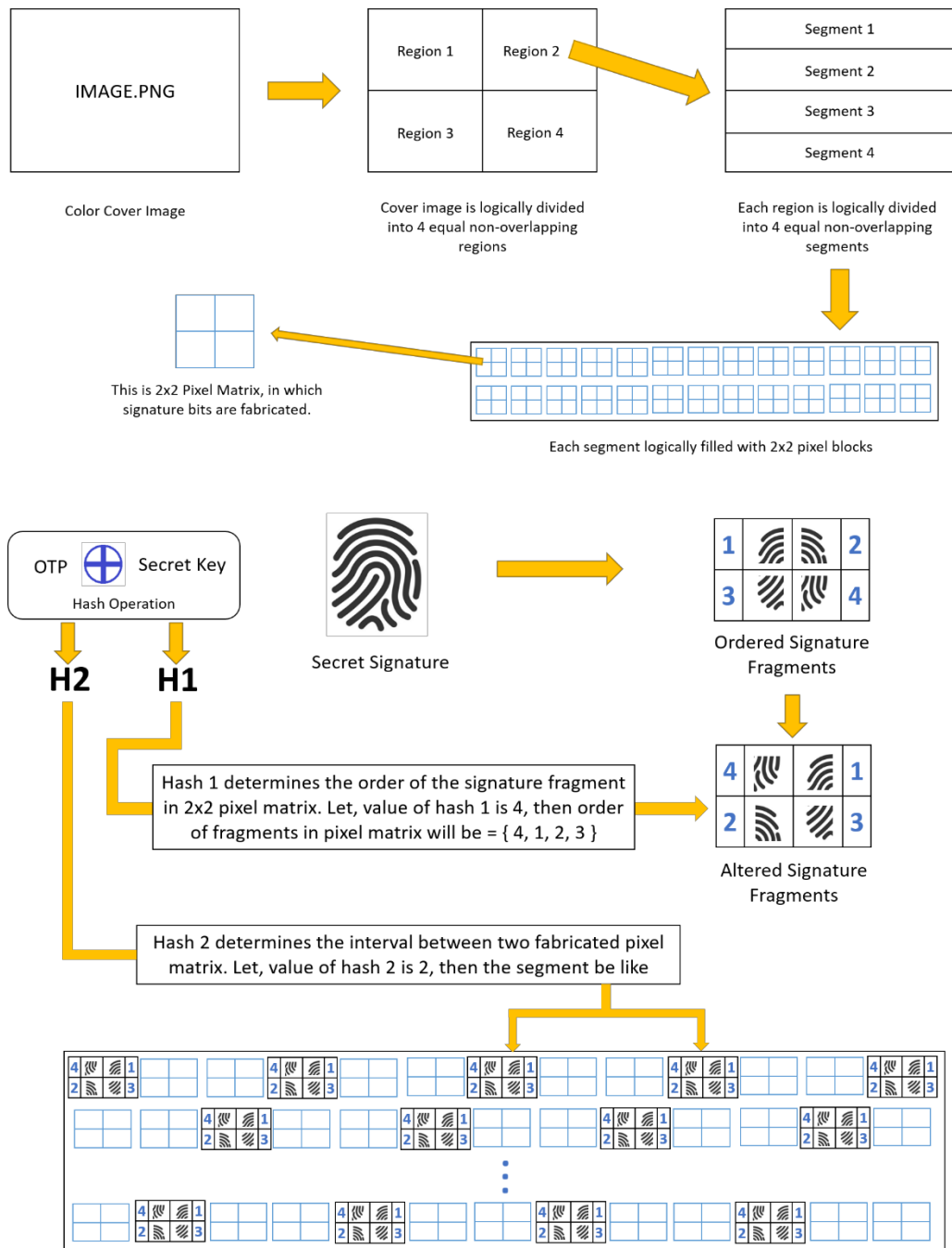


Figure 11: Bit fabrication in host image

5.1 Bit Insertion Algorithm

Let, $M_n = [A_1, A_2, A_3, A_4]$ be a 2x2 pixel byte matrix, where A_1, A_2, A_3, A_4 are its pixel byte values ranges from 0 to 255 and n is positive integer denotes the matrix number. The transformation is performed on each pixel bytes.

In spatial domain watermark technique, signature bits are encoded in each pixel byte of the pixel matrix. In this technique pixel matrix doesn't require any matrix transformation.

$$M_n = \begin{array}{|c|c|} \hline A_1 & A_2 \\ \hline A_3 & A_4 \\ \hline \end{array}$$

$$M_n' = \text{BIT_ENCODE}(M_n', b_1, b_2, b_3, b_4)$$

In transform domain watermarking, Elements of the pixel matrix, are forward transformed, then signature bits are encoded in each transform elements and then reverse transformed to get the final bit encoded pixel matrix.

Matrix Transformation Procedure

Forward Transform:

$$M_n' = \begin{array}{|c|c|} \hline A_1' = A_1 + X & A_2' = A_2 - X \\ \hline A_3' = A_3 + X & A_4' = A_4 - X \\ \hline \end{array} \dots\dots\dots(11)$$

Where,

$$X = \{ \text{Matrix Number} + (\text{Sum of digit of Matrix number}) \} \text{Mod } 4 \dots\dots\dots(12)$$

$$X = \{ n + (\text{sum of digit of } n) \} \text{Mod } 4$$

Here, $M_n' = [A_i']$ is the transformed matrix, where A_i denotes the transformed element at co-responding index $j \in \{ 1, 2, 3, 4 \}$. To encode one signature bit on each transformed element A_i' , bit encoding procedure is applied to the transformed matrix M_n' .

$$M_n'' = \text{BIT_ENCODE}(M_n'', b_1, b_2, b_3, b_4)$$

Then reverse transformation is applied to the bit encoded Matrix M_n'' using matrix operation $(x+1)$ to obtain final bit encoded matrix M_n''' .

Reverse Transform:

$$M_n''' = \begin{array}{|c|c|} \hline A_1''' = A_1'' - X & A_2''' = A_2'' + X \\ \hline A_3''' = A_3'' - X & A_4''' = A_4'' + X \\ \hline \end{array} \dots\dots\dots (13)$$

Pseudocode for the BIT_ENCODE algorithm is as follows-

BIT_ENCODE = function (M_n, b₁, b₂, b₃, b₄)

Start

N = Matrix number of M_n

X = {N + (Sum of digits of N)} Mod 4

If (X = 0 or X = 3) then

L₄ = Multiple of 4 that is lower than A₁

U₄ = Multiple of 4 that is greater than A₁

R₁ = (L₄ + U₄) / 2

If (b₁ = 1) then

A₁' = R₁ + 1

Else

A₁' = R₁ - 1

End If

L₆ = Multiple of 6 that is lower than A₂

U₆ = Multiple of 6 that is greater than A₂

R₂ = (L₆ + U₆) / 2

If (b₂ = 1) then

$$A_2' = R_2 + 1$$

Else

$$A_2' = R_2 - 1$$

End If

L_8 = Multiple of 8 that is lower than A_3

U_8 = Multiple of 8 that is greater than A_3

$$R_3 = (L_8 + U_8) / 2$$

If ($b_3 = 1$) then

$$A_3' = R_3 + 1$$

Else

$$A_3' = R_3 - 1$$

End If

End If

If ($X = 1$) then

L_6 = Multiple of 6 that is lower than A_1

U_6 = Multiple of 6 that is greater than A_1

$$R_1 = (L_6 + U_6) / 2$$

If ($b_1 = 1$) then

$$A_1' = R_1 + 1$$

Else

$$A_1' = R_1 - 1$$

End If

$L_8 =$ Multiple of 8 that is lower than A_2

$U_8 =$ Multiple of 8 that is greater than A_2

$$R_2 = (L_8 + U_8) / 2$$

If ($b_2 = 1$) then

$$A_2' = R_2 + 1$$

Else

$$A_2' = R_2 - 1$$

End If

$L_4 =$ Multiple of 4 that is lower than A_3

$U_4 =$ Multiple of 4 that is greater than A_3

$$R_3 = (L_4 + U_4) / 2$$

If ($b_3 = 1$) then

$$A_3' = R_3 + 1$$

Else

$$A_3' = R_3 - 1$$

End If

End If

If ($X = 2$) then

$L_8 =$ Multiple of 8 that is lower than A_1

$U_8 =$ Multiple of 8 that is greater than A_1

$$R_1 = (L_8 + U_8) / 2$$

If ($b_1 = 1$) then

$$A_1' = R_1 + 1$$

Else

$$A_1' = R_1 - 1$$

End If

L_4 = Multiple of 4 that is lower than A_2

U_4 = Multiple of 4 that is greater than A_2

$$R_2 = (L_4 + U_4) / 2$$

If ($b_2 = 1$) then

$$A_2' = R_2 + 1$$

Else

$$A_2' = R_2 - 1$$

End If

L_6 = Multiple of 6 that is lower than A_3

U_6 = Multiple of 6 that is greater than A_3

$$R_3 = (L_6 + U_6) / 2$$

If ($b_3 = 1$) then

$$A_3' = R_3 + 1$$

Else

$$A_3' = R_3 - 1$$

End If

End If

If ($b_4 = 0$) then

If (A_4 is even) then

$$A_4' = A_4$$

Else

$$A_4' = A_4 - 1$$

End If

End If

If ($b_4 = 1$) then

If (A_4 is even) then

$$A_4' = A_4 - 1$$

Else

$$A_4' = A_4$$

End If

End If

$$M_n = [A_1', A_2', A_3', A_4']$$

Return M_n

End function

5.2 Bit Detection Algorithm

In transform domain watermarking, Signature bits are extracted from forward transformed pixel byte matrix. Whereas in spatial domain watermarking bits are directly extracted from pixel byte matrix without any prior matrix transformation.

Let, $M_n = [A_1, A_2, A_3, A_4]$ is a bit encoded pixel matrix, where A_1, A_2, A_3, A_4 are the encoded pixel byte values and n is a positive integer denotes the concern matrix number.

Bit Detection in Spatial Domain Watermarking

$$b_{[1,2,3,4]} = \text{BIT_DETECT}(M_n)$$

Here $b_{[1,2,3,4]}$ denotes the extracted four bits from a single bit encoded matrix.

Bit Detection in Transform Domain Watermarking

M_n is forward transformed using the matrix operation (x), to obtain transformed matrix M_n' .

$$b_{[1,2,3,4]} = \text{BIT_DETECT}(M_n')$$

Here $b_{[1,2,3,4]}$ denotes the extracted four bits from a single bit encoded matrix.

Pseudocode for the BIT_DETECT algorithm is as follows-

BIT_DETECT = function (M_n)

Start

N = Matrix number of M_n

$X = \{N + (\text{Sum of digits of } N)\} \text{ Mod } 4$

If ($X = 0$ or $X = 3$) then

L_4 = Multiple of 4 that is lower than A_1

U_4 = Multiple of 4 that is greater than A_1

$R_1 = (L_4 + U_4) / 2$

If ($A_1 \geq R_1$) then

$b_1 = 1$

Else

$b_1 = 0$

End If

$L_6 =$ Multiple of 6 that is lower than A_2

$U_6 =$ Multiple of 6 that is greater than A_2

$$R_2 = (L_6 + U_6) / 2$$

If ($A_2 \geq R_2$) then

$$b_2 = 1$$

Else

$$b_2 = 0$$

End If

$L_8 =$ Multiple of 8 that is lower than A_3

$U_8 =$ Multiple of 8 that is greater than A_3

$$R_3 = (L_8 + U_8) / 2$$

If ($A_3 \geq R_3$) then

$$b_3 = 1$$

Else

$$b_3 = 0$$

End If

End If

If ($X = 1$) then

$L_6 =$ Multiple of 6 that is lower than A_1

$U_6 =$ Multiple of 6 that is greater than A_1

$$R_1 = (L_6 + U_6) / 2$$

If ($A_1 \geq R_1$) then

$$b_1 = 1$$

Else

$$b_1 = 0$$

End If

L_8 = Multiple of 8 that is lower than A_2

U_8 = Multiple of 8 that is greater than A_2

$$R_2 = (L_8 + U_8) / 2$$

If ($A_2 \geq R_2$) then

$$b_2 = 1$$

Else

$$b_2 = 0$$

End If

L_4 = Multiple of 4 that is lower than A_3

U_4 = Multiple of 4 that is greater than A_3

$$R_3 = (L_4 + U_4) / 2$$

If ($A_3 \geq R_3$) then

$$b_3 = 1$$

Else

$$b_3 = 0$$

End If

End If

If ($X = 2$) then

$L_8 =$ Multiple of 8 that is lower than A_1

$U_8 =$ Multiple of 8 that is greater than A_1

$$R_1 = (L_8 + U_8) / 2$$

If ($A_1 \geq R_1$) then

$$b_1 = 1$$

Else

$$b_1 = 0$$

End If

$L_4 =$ Multiple of 4 that is lower than A_2

$U_4 =$ Multiple of 4 that is greater than A_2

$$R_2 = (L_4 + U_4) / 2$$

If ($A_2 \geq R_2$) then

$$b_2 = 1$$

Else

$$b_2 = 0$$

End If

$L_6 =$ Multiple of 6 that is lower than A_3

$U_6 =$ Multiple of 6 that is greater than A_3

$$R_3 = (L_6 + U_6) / 2$$

If ($A_3 \geq R_3$) then

$$b_3 = 1$$

Else

$$b_3 = 0$$

End If

End If

If (A_4 is even) then

$$b_4 = 0$$

else

$$b_4 = 1$$

End If

Return [b_1, b_2, b_3, b_4]

End function

5.3 Signature Share Generation algorithm:

Two share image P1 and P2 can be produced from the original image by adding some encrypted value with the red, green, and blue intensities. Let X_r, X_g, X_b are the encrypted values of red, green, blue intensities of private share and Y_r, Y_g, Y_b are the encrypted values of red, green, blue intensities of public share respectively. Red, green and blue intensities of original image is denoted by O_r, O_g, O_b and POS denote position of the pixel.

$$POS = \{0, 1, 2, 3, \dots, n\}$$

$$X_{red}[POS] = (O_{red}[POS] \text{ Mod } 100) + (POS * 3) \text{ Mod } 100 \quad (14)$$

$$X_{green}[POS] = (O_{green}[POS] \text{ Mod } 100) + (POS * 7) \text{ Mod } 100 \quad (15)$$

$$X_{blue}[POS] = (O_{blue}[POS] \text{ Mod } 100) + (POS * 9) \text{ Mod } 100 \quad (16)$$

$$Y_{red}[POS] = 255 - (O_{red}[POS] / 100) \quad (17)$$

$$Y_{\text{green}}[\text{POS}] = 255 - (O_{\text{green}}[\text{POS}] / 100) - 253 \quad (18)$$

$$Y_{\text{blue}}[\text{POS}] = 255 - (O_{\text{blue}}[\text{POS}] / 100) \quad (19)$$

Algorithm:

Input: Original Image

Output: Public Share and Private Share

Method:

1. h = height of original image (O)
2. w = width of original image (O)
3. $P1$ = new image of dimension of $h \times w$
4. $P2$ = new image of dimension of $h \times w$
5. For i in range 1 to h

Start loop:

For j in range 1 to w

Start loop:

$$\text{pos} = (i * w) + j$$

$$P1_{\text{red}}[\text{pos}] = (O_{\text{red}}[\text{pos}] \text{ Mod } 100) + (\text{pos} * 3) \text{ mod } 100$$

$$P1_{\text{green}}[\text{pos}] = (O_{\text{green}}[\text{pos}] \text{ Mod } 100) + (\text{pos} * 7) \text{ mod } 100$$

$$P1_{\text{blue}}[\text{pos}] = (O_{\text{blue}}[\text{pos}] \text{ Mod } 100) + (\text{pos} * 9) \text{ mod } 100$$

$$P2_{\text{red}}[\text{pos}] = 255 - (O_{\text{red}}[\text{pos}] / 100)$$

$$P2_{\text{green}}[\text{pos}] = 255 - (O_{\text{green}}[\text{pos}] / 100) - 253$$

$$P2_{\text{blue}}[\text{pos}] = 255 - (O_{\text{blue}}[\text{pos}] / 100)$$

End loop

End loop

6. Return $P1$ & $P2$

CHAPTER 6

OCR IMPLEMENTATION CONCEPTS

Optical Character recognition technology is a business solution for automated data extraction from printed or written text from a scanned document or image file.

How OCR works?

Generally, OCR works as follows:

1. Pre-process image data.
2. Detect lines, words and characters.
3. Produce ranked list of candidate characters based on trained datasets.
4. Post process recognized characters, choose best characters based on confidence from previous step and language data. Language data includes dictionary, grammar rules, etc.

Tesseract-OCR:

Tesseract is an optical character recognition engine with support for unicode and ability to recognize more than 100 language, originally developed by Hewlett-Packard as a proprietary software in the 1980s. Later it was released as open source in 2005 and development has been sponsored by Google since 2006. It is available for Linux, Windows and Mac OS X.

Initial version of tesseract could only recognize English language. Later versions extended support for more languages. In addition, tesseract can be trained to work in other languages. It can also process right-to-left text such as Arabic or Hebrew and many Indic scripts.

Tesseract is executed from the command line interface, that's why it is suitable for use as a backend. Google uses it for text detection on mobile devices, in videos and in gmail image spam detection.

Tesseract can be integrated into applications using its C++ API. For other programming languages various wrapper APIs are available.

Installation:

- Step1: Installer for windows for Tesseract-OCR is available from <https://github.com/UB-Mannheim/tesseract/wiki>.
- Step 2: Download the “tesseract-ocr-w64-setup-vX.exe” executable file by clicking the hyperlink and save it in “Download” folder.
- Step 3: Run the executable setup file with administrative privilege.
- Step 4: Select the language and then click next.
- Step 5: Read the terms of the agreement and click on “I Agree” button.
- Step 6: Choose the user and click next.
- Step 7: Choose the additional languages and click on next.
- Step 8: Choose the installation location and click on next.
- Step 9: Click on Install to start the installation.
- Step 10: After the complete installation, click on finish to close the setup window.

Tess4J:

Tess4J is a java wrapper for the Tesseract APIs that provides OCR support for various image formats like JPEG, GIF, PNG and BMP. With Tess4J we can access the tesseract API in java.

Installation:

- Step 1: Download the Tess4J zip file from <http://tess4j.sourceforge.net> .
- Step 2: Extract the zip in E drive.

Code & Explanation

First, we have to create a new File object that represents the image data file.

```
File image = new File( "image_data.png" );
```

Then we have to create a Tesseract object to read data from the image file. Tesseract class is located in "net.sourceforge.tess4j" package. Before using the Tesseract class, we have to import that package. This package doesn't come with standard java packages. This package comes with the Tess4J and located in a JAR file named "tess4j-x.y.z.jar".

```
Tesseract tess = new Tesseract();
```

After instantiation of the Tesseract object, we have to set the trained dataset directory by calling the setDatapath() method of Tesseract class.

```
tess.setDatapath( "E:/Tess4J/tessdata" );
```

Next, we have to set the language we want to recognize by calling the setLanguage() method of Tesseract class.

```
tess.setLanguage( "eng" );
```

Character recognition process is started with the invocation of doOCR() method of Tesseract class and pass the file object in method parameter. doOCR() method returns the recognized characters as a string object.

```
String text = Tess.doOCR( image );
```

Next, display the string data in standard output.

```
System.out.println( text );
```

Here is the complete code of the OCR program in java:

```
import net.sourceforge.tess4j.*;
import java.io.*;
import javax.imageio.*;
import java.awt.image.*;
import java.awt.*;

class OCRtest{
    public static void main(String args[]){
        try{
            Tesseract tess = new Tesseract();
            File f = new File("host.png");
            tess.setDatapath("E:/Tess4J/tessdata");
            tess.setLanguage("eng");

            System.out.println();

            String text = tess.doOCR(f, new
            Rectangle(162,11,100,40));
            System.out.println("Customer ID = " + text);

            text = tess.doOCR(f, new Rectangle(100, 43,170,27));
            System.out.println("Customer Name = " + text);

            text = tess.doOCR(f, new Rectangle(111, 81,130,27));
            System.out.println("Test ID = " + text);

            text = tess.doOCR(f, new Rectangle(86, 115,170,27));
            System.out.println("Test Date = " + text);
        }
    }
}
```

```

        text = tess.doOCR(f, new Rectangle(192, 153,140,27));
        System.out.println("Transaction ID = " + text);

        text = tess.doOCR(f, new Rectangle(127, 190,170,27));
        System.out.println("Amount = " + text);
    }catch(Exception e){
        e.printStackTrace();
    }
}
}
}

```

Code compilation and execution:

During compilation of the java file in command line interface, we have to set classpaths of the Tesseract jar files. These jar files are located inside the “dist” and “lib” sub-directories of unzipped “Tess4J” directory.

Compilation of java code file:

```
javac -cp ".;E:\Tess4J\lib\*;E:\Tess4J\dist\*" OCRprogram.java
```

Execution of java bytecode:

```
java -cp ".;E:\Tess4J\lib\*;E:\Tess4J\dist\*" OCRprogram
```

Output:

```
C:\Windows\System32\cmd.exe
F:\FINAL_SEM_PROJECT\Testing\OCR>java -cp ".;E:\Tess4J\lib\*;E:\Tess4J\dist\*" OCRtest
Customer ID = : 108865

Customer Name = Akash Kumar

Test ID = 987654321

Test Date = 12 - 01 - 2019

Transaction ID = 8877660011

Amount = 12000

F:\FINAL_SEM_PROJECT\Testing\OCR>
```

Figure 12: Output of OCR Program

CHAPTER 7

EXPERIMENTAL RESULTS & DISCUSSION

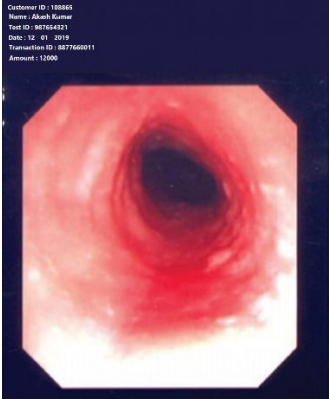

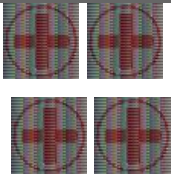






Proposed Image fabrication and detection scheme is applied on a sample medical color image. The standard benchmark color images in PNG format with cover image of size 1152x1408 and signature images of size 50x50. The testing is carried out in WINDOWS environment while the experimental data is evaluated using web version of MATLAB.

Comparison between original signature images and extracted signature images

Cover image is logically divided in four regions and each region is sub-divided into four segments. Four signature images are inserted in four different segments of each region of the cover image. Private share of hospital logo is fabricated in segment 1 of each region. Right hand fingerprint of client is fabricated in segment 2 of each region. Left hand fingerprint of client is fabricated in segment 3 of each region and the last segment is fabricated by the client's left/right fingerprint. In the extraction process, signature images are extracted from each segment of each region. During extraction process, four copies of each signature image is generated. Similarity between original signature and corresponding extracted signatures can be found by counting number of pixels matched between original and extracted signature.

Let, C be the number of extracted signature pixels that exactly matches with the original signature image and N is the total number of pixels in the original signature. Then similarity S can be calculated as

$$S = \frac{C}{N} \times 100$$

Cover Image	Segment No.	Signature Image	Extracted Image
	1		
	2		
	3		
	4		

```
C:\Windows\System32\cmd.exe
F:\FINAL_SEM_PROJECT\Testing\compare image>java CompareImage
Segment wise Image Comparison

Segment 1:
Original privateshare vs Extracted privateshare

Region 1 image matching % : 100.0
Region 2 image matching % : 100.0
Region 3 image matching % : 100.0
Region 4 image matching % : 100.0

Segment 2:
Original right fingerprint vs Extracted right fingerprint

Region 1 image matching % : 99.45333333333333
Region 2 image matching % : 100.0
Region 3 image matching % : 99.68
Region 4 image matching % : 100.0

Segment 3:
Original left fingerprint vs Extracted left fingerprint

Region 1 image matching % : 100.0
Region 2 image matching % : 100.0
Region 3 image matching % : 100.0
Region 4 image matching % : 93.8

Segment 4:
Original client fingerprint vs Extracted client fingerprint

Region 1 image matching % : 99.96000000000001
Region 2 image matching % : 99.97333333333333
Region 3 image matching % : 86.98666666666666
Region 4 image matching % : 86.18666666666667
```

Figure 13: Comparison between original signature and extracted signatures

Comparison between original hospital logo and extracted merged logos

Private share of the hospital logo is extracted from segment 1 of each four regions. Each extracted private shares are then merged with the public share of the hospital logo to

generated the merged logos. Merged logos are then compared with the original hospital logo.

```
Original Logo vs Merged Logo
Region 1 image matching % : 100.0
Region 2 image matching % : 100.0
Region 3 image matching % : 100.0
Region 4 image matching % : 100.0
```

Figure 14: Comparison between original hospital logo and merged logo

Comparison between extracted signatures with some other images

Comparison between extracted right hand fingerprint from segment 2 with the original left hand fingerprint.

```
Original left fingerprint vs extracted right fingerprint
Region 1 image matching % : 39.160000000000004
Region 2 image matching % : 39.44
Region 3 image matching % : 39.28
Region 4 image matching % : 39.44
```

Figure 15: Comparison between left hand fingerprint and extracted right hand fingerprint

Comparison between extracted left hand fingerprint from segment 3 with the original right hand fingerprint.

```
Original right fingerprint vs extracted left fingerprint
Region 1 image matching % : 39.44
Region 2 image matching % : 39.44
Region 3 image matching % : 39.44
Region 4 image matching % : 37.0
```

Figure 16: Comparison between right hand fingerprint and extracted left hand fingerprint

Comparison between extracted right hand fingerprint from segment 2 with someone else right or left hand fingerprint.

```
Someone else fingerprint vs extracted right fingerprint
Region 1 image matching % : 26.279999999999998
Region 2 image matching % : 26.506666666666668
Region 3 image matching % : 26.453333333333333
Region 4 image matching % : 26.506666666666668
```

Figure 17: Comparison between someone else fingerprint and extracted right hand fingerprint

Comparison between original cover image and signature fabricated image with PSNR, SSIM, MSE, CC values.

The quality of the signature fabricated image is qualitatively decided by visual objects in signature fabricated image. Peak Signal to Noise Ratio (PSNR) is used as a quality measurement between the original and a compressed image. The higher the PSNR, the better the quality of the compressed or reconstructed image.

$$PSNR = 10 \log \frac{(255)^2}{MSE}$$

The Mean Square Error (MSE) represents the cumulative squared error between the compressed and original image. The lower the value of MSE, the lower the error. MSE between a signature fabricated image (I_s) and original cover image (I) is

$$MSE = \frac{1}{N} \sum_{j=0}^N (I_w - I)^2$$

Structural similarity index measure (SSIM) is used for measuring the similarity between two images. SSIM index is full reference matrix, in other words, the measurement or prediction of image quality is based on an initial uncompressed or

distortion free image as reference. SSIM is perception-based model that considers image degradation as perceived change in structural information. The difference with other techniques such as MSE or PSNR is that these approaches estimate absolute errors.

Normalize Cross Correlation (NCC) is used to measure the quality of the stego image after extraction.

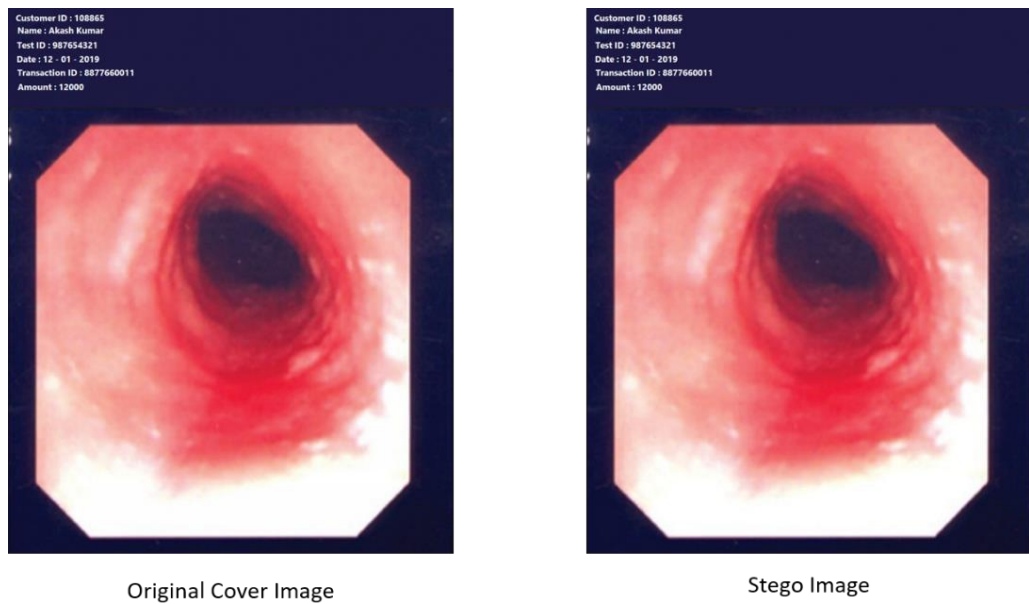


Figure 18: Original cover image and Signature fabricated image

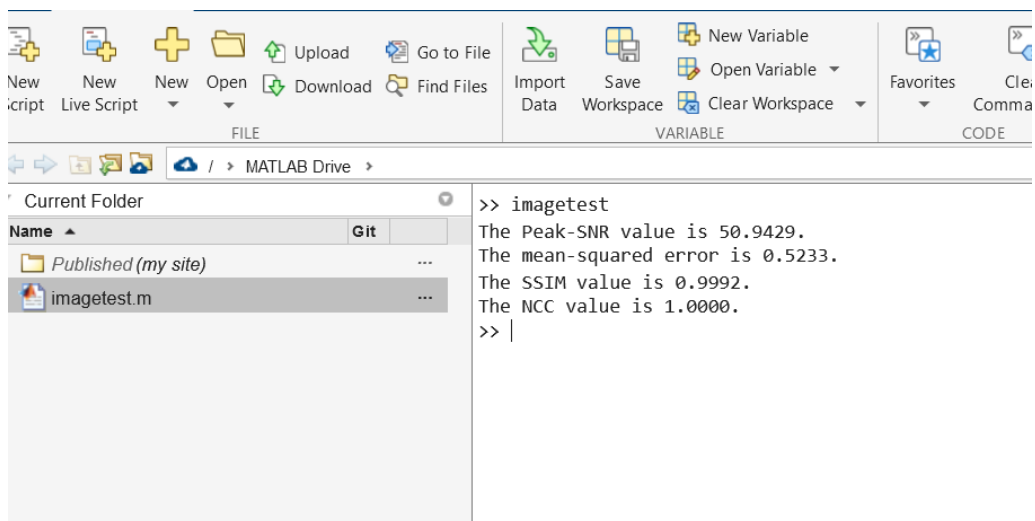


Figure 19: PSNR, MSE, SSIM, NCC values of signature fabricated image

Histogram comparison between Original Image and Signature Fabricated Image

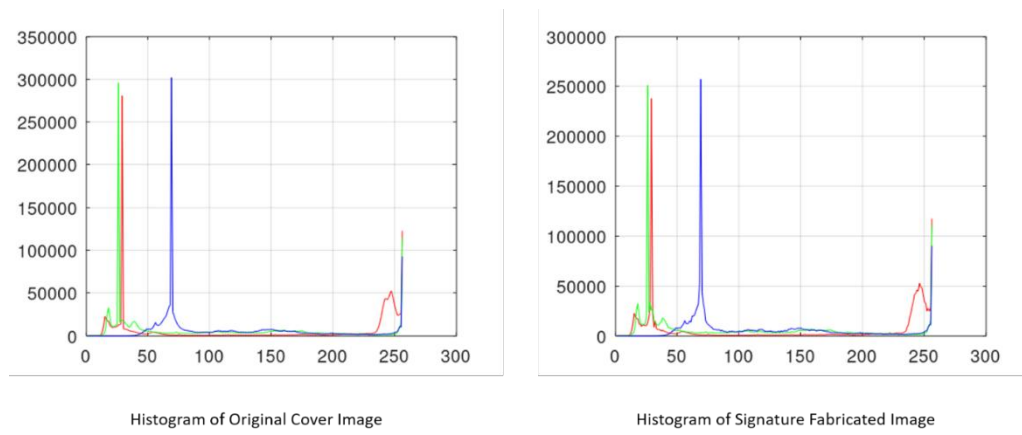


Figure 20: Histogram comparison between original and signature fabricated image

CHAPTER 8

CONCLUSION & FUTURE WORK

This proposed idea represents a trusted data security protocol for validation of e-document related to healthcare application. The project compiles all the data security issues (Authentication, Confidentiality, Integrity, Non-repudiation) in contrast to the existing approaches. Additionally, this proposed concept also introduces an OCR technique to validate the sensitive data of the digital medical document. Apart from that, the propose concept also promotes robust data hiding technique that support better imperceptibility as well. Further this concept also compiles the non-repudiation issues with the digital signature concept which is integrated with visual cryptographic approach. In this regard a novel signature share algorithm is designed with tested output. Further, another suitable technique will be designed for biometric authentication.

The proposed work will be further tested with different digital e-documents, in terms of data hiding imperceptibility and robustness along with biometric matching samples.

REFERENCE:

1. Anitha, V., & Velusamy, R. L. (2012) “Authentication of digital documents using secret key biometric watermarking”, *International journal of communication network security*, Vol. 1, Issue 4, pp. 5–11.
2. Mishra, K. N. (2016) “AAdhar based smartcard system for security management in South Asia”, In the Proceedings of International Conference on Control, Computing, Communication and Materials (ICCCCM), pp. 1–6.
3. Hasan, H. R. (2018) “Copyright Protection for Digital Certificate using Blind Watermarking Technique”, *Kurdistan Journal of Applied Research*, Vol. 3, Issue 1, pp. 75–79.
4. Gull S, Loan NA, Parah SA, Sheikh JA, Bhat GM (2018) An efficient watermarking technique for tamper detection and localization of medical images. *J Ambient Intell Humaniz Comput*.
5. Swaraja K, Meenakshi K, Padmavathi K (2020) An optimized blind dual medical image watermarking framework for tamper localization and content authentication in secured telemedicine. *Biomed Signal Process Control* 55:101665.
6. Alshanbari HS (2020) Medical image watermarking for ownership & tamper detection. *Multimed Tools Appl*.
7. Lee H-Y (2019) Adaptive reversible watermarking for authentication and privacy protection of medical records. *Multimed Tools Appl* 78(14):19663–19680.
8. Behnia, S., Teshnehlab, M., & Ayubi, P. (2010) “Multiple watermarking scheme based on improved chaotic maps”, *Communication in Nonlinear Science and Numerical Simulation*, Vol. 15, Issue 9, pp. 2469–78.

9. Thanki, R. M., & Borisagar, K. R. (2014) “Compressive Sensing Based Multiple Watermarking Technique for Biometric Template Protection”, *International Journal of Image Graphics and Signal Processing*, Vol. 7, Issue 1, pp 53–60.
10. Natarajan, M., & Govindarajan, Y. (2016) “Performance optimization of multiple watermarking using genetic algorithms”, *International Journal of Enterprise Network Management*, Vol. 7, Issue 3, pp. 237–249.
11. Horng, S. J., Rosiyadi, D., Li, T., Takao, T., Guo, M., & Khan, M. K. (2013) “A blind image copyright protection scheme for e-government”, *Journal of Visual Communication and Image Representation*, Vol. 24, Issue 7, pp. 1099–1105.
12. Al-Haj, A., & Barouqa, H. (2017) “Copyright protection of e-government document images using digital watermarking”, In the Proceedings of 3rd International Conference on Information Management (ICIM), IEEE, pp. 441–446.
13. Nasir, I., Weng, Y., Jiang, J., & Ipson, S. (2010) “Multiple spatial watermarking technique in color images”, *Signal Image & Video Processing*, Vol. 4, Issue 2, pp. 145–154.
14. Bhatnagar, G., & Wu, Q. J. (2015) “A new robust and efficient multiple watermarking scheme”, *Multimedia Tools & Application*, Vol. 74, Issue 19, pp. 8421–8444.
15. Babaei, M., Ng, K., Babei, H., & Niknajeh, H. G. (2014) “Robust multi watermarking scheme for multiple digital input images in DWT domain”, *International Journal of Computer and Information Technology*, Vol. 3, Issue 4, pp. 834–840.

FRUIT FRESHNESS MEASUREMENT USING ML TECHNIQUES

B.Tech Project Report

By

Name of the B.Tech. Students

**AKASH MUKHERJEE (GCECTB-R18-3035)
DEBMALYA SUR (GCECTB-R18-3007)
GOURAB CHATTERJEE (GCECTB-R18-3011)
SAYAN MONDAL (GCECTB-R18-3024)**

**Under Supervision of
Kingshuk Chatterjee**



**Department of Computer Sci. and Engineering
Government College of Engineering and
Ceramic Technology
Kolkata**

May 2024

FRUIT FRESHNESS MEASUREMENT USING ML TECHNIQUES

A Project Report

*Submitted in partial fulfilment of the
requirements for the award of the degree
of*

Bachelor of Technology

In

Computer Sci. and Engineering

By

**AKASH MUKHERJEE (GCECTB-R18-3035)
DEBMALYA SUR (GCECTB-R18-3007)
GOURAB CHATTERJEE (GCECTB-R18-3011)
SAYAN MONDAL (GCECTB-R18-3024)**



**Department of Computer Sci. and Engineering
Government College of Engineering and
Ceramic Technology
Kolkata**

May 2022

DECLARATION

We hereby declare that the project entitled **Fruit Freshness Measurement Using ML Techniques** was submitted for the B. Tech. (CSE) degree is our original work and the project has not formed the basis for the award of any other degree, diploma, fellowship, or any other similar titles.

Name and Roll No. of the Students

Signature of the Students

1. AKASH MUKHERJEE (GCECTB-R18-3035)

Akash Mukherjee..

2. DEBMALYA SUR (GCECTB-R18-3007)

Debmalya Sur

3. GOURAB CHATTERJEE (GCECTB-R18-3011)

Gourab Chatterjee

4. SAYAN MONDAL (GCECTB-R18-3024)

Sayan Mondal

Place: Kolkata

Date: 11/05/2022



Government College of Engineering and Ceramic Technology

73, A. C. Banerjee Lane, Kolkata, West Bengal 700010

BONAFIDE CERTIFICATE

Certified that this project report titled **FRUIT FRESHNESS MEASUREMENT**

USING **ML TECHNIQUES** is the authentic work carried out
by Akash Mukherjee, Debmalya Sui, Gourab Chatterjee
Sayan Mondal NAME OF THE
STUDENT(Roll.Nos). GCECTB-R18-3011, GCECTB-R18-3024
GCECTB-R18-3035, GCECTB-R18-3007 who

carried out the project work under **my / our** supervision. Certified further, that to the best of
my knowledge the work reported herein does not form part of any other project report or
dissertation on the basis of which a degree or award was conferred on an earlier occasion on
this or any other candidate.

Kingshuk Chatterjee

Kingshuk Chatterjee
SUPERVISOR

Assistant Professor

Department of Computer Science and Engineering
Government College of Engineering and
Ceramic Technology
Kolkata-700010

Mentel Mondal
11/5/2022

External Examiner

K. Saha 06.05.2022

Dr. Kalpana Saha Roy
HEAD OF THE DEPARTMENT

Assistant Professor & Head

Department of Computer Science and Engineering
Government College of Engineering and
Ceramic Technology
Kolkata-700010

Abstract

This project presents a comprehensive analysis of a variety of fruit and vegetable images for freshness grading using deep learning. A number of models have been used in this project, including DenseNet121 and the Custom model. Fruit and vegetable decaying occur in a gradual manner, this characteristic is included for freshness grading by interpreting chronologically-related fruit decaying information. The contribution of this project is to propose a novel neural network structure for fruit object locating and classification. It takes fruits and vegetables as an object and using its images we classify them into two categories bad and fresh.

Acknowledgment

We express our sincere gratitude towards our project mentor Kingshuk Chatterjee, Assistant Professor, Department of Computer Science and Engineering, Government College of Engineering and Ceramic Technology, Kolkata, West Bengal, for providing valuable guidance and constant encouragement throughout the project. We would also like to thank our HOD Mam Dr. Kalpana Saha Roy and Principal Sir Prof. Krishnendu Chakrabarty for providing us with this opportunity. It is our pleasure to record our sincere thanks to him for his constructive criticism and insight without which the project would not have shaped as it has.

We thank God for making all this possible, our parents and friends for their constant support and encouragement throughout the project work.

List of Figures

Figure	Page Number
Fig 2.1 Literature Survey	3
Fig 3.2.1 Examples of image from our dataset	5
Fig 3.2.2 Demonstration of our dataset	6
Fig 3.3.1.1 DenseNet-121 model architecture	8
Fig 3.3.2.1 Custom Model architecture	10
Fig 3.3.3.1 Error-vs-Complexity graph of Ridge Regressor	11
Fig 4.1.1 Training vs Validation loss and accuracy curves of DenseNet121	13
Figure 4.1.2 Confusion matrix of the validation set of DenseNet121	14
Figure 4.1.3 Confusion matrix of the test set of DenseNet121	14
Figure 4.1.4 Classification report of the validation set of DenseNet121	14
Figure 4.1.5 Classification report of the test set of DenseNet121	14
Figure 4.2.1 Training vs Validation loss and accuracy curves of FFCM	15
Figure 4.2.2 Confusion matrix of the validation set of FFCM	15
Figure 4.2.3 Confusion matrix of the test set of FFCM	15
Figure 4.2.4 Classification report of the validation set of FFCM	16
Figure 4.2.5 Classification report of the test set of FFCM	16
Figure 3.1 Mean Absolute Error Formula	17
Figure 4.3.2 Mean Squared Error Formula	17
Figure 4.3.3 Root Mean Squared Error Formula	18
Figure 4.3.4 Root Mean Squared Log Error Formula	18
Figure 4.3.5: R2 Score Formula	19
Figure 4.3.6: Adjusted R2 Formula	19
Figure 5.2.1 Data Flow Diagram	21
Figure 5.3.1 High Level Design	22
Figure 5.4.1 Home Page	22
Figure 5.4.2 Options for various Tasks	23
Figure 5.4.3 Classification Task	23
Figure 5.4.4 Regression Task	24
Figure 5.4.5 Combined Task	25

Table of Contents

	Title Page	i
	Declaration of the Students	iii
	Bonafide Certificate	iv
	Abstract	v
	Acknowledgment	vi
	List of Figures	vii
1.	INTRODUCTION	1
	1.1 Background	1
	1.2 Fruit Freshness Grading	1
	1.3 Project Motivation	2
2.	LITERATURE SURVEY	3
3.	PROPOSED WORK	4
	3.1 Objectives & Goals	4
	3.2 Dataset	4
	3.3 Model Building	7
	3.3.1 DenseNet-121 Model Architecture	7
	3.3.2 Custom Model Architecture	9
	3.3.3 Ridge Regression Model	11
4.	RESULTS / OUTPUTS	13
	4.1 Output of DenseNet-121	13
	4.2 Output of Custom Model	15
	4.3 Output of Ridge Regression Model	16
5.	SYSTEM ANALYSIS & DESIGN	20
	5.1 System Specifications	20
	5.2 DFD	20
	5.3 Design and Test Steps	21
	5.4 Web View	22
6.	CONCLUSIONS AND SCOPE FOR FUTURE WORK	26
	6.1 Conclusion	26
	6.2 Future Work	26
7.	REFERENCES	27

1 Introduction

In this project, we will provide an overview of fruit freshness grading system, including the identification of the research problem.

1.1 Background

Fruits and vegetables are an important constituent of a person's daily diet and thus play a significant role in their lives. However, grading the freshness of the fruits and vegetables is a manual operation and is time-consuming. Also, not many people are skilled in the process of manual detection which leads to a large margin of error. Automated grading by using computerized approaches is believed to be the solution to this problem. In this current scenario people are getting more conscious about their health and trying to get fresh fruits and vegetables but are not able to correctly distinguish between fresh and bad.

Established research evidence shows that when deterioration of fruit and vegetable occurs, they go through a series of biochemical transformation that leads to changes in their physical conditions, e.g., visual features including colour and shape. Most of these features can be captured. It is expected that the computer vision-based approach is the most economical solution. Given the advancement of deep learning technology, grading algorithms should produce satisfactory accuracy.

1.2 Fruit Freshness Grading

For the categorization of the fruit and vegetables depending upon their freshness, we have used a Hedonic [9] scale rating. Each image is associated with a Hedonic [9] Rating given by the Panel of Food Technology experts. Hedonic [9] rating is a Quality Measurement technique measuring 3 qualities, namely 'Colour', 'Shape' and 'Texture'. Each quality can take a value from 1 to 9. The average of three values should be taken. If the average is greater than 4, then the image associated with the particular Hedonic [9] Rating is considered as "Fresh". Otherwise, the image will be considered as "BAD". Then the images are classified into two groups- "FRESH" & "BAD".

1.3 Project Motivation

We consider fruit freshness grading as one step of post-harvest assessments. Everyone tries to eat fresh fruits and vegetables as much as possible and the only way most of the common people can judge whether it is fresh or not is using manual inspection which is time consuming as well as it leaves a large error of margin and is also not scientifically proved. Moreover, many people might not even know the manual techniques and end up buying the stale ones. This motivated us to pursue this project as everyone wants fresh fruits and vegetables but is not able to distinguish it from the stale ones. As a result, it motivated us to find a way so that anyone can just use their phone's camera to decide whether its fresh or not.

2 Literature Survey

We decided to do a literature survey to know the different models that we can use on our project.

The following table shows the various works being done in the area of fruit, vegetable classification or grading, the models being used and the accuracy achieved.

<u>Author Name</u>	<u>Fruit / Vegetable Used</u>	<u>Method used and Accuracy achieved</u>
Jahanbakhshi et al .[1]	Classified carrots based on their size to control waste	Artificial Neural Networks - 98.5% Support Vector Machine - 89.62%
Izadi et al .[2]	Graded tomatoes based on their size,shape and texture	Neural fuzzy networks (ANFIS) - 81%
Kheiralipour et al .[3]	Categorized cucumbers based on their size,shape and texture	Artificial Neural Networks - 97.1% Linear Discriminant Analysis - 91.2% Quadratic Discriminant Analysis - 93.1%
Wang et al. [4]	Classified fruits	Convolutional Neural Networks - 95.67%
Jahanbakshi et al.[5]	Classified lemons based on their imperfections	Convolutional Neural Networks - 100%
Chowdhury et al.[6]	Recognized 10 different types of vegetables based on colour and texture	Convolutional Neural Networks - 96.55%
Danti et al.[7]	Classified 10 different types of leafy vegetables	BP Neural Networks - 96.40%
Yuan et al.[8]	Created a database named Food-SK consisting of 2500 food images selected from three popular image sets for food recognition:	Fine Tuned GoogLeNet -99.2%

Figure 2.1 Literature Survey

3 The Proposed Work

3.1 Objectives & Goals

- The customers mainly use manual inspection techniques to distinguish between fresh and stale fruits and vegetables.
- This process is very time-consuming and we cannot determine the actual quality and there may be even some naive buyers who can't distinguish and end up buying the stale ones.
- In this project, we aim to automate the whole process so anyone can just go to the market and distinguish the fresh ones from the stale ones using their smartphone cameras.
- We aim to measure the freshness of the fruit utilizing a Hedonic [9] scale rating.
- Using the measurement, we can categorize the fruits and vegetables into two categories namely fresh and bad.
- Utilizing the categorization, we can determine whether it is consumable or not.

3.2 Dataset

In our project, we didn't use any readily available or existing dataset, rather we have created the dataset on our own. We selected Amla for our dataset because it is easily available at the market, the price is also lower compared to other fruit items, and being a rich source of vitamin-c, it is very useful especially in the COVID situation.

- We have image files and one CSV file containing Hedonic [9] ratings as our dataset.
- Seven Amlas of fine quality were collected.
- Those Amlas were observed for 15 days. Those were kept in the same environmental condition.
- The picture of each Amla was captured thrice a day.
- The time of capturing photos were 10 AM, 4 PM, and 10 PM.
- 21 images were captured per day for our dataset.
- There are 283 images of amla in total.

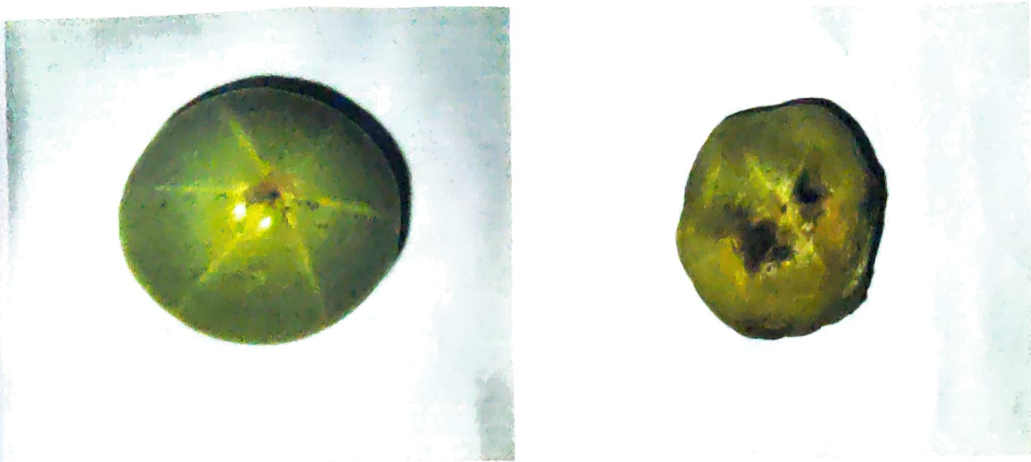


Figure 3.2.1 Examples of images from our Dataset

The process was started from 4th May 2021 onwards. We took 3 pictures of each amla per day. So, in total, we captured 21 images per day. 315 images should be there, but there are 283 images in our dataset. The rest of the images got eliminated due to the worst quality. After capturing the images and eliminating inappropriate images, the rest images are then renamed in a particular format, in order to easy accessibility with coding.

The other part of our dataset is the Hedonic [9] Rating. Each image is associated with a Hedonic [9] Rating given by the Panel of Food Technology experts. **Hedonic [9] rating is a Quality Measures technique.** 3 quality measures, namely 'Colour', 'Shape' and 'Texture' are there. Each quantity can take a value from 1 to 9, where "9" indicates the best condition and "1" stands for the worst condition. Each parameter should have an individual value. The average of three values should be taken. **If the average is greater than 4, then the image associated with the particular Hedonic [9] Rating is considered as "Fresh". Otherwise, the image will be considered as "BAD".** Then the images are classified into two groups- "FRESH" & "BAD".


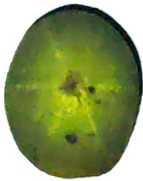
Image	Time & Date	Shape	Colour	Texture	Average	Status
	08/05/2021 4 pm Sample-1	8.5	8	8	8.2	Fresh
	18/05/2021 10 pm Sample-1	2	2	2	2	Bad

Figure 3.2.2 Demonstration of the dataset

So, in the above table, the first image was captured on the 8th day of May at 4 pm. This is sample-1. The shape rating of the image is 8.5. Texture and Colour ratings are 8.5 & 8 respectively. So, the average of these three parameters is 8.2, which is greater than 4. Hence, this particular image is classified as "Fresh". On other hand, the second image was captured on 18th May at 10 pm. It is sample-1. The value of Shape, Texture & Colour ratings are 2, 2 & 2 respectively. Since, the average of these three fields is 2, which is lesser than 4. That implies the corresponding item will be considered as "Bad" and it is inconsumable. So, in our dataset, we have image files and one CSV file containing Hedonic [9] Rating. Each image is associated with one Hedonic [9] rating, better to say one row of the CSV file.

3.3 Model Building

After creating our dataset, we did some data pre-processing to make the data ready before insertion into Deep Learning Models. We aim to build a CNN model to do classification, we want to build models using Transfer Learning and custom models of Convolutional Neural Networks. We are going to apply our model created to classify the fruit items as FRESH or BAD.

3.3.1 DenseNet-121 Model Architecture

Input Layer: Here we will give an input of (150, 150, 3) sized image to the model and the output of this layer will be (150, 150, 3)

Functional Layer: It is a combination of multiple layers, first we will do a max pooling on the current layer and then we will create two threads, on one thread we will do the following procedures sequentially:

- Batch normalization
- Applying an activation function (ReLU is preferred)
- Then applying a convolution 2D layer

we will follow these sequences multiple times, and lastly, the output of this thread will be concatenated with another thread. In this model we got (4, 4, 1024) as an output from this layer.

Flatten Layer: The main purpose of this layer is to flat the nodes of the previous layer, so the total number of nodes in this layer will be the simple multiplication of the output of its previous layer. Here, the input to this layer is (4, 4, 1024) thus the output from this layer will be $= 4 \times 4 \times 1024 = 16384$

Dense Layer: The main purpose of this layer is to make a dense connection between the input nodes and the output nodes. A dense connection means each node of its input layer will be connected with each node of the output layer, i.e. this layer will create a complete bipartite graph-like structure. In this model, we have got 128 nodes as an output from this layer.

Dropout Layer: Dropout is a technique used to prevent a model from overfitting. Dropout works by randomly setting the outgoing edges of hidden units (neurons that make up hidden

layers) to 0 at each update of the training phase. In this model, we have got 128 nodes as an output from this layer.

Dense Layer: It will be the last layer of our model. As an input to this layer, we have 128 nodes and this layer will simply make a complete connection with the 2 output nodes in this layer and those two output nodes will be the output of the whole model, more accurately one node will be standing for "FRESH" and another node will be considered as "BAD" conditioned fruits.

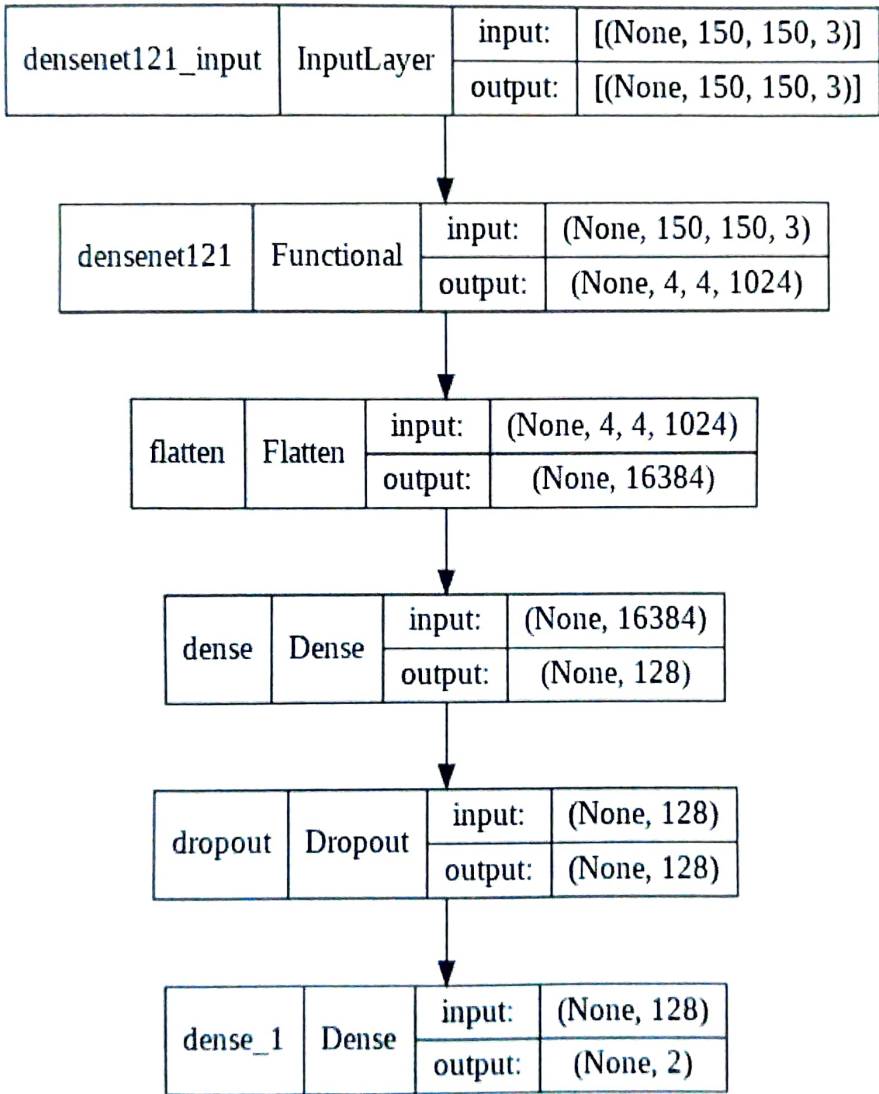


Figure 3.3.1 DenseNet-121 Model architecture

3.3.2 Custom Model Architecture

Input layer, the input shape is (224, 224, 1) and the output shape is also (224, 224, 1), which is then passed through Convolution2D layer with a filter of (3,3) and the input shape is (224, 224, 1) and output shape is (222, 222, 64) and in it Relu is used as an activation function. It is then passed through MaxPooling2D layer with a pool size of (3, 3) and the input shape is (222, 222, 64) and output shape is (222, 222, 64). It is then passed through Convolution2D layer with a filter of (3,3) and the input shape is (74, 74, 64) and output shape is (72, 72, 32) and in it Relu is used as an activation function. It is then passed through MaxPooling2D layer with a pool size of (2, 2) and the input shape is (72, 72, 32) and output shape is (36, 36, 32). It is then passed through Convolution2D layer with a filter of (3,3) and the input shape is (36, 36, 32) and output shape is (34, 34, 64) and in it Relu is used as an activation function. It is then passed through MaxPooling2D layer with a pool size of (2, 2) and the input shape is (34, 34, 64) and the output shape is (17, 17, 64). The data is then flattened where the input shape is (17, 17, 64) and the output shape is (18496), which is then passed through a dense layer where the input shape is (18496) and output shape is (128) and here Relu is used as an activation function and dropout (p=0.5) is used. It is then passed through a dense layer where the input shape is (128) and output shape is (64) and here Relu is used as an activation function and dropout (p=0.3) is used. It is then passed through a dense layer where the input shape is (64) and output shape is (1) and here Sigmoid is used as an activation function

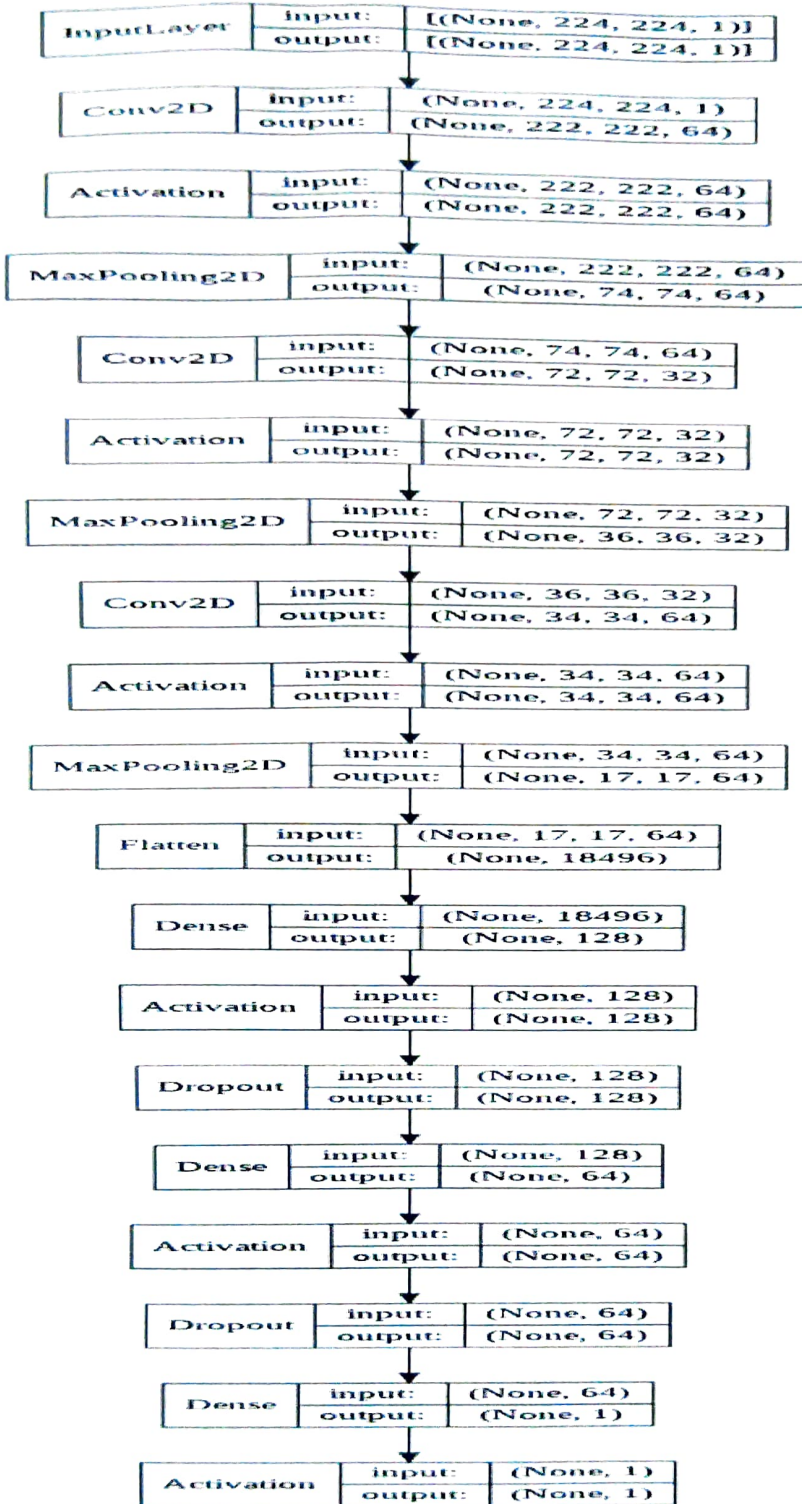


Figure 3.3.2.1 Custom Model architecture

3.3.3 Ridge Regressor

Ridge Regression is a special type of model tuning procedure. It is essentially used to analyse data that are suffering from multicollinearity. Multicollinearity means correlations between predictor variables. The mentioned method performs

L2 regularization techniques. It adds the Squared Magnitude of the coefficient as the penalty term to the loss function. Ridge Regression is a special way that creates a parsimonious model when the number of predictor variables in a set exceeds the number of observations. Alternatively, it is also very useful when data has multicollinearity. Ridge Regressor doesn't require unbiased estimators.

When there are some issues because of multicollinearity, least-squares are unbiased, and variances are large, which results in the predicted values being far away from the actual values.

The cost function of Ridge Regression is given here:

$$\text{Cost Function} = \text{Minimum}(\|y - x(\theta)\|^2 + \lambda \|\theta\|^2)$$

Here, is the Penalty term. It is denoted by an Alpha parameter in the Ridge Function. We can control the penalty term by changing the values for alpha. That means, bigger the values of alpha, the higher is the penalty and therefore the magnitude of coefficients will be reduced.

Since Ridge Regressor shrinks the parameters, this is used to prevent multicollinearity. It reduces the model complexity by shrinking the coefficients.

The Error vs Complexity scenario of the Ridge Regression is given below:

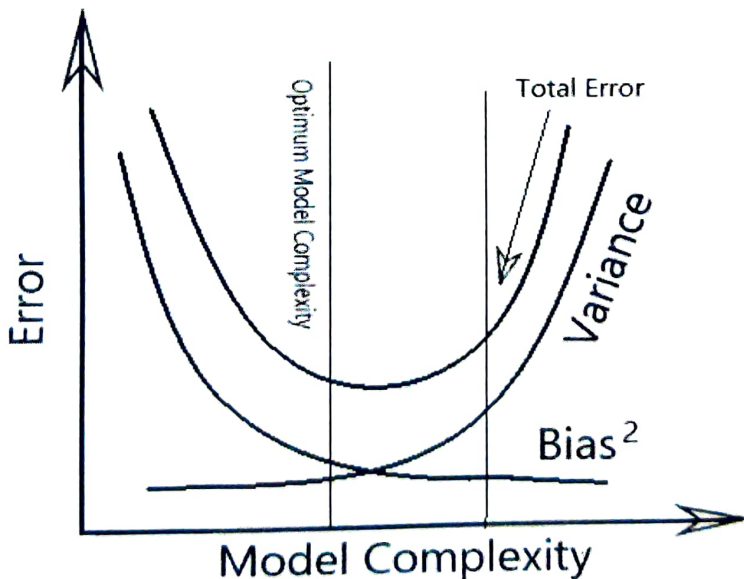


Figure 3.3.3.1: - Error vs Complexity graph of Ridge Regressor

This is the Error Vs Model Complexity graph for Ridge Regressor. We can see the Variance and the Square of Bias in the above graph. We can determine Total Error and the Optimum Model Complexity through this graph.

4. Results and Outputs

Here we tried out two different models, one using transfer learning and the name of the model is **Dense Net 121**, and another was our custom model named as Fruit Freshness Classification Model in short **FFCM**. Here are the results of those two models.

4.1 Output of DenseNet121

The model's training and validation loss and accuracy curves are given below

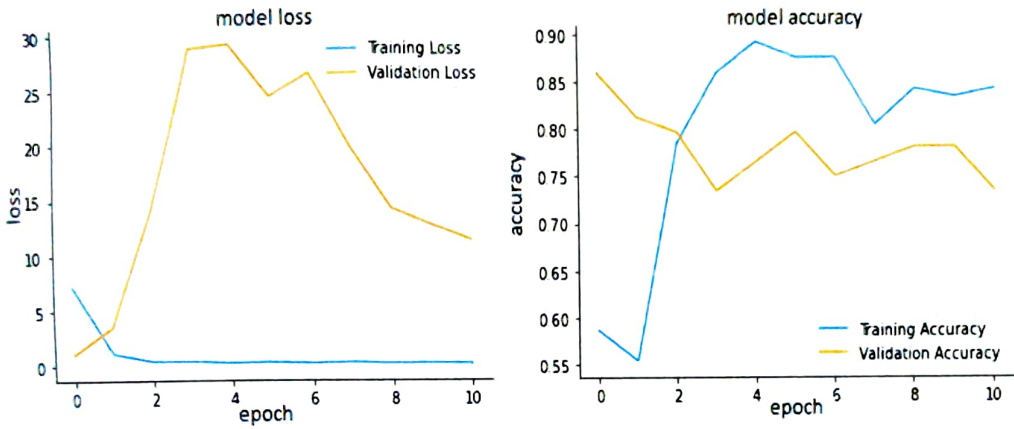


Figure 4.1.1 Training vs Validation loss and accuracy curves of DenseNet121

The confusion matrices of validation and test sets are given below

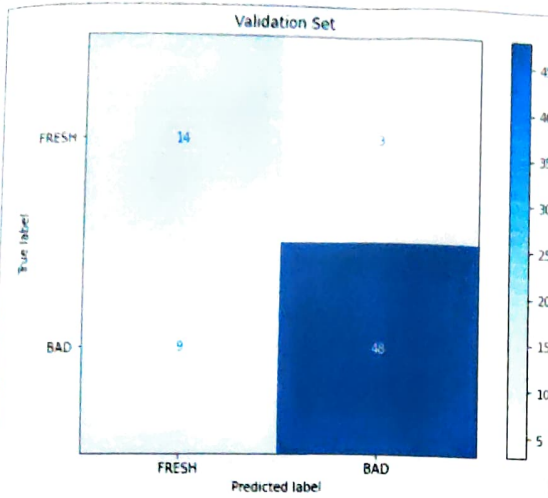


Figure 4.1.2 Confusion matrix of the validation set of DenseNet121

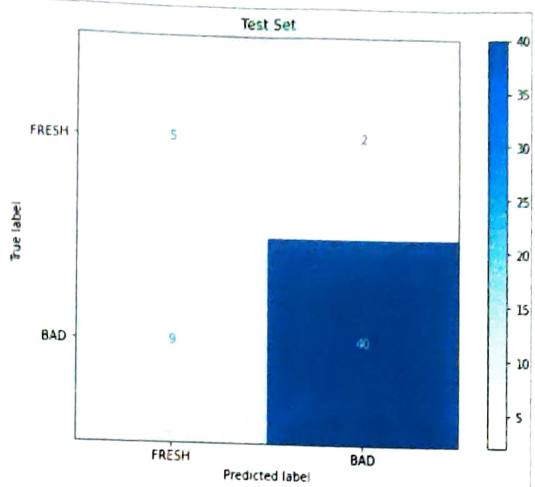


Figure 4.1.3 Confusion matrix of the test set of DenseNet121

The classification reports of the validation and test set are given below

	precision	recall	f1-score	support
BAD	0.61	0.82	0.70	17
FRESH	0.94	0.84	0.89	57
accuracy			0.84	74
macro avg	0.77	0.83	0.79	74
weighted avg	0.86	0.84	0.85	74

Figure 4.1.4 Classification report of the validation set of DenseNet121

	precision	recall	f1-score	support
BAD	0.36	0.71	0.48	7
FRESH	0.95	0.82	0.88	49
accuracy			0.80	56
macro avg	0.65	0.77	0.68	56
weighted avg	0.88	0.80	0.83	56

Figure 4.1.5 Classification report of the test set of DenseNet121

4.2 Output of FFCM

The model's training and validation loss and accuracy curves are given below

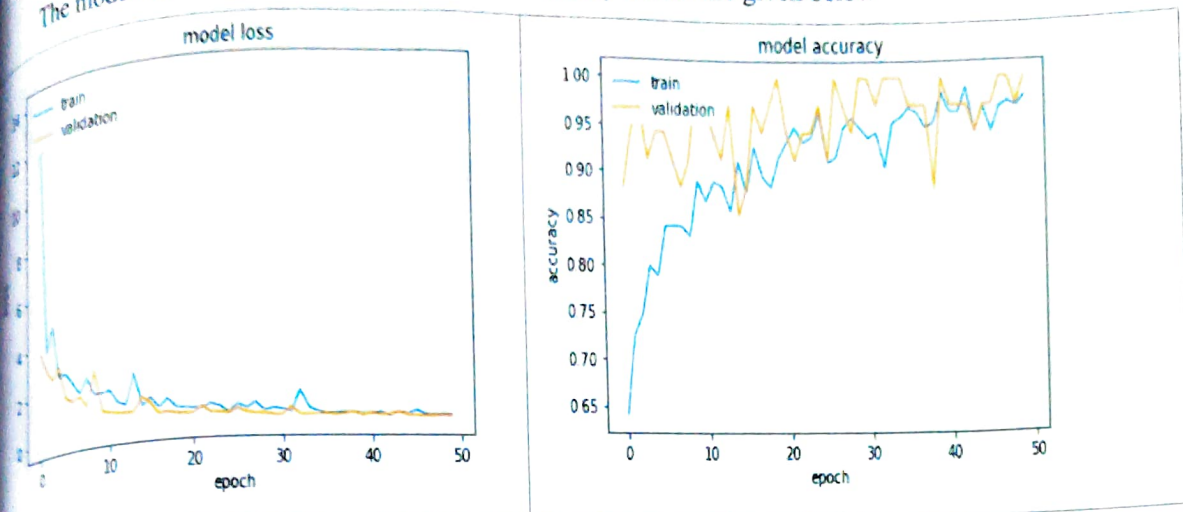


Figure 4.2.1 Training vs Validation loss and accuracy curves of FFCM

The confusion matrixes of validation and test sets are given below

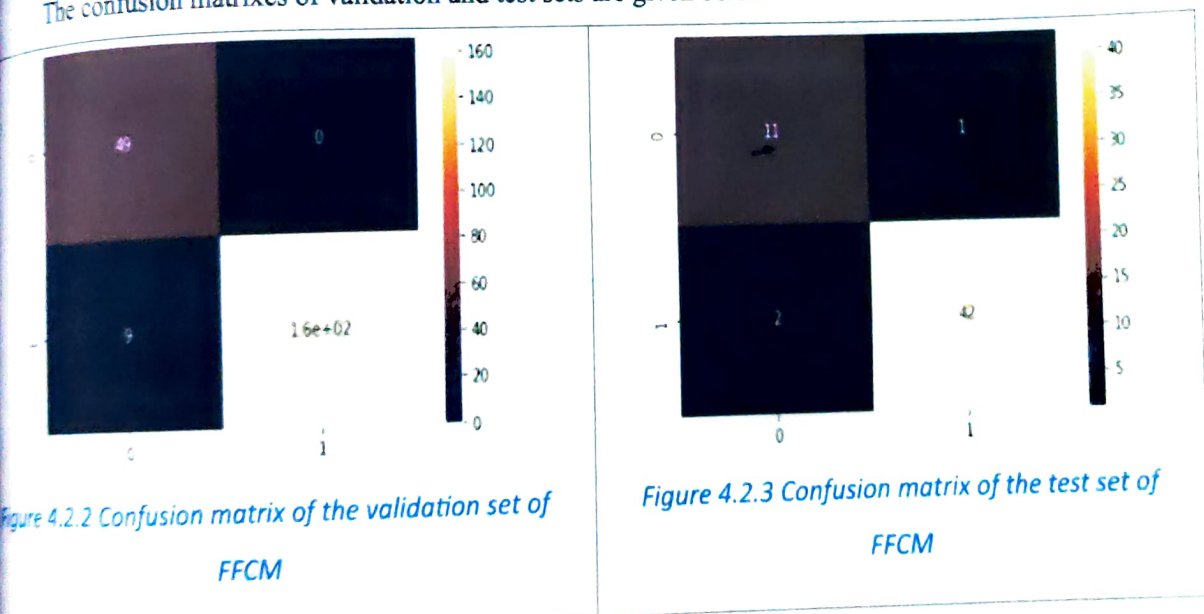


Figure 4.2.2 Confusion matrix of the validation set of FFCM

Figure 4.2.3 Confusion matrix of the test set of FFCM

The classification reports of the validation and test set are given below

	precision	recall	f1-score	support
BAD	0.84	1.00	0.92	49
FRESH	1.00	0.95	0.97	174
accuracy			0.96	223
macro avg	0.92	0.97	0.94	223
weighted avg	0.97	0.96	0.96	223

Figure 4.2.4 Classification report of the validation set of FFCM

	precision	recall	f1-score	support
BAD	0.85	0.92	0.88	12
FRESH	0.98	0.95	0.97	44
accuracy			0.95	56
macro avg	0.91	0.94	0.92	56
weighted avg	0.95	0.95	0.95	56

Figure 4.2.5 Classification report of the test set of FFCM

4.3 Output of FFRM

- **Mean Absolute Error:** - Absolute Error is nothing but the total error in our measurement. The Mean Absolute Error is measured by summing up all the absolute errors and dividing them by the total number of errors.

$$\text{Average MAE} = \frac{(\text{Sum Of } (|Y_i - X_i|) / (\text{Number of Errors}) + \text{Sum Of } (|Y_j - X_j|) / (\text{Number of Errors}) + \text{Sum Of } (|Y_k - X_k|) / (\text{Number of Errors}))}{3}$$

Here, i denotes "Shape", j denotes "Color" and k denotes the "Texture".

Figure.3.1: Mean Absolute Error Formula

The Average Mean Absolute Error for our model = 0.006478328295644295

- **Mean Squared Error:** - It is the mean of squared difference between target values and model predictions. We can measure the quality of an estimator through the term Mean Squared Error.

$$\text{Average MSE} = \left(\frac{1}{n} \sum_{i=1}^n (Y_i - \hat{Y}_i) + \frac{1}{n} \sum_{j=1}^n (Y_j - \hat{Y}_j) + \frac{1}{n} \sum_{k=1}^n (Y_k - \hat{Y}_k) \right) / 3$$

Here, n = total no of samples, Y represents the target values and \hat{Y} represents the model predictions and i denotes "Shape", j denotes "Color" and k denotes the "Texture".

Figure 4.3.2: Mean Squared Error Formula

The Average Mean Squared Error for our Model = 0.0016195524146293838

- **Root Mean Squared Error:** - It is the squared root of the mean of squared differences between the target values and model predictions. This term shows the differences between the observed or actual values and the predicted values.

$$\text{Average RMSE} = \left(\sqrt{\frac{\sum_{i=1}^n ((\text{Actual})_i - (\text{Predicted})_i)^2}{n}} + \sqrt{\frac{\sum_{j=1}^n ((\text{Actual})_j - (\text{Predicted})_j)^2}{n}} + \sqrt{\frac{\sum_{k=1}^n ((\text{Actual})_k - (\text{Predicted})_k)^2}{n}} \right) / 3$$

Here, i denotes "Shape", j denotes "Color" and k denotes the "Texture".

Figure 4.3.3: Root Mean Squared Error Formula

The Average Root Mean Squared Error of our model = 0.0402436630369227

- **Root Mean Squared Log Error:** - It is the squared root of the mean of squared differences between the log transferred target values and the log transferred model predictions.

$$\text{Average RMSLE} = \left(\sqrt{\frac{\sum_{i=1}^n (\log(\text{Actual})_i - \log(\text{Predicted})_i)^2}{n}} + \sqrt{\frac{\sum_{j=1}^n (\log(\text{Actual})_j - \log(\text{Predicted})_j)^2}{n}} + \sqrt{\frac{\sum_{k=1}^n (\log(\text{Actual})_k - \log(\text{Predicted})_k)^2}{n}} \right) / 3$$

Here, i denotes "Shape", j denotes "Color" and k denotes the "Texture".

Figure 4.3.4: Root Mean Squared Log Error Formula

The Average Root Mean Squared Log Error of our model = 3.2128027275890076

- **R2 Score:** - It indicates the degree of interrelation. It says about the variation of the dependent variables from independent variables.

$$\text{Average R Squared} = (A/B + C/D + E/F) / 3$$

$A = \sum_{i=1}^n (\widehat{Y}_i - \bar{Y})^2$. It is the sum of Squared Regression of a model.

$B = \sum_{i=1}^n (Y_i - \bar{Y})^2$. It is the total variance in the data.

\bar{Y} is the mean of Y values and \widehat{Y}_i is the predicted value of observation i for Y.

$C = \sum_{j=1}^n (\widehat{Y}_j - \bar{Y})^2$. It is the sum of Squared Regression of a model.

$D = \sum_{j=1}^n (Y_j - \bar{Y})^2$. It is the total variance in the data.

$E = \sum_{k=1}^n (\widehat{Y}_k - \bar{Y})^2$. It is the sum of Squared Regression of a model.

$F = \sum_{k=1}^n (Y_k - \bar{Y})^2$. It is the total variance in the data.

Here, i denotes "Shape", j denotes "Color" and k denotes the "Texture".

Figure 4.3.5 R2 Score Formula

The Average R2 score of our model = 0.9995107898512906

- **Adjusted R2:** - It is the modified version of the R Squared score. It is adjusted against the number of predictors.

$$\text{Adjusted } R^2 = 1 - \frac{(1-R^2)(N-1)}{N-P-1}$$

Here, N = Total sample Size, P = Number of Independent Variables.

Figure 4.3.6 Adjusted R2 Formula

The Adjusted R2 score of our model = 0.9994843460594685

Iterative Enhancement Model

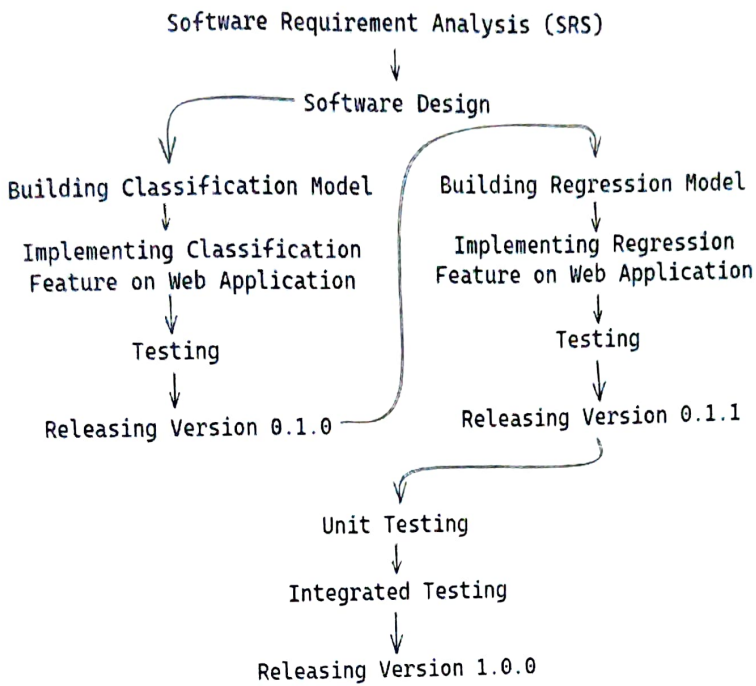


Figure 5.2.1 Data Flow Diagram

5.3 Design & Test Steps: -

Now, let's look into the internal mechanism of our system. We have stored the Regression and Classification model in the Database System. When the user will upload an image, it will be saved temporarily in the cloud. After running the requested model, the result will be generated and the user will get the required result. A diagram showing the High-Level Design is given in Figure.

High Level Design

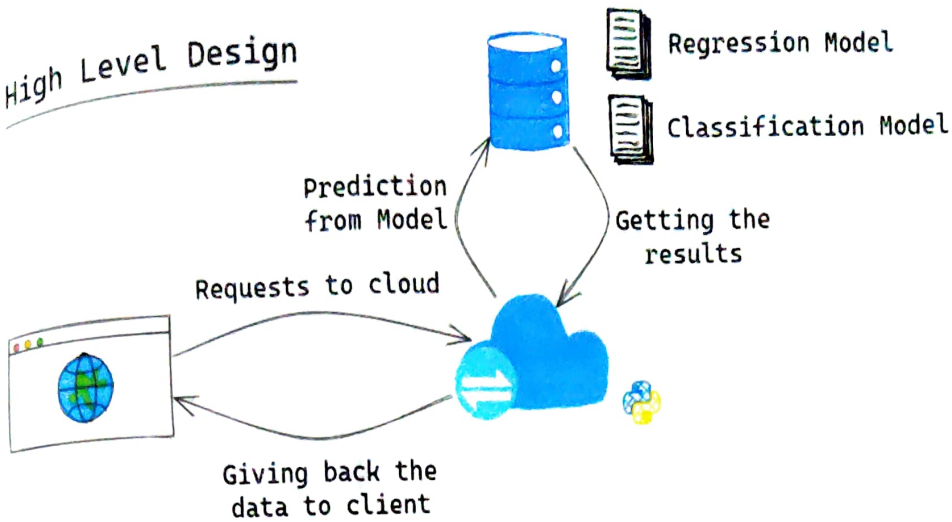


Figure 5.4.1 High Level Design

5.4 Web View

We have used Flask as the Backend and Bootstrap as the Frontend. There are 3 parts to our Web App. The first one is Classification Task. after uploading an image, our system will say whether the corresponding fruit item is consumable or not. The second one is the Regression part. This part will predict the 3 different ratings of the Hedonic System. And the average of these 3 fields Colour, Shape and Texture ratings will also be there. The final part is the Combined task of Classification and Regression. Some snapshots of the web app are given below:

- **Home Page:** - The Home Page of our Web App looks like the one below.

Fruit Image Classification and Regression Project

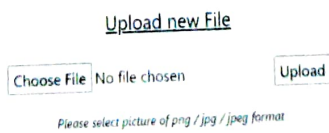
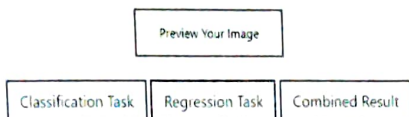


Figure 5.5.1 Home Page

• **After Successfully uploading an image by the user:** - When the user uploads an image successfully, then it will be sent to the server. And our App will look like the one below. We will have three options- Previewing the uploaded image, Classification, Regression and finally Combination of Classification and Regression tasks. Figure represents the above discussions.

Picture Uploaded to the server successfully



Meet the Developer | Fruit Freshness Measurement Team

Figure 5.5.2 Options for various Tasks

• **Classification Report:** - When the user wants to perform Classification, then our system will say like figure.

Fruit Image Classification Report



The Fruit Corresponding To The Given Image Is **FRESH**

Meet the Developer | Fruit Freshness Measurement Team

Figure 5.5.3 Classification Task

Regression Report: - After performing the Regression task, the page will look like the one below.

Fruit Image Regression Report



Hedonic Scale Ratings of The Given Image are:

Colour Rating: 5.05

Shape Rating: 5.08

Texture Rating: 5.39

Average Rating: 5.17

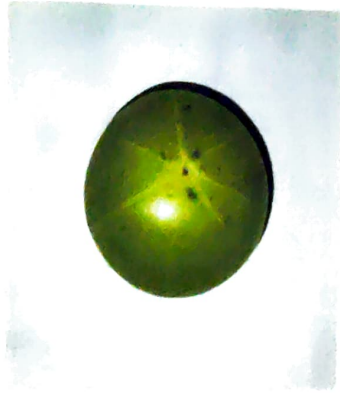
Wanna try another image? [Back To Home](#)

Meet the Developer | Fruit Freshness Measurement Team

Figure 5.5.4 Regression Task

Combined Report: - The page, after clicking Combined Task, will be as per figure.

Fruit Image Combined Report



1. Classification Report

The Fruit Corresponding To The Given Image Is **FRESH**

2. Regression Report

Hedonic Scale Ratings of The Given Image are:

Colour Rating: 8.5

Shape Rating: 8.51

Texture Rating: 8.5

Average Rating: 8.5

Wanna try another image? [Back To Home](#)

Meet the Developer | Fruit Freshness Measurement Team

Figure 5.5.5 Combined Task

Currently, we have not published our Web App in the cloud. It is running on our local server. In future, we will publish it in the cloud so that everyone can use the app.

6 Conclusion and Future Work

6.1 Conclusion

In this project we have created a new amla fruit dataset. We have also created a custom CNN model a DenseNet-121 and a Ridge Regression based model. The performances of the aforementioned neural networks are recorded. the final classification results for both the models show F1 scores of more than **80%** and the FFRM has RMSE score of **0.04024366303692277**.

6.2 Future Work

To develop a more robust and accurate fruit freshness assessment deep learning model, as a common deep learning practice, a large volume of source data is required. The data should include noises and pictures in different orientations.

In the future a cross platform application can be developed to give users more flexibility to use the app across multiple devices.

7 References

1. Jahanbakhshi, A., Kheiralipour, K., 2019. Carrot sorting based on shape using image processing and artificial intelligent. *J. Agric. Mach.* 9, 295–307.
2. Izadi, H., Kamgar, S., Raoufat, M.H., 2016. Tomato grading system using machine vision technology and neuro-fuzzy networks (ANFIS). *J. Agric. Mach.* 6, 49–59
3. Kheiralipour, K., Pormah, A., 2017. Introducing new shape features for classification of cucumber fruit based on image processing technique and artificial neural networks. *Food Process Eng.* 40, e12558.
4. Wang, S.H., Chen, Y., 2018. Fruit category classification via an eight-layer convolutional neural network with parametric rectified linear unit and dropout technique. *Multimed. Tools Appl.* 1–17.
5. Jahanbakhshi, Mohammad Momeny, Mahmoudi, Zhang, 2019. Classification of sour lemons based on apparent defects using stochastic pooling mechanism in deep convolutional neural networks
6. M. T. Chowdhury, M. S. Alam, M. A. Hasan and M. I. Khan, Vegetables detection from the glossary shop for the blind, *IOSR J. Electr. Electron. Eng.* 8 (2013), 43–53.
7. A. Danti, M. Madgi and B. S. Anami, Mean and range color features based identification of common Indian leafy vegetables. *Int. J. Sign. Proc. Image Proc. Pattern Recogn.* 5 (2012), 151–160.
8. Singla, A., Yuan, L., & Ebrahimi, T. (2016). Food/non-food image classification and food categorization using pre-trained GoogLeNet model. In *Proceedings of the 2nd International Workshop on Multimedia Assisted Dietary Management* (pp. 3–11).
9. Sukanya Wichchukit and Michael O'Mahony, 2014. The 9-point Hedonic scale and Hedonic ranking in food science: some reappraisals and alternatives.

DEEP LEARNING BASED DETECTION OF ABNORMAL HUMAN BEHAVIOUR

B. Tech. Project Report

By

Firhadweep Pramanick
Sombit Bose
Aisek Mondal
Sayantan Roy

Under Supervision of
Dr. Partha Ghosh



Department of Computer Sc. and Engineering

Government College of Engineering and
Ceramic Technology

Kolkata

May 2022

DEEP LEARNING BASED DETECTION OF ABNORMAL HUMAN BEHAVIOUR

A Project Report

*Submitted in partial fulfillment of the
requirements for the award of the degree
of*

Bachelor of Technology

In

Computer Sc. and Engineering

By

**TIRTHADWEEP PRAMANICK(GCECTB-L19-3011)
AVISEK MONDAL (GCECTB-R18-3005)
SOMBIT BOSE (GCECTB-R18-3028)
SAYANTAN ROY(GCECTB-R18-3025)**



Department of Computer Sc. and Engineering

**Government College of Engineering and
Ceramic Technology**

Kolkata

May 2022

DECLARATION

We hereby declare that the project entitled "DEEP LEARNING BASED DETECTION OF ABNORMAL HUMAN BEHAVIOUR" submitted for the B. Tech. (CSE) degree is our original work and the project has not formed the basis for the award of any other degree, diploma, fellowship or any other similar titles.

Name and Roll No. of the Students

Signature of the Students

1. Tirthadweep Pramanick (GCECTB-L19-3011)

Tirthadweep Pramanick

2. Sombit Bose (GCECTB-R18-3028)

Sombit Bose

3. Avisek Mondal (GCECTB-R18-3005)

Avisek Mondal

4. Sayantan Roy (GCECTB-R18-3025)

Sayantan Roy

Place: Kolkata

Date: 11/05/22



Government College of Engineering and Ceramic Technology

73, A. C. Banerjee Lane, Kolkata, West Bengal 700010

BONAFIDE CERTIFICATE

Certified that this project report titled **DEEP LEARNING BASED DETECTION OF ABNORMAL HUMAN BEHAVIOR** is the authentic work carried out by **Sombit Bose (Roll No: GCECTB-R18-3028)**, **Sayantana Roy (Roll No: GCECTB-R18-3025)**, **Avishek Monal (Roll No: GCECTB-R18-3005)** **Tirthadweep Pramanick (Roll No: GCECTB-L19-3011)** who carried out the project work under **my / our** supervision. Certified further, that to the best of my knowledge the work reported herein does not form part of any other project report or dissertation on the basis of which a degree or award was conferred on an earlier occasion on this or any other candidate.

Dr. P. Ghosh
SUPERVISOR

Assistant Professor
Department of Computer Science and Engineering
Government College of Engineering and
Ceramic Technology
Kolkata-700010

K. Saha 11.05.2022

Dr. K. Saha Roy
HEAD OF THE DEPARTMENT
Assistant Professor & Head

Department of Computer Science and Engineering
Government College of Engineering and Ceramic Technology
Kolkata-700010

External Examiner

1. Introduction

Human activity is the entire body or the different positions of the limbs . Abnormal Human Activity Recognition (Abnormal HAR) is very popular nowadays . However, it still remains a complex task due to complex issues such as sensor movement, placement etc. and how people perform their activities. Determining detailed activities is beneficial in human-centric applications, such as home care support, postoperative trauma rehabilitation, gesture detection, exercise, and fitness mainly related to HAR. Most of the person's daily tasks can be simplified or automated by the HAR system. Usually, HAR systems are based on either unsupervised or supervised learning. A supervised system requires pre-training using special datasets, but unsupervised systems have a set of rules. This literature survey paper surveys extensively the current progress made towards various activity recognition methods. Moreover, we provide a comprehensive analysis of three techniques, namely wearable devices-based approach, pose based approach, and smartphone sensors. The first one uses sensing devices to collect data from the sensors whereas smartphone sensors take input from the smartphone sensors such as gyroscope and accelerometer and in the last one activity is classified using pose estimation that require the estimation of body key points through neural network. The HAR system can be subdivided into three levels, as follows as given in the picture.

1.1 Project overview/specifications:

In this project we have made a new dataset **Anomalous Action Detection Dataset (Ano-AAD)** to study anomalous behavior using **deep learning models** like **convolutional LSTM-GRU** and **Long Recurrent Convolutional Network (LRCN)**. Our dataset is divided in 2 parts 1. Anomaly videos and 2. Normal videos. Total number of videos in the dataset 392. Anomaly part has 351 videos and there are 41 normal videos. Total number of class is 9. The name of the classes are in anomaly section :

Burglary (49 videos, 78 minutes), Fighting (50 videos, 85 minutes), Explosion (49 videos, 72 minutes), Fire raising (52 videos, 96 minutes), Ill treatment (32 videos ,68 minutes), Traffic Irregularities (5 videos, 3 minutes), Violence (26 videos, 37 minutes), Arrest (50 videos, 93 minutes), Attack (38 videos, 71 minutes). LRCN has achieved 68% testing accuracy and Convolutional LSTM has achieved 73% testing accuracy.

As of now, our resources are not enough to compute that huge amount of data. So our Accuracy is low.

1.2 Hardware Specification

GPU: 1xTesla K80 , compute 3.7, having 2496 CUDA cores , 12GB GDDR5 VRAM

CPU: 1xsingle core hyper threaded Xeon Processors @2.3Ghz i.e(1 core, 2 threads)

RAM: ~12.6 GB Available

Disk: ~33 GB Available

1.3 Software Specification

Google Colab is the software system that we used for working on our own Dataset.

2. LITERATURE SURVEY

There are **three** approaches to **HAR**

- (1) **Pose Based Approach** (Vision Based Approach):takes the pixel based coordinates of the body's key points used for activity recognition and feature extraction.
- (2) **Smartphone Sensor Based**:Here sensors are mounted on smartphones.
- (3) **Wearable Sensor Based**:Here sensors are mounted on the human body.They Collect data from the Human Body.

As per our research project topic we will be focusing on vision based approach Domain

2.1 Existing Methods

There are mainly three deep learning methodologies:-

1. **Generative Methods(unsupervised)**[e.g. Autoencoders, GANs]
2. **Discriminative Methods(supervised)**[e.g. DNN,CNN,RNN,RNN+LSTM]
3. **Hybrid Methods(integrates both)**

These methods are applied on other kinds of popular deep learning datasets.

2.2 Related Works

In recent years, recognition and understanding of human behavior have received much attention.Different techniques have been used to understand patterns of behavior activity and to understand the scene. In this work, we have **reviewed** some selected papers mainly from **201821**.There are related works (mostly related or close to HAR anomalies) on motion detection, face detecting,shoplifting, tracking , loiter detecting, abandoned luggage detecting , crowd behavior , and snatch detecting algorithms . Convolutional Neural Networks (CNN) have shown a remarkable performance in computer vision in the last recent years. Researchers used Alex Net, VGG-Net, Res Net , Inception-like pre-trained models to increase accuracy. Particularly 3DCNN focuses on extracting spatial and temporal features from videos. Researchers also used Autoencoders, RNN, LSTM, GAN like systems combined with new learning methods like Transfer learning and meta learning. They also used combined architecture models to achieve accuracy.

2.2.1 Features of Pretrained Network Model

Table -1: Features of pretrained network model[11]

Network Architecture	Features	Accuracy	Parameters
AlexNet	Deeper	84.70%	62 million
VGGNet	Fixed Size Kernel	92.30%	138 million
ResNet	Skip short connections	95.51%	60.3 million
Inception	Parallel wider kernels	93.30%	6.4 million

2.2.2 Considered Datasets in our survey:

We have done an extensive survey how researchers worked on anomaly related Datasets like UCF-Crime and it's subsets like **HR-Crime** , **XD-Violence**, **UCSD Anomaly Detection Dataset(crowd anomaly)**, **Shanghai-Tech**, **LAD(Large anomaly Dataset)**, **Avenue**, **CAVIAR**,**PETS-2016** etc. and we have listed their methods and achieved accuracy.

Waqas Sultani et al.[1] from University of Central Florida made the **UCF-Crime** dataset. It has a total of **1900** videos in **13** classes like **Abuse**, **Arson** etc. and a total video length of **128 hours**.

2.2.3 Mascorro's concept to analyze pre crime scenes

Mascorro et al. [2] used 3D-CNN to detect abnormal behavior on shoplifting cases. They introduced a new concept to analyze pre-crime scenes:-

- 1) **Strict Crime Moment (SCM):** The SCM is the video segment where a person commits shoplifting.
- 2) **Comprehensive Crime Moment (CCM):** It is the precise moment when an ordinary person can detect the suspect's behaviour. Unsuccessful attempts or reorder things is also noted in this step.
- 3) **Crime Lapse (CL):** The CL is the entire video segment where a crime happens. If we remove the Lapse from the video, it will be impossible to determine that there is a criminal act in the video.

4) **Pre-crime Behavior (PCB):** The PCB contains what happens from the first appearance of the suspect to the beginning of CCM.

2.2.4 Some popular works Done by other Researchers:

- **Sultani et al.** [1] combined deep neural networks with multiple instance learning to classify real-world anomalies, such as accident, explosion, fighting, abuse, arson, etc. Their AUC is 75.41%. They used C3D and TCNN Architecture and achieved an accuracy of 23.0% and 28.4% respectively.
- **Sabokrou et al.** [4] used CNNs with 3D deep autoencoders in order to detect anomalies in videos.
- **Ullah et al.** [3] used an approach where video is fed into a pre-trained ResNet50 model to extract features; a feature vector is generated from a 15 consecutive frames of the video; the acquired feature vector is passed to a multilayer Bi directional LSTM to recognise anomalous events. They achieved an accuracy of 85.53%. The VGG-19 with multi-layer BD-LSTM achieved 82% accuracy on UCF Crime. while the inception V3 with multi-layer BD-LSTM reached 80% accuracy on UCF-Crime.
- **Hasan et al.** [5] proposed a convolutional auto-encoder (Conv-AE) framework for the reconstruction of the scenes, and then computed the reconstruction costs for the identification of anomalies.
- **Dubey et al.** [6] proposed method 3D deep Multiple Instance Learning with ResNet (MILR) along with the new proposed ranking loss function. They achieved an AUC of 76.67% with that new ranking loss function.
- **Nasaruddin et al.** [7] In their proposed method, a robust background subtraction for extracting motion, indicating the location of attention regions were employed. The resulting regions are finally fed into a 3D CNN. They took the advantage of C3D (Convolution 3-dimensional), to completely exploit spatiotemporal relation, a deep convolutional network is developed to distinguish between normal and abnormal events. Their locality learning model achieved an accuracy of 99.25 percent

2.2.5 Datasets and Results of various Datasets:

Table 2:- AUC Results Based on Publicly Available Codes [10]

Methods	Learning Type	UCSD Ped2	ShanghaiTech	UCF Crime	Avenue	LAD
Sparse	Unsupervised	-	-	65.51	-	50.31
ConvAE	Unsupervised	-	-	50.60	-	53.24
GMM	Unsupervised	-	-	56.43	-	41.02
Stacked RNN	Unsupervised	52.58	67.66	-	70.09	49.42
U-Net	Unsupervised	71.26	56.69	-	55.26	53.96
MNAD	Unsupervised	46.72	51.13	56.20	73.58	45.84
OGNet	Unsupervised	69.08	69.26	-	63.23	55.07
DeepMIL	Weakly supervised	90.09	86.30	75.41	87.53	70.18
MLEP	Weakly supervised	-	73.40	50.01	89.20	50.57
AR-Net	Weakly supervised	93.64	91.24	74.36	89.31	79.84

Results given in Anomaly Detection in Video Sequences: A Benchmark and Computational Model by Boyang et. al IET Research Journal Papers arxiv preprint June 2021 [10]

3.OUR WORK

3.1 Our Own Dataset

We have made a new dataset to detect anomalous action and named it **Anomalous Action Detection Dataset(Anno-AAD)** to detect anomalous behaviour. Our dataset is divided in 2 parts

1. **Anomaly videos** and
2. **Normal videos.** (41 videos, 62 minutes)

Total **number** of videos in the dataset **392**. **Anomaly** part has **351** videos and there are **41 normal videos**. Total **number** of classes is **9**. The name of the classes are in anomaly section : **1.Burglary**(49 videos,78 minutes) **2.Fighting**(50 videos, 85 minutes) **3.Explosion**(49 videos, 72 minutes) **4.Fire raising**(52 videos, 96 minutes) **5.Ill treatment**(32 videos, 68 minutes) **6.Traffic irregularities**(5 videos,3 minutes) **7.Violence**(26 videos, 37 minutes) **8.Arrest**(50 videos, 93 minutes) **9.Attack**(38 videos, 71 minutes)

Anno-AAD Dataset:-

Total video length of the anomaly part is 10 hours 03 minutes. Total video length of the normal part is 62 minutes. Total video length of the criminal action detection dataset is 11 hours 05 minutes. Average length of a video is 1 minute 42 seconds.

3.2 Our own model and used libraries

Model

We have made our own convolutional long Short Term Memory Gated Recurrent Unit model (conv-LSTM-GRU) and Long Recurrent Convolutional Network (LRCN) model to predict.

Used python libraries:

- 1.os
- 2.cv2
- 3.math
- 4.random
- 5.numpy
- 6.tensorflow
- 7.collections
- 8.matplotlib
- 9.moviepy
- 10.matplotlib
- 11.sklearn

3.3 Dataset Preprocessing

We perform Data Preprocessing in the dataset mainly to reduce the number of computations and enhance easy training of our deep learning model. The following are done:-

1. Reading the video files from the dataset and resize the frames to a fixed width and height
2. Normalizing the data range in [0,1] by dividing 255.

- Here **frame size** is 64*64(height*width)
- **Sequence length** is 20
- We define **frames_extraction()** that will create a list containing the resized and normalized frames of a video whose path is passed as argument. The function will read the video frame by frame, but not all frames are added to the list as we will only need an evenly distributed sequence length of frames.
- **The dataset is split into Train(75%) and Test(25%)**

3.4 Conv-LSTM-GRU

Data collected over successive periods of time are characterized as a **Time Series**. In such cases, an interesting approach is to use a model based on LSTM (Long Short Term Memory), a Recurrent Neural Network architecture. In this kind of architecture, the model passes the previous hidden state to the next step of the sequence. Therefore holding information on previous data the network has seen before and using it to make decisions. In other words, the data order is extremely important.

When working with images, the best approach is a CNN (Convolutional Neural Network) architecture. The image passes through Convolutional Layers, in which several filters extract important features. After passing some convolutional layers in sequence, the output is connected to a fully-connected Dense network. In our case, sequential images, one approach is using Conv LSTM layers. It is a Recurrent layer, just like the LSTM, but internal matrix multiplications are exchanged with convolution operations. As a result, the data that flows through the Conv LSTM cells keeps the input dimension.

GRUs are very similar to Long Short Term Memory (LSTM). Just like LSTM, GRU uses gates to control the flow of information. They are relatively new as compared to LSTM. This is the reason they offer some improvement over LSTM and have simpler architecture. Thus we attempt to combine the features of Conv-LSTM and GRU to create a new model to do a prediction over a video as a Time Series Data of a set of frames.

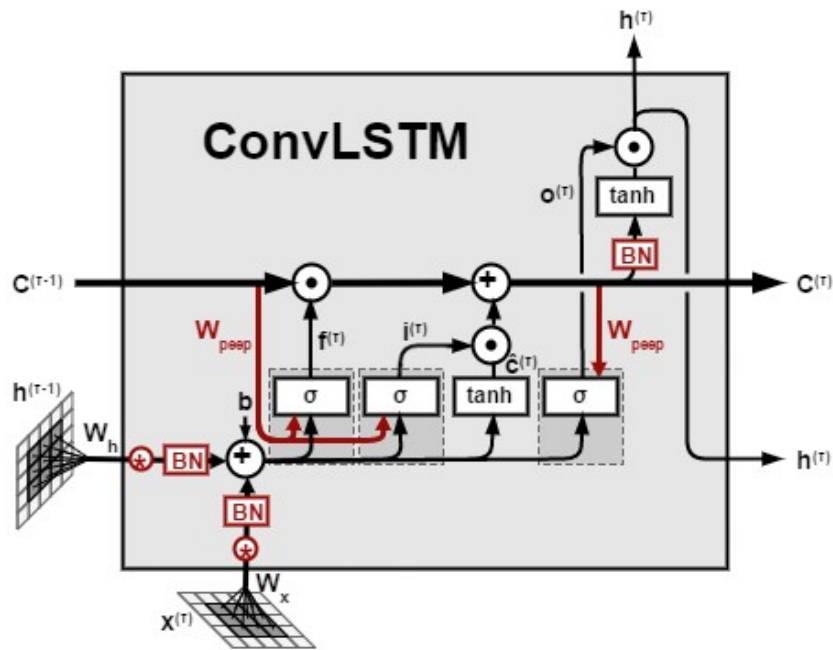


Fig 1: Convolutional Long Short Term Memory [9]

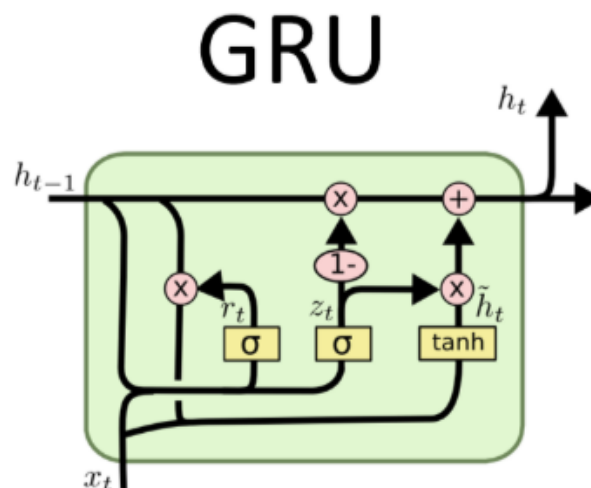


Fig 2: Gated Recurrent Unit

3.5 Long Recurrent Convolutional Network (LRCN)[8]

We propose Long-term Recurrent Convolutional Networks (LRCNs), a class of architectures leveraging the strengths of rapid progress in CNNs for visual recognition problems, and the growing desire to apply such models to time-varying inputs and outputs. LRCN processes the (possibly) variable-length visual input (left) with a CNN (middle-left), whose outputs are fed into a stack of recurrent sequence models (LSTMs, middle-right), which finally produce a variable-length

prediction (right). Both the CNN and LSTM weights are shared across time, resulting in a representation that scales to arbitrarily long sequences.

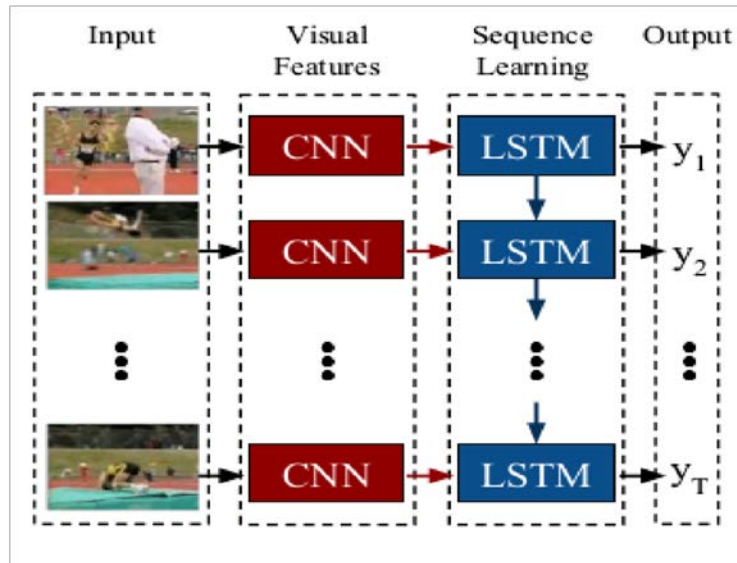


Fig 3: LRCN [8]

3.6 Model Description

3.6.1 Model Description: CONV-LSTM-GRU

Fig 4: Number of parameters in CONV-LSTM-GRU

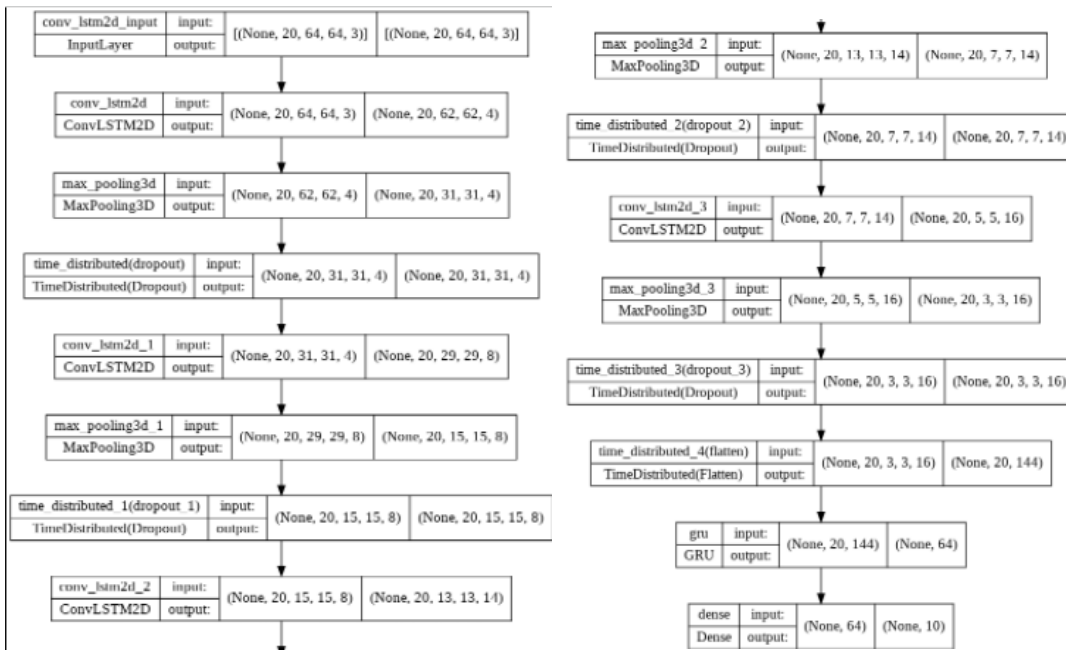


Fig 5 : Design of the CONV-LSTM-GRU model

3.6.2 Model Description:Our Model LRCN

Layer (type)	Output Shape	Param #
time_distributed_6 (TimeDistributed)	(None, 20, 64, 64, 16)	448
time_distributed_7 (TimeDistributed)	(None, 20, 16, 16, 16)	0
time_distributed_8 (TimeDistributed)	(None, 20, 16, 16, 16)	0
time_distributed_9 (TimeDistributed)	(None, 20, 16, 16, 32)	4640
time_distributed_10 (TimeDistributed)	(None, 20, 4, 4, 32)	0
time_distributed_11 (TimeDistributed)	(None, 20, 4, 4, 32)	0
time_distributed_12 (TimeDistributed)	(None, 20, 4, 4, 64)	18496
time_distributed_13 (TimeDistributed)	(None, 20, 2, 2, 64)	0
time_distributed_14 (TimeDistributed)	(None, 20, 2, 2, 64)	0
time_distributed_15 (TimeDistributed)	(None, 20, 2, 2, 64)	36928
time_distributed_16 (TimeDistributed)	(None, 20, 1, 1, 64)	0
time_distributed_17 (TimeDistributed)	(None, 20, 64)	0
lstm (LSTM)	(None, 32)	12416
dense_2 (Dense)	(None, 10)	330

=====
 Total params: 73,258
 Trainable params: 73,258
 Non-trainable params: 0
 =====
 Model Created Successfully

Fig 6: Number of parameters in LRCN

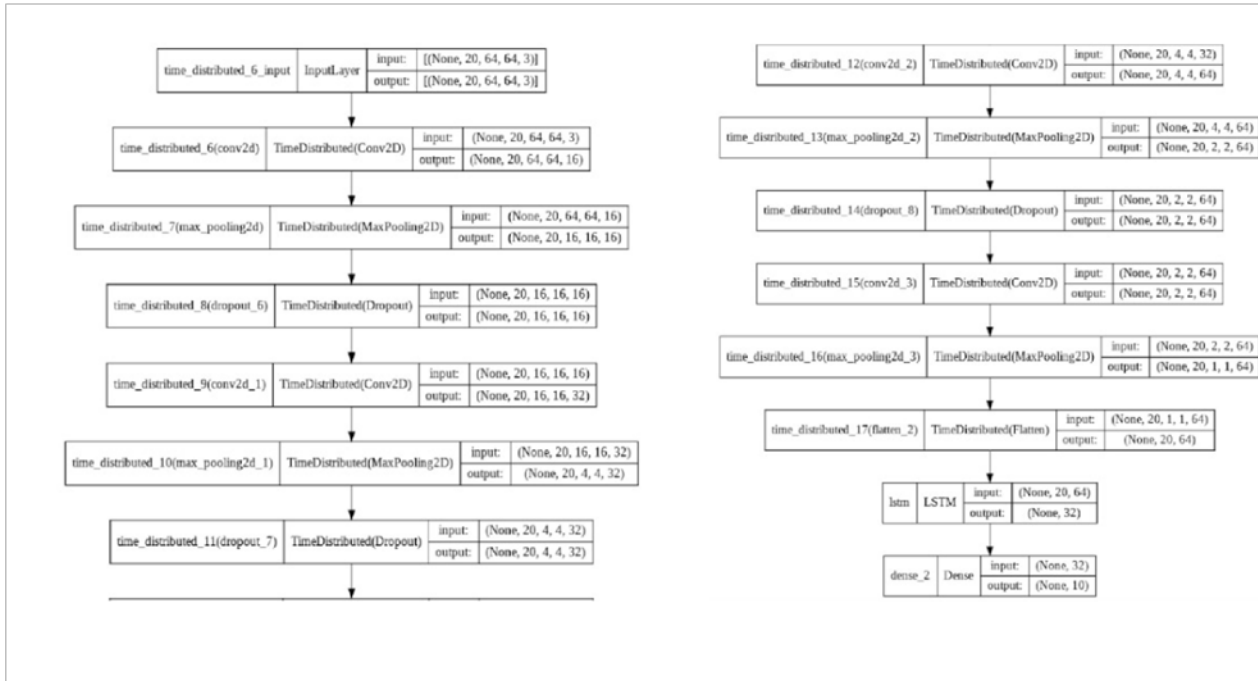


Fig 7: Design of LRCN Model

3.7 Training Parameters

- For LRCN, the model was trained with **adam** optimizer, categorical crossentropy as loss function with batch size=4 and epochs=90.
- For CONV-LSTM-GRU, the model was trained with **adam** optimizer, categorical crossentropy as loss function with batch size=4 and epochs=30.

4. Results of our work

4.1 Results on our Dataset

LRCN have achieved 86% testing accuracy and Conv-LSTM-GRU have achieved 84.5% testing accuracy on the dataset.

4.2.1 Conv-LSTM-GRU: Total loss vs validation loss graph

fig 8: Conv-LSTM-GRU :Total loss vs validation loss graph

4.2.2 Conv-LSTM-GRU: Total Accuracy vs Total validation Accuracy graph

fig 9: Conv-LSTM-GRU: Total Accuracy vs Total validation Accuracy graph

4.2.3 LRCN: Total loss vs validation loss graph

fig 10: LRCN :Total loss vs validation loss graph

4.2.4 LRCN: Total Accuracy vs Total validation Accuracy graph

fig 11: LRCN :Total Accuracy vs Total validation Accuracy graph

5. Evaluation of Models

5.1 AUC and ROC Curve

fig 12: Conv-LSTM-GRU: AUC and ROC plot

fig 13: LRCN: AUC and ROC plot

5.2 Confusion matrix, Precision, Recall and F1-Score

fig 14: Conv-LSTM-GRU: Confusion matrix, Precision, Recall and F1-Score

fig 15: Conv-LSTM-GRU: Confusion matrix, Precision, Recall and F1-Score

6. Challenges in HAR

- Modeling and Analyzing the interaction between human-human and human-object is a challenging issue.
- HAR systems are not yet able to detect and recognize various gestures under different background conditions and are not tolerant with the scalability and growth of gestures.
- Some activities are difficult to model because of their complex structure as well as the big variation in ways of performing the same activity.
- Limitation of scenes and human movements in 3D space, In addition, detection and extracting individuals from image sequences is another limitation that requires experience and knowledge. Therefore, when large volumes of data are processed at once, a realtime HAR system can achieve better results.
- Privacy problems- a person will be uncomfortable or forced to be monitored all times.

6. Conclusions and Future Scope

Conclusions:

(i) A literature survey has been completed by us on some selected research papers published mainly in 2018-2021 on various HAR technologies. We have categorized these

technologies into three main categories, smartphone sensors, and wearable sensors and vision based approaches. We studied that the emergence of wearable technology has become a better solution for providing support services to people. However, the system still has some limitations. Some actions have low recognition rates. Further research is needed to improve accuracy and increase the number of activities detected by the system. The main drawback of this CNN-based approach is the training time required is very large. As principle work is here to spot different human activities from the videos, the dataset used for training consists of actions with different classes. CNN-based methods undergo high computations for these videos.

(ii) Due to limited availability of computational power we had to train our model with less epochs and so our accuracy obtained is low.

Future Scope:

- Overcome the previously discussed Challenges to HAR.
- Selection of a deep learning model with comparable accuracy to detect abnormal behavior using the Human Activity Recognition System.
- Future models will use transfer learning, Meta learning, new pre-trained CNN models and combined deep learning models to increase accuracy.

7. References:

1. Sultani, W., Chen, C., Shah, M. (2018). Real-world anomaly detection in surveillance videos. In *Proceedings of the IEEE conference on computer vision and pattern recognition* (pp. 6479-6488).
2. Martínez-Mascorro, G. A., Abreu-Pederzini, J.R., Ortiz-Bayliss, J. C., Terashima-Marín, H. (2020). Suspicious behavior detection on shoplifting cases for crime prevention by using 3D convolutional neural networks. *arXiv preprint arXiv:2005.02142*.
3. Ullah, W., Ullah, A., Haq, I. U., Muhammad, K., Sajjad, M., Baik, S.W. (2021). CNN features with bi-directional LSTM for real-time anomaly detection in surveillance networks. *Multimedia Tools and Applications*, 80(11), 16979-16995.
4. M. Sabokrou, M. Fayyaz, M. Fathy, and R. Klette, "Deep-cascade: Cascading 3d deep neural networks for fast anomaly detection and localization in crowded scenes," *IEEE Transactions on Image Processing*, vol. 26, pp. 1992-2004, 2017.
5. Hasan, M., Choi, J., Neumann, J., Roy-Chowdhury, A. K., & Davis, L. S. (2016). Learning temporal regularity in video sequences. In *Proceedings of the IEEE conference on computer vision and pattern recognition* (pp. 733-742).
6. Dubey, S., Boragule, A., Jeon, M. (2019, October). 3D ResNet with Ranking Loss Function for Abnormal Activity Detection in Videos. In *2019 International Conference on Control, Automation and Information Sciences (ICCAIS)* (pp. 1-6). IEEE.
7. Nasaruddin, N., Muchtar, K., Afdhal, A., Dwiyanoro, A. P.J. (2020). Deep anomaly detection through visual attention in surveillance videos. *Journal of Big Data*, 7(1), 1-17.
8. Donahue, J., Anne Hendricks, L., Guadarrama, S., Rohrbach, M., Venugopalan, S., Saenko, K., & Darrell, T. (2015). Long-term recurrent convolutional networks for visual recognition and description. In *Proceedings of the IEEE conference on computer vision and pattern recognition* (pp. 2625-2634).
9. <https://medium.com/neuronio/an-introduction-to-convlstm-55c90lutional%20lstm%20ARXIV25563a7>

10. Wan, B., Jiang, W., Fang, Y., Luo, Z., & Ding, G. (2021). Anomaly detection in video sequences: A benchmark and computational model. *arXiv preprint arXiv:2106.08570*.
11. Begampure, S., Jadhav, P. (2021). Intelligent video analytics for human action detection: a deep learning approach with transfer learning. *International Journal of Computing and Digital System*.

PROJECT REPORT ON
**EFFECT OF Cr₂O₃ AND B₂O₃ ON THE DENSIFICATION AND
MICROSTRUCTURAL CHARACTERISTICS OF ALUMINA CERAMIC**

A THESIS SUBMITTED IN PARTIAL FULFILLMENT OF THE REQUIREMENTS FOR THE
DEGREE OF

BACHELOR OF TECHNOLOGY

IN

CERAMIC TECHNOLOGY

By

DIPIKA SARKAR

Roll No.-GCECTB-R15-1011

Reg. No.-151130110088 of 2015-16

&

MD SAFIQL ISLAM

Roll No.-GCECTB-R15-1013

Reg. No.-151130110090 of 2015-16

Under the guidance of

Dr. Kaberi Das

Department of Ceramic Technology

Govt. College of Engineering & Ceramic Technology

73, A.C Banerjee Lane, Kolkata-700010



2019

DECLARATION

It is hereby stated that the Project Report entitled “**Effect of Cr₂O₃ and B₂O₃ On The Densification And Microstructural Characteristics Of Alumina Ceramic**” which is submitted by us in partial fulfillment of the requirements for the degree of B. Tech in Ceramic Technology at Govt. College of Engineering & Ceramic Technology which is under the West Bengal University of Technology, Kolkata, West Bengal comprises only our original work done under the guidance of Dr. Kaberi Das, Asst. Prof., Dept. of Ceramic Technology, Govt. College of Engineering & Ceramic Technology, Kolkata-700010. Due acknowledgement has been made in the text to everyone concerned and detailed information of every literature cited in this report has been provided in the References section.

.....

Dipika Sarkar

(Roll No.-GCECTB-R15-1011 & Reg. No.-151130110088 OF 2015-16)

&

.....

Md Safiqul Islam

(Roll No. GCECTB-R15-1013 & Reg. No. 151130110090 of 2015-16)

Final year students of B. Tech, Ceramic Technology

Govt. College of Engineering & Ceramic Technology, Kolkata-700010

Dated-



Government College of Engineering & Ceramic Technology

(An Autonomous Institute affiliated to WBUT)

**Government of West Bengal
73, Abinash Chandra Banerjee Lane, Kolkata-700010, India**

Tele/Fax- +91 33 2370 1264, E- mail - gcect@rediffmail.com

30.04.2019

TO WHOM IT MAY CONCERN

This is to certify that the thesis entitled, “**Effect of Cr₂O₃ and B₂O₃ Addition on The Densification and Microstructural Characteristics of Alumina Ceramics**” submitted by **Dipika Sarkar (GCECTB-R15-1011) & Md Safiqul Islam (GCECTB-R15-1013)** in partial fulfillment of the requirements for the award of Bachelor of Technology Degree in Ceramic Technology at Govt. College of Engineering & Ceramic Technology, an autonomous College under MAKAUT, Kolkata, West Bengal, is an authentic work carried out by them under my supervision and guidance.

To the best of my knowledge, the matter embodied in the thesis has not been submitted to any other University / Institute for the award of any Degree or Diploma.

Dr. Kaberi Das,

Assistant Professor,

Dept. of Ceramic Technology.

ACKNOWLEDGEMENT

We earnestly thank our project supervisor & guide Dr. Kaberi Das (Asst. Professor, Dept. of Ceramic Technology, GCECT, Kolkata) for her constant advice, follow up, hard work, literatures & most important of all the encouragement which she gave us throughout the course of this project work which started in August 2018 & ended in May 2019. There are hundreds of concepts, skill of using different machines, technique of thinking deeply, discussing productively & documenting impressively which we learned while working under her & which we will cherish for a lifetime.

We express our gratitude to Dr. R. Sen (HOD), Dr. S. Patra & Dr. T. K. Bhattacharyya, Prof. P. Guha who are professors at Dept. of Ceramic Technology of this college for giving us suggestions and letting us work in their laboratories. We thank our respected principal Dr. Krishnendu Chakraborty for his encouragement.

We thank Asst. Professor Mr. Partha Haldar (Mechanical Engg.), Ram Karan (research fellow), and Pameeli Pal (research fellow) for support and encourage us by giving his valuable time.

We thank Mr. Rahul Mitra of mechanical workshop and Mr. Jiban Dey for assisting us every day in laboratory without whose presence & helping hands we wouldn't have completed this work.

Lastly we thank everybody who helped us but whose name we forgot to mention here.

CONTENTS

	Page No.
1. INTRODUCTION	6-7
2. LITERATURE REVIEW	8-41
3. PLAN OF THE WORK	42
4. EXPERIMENTAL WORK	43-50
5. RESULT & DISCUSSION	51-62
6. SUMMARY	63-64
7. REFERENCES	65-69

1. INTRODUCTION

Alumina is one of the more widely used and studied advanced ceramic materials. The relative abundance & low cost of the material resources is advantageous for commercial application. Availability of the material in highly purified grades makes it well studied in material research. Alumina based ceramics show high values of refractoriness, hardness, strength & resistances to chemical attack.

Sintering of alumina & alumina based ceramic has been the subjects of many investigations. It is well known that firing temperatures above 1600°C is needed if pure alumina is to be sintered to high density. It has been shown that some additions allows the sintering temperature to be lowered, resulting in a densifications to 90% to 95% of theoretical density.

There are two general approaches to enhancing sintering kinetics or lowering the sintering temperature for ceramics. The first is by improving powder processing that means to use fine starting powders and to eliminate agglomerates in the green preforms. The second approach is to use sintering aids or additives. Additives in solid solution can enhance diffusion and hence sintering by increasing defect population, while additives forming a liquid phase can facilitate particle rearrangement & solution reprecipitation ^[27].

Most frequently used additives are MgO, silicates compound such as clay, talc or various silicates mixture, transitional metal oxides such as TiO₂, MnO₂. The effect of the additions is connected to an enhancement of ions mobility caused by various phenomena such as formation of a liquid phase or creation of lattice vacancies.

Chromia (Cr₂O₃) has long been used to improve the physical properties of alumina. Cr₂O₃ forms a solid solution with Al₂O₃ over the full range of compositions. Addition of Cr₂O₃ was formed to increase the hardness, tensile strength & thermal shock resistance of Al₂O₃.

Boron containing alumina materials have attracted special attention due to stable crystalline compound aluminum borate ($9\text{Al}_2\text{O}_3 \cdot 2\text{B}_2\text{O}_3$), orthorhombic crystalline structure & a density of 2.93 gm/cc when it is synthesized from end members of the binary system by conventional ceramic processing techniques, a porous material of a low bulk density having whisker like grain morphology can be obtained. This compound has a high melting point of 1950°C & it is quite stable in oxidizing atmosphere up to 1700°C . Such good properties along with easy & cheap processing means make this materials a potential candidate for filtration of molten materials, high temperature thermal insulation, support for catalytic reactions, filtration of particulate from diesel engine exhaust gases & filtration of hot corrosion gases in various industrial processes ^[43].

In this work, two additives were selected for alumina sintering, one solid solutions forming additives Cr_2O_3 & another eutectic compound forming additives B_2O_3 . The effect of these oxides on the sintering characteristics, crystalline phase development the microstructural of the alumina ceramics were studied.

2. LITERATURE REVIEW

2.1 LITERATURE REVIEW ON $\text{Al}_2\text{O}_3\text{-Cr}_2\text{O}_3$:

Alumina (Al_2O_3) is one of the most widely used ceramic materials because of its excellent physical and thermo-mechanical properties. Aluminum oxide is a major engineering material. A wide variety of ceramic processing methods can be applied including machining or net shape forming to produce a wide variety of size and shapes of the components. Alumina is an oxide ceramic, formed in almost all cases by conventional powder forming. In essence, form a shape from the powdered ceramic (dry or wet), dry the shape (if it was wet formed), rebind if it was formed with a binder, then densify by solid-state sintering in a furnace. In special cases alumina is formed by unconventional powder forming, or non-powder forming methods.

According to the **Ruys, Andrew** et. al. ^[1] the key ceramic engineering principles that underlie alumina ceramic technology. Processing of alumina ceramics includes — forming, and sintering; structure of the various alumina polymorphs from a crystallographic perspective; properties of alumina ceramics (mechanical, electrical, and thermal). Specifically the three key reasons for the dominance of alumina in the global advanced ceramics industry are -

- 1) Alumina has a set of very industrially valuable properties.
- 2) High-quality alumina raw material is abundant and inexpensive.
- 3) Alumina can be pressure less sintered to full density in air.

Aside from its impressive mechanical, electrical, and chemical inertness properties, the main reason for the great success of alumina commercially is its low production cost, for a material of such outstanding properties. Alumina is unique in combining a low cost with a very high refractoriness. Its melting point is around 2050°C . There is great variation in the reported melting point of alumina within the $2000\text{--}2100^\circ\text{C}$ range, depending on the method used and the alumina tested, but it is approximately in the mid-2000s. The maximum use temperature of pure alumina is 1750°C which is above virtually all common industrial processes.

It is significantly above the 1540°C melting point of steel, well above the sintering temperature of all clay-based ceramics, and well above the processing temperature of most glass formulations. This combined with the chemical inertness of alumina make it one of the leading refractory materials in the world. Alumina of varying purity levels is a standard liner in most high-temperature kilns. In addition with alumina, it can be readily joined to different oxide (like chromium oxide which has been mixed and discussed in this project) using different process (like solid state sintering) showing improved properties.

Doh-Hyung Riu et. al. [2] reported that the effects of chromia (Cr_2O_3) additions on the microstructural evolution and the mechanical properties of alumina (Al_2O_3) were investigated. When small amounts (<5 mol. %) of Cr_2O_3 were added in samples hot pressed at 1500°C, the grain size distribution became bimodal; large plate like grains were dispersed in a relatively small grained matrix. When a small amount of Cr_2O_3 (2mol. %) was added, the grains became larger and bi-modal in size distribution. The large grains had plate like shape and were composed of a core region that is free of Cr^{3+} and a surrounding shell region rich in Cr^{3+} . The high diffusion rate of Cr^{3+} ions through the surface of alumina was attributed to this microstructural evolution. The mechanical properties of the specimens were strongly influenced by this microstructural change. The hardness and the elastic modulus also increased, however, the fracture strength decreased by the addition of Cr_2O_3 . The effect of chromium oxide is so significant as to decrease the sintered density of the alumina ceramics. This is correlated with the influence of Cr_2O_3 in increasing the dihedral angle. As a result, the distinct deterioration of the mechanical properties of alumina ceramics is observed.

H. Tomaszewski et. al. [3] investigated that the effect of Cr_2O_3 additions on the penetration of the intergranular phase between alumina grains of 96 wt% alumina ceramics has been investigated by applying the principles of quantitative metallography. From micro-sections, values of the true dihedral angle have been measured. Cr_2O_3 additions increased the dihedral angle and decreased the density of alumina ceramics. As a result, distinct deterioration of the mechanical properties of alumina ceramics was observed. This study indicates a disadvantageous effect of Cr_2O_3 on the sintering of alpha-alumina in the presence of a liquid phase. The effect of chromium oxide is so significant as to decrease the sintered density of the alumina ceramics. This is correlated with the

influence of Cr_2O_3 in increasing the dihedral angle. As a result, the distinct deterioration of the mechanical properties of alumina ceramics is observed. That Chromia (Cr_2O_3) has long been used to improve the physical properties of Al_2O_3 . Different from the other additives mentioned above, Cr_2O_3 forms a solid solution with Al_2O_3 over the full range of compositions. The addition of Cr_2O_3 was found to increase the hardness, tensile strength, and thermal shock resistance of Al_2O_3 . Even though not thoroughly investigated yet, the improvement are believed to be closely related to the changes in microstructure. When the Cr_2O_3 is added, the sinterability of Al_2O_3 decreased markedly due either to the evaporation of the Cr-containing species or to the change in the sintering mechanism.

H.J Reynolds et. al. ^[4] illustrated that the sintering and grain growth of alumina as a function of the type of impurity (oxide) added was studied. One weight percent of the impurity was added to a commercial fine-grained alumina or was co-precipitated with AlCl_3 to form hydroxides. Fired shrinkage, bulk density, and apparent porosity measurements were used to correlate sintering with grain growth as observed by the petrographic and electron microscope. Some additives which increased grain growth were believed to enter into solid solution with alumina and to strain the lattice sufficiently to increase material transport. Other additives were believed to produce a glassy phase which would greatly increase surface diffusion and resulting grain growth. Some additives decrease grain growth because of the relatively large vapor phase produced by the impurity upon heating which may have been absorbed on the alumina; other additives may have filled anion vacancies to reduce material transport or may have produced complex anions whose flow or diffusion may have been impeded.

J. Christensen et. al. ^[5] investigated that the sintering (densification) and grain growth of alumina were studied to determine the effect of the variables raw material, particle size, grinding in acid media, molding pressure, various single additives in different amounts, and firing temperature. Fine grinding promoted sintering and the, growth of large grains and caused the grains to be more elongated inhabit. Sintering was facilitated by additions of iron oxide, manganese oxide, copper oxide, and titanium oxide, provided the amounts of these oxides and the temperature of firing were within certain bounds. The growth of large grains was facilitated by additions of iron oxide and manganese oxide. Nineteen other additives had no effect or retarded sintering and large-grain

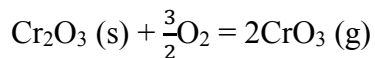
growth. Both magnesium oxide and silica had a marked effect in inhibiting the growth of large grains. The alkali metal oxides, added singly, were especially deleterious to the production of strong alumina bodies. The maximum density and maximum strength of the fired body were attained approximately simultaneously with the onset of large-grain growth. The habit of the large grains was markedly altered by increasing amounts of each additive; the grains lost their characteristic crystalline shape and became nearly spheroidal particles. It is suggested that two grain-growth phenomena exist which are independent of each other. One is termed “small-grain growth” and is associated with densification; the other is referred to as “large-grain growth” and occurs in certain specimens, depending on the additions to the alumina, after the sintering (densification) is substantially completed.

Pengda Zhao et. al. ^[6] demonstrated that Al_2O_3 and Cr_2O_3 form complete substitutional solid solutions over the entire composition range at 1650 °C without forming any other compounds. Lattice parameters a and c increase linearly with an increase in the Cr_2O_3 content, with doping with Cr^{3+} ions resulting in more severe lattice strain in the c -axis direction. The angles of the different diffraction peaks also decrease linearly with an increase in Cr_2O_3 content. Furthermore, it was found that the relationship between the theoretical density of each solid solution and its Cr_2O_3 content could be fitted using a second-order polynomial. Properties of Al_2O_3 - Cr_2O_3 solid solutions strongly depend on their crystal structure. It is well known that Al_2O_3 - Cr_2O_3 solid solutions have a crystal structure similar to that of corundum. In this compound, the oxygen ions form an approximately hexagonal close-packed structure, with Al^{3+} filling two-thirds of the octahedral interstices and each Al^{3+} and Cr^{3+} center filling an octahedron. However, the effect of the Cr_2O_3 content on the crystal structure of Al_2O_3 - Cr_2O_3 solid solutions remains a matter of debate.

H.G. Emblem et. al. ^[7] investigated that there are two distinct aluminum (III) oxide gradually raises the temperature at which liquid is formed. Aluminium (III) oxide (corundum) and chromium (III) oxide (eskolaite) have the same crystal structure. Because the crystal structures of oxides are the same and the ionic radius of Al^{3+} and Cr^{3+} differ by only about 12%, corundum is an excellent host for the Cr^{3+} ion. A complete series of solid solutions is formed. The formation of solid

solutions is shown by XRD studies of the aluminium (III) oxide-chromium (III) oxide regions of aluminium (III) oxide-chromium (III) oxide solid solutions. The first region extends from 0 to 8 mol. % chromium (III) oxide. The crystals are red, the color becoming increasingly deep as the percentage of chromium (III) oxide increases. These crystals represent the gem stone material ruby [16]. The second region extends from 8 mol. % chromium (III) oxide upwards. Crystals in which the percentage of chromium (III) oxide is slightly in excess of 8 mol. % are green. The color changes to dark grey as the chromium (III) oxide percentage increases. The color changes could be due to ligand field splitting. In the solid state at high temperature, aluminium(III) oxide and chromium(III) oxide are completely miscible, but at lower temperatures there is a miscibility gap (T = 950°C), shown. The mechanism of the separation is spinodal. A spinodal transformation is where a "phase" separation occurs in the otherwise homogeneous solid solution due to small differences in composition within the phase. In alumina-chrome refractories, the quantity of chromium (III) oxide is generally insufficient to cause miscibility problems. At the usual operating temperatures of alumina-chrome refractory bodies, the two components are completely miscible in the solid state.

V. Tsantzalou et. al.^[8] discovered that incorporating chromium oxide in alumina refractories improves resistance to thermal-shock damage and slag attack. In manufacturing alumina-chrome refractories, the chromium oxide can be added to a coarse alumina as a fine chrome ore or to corundum as purified chrome ore when preparing ethyl-silicate-bonded alumina-chrome refractories the source of chromium is usually chromium (III) oxide. The low density of some sintered compacts prepared, may be due to loss chromium, which could occur by the reaction



Chromium loss is consistent with the large primary particle size, suggesting that loss of chromium by volatilization is faster than solid solution formation.

It was reported that the changes in the lattice parameters with an increase in Cr₂O₃ content were not completely linear. However, they later observed that the changes were linear and in agreement with **Vegard's law** [41]. Vegard's law is an approximate empirical rule stating that a linear relation

exists, at a constant temperature, between the crystal lattice constant of an alloy and the concentrations of the constituent elements. However, Vegard's law seldom holds true for binary continuous solid solutions. Whether an $\text{Al}_2\text{O}_3\text{-Cr}_2\text{O}_3$ solid solution satisfies Vegard's law is still controversial. The near expansion coefficient of the solid solutions decreases with an increase in the Cr_2O_3 content.

A. Harabi et. al. ^[9] stated that the effect of certain oxides (such as MgO, TiO_2 , Fe_2O_3 , FeO and CaO) on grain growth in alumina. Microstructurally it has been found that chromia additions promotes a change from polygonal grains to tabular grains and promotes grain growth up to 10 wt% but inhibit grain growth when more chromia is added. For 7.5 and 10 wt % chromia samples sintered at 1700°C for longer times a third stage corresponding to saturation of grain growth capacity, was observed. The grain size change during sintering were compatible with a surface diffusion-controlled pore drag mechanism for pure alumina and 2.5 wt% chromia whereas the 7.5wt% chromia composition obeyed a simple cubic relationship between grain size and sintering time. It was found that when chromia is added to alumina composites, wedge-shaped crystals were observed and grain grew with increasing chromia content. But the addition of small amount of chromia is effective as a grain growth inhibitor.

E. N. Bunting et. al. ^[10] stated that a dilute solution of Cr_2O_3 in Al_2O_3 has long been known as the ruby ^[16]. More concentrated solutions do not possess the desirable color of the ruby, but are of interest because of their refractory properties. A study of the phase equilibria in the $\text{Cr}_2\text{O}_3\text{-Al}_2\text{O}_3$ system has shown one oxides to be completely miscible in the liquid and solid states, with compound formation. The melting point of Cr_2O_3 has been re-determined to be $2,275^\circ \pm 25^\circ \text{C}$.

It was also reported that on heating mixtures of Cr_2O_3 and Al_2O_3 to a "red white" heat, from 15 to 16 per cent Cr_2O_3 united with the Al_2O_3 . Another author made an examination by X-rays of mixtures which had been heated to 600°C . and found that limited solution in the solid state occurred at this temperature.

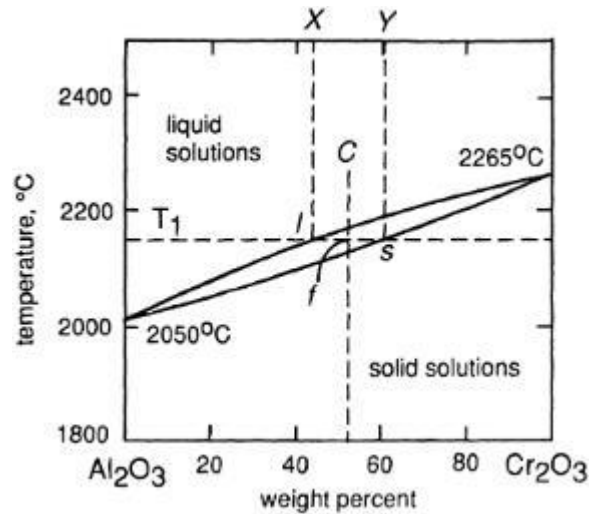


Fig: 1 Phase diagram

P.H. Sydenhum et. al. ^[11] stated that The sub-solidus phase equilibria in the system Al_2O_3 - Cr_2O_3 were investigated hydrothermally at a pressure of 1 kbar in the temperature range 370°C to 1200°C . Intimate mixtures were prepared from reagent grade nitrates utilizing the method of hydroxide co-precipitation^[27]. It is reported the presence in the system of a miscibility gap with limits at compositions of approximately 10 and 60mol% Cr_2O_3 , decreasing in extent with increasing temperature to close at 800°C a composition of 40mol% complete phase diagram for the system.

M. Risti et. al. ^[12] have discovered that structural properties of the system $(1-x)\text{Al}_2\text{O}_3+x\text{Cr}_2\text{O}_3$ were investigated in the whole concentration range. The samples were prepared by mechano-chemical activation of γ - AlOOH and Cr_2O_3 , sintering the resulting powder up to 1300°C . The formation of solid solutions $(\text{Al}_{1-x}\text{Cr}_x)_2\text{O}_3$ was observed in the whole concentration range. The replacement of Al^{3+} with Cr^{3+} resulted in a gradual increase of the unit-cell parameter with x . For the molar fraction of Cr_2O_3 , $x > 0.5$, a phase closely related to Cr_2O_3 was also found. The unit-cell

parameters of this phase also increased with x , although the rate of increase was much smaller. The samples of $(1-x) \text{Al}_2\text{O}_3 + x \text{Cr}_2\text{O}_3$ showed gradual changes in the FTIR spectra with x . α - Al_2O_3 , Cr_2O_3 and are mutually iso-structural, the space group being $R3c$. The ionic radii of Al, Cr and Fe are nearly similar (0.057 nm for Al^{3+} , 0.064 nm for Cr^{3+}), and this fact favors the formation of solid solutions between their oxides. In general, the temperature and the concentration range of the formation of solid solutions in mixed metal oxides are strongly dependent on the experimental conditions of their preparation (co-precipitation, sol-gel procedures, ceramic sintering, mechano-chemical activation, etc.)

K. Shibata et. al. [13] expatiated that in the system Cr_2O_3 - Al_2O_3 , Cr_2O_3 solid solution (ss) powders containing up to 25 mol % Al_2O_3 have been prepared by the hydrazine method. Dense Cr_2O_3 (ss) ceramics (99-99.2% of theoretical) have been fabricated by HIPing (1500°C/2h/196MPa) of the compacts sealed under reduced pressure. Their mechanical data are discussed, in comparison with those of Al_2O_3 (ss) ceramics in this system. Micro-hardness (23.4 GPa) and fracture toughness are not dependent on the compositions of Cr_2O_3 ceramics. The former value is higher than that of much improved Al_2O_3 ceramics. Bending strength increases linearly with increasing Al_2O_3 content; the maximum value of 380 MPa is achieved in the ceramics containing 25mol. % Al_2O_3 . Both Cr_2O_3 and Al_2O_3 possess the same crystal structure having a hexagonal system.

The binary system forms a continuous solid solution at high temperatures. Several investigations have been undertaken on the fabrication and mechanical properties of Al_2O_3 solid solution ceramics. It is reported that the micro hardness of dense Al_2O_3 (ss) ceramics (99.8% of theoretical) fabricated by hot pressing (1500- 1700°C (hydrogen atmosphere) increased with increasing Cr_2O_3 content. Although the densities of hot-pressed (1425°C/27.6MPa/vacuum) Al_2O_3 (ss) ceramics decreased (99.4+97.4%) rapidly with increasing Cr_2O_3 content, they caused significant increases in micro hardness and wear resistance up to 25 mol% Cr_2O_3 additions. Based on the results thus obtained, it has been accepted that the mechanical properties of Al_2O_3 ceramics were enhanced by Cr_2O_3 , in solid solution. On the other hand, no data for the fabrication and mechanical properties of Cr_2O_3 (ss) ceramics in this system have been reported. This is due to the poor sinterability of Cr_2O_3 , in air; the oxide requires high temperatures >1600°C in a reducing pressure to achieve high density. It is reported that, below 25 mol% Al_2O_3 additions, Cr_2O_3 (ss) were formed at very

low temperatures (405-480°C) from amorphous materials prepared by a sol-gel technique. Investigations were carried out with different types of bauxites and chromites to prepare chrome-alumina refractories. Raw materials mixed in suitable proportions to give 10-12 % Cr₂O₃ in the product were calcined at 1600° and then graded. Bricks formed under pressure and fired to 1600° indicate promising results but high porosity. Lime addition (2-3%) in the mixes appreciably reduces porosity but slightly affects the refractoriness. Chrome ore containing about 5 percent silica is suitable for the purpose. Chrome-alumina refractories thus made possess desirable properties and their use in steel pouring ladles and regenerators of open hearth furnaces may be considered.

Chrome ore is represented by the formula (Fe, Mg)O (Or, Al, Fe)₂O₃ • Impurities present in the chrome ore are generally serpentine, chlorite, olivine, talc and pyroxene. On heating, ores get oxidised and ferrous spinels are converted to solid solutions of sesquioxides Fe₂O₃, Cr₂O₃ and Al₂O₃. Magnesia present in the chrome ores or introduced by addition forms spinels like MgO.Fe₂O₃, MgO.Cr₂O₃ and MgO.Al₂O₃ and the spinel structure of the ore is preserved. When alumina or bauxite is added to chrome ores and are oxidised solid solutions of Cr₂O₃-Al₂O₃-Fe₂O₃ might be formed together with some magnesia-spinels depending upon the limit of MgO present in the chrome ores. Thus chrome-alumina refractories with high percentage of alumina are mainly solid solutions of Cr₂O₃-Fe₂O₃-Al₂O₃. Mechanical strength of the brick depends upon the amount of melt formed during firing. Formation of the melt varies on the nature and amount of the impurities present in the ores and the grain size of the batch. Low underload values of half bricks prepared from coarse fractions might be due to inadequate sintering of the grains when fired to 1500°. Mechanical strength as indicated by refractoriness underload values increases due to better sintering when fine fractions are used. Addition of lime decreases porosity considerably possibly due to formation of more calcium aluminate and monticellite.

Ravindra Jangir et. al. ^[14] discovered we report on structural and optical properties for ternary α -(Al_xCr_{1-x})₂O₃ (0 < x < 1) solid solutions synthesized by using solid state reaction method. Single R-3c phase was obtained for the Aluminum composition of 0 < x < 1. Due to difference in the ionic radius of Al³⁺ and Cr³⁺, in plane lattice parameter showed deviation from the **vegard's law** ^[41].

Optical absorption spectra for the solid solutions showed a blue shift of ~ 0.5 eV in the optical gap. It has also been observed that Cr 3d level shifted towards the O 2p level in the valence band which indicates the enhancement of hybridization in the d and p levels, which is related to the delocalization of hole states, responsible for p-type conduction in wide band gap semiconductors. The results suggest that ternary $\alpha\text{-(Al}_x\text{Cr}_{1-x})_2\text{O}_3$ ($0 < x < 1$) can be useful in the field of UV transparent electronics and UV photodetectors. Synthesis of ternary $\alpha\text{-(Al}_x\text{Cr}_{1-x})_2\text{O}_3$ ($0 < x < 1$) material system has been carried out using solid state reaction method. XRD measurements reveal that Aluminium (Al) can be substituted with chromium (Cr) for full composition range. Polycrystalline solid solutions of ternary $\alpha\text{-(Al}_x\text{Cr}_{1-x})_2\text{O}_3$ ($0 < x < 1$) were prepared using conventional solid state reaction method with starting materials; Al_2O_3 (99.999% Sigma Aldrich) and Cr_2O_3 (99.97% Sigma Aldrich). Al_2O_3 powder was mixed with the Cr_2O_3 powder in different molar ratio to vary the Al (x) concentration in ternary $\alpha\text{-(Al}_x\text{Cr}_{1-x})_2\text{O}_3$ solid solution.

J. Graham et. al. ^[15] investigated that precision lattice spacing determinations have been made on well crystallized specimens throughout the system, and the diffuse reflectivity of the samples measured. There is no anomaly at 8 mol percent Cr_2O_3 as found by earlier workers, the change in both the colour and the crystal field surrounding the chromium ions being continuous and smooth, though changes in the crystallographic environment of these ions cannot be followed in detail. Atomic parameters have been obtained for pure chromic oxide, revealing that the structure is rather less distorted than the similar structures of α -alumina and $\alpha\text{-Fe}_2\text{O}_3$. The positive deviations from linearity which are found in our lattice spacing curves indicate an apparent diameter for the Cr^{3+} ion greater than that in Cr_2O_3 ; the average molar volume increases initially more rapidly than the simple linear law predicts, so that there is no abnormal compression in this region.

J.E. Lovelock et. al. ^[16] showed that the abnormal red color of ruby compositions (solid solutions containing less than 8 mol % Cr_2O_3 in Al_2O_3) is due to compression of chromite ions. This conclusion is based on the shift towards shorter wave from about 17000 cm^{-1} in green chromic oxide to about 19000 cm^{-1} in the red rubies, the shift of the absorption bands, in fact, takes place gradually as the concentration of chromic oxide is reduced down to 8 mol%. The colour of mixed crystals remains green in varying shades down to 30mol% of chromic oxide, when it changes

gradually to greyish-green, grey, greying-red and then to bright red which remains stable below 8 mol% . The position of the absorption bands remains almost fixed in the red compositions below this concentration. Thus, it is obvious that this phenomena of ion-compression takes place gradually and in the green region only. (For convenience, the whole of the green-to-red region above 8 mol% chromium oxide has been designed as the green region). No extraordinary compression of the chromic ion is associated with the critical concentration.

Sun Hong gang et. al. ^[17] reported that the character of $\text{Al}_2\text{O}_3\text{-Cr}_2\text{O}_3$ refractories service is affected by multiple factors such as temperature fluctuation, slag corrosion and penetration. To simulate service, some kinds of $\text{Al}_2\text{O}_3\text{-Cr}_2\text{O}_3$ refractories were estimated with slag resistance test under temperature fluctuation. The result showed that, slag resistance and penetration resistance increased with increasing chromium oxide content in bricks. With the increase of Cr_2O_3 content, the slag corrosion rate of $\text{Al}_2\text{O}_3\text{-Cr}_2\text{O}_3$ material decreased, which indicated that the Cr_2O_3 content played a decisive role in the slag resistance of $\text{Al}_2\text{O}_3\text{-Cr}_2\text{O}_3$ material. Dense spinel layer was formed by the reaction of Cr_2O_3 with Fe_2O_3 and MgO , which had a high melting point and prevented the further infiltration of slag into the materials. The improvement of the thermal shock resistance was verified by introducing mullite-zirconia particles or m- ZrO_2 particles as additives into $\text{Al}_2\text{O}_3\text{-Cr}_2\text{O}_3$ refractories. Moreover, microporous microstructure was very favourable for both slag penetration resistance and thermal shock resistance. The addition of zirconium oxide and the microstructural design of micro pores can make up for the decline in the performance of chromium oxide in $\text{Al}_2\text{O}_3\text{-Cr}_2\text{O}_3$ refractories. Thermodynamic evaluation also showed that the content of Cr_2O_3 in refractories had a significant influence on the formation of dense spinel layer. Moreover, the additives had benefit on improving the slag penetration resistance because it effectively suppressed the micro crack propagations under the condition of temperature fluctuation. Therefore, it will be also an effective way to promote slag resistance of $\text{Al}_2\text{O}_3\text{-Cr}_2\text{O}_3$ refractories with lower content of Cr_2O_3 by the designation and preparation of microporous structural materials.

Takehiko Hirata et. al. ^[18] demonstrated that the corrosion of ceramic materials in molten slag depended strongly on the viscosity of the slag and the basicity gap between the ceramics and the slag. In this study, we propose experimental equation to predict the corrosion rate of a ceramic

material in a molten slag as functions of the viscosity and the basicity gap on the basis of the corrosion tests. Generally, the corrosion rate seems to be influenced of oxide. However, the ceramic materials, which exhibit the superior stability in the molten slag, have been found out experientially or empirically, since the understanding about corrosion chemistry in a slag was still insufficient. The investigated the corrosion behaviour of $\text{Cr}_2\text{O}_3\text{--Al}_2\text{O}_3$ ceramics in the $\text{CaO--SiO}_2\text{--B}_2\text{O}_3$ model slag system. The obtained results suggest that the basicity and viscosity of slag were the critical factors, which control the corrosion behaviour.

Hiroyuki Sunayama et. al. ^[19] described that Chromium oxide particle, which composed the matrix of brick, surrounded the surface of brick in suspension. Furthermore, the content of chromium oxide in penetrated slag was saturated with the dissolution of inner wall of pore in the brick, as a result, the chemical reaction between Fe_xO and Cr_2O_3 at the interface on the top of penetrating slag might be negligible. $\text{Al}_2\text{O}_3\text{--Cr}_2\text{O}_3$ refractory had the high corrosion resistance because of the suspension of Cr_2O_3 particles and the saturated solubility of Cr_2O_3 in the penetrated slag. Generally, it is considered that the viscosity of the slag which penetrates into the $\text{MgO--Cr}_2\text{O}_3$ refractory becomes high because of dissolving of Cr_2O_3 in the penetrated slag. In the present study, the measurement of the dissolution rate of the $\text{Al}_2\text{O}_3\text{--Cr}_2\text{O}_3$ refractory and of the penetration rate of slag into the Cr_2O_3 capillary were carried out to clarify the role of Cr_2O_3 constituent in the refractory on the high corrosion resistance of $\text{Al}_2\text{O}_3\text{--Cr}_2\text{O}_3$ refractory. So, One of disposal of waste is to incinerate waste at high temperature. Alumina-chrome refractory, $\text{Al}_2\text{O}_3\text{--Cr}_2\text{O}_3$, is used as aligning of an incinerator because $\text{Al}_2\text{O}_3\text{--Cr}_2\text{O}_3$ has a high corrosion resistance against molten slag.

Ding Chena et. al. ^[20] reported that $\text{Al}_2\text{O}_3\text{--Cr}_2\text{O}_3$ refractories containing a minor amount of ZrO_2 usually have excellent heat stability and corrosion resistance. However, a short service life is observed in high-temperature solid waste incinerators. Therefore, the phase compositions and microstructure of the $\text{Al}_2\text{O}_3\text{--Cr}_2\text{O}_3$ refractory linings, both with and without corrosion, were analyzed. The results show that $\text{Al}_2\text{O}_3\text{--Cr}_2\text{O}_3$ bricks were corroded by both molten slag and gas in the solid waste incinerator. Regarding the corrosion by molten slag, SiO_2 and CaO contained in the slag entered into the bricks along pores, which caused densification of the matrix and reaction of SiO_2 , CaO , and Al_2O_3 to form CAS_2 ; FeO entered into the refractory and reacted with Al_2O_3 and Cr_2O_3 , forming the composite spinel $\text{FeO.Cr(Al)}_2\text{O}_3$. Moreover, the gas mixture of CO and

Cl₂ also infiltrated into the Al₂O₃-Cr₂O₃ brick and accelerated brick corrosion by reacting with ZrO₂, Al₂O₃, and Cr₂O₃ one after another.

Mithun Nath et. al. [21] interpreted that visible corrosion has not been observed even after 36 hrs of corrosion test, but microscopic analysis revealed the corroded region which increases with time. Corrosion occurs via dissolution of Al₂O₃ fractions from the Al₂O₃- Cr₂O₃ solid solution by the molten glass followed by mass exchange. The Al₂O₃ fraction in the Al₂O₃-Cr₂O₃ solid solution is occupied by Fe₂O₃ there by forming of Fe₂O₃- Cr₂O₃ solid solution and plausibly this layer acts a barrier to molten glass which ceases the corrosion rate. However, Cr₂O₃ fraction remained unaffected by the molten glass. The properties of molten glass/slag such as chemical composition, acid or basicity, viscosity, density, temperature and surface tension are the important variables which come into play during interactions with refractories. Researchers have investigated the interaction Al₂O₃- Cr₂O₃ with various slag/glass containing iron oxides and established that the dissolution and penetration of liquid melts occurs via formation of different spinel phases of Al and Cr with Fe. Therefore, investigation of affected grains in the corroded region in terms of phase analysis by XRD and detail elemental analysis by EDX are per-formed to find out the formation of new phases and the corrosion mechanism.

Kyeising Kwong et. al. [22] showed that the effect of operational conditions and slag chemistry on the wear of Cr₂O₃ refractory has been discussed. Structural spalling and corrosion have been identified by post mortem analysis and field investigation as major failure mechanisms for the premature service life of refractory. The use of phosphate additives in a Cr₂O₃ refractory has been proved to be an effective way to enhance the slag penetration resistance and to eliminate the structural spalling of refractory brick. The hot-face refractory lining is a key component of gasification systems. The refractory liner protects the gasification system from the high-temperature corrosive gaseous and from the molten slag environment associated with the conversion of carbon feed stocks. The ability to produce combinations of electricity, hydrogen, and chemicals, while eliminating nearly all air pollutants and potential greenhouse gases, makes gasification one of the most promising technologies for the energy plants of tomorrow, especially at a time when oil and natural gas prices are rising and reserves are being depleted. Compared with

traditional coal combustion plants, slagging gasifiers have several potential environmental benefits.

U. Rothhaar et. al. ^[23] reported on annealing-induced interface and bulk effects in thin Cr_2O_3 films on aluminium oxide substrates. The samples consisted of ceramic Al_2O_3 substrates with 825 Å Cr_2O_3 over layers, deposited by reactive R.F. magnetron sputtering. Annealing in the range from 1100°C to 1250°C, and the subsequent AES sputter depth profiling were carried out in situ under ultrahigh vacuum conditions. With increasing temperature and heating time an interface broadening and a nearly constant concentration of Al developing in the Cr_2O_3 film are observed. On the basis of Whipple's theory for combined grain boundary and intragranular diffusion, bulk diffusion coefficients are determined leading to an activation energy of 4.67 eV for Al diffusion in Cr_2O_3 . Interdiffusion effects in Cr_2O_3 - Al_2O_3 systems prepared and annealed in situ under ultrahigh vacuum conditions have been investigated in the temperature range of 1100°C-1250°C. Auger sputter depth profiling was shown to enable the determination of the temperature induced compositional changes despite the electrically non-conducting ceramic alumina substrates. The bulk diffusion coefficients derived via the plateau-rise method developed. It obeys an Arrhenius law and yield an activation energy of 4.67 eV for the diffusion of Al in bulk Cr_2O_3 .

Hwan-Tang et. al. ^[24] investigated that activity -composition relations in Al_2O_3 - Cr_2O_3 solid solutions at 1500°C and 1600°C were determined by equilibrating members of this solid-solution series with Mo-Cr alloys of known activity-composition relations and a gas phase of known oxygen potentials. The oxide solid solution shows considerable positive deviation from ideality. Activity composition relations of the system Cr_2O_3 - Al_2O_3 at high temperatures are of interest in the physical chemistry of refractories used in steelmaking and in coal gasification. Such data, in combination with acknowledge of phase relations in ternary systems of the type MO - Cr_2O_3 - Al_2O_3 , where MO is a divalent oxide, for instance FeO or MnO , will be useful for evaluating the interaction between metal oxides and Cr_2O_3 - Al_2O_3 containing refractory materials. In the present study, the activity -composition relations of the Cr_2O_3 - Al_2O_3 solid solutions were determined at relatively high temperatures (1500°C and 1600°C) from data on the equilibrium between these solid solutions, Mo-Cr alloys, and atmosphere of known oxygen pressures.

A. Bettinelli et. al. ^[25] elucidated that densification of alumina-based ceramics can be achieved (95% of the theoretical value) by liquid phase sintering at 1400°C. The optimum amount of silicate additions was determined in order to achieve the best densification. Using a fine grained alumina (0.5 to 1µm average grain size) 94% of the theoretical density is obtained in air and 93% in hydrogen with an addition of 2.25 wt% of CaSiO₃. The densification kinetics were studied under these two atmospheres and the influence of some transition metal oxides (TiO₂, Nb₂O₅) under a reducing atmosphere is also discussed. Ninety five per cent dense ceramics having an alumina content of 96% are obtained after four hours firing at 1400°C. The results show that it is possible to densify pure fine grained alumina at 1400°C, by adding 2 wt% of an additive with a low melting point. The density, which can be obtained, is nearly 95% of the theoretical value. A supplementary addition of TiO₂ or Nb₂O₅ fired in air or in hydrogen, or MoO₃ fired in hydrogen has little effect on sintering. In the case of firing in hydrogen the oxides may be of interest if a black alumina is required.

Motonari Fujita et. al. ^[26] described that the sol-gel method was applied to create Al₂O₃-Cr₂O₃ ceramics using aluminum ethyl acetoacetate di-isopropylate and chromium chloride hexahydrate as starting materials. In the calcinations at 600-1200°C it was found that the grains of Cr₂O₃-rich solid solution grew when they were exposed to the surrounding Al₂O₃-rich amorphous particles. The composition of the powders obtained by the sol-gel process changed with calcining temperature. Cr₂O₃-rich solid solutions first crystallize at low temperature and the composition of the crystallites changes as the crystals grow and react with the surroundings Al₂O₃ -Rich Phase. The final sintered bodies fired under an Ar atmosphere showed higher relative densities as compared with those fired in air. A dense sintered body was not obtained when abnormal grains grew when calcining occurred. Melting type incinerators such as gasification melting furnace^[22] have been developed as a solution to this problem. In high temperature melting type incinerators the waste are burnt and melted above 1300°C. Generally Al₂O₃-Cr₂O₃ refractories are used in such conditions. The alkali alkali-earth elements such as Na, K and Ca are present in the municipal wastes and corrode furnace lining refractories. Porous microstructure refractories are attacked so a dense body is used to avoid damage.

Federica Bondioli et. al. [27] investigated that concerning iso-valent solid solutions, in which an atom or ion replaces an atom or ion of the same charge in the parent structure, the study of the $\text{Al}_2\text{-}_x\text{Cr}_x\text{O}_3$ ($0 \leq x \leq 2$) system is of great interest because of its high refractoriness and chemical stability. Al_2O_3 and Cr_2O_3 are sesquioxides having the same corundum crystal structure (approximately hexagonal close-packed oxide ions with the Al^{3+} and Cr^{3+} ions occupying two thirds of the available octahedral interstitial sites), and by reaction at high temperatures ($T > 1000^\circ\text{C}$) complete ranges of substitutional solid solutions are obtained. Below 950°C a miscibility dome is present, inside which two crystalline phases (alumina-rich and chromia rich solid solutions) are present. The actual decomposition of a homogeneous solid solution into two phases takes place very slowly, but it may be speeded up using hydrothermal or high pressure treatments. In this system the co-precipitated powders present faster reaction kinetics, not only because of the smaller particle size, and consequently greater reactivity, but also because of Cr–O–Al bonds due to the co-precipitation process. In particular, for compositions inside the miscibility gap, because of these bonds, the thermodynamic equilibrium, characterized by the presence of two solid solutions, has been obtained in a shorter time and at ambient pressure.

V.A. Bron et. al. [28] described that the firebrick linings of steel plant ladles at the Chelyabinsk iron and steel plant do not last more than six to ten heats. In order to improve ladle life, trials were, therefore, carried out with alumina-chrome brick produced at the Semiluksk refractories plant and characterized by a high Al_2O_3 content and good thermal stability. The refractoriness of these bricks and the initial softening temperature under load are markedly superior to those of fireclay. The chemical composition of alumina-chrome brick is: 77.38% Al_2O_3 , 6.70% SiO_2 , 10.81% Cr_2O_3 , 1.17% Fe_2O_3 , 1.02% MgO , 3.29% R_2O . Overall lining life of the ladle walls was 7 heats. The ladle bottom bricked with alumina-chrome was left for a second campaign. After two campaigns (14 heats), the residual brick thickness of the bottom was 110 to 135 mm. Some difficulties associated with alumina-chrome refractories were encountered during ladle operations:

- 1) Slagging of the brick surface and partial spalling of the brick;
- 2) Difficulty in removing slag because of its high viscosity;
- 3) Partial skulling of the ladle

Although the superior wear resistance of the alumina-chrome brick was also apparent in the remaining trial ladles. A ladle was tried with the bottom and lower 13 rings of the side wall bricked completely in alumina-chrome and the remaining lining in firebrick.

M.T. Hernandez et. al. ^[29] reported that alumina is an important technological material due to its excellent physical and thermomechanical properties. Binary compositions enhance some of these properties; especially Cr additions significantly increase the mechanical behavior of pure alumina. It is well known that the sintered bodies of chromium oxide doped-alumina do not become dense when sintering in air because vaporization and condensation of Cr_2O_3 during the high temperature densification process. The aim of this work is to assess the hot press sintering as an adequate processing method to obtain full dense sintered bodies from well homogeneous powders on chromia-alumina system. Using solutions of the desired nitrates, powders were prepared by the Pechini process in the range 0–6 Cr_2O_3 wt% and hot-pressed at 1500° C. C-diffusion and microstructure of the final densified bodies were studied in order to evaluate synthesis process feasibility. The Pechini process is a good method of obtaining high quality powders in the system Al_2O_3 - Cr_2O_3 . It can supply a large amount of product in a short period of time. Due to an absolutely homogeneous chromium distribution along CIT samples, the resultant microstructure of the densified ceramics is composed of isotropic rounded grains. On the contrary, the anisotropic structure of elongated grains, observed on JP samples is the consequence of the irregular incorporation of chromium oxide into the alumina matrix before to the heating process. The hot press sintering has been demonstrated to be a successful process to obtain fully densified chromia-alumina compositions, avoiding the loss of gaseous chromium-based oxides at high temperatures. But an uncontrolled amount of carbon is diffused into the corundum structure due to a gas flow from the graphite moulds through the powder pore network. However, the existence of that carbon-rich flow seems to provoke the formation of some chromium carbides, detected when chromium content exceeds 5wt% of the solid solution by XRD. In compositions with a lower chromium content, the incorporated carbon is located both at grain boundaries and triple points as low crystallinity carbon phases, as demonstrated by XRD and TEM studies.

A.A. Shaposnikova et. al. ^[30] demonstrated that Chrome-alumina slag is a waste product from the production of chrome metal. A number of publications have pointed out the advisability of

using high-alumina slag for making refractories. On the basis of experimental data, the slag: clay ratio providing the greatest density in industrial grinding was taken as 65:35. The jointly ground mixture contained 1% fraction coarser than 0.5 mm and 64% finer than 0.088 mm. The experimental batches of ladle brick were made with equipment used for the present production by semi-dry pressing. Water absorption of the chamotte was 8 - 10%. They manufactured experimental batches of ladle brick with the addition of 20% and 28% chrome-alumina slag and tested it in 140-ton ladles. The slag was added in finely-ground form to the charge binder during joint grinding with the clay. In order to manufacture the chrome-alumina ladle brick at the refractory shop of the NTMK in accordance with the set technology, it is necessary to arrange a separate production line with a tube mill. Wear and tear in the experimental brick with 28% chrome-alumina slag amounted to 4.2 mm/melt, with 26% chrome-alumina slag to 4.4 mm/melt, with 20% chrome-alumina slag to 4.4 mm/melt, and in the case of the ordinary brick to 8.1 mm/melt. The tests showed the possibility of increasing the wear resistance of ladle linings made of experimental brick to 13 - 15 melts, as against 9.3, when ordinary brick is used.

V. V. Viktorov et. al. [31] expatiated that Statistical homogeneity of $(Cr_xAl_{1-x})_2O_3$ solid solutions is investigated. It is shown, that there may be distinguished the region of statistical regularities and regions where prevail the clusters of two, three, and four chromic ions (III). The formation mechanism of solid solutions mentioned is proposed. The only thermodynamically equilibrium phase of the $Al_2O_3-Cr_2O_3$ system above 1500K in air is the continuous range of solid solutions $(Cr_xAl_{1-x})_2O_3$, having a great significance in the production of ceramics, fireproofs, catalysts, and other materials. The synthesis of these solid solutions is performed either by means of fusion or by heating a chromic oxide (III) and aluminium oxide (III) mixture in the sub-solidus temperature range. The question of homogeneity of solid solutions in the $Al_2O_3-Cr_2O_3$ system has been discussed. The regularities of the chromium distribution in the lattice of $(Cr_xAl_{1-x})_2O_3$ solid solutions have not been sufficiently investigated. It is considered the chromic ion distributions to be close to statistical in solutions with chromic concentration $x \leq 0.17$. However, other authors discovered an abnormal content of two Cr^{3+} ion clusters in the solid solution lattice. One of the most effective methods to investigate the Cr^{3+} ion distributions in the lattice of $(Cr_xAl_{1-x})_2O_3$ having

corundum structure, is the magneto-chemical analysis, i.e. the measurement of the statistical magnetic susceptibility X at different temperatures and chromium concentrations x . Thus in the structure of $(\text{Cr}_x\text{Al}_{1-x})_2\text{O}_3$, solid solutions. The latter groups, as was mentioned above, present the elements of the crystalline Cr_2O_3 structure. During the formation of the $(\text{Cr}_x\text{Al}_{1-x})_2\text{O}_3$ structure the successive substitution of clusters consisting of two, three, and four Cr^{3+} ions takes place, which causes the successive transition from the properties of alumina to those of pure chromia.

S. G. Yanga et. al. ^[32] investigated that Solid solution ceramics $(\text{Al}_2\text{O}_3)_x(\text{Cr}_2\text{O}_3)_{1-x}$ with different x in the range of $0 < x < 1$ were synthesized via traditional ceramic production method. X ray diffraction results and Rietveld refinements indicated that all samples possessed rhomb-centered structure and continuous solid solutions were synthesized. The samples were composed of irregular grains with several micrometers in diameter. Temperature dependence of magnetization measurements showed monotonous decreasing Neel temperature with increasing x and percolation effect happened with threshold of $x = 0.65$. As x became higher, weak ferromagnetism was observed in the samples. Field dependence of magnetization measurements further confirmed the weak ferromagnetism in the samples with $x = 0.7, 0.8$ and 0.9 .

F. S. Stone et. al. ^[33] reported that magnetic susceptibilities (77-1000 K) and E.P.R spectra (100-573 K) have been measured for α - Cr_2O_3 and ten corundum-phase solid solutions α - $\text{Cr}_x\text{Al}_{2-x}\text{O}_3$ with x varying from 0.002 to 1.6. The Racah parameter B has been obtained from optical reflectance spectra. Solutions dilute in chromium obey the Curie-Weiss law and effective magnetic moments decrease from $\mu_{\text{eff}} = 3.9, \mu_B$ at $x = 0.002$ to $\mu_{\text{eff}} = 3.5, \mu_B$ at $x = 0.18$. Above $x = 0.2$ the susceptibility temperature variation reveals long-range antiferromagnetic interactions, which remain detectable up to 700 K. E.P.R spectra show that the ruby spectrum is replaced by the broad β -phase resonance in the range $x = 0.02$ to $x = 0.20$, and the variation of the β -phase line width with concentration ($0.1 < x < 1.6$) has a minimum at $x = 0.8$. These results and the change in the number of spins with temperature are correlated with the susceptibility and optical measurements. As x increases, exchange coupling is first felt as an influence of pair-wise M-M interaction of Cr^{3+} ions, reducing the magnetic moment, but above $x = 0.20$ coupling of the M-O-M super exchange type becomes important and eventually dominates the magnetic behavior. When x reaches 1.6, the susceptibility is characteristic of an antiferromagnetic with $T_N = 300$ K and properties are similar to those of α - Cr_2O_3 . When a Cr^{3+} ion is replaced by an Al^{3+} ion (say, at M_1), the exchange coupling within a

sub lattice as well as between the sub lattices suffers a severe disruption. Hence relatively few Al^{3+} ions will cause a breakdown of the complete anti ferromagnetic ordering. Under these circumstances the partner ions (M_2) will behave in an almost paramagnetic fashion, and ferrimagnetism will be the result.

P. N. Bobin et. al. [34] demonstrated that electro-melted chromium containing refractories are distinguished by the excellence of the physico-chemical processes of mineral formation which occur via a liquid phase. Smelting provides single-phase materials or materials which correspond in composition to solid solutions and eutectics. The structure-forming processes in the production of chromite-containing fused refractories are made difficult because the Cr_2O_3 and Fe_2O_3 are easily reduced in the electro-melting conditions and this makes it difficult to choose the optimal composition for the batch. This can be avoided by smelting the materials in a weakly oxidizing atmosphere in electric furnace with bare electrodes. The future prospects for the development of fused refractories of an oxide-spinel type have been demonstrated. Such refractories are highly resistant to silicate melts and acid slags. However, information on the mineral formation and the industrial properties of fused mixtures of chromite and alumina is very limited.

N. B. Chatterjee et. al. [35] investigated on different types of bauxites and chromites to prepare chrome-alumina refractories. Raw materials mixed in suitable proportions to give 10-12 % Cr_2O_3 in the product were calcined at 1600°C and then graded. Bricks formed under pressure and fired to 1600°C indicate promising results but high porosity. Lime addition (2-3)% in the mixes appreciably reduces porosity but slightly affects the refractoriness. Chrome-alumina refractories thus made possess desirable properties and their use in steel pouring ladles and regenerators of open hearth furnaces may be considered. Cr_2O_3 and Al_2O_3 form a continuous series of solid solutions of complete miscibility as reported by E.N. Bunting [10]. The effect of addition of alumina or calcined Indian bauxite to chrome bricks was studied by T.R.Lynam and W.J. Rees. They obtained high mechanical strength with increasing bauxite content. Addition of more than 50% bauxite lowered the resistance to slag attack. Thermal expansion and spalling tendency decreased when bauxite was added to chromite.

H.S Tripathay et. al. [36] interpreted that highly dense alumina–chrome bodies with low porosity are usually used as corrosion and thermal resistant refractories. Alumina–chrome refractory with

molar ratio 1:1 was developed using chemical grade hydrated alumina and chromium (III) oxide by conventional sintering route. Batch materials were attrition milled, isostatically pressed and sintered in the temperature range from 1000°C to 1700°C with 2h soaking at peak temperature. Phase development of the sintered materials with temperature was studied by X-ray diffraction. Sintering temperature, sintering condition and addition of sintering aid (TiO₂) have immense effect on the densification of the alumina–chrome refractory. Highly dense alumina–chrome refractory with almost nil apparent porosity was developed at 1500°C in reducing atmosphere. Flexural strength of the sintered materials at room temperature and at 1200°C was also measured. 1wt% TiO₂ gives the optimum result with respect to densification and flexural strength. Highly dense alumina–chrome refractories were developed by conventional sintering route. It is not possible to get dense sintered Al₂O₃–Cr₂O₃ body in air/oxidizing atmosphere due to the removal of Cr compound. Al₂O₃–Cr₂O₃ samples without TiO₂ sintered in reducing condition, always exhibit higher bulk density than the samples sintered in air atmosphere. At 1600°C, sintered body of Al₂O₃–Cr₂O₃ without TiO₂ having almost nil apparent porosity is obtained in reducing atmosphere. Addition of TiO₂ as sintering aid favours the densification by the formation of cation vacancy. TiO₂ containing samples achieve highest density and almost nil apparent porosity at 1500°C in reducing condition. Hot modulus of rupture at 1200°C is almost same to the room temperature flexural strength. The TiO₂ containing sintered Al₂O₃–Cr₂O₃ body shows more compact grains with bigger grain size. 1wt% TiO₂ gives the optimum results with respect to densification and flexural strength of Al₂O₃–Cr₂O₃ ceramics.

Wen Yan et. al. ^[37] investigated that the porous MgO–Al₂O₃ refractory aggregates containing 30–92 wt% Al₂O₃ were prepared via an in-situ decomposition pore-forming route using magnesite and Al(OH)₃ as starting raw materials. The phase compositions, pore characteristics and mechanical strengths were characterised by means of X-ray diffractometer (XRD), scanning electron microscopy (SEM), and mercury porosimetry measurements, etc. The results showed that the Al₂O₃ contents in the porous refractory aggregates strongly affected the spinel formation, change of the neck bonds between the particles, pore structure (porosity, average pore size and pore size distributions), and then affected the strengths. The porous MgO–Al₂O₃ refractory aggregates of 62–72 wt% Al₂O₃ showed the best combination of high apparent porosities of 42.1–44.2%, high compressive strengths of 51.1– 52.0 MPa, high flexural strengths of 17.7–18.6 MPa and small

average pore size of 10.81–12.07 μm . Thus Porous MgO–Al₂O₃ refractory aggregates with micro-sized pore, high porosities and strengths were successfully fabricated using an in-situ decomposition pore-forming technique.

Sunggi Baiket et. al. [38] described that the effects of MgO on sintering and grain growth of alumina in the absence of any other impurities as well as in the presence of various amounts of CaO were investigated using ultrapure (>99.999 %) alumina and sintering at 1900°C for 1 h in a clean contamination-free condition. Critical concentrations of MgO required for the prevention of abnormal grain growth were linearly dependent on the CaO concentration. For a given concentration of CaO, at least the same amount of MgO has to be added to prevent abnormal grain growth. MgO addition alone to the ultrapure alumina enhanced both grain growth and densification kinetics during pressure less sintering. The beneficial effect of MgO doping could not be explained based on the solute drag (or pinning) model. It was more likely to be understood in terms of either a glass modification model or a solid-liquid interface modification model.

Ritwik Sarkar et. al. [39] investigated that effect of addition of Cr₂O₃ up to 4 wt.% was studied on three different spinel compositions with MgO: Al₂O₃ molar ratios 2:1, 1:1 and 1:2. Attritor mill was used to reduce the particle size of the starting materials and a single stage sintering technique was employed in the temperature range of 1550–1650°C for all the compositions. Final sintered products were then characterised in terms of densification and shrinkage studies, phase analysis, strength evaluation both at the ambient temperature and at 1300°C, strength retention capacity after different cycles of thermal shock at 1000°C, quantitative elemental analysis and microstructural studies. Cr₂O₃ showed the greatest effect on densification for the alumina rich spinel at 1550°C. No Cr-bearing phase was observed in XRD for all the three spinel compositions. Cr₂O₃ was found to decrease the temperature of complete solid solubility of excess alumina in spinel for the alumina rich composition. Strength was not highly affected by the addition of lower percentages of Cr₂O₃ but 4 wt.% of additive was found to be detrimental for all the compositions on sintering at 1650°C. Deleterious effect was much pronounced for the hot strength values and mainly for the magnesia rich composition. 1 wt.% of Cr₂O₃ was found to be beneficial in restricting the strength degradation after thermal shock for quantitative elemental analysis by EDAX study shows that Cr₂O₃ was uniformly distributed throughout the grains and grain boundaries, which confirms the solid solubility of Cr₂O₃ in spinel. Cr₂O₃ was also found to be effective for the grain growth of all three

different spinel compositions at high temperature. The effect was much pronounced for the alumina rich composition.

S. Maitra et. al. ^[40] discovered that precursor powder for zirconia–mullite composite was synthesized by co-precipitation in aqueous medium taking inorganic salts of aluminium, silicon and zirconium in requisite amounts. The powder was thoroughly characterized in terms of chemical composition, surface area, DTG behavior and FT–IR spectra. Role of two additives, namely, MgO and Cr₂O₃, on the densification of the compacted powder at different elevated temperatures ca. 1300–1500 °C was studied by the measurement of different physico-mechanical properties, such as bulk density, apparent porosity, specific gravity, compressive strength, bending strength and fracture toughness. Phase analysis by XRD technique and phase distribution by SEM technique was carried out to evaluate the microstructure of the sintered materials. Inorganic salts can be used to synthesize precursor powders of high surface area and very fine particle size with considerable surface activity by solution technique. MgO and Cr₂O₃ as additives play a positive role in the densification and proper microstructure development in the sintered ZrO₂–mullite products. The batch containing only MgO as an additive showed a progressive and steady increase in bulk density and specific gravity. The batch containing both MgO and Cr₂O₃ as sintering aid contained more glassy phase compared to the batch containing only MgO as a sintering aid. Mechanical properties like compressive strength, flexural strength and fracture toughness of the batch containing both MgO and Cr₂O₃ was better than the others. Probably Cr⁺³ doped expanded mullite crystals containing better interlocking matrix with reinforcement from t and m- ZrO₂, and MgO-containing liquid phase is a reason for this. All the batches contained mullite, corundum, cristobalite, tetragonal, monoclinic and cubic zirconia and some amount of glassy phase. The additives improved the microstructure, in terms of grain growth, phase distribution, strain development etc.

Lei Zhang et. al. ^[41] investigate that Vegard's law seldom holds true for most binary continuous solid solutions. When two components form a solid solution, the atom radii of component elements will change to satisfy the continuity requirement of electron density at the interface between component atom A and atom B so that the atom with larger electron density will expand and the atom with the smaller one will contract. If the expansion and contraction of the atomic radii of A

and B respectively are equal in magnitude, Vegard's law will hold true. However, the expansion and contraction of two component atoms are not equal in most situations. The magnitude of the variation will depend on the cohesive energy of corresponding element crystals. An empirical atom model of Vegard's law has been proposed to account for signs of deviations according to the electron density at Wigner–Seitz cell from Thomas–Fermi–Dirac–Cheng model.

When two components form a solid solution, the atom volumes of component elements will change to satisfy the continuity requirement of electron density at the interface between component atom A and atom B. Here the equilibrium electron density ρ_P at the interface can be obtained by one so-called empirical lever law as follows:

$$(\rho_B - \rho_P) \times E_B = (\rho_P - \rho_A) \times E_A$$

ρ_A and ρ_B are electron density of component atoms A and B, E_A and E_B are cohesive energy of components A and B. The empirical atom model of Vegard's law in this paper is just built on such an idea.

2.2 Literature review on $\text{Al}_2\text{O}_3\text{-B}_2\text{O}_3$:

T. R. Karpova et. al. ^[42] stated that the effect of chemical composition on the formation of the crystal structure and texture characteristics of the oxide system $\text{B}_2\text{O}_3\text{-Al}_2\text{O}_3$ obtained through impregnation of pseudoboehmite with the solutions of ortho-boric acid was studied. It was shown that the modification with boron oxide slows down the crystallization of aluminium oxide. According to the high-resolution TEM data, borate-containing aluminium oxides are composed of amorphous and crystalline primary particles. It was established that aluminium atoms in the samples occur in octahedral, tetrahedral and penta-co-ordination, while boron atoms occur in trigonal and tetrahedral co-ordinations; their relative content depends on chemical composition. The dependence of the specific surface of $\text{B}_2\text{O}_3\text{-Al}_2\text{O}_3$ system on its composition has an extreme character; the maximum is achieved with B_2O_3 content 5 mass %. According to the data of thermogravimetry and X-ray phase analysis, the introduction of boron oxide into pseudoboehmite hinders crystallization of aluminium oxide from it during thermal treatment, while the introduction of the modifying agent in the amount of 15mass % and more promotes the formation of X-ray amorphous

material. In this situation, according to the data of HRTEM, the obtained X-ray amorphous borate-containing aluminium oxides are composed of amorphous and crystalline primary particles. It was established that an increase in the concentration of B_2O_3 in the samples causes a decrease in the fraction of aluminium atoms in tetrahedral coordination and an increase in the fraction of penta-co-ordinated aluminium atoms and boron atoms in the tetrahedral coordination.

Hilkat Erkalfa et. al. ^[43] showed that Boron-containing alumina materials in the Al_2O_3 - B_2O_3 binary phase system have attracted special attention recently due to the stable, whisker-like crystalline compound aluminum borate ($9Al_2O_3 \cdot 2B_2O_3$). Hence in this study, the effect of the addition of B_2O_3 up to 1.5 wt% on the sintering characteristics of α - Al_2O_3 has been investigated in the sintering temperature range of 1450-1650°C. The effect of B_2O_3 addition on the bulk density and porosity, on the mechanical properties and on the microstructure of α - Al_2O_3 have been elucidated. The formation and the stability of the aluminum borate phase was also investigated in the range of sintering temperatures studied. The spray-drying technique gives good results in the preparation of uniform-sized alumina granules from alumina slip having boric acid as the B_2O_3 additive. The boric acid also acts as a binder both for the granulation and for the die-pressing process. The formation of the aluminum borate phase is found to be complete at 1000°C and the fibrous microstructure which is characteristic of this phase is developed between 1000 and 1100°C. The addition of B_2O_3 between 0.5 and 1.5 wt% to alumina results in a discontinuous grain growth in the sintered samples. The incompatible characteristics of the aluminum borate phase to those of the α - Al_2O_3 , result in a porous microstructure which in turn reduces the strength of the sintered material. The porosity level can be controlled by the B_2O_3 addition levels. The porous structure and reasonable strength values make the material a potential candidate to be used as ceramic filters and for ceramic-metal composite performs.

According to **Foster** et. al. ^[44] numerous investigations have been made of the thermal behavior of alumina-boric oxide mixture. In 1887 Mallard identified a compound believed to be $3Al_2O_3 \cdot B_2O_3$. Later work by Baumann and Moore and by Scholze indicated the formula to be $9Al_2O_3 \cdot B_2O_3$. Scholze reported an additional compound, $2Al_2O_3 \cdot B_2O_3$. Alumina-boric oxide mixtures were prepared from high purity γ -alumina and crystalline boric oxide, or from the previously prepared boroaluminate compounds, $9Al_2O_3 \cdot B_2O_3$ and $2Al_2O_3 \cdot B_2O_3$. Samples were sealed in platinum tubes to eliminate volatilization losses, and to ensure a water-free environment.

They were held for 16-24 hrs, and occasionally up to 120 hrs, in a platinum 60 rhodium 40 resistance furnace. Temperature were read with a platinum, platinum 90-rhodium 10 thermocouple frequently calibrated against the melting points of gold (1063°C), dropsied (1391.5°C), and palladium (1555°C). The fired charges were quenched in air or mercury, and phases were identified with the polarizing microscope and the X- ray diffractometer.

Siba E Ray et. al. [45] discovered that Aluminum borate, ($9\text{Al}_2\text{O}_3, 2\text{B}_2\text{O}_3$) or $\text{Al}_{18}\text{B}_4\text{O}_{33}$, was synthesized by the reaction of stoichiometric amounts of $\alpha\text{-Al}_2\text{O}_3$ and B_2O_3 . The $\text{Al}_{18}\text{B}_4\text{O}_{33}$ material was formed into a dense ceramic by pressure less sintering with CaO , MgO , or $\text{CaAl}_2\text{B}_2\text{O}_7$ additives. The material was characterized by low bulk density, moderate coefficient of thermal expansion ($3 \times 10^{-6}/^\circ\text{C}$ to $5 \times 10^{-6}/^\circ\text{C}$), moderate strength (210 to 324 MPa), and low dielectric constant Aluminum borate, $9\text{Al}_2\text{O}_3, 2\text{B}_2\text{O}_3$ or $\text{Al}_{18}\text{B}_4\text{O}_{33}$ was synthesized from Al_2O_3 and B_2O_3 and fabricated into ceramic shapes for evaluation of properties. $\text{Al}_{18}\text{B}_4\text{O}_{33}$ was hot-pressed to 99.6% density, but cold-pressing and sintering without additives did not result in densification. However, the addition of liquid-forming additives (e.g., $\text{CaAl}_2\text{B}_2\text{O}_7$, melting point 1098°C; CaO , which likely forms $\text{CaAl}_2\text{B}_2\text{O}_7$; and MgO) allowed densification by pressure less sintering. Densities of 96% to 98% of theoretical were achieved. The material contains 86.8 wt% Al_2O_3 but has a density of $\alpha\text{-Al}_2\text{O}_3$. The material has a moderate thermal expansion coefficient, only $3 \times 10^{-6}/^\circ\text{C}$ to $5 \times 10^{-6}/^\circ\text{C}$ compared to $6 \times 10^{-6}/^\circ\text{C}$ to $8 \times 10^{-6}/^\circ\text{C}$ for $\alpha\text{-Al}_2\text{O}_3$. The sintered material is characterized by a fine-grained microstructure, with grainsizes of the order of 1 to 2 μm ; the material has a moderate strength of 210 to 242 MPa, which is somewhat lower than $\alpha\text{-Al}_2\text{O}_3$. The material melts at 1950°C, but the useful temperature is probably below 1500°C because of the reported loss of B_2O_3 at elevated temperatures.

Ahmet Atasoy et. al. [46] stated that the effect of metallic aluminium powder on the production of boron carbide–alumina composite was studied. Boric acid, carbon and aluminium powders were mixed in stoichiometric ratio, ball milled and heat treated at temperatures between 1300°C and 1650 °C for 1–5 hrs in the presence of argon flow. Depending on the ratio of boron oxide to carbon, the formation of boron carbide by the carbothermal reduction, was possible at a temperature of around 1500°C, but with the addition of metallic aluminium to the mixture of boric acid and

carbon, the carbide formation temperature was reduced at least 300 °C. At 1300 °C, B₄C was the major phase with alumina in the reaction products. The liquid–solid reaction mechanism, which occurred during the aluminothermic process, had a specific influence on the formation of boron carbide. The reaction temperature is lower than the corresponding temperature needed for the carbothermic reduction of a boron oxide–carbon mixture. The production of boron carbide by aluminothermic reduction shows that the overall reduction would proceed through a number of steps involving the formation of subs boron oxides and the dehydration of boric acid, the melting of Al, the reduction of boron oxide by Al, and the formation of reaction products such as boron carbide and alumina. The results suggest that a faster reaction occurs when the aluminium is molten, and that the mixture undergoes better reduction than the conventional carbothermic reduction under the conditions investigated.

Hui-xian Wei et. al. ^[47] showed that the effect of boric acid on the properties of high-alumina phosphate-bonded plastic refractory materials at medium temperature is investigated in this work. Powder X-ray diffraction (XRD), thermogravimetric analysis/differential thermal analysis (TG/DTA), and scanning electron microscopy (SEM) techniques are used to investigate the compositions and microstructures of the Al₂O₃–H₃BO₃ sintering products, in order to study the influence of the generated aluminum borate on the high aluminum refractories. Additionally, the effect of the addition of H₃BO₃ on the densification and mechanical strength of high-aluminum phosphate-bonded plastic refractories is studied by the permanent linear change, apparent porosity, cold compressive strength, flexural strength, and scanning electron microscopy pattern. The densification and mechanical strength of the refractories can be improved significantly by the optimal addition of H₃BO₃. However, excess H₃BO₃ will bring about a large amount of bound water into the refractories, and superabundant aluminum borate whiskers will be generated by the excess addition of H₃BO₃, both of them resulting in the reduction of the densification and mechanical strength of the refractory. In conclusion, the optimum dosages of H₃BO₃ in the powder system of high alumina phosphate-bonded plastic refractories are 5, 4, and 3 wt%, sintered at 700, 900, and 1100 °C, respectively. Besides, the optimum dosage of boric acid in the high-alumina refractory materials was seen to depend on the operating temperature. In summary, the high-alumina phosphate-bonded plastic refractory materials enhanced by H₃BO₃ at medium temperature

have achieved good results. And, the optimum dosage of boric acid in the high-alumina refractory materials should be adjusted depending on the operating temperature.

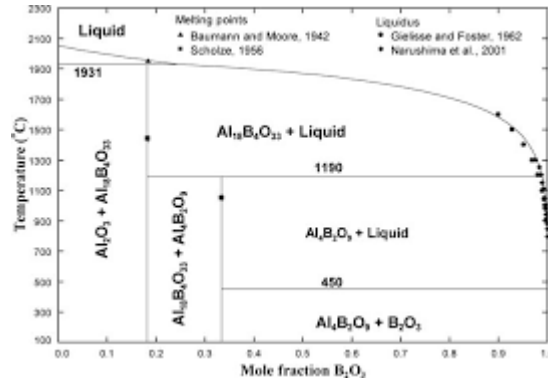


Figure-2: Phase diagram of Al₂O₃- B₂O₃

Maria F. Hernandez et. al. [48] investigated that the formation of aluminum borates (Al₁₈B₄O₃₃ & Al₄B₂O₉) from alumina and boron oxide occurs between 600 and 800 °C. These materials have refractory properties and corrosion resistance. The objective of this work is to develop materials from the Al₂O₃-B₂O₃ system, employing alumina and boric acid as starting powders, to study the critical processing variables and describe the developed microstructure and properties. Three formulations (13, 19.5 and 26 wt% B₂O₃) were studied. In order to confirm the formation of borates, the differential thermal analysis and thermogravimetric analysis were carried out. Afterwards, uniaxially pressed disc-shaped specimens were fired at four temperatures above the formation temperature. The textural properties of the ceramics were evaluated by the immersion method, this permit to evaluate the sintering processes. Then the degree of borate formation was confirmed by X-ray diffraction. Finally, the developed microstructures were characterized by scanning electron microscopy, and the diametric compression behavior was evaluated. A series of porous (≈50%) refractory materials from the Al₂O₃-B₂O₃ system were developed. The processing strategy resulted in materials with Al₁₈B₄O₃₃ as the main crystalline phase. Needle grains with diameters between 0.2 and 1 μm and an aspect ratio over 20:1 were obtained. Thus, based on the information gathered from their research, aluminum borate ceramic materials can be designed for structural, insulating or filtering applications employing only alumina and boric acid as boron oxide source.

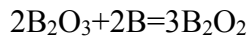
M. Rendtorff et. al. [49] compared the complex mechanical behavior of two complex ceramics material formed within the reaction sintering framework. Two comparable pairs of materials with

respectively similar microstructures were obtained by reaction sintering from boric acid and alumina. Two single phase porous ceramics were compared with two composite (1:1) porous ceramic. The first and second phases were aluminum borate needles ($\text{Al}_{18}\text{B}_4\text{O}_{33}$) and alumina (Al_2O_3). The four with comparable grain size and analogous apparent porosities: in diameter ($\approx 0.7 \mu\text{m}$) and in volume fraction ($\approx 45\%$). The mechanical behavior was studied by means of the diametral compression test at low displacement rate and explained in terms of the texture, microstructure features evaluated by mercury intrusion porosimetry and scanning electron microscopy. Single $\text{Al}_{18}\text{B}_4\text{O}_{33}$ phase porous materials presented higher mechanical strengths than the composite materials. Within the respective microstructural configurations the whisker thickness did not affect significantly the mechanical behavior and parameters. A well-defined fragile behavior was observed and described in the composite material. On the other hand the single $\text{Al}_{18}\text{B}_4\text{O}_{33}$ needle porous material presented a distinctive behavior with local discontinuities without loss of integrity in the diametral stress behavior, and achieved strength up to 50% higher than the corresponding composite.

Yan Li et. al. ^[50] showed that Single crystal aluminum borate, including $\text{Al}_{18}\text{B}_4\text{O}_{33}$ and $\text{Al}_4\text{B}_2\text{O}_9$, nanowires and nanotubes have been synthesized on sapphire substrates covered by NiB powder, Pt powder and Al films. For NiB powder covered sapphire substrates, $\text{Al}_{18}\text{B}_4\text{O}_{33}$ nanowires and nanotubes are formed by heating the substrates at 1100°C under Ar gas flow. For Pt powder covered sapphire substrates, $\text{Al}_{18}\text{B}_4\text{O}_{33}$ nanowires and nanotubes are produced by a chemical vapor deposition (CVD) method using boron tri-iodide and boric acid ($\text{BI}_3/\text{H}_3\text{BO}_3$) vapor with Ar gas as precursor at 1000°C . The nanowires are several micrometers long with diameters ranging from 50 to 200 nm, while the diameters of the nanotubes are usually larger than 200 nm. For Al film covered sapphire substrates, $\text{Al}_4\text{B}_2\text{O}_9$ nanowires and nanotubes are synthesized by the CVD method using boron tri-iodide (BI_3) vapor with Ar gas as precursor at $750\text{--}850^\circ\text{C}$. The size of the nanostructures can be manipulated by the growth time, the growth temperature, the BI_3 vapor concentration, and the Al film thickness. The nanostructure diameter and length can be varied in the range of 10–500 nm and 300 nm–2 μm , respectively. All the nanostructures have been characterized by scanning electron microscope (SEM), X-ray diffraction (XRD), transmission electron microscope (TEM), selected area electron diffraction (SAD), electron energy-loss

spectrometry (EELS) and X-ray energy-dispersive spectrometry (XEDS). The growth mechanism of the aluminum borate nanowires and nanotubes is discussed.

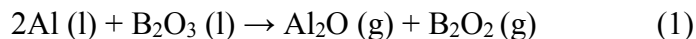
Chun Cheng et. al. ^[51] showed that Single-crystal aluminum borate nanowires ($\text{Al}_{18}\text{B}_4\text{O}_{33}$) with uniform diameter distribution were synthesized by a chemical reaction of alumina with boron monoxide in the presence of a support catalyst. Three comparative experiments were carried out and demonstrated the detailed crystal growth process of the nanowires. It is found that two factors, the isolated reaction area with nanometer scale and abundant local reactants at an appropriate reaction temperature, play important roles in determining the diameter, length and yield of the nanowires. The growth mechanism was also prepared. The addition of boron is believed to increase the concentration of reacting boron-containing vapor during the experiments as a result of the following chemical reactions taking place at the reaction temperature:



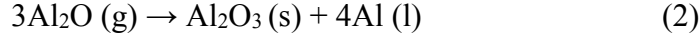
B_2O_2 vapor reacted with the Al_2O_3 and yielded more aluminum borate nanowires with perfect morphology because the superfluous boron monoxide gas was transported away by argon from the reaction area.

J. Zhang et. al. ^[52] reported that single-crystal and uniform aluminum borate ($\text{Al}_4\text{B}_2\text{O}_9$) coated aluminum oxide nanowires have been synthesized in high purity and in large yield via a reaction of metal aluminum with boron oxide in the presence of carbon nanotubes (CNTs). The aluminum oxide nanowires exhibit a well-crystallized one-dimensional structure with diameters ranging from 50 to 70 nm, and the $\text{Al}_4\text{B}_2\text{O}_9$ have a coating thickness of about 1–5 nm. CNTs play a crucial role in the formation of the important ceramic nanowires, by providing a platform to grow the composite structure. The growth mechanism was proposed by the detailed microscopy observations.

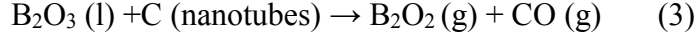
The following reaction starts when heating B_2O_3 and Al at a high Temperature:



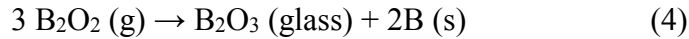
The generated Al_2O vapors transfer and deposit onto the surfaces of CNTs to form Al_2O_3 lumps, or form Al_2O_3 nanowires along with CNTs, according to the process



Once the nanowires are formed, this trend might be maintained and Al_2O_3 nanowires would grow continuously along the initially formed crystal directions. Simultaneously, the vapor B_2O_2 reacts with Al_2O or Al_2O_3 to form $\text{Al}_4\text{B}_2\text{O}_9$ crystal. At the same time, B_2O_2 gas can also be supplied by the chemical reaction



Therefore, the existence of CNTs avoids the formation of the glassy B_2O_3 in the product due to the decomposition of B_2O_2 to B_2O_3 at low temperature according to the reaction



B_2O_2 gas can escape and react with Al or its oxides, forming $\text{Al}_4\text{B}_2\text{O}_9$ coating at the surface of the as-grown Al_2O_3 .

S.A. El-Hakam et. al. ^[53] investigated that a series of aluminum borate alumina catalysts of different composition was prepared with the co precipitation method. The structural and phase changes were studied by thermal analysis, X-ray diffraction (XRD) and FT-IR techniques. Thermal treatment of solid aluminum borates–alumina led to the formation of different phases namely, $\gamma\text{-Al}_2\text{O}_3$, $\alpha\text{-Al}_2\text{O}_3$, $2\text{Al}_2\text{O}_3 \cdot \text{B}_2\text{O}_3$ and $9 \text{Al}_2\text{O}_3 \cdot 2\text{B}_2\text{O}_3$, where the formation of the latter two phases was observed in the temperature range of 840–900°C. The surface acidities were determined using the spectrophotometric method. Cracking of ethylbenzene and dehydration (DHD) of isopropanol and ethanol were investigated on the calcined catalyst using the pulse micro catalytic technique. The boron contents and the calcinations temperature are important factors in determining the structural properties and catalytic activities of these catalysts. The results also indicated that the surface acidities were found to increase with increasing boron contents of the samples and decreased with the calcination temperatures. Therefore, the catalytic activities of the investigated catalysts were found to be structurally sensitive.

R. K. Gupta et. al. [54] have discovered that nanostructured aluminum borate was synthesized using sol–gel technique. X-ray diffraction study revealed that the synthesized aluminum borate was single crystal. These nano rods have very uniform diameter. High resolution transmission electron microscope images indicate that aluminum borate is well crystallized. The alternating current (AC) conductivity of the aluminum borate was studied as a function of temperature and frequency. The AC conductivity mechanism of the aluminum borate was found to be proportional to ω^s . The exponents is almost independent with temperature. This suggests that AC conductivity mechanism of the aluminum borate can be interpreted by localized hopping model. Nanostructured aluminum borate was synthesized using sol–gel method. The results indicate that the synthesized aluminum borate is phase pure. The nanowires have lengths of several nanometers and diameters ranging from 15 to 20 nm. The AC conductivity was found to depend both on frequency and temperature. The value of the frequency exponent and its temperature dependence confirmed the localized hopping conduction mechanism.

Ana Paula Luz et. al. [55] described that this work addresses the optimization of alumina-based castables designed for petrochemical applications by adding an additive able to speed up the samples' densification at lower temperatures. Hot elastic modulus, thermal shock, hot modulus of rupture, and erosion resistance measurements were carried out to evaluate these castables. The E profiles confirmed the transient feature of the generated liquid phase, as it was crystallized throughout subsequent heating cycles. Thermal fatigue effect was also observed for the compositions with higher boron content. Nevertheless, the boron-containing castables showed outstanding properties, which could be attained only with using suitable amounts of this engineered additive. According to the results presented in this work, the addition of a boron-based sintering additive can lead to a remarkable improvement of the high-alumina refractory castables properties (i.e., hot mechanical strength, erosion, and thermal shock resistance) mainly at 800°C. It must be highlighted that although a liquid is formed at high temperatures in the boron-containing refractories, this phase will react with the castable components (mainly the calcium aluminate cement and reactive alumina of the matrix portion) giving rise to aluminum borates (A_2B , A_9B_2) and a ternary compound (CAB). Hence, it was concluded that the liquid phase presented a transient feature, as it was consumed with subsequent thermal treatments. Furthermore, the presence of a great amount of those new boron-containing phases (A_2B , A_9B_2 and CAB) led to a

decrease in the castables' stiffness due to a thermal fatigue effect (related to the thermal expansion mismatch of the formed phases and the castable original components).

M.F. Hernández et. al. ^[56] investigated that dense aluminum borate ($\text{Al}_{18}\text{B}_4\text{O}_{33}$) materials were processed by simple milling-sintering of aluminum borate powders obtained by reacting calcined alumina and fine boric acid at temperatures of around 600- 800°C. The effect of milling on the grain size and sintering behavior of the aluminum borate powders was also determined. Sintering began at around 1000°C and was limited by the thermal decomposition ($T > 1300$ °C) of the borate in to alumina and boron oxide, which volatilize at this temperature. Sub angular and medium spherical sintered grain microstructures were developed. A hardness of 6 GPa and bulk density below 2.5 g/cm^3 were achieved. The results are accomplished encouraging for the structural applications of borate materials. The attrition milling was demonstrated to be adequate for milling the initially whisker shape borate powder. An almost complete loss of the whisker-shaped was achieved after 180 min grinding. All the analyses of this system encourage the structural application of borate materials sintered at up to 1300 °C. The results also reveal important information on the thermal behavior of the Al_2O_3 - B_2O_3 system that is being proposed as a setting (bonding) phase at intermediate temperatures (800-1200 °C) of high alumina and/or spinel refractory castables.

Andre R. Studart et. al. ^[57] demonstrated that macro porous ceramics with pore sizes from 400 nm to 4 mm and porosity within the range 20%–97% have been produced for a number of well-established and emerging applications, such as molten metal filtration, catalysis, refractory insulation, and hot gas filtration. These applications take advantage of the unique properties achieved through the incorporation of macro-pores into solid ceramics. In this article, we review the main processing routes that can be used for the fabrication of macro-porous ceramics with tailored microstructure and chemical composition. Emphasis is given to versatile and simple approaches that allow one to control the micro-structural features that ultimately determine the properties of the macro-porous material. Replica, sacrificial template, and direct foaming techniques are described and compared in terms of microstructures and mechanical properties that can be achieved. Finally, directions to future investigations on the processing of macro-porous

ceramics are proposed. Highly oriented open pores ranging from 10 to 300 nm can be produced with this method at porosities between 25% and 95%. The most important processing step in this route is the conversion of the wood-derived carbon preform into a ceramic phase. Predominantly open pores of various different morphologies can be produced with this method.

Hanna Luhrs et. al. [58] showed that A series of boron doped mullites (B-mullite) was prepared from single-phase gels with initial compositions based on a 1:1 isomorphous substitution of Si by B, starting from a 3:2 mullite composition ($\text{Al}_{4.5}\text{Si}_{1.5}\text{O}_{9.75}$). A high amount of boron (>10 mol.%) can be incorporated into the crystal structure of mullite where it most likely replaces Si. In situ phase formation of B-mullites was studied with high temperature X-ray diffraction and thermal analysis. A decrease of the formation temperature for B-mullite with increasing boron content was observed. With increasing boron content lattice parameters b and c significantly decrease, while no systematic evolution is observed. Long annealing at 1400°C results in decomposition of B-mullite to boron free mullite and α -alumina. At 800°C B-mullite appears to be stable over a period of at least 12 days. The mean thermal expansion coefficient was reduced by 15% upon incorporation of boron which makes the material technologically interesting.

3. PLAN OF THE WORK

Calcined alumina was used as the principle raw material. Chromium oxide and boron tri-oxide was used as sintered aid for the densification of alumina.

For the densification of the alumina presence of chromium oxide and boron oxide, different amount of the additive oxides was chosen. For the uniform and homogeneous mixing each batch was thoroughly mixed in presence of alumina ball. For getting green strength, green binder was used before granulation of the powder binder mixtures. For uniform green density, the binder powder mix was granulated followed by uniaxial pressing. Effect of firing temperature was evaluated by sintering the pressed body at different temperature with 2hs.

The densification was evaluated by measuring linear shrinkage, bulk density, and apparent porosity. The crystalline phase was evaluated by powder X-ray diffraction study. To access the chemical corrosion resistance property, the slag corrosion test was performed on the sintered body. To get the idea about the morphology, size of different phases including pores, scanning electron microstructural study was done on the chemically etched fractured surface. To identify different phase with their chemical composites, EDX analysis was also performed.

4. Experimental work

Stage 1: Preparation of Alumina-Chrome refractory

We have prepared five batches of mixture of alumina (Al_2O_3) and chromia (Cr_2O_3) by changing the amount of chromia content. Total amount of mixture in each batch is 100 gm. The detail of batch composition and batch code is displayed in table 1.

Table 1: Batch composition of raw materials

Sl. No.	Batch no.	Al_2O_3 (wt.%)	Al_2O_3 (mol%)	Cr_2O_3 (wt.%)	Cr_2O_3 (mol%)
1.	Cr ₀	100	100	0	0
2.	Cr ₃	97	97.97	3	2.029
3.	Cr ₅	95	96.59	5	3.41
4.	Cr ₇	93	95.19	7	4.81
5.	Cr ₁₀	90	93.05	10	6.94

Stage 2: Preparation of Alumina-Boron trioxide:

We have prepared four batches of mixture of alumina (Al_2O_3) and boron trioxide (B_2O_3) by changing the amount of boron trioxide content. Total amount of mixture in each batch is 80 gm. The detail of batch composition and batch code is displayed in table 2.

Table 2: Batch composition of raw materials

Sl. No.	Batch no.	Al_2O_3 (wt.%)	B_2O_3 (wt.%)	H_3BO_3 (wt.%)
1.	AlB ₂₅	79.8	0.2	0.359
2.	AlB ₅₀	79.6	0.4	0.71
3.	AlB ₇₅	79.4	0.6	1.069
4.	AlB ₁₀₀	79.2	0.8	1.42

4.1. Procedure:

Stage 1: The Cr_2O_3 content differ in every batch starting from 0 wt% in the 1st batch to the 10 wt% in the 5th batch.

Calcined alumina (HGRM-30) and chromia (Cr_2O_3) are mixed for 45 min in a plastic jar by hand. The plastic jars are jerked continuously and equally so the mixing should be a homogeneous. After that PVA (5%) is mixed with the samples for binding purpose for 20 min. The mixture should be passed to 30 mesh for 3 times so that a granulation should be proper. The batch is taken in a cylindrical mould of 20 millimeter and 12 millimeter diameter & pressed at 1200 kg/cm^2 for 1 min using hydraulic press after that the pellets are again sent into the dryer for 24 hrs. After overnight drying, the pressed sampled are sintered at the temperature of 1600°C & 1650°C maintaining oxidizing atmosphere. Reducing atmosphere has been maintained for same sample at 1600°C .

The firing schedule of sintering being programmed in furnaces are as follows:

Room Temp. $\xrightarrow{5^\circ\text{C/min}}$ 1000°C (10 min for soaking) $\xrightarrow{3^\circ\text{C/min}}$ 1600°C (2 hrs for soaking)

The temperature is raised from room temperature to 1000°C at the rate of 8°C/min . The soaking time at 1000°C is 10 min.

Again the temperature is raised to the respective optimum temperature (1600°C / 1650°C) at the rate of 3°C/min and the final soaking time at reached temperature is given for 2 hours.

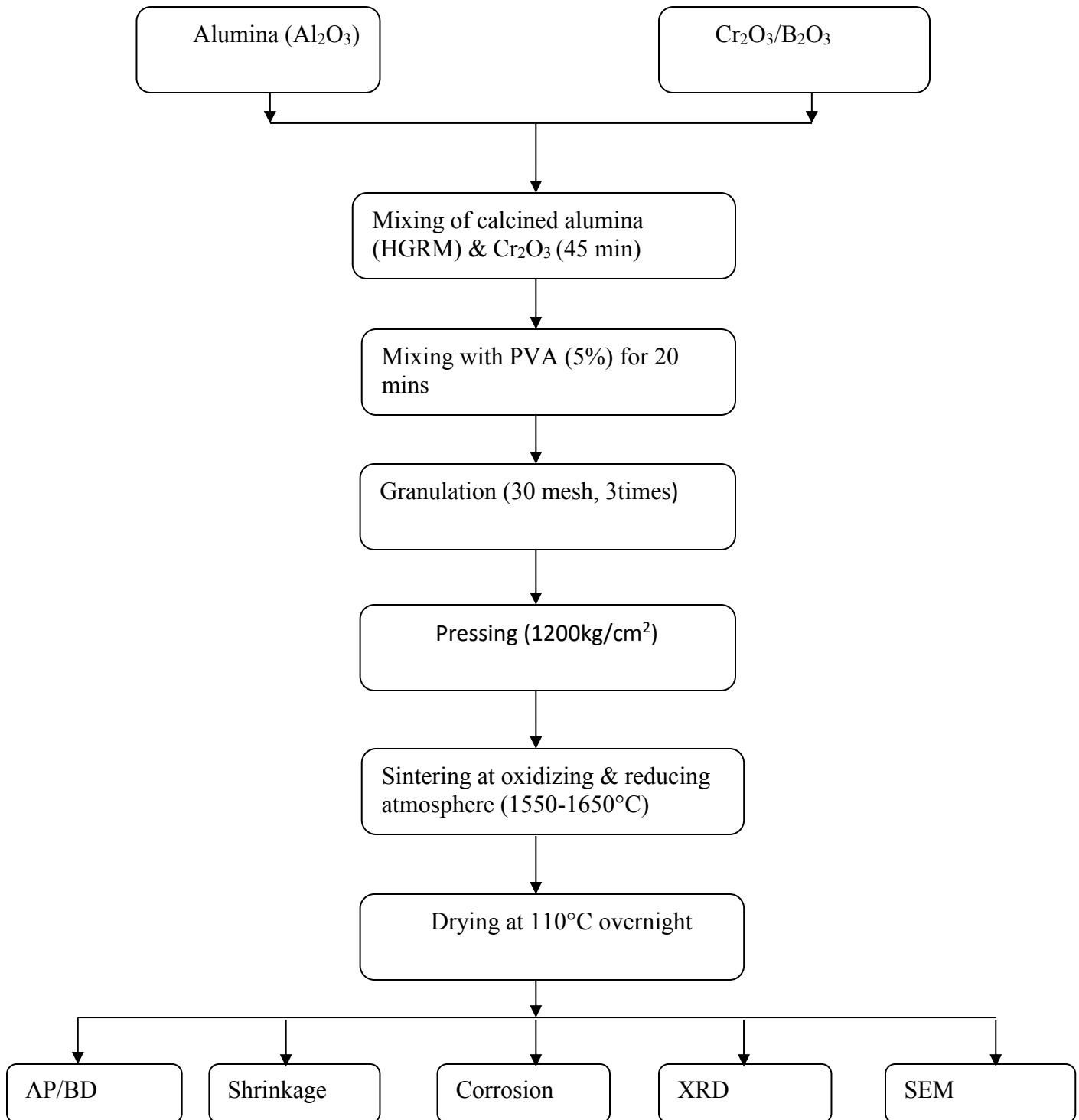
Stage 2: For B_2O_3 the experimental processes are same and rate also same but the firing has been done only at oxidizing atmosphere. The heating schedule also same for sintering but different only for slag corrosion test due to porous microstructure of B_2O_3 and high porosity of Cr_2O_3 .

The firing schedule of sintering for slag corrosion test:

Room Temp. $\xrightarrow{8^\circ\text{C/min}}$ 1000°C (10 min for soaking) $\xrightarrow{5^\circ\text{C/min}}$ 1450°C (1 hrs for soaking)

Sintered samples are placed into electrically heated dryer for further characterization.

4.2 Process flow chart:



4.3 Tests:

Finally, the samples undergo different characterization as follows:

4.3.1 Percentage of linear shrinkage(%)

The diameter of the samples was measured before firing (a) and after firing (b). Then it is calculated by

$$\frac{(b-a)}{a} \times 100$$

Where a = Diameter before firing, b = Diameter after firing

It is calculated in percentage.

4.3.2 Apparent Porosity (AP)

Apparent porosity is defined as the ratio of the volume of the open pores to the bulk volume of the material. It is expressed as a percentage.

The test specimen having a diameter 20mm are taken. Then, such test pieces are tied with a thread and is thereby hanged from the test rod. Such a Glass rod containing the test specimen is placed inside the beaker containing water such that the test specimen suspended in water so that any part of it should not be touched with the walls or bottom of the beaker.

The whole assembled beaker is placed n heater and water at 110°C for 2hrs. So that the open pores in the piece are filled up with the water quickly. Then, the samples are placed in cold water for a few minutes to get it cooled and then, the test pieces are tied with a wire which hangs from the knot of the weight to get it cooled and then, the test piece is tied with a wire which hangs from the knot of the wight balance such that the test piece should remain completely immersed in the water in the beaker.

Thus dry weight (D), suspended weight (S) and soaked weight (W) is calculated for the test specimen. Dry weight (D) should be calculated by drying the test specimen for 24Hrs. in an air oven.

Suspended weight (S) and soaked weight (W) is calculated. The apparent porosity (AP) is then calculated by the following equation.

$$\mathbf{A.P. = \frac{W-D}{W-S} * 100}$$

4.3.3 Bulk density

Bul density is a property of powders, granules, and other “divided” solids, especially used in reference to mineral component (soil, gravel), chemical substances, (pharmaceutical) ingredients, foodstuff, or any other or particular matter. It is defined as the mass of many particles of the material divided by the total volume they occupy. The total volume includes particle volume, inter-particle void volume, and internal pore volume.

This method of determining bulk density is preferable for specimens which are branded deeply or are irregular in contour. It is more than the direct measurement method.

The dry weight (D), suspended weight (S) and soaked weight (W) is calculated for the test specimen. Dry weight (D) should be calculated by drying the specimen for 24hrs in an air oven.

Suspended weight (S) and soaked weight Weight (W) are calculated by evacuation method. Bulk density is calculated in gm/cm³. The bulk density is given by the formula.

$$\mathbf{BD = \frac{D}{W-S}}$$

4.3.4 X-ray Diffraction (XRD) analysis

A scattering of X-ray by the atom of a crystal that produces an interference effect so the diffraction pattern gives information on the structure of the crystal or the identity of a crystalline substance.

The objective of Xrd is to know the composition of a crystalline object, which helps to determine different properties of that substance.

Selected sample was crushed into an iron mortar and pestle, passed through 30 mesh B.S. demagnetized and finely ground (much below 200 mesh) in a gate.

The nearly 5gm sample is required.

Bragg’s law is employed.

The instrument uses Ni-filtered Cu K_a radiation with a scanning rate of 2° per minute. The data had to be either compared using monographs already collected or using software crystalline phases are detected.

They were finally plotted neatly using ORIGIN software.

4.3.5 Scanning Electron Microscopy (SEM)

. A scanning electron microscope (SEM) is a type of electron microscope that produces an image of a sample by scanning it with a focused beam of electrons. The electrons with atoms in the sample, producing various signals that contain information about the samples surface topography and composition.

Samples were first broken into a thin plate.

Then samples were chemically etched. Chemical etching was done by treating the factured surface of the sample with 40% HF for 1 min. Then the surface was washed by 1:1 rectified spiritand distilled water in ultrasonic cleaner for 8 mins. After that the samples were dried at 110°C for 2 hrs.

Sample tester firstly coated the sample with the platinum nanoparticle to make the surface conductive. Then SEM pictures were taken and grain composition was found out by EDXA

4.3.6 Slag Corrosion Test of Refractories

Slag attack is particularly important. The structural strength of the refractory may be critically reduced by the solvent action of liquid slags. The slag attack on the refractories in contact may be in two ways: Corrosion - It is the wear and tear of refractories caused by a static chemical attack of slag.

Erosion - It is wear caused by mechanical action i.e. the process of breaking and washing away of refractory materials by molten slag.

Firstly, we have prepared cylindrically shaped specimens having a diameter 20mm. Then we make 5mmhole at the center and Depth around 2/3rd of specimens. Fired the sample according to the schedule.

The temperature is raised from room temperature to 1000°C at the rate of 8°C/min. the soaking time at 1000°C is 10 min.

Again, the temperature is raised to the respective optimum temperature at the rate of 5°C/min and the final soaking time at reached temperature is given for 1 hours.

Now, the fired samples are half filled with BF slag and fired at 1450°C for 1Hrs. The corroded samples are cut into two pieces by the help of cutting machine.

The depth of the penetration of the samples is observed and measured by a vernier scale.

5. RESULT AND DISCUSSION

Table-3: physico-chemical characteristics of raw materials in weight %

Raw Material	MgO	Al ₂ O ₃	Cr ₂ O ₃	B ₂ O ₃	Na ₂ O	SiO ₂	CaO	TiO ₂	Fe ₂ O ₃	Specific Gravity	XRD (main crystalline phase)
Chromium Oxide(Loba Chemie pvt. Ltd.	-	-	99.08	-	-	-	-	-	0.02	5.22	Eskolaite
Calcined Alumina	Trace	99.5	-	-	0.35	0.04	Trace	-	0.06	3.95	α-Al ₂ O ₃
Boric acid powder	-	-	-	99.5	-	-	-	-	-	1.44	-

Densification of the sintered body can be evaluated by measuring diametral shrinkage of the samples after firing from green stage, bulk density and apparent porosity . Here in case of Al₂O₃-Cr₂O₃ system, sintering was done separately in oxidising and reducing atmosphere.

Fig-3 & 4 shows the dimetral shrinkage (%) as function of Cr₂O₃ content sintered at oxidising condition at 1600°C & 1650°C for two hours. The percentage shrinkage of sample sintered was reduced with the increasing content of Cr₂O₃. Smamples fired at 1650°C for two hours showed higher shrinkage wuth respect to the samples fired at 1600C for two hours.

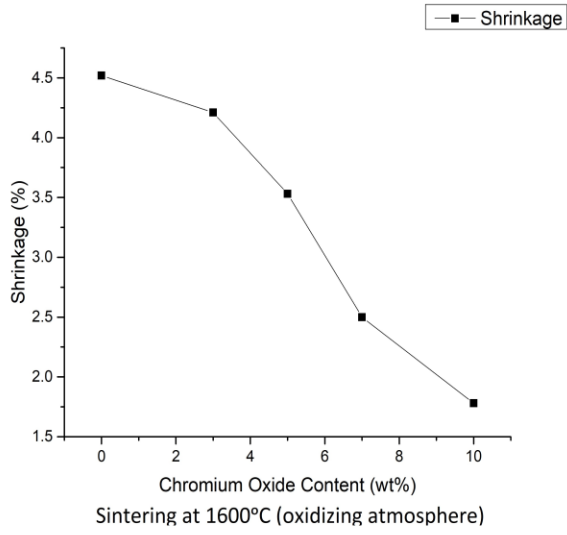


Fig-3

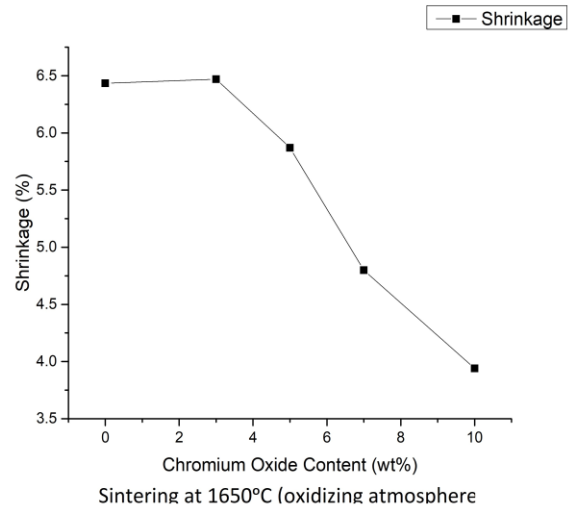
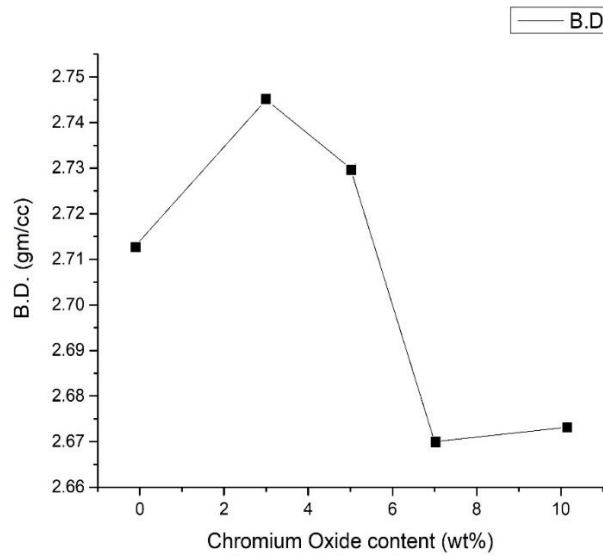


Fig-4



BD test after sintering at 1600°C of $\text{Al}_2\text{O}_3\text{-Cr}_2\text{O}_3$
Oxidizing atmosphere

Fig-5

Fig-5 displays the bulk density (B.D.) of sintered body as function of Cr_2O_3 content when sintered at 1600°C in oxidizing atmosphere. Here best B.D was observed with 3 weight % Cr_2O_3 content Alumina and then B.D was decreased with increasing Cr_2O_3 content.

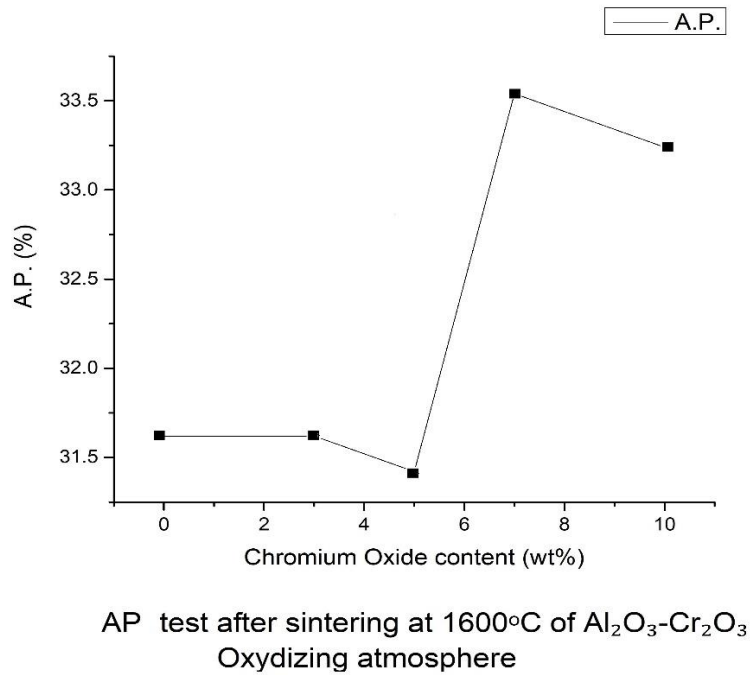


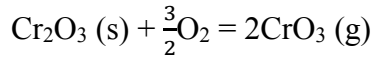
Fig-6

Fig-6 reports that the apparent porosity(A.P) versus Cr_2O_3 content graph showed the same values for without & 3 wt% Cr_2O_3 samples, but the B.D of 3wt% is high due to the higher specific gravity of Cr_2O_3 (5.22) as compared to Alumina (3.96).

The difficulty of sintering in oxidising condition is confirmed by the reduction in B.D with higher percentage of Cr_2O_3 . The characteristics white colour of Alumina turned into pink.

This colour is characteristic of the solid solution formation in which Cr³⁺ ions are occupying part of the octahedral interstitial sites of Al³⁺ in the approximate hexagonal closed packed structure[6].

The low B.D of the sintered samples with high Cr₂O₃ oxide content may be decrease due to the ion of Cr³⁺ which would occur by reaction:



Chromium ions are consistent with the large primary particle size suggesting ion of chromium by volatilization is faster than solid solution.^[8] Fig-7 shows A.P decrease with increasing Cr₂O₃ content in reducing atmosphere.

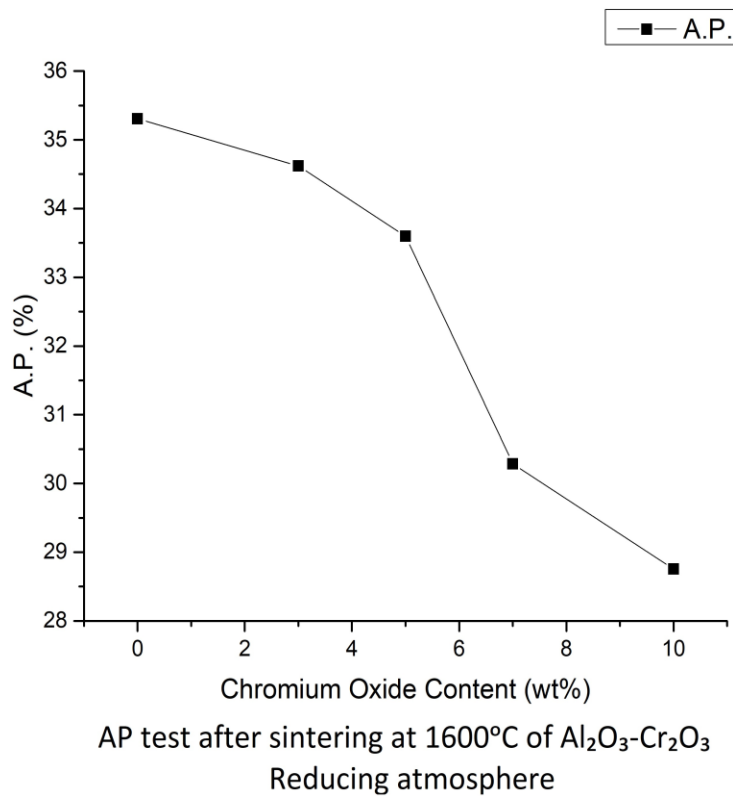
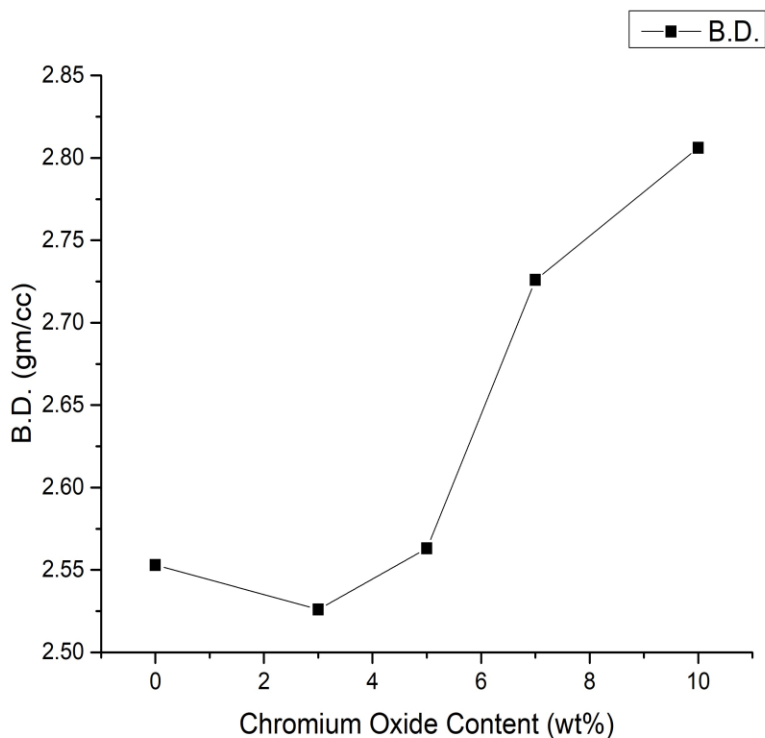


Fig-7



BD test after sintering at 1600°C of Al₂O₃-Cr₂O₃
Reducing atmosphere

Fig-8

If the sintering atmosphere is reducing then the value of B.D. was increased with the Cr₂O₃ content in the samples. Due to the reducing condition volatilization of chromium as CrO₃ was reduced led to the high value of B.D. According **fig-8** highest B.D. 2.806 g/cc was observed 10wt% Cr₂O₃ content body.

In the powder X-Ray diffraction (10wt% Cr₂O₃) study of the Al₂O₃- Cr₂O₃ batch shown in **fig-9**, corundum is the only crystalline phase in the sintered body in oxidizing atmosphere. A small peak of chromium was identified in the sample in reducing condition. **AIB** denotes Al₂O₃-B₂O₃ with 1wt% B₂O₃, **Cr-R** denotes Al₂O₃-Cr₂O₃ system with 10 wt % Cr₂O₃ in reducing atmosphere and

Cr-O denotes $\text{Al}_2\text{O}_3\text{-Cr}_2\text{O}_3$ system with 10 wt % Cr_2O_3 in oxidizing atmosphere. In XRD figure Cd = Corundum & Cr = Chromium.

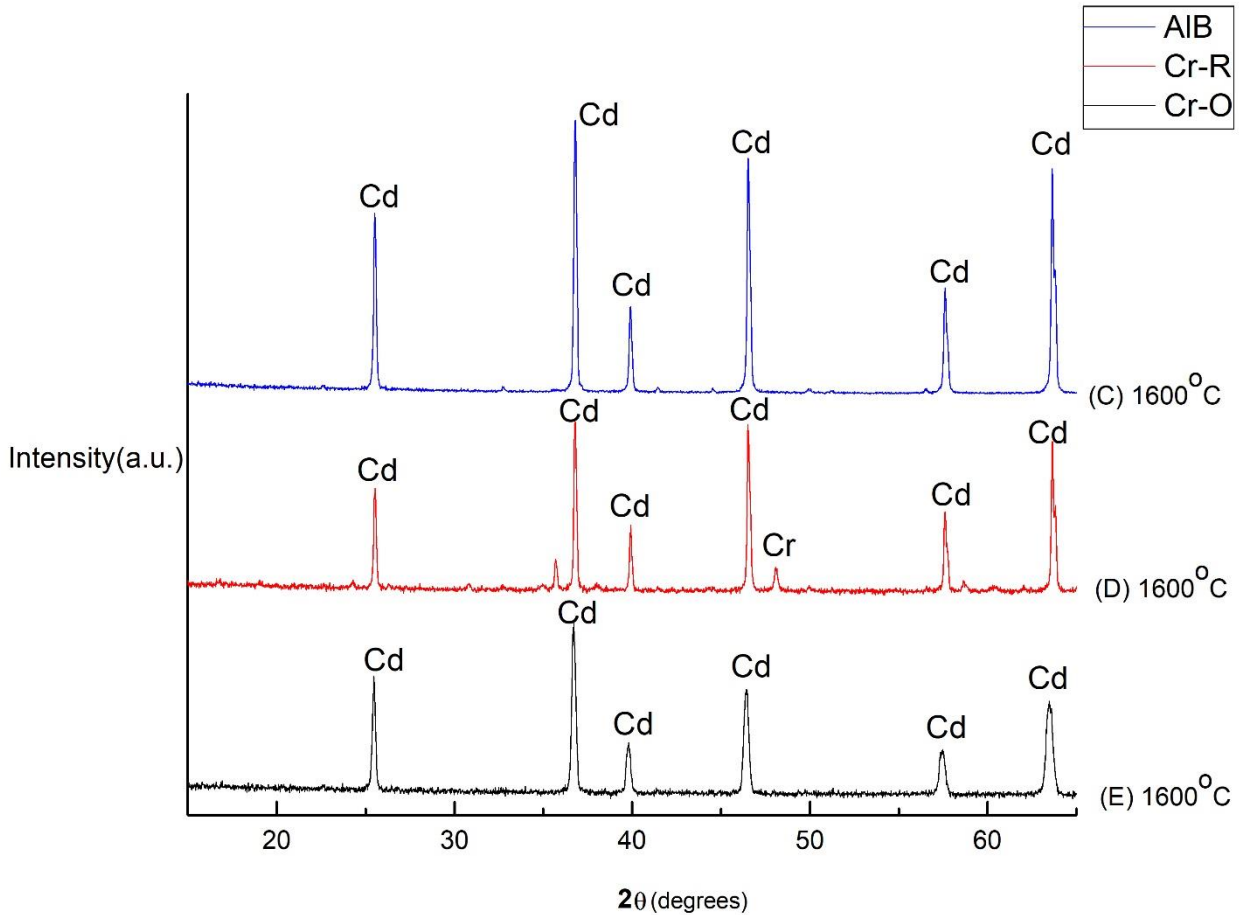


Fig-9: Powder XRD of Cr-O, Cr-R & AIB sintered at 1600°C

Microstructure can explain the various characteristics of the sintered body which include:

- Identification of different phase including pores
- relative amount & distribution of different phases
- morphology of different phases

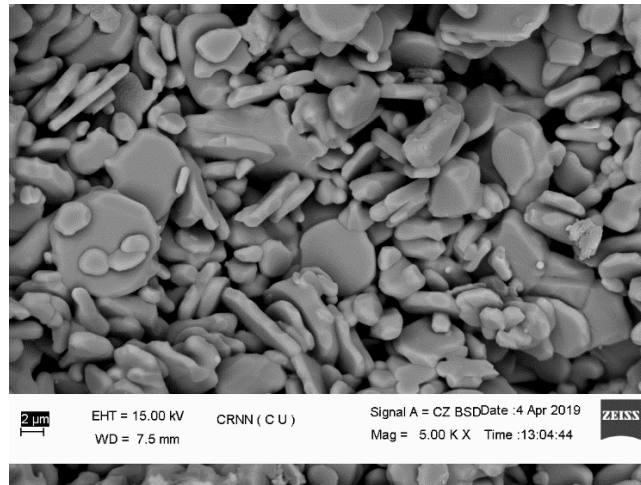


Figure-10: SEM image of Cr₀ sintered at 1600°C/2hrs in Oxidizing atmosphere.

Fig-10 shows the secondary electron image of chemically etched fractured surface of Cr-O sample sintered at 1600°C/2hrs. Plate like hexagonal crystals of corundum are observed.

The microstructure is porous. In presence of Cr₂O₃ (10wt%) the grain size of corundum was increased (**fig-11**).

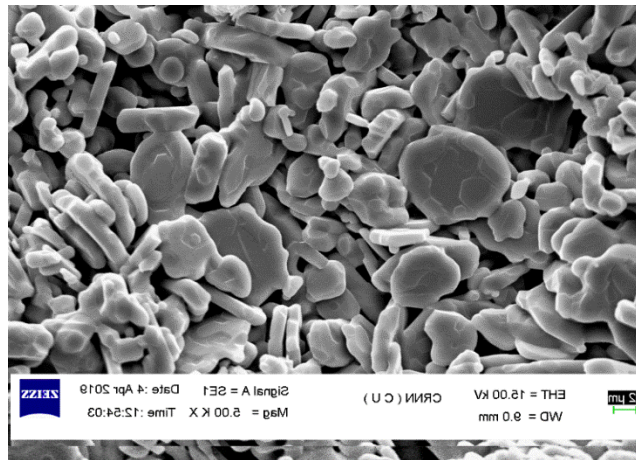


Figure-11: SEM image of Cr₁₀ sintered at 1600°C in oxidizing atmosphere.

Exaggerated grain growth of corundum grains are observed. Difficulty of sintering in oxidizing condition is observed. The same magnifications are displayed in both pictures.

The microstructure was changed when the sample was sintered in reducing condition.

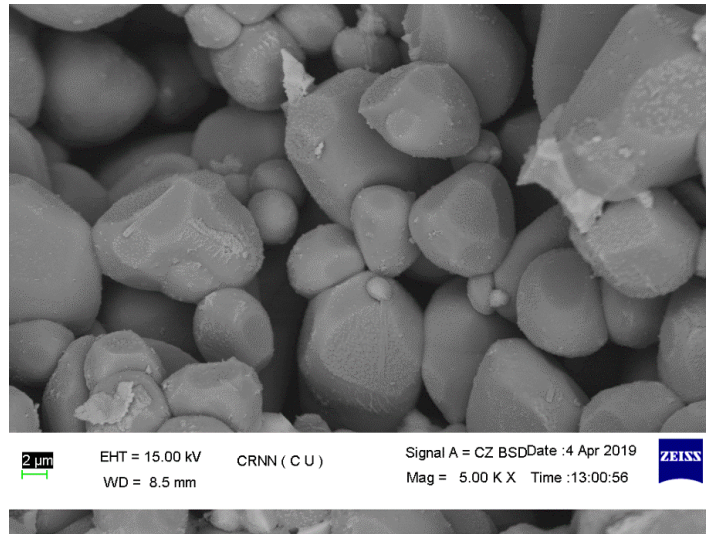


Figure-12: SEM image of Cr_{10} sintered at $1600^{\circ}\text{C}/2\text{hrs}$ in reducing atmosphere

Fig-12 shows the secondary image of Cr-10 sample sintered at $1600^{\circ}\text{C}/2\text{hrs}$ in reducing atmosphere. The microstructure is porous.

The corundum grains are irregular shaped. White spots are observed may be the Cr_2O_3 . The grain sizes varies from $2\ \mu\text{m}$ to several micrometres.

For the densification study, another oxide B_2O_3 was used varing $0.25 - 1.0\ \text{wt}\%$ with calcined alumina. Sintering temperature selected are 1550°C and 1600°C for 2hrs.

It was proposed that two stage reactions are there for formation of $\text{Al}_{18}\text{B}_4\text{O}_{33}$ phase. No reaction took place between B_2O_3 & Al_2O_3 below 800°C . Between 800°C & 900°C formation of $2\text{Al}_2\text{O}_3 \cdot \text{B}_2\text{O}_3$ was formed which above 900°C reacted gradually with excess alumina to form the $\text{Al}_{18}\text{B}_4\text{O}_{33}$ phase.

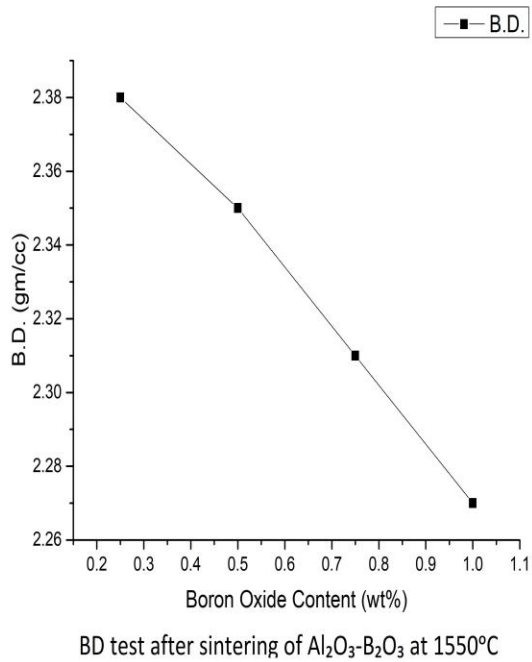


Fig-13

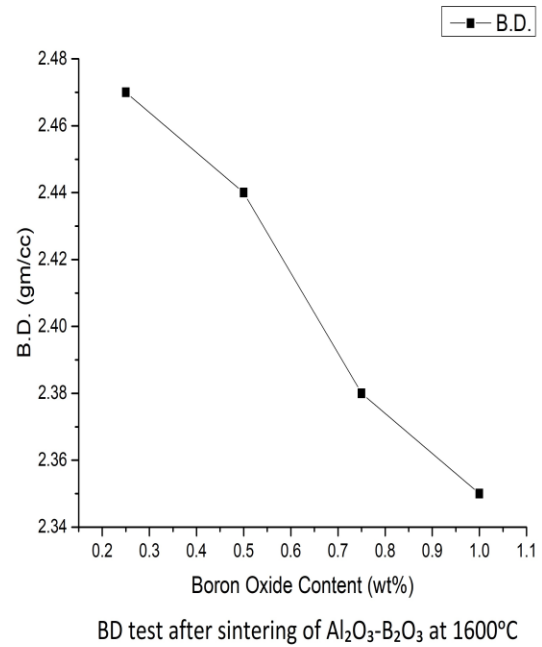


Fig-14

Fig-13 & 14 shows the effect of B₂O₃ of the bulk density of corundum samples after sintering at 1550°C & 1600°C /2hrs. In both temperatures the B.D. decreased with increase in B₂O₃ content. Addition of B₂O₃ to alumina has pronounced effect in lowering B.D. which in term results in porous microstructures^[43].

These results can be explained by the formation of aluminium borate phase which has chemical & physical properties in compatible to that of α -Al₂O₃ matrix. This are the lack of solid solubility between the two phases. Low theoretical densities (2.93 gm/cc) of aluminium borate phase results in volume expansion during its formation.

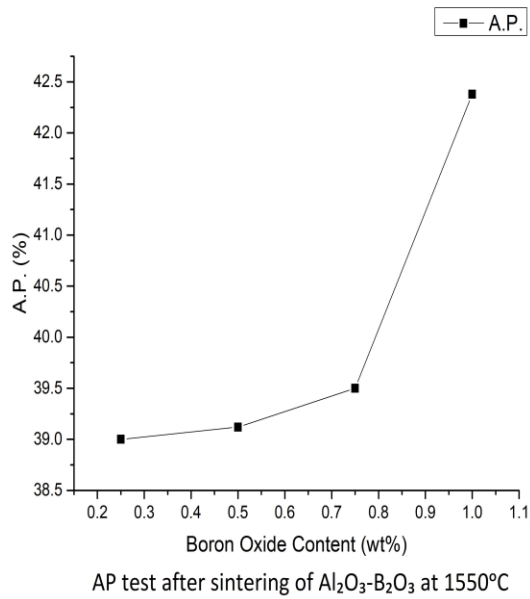


Fig-15

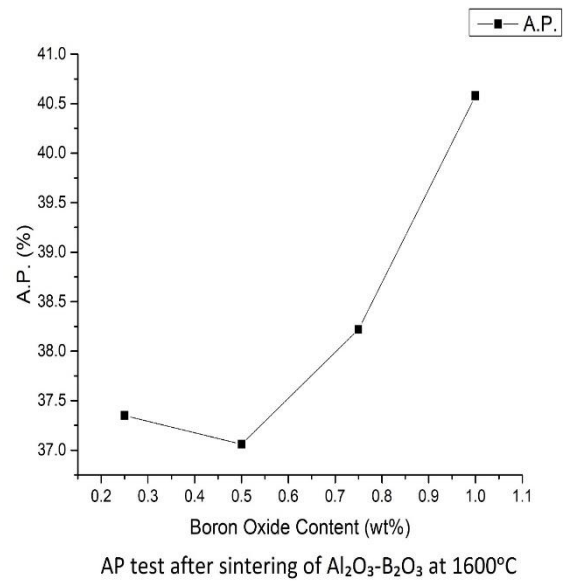


Fig-16

Fig 15 & 16 indicate that the effect of B₂O₃ content on the apparent porosity of Al₂O₃ B₂O₃ samples sintered at 1550°C & 1600°C / 2hrs. Apparent porosity reduced due to the increase in temperature from 1550°C to 1600°C which is also reflected in B.D. But with increasing in B₂O₃ content A.P. was increased which is 37.35% without any B₂O₃ to 40.58% with 1.00 wt% B₂O₃.

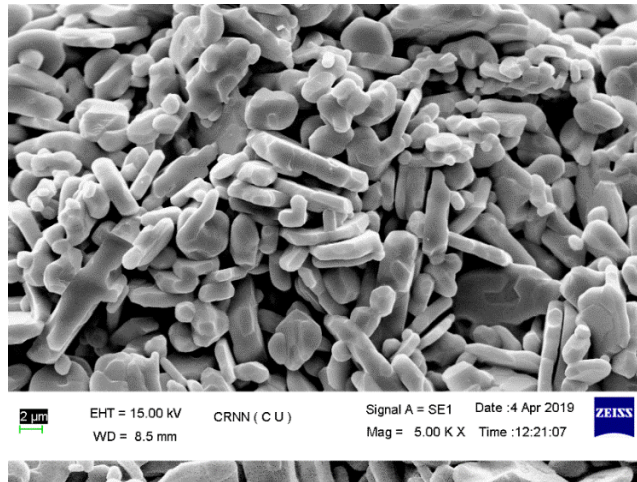


Figure-17: SEM image of AlB₁₀₀ sintered at 1600°C

Fig-17 showed that the secondary electron image of 1.00 wt% of B₂O₃- Al₂O₃ sample sintered at 1600°C/2hrs. The pure alumina or stated above, gives small & uniform plate like grained microstructure. In presence of 1.00 wt% B₂O₃ , the alumina grains lose their sharp definition & a discontinuous grain growth is observed within the microstructure. This addition level, which corresponds to the presence of ~ 7 wt% of aluminium borate phase within the matrix, gives rise to a porous microstructure due to volume expansion of these phase during its formation.



Fig-18: Corroded of Cr₁₀(O) sintered at 1450°C **Fig-19:** Corroded of Cr₁₀(R)



Fig-20: Corrosion of Cr₀ sintered at 1450°C

Slag corrosion test was done with the $\text{Cr}_2\text{O}_3\text{-Al}_2\text{O}_3$ samples. Fig-18,19 & 20 shows the corrosion after test. The slag was penetrated into the sample due to the high porosity. The alumina without Cr_2O_3 shows the highest corrosion.

6. SUMMARY

STAGE I:

1. When the Cr_2O_3 is added, the sinterability of Al_2O_3 decreased markedly due either to the evaporation of the Cr-containing species or to the change in the sintering mechanism.
2. The low density of some sintered compacts prepared, may be due to loss chromium, which could occur by the reaction
$$\text{Cr}_2\text{O}_3 (\text{s}) + \frac{3}{2}\text{O}_2 = 2\text{CrO}_3 (\text{g})$$
3. Chromium loss is consistent with the large primary particle size, suggesting that loss of chromium by volatilization is faster than solid solution formation.
4. Properties of Al_2O_3 - Cr_2O_3 solid solutions strongly depend on their crystal structure. It is well known that Al_2O_3 - Cr_2O_3 solid solutions have a crystal structure similar to that of corundum.
5. Later, it had been tried to maintain reducing atmosphere to get low apparent porosity by reducing volatilization of Cr^{3+} and A.P had been decreased compared to oxidizing atmosphere.
6. With the increase of Cr_2O_3 content, the slag corrosion rate of Al_2O_3 - Cr_2O_3 material decreased, which indicated that the Cr_2O_3 content played a decisive role in the slag resistance of Al_2O_3 - Cr_2O_3 material.
7. In this compound, the oxygen ions form an approximately hexagonal close-packed structure, with Al^{3+} filling two-thirds of the octahedral interstices and each Al^{3+} and Cr^{3+} center filling an octahedral. However, the effect of the Cr_2O_3 content on the crystal structure of Al_2O_3 - Cr_2O_3 solid solutions remains a matter of debate.

STAGE II:

1. The boric acid also acts as a binder both for the granulation. The formation of the aluminum borate phase is found to be complete at 1000°C and the fibrous microstructure which is characteristic of this phase is developed between 1000°C and

1100°C. The addition of B₂O₃ between 0.25 and 1wt% to alumina results in a discontinuous grain growth in the sintered samples.

2. The incompatible characteristics of the aluminum borate phase to those of the α -Al₂O₃, result in a porous microstructure which in turn reduces the strength of the sintered material. The porosity level can be controlled by the B₂O₃ addition levels.
3. The porous structure and reasonable strength values make the material a potential candidate to be used as ceramic filters and for ceramic-metal composite performs.

7. REFERENCES

1. Ruys, Andrew—**processing, structure, and properties of alumina ceramics.**
2. Doh-Hyung Riu, Young-Min Kong, Hyoun-Ee Kim, **Effect of Cr₂O₃ addition on microstructural evolution and mechanical properties of Al₂O₃.** *Journal of the European Ceramic Society*, 20 (2000), 1475±1481.
3. H. Tomaszewski, **Effects of Cr₂O₃ Additions on the Sintering And Mechanical Properties of Al₂O₃.** *Ceramics International*, Vol 8, 2, 1982.
4. W. J. Smothers and H. J. Reynolds, **Sintering and Grain Growth of Alumina.** *Journal of the American Ceramic Society*, Vol. 37, No. 12, 588-595
5. Harold, P. Cahoon, and Carl, J. Christensen, **Sintering and Grain Growth of Alpha-Alumina.** *Journal of the American Ceramic Society*, Vol. 39, No. 10, 337-344.
6. Pengda Zhao, Huizhong Zhao, Jun Yu, Han Zhang, Hongjun Gao, Qi Chen, **Crystal structure and properties of Al₂O₃-Cr₂O₃ solid solutions with different Cr₂O₃ contents,** *ceramic international*, 2017.
7. H.G. Emblem and T.J. Davies, **Solid-state chemistry of alumina-chrome refractories,** Vol 13, No. 2, 1993.
8. H. G. Emblem, T. J. Davies, A. Harabi, A. A. Ogwu, C. S. Nwobodo, V. Tsantzalou, **Solid-state chemistry of alumina-chrome refractories.** *Journal of materials science letters ll*, (1992), 820-821.
9. A. harabi and T.J Davies, **Effect of chromia on grain growth in alumina.** *Material science*, Vol 94-96(1992), pp 797-802.
10. E. N. Bunting, **Phase equilibria in the system Cr₂O₃-Al₂O₃,** Washington, March 19, 1931, 947-949.
11. P.H Sydenham, B.C Preston, B.W Mcknight, A.R. Limber, R Greent, **Sub-solidus phase equilibria in Cr₂O₃-Al₂O₃.** *Nature physical science*, Vol 235, Feb 7, 1972.
12. M. Risti, S. Popovi and S. Musi, **Structural properties of the system Cr₂O₃- Al₂O₃.** *Materials Letters*, 16 (1993), 309-312.
13. K. Shibata, M. Yoshinaka, K. Hirota and O. Yamaguchi, **Fabrication and mechanical properties of Cr₂O₃ solid solution ceramic in the system Cr₂O₃-Al₂O₃.** *Materials Research Bulletin*, Vol. 32, No. 5, pp. 627-632. 1997.

14. RavindraJangir, Dharmendra Kumar, Velaga Srihari, and Tapas Ganguli, **Study On Structural and Optical Properties of α -(Al_xCr_{1-x})₂O₃ (0 < x < 1) Solid Solutions**. *AIP Conference Proceedings*, 1942, 120025 (2018).
15. J. Graham, **Lattice spacings and color in the system alumina-chrome oxide**. *J. Phys. Chem. Solids* Pergamon Press, 1960, Vol. 17, Nos. 1/2, pp. 18-25.
16. J.E. Lovelock, T. Nash **The color problem of ruby**, *Nature*, May 3, 1958, Vol-181, 1264.
17. Sun Honggang, Li Hongxia, Li Pengtao, Zhao Shixian, **Research on slag resistance of Al₂O₃ - Cr₂O₃ refractory under temperature fluctuation condition**.
18. Takehiko Hirataa, Tatsuo Morimotob, Satoshi Ohtab, Nozomu Uchidac, **Improvement of the corrosion resistance of alumina–chromia ceramic materials in molten slag**. *Journal of the European Ceramic Society*, 23 (2003), 2089–2096.
19. Hiroyuki Sunayama, Takayuki Kasahara, and Masayasu Kawahara, **High Corrosion Resistance of Alumina-Chrome Refractory**. *The electro-chemical society*,
20. Ding Chena, AoHuangan, HuazhiGua, MeijieZhanga, ZhijunShaob, **Corrosion of Al₂O₃ - Cr₂O₃ refractory lining for high-temperature solid waste incinerator**. *Ceramic International*, Vol 41, Issue 10, Part B, December 2015, Pages 14748-14753.
21. Mithun Nath, A. Ghosh, H.S. Tripathi, **Hot corrosion behavior of Al₂O₃-Cr₂O₃ refractory by molten glass at 1200°C under static condition**. Vol1102, January 2016, Pages 153-160.
22. Kyeising Kwong, Art Petty, James Bennett, Rick Krabbe, and Hugh Thomas, **Wear Mechanisms of Chromia Refractories in Slagging Gasifiers**, *Int. J. Appl. Ceram. Technol.*, 4 [6], 503–513 (2007).
23. U. Rothhaar, H. Oechsner, **Interdiffusion studies of Cr₂O₃ layers on ceramic Al₂O₃ substrates**. *Thin Solid Films*, 324, 1998, 165–169.
24. Hwan-Tang, T. Tsai and Arnulf Muan, **Activity-Composition Relations in Refractory Oxide Solid Solutions at High Temperatures: The System Cr₂O₃-Al₂O₃**, *Am Gram Soc*, 75 [6], 1412-15, (1992).
25. A. Bettinelli, J. Guille and J. C. Bernier, **Densification of Alumina at 1400°C**, *Ceramics International*, 14 (1988), 31-34.

26. Motonari Fujita, Keisuke Inukai, Shinichi Sakida, Tokuro Nanba, Junji Ommyogi, Akira Yamachuchi, Yoshinari Miura, **sintering of Al₂O₃- Cr₂O₃ powder prepared by sol-gel process**. *Journal of the material science*, Vol.56, No.6, pp.526-530, June 2007.
27. Federica Bondioli, Anna Maria Ferrari, Cristina Leonelli and Tiziano Manfredini, **Reaction Mechanism in Alumina/Chromia (Al₂O₃–Cr₂O₃) Solid Solutions Obtained by Coprecipitation**, *J. Am. Ceram. Soc.*, 83 [8] 2036–40 (2000).
28. V.A. Bron and P.A. Lande, **Alumina-chrome refractories for lining steel plant ladles**. *Metallurgist*, volume 1, issue 9 (1957).
29. M.T. Hernandez, M. Gonzalez, De Pablos, **C-diffusion during hot press in the Al₂O₃-Cr₂O₃ system**. *Acta Materialia*, 51 (2003), 217–228.
30. A. A. Shaposhnikova, Kh. M. Papakin, T. S. Ignatova, V. G. Flyagin, **Production and testing of ladle brick with chrome-alumina slag additives**. *Refractories and industrial ceramics*, volume 2, issue 1-2 (1961).
31. V. V. Viktorov, I.V. Evdokimov and A. A. Fotiev, **Magnetic Properties and Structure of (Cr_xAl_{1-x})₂O₃ Solid Solutions**. *phys. stat. sol. (b)* 166, 453 (1991).
32. S.H. Yanga, S.J. Liub, Z.H. Huaa, S.G. Yanga, **Magnetic properties of Al₂O₃–Cr₂O₃ solid solutions**, *Journal of Alloys and Compounds*, 509 (2011), 6946–6949.
33. F. S. Stone and J. C. VickermaI, **Magnetic Properties of Chromium Ions in Oxide Matrices**. *Transaction of the faraday society*, volume 67 (1971).
34. G.M Dodis, T.V. Dodis and P.N Bobin, **structure and properties of fused refractories made from chromite and mixture of chromite and alumina**. *Academy of science of the translated from Ogneupory*, No. 1, pp.33-38, Jan.1982.
35. N. B. Chatterjee and B. N. Anti, **Chrome-Alumina Refractories**. *Transactions of the Indian Ceramic Society*, 23:1, 125-130, 2014.
36. Mithun Nath, Sandipan Sen, K. Banerjee, A. Ghosh, H.S. Tripathi, **Densification behavior and properties of alumina–chrome ceramics: Effect of TiO₂**. *Ceramics International*, Vol.39, Issue 1, January 2013, Pages 227-232.
37. Wen Yan, Junfeng Chena, Nan Li, Wendong Qiub, Yaowu Wei, Bingqiang Han, **Preparation and characterization of porous MgO–Al₂O₃ refractory aggregates using an in-situ decomposition pore-forming technique**, *Ceramics International*, 41(2015), 515–520.

38. Soik Bae and Sunggi Baik, **Critical Concentration of MgO for the Prevention of Abnormal Grain Growth in Alumina**, *J. Am. Ceram. Soc.*, 77[10], 2499-504 (1994).
39. Ritwik Sarkar, Samir Kumar Das, Goutam Banerjee, **Effect of addition of Cr₂O₃ on the properties of reaction sintered MgO–Al₂O₃ spinels**, *Journal of the European Ceramic Society*, 22 (2002), 1243–1250.
40. S. Maitra, S. Pal, S. Nath, A. Pandey, R. Lodha, **Role of MgO and Cr₂O₃ additives on the properties of zirconia–mullite composites**, *Ceramics International*, 28 (2002), 819–826.
41. Lei Zhang, Shichun Li, **Empirical atom model of Vegard's law**, *Science direct*, Vol 434, 1 February 2014, Pages 38-43.
42. T. R. Karpova, E. A. Buluchevskii, A. V. Lavrenov, N. N. Leontyeva, M. V. Trenikhin, T. I. Gulyaeva and V. P. Talzi, Synthesis, **Structure and Properties of the System B₂O₃/Al₂O₃**. *Chemistry for Sustainable Development*, 21 (2013), 53-60.
43. Zulal Misirli, Hilka Erkalfa & Osman T. dzkar, **Effect of B₂O₃ Addition on the Sintering of α -Al₂O₃** *Ceramics International*, 22 (1996), 33-37.
44. Gielisse, P. J. M, Foster, W. R, **The System of Al₂O₃-B₂O₃**. Volume 195, issue 4836 (1962).
45. Siba E Ray, **Preparation and Characterization of Aluminum Borate**. *J. Am. Ceram. Soc.*, 75[9], 2605-609 (1992).
46. Ahmet Atasoy, **The aluminothermic reduction of boric acid**, Vol.28, Issue 5, September 2010, Pages 616-622.
47. Hui-xian Wei, Yan-wei Jiang, Qiang Zhang, Cheng-hao Mo, Dong-yin Liu, **Effect of boric acid on properties of high-alumina phosphate-bonded plastic refractory materials**. *Journal of the Chinese chemical society*, 2018.
48. María F. Hernández, Gustavo Suárez, Mariano Cipollone, María S. Conconi, Esteban F. Aglietti, Nicolás M. Rendtorff, **Formation, microstructure and properties of aluminum borate ceramics obtained from alumina and boric acid**. *Ceramic International*, Vol.43, Issue 2, 1 February 2017, Pages 2188-2195.
49. Maria. Hernández, Gustavo Suárez, Mariano Cipollone, Esteban F. Aglietti, Nicolás M. Rendtorff, **Mechanical behavior and microstructure of porous needle: aluminum**

- borate ($\text{Al}_{18}\text{B}_4\text{O}_{33}$) and Al_2O_3 - $\text{Al}_{18}\text{B}_4\text{O}_{33}$ composites**, *Ceramic international*, Vol.43, Issue 15, 15 October 2017, Pages 11759-11765.
50. Yan Li, R.P.H. Chang, **Synthesis and characterization of aluminum borate ($\text{Al}_{18}\text{B}_4\text{O}_{33}$, $\text{Al}_4\text{B}_2\text{O}_9$) nanowires and nanotubes**. *Materials Chemistry and Physics*, 97 (2006) 23–30.
 51. Chun Cheng, X.X. Ding, F.J. Shi, Yun Cheng, X.T. Huang, S.R. Qi, C. Tang, **Preparation of aluminum borate nanowires**, *Journal of Crystal Growth* 263 (2004) 600–604
 52. J. Zhang, Y. Huang, J. Lin, X.X. Ding, C. Tang, S.R. Q, **Large-scale preparation of aluminum borate-coated aluminum oxide nanowires**. *Journal of Solid State Chemistry*, 178 (2005), 2262–2266.
 53. S.A. El-Hakam, E.A. El-Sharkawy, **Structural characterization and catalytic properties of aluminum borates–alumina catalysts**. *Materials Letters* 36 _1998. 167–173
 54. R. K. Gupta, A. A. Al-Ghamdi, Omar A. Al-Hartomy, **Synthesis and characterization of nanostructured aluminum borate by sol–gel method**. *J Sol-Gel Sci. and Technology*, (2012) Vol 64, Issue 1, pp 100–103.
 55. Ana Paula Luz, Tiago Santos Jr, and Victor Carlos Pandolfelli, **High-Alumina Boron-Containing Refractory Castables**. *Int. J. Appl. Ceram. Techno*, 11 [6] 977–983 (2014).
 56. M.F. Hernández, G. Suárez, C. Baudin, P. Pena Castro, E.F. Aglietti & N.M. Rendtorff, **Densification of lightweight aluminum borate ceramics by direct sintering of milled powders**. *Journal of Asian Ceramic Society*, Vol 6, Issue 4, 2018, pp.374-383.
 57. Andre R. Studart, WUrs, T. Gonzenbach, Elena Tervoort, and Ludwig J. Gauckler, **Processing Routes to Macroporous Ceramics: A Review**. *J. Am. Ceram. Soc.*, 89 [6] 1771–1789 (2006).
 58. Hanna Luhrs, Reinhard X. Fischer, Hartmut Schneider, **Boron mullite: Formation and basic characterization**. *Materials Research Bulletin* 47, (2012) 4031–4042.

Effect of Bauxite & Zirconia Addition on the Densification and Microstructural Properties of Mullite Aggregates Derived from Sillimanite Beach Sand

*A project submitted in partial fulfilment of the requirements for
the degree*

of

Bachelor of Technology

In

Ceramic Technology

Submitted by

Abhishek Das (GCECTB-R15-1001)

Tilak Matabbar (GCECTB-R15-1035)

Under the guidance of

Dr. Kaberi Das

Assistant Professor (Dept. of Ceramic Technology)



**Government College of Engineering
& Ceramic Technology**

(An Autonomus Institution under MAKAUT, NAAC accredited A Grade)

Acknowledgement

With deep regards and profound respect, we avail this opportunity to express our deep sense of gratitude and indebtedness to **Dr. Kaberi Das** (Assistant Professor, Dept of Ceramic Technology, GCECT, Kolkata) for his inspiring guidance, constructive criticism and valuable suggestion throughout in this project work.

It was very enriching and enlightening experience to work under her guidance. she has been very helpful and supportive; without her support this project would not have been possible. It was she who took initiative to send us to give oral presentation in 82nd annual session of Indian Ceramic Society at Jamshedpur on 8-9th January, 2019. For all of these invaluable helps we will be ever grateful to her.

We thank our Principle **Prof.(Dr.) K. Chakraborty** for his encouragement. We also would like to express our gratitude to our professors **Dr. R. Sen, Dr. R.C. Das, Dr. T.K. Bhattacharya, Dr. S. Patra, Dr. B.K. Sanfui**, who give us support, guidance & suggestions throughout the project.

We thank Mr. Jiban Dey for assisting us every day in laboratory.

We are heartily thanks to **Ramkaran Mosalpuri** (PhD. Scholar, CU) & **Pameli Paul** (PhD. Scholar, CU)

We are grateful to University college of Science & Technology, Calcutta University, Razabazar, Kolkata, Indian Institute of Engineering Science and Technology, Shibpur and Central Glass & Ceramic Research Institute (CGCRI), Kolkata for carrying out our SEM, EDX and XRD.

Lastly, we thank everyone who has helped us in all respect for giving our project a success.

Mr. Abhishek Das
(GCECTB-R15-1001)

Mr. Tilak Matabbar
(GCECTB-R15-1035)

B.Tech (Ceramic Technology)
GCECT, Kolkata.

Table of Contents

Sl. No.	Contents	Page No.
1.	Introduction	1-3
2.	Literature Review	4-17
3.	Plan of the work	18-19
4.	Experimental work	20-29
5.	Result and Discussion	30-45
6.	Summary & Conclusion	46-47
7.	Reference	48-52

CHAPTER 1

INTRODUCTION

1. Introduction

Sillimanite, Andalusite and Kyanite comprises the anhydride aluminium silicate polymorphs, commonly known as the Sillimanite group of minerals. Such minerals have the same composition ($\text{Al}_2\text{O}_3 \cdot \text{SiO}_2$) and transform into mullite and silica at temperature between 1300-1600°C depending on the polymorphic form, particle size and level of impurity. These raw materials are consumed primarily in refractory industry due to their transformation to mullite at high temperature. The mullite phase shows high hot strength with good resistance to chemical corrosion & physical erosion. [1]

Sillimanite group of minerals decompose to mullite and silica during thermal decomposition. These minerals show various characteristics of thermal expansion in which kyanite has the highest value. The nature of the silica that is liberated on heating also varies. It is in the form of cristobalite for kyanite and amorphous silica for sillimanite and andalusite. SiO_2 released during thermal transformation and partially reacts with impurity to form a glassy phase, which impairs the product quality. Product quality can be improved by alumina to form more mullite.



Mullite is widely used in various applications due to its several important properties such as good chemically inert, low thermal conductivity, high creep resistance, high refractoriness, low thermal expansion coefficient & good thermal shock resistance.

It is extremely rare natural material. Commercially mullite products are usually synthesized from various alumina and silica precursors through technique such as Co-Precipitation, Sol-gel, hydrothermal and chemical vapour deposition. In this process's alumina precursors are naturally γ -alumina, aluminium fluoride, aluminium hydroxide, α -alumina or other aluminium salts, whereas silica sources can be pure natural quartz, cristobalite, amorphous silica, colloidal, fumed and precipitated silica etc. However, mullite products produced from high purity reagents and precursors are not commercially available for bulk refractory applications. Normally, cheap, readily, locally, abundantly available natural raw materials are preferred to produce refractory-grade mullite aggregates. So far, raw materials used for this purpose include kaolinite, sillimanite and bauxite. Most of mullite obtained from these natural materials show an

inferior property in proportion to impurity levels. Further, a gradual depletion of the currently used raw materials represent a serious challenge to the refractory community to keep up the continuous production to mullite that as in high demand. Therefore, finding alternate alumina sources to meet the mullite requirement in term of production demand and properties has become imperative. Recently, beach sand sillimanite (BSS) has been identified as an alternative low-cost raw material which is abundantly available in nature. An estimated amount of BSS available in India about is 54 million tons, out of which a very small percentage is used in refractory industries and the rest remains unused as waste. The utilization of this mineral will contribute to environmental safety and to preserve valuable naturally occurring mineral resources. [2]

Sillimanite occurs in nature in rock form. But the rock form sillimanite has been depleted/exhausted in many parts of the world. Placer deposits of beach sand sillimanite minerals occur in a number of coastal areas. Placer deposits are two types, viz beach placers and inland placers. India is gifted with a coastline of over 6000km, hosts some of the largest and richest shoreline placers. Sillimanite beach placer deposits found in the eastern & southern coasts [3]

Previous studies revealed that the submicron sized BSS & alumina mixtures reacted to form mullite with 99% of the theoretical density after sintering at 1500-1575°C in presence of sintering aids. However, the use of submicron sized powders not viable for commercial production. Further precursors mixtures containing BSS with an average particle size (APS) of 5-6 μm require sintering temperature greater than 1700°C to form dense mullite aggregates. Lowering the sintering temperature while achieving the same degree of densification and mullite phase transformation would have some distinct advantages, including energy savings, finer microstructure and hence improved mechanical properties. Volume expansion associated with the 3:2 mullite formation from aluminosilicates was found to be one of the main factors restricting the densification of the aggregates.

In the present work, in first phase of work bauxite was added with different amount as source of alumina with sillimanite beach sand. The bauxite amount was optimised. In the second phase of the study, one additive was used (ZrO_2) to improve the densification and microstructure with two bauxite containing bauxite containing batches.

CHAPTER 2

LITERATURE REVIEW

2. Literature Review

The high temperature transformation of sillimanite to elongated mullite crystals has been studied by **A. Tomba** et. al [1]. Sillimanite group minerals have the composition $(Al_2O_3.SiO_2)$, can transform into mullite and silica at temperatures between 1300°C and 1600°C depending on the polymorphic form. Sillimanite beneficiated mineral was cold isopressed at 200 MPa into cylindrical bars and then fired in air between 1500°C and 1650°C for 4h. From the microstructure and characteristic properties, it can be concluded that the larger part of the mullitization of sillimanite takes place in a temperature interval between 1550°C and 1650°C. At these temperatures, the transformation produces liquid and mullite. Elongated mullite grains with a high degree of orientation are always produced. A rapid nucleation occurs above a critical temperature, 1550°C, due to the resemblance of sillimanite and mullite structures. Below 1500°C, there is no evidence of sillimanite-mullite transformation. The critical temperature (1550°C) of sillimanite to mullite transformation was not modified by presence of liquid phase due to the minor impurities in the starting material. Finally, a step of acid leaching was employed to remove the glassy phase and high-grade purity mullite powders were obtained.

Ibram Ganesh et. al [2] found that dense mullite aggregates with 60% and 70% Al_2O_3 can be prepared from precursor mixtures consisting of beach sand sillimanite and a high-purity aluminium hydroxide following conventional single-stage and double-stage firing processes. The bulk density, apparent porosity, and water absorption capacity of sintered mullite aggregates were found to be strongly influenced by the premullitization step of this precursor mixture. The premullitization step of precursor mixtures followed by a milling process enhanced the phase transformation into mullite and densification, enabling one to obtain 100% mullite phase aggregates denser than the current commercial products in a double-stage firing process (1250°C, 1 h + 1550°C, 1 h). Mullite aggregates formed in a double-stage firing process exhibited higher BD and mullite content and lower AP and WA capacity in comparison with those obtained by the single-stage firing process.

H.S. Tripathi et. al [3] discussed the Mullite development by reaction sintering of sillimanite beach sand and calcined alumina. In the test, batches were prepared with the sillimanite beach

sand as well as by the addition of calcined Al_2O_3 to convert the SiO_2 available into mullite. Sintered products thus obtained were characterized in terms of bulk density, apparent porosity, mechanical and thermo-mechanical properties and microstructure. The result showed that highest bulk density 3.04 gm/cc is achieved. Alumina addition always lower the hot MOR at 1200°C due to the reduction of high silica glass content. Higher amount of impurities containing sand densifies at lower temperature through liquid phase sintering. X-ray diffraction pattern of some sintered samples are showed that the main crystalline phase present is mullite. Mullite formed in the samples retains the orthorhombic habit of sillimanite. Mullite crystals are interlocked with each other. Small amount of rounded to sub rounded ZrO_2 embedded in the mullite matrix is also noticed. ZrO_2 reduces the grain growth of the mullite which is formed in situ.

Microstructure and properties of sintered mullite developed from Indian bauxite studied by **H.S. Tripathi** et. al [4]. Dense mullite aggregates with 72% Al_2O_3 have been synthesized by reaction sintering of two varieties of Indian bauxite and silica sol. The bauxites used are of inferior grade with different levels of accessory impurities such as Fe_2O_3 , TiO_2 , CaO . The phase and microstructure development of sintered samples were investigated by XRD and SEM. Mullite formed from low impurity bauxite is mostly equiaxed, whereas mullite developed from bauxite with higher impurity particularly CaO is needle shaped. At 1050°C the initial peaks of mullite appear and the nature of the peaks shows that the initial mullitization has started. It was found that the bulk density gradually increases with sintering temperature up to 1600°C followed by decrease in density at 1650°C. Gradual removal of open pores with an increase in sintering temperature is the reason for higher densification.

Thermo-mechanical properties of mullite–zirconia composites derived from reaction sintering of zircon and sillimanite beach sand: Effect of CaO has been studied by **P. KUMAR** et. al [5]. Mullite–zirconia composites containing 20% zirconia (mass fraction) were prepared by reaction sintering route utilizing Indian coastal zircon flour and sillimanite beach sand. 4%–12% of CaO (mole fraction) with respect to zirconia was used as additive. The effect of additive on densification, microstructure as well as various mechanical and thermo-mechanical properties was studied. Incorporation of CaO reduced the densification temperature of the composites to 1550 °C compared to 1600 °C (for CaO free samples). CaO formed small amount of liquid phase

(calcium aluminosilicate), which facilitated sintering. Average grain size of the composites decreased up to 4% CaO addition, afterwards grain size increased with further addition of CaO. Samples with 4% CaO exhibited ~225 MPa of flexural strength, ~6 MPa·m^{1/2} of fracture toughness and significant improvement in thermal shock resistance. CaO stabilized the tetragonal zirconia phase and thus improved the mechanical properties. Also, CaO stabilized the tetragonal zirconia phase and improved the thermal shock resistance. Samples with 4% CaO retained around 64% of its initial flexural strength even after 15 thermal shock cycles.

S. Rahman et. al [6] discussed the Structure description of the thermic phase transformation of sillimanite–mullite. The thermic phase transformation of sillimanite to 3:2 mullite was structurally examined with the main focus on the initial stage of this transformation. Single crystals of very pure sillimanite were annealed for different time periods (1600°C; 45 min–96 h) and then analysed employing X-ray and electron microscopic investigations. Using the videographic reconstruction method, the initial stage of the transformation (2–6 h, 1600°C) of sillimanite to 3:2 mullite is characterized as follows: (1) Splitting of the oxygen sites, resulting in tetrahedra- and octahedra-tilts and/or rotations; (2) statistical distribution of Si and Al on the tetrahedral sites. The results of the videographic reconstruction were confirmed via videographic simulations. A prolonged period of thermal treatment (24 h, 1600°C) leads to the complete transformation of sillimanite to 3:2 mullite with precipitations of amorphous SiO₂.

Synthesis and thermo-mechanical properties of mullite–alumina composite derived from sillimanite beach sand: Effect of ZrO₂ studied by **H.S. Tripathi** et. al [7]. The raw materials and additive were mixed, attrition milled and sintered in compacted form at 1400–1600°C with 2 h soaking. Then the effect of ZrO₂ on the densification behaviour, thermo-mechanical properties and microstructure was studied. It was found that addition of ZrO₂ slightly retards the densification process. All the samples achieved their highest bulk density at 1600°C. X-ray diffraction pattern showed the major crystalline phase was mullite with some amount of corundum. A small amount of zirconia both in monoclinic and tetragonal form was also noticed. Scanning electron micrography shows that ZrO₂ occupies both an intergranular and intragranular position in the mullite matrix. The mullite formed at 1600°C is mostly equiaxed in nature that

suggests densification mainly occurs through solid state sintering. Thermo-mechanical properties of the sintered samples are not effectively altered by the presence of ZrO_2 . ZrO_2 containing samples always show better resistance to thermal shock than the ZrO_2 free samples. Mullite formed is non stoichiometric in nature and maximum solid solubility of ZrO_2 within the mullite structure is 1.70 wt.%

Sasmita Prusty et. al [8] investigate the effect of MgO additive on the structural, microstructural and hardness properties of zirconia mullite (MUZ). The MgO additive in MUZ not only stabilizes the cubic zirconia phase but also acts as a sintering aid for the formation of cross-linked mullite grains. The micrograph of plasma sintered composites shows a ladder like structure and a complete cross-linked mullite grains whereas the surface morphology of conventionally sintered composites clearly indicates the presence of small and big grains close packed to each other. From the X-ray diffraction and Fourier transform infrared studies, it has been realized that complete dissociation of sillimanite and zircon has been occurred for the conversion of zirconia/mullite aggregates in plasma fused MgO–MUZ composites within the 5 min of plasma arching. Uniform arrangement of mullite platelets and dendritic structure of zirconia has been observed in the surface of plasma fused MgO–MUZ composites whereas ladder like structure with complete interconnected mullite grains has been observed for plasma sintered composites. Appreciable hardness and higher optical band gap have been observed for plasma fused MgO–MUZ composites. The total sillimanite and zircon mixtures have been utilized for the complete conversion of mullite and zirconia composites in plasma fusion whereas the complete conversion of sillimanite and zircon has not observed in plasma sintered and conventionally sintered composites.

Preparation and properties of Y_2O_3 containing zirconia–mullite composites derived from sillimanite beach sand discussed by **Manas K. Haldar** et. al [9]. All raw materials have been attrition milled and then isostatically pressed followed by sintering in the range of 1500–1600°C with a 2-h soaking period. Then the sintered materials have been characterised in terms of bulk density, linear shrinkage, hot modulus of rupture, X-ray diffraction, infrared spectroscopy and microstructural features. The addition of yttrium oxide overall improves the physical, thermo-mechanical properties of the composites. As the sintering temperature increases, yttrium oxide

helps in grain growth of the samples. Exaggerated grain growth is responsible for higher porosity as the temperature increases. But the samples without additive show a down trend in porosity with rise in temperature. The microstructure of zirconia-mullite composites are characterized by of elongated mullite grains along with sub rounded to rounded zirconia grains. There are two types of zirconia particles present in the microstructures. One is intergranular and other one is intragranular. The microstructure contains elongated and equiaxed mullite grains (black) along with zirconia grains (white). Most of zirconia grains are intergranular and few are intragranular.

Sintering of Mullite-Containing Materials: Effect of Composition found by **D. Sackset**. al [10] found the Sintering behaviour of mullite-containing powder over a range of chemical compositions ($\text{Al}_2\text{O}_3/\text{SiO}_2$ ratio). Densification measurements were made for both liquid phase-containing and solid-state systems. Small amounts of liquid phase were observed to have a significant effect on densification rate. A linear relation was obtained between the percent of theoretical density and the logarithm of time for compositions in the range 73 to 75 wt.% Al_2O_3 . Grain-boundary transport or diffusion appeared to be the primary mechanism of densification. A glass phase, however, persisted up to 74 wt.% Al_2O_3 , presumably because of metastable behaviour driven by a lowering of high mullite-mullite interfacial energies. A sharp decrease in densification rate was observed on transition from the mullite solid solution range to the mullite and alumina phase region. This decrease was associated with elimination of the residual glassy phase.

G. Orange et. al [11] studied the mechanical behaviour of reaction-sintered mullite/zirconia composites (RSMZ) at room temperature and up to 1200°C . It is well established that fully dense fine-grain mullite/zirconia or mullite/alumina/zirconia composites with enhanced mechanical properties can be produced by reaction-sintering routes. These materials, obtained with a low-cost process have potential uses as structural ceramics up to at least 1000°C . It appears that published toughening mechanisms cannot explain by themselves the mechanical properties of these composites. The needle-like morphology of mullite grains leads to a lengthening of the fracture path and a higher proportion of trans granular fracture mode. Thermal shock resistance has also been determined. It was found that dispersion of zirconia particles and the particular microstructure of mullite obtained by means of an in situ reaction process leads to improved

properties, with room temperature fracture toughness of about 5.25 MPa m^{1/2}. Up to 1000°C fracture strength and toughness values are quite high, which make these materials potential candidates for high temperature applications.

Controllable preparation and synthetic mechanism of mullite from the bauxite with Fe-rich oxide content studied by **Mingwei Yan** et. al [12]. In this paper, controllable preparation of mullite was attained using the bauxite with Fe-rich oxide content as raw materials, by adjusting its mass ratio of (Fe₂O₃+Al₂O₃)/SiO₂ to about 2.57 based on the theoretical design of Fe₂O₃-Al₂O₃ binary diagram and Al₂O₃-SiO₂-TiO₂ ternary diagram. Phase and synthetic mechanism of mullite from the Fe-rich bauxite have been characterized and analysed by XRD, SEM, EDS. Crystal phases of the bauxite with Fe-rich oxide content after sintering are composed of mullite solid solution, aluminium titanate solid solution and cristobalite with aluminium titanate solid solution distributed dispersively and surrounded by mullite solid solution. The synthetic mechanism of mullite solid solution can be expressed as follow: in the sintering process of the bauxite with mid-low grade, mullite is firstly formed by mullitization behaviour, and then Fe³⁺ and Ti⁴⁺ ions occupy and replace Al³⁺ located in the octahedral or tetrahedral sites for mullite. Si⁴⁺ in the tetrahedral site will be simultaneously substituted by Al³⁺ to maintain electrovalence equilibrium. As a result, mullite solid solution containing Fe³⁺ and Ti⁴⁺ is eventually developed. A very little of amorphous phase exists between mullite crystals, and aluminium titanate solid solution is distributed dispersively and surrounded by mullite solid solution.

Correlation between properties of zirconia mullite and Y₂O₃ stabilised zirconia mullite derived by various processing techniques described by **S. Prusty** et. al [13]. Zirconia mullite (MUZ) and Y₂O₃-MUZ composites were synthesised by plasma melting, plasma sintering and conventional sintering techniques. Mixtures of tetragonal and cubic phases have been observed in all the processed Y₂O₃-MUZ composites. The XRD and micro-Raman studies indicate that the addition of Y₂O₃ in MUZ transforms the monoclinic zirconia to cubic zirconia phase. The optical absorption studies completely reflect the improvement in optical band gap of Y₂O₃-MUZ composites to prove it as a suitable candidate for refractory applications. The bulk density, hardness and higher crystalline nature of plasma sintered composites indicate that better products can be synthesised by direct current extended arc thermal plasma heating technique

within a short duration of time. In conclusion, their correlation studies on the properties of MUZ and Y_2O_3 -MUZ open an avenue to determine the appropriate melting and sintering procedures for enhancing the physical properties of the materials as desired for industrial applications.

Manas K. Haldar et. al [14] found the effect of magnesia additions on the properties of zirconia-mullite composites derived from sillimanite beach sand. Zirconia-mullite composites with 4–8 mol% magnesium oxide has been prepared from Indian coastal sillimanite beach sand, zirconia and alumina. The X-ray diffraction study reveals that in zirconia, monoclinic is the major phase, Alumina is having $\alpha-Al_2O_3$ as main constituent & in magnesia periclase is the major phase. Milling of the mixtures of all raw materials has been carried out in an attritor mill for 9 h. After drying and pressing the samples were sintered between 1500°C and 1600°C with 2 hrs of soaking. The physical, mechanical & thermo-mechanical properties of the sintered materials namely bulk density, linear shrinkage, hot modulus of rupture, hardness and fracture toughness have been evaluated. The infra-red spectrums of sillimanite sand and sintered samples have been described. The bulk density of the sintered samples falls with increase in temperature with varying amount of magnesia. The linear shrinkage of the sintered samples increases with higher content of magnesia. The hot modulus of rupture for all samples is showing lower value at 1600°C. The sintered materials are having higher value of fracture toughness than pure mullite. All the sintered composites are showing an overall decreasing trend in modulus of elasticity as the sintering temperature increases. The scanning electron microstructures of the sintered samples show bright zirconia grains are uniformly distributed throughout the darker mullite matrix.

High-temperature characterization of reaction-sintered mullite-zirconia composites discussed by **Philippe Descamps** et. al [15]. Mullite-zirconia composites are prepared by reaction sintering of zircon and alumina, either using reaction and sintering additives (Titania (T-MZ) or Magnesia (M-MZ)) or starting from highly reactive powder mixtures obtained by an ultra-rapid-quenching technique (URQ-MZ). In the latter case, the presence of large amounts of an amorphous phase in the quenched powders enables sintering without the use of additives. The various composites differ mainly by their microstructure-i.e., the mullite grains aspect ratio and grain size-and by the quantity and nature of impurities or additives. Within this work, the modulus of rupture and

critical stress intensity factor of each material are measured from room temperature to 1200°C. Bending creep is also investigated for various temperature and stress ranges. For the three materials, the fracture toughness decreases with temperature, according to tetragonal zirconia stabilization, up to 600°C to 700°C, above which a significant increase occurs. The reinforcement is more efficient for T-MZ because of the higher viscosity of the glassy phase. Despite its larger amount of glassy phase, the M-MZ ceramic shows the better creep resistance because of its particular microstructure consisting of cross-linked elongated mullite grains-which impedes grain-boundary sliding.

Manas K. Haldar et. al [16] found that Zirconia–mullite composites can be prepared from beach sand sillimanite in the presence of magnesia as an additive. The raw materials were attrition milled. Samples were isostatically pressed and sintered in the temperature range of 1500–1600°C with 2hr of soaking. The resulting composites were characterized in terms of densification, thermal expansion, martensite start (Ms) temperature. The presence of magnesia changes the value of thermal expansion coefficient. The mechanical and thermo-mechanical properties, namely flexural strength and thermal spalling of the sintered composites, were characterized and effect of magnesia on it is discussed. The interrelation between microstructure and properties of a material is very important for greater understanding of material property and possibility of improvement. Zirconia has higher atomic number compared to aluminium and silica. So, it appears clearly from its surrounding mullite matrix under SEM and shows a brighter image (white). The EDAX analyses of zirconia, mullite and zirconia–mullite grain boundary showed that the mullite phase contains around 72% Al₂O₃ and 27% SiO₂, whereas zirconia phase contains 90% ZrO₂. A small amount of magnesia of 0.37% in mullite and 0.12% in zirconia is present. The most of magnesia (around 2.35%) is present in the zirconia–mullite grain boundary. Both zirconia and mullite contain a small amount of TiO₂, which comes from raw material.

Mechanical properties of mullite–corundum composites prepared from bauxite having considerable amount of impurities and silica sol has been studied by **Atul V. Maldhure** et. al [17]. The effect of changing mullite phase proportion on the mechanical properties (i.e., flexural

strength, elastic modulus, hot modulus of rupture, thermal shock resistance) of prepared composites has been studied. Flexural strength and elastic modulus increase with increasing free corundum phase content in the composites. Hot modulus of rupture for the sample containing only mullite phase increases with increasing test temperature over entire temperature range. Only mullite/highest mullite phase proportion showed the highest resistance to both crack initiation and propagation. The values of these parameters decrease with increasing corundum phase proportion in the composites. Retention of mechanical strength after successive thermal shock cycles decreases with increasing corundum phase proportion in the composites. The reason for such behaviour is two fold, the thermal expansion mismatch between individual mullite and corundum phases, and increase in amount of glassy phase due to high impurity phase. The refractory composites containing only mullite showed the greatest performance in terms of high-temperature mechanical strength, loss of strength on thermal shocking, and ability of a material to resist crack propagation and further damage.

Effect of the calcining temperatures of low-grade bauxite on the mechanical property of mullite ceramics without any other additives discussed by **Qiang Ren** et. al [18]. The variations in physical and chemical properties in the process of sintering, the specific surface area of calcined bauxite at different calcining temperatures, and the phase composition of the mullite ceramic and its microstructure were investigated by thermal analysis, laser particle analysis, the X-ray diffraction, and scanning electron microscope, respectively. The mechanical properties of mullite ceramics prepared by calcined bauxite are superior to the properties of mullite ceramics made by raw bauxite, and the flexural strength of mullite ceramics improved with the increase of calcining temperatures at the range of 650-1200°C. The influence of calcining temperature of raw bauxite on the mechanism of sintering of mullite ceramics is reflected in these aspects, (i) the crystalline moisture and other impurities; (ii) the specific surface area of calcined bauxite powders; (iii) crystals in calcined bauxite. Using calcined bauxite to produce mullite ceramic was an applicable way, at the same time, this provides the application of low-grade bauxite for new thoughts. The deeper studies needed to be done before the research achievements are applied to manufacture effectively.

Preparation of low-cost mullite ceramics from natural bauxite and industrial waste fly ash studied by **Yingchao Dong** et. al [19]. The fired samples, including fly ash, bauxite and their mixture based on the composition of 3:2 mullite, were characterized respectively by XRD (X-ray diffraction). The results indicate that the secondary mullitization occurred by the solid-state reaction of cristobalite and corundum below 1300°C, followed by the dissolution of corundum into transitory glassy phase at higher temperatures. The dilatometric results reveal that the formation of secondary mullite resulted in aslight expansion in spite of the shrinkage induced by sintering. In addition, the samples were fired at elevated temperatures and then characterized in terms of relative density, porosity, micro-structure and fracture strength. At 1600°C, the relative density and fracture strength are 93.94% and 186.19MPa, respectively. After sintering at 1600°C for 4 h, the sample exhibited a closed porosity of 5.44% and open porosity of 0.62%. It is crucial to prepare denser mullite ceramics by avoiding the formation of closed pores. The development of mullite ceramics would add great economic value to industrial waste fly ash that existed abundantly throughout the world, most of which are not well utilized currently. Moreover, inexpensive raw natural mineral bauxite was testified as an effective substitute for industrial alumina for the production of mullite. This fact supports the practicability of the direct use of natural raw materials, instead of alumina produced by the complicated process.

Toshiyuki Koyama et. al [20] found that Mullite-zirconia composites can be prepared from three kinds of combination of starting materials such as mullite-zirconia (MM), alumina-silica-zirconia (RS3) and alumina-zircon (RS2). Phase formation reaction, sinterability and microstructures of these samples were investigated. The following conclusions can be drawn.

- (1) The mixture of mullite and zirconia powders (MM): Sinterability of this sample was not so good compared with the others. At high temperature, it released silica from mullite and formed a liquid phase, which caused the growth of elongated large mullite grains in the microstructure.
- (2) The mixture of alumina, amorphous silica and zirconia powders (RS3): Sinterability of this sample was good because of the enhancement of densification by a viscous flow mechanism due to amorphous silica phase. Equiaxed mullite grains and intergranularly dispersed zirconia grains formed the microstructure.
- (3) The mixture of alumina and zircon (RS2): Extremely alumina-rich mullite were formed transiently in this sample. Their microstructures were composed of irregularly shaped mullite

and intra/intergranularly dispersed zirconia grains. Some extent of Zr atoms was considered to be incorporated in the transient state mullite.

H.S. Tripathi et. al [21] discussed the Sintered mullite from aluminous ore for refractory application. Mullite aggregate was prepared by reaction sintered from Aluminous ore with calcined alumina and added Titania to enhance the densification process without deterioration of thermo-mechanical properties. The major raw materials used in this investigation were kyanitic aluminous ore and Bayer's alumina. Batches were mixed and milled in a vibroenergy mill 8 h. Then rectangular bars were uniaxially pressed at 100 MPa and sintered in air at 1500, 1550, 1600 and 1650°C with 2 h soaking time. Sintered products thus obtained were characterized in terms of bulk density, apparent porosity, high-temperature flexural strength and microstructure. So, results showed that at 1600°C, 1 wt.% TiO₂ addition decreases the porosity from 2.2 to 0.5%. An XRD pattern of the mullite aggregate developed at 1600°C shows that the main crystalline phase is mullite, with a small amount corundum. A SEM photomicrograph of the same sample shows that the mullite grain developed from kyanite. Aluminous materials are mostly acicular in shape and the glassy phase is evenly distributed in the intergranular position. Some equiaxed mullite grains smaller in size also are observed. Flexural strength at 1300°C of the mullite aggregate developed at 1600°C shows that mullite with no additive exhibits the highest flexural strength of 73.5 MPa at 1300°C. Beyond 1 wt.% TiO₂ addition, the decrease in strength is not appreciable (up to 3 wt.% TiO₂). Because TiO₂ forms solid solution with mullite, it does not significantly alter the amount of glassy phase or glass composition.

Structure and properties of mullite discussed by **H. Schneider** et. al [22]. Mullite has achieved outstanding importance as a material for both traditional and advanced ceramics because of its favourable thermal and mechanical properties. Depending on the synthesis temperature and atmosphere mullite is able to incorporate a number of transition metal cations and other foreign atoms. In more detail: Parallel to **a** the tetrahedra are linked to the relatively short stiffer Al–O (A, B) bonds, whereas parallel **b** they are linked parallel to the relatively long more compliant Al–O(D) bonds. In mullite some of the oxygen atoms bridging the tetrahedra are removed for charge compensation. This gives rise to the formation of oxygen vacancies and of T₃O groups (so-called tetrahedral triclusters). The anisotropy of the bonding system of mullite has a major

influence on the anisotropy of its physical properties. Heat capacity and thermal expansion measurements of mullite display reversible anomalies in the temperature range between about 1000 and 1200°C. It is believed that tetrahedral cations, bridging O atoms, and O vacancies undergo dynamical site exchange processes at high temperatures. At lower temperatures the dynamic disorder may transform to a static one. Diffraction experiments revealed that also partially ordered states may exist.

Thermo-mechanical properties of mullite/zirconia reinforced alumina ceramic composites investigate by **M.M.S. Wahsh** et. al [23]. Alumina–mullite–zirconia ceramic composites was prepared by reaction bonding of alumina and zircon mixtures after firing at different temperatures 1300°C, 1400°C and 1500°C. Constant amount of magnesia was added as a sintering aid. The technological parameters of the sintered ceramic composites, i.e. the mechanical properties and densification parameter as well as thermal shock resistance, have been investigated. The main phases in all samples fired at 1500°C are corundum (α -Al₂O₃), monoclinic zirconia (m-ZrO₂) and tetragonal zirconia (t-ZrO₂). In addition, some diffraction peaks of mullite (3Al₂O₃.2SiO₂) and magnesium-aluminium-silicate (Mg_{3.5}Al₉Si_{1.5}O₂₀; Sapphire) were detected in samples containing higher amounts of zircon. All ceramic composites achieved an excellent thermal shock resistance (TSR). Ceramic composite containing 66.79 mass% calcined alumina, 30.52 mass% zircon and 2.69 mass% magnesia fired at 1500°C exhibited higher densification parameter (BD~3.31 g/cm³, AP~5.5%) and mechanical properties (CCS~550 MPa) as well as excellent thermal shock resistance. This alumina–mullite zirconia ceramic composite can be suggested for using in refractory and high temperature applications where severe thermal shock and high mechanical properties are required.

Cemil Aksel et. al [24] described the role of fine alumina and mullite particles on the thermo-mechanical behaviour of alumina–mullite refractory materials. Fine grain alumina and mullite particles were incorporated into slip-cast alumina–mullite refractories in order to investigate their effects on the microstructure, mechanical properties and thermal shock behaviour of the refractories. The addition of fine mullite resulted in a high porosity and low mechanical properties, both densification and mechanical properties increased with the incorporation of fine alumina particles significantly through improvement of interparticle bond strength amongst the

coarser grains. Therefore, more fracture surface energy was required to connect the cracks for propagation, associated with a high value of fracture toughness. The strength and Young's modulus were also improved with increasing quench temperature, leading to a high thermal shock resistance. Furthermore, the crack initiation resistance was also increased with higher alumina content. Thermal shock tests confirmed that the addition of fine alumina rather than fine mullite particles into an alumina–mullite slip-cast refractory material improved both strength and modulus values with increasing quench temperature, indicating better thermal shock resistance.

H. Schneider et. al [25] studied the temperature dependent solubility of titanium, iron, and magnesium in mullites coexisting with SiO₂-rich partial melts in a used chamotte brick was studied with a high-resolving microprobe. The mullites of the starting material have relatively high mean Fe₂O₃ (~ 2.4 wt.%), but lower TiO₂ (~ 1.4 wt.%), and very low MgO contents (~0-5wt.%). Cation removal from mullite to coexisting glass phase is observed at high temperature: the onset of exsolution is about 1300°C for magnesium, 1350°C for iron, and 1400°C for titanium. Sample specimens annealed at 1650°C have mullites with about 0-5 wt.% Fe₂O₃, 0.9wt.% TiO₂, and traces of MgO. Cation exsolution curves follow exponential laws, the exsolution rate being considerably higher for Fe₂O₃ than for TiO₂ and MgO. The study documents amuch higher mobility of the iron ion as compared to that of titanium. Eutectic melting of mullite with associated limited solid solution of iron, titanium, and magnesium cannot be the only reason for cation removal from mullite to the coexisting melt because the amount of mullite dissolution between 1300 and 1650°C is too low. A cation distribution between mullite and coexisting melt, the value of which decreases with temperature is believed to be a further driving force for cation exsolution.

CHAPTER 3

PLAN OF THE WORK

3. Plan of the Work:

The present work was performed to study the effect of bauxite on the mullitization and densification of sillimanite. The effect of zirconia addition on the bauxite-sillimanite mixture was also studied.

For this purpose, Indian sillimanite beach sand (Kerala) and Saurashtra bauxite were selected. The physio-chemical characteristics of the principle raw materials were studied through chemical analysis, phase analysis by powder XRD, Differential thermal analysis and specific gravity measurement.

The batch compositions were selected, and thoroughly mixed & ground and then calcined at appropriate temperature to get reactive powder. Sintering study was reformed on small discs. The green samples after proper drying were subjected to firing. The firing was done in oxidising atmosphere.

The sintered compact bodies were characterised with respect to the variables through the determination of some physical properties. These included bulk density, apparent porosity, diameter, shrinkage etc. the different crystalline phases developed in the sintered body were examined by powder X-ray diffraction study.

The properties of sintered products depend on the microstructure developed in the body that means the nature and distribution of different phases. A thorough investigation on the densification of different phases, their morphology and their size were determined by examining the chemically etched fractured surface. The approximate chemical composition of the different crystalline and amorphous phase developed were estimated by energy dispersive x-ray analysis (EDX). The study this microstructural analysis will help to understand its relation with other physio-chemical and thermo-chemical properties.

For refractory application, cold crushing strength, chemical corrosion and pyrometric cone equivalent tests are also measured

CHAPTER 4

EXPERIMENTAL WORK

4. Experimental Work

At first raw materials, Sillimanite fine (-300 mesh), Bauxite (supplied by Shri Nataraj Ceramic & Chemicals Industries Ltd, Gujarat), Zirconium Dioxide (LOBA CHEMIE) were used for the study. The main raw materials were characterized by chemical analysis, phase identification by powder XRD, specific gravity measurement and differential thermal analysis (DTA). Bauxite was ground in a rubber lined pot with alumina as grinding media for 5 hours. The slurry from the pot mill was dried at $110^{\circ}\text{C}\pm 5^{\circ}\text{C}$. The batch composition and the sample codes of different batches are listed in **Table 1**.

Table 1: Batch Composition and batch code for the stage-I

Batch code	Sillimanite	Bauxite
SB0	100	0
SB2	80	20
SB3	70	30
SB4	60	40
SB5	50	50

Each batch was thoroughly mixed in a plastic container with small alumina ball for 45 mins. After that mixed batch was calcined at 600°C for 2 hrs. The batch powder was mixed with 5% PVA and granulated through 30 BS sieve. The granulated materials were pressed at 120MPa into 20mm and 25mm diameter discs, dried at 110°C and fired at 1500° to 1650°C with 2hr soaking time. Bauxite was added in 20, 30, 40 and 50wt% to the mixture.

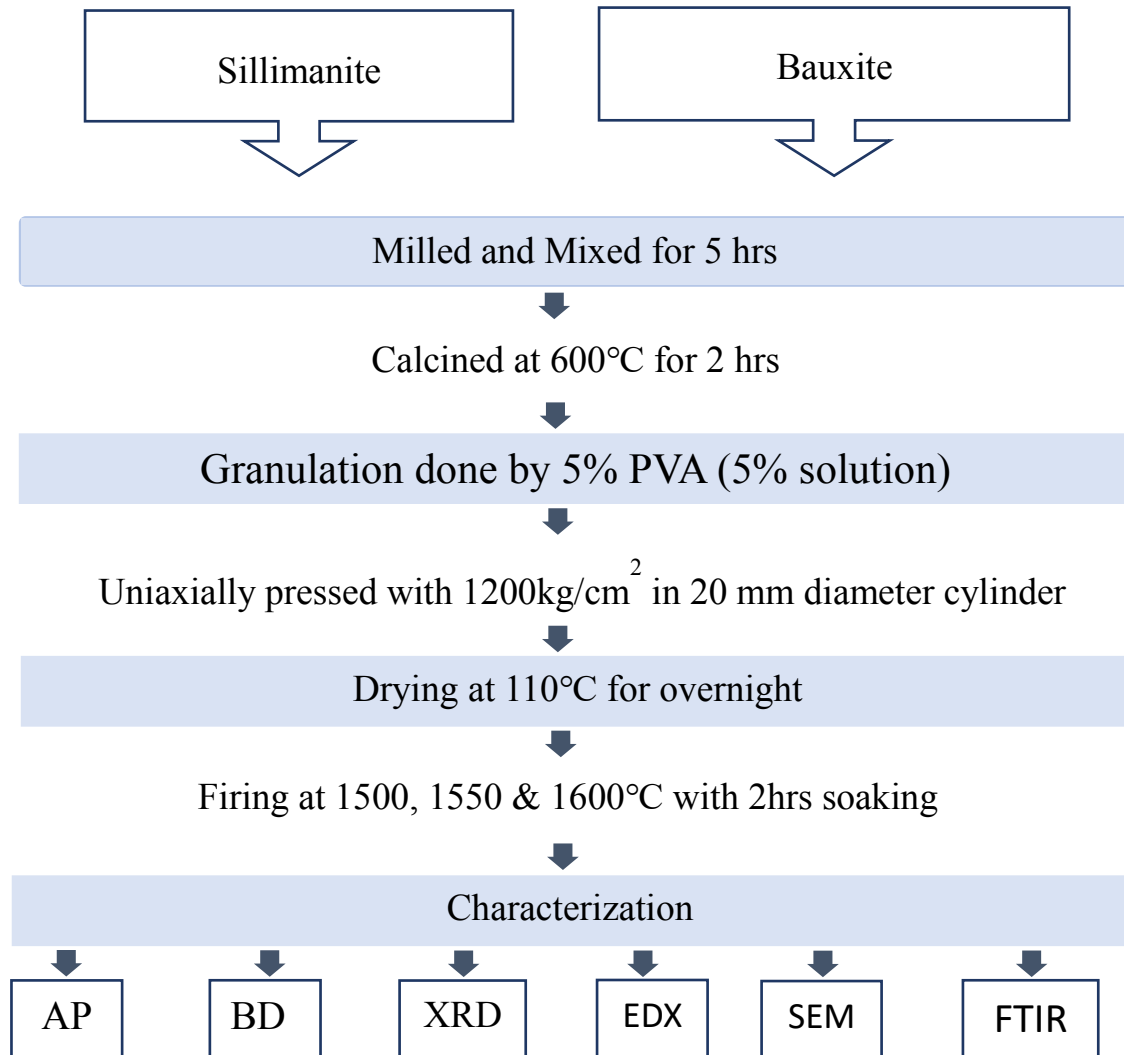
After that from the optimized batches, we have taken two batches and add zirconium dioxide in stage-II. Zirconia was added in 1, 3 and 5wt% to the mixture. The same mixing, calcining, granulation, pressing and firing were followed as in stage-I. The batch composition and the sample codes of different batches for stage-II are listed in **Table 2**.

Table 2: Batch Composition and batch code for the stage-II

Batch code	Sillimanite	Bauxite	Zirconia	Batch code	Sillimanite	Bauxite	Zirconia
SB4-Z0	60	40	0	SB5-Z0	50	50	0
SB4-Z1	60	40	1	SB5-Z1	50	50	1
SB4-Z3	60	40	3	SB5-Z3	50	50	3
SB4-Z5	60	40	5	SB5-Z5	50	50	5

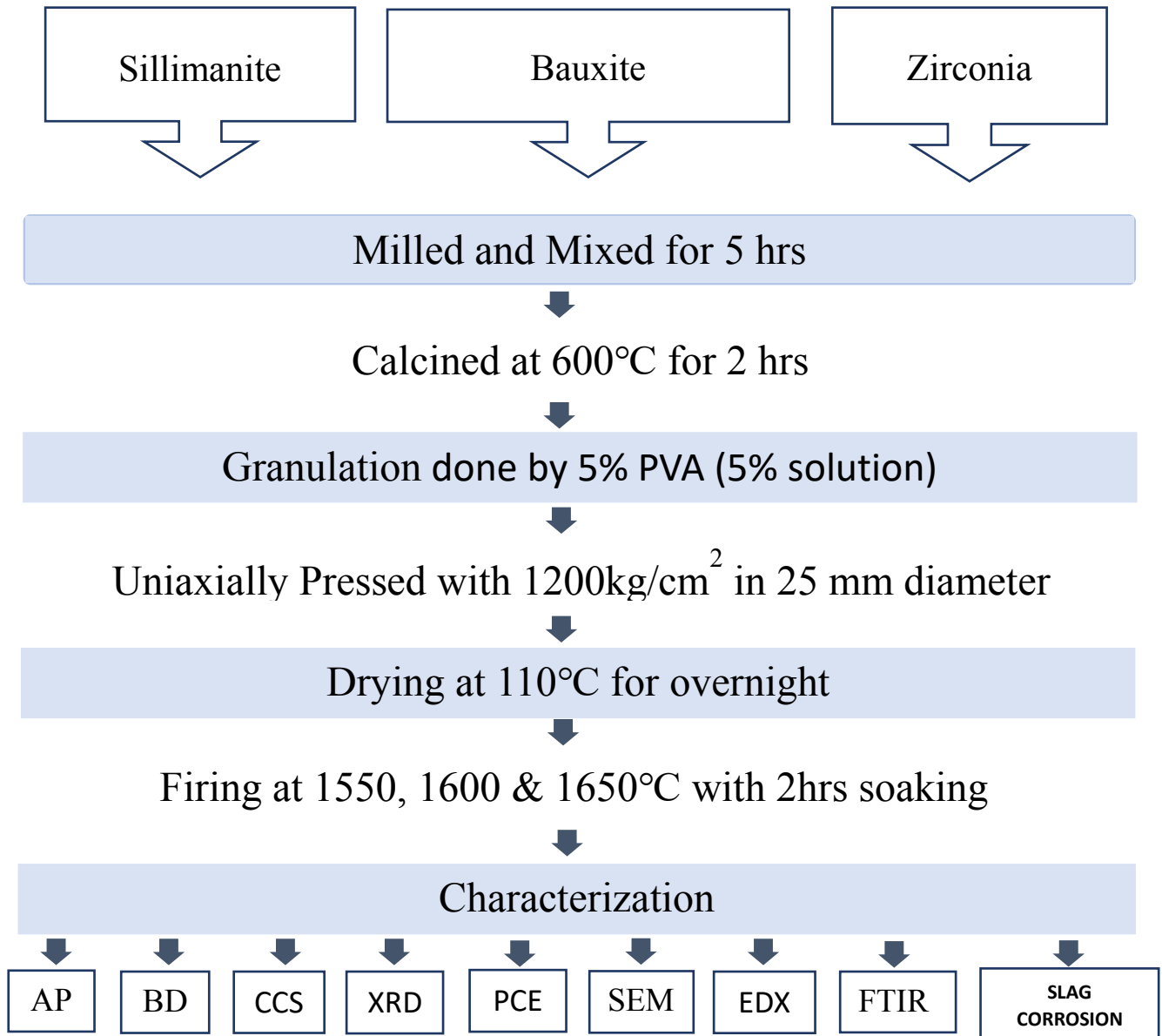
The process flow chart is given below-

Figure1: Process flow chart for the stage-I



The process flow chart for stage two is given below-

Figure 2: Process flow chart for the stage-II



4.1 Characterization of Raw Materials

The following physical and thermal tests was conducted for the raw materials, Saurashtra Bauxite and Kerala Sillimanite.

- a) Specific gravity (ρ)
- b) X-ray Diffraction (XRD)
- c) Differential Thermal Analysis (DTA)
- d) Fourier-transform infrared spectroscopy (FTIR)

a) Specific gravity

Specific gravity, also referred to as relative density, is used to relate the weight or density of liquids to that of water. Specific gravity is the ratio of the mass of a substance to the mass of a reference substance for the same given volume. *Apparent* specific gravity is the ratio of the weight of a volume of the substance to the weight of an equal volume of the reference substance.

Here we measure the sp. Gravity by pycnometer. A pycnometer allows measuring the volume and the density of solid objects in a non-destructive manner. The latter is accomplished by employing Archimedes' principle of fluid displacement for liquid pycnometer.

The specific gravity of sample is determined using the relation:

$$G = \frac{M_2 - M_1}{(M_2 - M_1) - (M_3 - M_4)}$$

Where, M_1 = mass of empty Pycnometer.

M_2 = mass of the Pycnometer with dry sample.

M_3 = mass of the Pycnometer and sample and xylene.

M_4 = mass of Pycnometer filled with xylene only.

G = Specific gravity of sample.

b) X-ray Diffraction(XRD) analysis

A scattering of X-ray by the atom of a crystal that produces an interference effect so the diffraction pattern gives information on the structure of the crystal or the identity of a crystalline substance.

The objective of XRD is to know the composition of a crystalline material, which helps to determine different properties of that substance.

Selected sample was crushed into iron mortar and pestle, passed through 30 mesh B.S. demagnetized and finely ground (much below 200 mesh) in anagate.

The nearly 3gm sample is required.

Bragg's law is employed.

The instrument uses Ni-filtered Cu K_a radiation with a scanning rate of 2° per minute. The data had to be either compared using monographs already collected or using software crystalline phases are detected.

They were finally plotted neatly using ORIGIN software.

c) Differential Thermal Analysis (DTA)

It is a thermo-analytic technique that is similar to differential scanning calorimetry. In DTA, the material under study and an inert reference are made to undergo identical thermal cycles, (i.e., same cooling or heating programme) while recording any temperature difference between sample and reference. This differential temperature is then plotted against time, or against temperature (DTA curve, or thermogram). Changes in the sample, either exothermic or endothermic, can be detected relative to the inert reference. Thus, a DTA curve provides data on the transformations that have occurred, such as glass transitions, crystallization, melting and sublimation. The area under a DTA peak is the enthalpy change and is not affected by the heat capacity of the sample.

A DTA consists of a sample holder, thermocouples, sample containers and a ceramic or metallic block; a furnace; a temperature programmer; and a recording system. The key feature is the existence of two thermocouples connected to a voltmeter. One thermocouple is placed in an inert material such as Al₂O₃, while the other is placed in a sample of the material under study. As the temperature is increased, there will be a brief deflection of the voltmeter if the sample is undergoing a phase transition. This occurs because the input of heat will raise the temperature of the inert substance, but be incorporated as latent heat in the material changing phase.

d) Fourier-transform infrared spectroscopy (FTIR)

A technique used to obtain an infrared spectrum of absorption or emission of a solid, liquid or gas. An FTIR spectrometer simultaneously collects high-spectral-resolution data over a wide spectral range. This confers a significant advantage over a dispersive spectrometer, which measures intensity over a narrow range of wavelengths at a time.

Firstly, The KBr thin plates are prepared and scanned in FTIR machine. Then, the powder sample and KBr are mixed together and thin plates are prepared. These plates are scanned in FTIR machine. Final result is analysis with paper.

4.2 Analysis of Sintered Material

- a) Apparent Porosity
- b) Bulk Density
- c) Shrinkage
- d) Scanning Electron Microscopy
- e) Energy Dispersive X-ray Analysis
- f) Slag Corrosion
- g) Fourier-transform infrared spectroscopy
- h) X-ray Diffraction

a) Apparent Porosity (AP)

Apparent porosity is defined as the ratio of the volume of the open pores to the bulk volume of the material. It is expressed as a percentage.

The test specimen are taken. Then, such test pieces are tied with a thread and is thereby hanged from the test rod. Such a Glass rod containing the test specimen is placed inside the beaker containing water such that the test specimen suspended in water so that any part of it should not be touched with the walls or bottom of the beaker.

The whole assembled beaker is placed on heater at 110°C for 2hrs. So that the open pores in the piece are filled up with the water quickly. Then, the samples are placed in cold water for a few minutes to get it cooled and then, the test pieces are tied with a wire which hangs from the knot of the weight to get it cooled and then, the test piece is tied with a wire which hangs from the knot of the wight balance such that the test piece should remain completely immersed in the water in the beaker.

Thus dry weight (D), suspended weight (S) and soaked weight (W) is calculated for the test specimen. Dry weight (D) should be calculated by drying the test specimen for overnight.

Suspended weight (S) and soaked weight (W) is measured. The apparent porosity (AP) is then calculated by the following equation.

$$\text{A.P.} = \frac{W-D}{W-S} * 100 \%$$

b) Bulk Density

Bulk density is a property of powders, granules, and other “divided” solids, especially used in reference to mineral component (soil, gravel), chemical substances, (pharmaceutical) ingredients, foodstuff, or any other or particular matter. It is defined as the mass of many particles of the material divided by the total volume they occupy. The total volume includes particle volume, inter-particle void volume, and internal pore volume.

This method of determining bulk density is preferable for specimens which are branded deeply or are irregular in contour. It is more than the direct measurement method.

The dry weight (D), suspended weight (S) and soaked weight (W) is calculated for the test specimen. Dry weight (D) should be calculated by drying the specimen for overnight.

Suspended weight (S) and soaked weight Weight (W) are measured by water displacement method. Bulk density is calculated in gm/cm³. The bulk density is given by the formula.

$$\text{BD} = \frac{D}{W-S} \text{ gm/cc}$$

c) Shrinkage

The diameter of the samples was measured before firing (a) and after firing (b). Then it is calculated by $((b-a)/a)*100$. It is calculated in percentage.

$$\text{Shrinkage} = \frac{b - a}{a} * 100 \%$$

d) Scanning Electron Microscopy (SEM)

A scanning electron microscope (SEM) is a type of electron microscope that produces an image of a sample by scanning it with a focused beam of electrons. The electrons with atoms in the sample, producing various signals that contain information about the sample's surface topography and composition.

Samples were first broken into a thin plate.

Then samples were chemically etched. Chemical etching was carried out by treating the sample surface using 40vol% HF for 1min. The etched surface was washed by 1:1 water and rectified spirit mixture in an ultrasonic cleaner.

Sample is coated with the platinum nanoparticle to make the surface conductive. Then SEM pictures were taken and grain composition was found out by EDXA.

e) Energy Dispersive X-ray Analysis (EDX)

Energy-dispersive X-ray spectroscopy (EDS, EDX, EDXS or XEDS), sometimes called energy dispersive X-ray analysis (EDXA) or energy dispersive X-ray microanalysis (EDXMA), is an analytical technique used for the elemental analysis or chemical characterization of a sample. It relies on an interaction of some source of X-ray excitation and a sample. Its characterization capabilities are due in large part to the fundamental principle that each element has a unique atomic structure allowing a unique set of peaks on its electromagnetic emission spectrum.

EDS makes use of the X-ray spectrum emitted by a solid sample bombarded with a focused beam of electrons to obtain a localized chemical analysis. All elements from atomic number 4

(Be) to 92 (U) can be detected in principle, though not all instruments are equipped for 'light' elements ($Z < 10$). Qualitative analysis involves the identification of the lines in the spectrum and is fairly straight forward owing to the simplicity of X-ray spectra. Quantitative analysis (determination of the concentrations of the elements present) entails measuring line intensities for each element in the sample and for the same elements in calibration Standards of known composition.

e) **Slag Corrosion Test of Refractories**

Slag attack is particularly important. The structural strength of the refractory may be critically reduced by the solvent action of liquid slags. The slag attack on the refractories in contact may be in two ways: Corrosion - It is the wear and tear of refractories caused by a static chemical attack of slag, i.e. the process of breaking and washing away of refractory materials by molten slag.

First, we have prepared cylindrically shaped specimens having a diameter 25mm. Then we make 10mm hole at the center and Depth around $2/3^{\text{rd}}$ of specimens. Fired the sample according to the schedule.

Now, the fired samples are $2/3$ filled with BF slag and fired at 1450°C for 2 Hrs. The corroded samples are cut into two pieces by the help of cutting machine. Then the diameter of the penetration of the samples are observed and measured by a vernier scale.

CHAPTER 5

RESULT & DISCUSSION

5. Results and discussion:

Stage-I

The physico-chemical properties of the sillimanite and bauxite are presented in **Table-3**. Impurities in sillimanite is relatively low which constituted of only 1.64 wt.% with respect to bauxite one (12.59wt. %). Specific gravity of sillimanite is 3.24 higher than that reported by Grimshaw (3.08). [26] Mole ratio of Alumina to silica ratio is 1:1.1 means silica rich sillimanite. The powder X-ray shows small peaks of quartz with main sillimanite phase. FTIR spectra of sillimanite shown in **fig 3**, shows the characteristics transmittance peak at of sillimanite 1185cm^{-1} . [14] FTIR of SB4 and SB5 shows the absence of sillimanite characteristics transmittance peak at 1185cm^{-1} , confirms the total decomposition of sillimanite at this temperature.

Table 3: Physio-chemical properties of raw materials

Composition	Sillimanite	Bauxite
Al ₂ O ₃	59.46	58
SiO ₂	38.9	5.4
TiO ₂	0.36	1.56
Fe ₂ O ₃	0.72	1.72
CaO	0.56	1.6
MgO	----	0.1
P ₂ O ₅	-----	1.0
Na ₂ O	-----	0.15
LOI	-----	28
Specific Gravity	3.24	2.46
Crystalline phases present		
Major	Sillimanite	Gibbsite
Minor	Quartz	Anatase

Main detrimental impurities present in bauxite are CaO, Fe₂O₃ and TiO₂ totalling about 12.59% on loss free basis. Specific gravity of bauxite is 2.46 little bit higher than that reported by Grimshaw (2.3-2.4) may be due to the presence of high density anatase. [26] Gibbsite is the main crystalline phase along with anatase minor phase. Linear shrinkage (%) as function of bauxite content (wt.%) is shown in **Fig 4**. Maximum shrinkage is observed at 1600°C with highest bauxite containing batch (SB5). Generation of large volume of liquid phase from impurity present with higher amount of bauxite helps in particle rearrangement and effective packing

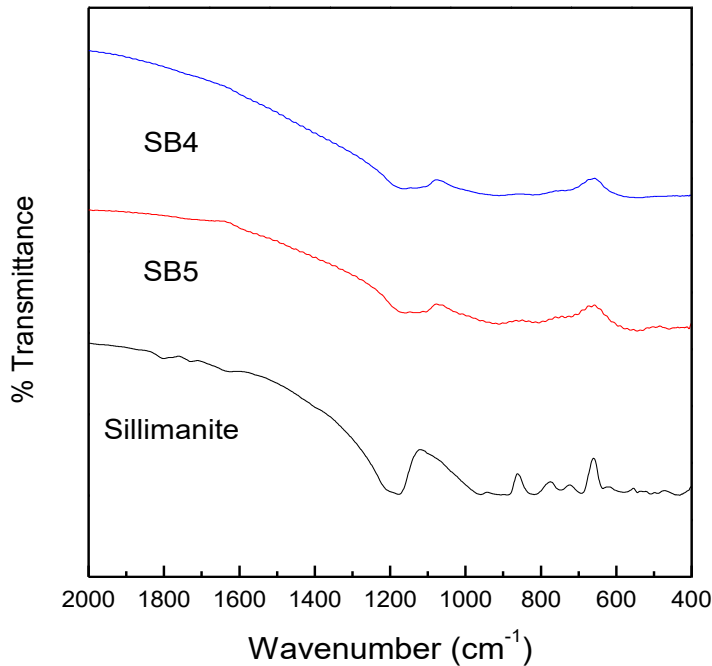


Fig 3: FTIR spectra of raw sillimanite and sintered batch fired at 1550°C/2hr

of particles leading to highest shrinkage (14%). (**Fig 5**) shows the relationship between BD and wt. % of bauxite. Higher the bauxite higher is the BD at all three-sintering temperature. But the change in BD from 40% to 50% bauxite content is steep with respect to the other bauxite content batch. This is may be due to the corundum phase present in the SB5 batch which was detected in powder XRD. Highest BD of 2.82 gm/cc was achieved with 50% bauxite batch (SB5). AP versus bauxite content also reflects (**Fig 6**) the above observation. Larger volume of low melting low viscous glassy phase formed due to presence of higher impurity in bauxite (12.59%) at 1600°C accelerates the pore removal of SB5 batch.

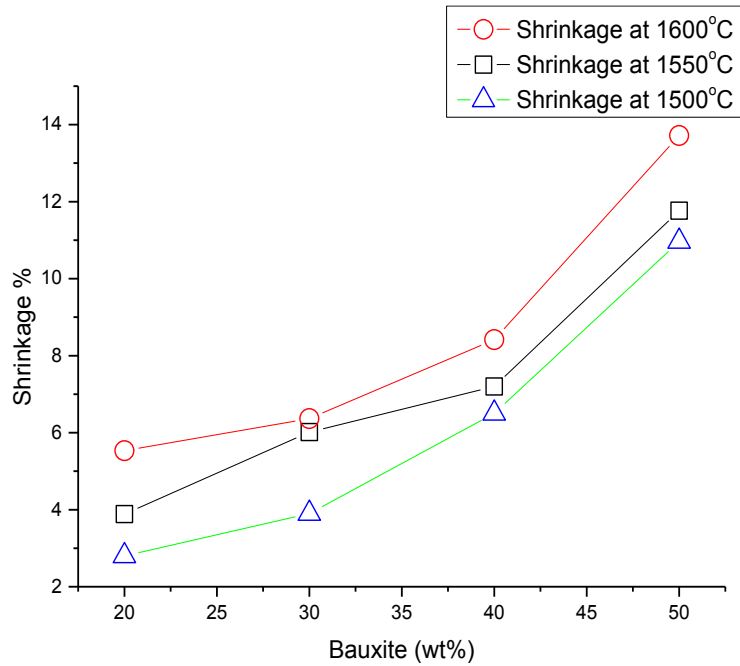


Fig 4: Effect of linear shrinkage (%) on the bauxite content at different sintering temperature

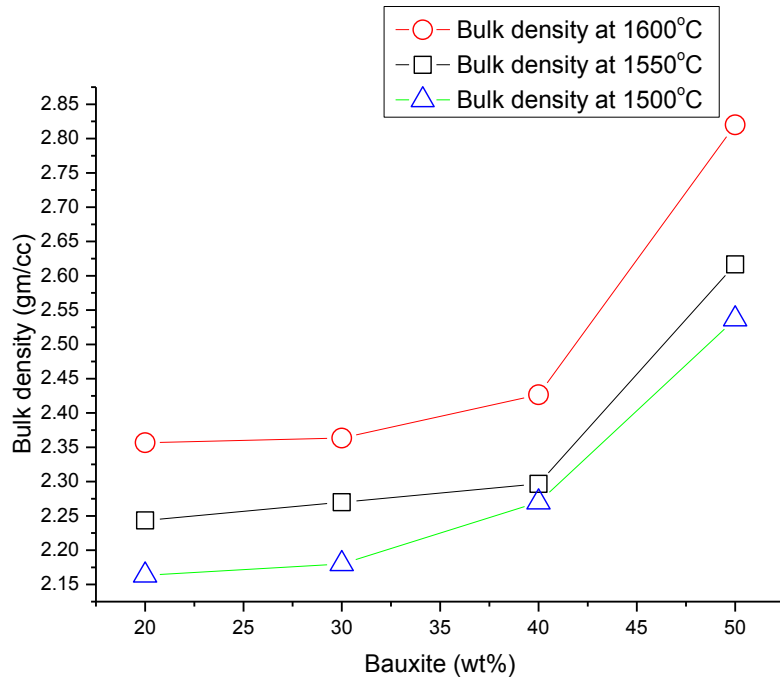


Fig 5: Variation of Bulk Density (BD) with the bauxite content at different sintering temperature

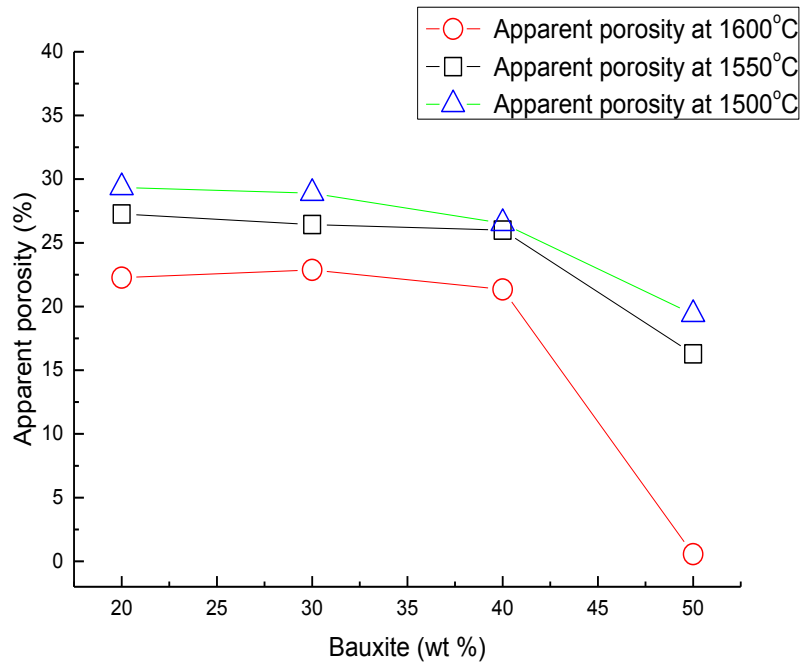


Fig 6: Variation of Apparent Porosity (AP) as function of bauxite content at different sintering temperature

Fig 7 is the powder XRD of SB4 and SB5 samples sintered at 1600°C/2hrs. SB4 shows mullite as the only main crystalline phase but SB5 containing 50wt% bauxite shows mullite as crystalline phase with few peaks of corundum

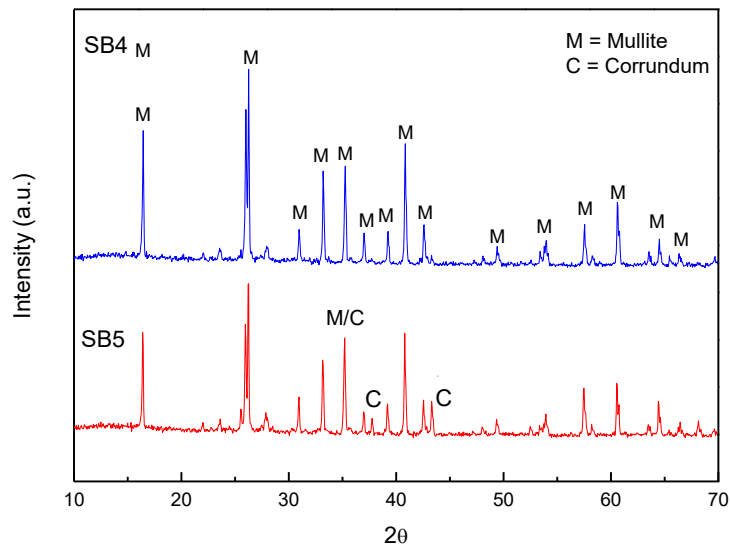
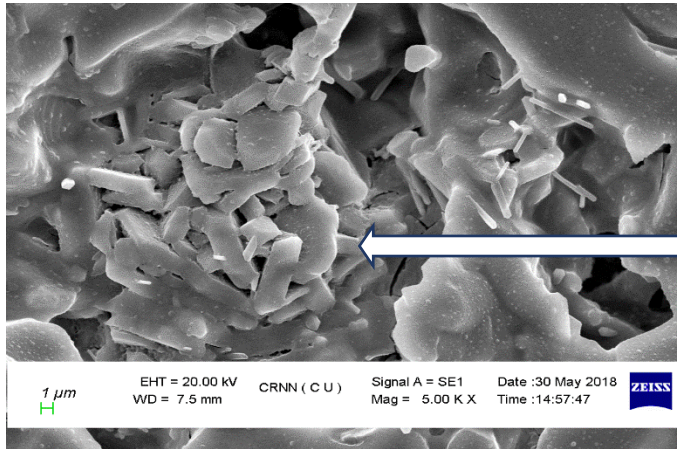


Fig7: Powder XRD pattern of samples sintered at 1550°C/2hrs

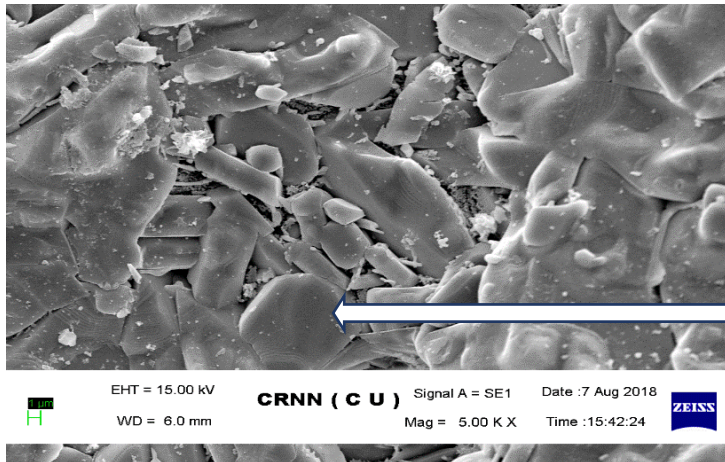
Fig 8 is the secondary electron image of chemically etched fracture surface of SB4 batch sintered at 1600°C/2hr. Elongated columnar shaped grains are mullite. Elongated mullite grains are interlocked. The energy dispersive x-ray analysis shows the presence of titanium, iron, calcium, magnesium, sodium in mullite grains suggesting mullite forms solid solution with these oxides. Glassy phase is also observed with dark colour.



Element	Weight%	Atomic%
O K	37.93	53.36
Na K	1.34	1.31
Mg K	0.51	0.47
Al K	27.78	23.17
Si K	18.66	14.95
Ca K	7.00	3.93
Ti K	1.25	0.59
Fe K	5.53	2.23
Totals	100.00	

Fig 8: Secondary electron image and EDX of SB4 sample sintered at 1600°C/2hrs.

Fig 9 is the secondary electron image of SB5 batch sintered at 1600°C/2hr. Columnar shaped grains are mullite. Equiaxed grains are corundum. EDX analysis shows the amount of titanium, iron, calcium, magnesium, sodium is much high in mullite grain with respect to that in corundum grains.



Element	Weight%	Atomic%
O K	46.83	60.32
Na K	0.04	0.04
Mg K	0.35	0.30
Al K	49.89	38.11
Si K	0.43	0.31
Ca K	0.07	0.04
Ti K	0.04	0.02
Fe K	2.34	0.86
Totals	100.00	

Fig 9: Secondary electron image and EDX of SB5 sample sintered at 1600°C/2hrs

Stage -II

From the stage one, we got best properties from alumina rich batch (SB5), that's why we choose SB5 batch and stoichiometric batch (SB4) for next stage.

The chemical analysis of the sintered sample is shown in **Table 4**. The chemical analysis confirms the presence of excess alumina after formation of stoichiometric mullite.

Table 4: Chemical composition of sintered aggregates fired at 1650°C

Parameter (%)	SB4-Z0	SB5-Z0
LOI	0	0
Al ₂ O ₃	67.24	70.05
Fe ₂ O ₃	2.11	2.64
TiO ₂	1.37	1.83
CaO	1.51	1.51
SiO ₂	27.77	23.97

Densification results can be confirmed by measuring linear shrinkage of the compacts. Batches without any ZrO₂ shows lower shrinkage (**fig10-a,b**) with respect to the zirconia containing batches. On increasing firing temperature diametral shrinkage increases. Maximum shrinkage was observed with 50% bauxite containing batch with 5% ZrO₂ content. The value is 15.41% at 1650°C/2hrs.

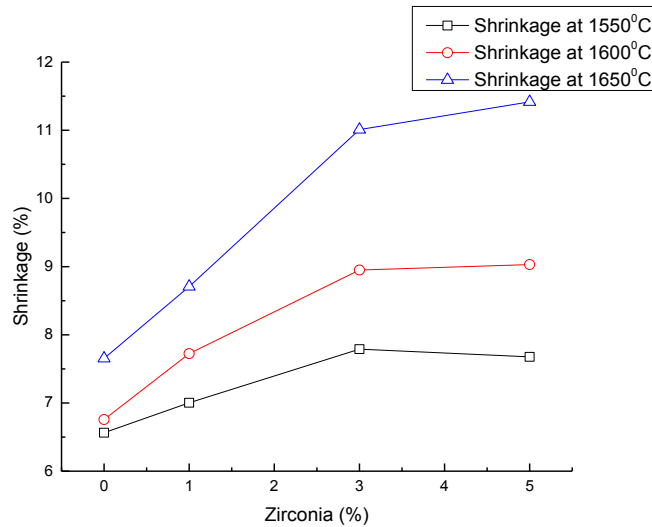


Fig 10(a): Effect of linear shrinkage (%) on the zirconia content and different sintering temperature on 40% bauxite content batch.

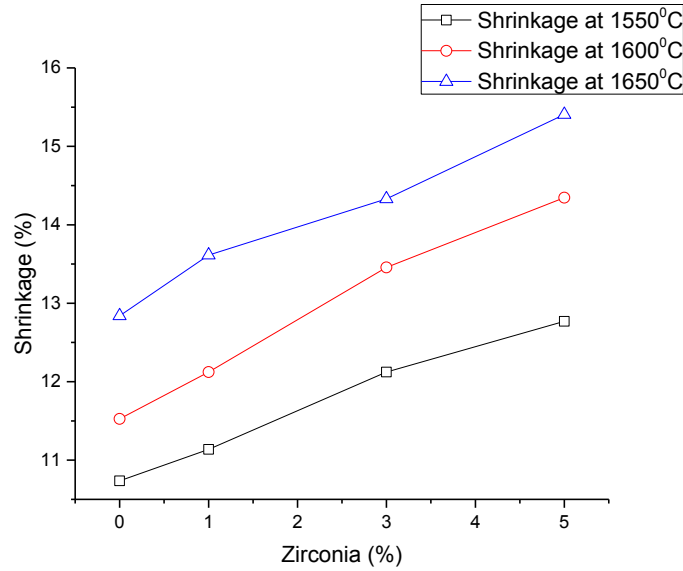


Fig 10(b): Effect of linear shrinkage (%) on the zirconia content and different sintering temperature on 50% bauxite content batch.

The shrinkage value also is also corroborated the value of apparent porosity (fig11-a,b). Minimum AP was observed in 50% bauxite batch with 5% ZrO₂ content batch. High percentage zirconia batch may have some pinning effect at the grain boundaries of mullite and corundum resulting in uniform grain size.

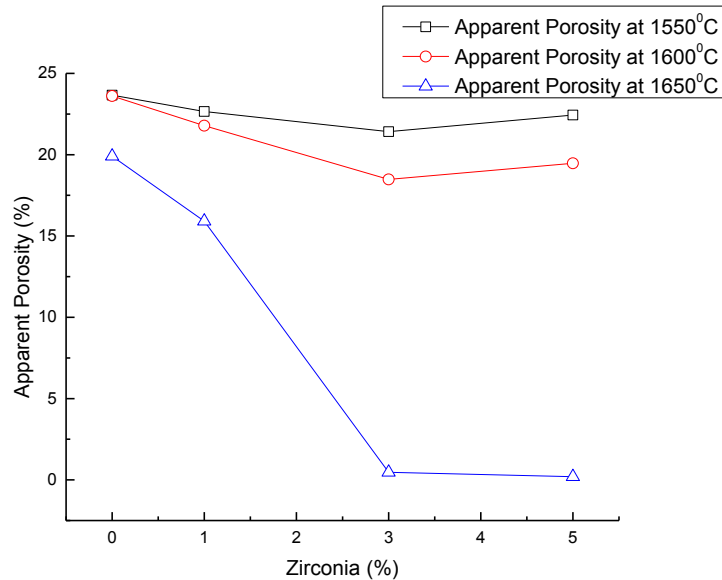


Fig 11(a): Variation of Apparent Porosity (AP) as function of zirconia content at different sintering temperature on 40% bauxite batch

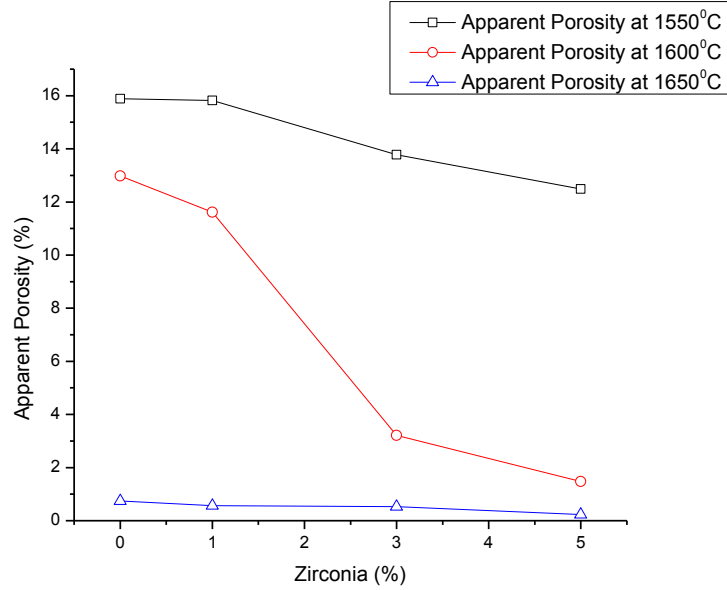


Fig 11(b): Variation of Apparent Porosity (AP) as function of zirconia content at different sintering temperature on 50% bauxite batch

The bulk density (BD) (fig12-a,b) of zirconia containing batches are high due to the high density of m-ZrO₂ (5.85 gm/cc) with respect to mullite (3.16 gm/cc) and corundum (3.99 gm/cc). BD of 40% bauxite containing 5 wt.% ZrO₂ is low (2.83 gm/cc) with respect to that of 50%Bauxite containing corundum along with mullite phase.

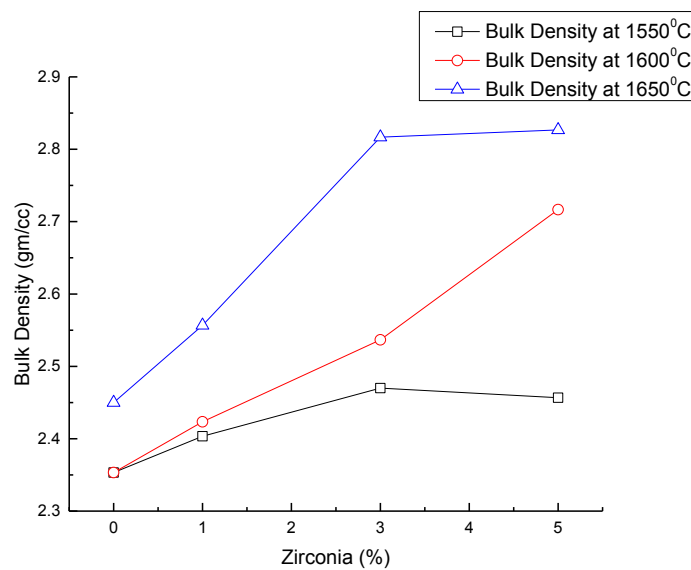


Fig 12(a): Variation of Bulk Density (BD) with the zirconia content at different sintering temperature in 40% batch

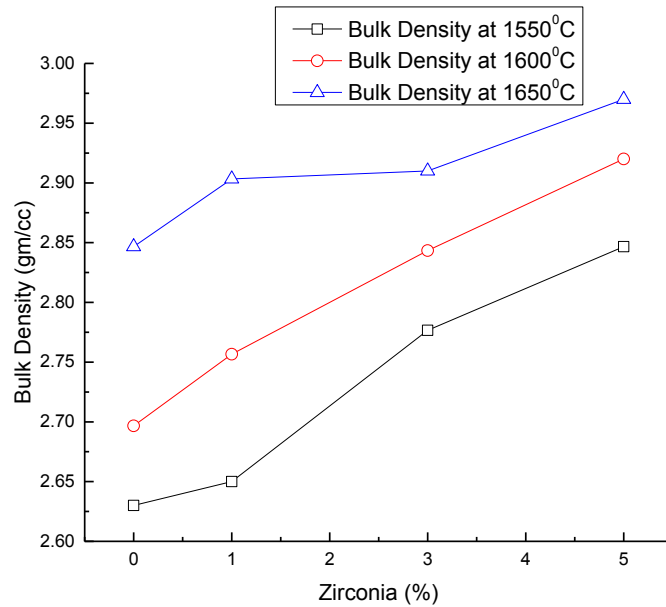


Fig 12(b): Variation of Bulk Density (BD) with the zirconia content at different sintering temperature in 50% batch

The powder x-ray diffraction of SB4-Z5 & SB5-Z5 is displayed in **fig-13**. Zirconia added to both the batches are present as m-Zirconia (01-083-0944). SB5-Z5 batch contain corundum (00-005-0712) along with and m-zirconia. And the major phases are mullite (01-074-2419).

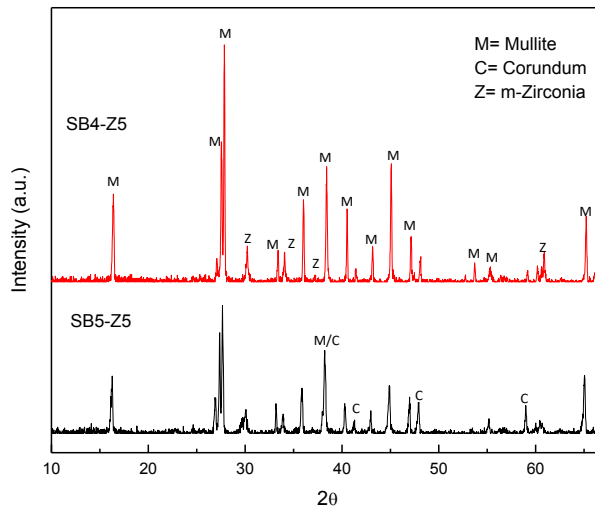


Fig 13: Powder XRD pattern of samples sintered at 1650°C/2hrs

FTIR of SB4-Z5 and SB5-Z5 shows (**fig-14**) the presence of double transmittance peaks at 1164 and 1135 cm^{-1} (Al-O & Si-O bond stretching vibration modes) assigned to mullite shows the

formation of this phase from sillimanite [1]. Bonds at 1185 and 950 cm^{-1} (Al-O & Si-O bond stretching vibration modes) are absent confirms the complete decomposition of sillimanite to mullite.

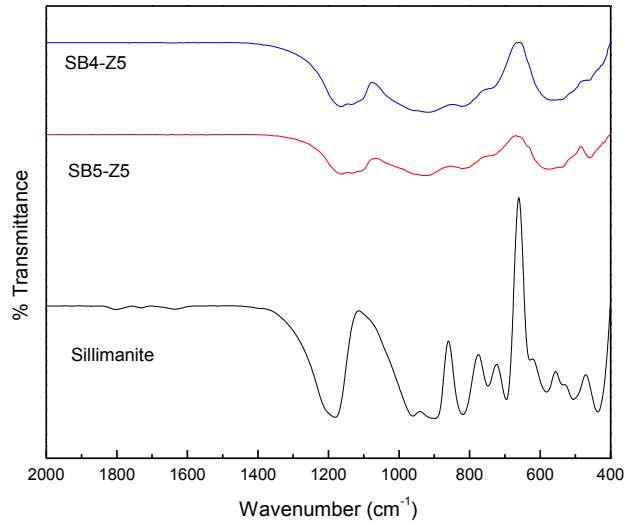


Fig 14: FTIR spectra of raw sillimanite and sintered batch fired at 1650°C/2hr

Fig-15 is the secondary electron image of chemically etched fractured surface of SB4 batch sintered at 1650°C. Elongated, rounded cornered columnar shaped grains are mullite. Glassy phases are present in the pockets. Black phases may be pores.

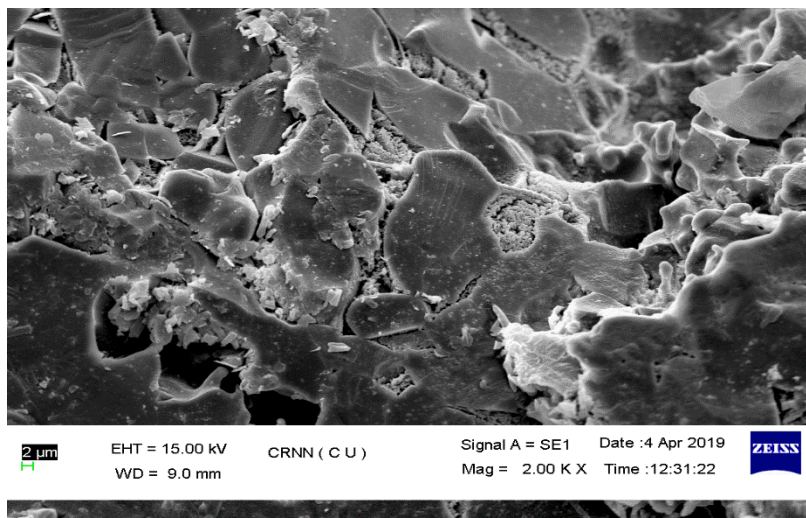


Fig 15: Secondary electron image of SB4-Z0 sample sintered at 1650°C/2hrs.

Fig-16 is the secondary electron image of chemically etched fractured surface of SB4 with 3 wt% zirconia (SB4-Z3). Mullite grains are angular, equiaxed and small with respect to the previous one. The structure is also compact than the previous one. Glassy phases (granular) are also observed in the inter-granular space. Grain to grain direct bonding is also noticed here. The presence of zirconia changes the morphological of the crystalline phases (changing rounded shaped grain to angular shaped one).

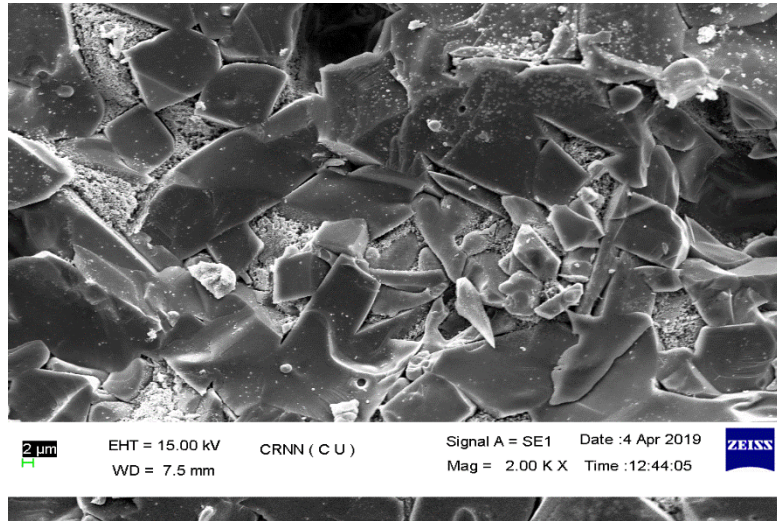


Fig 16: Secondary electron image of SB4-Z3 sample sintered at 1650°C/2hrs.

Fig-17 is the back scattered electron image (BSE) of SB4 batch with 3wt% zirconia. Bright white phases are zirconia wheares angular slate coloured grain are mullite crystals. Direct bonded mullite grains are present. Granular glassy phase is noticed in between the mullite grains.

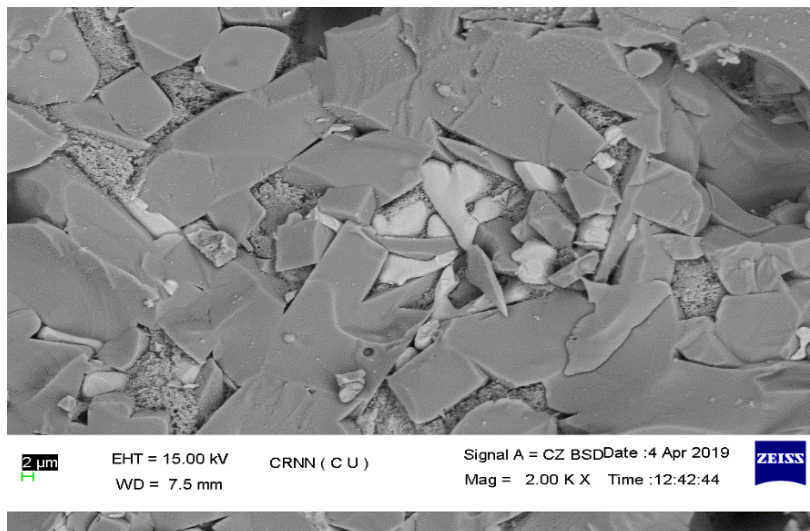


Fig 17: Back Secondary electron image of SB4-Z3 sample sintered at 1650°C/2hrs.

Fig-18 is the secondary image of 50% bauxite containing sillimanite batch sintered at 1650°C/ 2hr. Here the amount of glassy phase is higher with respect to the 40% bauxite batch. The microstructure is compact with low porosity. The mullite grains are rounded cornered elongated.

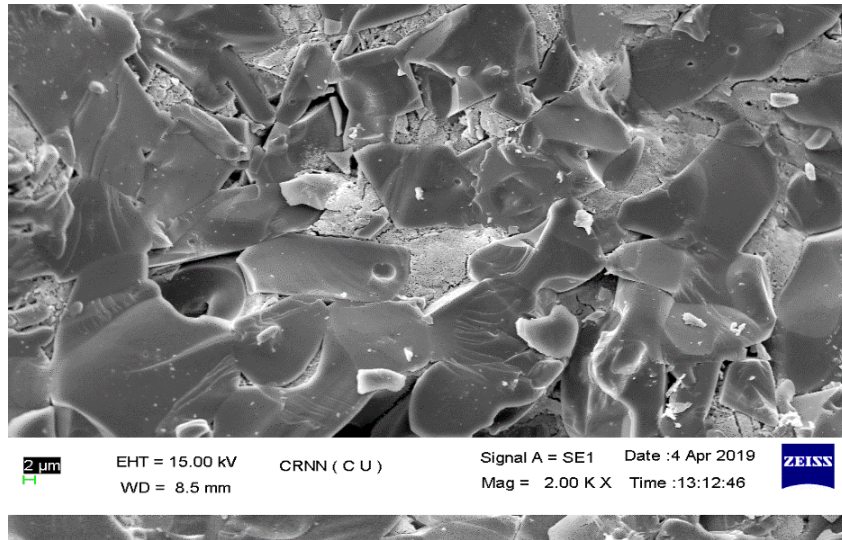


Fig 18: Secondary electron image of SB5-Z0 sample sintered at 1650°C/2hrs.

With the addition of 3 wt% of zirconia to the 50wt% bauxite containing batch (**fig-19**), the grain size are smaller one with respect to the previous one. Here aspect ratio is high and equiaxed grain may be corundum. Pores are not observed here and the structure is compact.

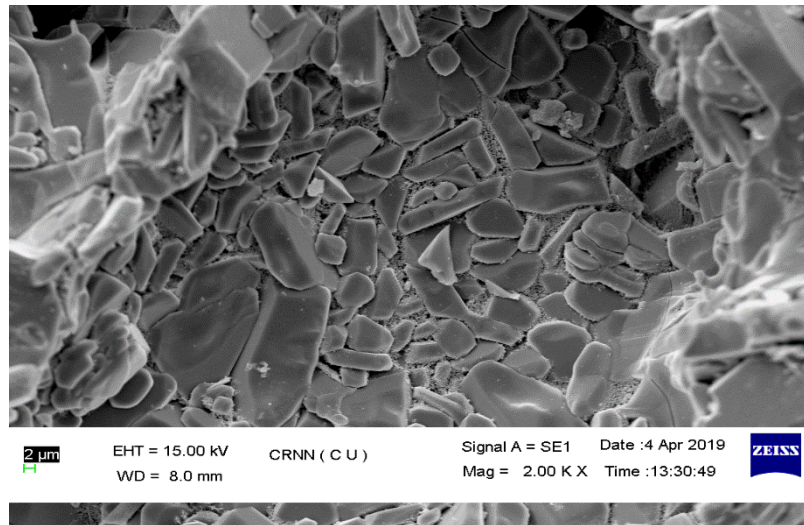


Fig 19: Secondary electron image of SB5-Z3 sample sintered at 1650°C/2hrs.

Further addition of ZrO₂ (batch SB5-Z5) shows much more elongated mullite with high aspect ratio with sharp corner (**fig-20**). Here the mullite grains are interlocked. Glassy phase (granular) are present in between the crystalline phases. Though it has more glassy phase respect to 40% batch but for this interlocked structure, it has higher CCS value.

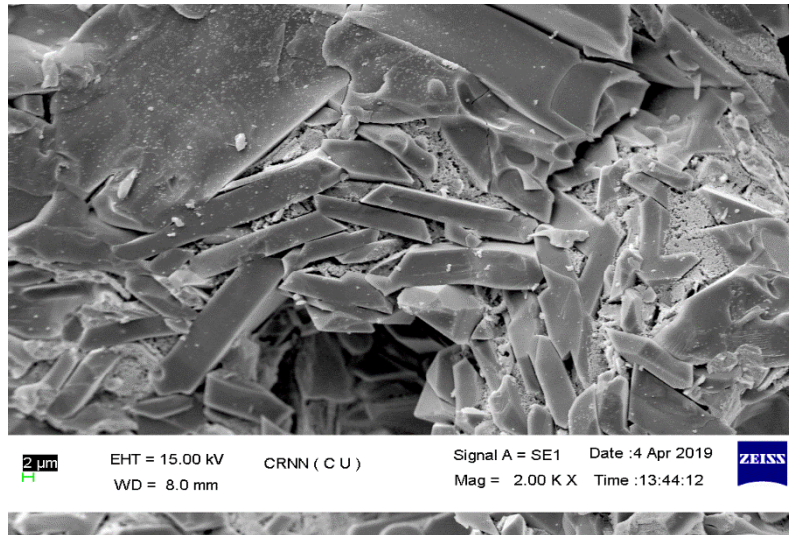


Fig 20: Secondary electron image of SB5-Z5 sample sintered at 1650°C/2hrs.

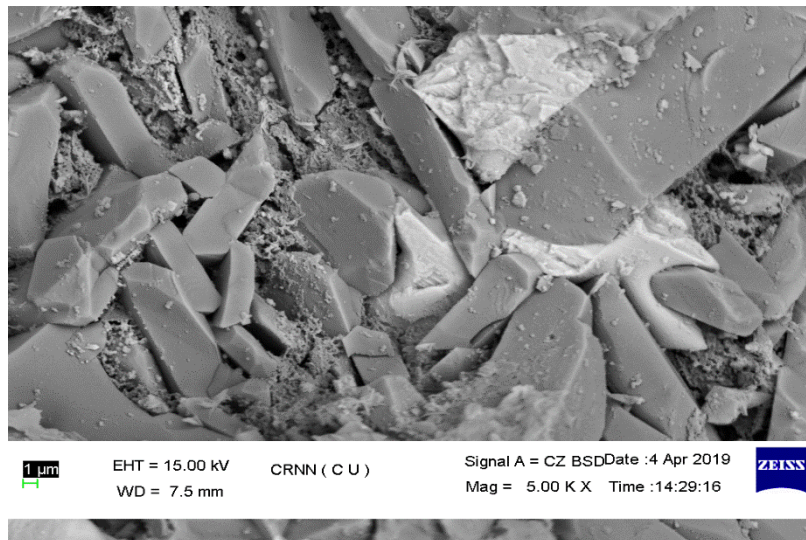


Fig 21: Back Secondary electron image of SB5-Z5 sample sintered at 1650°C/2hrs

Back scattered electron image (**fig-22**) at low magnification confirmed the uniform distribution of zircon within the matrix.

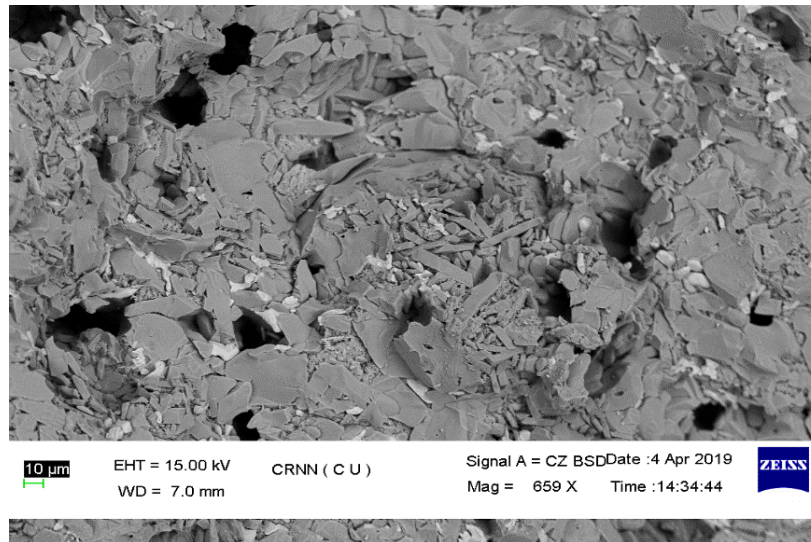


Fig 22: Back Secondary electron image of SB5-Z5 sample sintered at 1600°C/2hrs

Fig-23 shows the bar chart of slag corrosion resistance of the samples. The figure showed the highest slag resistance in 50% bauxite batch with 5% zirconia. And the 40% bauxite batch without zirconia showed the lowest resistance. This may be due to the presence of higher amount of porosity in 40% bauxite batch. But zirconia added batches in both 40% and 50% batches showed better slag resistance. The high resistance may be due to the presence of zirconia at the grain boundary.

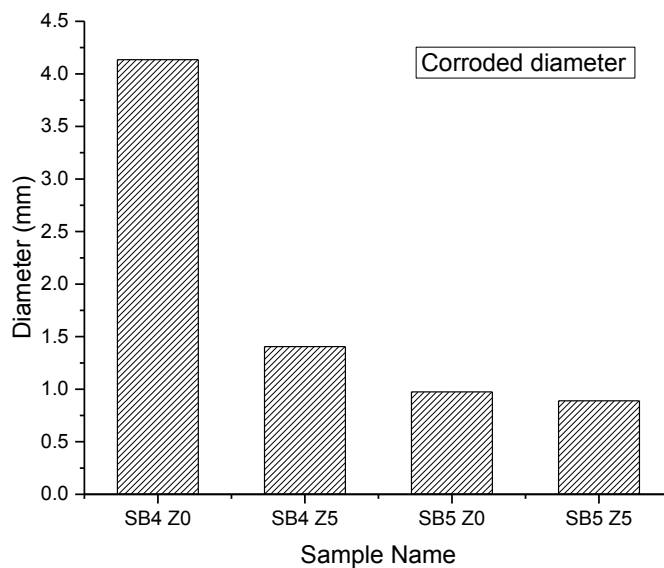


Fig 23: Slag corrosion resistance of sintered samples at 1450°C/2hrs

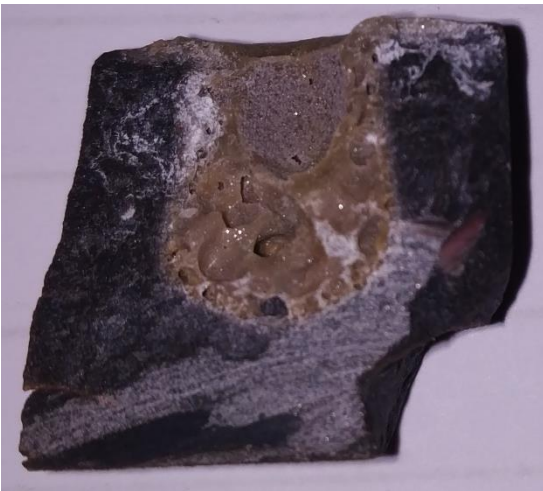


(a)



(b)

Fig 24: Cut surface photograph of 40% bauxite containing batch with 0% zirconia (a) and 5% Zirconia (b) after slag corrosion test



(a)



(b)

Fig 25: Cut surface photograph of 50% bauxite containing batch with 0% zirconia (a) and 5% Zirconia (b) after slag corrosion test

CHAPTER 6

SUMMARY & CONCLUSION

6. Summary & Conclusion

Mullite ceramics can be prepared from beach sand sillimanite fine after addition of natural bauxite as alumina source. Higher amount bauxite facilitates the higher sintering rate by providing high amount of liquid phase forming oxide present in bauxite.

Zirconia addition improved the densification as well as the bulk density and it also reduced the apparent porosity. The batch with 5% zirconia and 50% bauxite showed the lowest porosity, highest shrinkage and highest bulk density when sintered at 1650°C. With the higher amount of zirconia bulk density and shrinkage also increased. But it takes higher sintering temperature to densification.

FTIR of samples shown the presence of double transmittance peaks at 1164 and 1135 cm^{-1} (Al-O & Si-O bond stretching vibration modes) assigned to mullite shows the formation of this phase from sillimanite. Bonds at 1185 and 950 cm^{-1} (Al-O & Si-O bond stretching vibration modes) are absent confirms the complete decomposition of sillimanite to mullite.

High percentage of bauxite addition developed corundum along with mullite crystalline phase. XRD peak showed the presence of mullite ($3\text{Al}_2\text{O}_3 \cdot 2\text{SiO}_2$) phase, corundum ($\alpha\text{-Al}_2\text{O}_3$) phase in 50% bauxite batch and in zirconia added batch, monoclinic zirconia ($m\text{-ZrO}_2$) phase.

Elongated columnar shaped mullite grains were observed in SEM of chemically etched fracture surface. Back scattered electron image (BSE) shows the bright white phases are zirconia wheares angular slate coloured grain are mullite crystals. The presence of zirconia changes the morphology of the crystalline phases (changing rounded shaped grain to angular shaped one). Glassy phases (granular) are also observed in the inter-granular space. Further addition of ZrO_2 shows much more elongated mullite with high aspect ratio with sharp corner. Low magnification image confirmed the uniform distribution of zirconia within the matrix.

The EDX analysis shows that the detrimental impurities present in bauxite forms solid solution with mullite. Small amounts of Ti, Fe, Ca, Mg and Na are also detected in corundum grain in higher bauxite content batch (50%).

Zirconia addition showed higher amount of slag corrosion resistance than the non-zirconia batches. PCE shows that the samples can withstand up to 1800°C.

CHAPTER 7

REFERENCE

7. Reference:

1. A. Tomba, M.A. Camerucci, G. Urretavizcaya, A.L. Cavalieri, M.A. Sainz, A. Caballero, **“Elongated mullite crystals obtained from high temperature transformation of sillimanite”**, Ceramics International 25(1999) 245-252.
2. Ibram Ganesh, Govindan Sundararajan, JoseM. F. Ferreira, **“Formation and Densification Behavior of Mullite Aggregates from Beach Sand Sillimanite”**, Journal of American ceramic society 91 [8] 2464–2468 (2008).
3. H. S. Tripathi, B. Mukherjee, S K Das, A Ghosh and G Banerjee, **“Effect of sillimanite beach sand composition on mullitization and properties of Al₂O₃–SiO₂ system”**, Bull. Mater. Sci., Vol. 26, No. 2, February 2003, pp. 217–220.
4. H. S. Tripathi, A. Ghosh, M. K. Halder, B. Mukherjee and H. S. Maiti **“Microstructure and properties of sintered mullite developed from Indian bauxite”**, Bull. Mater. Sci., Vol. 35, No. 4, August 2012, pp. 639–643.
5. P. Kumar, M. Nath, A. Ghosh, H. S. Tripathi, **“Thermo-mechanical properties of mullite–zirconia composites derived from reaction sintering of zircon and sillimanite beach sand: Effect of CaO”**, Trans. Nonferrous Met. Soc. China 26(2016) 2397–2403.
6. S. Rahman, U. Feustel, S. Freimann, **“Structure description of the thermic phase transformation sillimanite–mullite”** Journal of the European Ceramic Society 21 (2001) 2471–2478.
7. H.S. Tripathi, S.K. Das, B. Mukherjee, A. Ghosh, G. Banerjee, **“Synthesis and thermo-mechanical properties of mullite–alumina composite derived from sillimanite beach sand: effect of ZrO₂”**, Ceramics International 27 (2001) 833–837.

8. Sasmita Prusty, D.K. Mishra, B.K. Mohapatra, S.K. Singh, **“Effect of MgO in the microstructure formation of zirconia mullite composites from sillimanite and zircon”**, *Ceramics International* 38 (2012) 2363–2368.
9. Manas K. Haldar, T.K. Pal, G. Banerjee, **“Preparation and properties of Y₂O₃ containing zirconia–mullite composites derived from sillimanite beach sand”**, *Ceramics International* 28 (2002) 311–318.
10. Michael D. Sacks, Joseph A. Pask, **“Sintering of Mullite-Containing Materials: I, Effect of Composition”**, *Journal of the American Ceramic Society*, Volume 66, Number 2 February 1982.
11. F. Cambier, C. Leblud, M. R. Anseau, A. Leriche, **“High temperature mechanical properties of reaction-sintered mullite/zirconia and mullite/alumina/zirconia composites”**, *Journal of Materials Science* 20 (1985) 2533—2540.
12. Mingwei Yan, Yong Li, Yang Sun, Ling Li, Shanghao Tong, JialinSun, **“Controllable preparation and synthetic mechanism of mullite from the bauxite with Fe-rich oxide content”**, *Material Chemistry and Physics* 202(2017)245-250.
13. S. Prusty, D. K. Mishra, B. K. Mohapatra and S. K. Singh, **“Correlation between properties of zirconia mullite and Y₂O₃ stabilized zirconia mullite derived by various processing techniques”**, *Advances in Applied Ceramics*, Vol. 110 (2011) 360-366.
14. Manas Kamal Haldar, **“Effect of magnesia additions on the properties of zirconia–mullite composites derived from sillimanite beach sand”**, *Ceramics International* 29 (2003) 573–581.

15. Philippe Descamps, Shuji Sakaguchi, Marc Poorternan, and Francis Cambier, **“High-Temperature Characterization of Reaction-Sintered Mullite-Zirconia Composites”** journal of American ceramic society 74 [10] 2476-81 (1991).
16. Manas K. Haldar, G. Banerjee, **“Properties of zirconia–mullite composites prepared from beach sand sillimanite”**, Materials letter 57 (2003) 3513-3520.
17. Atul V. Maldhure, Himansu S. Tripathi, Arup Ghosh, **“Mechanical Properties of Mullite–Corundum Composites Prepared from Bauxite”**, Int. J. Appl. CeramTechnology, 12 [4] 860–866 (2015).
18. Qiang Ren, Huanhuan Li, Xiulan Wu, Zhe zhe Huo, Ou Hai, Fei Lin, **“Effect of the calcining temperatures of low-grade bauxite on the mechanical property of mullite ceramics”**, Int J Appl Ceram Technol. 2017,1–9.
19. Yingchao Dong, Xuyong Feng, Xuefei Feng, Yanwei Ding, Xingqin Liu, Guangyao Meng, **“Preparation of low-cost mullite ceramics from natural bauxite and industrial waste fly ash”**, Journal of Alloys and Compounds, 460 (2008) 599–606.
20. Toshiyuki Koyama, Shigeo Hayashi, Atsuo Yasumori, Kiyoshi Okada, **“Preparation and Characterization of Mullite-Zirconia Composites from Various Starting Materials”**, Journal of the European Ceramic Society 14 (1994) 295-302.
21. H. S. Tripathi, S. K. Das, B. Mukherjee, A. Ghosh, **“Sintered Mullite from Aluminous Ore for Refractory Application”** American Ceramic Society Bulletin, Vol. 86, No. 5 (9301-9304).
22. H. Schneider, J. Schreuer, B. Hildmann, **“Structure and properties of mullite—A review”**, Journal of the European Ceramic Society 28 (2008) 329–344.
23. M.M.S. Wahsh, R.M. Khattab, M. Awaad **“Thermo-mechanical properties of mullite/zirconia reinforced alumina ceramic composites”**, Materials and Design 41 (2012) 31–36.

24. Cemal Aksel, “**The role of fine alumina and mullite particles on the thermo mechanical behavior of alumina–mullite refractory materials**”, *Materials Letters* 57 (2002) 708 – 714.
25. H. Schneider, “**Solubility of TiO₂, Fe₂O₃ and MgO in Mullite**”, *Ceramics International* 13 (1987) 77-82.
26. **The chem. And Physics of clay and allied materials** by R.W. Grimshaw (London, Ernest Benn Ltd) 4th ed p 329.

STUDIES ON IMAGE SEGMENTATION USING DIFFERENT CLUSTERING TECHNIQUES

A PROJECT REPORT

Submitted by

**Aditi Mandal
Aniruddha Chatterjee
Ayan Mondal
Bratati Chakraborty**

Supervised by

Dr Mousumi Maitra

in partial fulfillment for the award of the degree

of

Bachelor of Technology

IN

INFORMATION TECHNOLOGY

Year:2021-2022



**GOVERNMENT COLLEGE OF ENGINEERING AND
CERAMIC TECHNOLOGY**

73, Avinash Chandra Banerjee Ln, Kolkata- 700010

BONAFIDE CERTIFICATE

Certified that this project report "Studies on Image Segmentation using Different clustering techniques" is the bonafide work of "Bratati Chakraborty, Ayan Mondal, Aniruddha Chatterjee, Aditi Mandal" who carried out the project work under my supervision.

SIGNATURE

M. Maitra . 23.5.22.
DR MOUSUMI MAITRA

HEAD OF THE DEPARTMENT

INFORMATION TECHNOLOGY

73, Avinash Chandra
Banerjee Ln,
Kolkata- 700010

SIGNATURE

M. Maitra . 23.5.22.
DR MOUSUMI MAITRA

SUPERVISOR

HEAD OF THE DEPARTMENT
INFORMATION TECHNOLOGY

73, Avinash Chandra
Banerjee Ln,
Kolkata- 700010

SIGNATURE

[Signature]

External Examiner:

ACKNOWLEDGEMENT

We would like to express our sincere gratitude to several individuals and organizations for supporting us.

First, we wish to express our sincere gratitude to our supervisor, **Dr. Mausumi Maitra**, for her enthusiasm, patience, insightful comments, helpful information, practical advice, and unceasing ideas that have helped us tremendously at all times in our project on "**STUDIES ON IMAGE SEGMENTATION USING DIFFERENT CLUSTERING TECHNIQUES**" and writing of this project report.

Her immense knowledge, profound experience, and professional expertise in Networking and Image Processing had enabled us to perform this project successfully. Without her support and guidance, this project would not have been possible. We could not have imagined having a better supervisor in our study.

Secondly, we wish to express sincere thanks to our Head of The Department,

Dr. Mousumi Maitra, for giving us such an opportunity.

Last but not least we would like to thank the entire "**GOVERNMENT COLLEGE OF ENGINEERING AND CERAMIC TECHNOLOGY**" INFORMATION TECHNOLOGY DEPARTMENT for allowing us to proceed with the project.

Thanks for all the encouragement.

Aditi Mandal
Aniruddha Chatterjee
Ayan Mondal
Bratati Chakraborty

Aditi Mandal (GCECTB-R18-2001)
Aniruddha Chatterjee (GCECTB-R18-2004)
Ayan Mondal (GCECTB-R18-2006)
Bratati Chakraborty (GCECTB-R18-2010)

STUDIES ON IMAGE SEGMENTATION USING DIFFERENT CLUSTERING TECHNIQUES

A PROJECT REPORT

Submitted by

**Aditi Mandal
Aniruddha Chatterjee
Ayan Mondal
Bratati Chakraborty**

in fulfillment for the award of the degree

of

Bachelor of Technology

IN

INFORMATION TECHNOLOGY

Year:2021-2022



**GOVERNMENT COLLEGE OF ENGINEERING AND
CERAMIC TECHNOLOGY**

73, Avinash Chandra Banerjee Ln, Kolkata- 700010

BONAFIDE CERTIFICATE

Certified that this project report “**Studies on Image Segmentation using Different clustering techniques**” is the bonafide work of “**Bratati Chakraborty, Ayan Mondal, Aniruddha Chatterjee, Aditi Mandal**” who carried out the project work under my supervision.

SIGNATURE

DR MOUSUMI MAITRA

HEAD OF THE DEPARTMENT

INFORMATION TECHNOLOGY

73, Avinash Chandra
Banerjee Ln,
Kolkata- 700010

SIGNATURE

External Examiner:

SIGNATURE

DR MOUSUMI MAITRA

SUPERVISOR

**HEAD OF THE DEPARTMENT
INFORMATION TECHNOLOGY**

73, Avinash Chandra
Banerjee Ln,
Kolkata- 700010

ACKNOWLEDGEMENT

We would like to express our sincere gratitude to several individuals and organizations for supporting us.

First, we wish to express our sincere gratitude to our supervisor, **Dr. Mausumi Maitra**, for her enthusiasm, patience, insightful comments, helpful information, practical advice, and unceasing ideas that have helped us tremendously at all times in our project on “**STUDIES ON IMAGE SEGMENTATION USING DIFFERENT CLUSTERING TECHNIQUES**” and writing of this project report.

Her immense knowledge, profound experience, and professional expertise in Networking and Image Processing had enabled us to perform this project successfully. Without her support and guidance, this project would not have been possible. We could not have imagined having a better supervisor in our study.

Secondly, we wish to express sincere thanks to our Head of The Department,

Dr. Mousumi Maitra, for giving us such an opportunity.

Last but not least we would like to thank the entire “**GOVERNMENT COLLEGE OF ENGINEERING AND CERAMIC TECHNOLOGY**” INFORMATION TECHNOLOGY DEPARTMENT for allowing us to proceed with the project.

Thanks for all the encouragement.

Aditi Mandal (GCECTB-R18-2001)
Aniruddha Chatterjee (GCECTB-R18-2004)
Ayan Mondal (GCECTB-R18-2006)
Bratati Chakraborty (GCECTB-R18-2010)

ABSTRACT

In this paper, we have studied various clustering algorithms and implemented K-means clustering algorithm and Fuzzy-C means clustering algorithm on some random images. Then, we have studied the results and presented a comparative analysis of how effective both these algorithms are in terms of image segmentation.

Most automatic pictorial pattern identification and scene analysis tasks use image segmentation as a necessary first step. In practice, image segmentation is the assignment of each image pixel to one of the picture sections. Over the last three decades, image segmentation has been the focus of a lot of studies. It separates an image into discrete regions with the high similarity between pixels in each zone and high contrast between regions.

It is useful in a variety of fields, including health care, image processing, traffic image analysis, and pattern identification.

Image segmentation approaches include threshold-based, edgebased, cluster-based, and neural network-based.

Clustering is one of the most efficient strategies among the various techniques. K-means clustering, Fuzzy C-means clustering, mountain clustering method, and subtractive clustering method are all examples of clustering.

Clustering is the process of looking for unique groupings of features in a feature space. It is envisaged that these groups will have distinct structures that can be distinguished. The data is partitioned into a number of partitions, which are volumes in the n-dimensional feature space, by the clustering task. K-means clustering is a popular clustering algorithm as it is simple and computationally faster. The Fuzzy C-Means (FCM) technique is another popular fuzzy clustering algorithm. FCM (fuzzy c-means) is a clustering approach that allows one piece of data to belong to two or more clusters.

TABLE OF CONTENTS

Title Page	
Acknowledgment.....	
Abstract.....	

Chapter 1: INTRODUCTION

1.1 Image Segmentation	
1.2 Applications Of Image Segmentation	
1.2.1 Different Types Of Segmentation	
1.3 CLUSTERING	

Chapter 2: TYPES OF CLUSTERING

2.1 K Means Clustering	
2.1.1 Features	
2.1.2 K-Means Algorithm	
2.1.3 Choice Of K	
2.1.4 Disadvantages Of K-Means Clustering	
2.2 Fuzzy C Means Clustering	
2.2.1 Algorithm Flow	
2.2.2 Advantages And Disadvantages	
2.3 Literature Review On Related Work	

Chapter 3: PROJECT IMPLEMENTATION

3.1 Implementation And Results Of K-Means Algorithm

3.2 Implementation And Results Of Fuzzy-C Means Algorithm

3.3 Implementation Of K-Means Means Algorithm On
Mammography Images

3.4 Implementation Of Fuzzy-C Means Algorithm On
Mammography Images

Chapter 4: CANNY EDGE DETECTION

4.1 Implementation of Canny Edge Detector in Python

Chapter 5: CONCLUSION

Chapter 6: FUTURE SCOPE

Chapter 7: REFERENCES

LIST OF FIGURES

Figure No.	TITLE
Fig 1	Pseudo-code of K-means algorithm
Fig 2	Graph representing Elbow method
Fig 3	Flow chart of Fuzzy-C means algorithm
Fig 4	Code snippet of K-means clustering algorithm
Fig 5	Comparison of image segmentation using k-means on real images named i) scene, ii) butterfly, iii) mountain, and iv) bird.
Fig 6	Code snippets of Fuzzy-C means algorithm
Fig 7	Comparison of image segmentation using fuzzy-c means on real images named i) scene, ii) butterfly, iii) mountain, and iv) bird
Fig 8	Code snippet of K-means algorithm for black and white images
Fig 9	Image Segmented Results on Mammogram images when k=3 a. Benign Tumor b. Malignant c. Malignant d. Benign
Fig 10	Image Segmented Results on Mammogram images when k=5 a. Benign Tumor b. Malignant c. Malignant d. Benign

- Fig 11 Image Segmented Results on Mammogram images when $k=10$ a. Benign Tumor b. Malignant c. Malignant d. Benign
- Fig 12 Image Segmented Results on Mammogram images when $c=3, m=2$ a. Benign Tumor b. Malignant c. Malignant d. Benign
- Fig 13 Image Segmented Results on Mammogram images when $c=3, m=2$ a. Benign Tumor b. Malignant c. Malignant d. Benign
- Fig 14 Image Segmented Results on Mammogram images when $c=3, m=2$ a. Benign Tumor b. Malignant c. Malignant d. Benign
- Fig 15 Equation for a Gaussian filter kernel of size $(2k+1) \times (2k+1)$
- Fig 16 Gradient magnitude and angle
- Fig 17 Code Snippets of Canny Edge Detection Algorithm
- Fig 18 Comparison of Canny Edge Detection on Real Images named (a) *scene* (b) *sunset* (c) *butterfly*

1. INTRODUCTION

Image segmentation is a subset of digital picture processing that focuses on dividing an image into distinct portions based on its characteristics and attributes. The basic purpose of picture segmentation is to make the image simpler so that it can be analyzed more easily. Picture segmentation is the process of dividing an image into segments with comparable characteristics. Image Object refers to the sections of the image that you divide.

You can separate and group certain pixels from an image using image segmentation algorithms, assign them labels, then categorize additional pixels based on these labels.

You can draw lines, establish borders, and separate specific objects (important components) from the rest of the objects in a picture (unimportant components).

For both supervised and unsupervised training in machine learning, you can use the labels created from image segmentation. You'd be able to solve a variety of business issues as a result of this.

1.1 IMAGE SEGMENTATION

An image is made up of pixels and Google says segmentation means the act of dividing something into different parts. Now for an image, the different parts are the different objects in that image.

The objects are made up of groups of pixels with similar characters which can be Gray level, color, texture, and many other qualities. So image segmentation is the process of partitioning a digital image into multiple segments made up of pixels of similar properties.

The purpose of segmentation is to make an image more intelligible and easier to examine by simplifying and/or changing its representation. We have to work on that image at the end of the day.

1.2 APPLICATIONS OF IMAGE SEGMENTATION

Image is a very interesting topic to work on, we also can't ignore the fact that it has several applications related to the real world

It is a large aspect of computer vision and is used in several areas:-

- Face Recognition
- Number Plate Recognition
- Medical Imaging
- Object Recognition

Like face recognition, in our phones we have face lock features what it does is stores the unique properties of the owners face and matches it with the face that tries to unlock it, if it does not match it shows an error

If one breaks a traffic rule and is relaxed just because he/she was not seen by any police, then he/she is living a myth and it will be broken when he/she will receive a message of traffic challan. Thanks to technology we can do so and decrease the number of rule-breakers.

It plays a very important role in medical imaging, it can be used to identify different parts of our brain, we can use it to find the irregular cells which can or are causing the disturbance in our body.

It can also be used to identify a specific object differentiating it from others, identify lines curves, remove background and many more.

1.2.1 TYPES OF IMAGE SEGMENTATION

- Histogram-based segmentation.

- Region-based segmentation
 - Edge detection
 - Region growing
 - Region splitting and merging

- Clustering-based segmentation
 - K-means clustering
 - Fuzzy C- means clustering

- Neural Networks for Segmentation

1.3 CLUSTERING

A clustering algorithm separates an image into clusters (disjoint groups) of pixels with comparable properties, as the name implies. It would divide the data items into clusters, with the components in one cluster being more similar to the elements in other clusters.

Fuzzy c-means (FCM), k-means, and enhanced k-means algorithms are some of the most used clustering techniques.

The k-means clustering algorithm is commonly used in picture segmentation because it is simple and efficient.

The FCM method, on the other hand, divides pixels into separate groups based on their degree of membership.

2. TYPES OF CLUSTERING ALGORITHMS

There are various types of clustering algorithms and improvised versions of them. In this paper, we'll study and review K-means clustering algorithm and Fuzzy-C means clustering algorithm.

2.1 K-MEANS CLUSTERING:

The K-means clustering technique is a well-known and effective unsupervised machine learning algorithm. Many complex unsupervised machine learning issues are solved with it. Let's have a look at the points we'll be discussing before we get started.

Assume you're given a data set with a set of features but no labels for each observed sample. A supervised algorithm like Support Vector Machines, which trains a hypothesis function to predict labels given features, requires labels. As a result, we are unable to conduct supervised learning. What options do we have?

Finding groups of data in our dataset that are similar to one another — what we call clusters — is one of the easiest activities we can perform on a data set without labels.

2.1.1 Features:

- Unsupervised learning
- Hard clustering algorithm
- Produces k number of clusters
- Fast computational speed

2.1.2 K-Means Algorithm:

The K-means algorithm is an iterative algorithm that attempts to partition a dataset into K distinct non-overlapping subgroups (clusters), with each data point belonging to only one of these groups.

It aims to make intra-cluster data points as comparable as possible while maintaining clusters as distinct (far) as possible. It distributes data points to clusters in such a way that the sum of the squared distances between them and the cluster's centroid (arithmetic mean of all the data points in that cluster) is as small as possible.

Within clusters, the less variance there is, the more homogenous (similar) the data points are.

The following is how the K-means algorithm works:

1. K is the number of clusters to specify.
2. Initialize the centroids by shuffling the dataset and then picking K data points at random for the centroids without replacing them.

3. Continue iterating until the centroids do not change. i.e. the clustering of data points does not change.

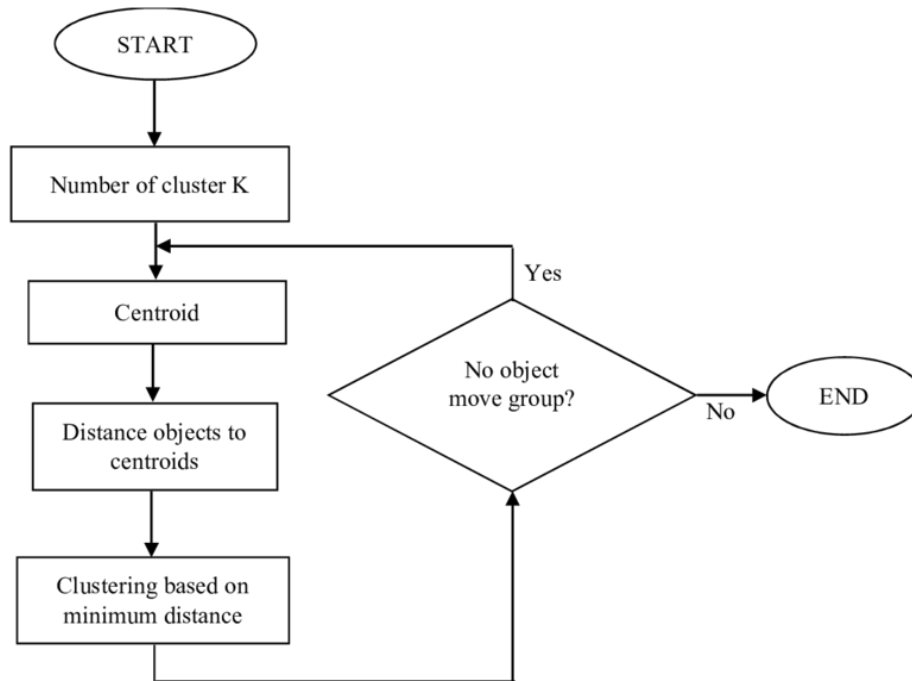


Fig. 1. Pseudo-code of K-means algorithm

2.1.3 CHOICE OF K

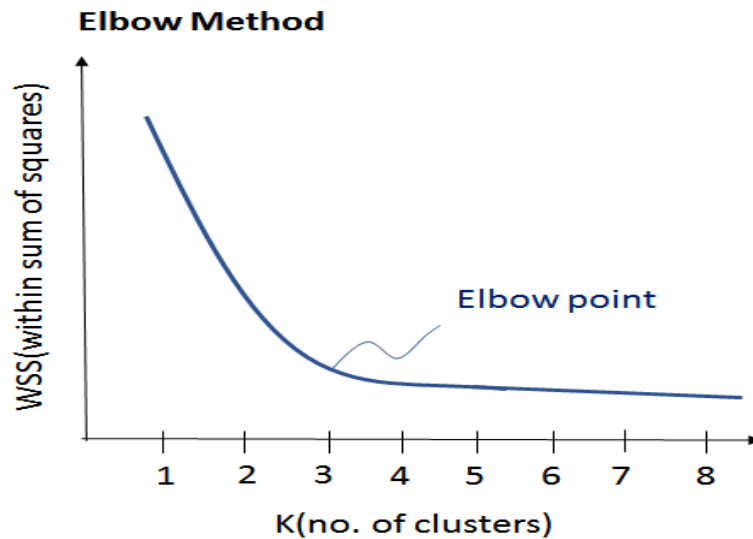


Fig. 2. Graph representing Elbow method

The optimal number of clusters into which the data can be grouped is a crucial stage in any unsupervised technique. One of the most prominent approaches for determining the ideal value of k is the Elbow Method.

2.1.4 DISADVANTAGES OF K-MEANS CLUSTERING

Appropriate choice of k is very important

Only works on numerical data

Shows poor results with irregularly shaped clusters

Mediocre performance if the parameters are fuzzy

2.3. FUZZY C MEANS CLUSTERING ALGORITHM

The Fuzzy C-Means (FCM) algorithm [S] is the most popular in fuzzy clustering. FCM (fuzzy c-means) is a clustering technique that allows a single piece of data to belong to two or more clusters.

A traditional clustering algorithm finds a “hard partition” of a given dataset based on certain criteria that evaluate the partition's goodness. The term "hard partition" refers to the fact that each datum belongs to exactly one cluster of the partition. Fuzzy C-Means algorithm is a soft clustering algorithm, unlike K-means which is a hard clustering algorithm.

The soft clustering algorithm, on the other hand, finds a “soft partition” of a given dataset. In a “soft partition,” a datum can be assigned to multiple clusters in part.

2.3.1 ALGORITHM FLOW OF FUZZY C MEANS

The Fuzzy C Means algorithm assigns membership to every data point that corresponds to each cluster center based on how distant the cluster center is from the data point. The closer the data is to the cluster center, the more its membership with that cluster center. Obviously, the sum of each data point's membership should equal one. After each iteration, update the

membership and cluster centers according to the formula given below:

$$J(U, V) = \sum_{i=1}^n \sum_{j=1}^c (\mu_{ij})^m \|x_i - v_j\|^2$$

where,

' n ' is the number of data points.

' v_j ' represents the j^{th} cluster center.

' m ' is the fuzziness index $m \in [1, \infty]$.

' c ' represents the number of cluster centers.

' μ_{ij} ' represents the membership of i^{th} data to j^{th} cluster center.

' d_{ij} ' represents the Euclidean distance between i^{th} data and j^{th} cluster center.

The main objective of fuzzy c-means algorithm is to minimize:
Where, ' $\|x_i - v_j\|$ ' is the Euclidean distance between i^{th} data and j^{th} cluster center

Algorithmic steps for Fuzzy c-means clustering

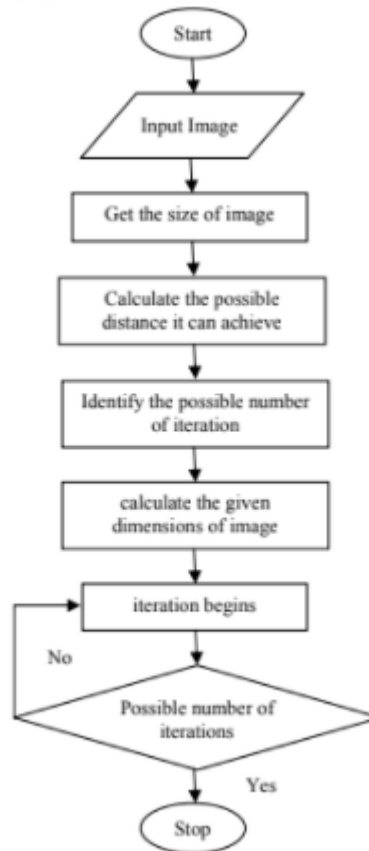


Fig. 3. Flow chart of Fuzzy-C means algorithm

Let $X = \{x_1, x_2, x_3 \dots, x_n\}$ be the set of data points and $V = \{v_1, v_2, v_3 \dots, v_c\}$ be the set of centers.

- 1) Randomly select 'c' cluster centers.
- 2) Calculate the fuzzy membership ' μ_{ij} ' using:
- 3) Compute the fuzzy centers ' v_j ' using:
- 4) Repeat step 2) and 3) until the minimum 'J' value is achieved or $\|U^{(k+1)} - U^{(k)}\| < \beta$.

where

' k ' is the iteration step.

' β ' is the termination criterion between [0, 1].

' $U = (\mu_{ij})_{n \times c}$ ' is the fuzzy membership matrix.

' J ' is the objective function.

Parameters:

The following parameters must be specified before using the FCM algorithm:

- c , the number of clusters
- m , the fuzziness exponent
- the tolerance for termination

2.3.2 ADVANTAGES AND DISADVANTAGES OF USING FUZZY C MEANS CLUSTERING FOR IMAGE SEGMENTATION

Unlike the k-Means algorithm where the data points exclusively belong to one cluster, in the case of the fuzzy c-means algorithm, the data point can belong to more than one cluster with a likelihood. Fuzzy c-means clustering gives comparatively better results for overlapped data sets. Due to the same reason, the Fuzzy c-means (FCM) algorithm is the most popular method used in image segmentation.

Although the Fuzzy C-means clustering algorithm is quite efficient as an image segmentation technique, it is sensitive to image noise. [10] Other limitations include the slow implementation (it is slower than K-means), prior random selection of clusters, initializing cluster centers, etc.

2.3 LITERATURE REVIEW ON IMAGE SEGMENTATION USING FUZZY-C MEANS ALGORITHM

Pingale et al [5] propose a method where brain tumor images procured from MRI scans of patients are fed into a Median filtering algorithm to cancel all unwanted noises. Then, the K-means algorithm is applied on noise filtered brain tumor images. It is said that the areas having higher intensity values are supposed to contain a tumor. After implementing K means clustering on the image, Fuzzy C- means segmentation is implemented on the resultant image. Lastly, thresholding segmentation is applied and the tumor part in the MRI image is shown. They have also applied approximate reasoning to calculate brain tumor area and SVM classification to detect the stage of brain tumor from the tumor area.

Keerthana et al [3] has employed the Fuzzy C-Means clustering algorithm to segment the brain stroke region from the input MRI scan image via three different clustering classes. In addition to that, their proposed segmentation work has also calculated the

stroke size on the basis of pixel intensity values.

Kumar et al [4] have implemented a low-cost and efficient strategy to detect skin cancer quickly and accurately. In the proposed method, they have applied image segmentation using fuzzy C-means along with Local Binary Pattern (LBP), GLCM methods, and artificial neural network (ANN). Their results have been highly accurate at identifying skin cancer as compared to other traditional approaches in the domain.

Karthikeyan et al [6] have worked with fuzzy c-means and K-means clustering algorithms to come up with a method that automates the procedure of leukemia detection.

As the traditional testing methods of leukemia are costly and time consuming, the proposed solution using image analysis via Fuzzy C means along with Gabor Texture Extraction, and Support Vector Machine, proves to be quite efficient in comparison.

3. PROJECT IMPLEMENTATION AND EXPERIMENTAL RESULTS

In this section, we shall discuss our implementation of the K-means algorithm and Fuzzy-C-means algorithm using Python and analyze the output received via the respective algorithms. Then, we will be presenting a conclusion of the results of these algorithms.

3.1 IMPLEMENTATION AND RESULTS OF COLOR-BASED K-MEANS ALGORITHM

We have implemented the K-means algorithm using Python, Numpy, Matplotlib and OpenCV. The code has been run on several random input images and we have tested the segmentation on different 'k' values (k=3, 5, 20).

Given below is the code snippet of our K-means implementation:

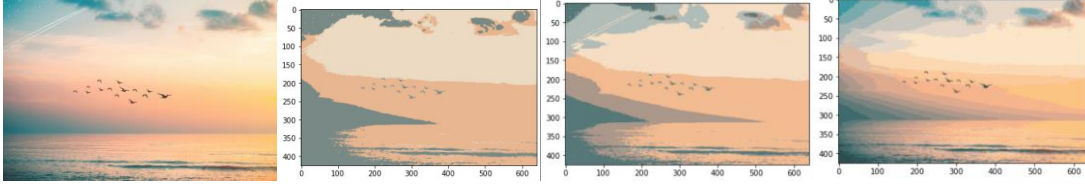
```

2
3 import numpy as np
4 import matplotlib.pyplot as plt
5 import cv2
6
7 # Read in the image
8 image = cv2.imread('images/butterfly.jpg')
9
10 # Change color to RGB (from BGR)
11 image = cv2.cvtColor(image, cv2.COLOR_BGR2RGB)
12
13 plt.imshow(image)
14 # Reshaping the image into a 2D array of pixels and 3 color values (RGB)
15 pixel_vals = image.reshape((-1,3))
16
17 # Convert to float type
18 pixel_vals = np.float32(pixel_vals)
19 #the below line of code defines the criteria for the algorithm to stop running,
20 #which will happen is 100 iterations are run or the epsilon (which is the required accuracy)
21 #becomes 85%
22 criteria = (cv2.TERM_CRITERIA_EPS + cv2.TERM_CRITERIA_MAX_ITER, 100, 0.85)
23
24 # then perform k-means clustering with number of clusters defined as 3
25 #also random centres are initially choosed for k-means clustering
26 k = 6
27 retval, labels, centers = cv2.kmeans(pixel_vals, k, None, criteria, 10, cv2.KMEANS_RANDOM_CENTERS)
28
29 # convert data into 8-bit values
30 centers = np.uint8(centers)
31 segmented_data = centers[labels.flatten()]
32
33 # reshape data into the original image dimensions
34 segmented_image = segmented_data.reshape((image.shape))
35
36 plt.imshow(segmented_image)
37

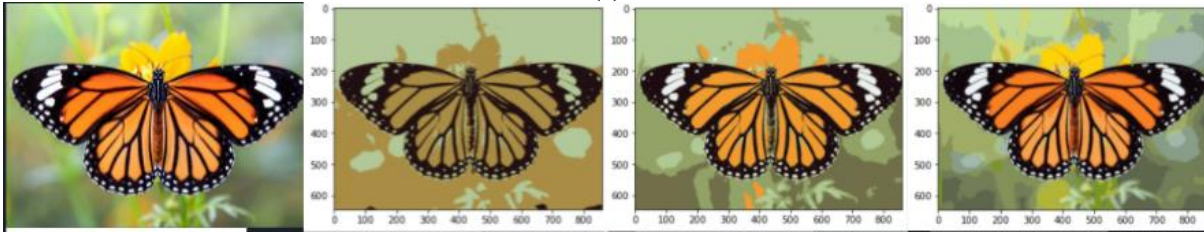
```

Fig. 4. Code snippet of color-based K-means clustering algorithm [13]

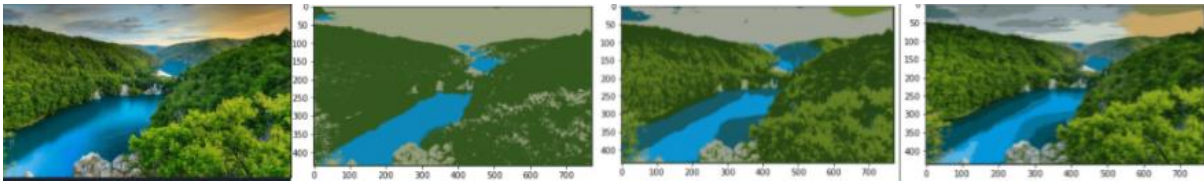
The following are the output results of our implementation of the K-means algorithm for image segmentation:



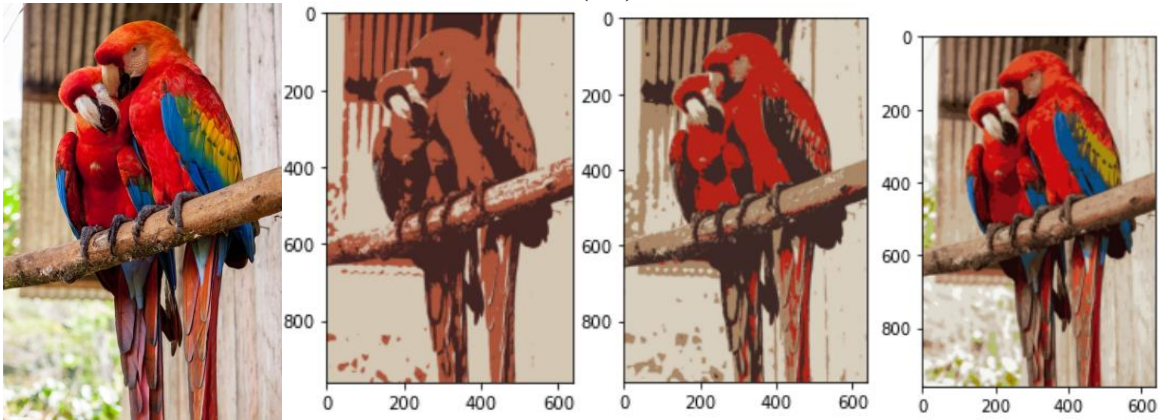
(i)



(ii)



(iii)



(iv)

a. Original images b. $k=3$ c. $k=5$ d. $k=20$

Fig. 5. Comparison of image segmentation using k-means on real images named i) scene, ii) butterfly, iii) mountain, and iv) bird.

The results presented above prove that with an increase in the value of K, the segmented image becomes clearer and more detailed because the K-means algorithm can classify more classes/clusters of colors.

3.2 IMPLEMENTATION AND RESULTS OF FUZZY-C MEANS ALGORITHM

We have implemented the Fuzzy-C means algorithm using Python, Numpy, Matplotlib, and OpenCV. The code has been run on several random input images (same images used for the K-means algorithm and we have tested the segmentation on a different number of clusters ‘c’ (c=3, 5, 20) but the same ‘m’ (fuzziness) value (m=2).

Given below is the code snippet of our Fuzzy-C means implementation:

```

import os
from os import listdir
from os.path import isfile, join
import cv2
import numpy as np
import matplotlib.pyplot as plt
from utils import maskedir

class FCM():
    def __init__(self, image, image_bit, n_clusters, m, epsilon, max_iter):
        """Fuzzy C-means clustering"""

        (image): 2D array, grey scale image.
        (n_clusters): int, number of clusters/segments to create.
        (m): float > 1, fuzziness parameter. A large (m) results in smaller
            membership values and fuzzier clusters. Commonly set to 2.
        (max_iter): int, max number of iterations.
        ...

        #-----Check inputs-----
        if np.ndim(image) != 2:
            raise Exception("image needs to be 2D (gray scale image).")
        if n_clusters <= 0 or n_clusters != int(n_clusters):
            raise Exception("n_clusters needs to be positive integer.")
        if m < 1:
            raise Exception("m needs to be >= 1.")
        if epsilon <= 0:
            raise Exception("eps(om) needs to be > 0")
        self.image = image
        self.image_bit = image_bit
        self.n_clusters = n_clusters
        self.m = m
        self.epsilon = epsilon
        self.max_iter = max_iter

        self.shape = image.shape # image shape

        self.X = image.flatten().astype('float') # flattened image shape: (number of pixels,1)
        self.numPixels = image.size

        #-----
        def initial_U(self):
            """Compute initial U"""
            U = zeros((self.numPixels, self.n_clusters))
            idx = np.arange(self.numPixels)
            for li in range(self.n_clusters):
                idell = idx[self.n_clusters-1-li]
                U[idell,li] = 1
            return U

        def update_U(self):
            """Compute weights"""
            c_mesh, idx_mesh = np.meshgrid(self.C, self.X)
            power = 2. / (self.m - 1)
            p1 = abs(idx_mesh - c_mesh)**power
            p2 = np.sum([1./abs(idx_mesh - c_mesh)**power, axis=1])
            return 1. / (p1**power)

        def update_C(self):
            """Compute centroid of clusters"""
            numerator = np.dot(self.X, self.U**self.m)
            denominator = np.sum(self.U**self.m, axis=0)
            return numerator/denominator

        def form_clusters(self):
            """Iterative training"""
            d = 100
            self.U = self.initial_U()
            for self.max_iter in range(1, d):
                i = 0
                while True:
                    self.C = self.update_C()
                    old_u = np.copy(self.U)

```

a.

```

old_u = np.copy(self.U)
self.U = self.update_U()
d = np.sum(abs(self.U - old_u))
print("Iteration %d : cost = %f" %(i, d))

if d < self.epsilon or i > self.max_iter:
    break
i+=1
else:
    i = 0
    while d > self.epsilon:
        self.C = self.update_C()
        old_u = np.copy(self.U)
        self.U = self.update_U()
        d = np.sum(abs(self.U - old_u))
        print("Iteration %d : cost = %f" %(i, d))

        if d < self.epsilon or i > self.max_iter:
            break
        i+=1
    self.segmentImage()

def deFuzzify(self):
    return np.argmax(self.U, axis = 1)

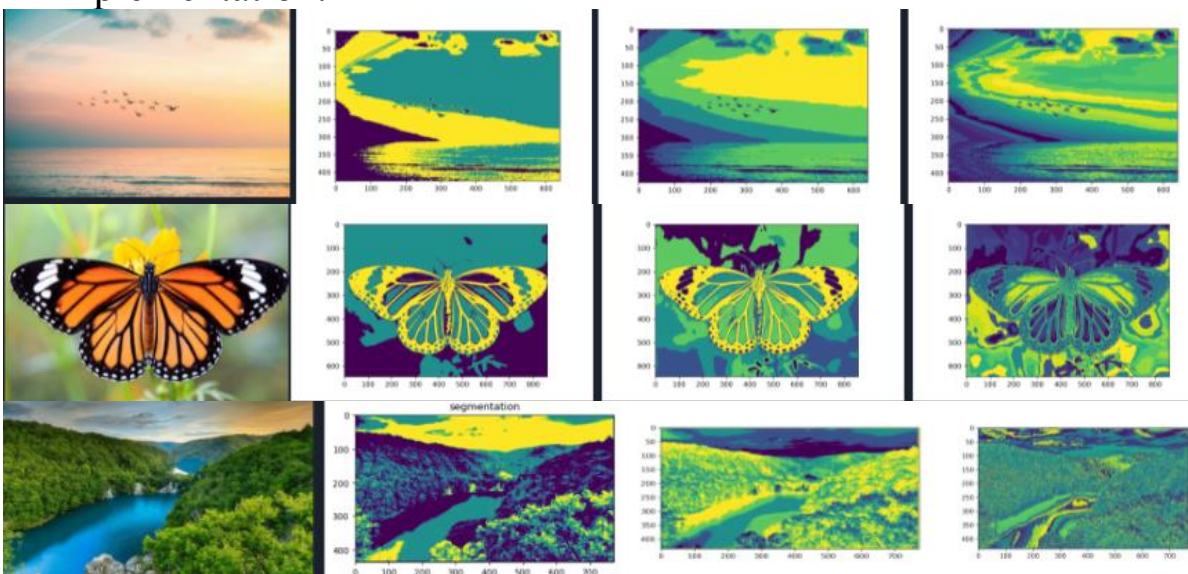
def segmentImage(self):
    '''Segment image based on max weights'''
    result = self.deFuzzify()
    self.result = result.reshape(self.shape).astype('int')
    return self.result

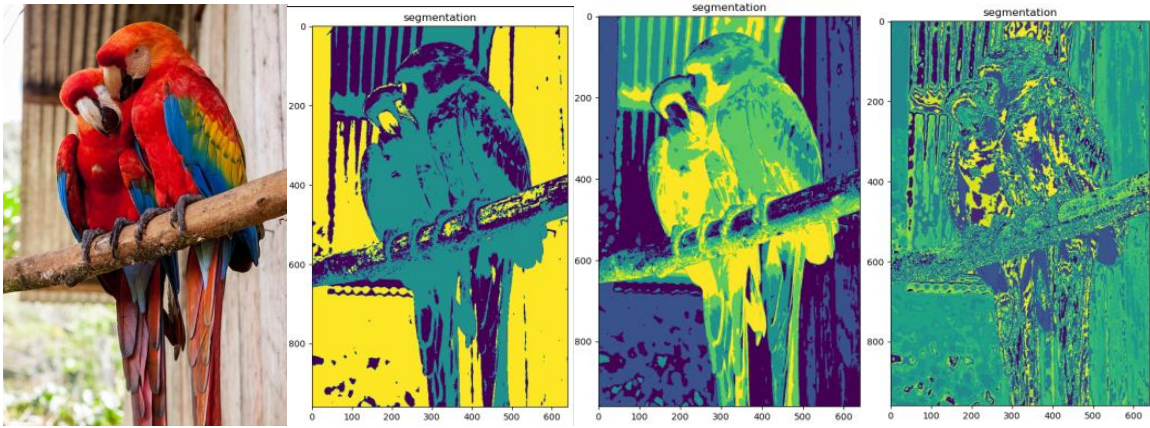
```

b.

Fig. 6. Code snippets of Fuzzy-C means algorithm

The following are the output results of Fuzzy-C means implementation:





a. Original images b. $c=3, m=2$ c. $c=5, m=2$ d. $c=20, m=2$

Fig. 7. Comparison of image segmentation using fuzzy-c means on real images named i) scene, ii) butterfly, iii) mountain, and iv) bird.

Again, we see with increasing cluster numbers we obtain a more detailed and better-segmented result. Also, the results are crisper or more detailed as compared to k means.

3.3 IMPLEMENTATION OF K-MEANS MEANS ALGORITHM ON MAMMOGRAPHY IMAGES

In this section, we have implemented a modified form of the color-based k-means code that works for black and white images as well. Then, we run the code on certain mammogram images[14]. Given below is the snippet of the code used:

```

7
8 import numpy as np
9 import cv2
10 import matplotlib.pyplot as plt
11 image=cv2.imread('images/mdb005.jpg')
12 image = cv2.cvtColor(image, cv2.COLOR_BGR2RGB)
13
14 def clust_gray(image,k=5,itters=3): # expects img in grayscale
15 image=cv2.cvtColor(image,cv2.COLOR_BGR2GRAY)
16 img=image.copy()
17 h,w=img.shape
18 orig=image.copy()
19 Klusters=np.random.randint(0,255,size=k)
20 print('init clusters', Klusters)
21 for it in range(itters):
22 img=image.copy()
23 for i in range(h):
24     for j in range(w):
25         pnt=img[i][j]
26         diff=np.abs(Klusters-pnt)
27         c=np.argmin(diff)
28         img[i][j]=Klusters[c]
29
30 loss=0
31 l=[]
32 for i in range(k):
33     Ys,Xs=np.where(img==Klusters[i])
34     kth_points=orig[Ys,Xs]
35     l.append(np.sum(Klusters[i]-kth_points))
36     Klusters[i]=np.mean(kth_points)
37 loss=sum(l)
38 print('Cluster centroids at iteration-{}'.format(it+1), Klusters)
39 print('loss at iteration-{}'.format(it+1),loss)
40 return img

```

Fig 8: Code Snippet of K-means algo for black and white images

Given below are the results we get after running the above code on some sample mammography images [14]:

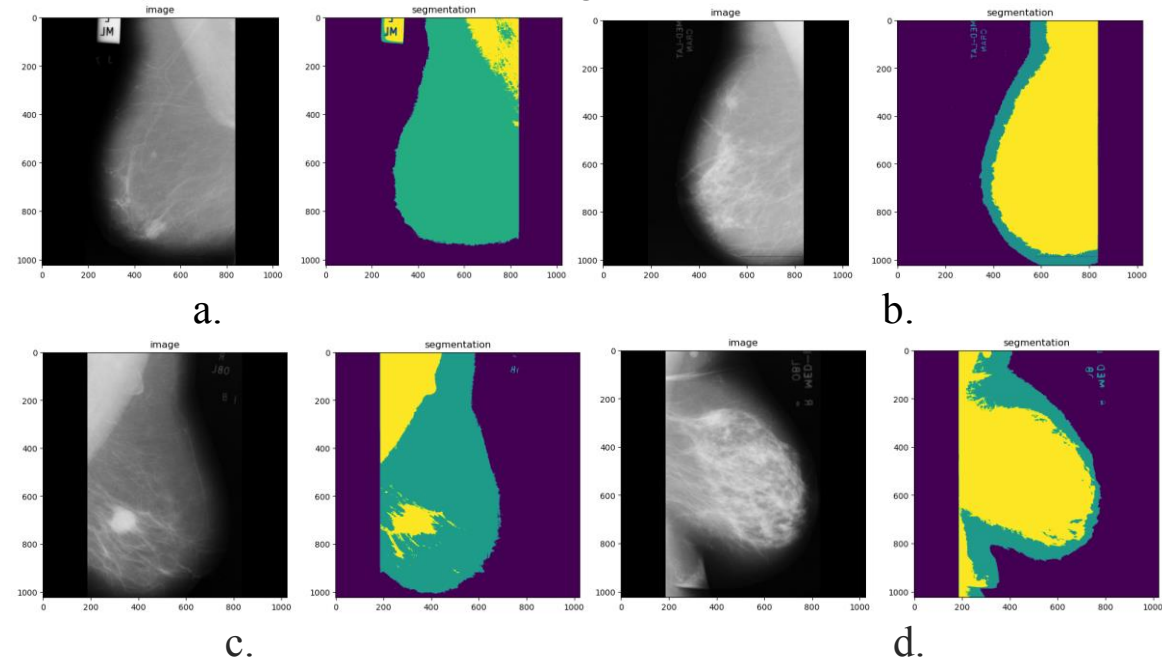


Fig 9. Image Segmented Results on Mammogram images when $k=3$ a. Benign Tumor b. Malignant c. Malignant d. Benign [14]

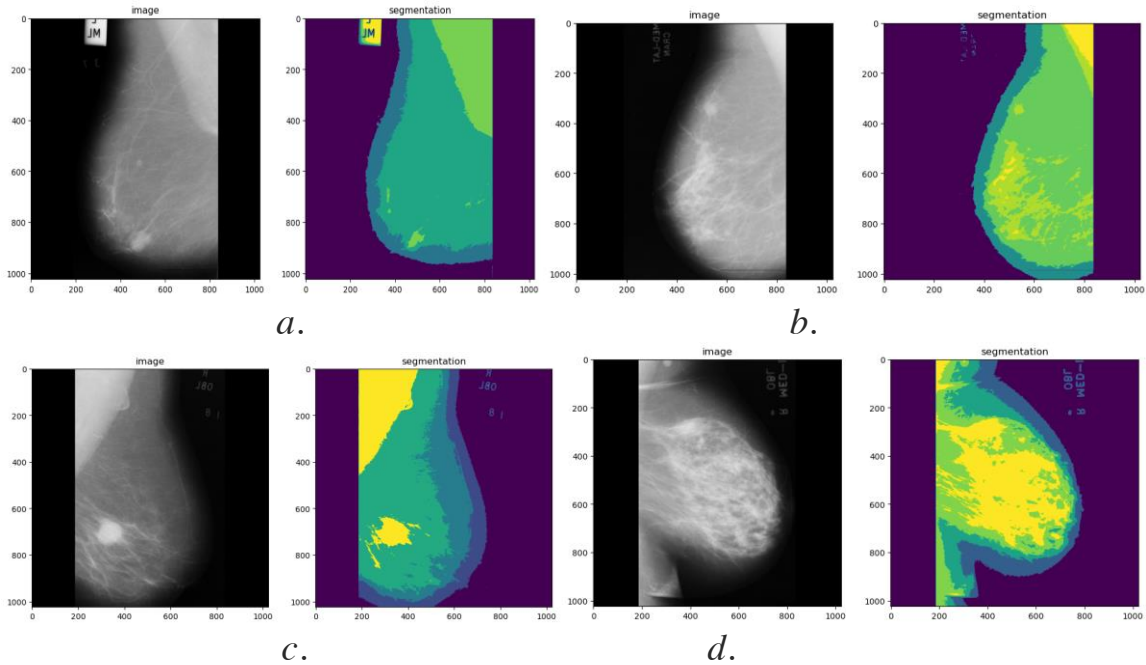
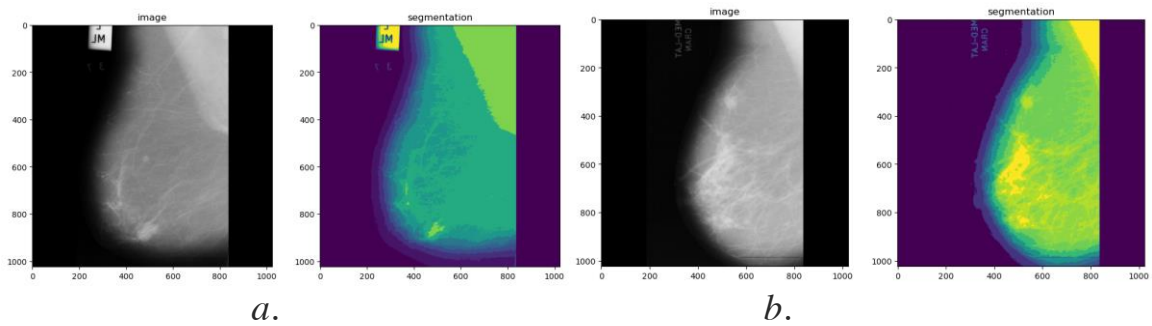


Fig 10. Image Segmented Results on Mammogram images when $k=5$ a. Benign Tumor b. Malignant c. Malignant d. Benign [14]



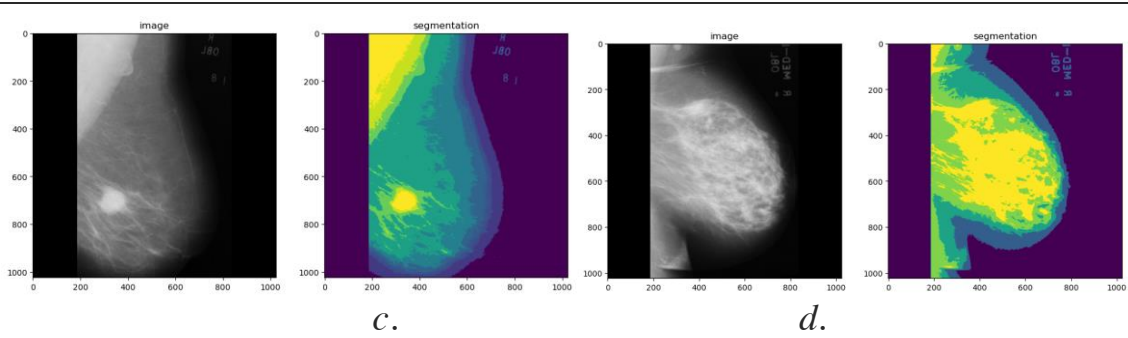


Fig 11. Image Segmented Results on Mammogram images when $k=10$
a. Benign Tumor b. Malignant c. Malignant d. Benign [14]

3.4 IMPLEMENTATION OF FUZZY-C MEANS ALGORITHM ON MAMMOGRAPHY IMAGES

Next, we have run the above Fuzzy-C means code on several mammogram images and presented the results below:

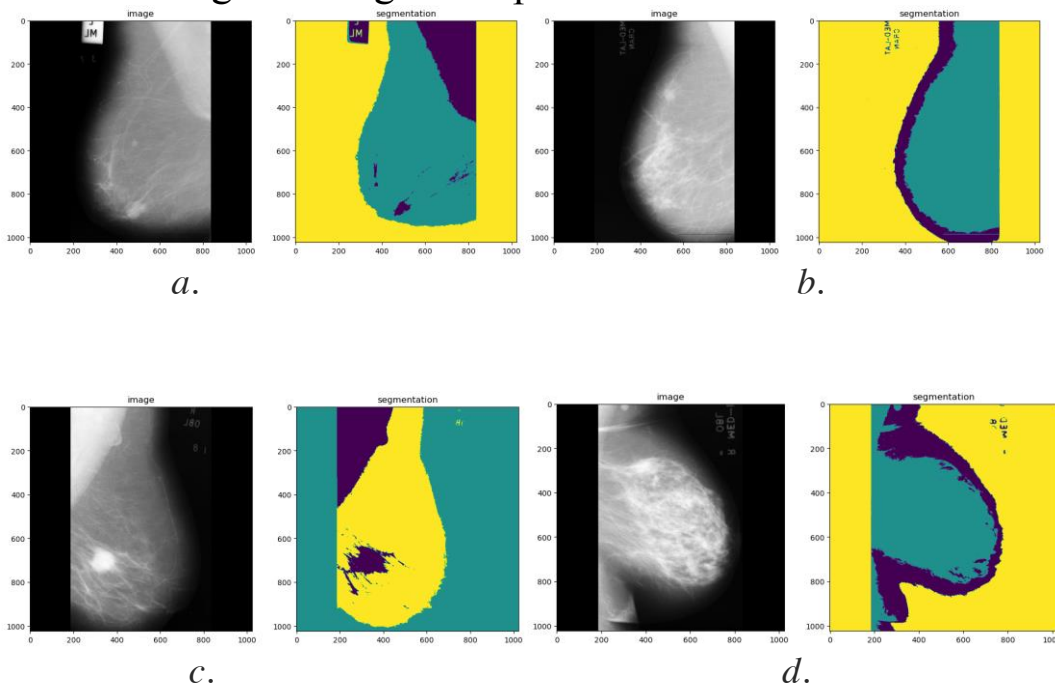
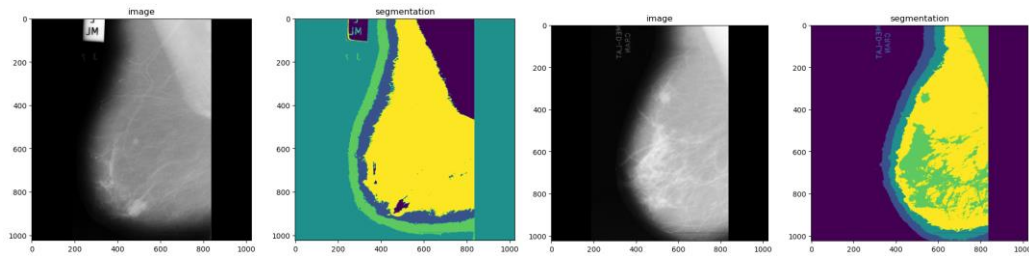
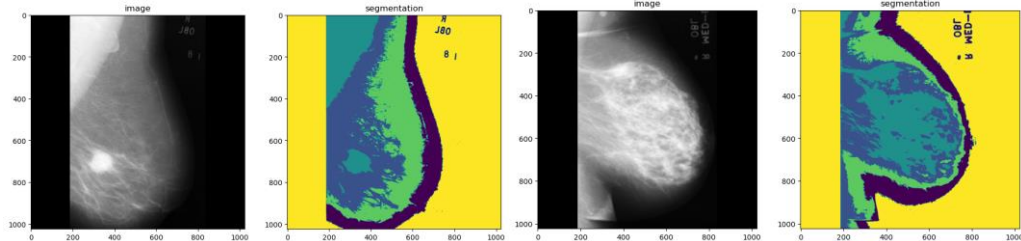


Fig 12. Image Segmented Results on Mammogram images when $c=3, m=2$
a. Benign Tumor b. Malignant c. Malignant d. Benign [14]



a.

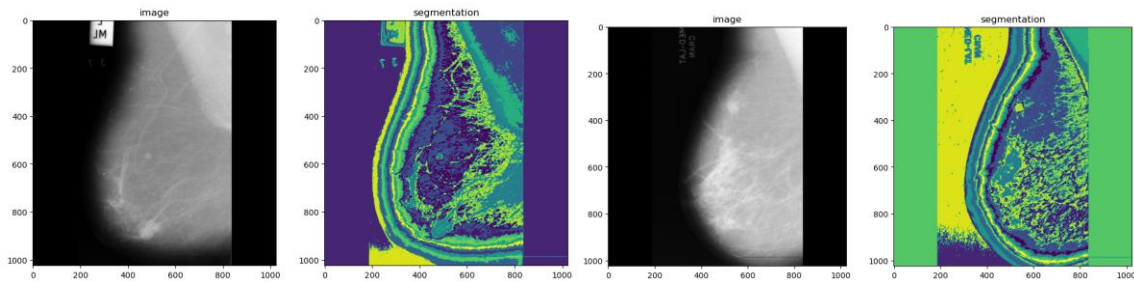
b.



c.

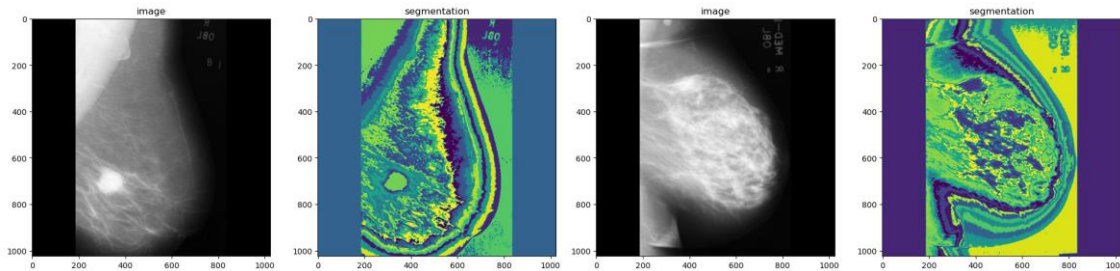
d.

Fig 13. Image Segmented Results on Mammogram images when $c=5$, $m=2$ a. Benign Tumor b. Malignant c. Malignant d. Benign [14]



a.

b.



c.

d.

Fig 14. Image Segmented Results on Mammogram images when $c=20$, $m=2$ a. Benign Tumor b. Malignant c. Malignant d. Benign [14]

From the images above, we can conclude that the results become clearer and far more detailed as we increase the value of 'c'.

4. Canny Edge Detection

Edge detection is a part of image segmentation. The effectiveness of many image processing and also computer vision tasks depends on the perfection of detecting meaningful edges. It is one of the techniques for detecting intensity discontinuities in a digital image.

Edge detection is a difficult task in noisy images, since both the edges and noise hold high-frequency content. Efforts to reduce the noise result in unclear and distorted edges.

Techniques used on noisy images are typically larger in scope; therefore they can share enough data to discount localized noisy pixels. This results in less perfect localization of the detected edges.

In image processing, especially in computer vision, edge detection treats the localization of important variations of a gray level image and the detection of the physical and geometrical properties of objects of the scene. It is a fundamental process that detects and outlines an object and boundaries among objects and the background in the image.

There are many edge detection techniques in the literature for image segmentation. The most commonly used discontinuity-based edge detection techniques are Roberts edge detection, Sobel Edge Detection, Prewitt edge detection, Kirsh edge detection, Robinson edge detection, Marr-Hildreth edge detection, LoG edge detection and Canny Edge Detection. In this paper we have studied about Canny Edge Detection.

Canny edge detection is a technique to extract useful structural information from different vision objects and dramatically reduce the amount of data to be processed. It was developed by John F. Canny in 1986. Canny also produced a computational theory of edge detection explaining why the technique works.

The general criteria for edge detection include:

1. Detection of edge with low error rate, which means that the detection should accurately catch as many edges shown in the image as possible
2. The edge point detected from the operator should accurately localize on the center of the edge.
3. A given edge in the image should only be marked once, and where possible, image noise should not create false edges.

To satisfy these requirements Canny used the calculus of variations – a technique which finds the function which optimizes a given functional. The optimal function in Canny's detector is described by the sum of four exponential terms, but it can be approximated by the first derivative of a Gaussian.

Among the edge detection methods developed so far, Canny edge detection algorithm is one of the most strictly defined methods that provides good and reliable detection. Because of its optimality to meet with the three criteria for edge detection and the simplicity of process for implementation, it became one of the most popular algorithms for edge detection.

The process of Canny edge detection algorithm can be broken down to five different steps:

1. Apply Gaussian filter to smooth the image in order to remove the noise
2. Find the intensity gradients of the image
3. Apply gradient magnitude thresholding or lower bound cut-off suppression to get rid of spurious response to edge detection
4. Apply double threshold to determine potential edges
5. Track edge by hysteresis: Finalize the detection of edges by suppressing all the other edges that are weak and not connected to strong edges.

Gaussian filter

Since all edge detection results are easily affected by the noise in the image, it is essential to filter out the noise to prevent false detection caused by it. To smooth the image, a Gaussian filter kernel is convolved with the image. This step will slightly smooth the image to reduce the effects of obvious noise on the edge detector. The equation for a Gaussian filter kernel of size $(2k+1) \times (2k+1)$ is given by:

$$H_{ij} = \frac{1}{2\pi\sigma^2} \exp\left(-\frac{(i - (k + 1))^2 + (j - (k + 1))^2}{2\sigma^2}\right); 1 \leq i, j \leq (2k + 1)$$

Fig. 15. Equation for a Gaussian filter kernel of size $(2k+1) \times (2k+1)$

Gradient calculation

When the image is smoothed, the derivatives I_x and I_y are calculated w.r.t x and y axis. It can be implemented by using the

Sobel-Feldman kernels convolution with image and after applying these kernel we can use the gradient magnitudes and the angle to further process this step. The magnitude and angle can be calculated as:

$$|G| = \sqrt{I_x^2 + I_y^2},$$
$$\theta(x, y) = \arctan\left(\frac{I_y}{I_x}\right)$$

Fig. 16. Gradient magnitude and angle

Non-Maximum Suppression

In order to reduce the duplicate merging pixels along the edges and to make them uneven, this step is used. For each pixel find two neighbors in the positive and negative gradient directions, supposing that each neighbor occupies the angle of $\pi/4$, and 0 is the direction straight to the right. If the magnitude of the current pixel is greater than the magnitude of the neighbors, nothing changes, otherwise, the magnitude of the current pixel is set to zero.

Double Thresholding

Even after Non-maximum suppression, some edge pixels remain that are caused by noise and color variation. To account for these responses, it is essential to filter out edge pixels with a weak gradient value and preserve edge pixels with a high gradient value. The gradient magnitudes are compared with two specified threshold values, the first one is lower than the second.

The gradients that are smaller than the low threshold value are suppressed, the gradients higher than the high threshold value are marked as strong ones and the corresponding pixels are included in the final edge map. All the rest gradients are marked as weak ones and pixels corresponding to these gradients are considered in the next step.

Edge Tracking using Hysteresis

To achieve an accurate result, the weak edges should be removed. Usually, a weak edge pixel caused by true edges will be connected to a strong edge pixel while noise responses are unconnected.

To track the edge connection, blob analysis is applied by looking at a weak edge pixel and its 8-connected neighborhood pixels. Since a weak edge pixel caused by true edges will be connected to a strong edge pixel, pixel W with weak gradient is marked as edge and included in the final edge map if and only if it is involved in the same connected component as some pixel S with strong gradient.

4.1 Implementation of Canny Edge Detector in Python

We have implemented Canny Edge Detector using Python, Numpy, Matplotlib, and OpenCV.

The code has been run on several random input images and below is the code snippet of Canny Edge Detection algorithm:-

```

1 import numpy as np
2 import os
3 import cv2
4 import matplotlib.pyplot as plt
5
6
7 # defining the canny detector function
8
9 # here weak_th and strong_th are thresholds for
10 # double thresholding step
11 def Canny_detector(img, weak_th = None, strong_th = None):
12
13     # conversion of image to grayscale
14     img = cv2.cvtColor(img, cv2.COLOR_BGR2GRAY)
15
16     # noise reduction step
17     img = cv2.GaussianBlur(img, (5, 5), 1.4)
18
19     # Calculating the gradients
20     gx = cv2.Sobel(img, cv2.CV_64F, 1, 0, 1)
21     gy = cv2.Sobel(img, cv2.CV_64F, 0, 1, 1)
22
23     # Conversion of Cartesian coordinates to polar
24     mag, ang = cv2.cartToPolar(gx, gy, angleInDegrees = True)
25
26     # setting the minimum and maximum thresholds
27     # for double thresholding
28     mag_max = np.max(mag)
29     if not weak_th: weak_th = mag_max * 0.1
30     if not strong_th: strong_th = mag_max * 0.5
31
32     # getting the dimensions of the input image
33     height, width = img.shape
34
35     # Looping through every pixel of the grayscale
36     # image
37     for i_x in range(width):
38         for i_y in range(height):
39
40             grad_ang = ang[i_y, i_x]
41             grad_ang = abs(grad_ang-100) if abs(grad_ang)>100 else abs(grad_ang)
42
43             # selecting the neighbours of the target pixel
44             # according to the gradient direction
45             # in the x axis direction
46
47             if grad_ang<= 22.5:
48                 neighb_1_x, neighb_1_y = i_x-1, i_y
49                 neighb_2_x, neighb_2_y = i_x+1, i_y
50
51             # Top right (diagonal-1) direction
52             elif grad_ang>22.5 and grad_ang<=(22.5 + 45):
53                 neighb_1_x, neighb_1_y = i_x-1, i_y-1
54                 neighb_2_x, neighb_2_y = i_x+1, i_y+1
55
56             # In y-axis direction
57             elif grad_ang>22.5 + 45 and grad_ang<=(22.5 + 90):
58                 neighb_1_x, neighb_1_y = i_x, i_y-1
59                 neighb_2_x, neighb_2_y = i_x, i_y+1
60
61             # Top left (diagonal-2) direction
62             elif grad_ang>22.5 + 90 and grad_ang<=(22.5 + 135):
63                 neighb_1_x, neighb_1_y = i_x-1, i_y+1
64                 neighb_2_x, neighb_2_y = i_x+1, i_y-1
65
66             # Now it restarts the cycle
67             elif grad_ang>22.5 + 135 and grad_ang<=(22.5 + 180):
68                 neighb_1_x, neighb_1_y = i_x+1, i_y
69                 neighb_2_x, neighb_2_y = i_x-1, i_y
70
71             # Non-maximum suppression step
72             if width>neighb_1_x+1 and height>neighb_1_y+1:
73                 if mag[i_y, i_x]<max(mag[neighb_1_y, neighb_1_x],
74                                     mag[i_y, i_x+1]):
75                     continue
76
77             if width>neighb_2_x+1 and height>neighb_2_y+1:
78                 if mag[i_y, i_x]<max(mag[neighb_2_y, neighb_2_x],
79                                     mag[i_y, i_x-1]):
80                     continue
81
82             weak_ids = np.zeros_like(img)
83             strong_ids = np.zeros_like(img)
84             ids = np.zeros_like(img)
85
86             # double thresholding step
87             for i_x in range(width):
88                 for i_y in range(height):
89                     grad_mag = mag[i_y, i_x]
90
91                     if grad_mag<weak_th:
92                         mag[i_y, i_x]= 0
93                     elif strong_th>grad_mag>= weak_th:
94                         ids[i_y, i_x]= 1
95                     else:
96                         ids[i_y, i_x]= 2
97
98             # finally returning the magnitude of
99             # gradients of edges
100             return mag
101
102 frame = cv2.imread('img5.jpg')
103
104 # calling the designed function for
105 # finding edges
106 canny_img = Canny_detector(frame)
107
108 # Displaying the input and output image
109 plt.figure()
110 f, plots = plt.subplots(2, 1)
111 plots[0].imshow(frame)
112 plots[1].imshow(canny_img)

```

a.

```

88         grad_mag = mag[i_y, i_x]
89
90         if grad_mag<weak_th:
91             mag[i_y, i_x]= 0
92         elif strong_th>grad_mag>= weak_th:
93             ids[i_y, i_x]= 1
94         else:
95             ids[i_y, i_x]= 2
96
97
98         # finally returning the magnitude of
99         # gradients of edges
100         return mag
101
102 frame = cv2.imread('img5.jpg')
103
104 # calling the designed function for
105 # finding edges
106 canny_img = Canny_detector(frame)
107
108 # Displaying the input and output image
109 plt.figure()
110 f, plots = plt.subplots(2, 1)
111 plots[0].imshow(frame)
112 plots[1].imshow(canny_img)

```

b.

Fig. 17. Code snippets of Canny Edge Detection Algorithm

The following are the output results of Canny Edge Detection algorithm implementation:-

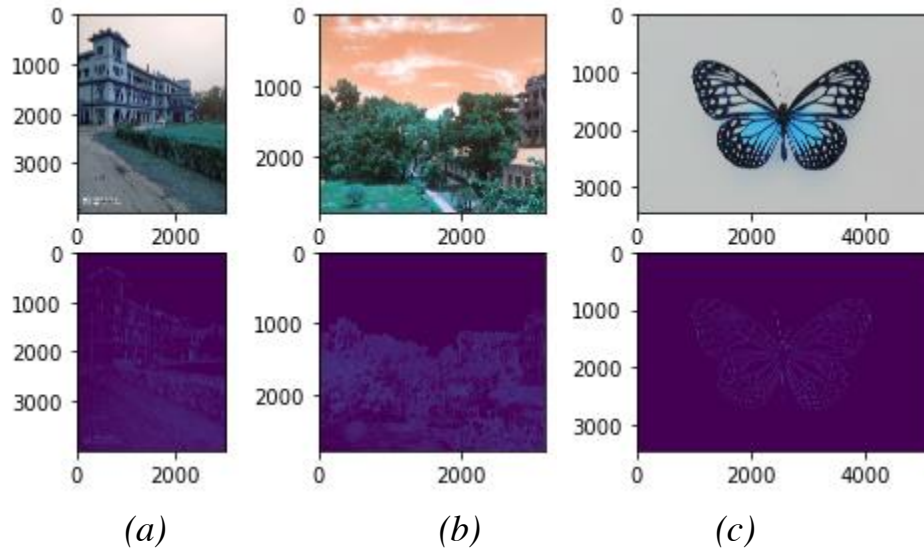


Fig 18. Comparison of Canny Edge Detection on Real Images named (a) scene (b) sunset (c) butterfly

5. CONCLUSION

In this project, we have studied image segmentation, clustering algorithms, and implemented K-means and Fuzzy-C means algorithms. We have run the algorithms on several real-world images and presented the segmented image results for various conditions. The results have shown us that with increasing the value of 'k' (number of clusters), we get better image segmentation.

We have found that the Fuzzy-C means algorithm gives more detailed and better results as compared to K-means. In the case of Fuzzy-C means, a higher value of 'c', i.e. clusters, gives us more details in the segmented images. But, increasing the value of 'm' makes the segmented image quite distorted.

6. FUTURE SCOPE

In the near future, we would like to calculate the image segmentation time of both K-Means and Fuzzy-C means algorithms to provide a better comparison between the two. We want to test the algorithms on brain tumor MRI images as well and present a comparative study of the same and try to provide a modified and optimized code for better performance.

7. REFERENCES

1. <https://jp.mathworks.com/help/fuzzy/fuzzy-c-means-clustering-for-iris-data.html>
2. Soheli AHmed, Snigdha Dey and Kandarpa Kumar Sarma. Image texture classification using artificial neural network(ANN), 2011: sci-hub.do/10.1109/NCETACS.2011.5751383
3. Keerthana, S. and K. Sathiyakumari. "Brain Stroke Segmentation using Fuzzy C-Means Clustering." International Journal of Computer Applications 154 (2016): 26-30.
4. Kumar, M., Alshehri, M., AlGhamdi, R. et al. A DE-ANN Inspired Skin Cancer Detection Approach Using Fuzzy C-Means Clustering. Mobile Netw Appl 25, 1319–1329 (2020). <https://doi.org/10.1007/s11036-020-01550-2>
5. Pingale, Divyata & Todmal, S.. (2018). Brain Tumor Segmentation Using K-Means and Fuzzy C-Means Clustering and Its Area Calculation and Stage Using SVM Algorithm. Journal of Advances and Scholarly Researches in Allied Education. 15. 27-32. 10.29070/15/56750.
6. Karthikeyan, T., and Narayana Poornima. "Microscopic image segmentation using fuzzy c means for leukemia diagnosis." Leukemia 4.1 (2017): 3136-3142.
7. Dhanachandra, Nameirakpam, Khumanthem Manglem, and Yambem Jina Chanu. "Image segmentation using K-means clustering algorithm and subtractive clustering algorithm."

Procedia Computer Science 54 (2015): 764-771.

8. N. Manahoran, M.V. Srinath. "K-Means Clustering Based Marine Image Segmentation" International Journal of MC Square Scientific Research Vol.9, No.3, 2017
9. M. C. J. Christ and R. M. S. Parvathi, "Fuzzy c-means algorithm for medical image segmentation," 2011 3rd International Conference on Electronics Computer Technology, 2011, pp. 33-36, doi: 10.1109/ICECTECH.2011.5941851.
10. Jinlin Chen et al 2018 J. Phys.: Conf. Ser. 1004 012035
11. J. Song and Z. Zhang "A Modified Robust FCM Model with Spatial Constraints for Brain MR Image Segmentation." Information 2019.
12. https://github.com/jeongHwarr/various_FCM_segmentation
13. <https://www.geeksforgeeks.org/image-segmentation-using-k-means-clustering/>
14. mini-MIAS database of mammograms:
<http://peipa.essex.ac.uk/info/mias.html>

DATA LEAKAGE DETECTION SYSTEM

A PROJECT REPORT

Submitted by

KOYENA MITRA
MAHASWATA KUNDU
PRITAM DOLUI
PRITAM JANA

Supervised by

Prof. Atanu Kumar Pal

in partial fulfillment for the award of the degree of

BACHELOR OF TECHNOLOGY

IN

INFORMATION TECHNOLOGY

Year: May, 2022



**GOVERNMENT COLLEGE OF ENGINEERING AND CERAMIC
TECHNOLOGY**

73, Avinash Chandra Banerjee Ln, SubhasSaroar Park, PhoolBagan, Belegkata, Kolkata,
West Bengal 700010

BONAFIDE CERTIFICATE

Certified that this project report "DATA LEAKAGE DETECTION SYSTEM"
is the bonafide work of "MAHASWATA KUNDU, PRITAM DOLUI ,
PRITAM JANA, KOYENA MITRA" who carried out the project work under
my supervision.

SIGNATURE

M. Maitra . 23.5.22.

Mousumi Maitra

HEAD OF THE DEPARTMENT

INFORMATION TECHNOLOGY

73, Avinash Chandra Banerjee Ln,
SubhasSaroobar Park, PhoolBagan,
Beleghata,Kolkata,

West Bengal 700010

SIGNATURE

AKP 23/05/22

Atanu Kumar Pal

SUPERVISOR

INFORMATIONTECHNOLOGY

73, Avinash Chandra Banerjee Ln,
SubhasSaroobar Park, PhoolBagan,
Beleghata,Kolkata,

West Bengal 700010

SIGNATURE

[Signature]

External Examiner

DECLARATION

We hereby declare that this project work entitled “ **DATA LEAKAGE DETECTION SYSTEM** ” under the guidance of **Prof. Atanu Kumar Pal** submitted for the B.tech Degree in our original work.

We also declare that this project is the outcome of our own effort, that has not been submitted to any other university for the award of any degree.

Name and roll of the students :

1. KOYENA MITRA (GCECTB-L19-2004)
2. MAHASWATA KUNDU (GCECTB-L19-2005)
3. PRITAM DOLUI (GCECTB-L19-2006)
4. PRITAM JANA (GCECTB-L19-2007)

Signature :

Koyena Mitra .
.....
Mahaswata Kundu.
.....
Pritam Dolui.....
.....
Pritam Jana.....
.....

PLACE: KOLKATA

DATE: 23.05.2022

ACKNOWLEDGEMENT

We would like to express our sincere gratitude to several individuals and organizations for supporting us.

Firstly, we wish to express our sincere gratitude to our supervisor, **Prof. Atanu Kumar Pal**, for his enthusiasm, patience, insightful comments, helpful information, practical advice, and unceasing ideas that have helped us tremendously at all times in our project on **“DATA LEAKAGE DETECTION”** and writing of this project report.

His immense knowledge, profound experience, and professional expertise in the field of Data Leakage detection had enabled us to perform this project successfully. Without her support and guidance, this project would not have been possible. We could not have imagined having a better supervisor in our study.

Secondly, we wish to express sincere thanks to our Head of The Department, **Dr. Mousumi Maitra**, for giving us such an excellent opportunity.

Last but not least we would like to thank the entire **“GOVERNMENT COLLEGE OF ENGINEERING AND CERAMIC TECHNOLOGY”** and **INFORMATION TECHNOLOGY DEPARTMENT** for allowing us to proceed with the project. Thanks for all the encouragement.

KOYENAMITRA (GCECTB-L19-2004)

MAHASWATAKUNDU (GCECTB-L19-2005)

PRITAMDOLUI (GCECTB-L19-2006)

PRITAM JANA (GCECTB-L19-2007)

ABSTRACT

- A data distributor has given sensitive data to a set of supposedly trusted agents.
- Sometimes data is leaked and found in unauthorized place e.g., on the web or on somebody's laptop.
- Data leakage happens every day when confidential business information are leaked out.
- When these are leaked out it leaves the company unprotected and goes outside the jurisdiction of the corporation.

TABLE OF CONTENTS

CHAPTER NO.	TITLE	PAGE NO.
	ABSTRACT	iii
	TABLE OF CONTENTS	iv-v
	LIST OF FIGURES	vi
1.	INTRODUCTION	1-3
	1.1 WHAT IS DATA LEAKAGE	2
	1.2 HOW DOES DATA LEAKAGE TAKE PLACE	2-3
2.	OBJECTIVES	4-5
	2.1 OBJECTIVES OF DATA LEAKAGE	4
	2.2 DATA LEAKAGE INCIDENTS	5
	2.3 OUR GOALS	5
3.	EXISTING SYSTEM LIMITATIONS	6-8
	3.1 INTRODUCTION	6
	3.2 DATA LEAKAGE DETECTION STEPS	6-7
	3.2.1 WATERMARKING	6
	3.2.2 STEGANOGRAPHY	7
	3.3 PROCEDURE & LIMITATIONS	8

	3.3.1 PROCEDURE OF WATERMARKING	8
	3.3.2 LIMITATIONS OF WATERMARKING	8
4.	PROPOSED SYATEM	9
5.	TYPES OF EMPLOYEES THAT MAY LEAK DATA	10
6.	IMPACT OF ORGANIZATIONS	11
7.	IMPLEMENTATION	12-13
8.	MODULES	14
	8.1 ADMIN MODULE	14
	8.2 USER MODULE	14
9.	APPLICATIONS OF DATA LEAKAGE DETECTION	15
10.	DATA LOSS PREVENTION	16
11.	CLOUD DATA LOSS PREVENTION	24-28
12.	ER DIAGRAM	29-36
13.	DASHBOARD AND OUTPUT	32-39
14.	DESCRIPTION OF DATABASE	40-42
15.	TECHNOLOGY USED	43
16.	FUTURE WORK	44
17.	CONCLUSION	45
18.	REFERENCES	46

LIST OF FIGURES

Fig no	Title	Page no
1	How data leakage take place	3
2	Data leakage incidents	5
3	Example of watermarking	6
4	Steganography	7
5	Procedure of watermarking	8
6	Proposed system	9
7	Types of employees	10
8	Impact of organization	11
9	Implementation	13
10	Admin & User module	14
11	Application of data leakage	15
12	Data loss prevention	16
13	Protection of User Data	21
14	Classification of DLP	22
15	Application of DLP	23
16	Cloud DLP	24
17	Architecture of Cloud DLP	26
18	Dashboard (New Item)	29
19	Dashboard (New Request Passcode)	29
20	My item Add	33

21	My item	33
22	Passcode Request	34
23	Passcode Request Rejected	34
24	Requested Item	35
25	Item uploaded	35
26	Passcode	36
27	Item Passcode	36
28	Request Send	37
29	Item Download	37
30	Passcode Request Rejected	38
31	Passcode	38
32	Password Accepted Successfully	39
33	Logout	39
34	Authorized Table	40
35	User Table	40
36	Profile Picture Table	41
37	Item Table	41
38	Passcode Request Table	42
39	Data Leakage Table	42

1. INTRODUCTION

- Data leakage is defined as the accidental or unintentional distribution of private or sensitive data to an unauthorized entity. Data leakage can be defined as an event in which classified information, e.g. sensitive, protected or confidential data has been viewed, stolen or used by somebody who is not authorized to do so.
- Data leakage poses a serious issue for companies as the number of incidents and the cost to those experiencing them continue to increase.
- Data leakage is enhanced by the fact that transmitted data including emails, instant messaging, website forms, and file transfers among others, are largely unregulated and unmonitored on their way to their destinations.

1.1 WHAT IS DATA LEAKAGE

- Data leakage is the unauthorized transmission of sensitive data or information within an organization to an external destination or recipient.
- Sensitive data of companies and organization includes
 - intellectual property,
 - financial information ,
 - patient information, personal credit card data ,
 - and other information depending upon the business and the industry.

1.2 HOW DOES DATA LEAKAGE TAKE PLACE?

- In the course of doing business, sometimes data must be handed over to trusted third parties for some enhancement or operations.
- Sometimes these trusted third parties may act as points of data leakage.
- Examples:
 - A hospital may give patient records to researcher who will devise new treatments.
 - A company may have partnership with other companies that require sharing of customer data.
 - An enterprise may outsource its data processing , so data must be given to various other companies.

- ❑ Owner of data is termed as the distributor and the third parties are called as the agents .
- ❑ In case of data leakage, the distributor must assess or judge the likelihood that the leaked data came from one or more agents, as opposed to having been independently gathered by other means.

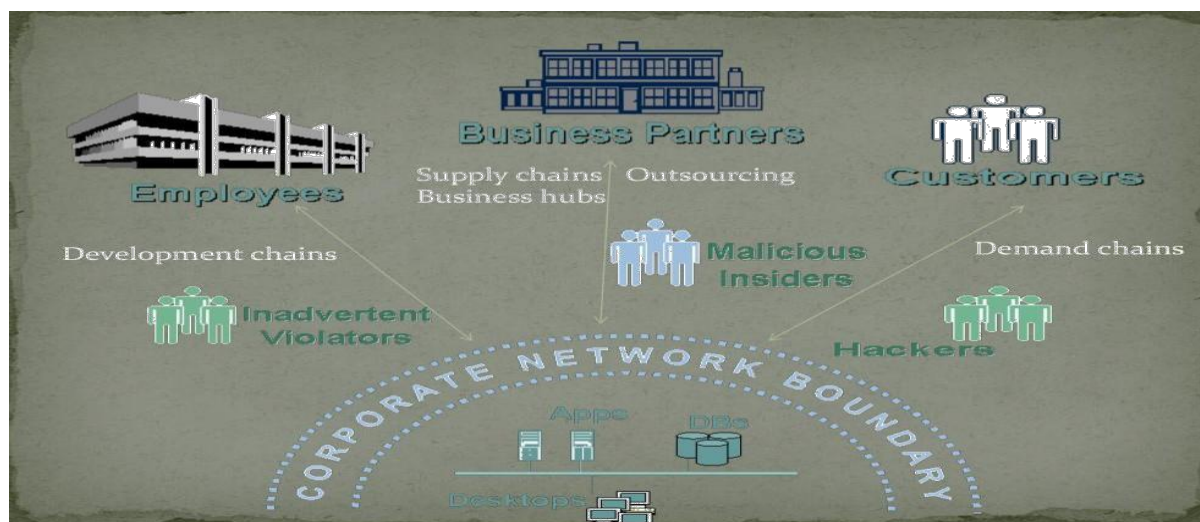


Fig 1: HOW DATA LEAKAGE TAKE PLACE

2. OBJECTIVES

2.1 DATA LEAKAGE OBJECTIVES

- A data distributor has given sensitive data to a set of supposedly trusted agents (third parties).
- Some of the data is leaked and found in an unauthorized place (e.g., on the web or somebody's laptop).
- The distributor must assess the likelihood that the leaked data came from one or more agents, as opposed to having been independently gathered by other means.
- Some propose data allocation strategies (across the agents) that improve the probability of identifying leakages.
- These methods do not rely on alterations of the released data (e.g., watermarks). In some cases we can also inject "realistic but fake" data records to further improve our chances of detecting leakage and identifying the guilty party.

2.2 DATA LEAKAGE INCIDENTS

Data leakage incidents

Sept. 2011	Science Applications International Corp	Backup tapes stolen from a car containing 5,117,799 patients' names, phone numbers, Social Security numbers, and medical information.
July 2008	Google	Data were stolen, not from Google offices, but from the headquarters of an HR outsourcing company, Colt Express.
July 2009	American Express	DBA stole a laptop containing thousands of American Express card numbers. The DBA reported it stolen.
Aug. 2007	Nuclear Laboratory in Los Alamos	An employee of the U.S. nuclear laboratory in Los Alamos transmitted confidential information by email.

Fig 2: DATA LEAKAGE INCIDENTS

2.3 OUR GOALS

- Our goal is to detect when the distributor's sensitive data has been leaked by agents, and if possible to identify the agent that leaked the data.
- The objective of this project is to improve the probability of identifying leakages using Data allocation strategies across the agents and also to identify the guilty party who leaked the data by injecting "realistic but fake" data records.

3. EXISTING SYSTEM LIMITATIONS

3.1 INTRODUCTION

We consider applications where the original sensitive data cannot be perturbed. Perturbation is a very useful technique where the data are modified and made “less sensitive” before being handed to agent. In some cases it is important not to alter the original distributor’s data.

3.2 DATA LEAKAGE DETECTION STEPS

3.2.1 WATERMARKING

A unique code is embedded in each distributed copy. If that copy is later discovered in the hands of an unauthorized party, the leaker can be identified. The watermark is difficult for an attacker to remove, even when several individuals conspire together with independently watermarked copies of the data.



Fig 3: EXAMPLE OF WATERMARKING

3.2.2 STEGANOGRAPHY

Steganography is a technique for hiding a secret message within a larger one in such a way that others can't discern the presence or contents of the hidden message.

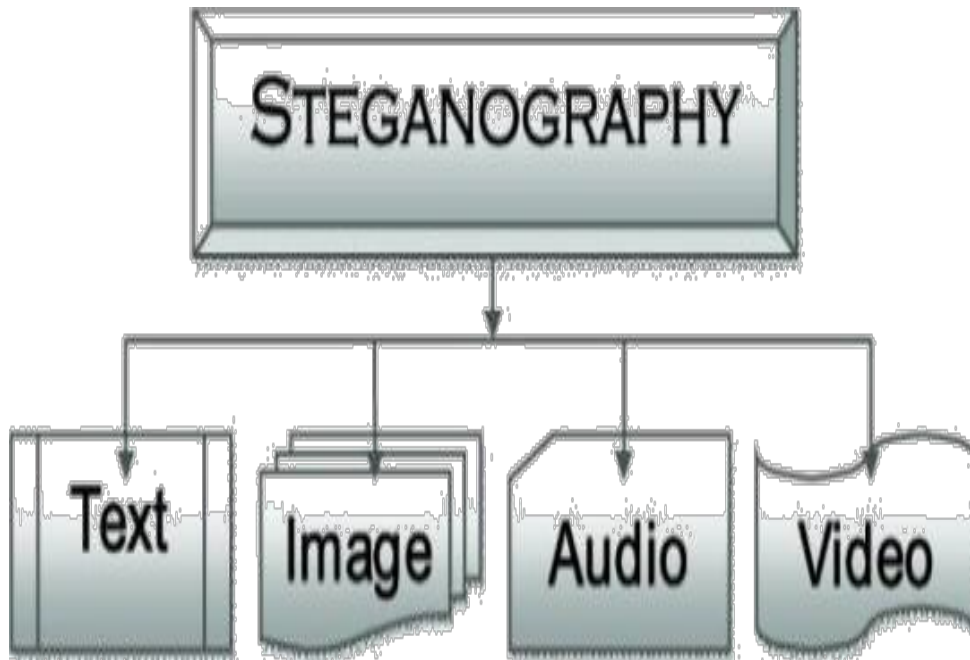


Fig 4: STEGANOGRAPHY

3.3 PROCEDURE & LIMITATIONS

3.3.1 PROCEDURES OF WATERMARKING

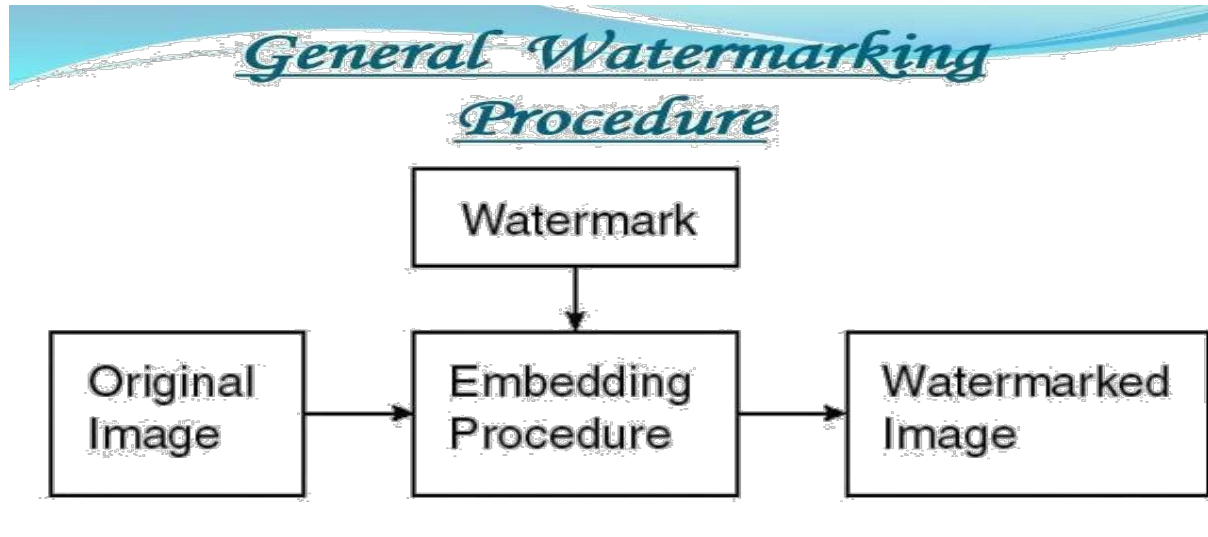


Fig 5: PROCEDURE OF WATERMARKING

3.3.2 LIMITATIONS OF WATERMARKING

- ❖ Watermarks can be very useful in some cases, but again, it involves some modification of the original data that is making the data less sensitive by altering attributes of the data.
- ❖ The second problem is that, these watermarks can sometimes be destroyed if the data recipient is malicious. E.g. A hospital may give patient records to researchers who will devise new treatments. Similarly, a company may have partnerships with other companies that require sharing customer data. Another enterprise may outsource its data processing, so data must be given to various other companies.

4. PROPOSED SYSTEM

- Our goal is to detect when the distributor's sensitive data has been leaked by agents, and if possible to identify the agent that leaked the data.
- Perturbation is a very useful technique where the data is modified and made "less sensitive" before being handed to agents. We develop unobtrusive techniques for detecting leakage of a set of objects or records.
- We develop a model for assessing the "guilt" of agents.
- Finally, we also consider the option of adding "fake" objects to the distributed set. Such objects do not correspond to real entities but appear realistic to the agents.
- In a sense, the fake objects acts as a type of watermark for the entire set, without modifying any individual members. If it turns out an agent was given one or more fake objects that were leaked, then the distributor can be more confident that agent was guilty.

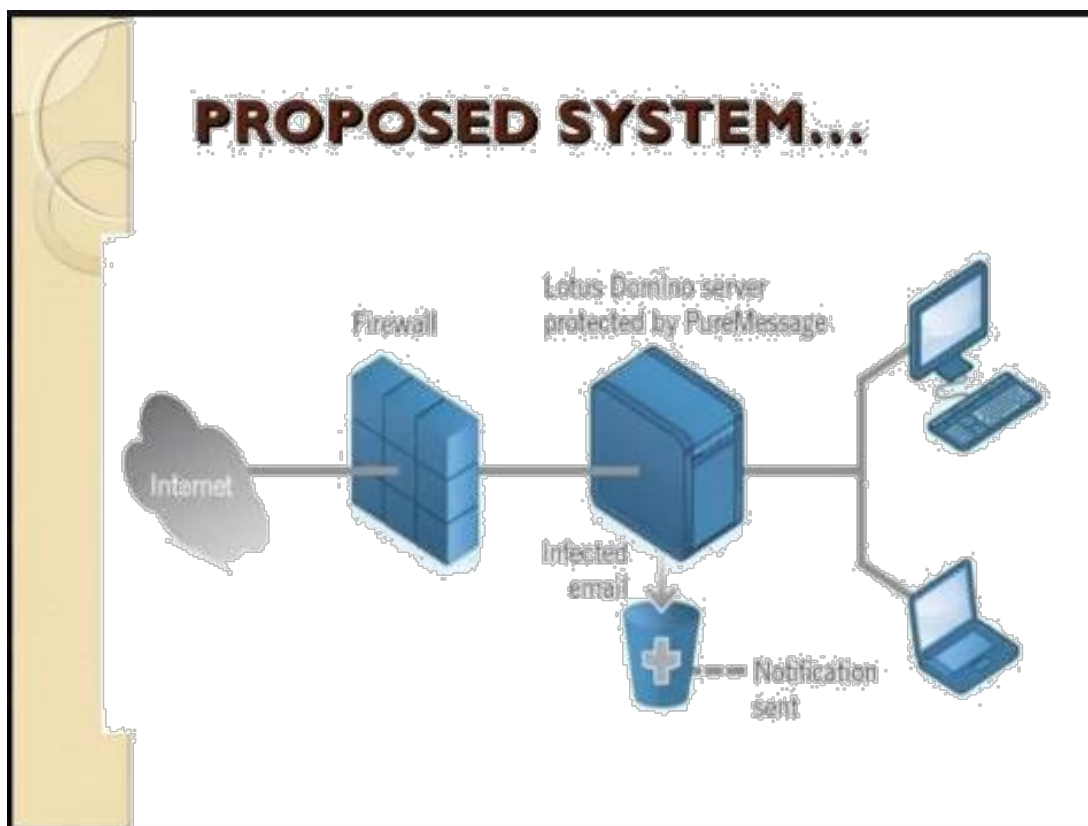


Fig 6: PROPOSED SYSTEM

5. TYPES OF EMPLOYEES THAT MAY LEAK DATA

- The security illiterate
 - Majority of employees with little or no knowledge of security
 - Corporate risk because of accidental breaches
- The unlawful residents
 - Use the company IT resources in ways they shouldn't
 - i.e., by storing music, movies, or playing games
- The malicious/disgruntled employees
 - Typically minority of employees
 - Gain access to areas of the IT system to which they shouldn't
 - Send corporate data(e.g., customer lists, R&D, etc.) to third parties.



Fig 7: TYPES OF EMPLOYEES

6. IMPACT OF ORGANIZATIONS

- Financial reputational loss
- Small leak & accumulate to big loss
- Loss of customer employee private information
- Loss of competitive position
- consequences Lawsuits or regulatory



Fig 8: IMPACT OF ORGANIZATION

7. IMPLEMENTATION

The system has the following

- Data Allocation
- Fake Object
- Optimization
- Data Distributor

7.1 DATA ALLOCATION

The main focus of our project is the data allocation problem as how can the distributor “intelligently” give data to agents in order to improve the chances of detecting a guilty agent.

7.2 FAKE OBJECT

Fake objects are objects generated by the distributor in order to increase the chances of detecting agents that leak data. The distributor may be able to add fake objects to the distributed data in order to improve his effectiveness in detecting guilty agents. Our use of fake objects is inspired by the use of “trace” records in mailing lists.

7.3 OPTIMIZATION

The purpose of optimization is to achieve the “best” design relative to a set of prioritized criteria or constraints. These include maximizing factors such as productivity, strength, reliability, longevity, efficiency, and utilization.

7.4 DATA DISTRIBUTOR

A data distributor has given sensitive data to a set of supposedly trusted agents (third parties). Some of the data is leaked and found in an unauthorized place (Eg, On the web or somebody’s laptop). The

distributor must assess the likelihood that the leaked data came from one or more agents, as opposed to having been independently gathered by other means.

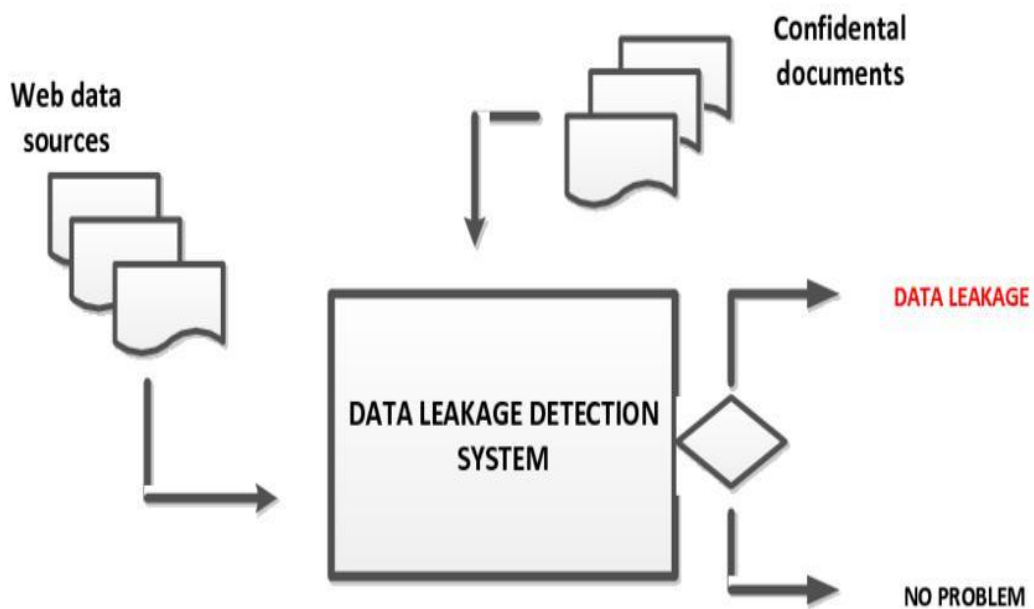


Fig 9: IMPLEMENTATION

8. MODULES

8.1 ADMIN MODULE

- Administrator has to logon to the system.
- Admin can add information about a new user.
- Admin can add/view/delete/edit the user details. Admin can create user groups and place users in it.

8.2 USER MODULE

- A user must login to use the services.
- A user can send data sharing requests to other users.
- A user can accept/reject data sharing requests from other users.
- A user can trace the flow of its data i.e. can see what all users possess its data.

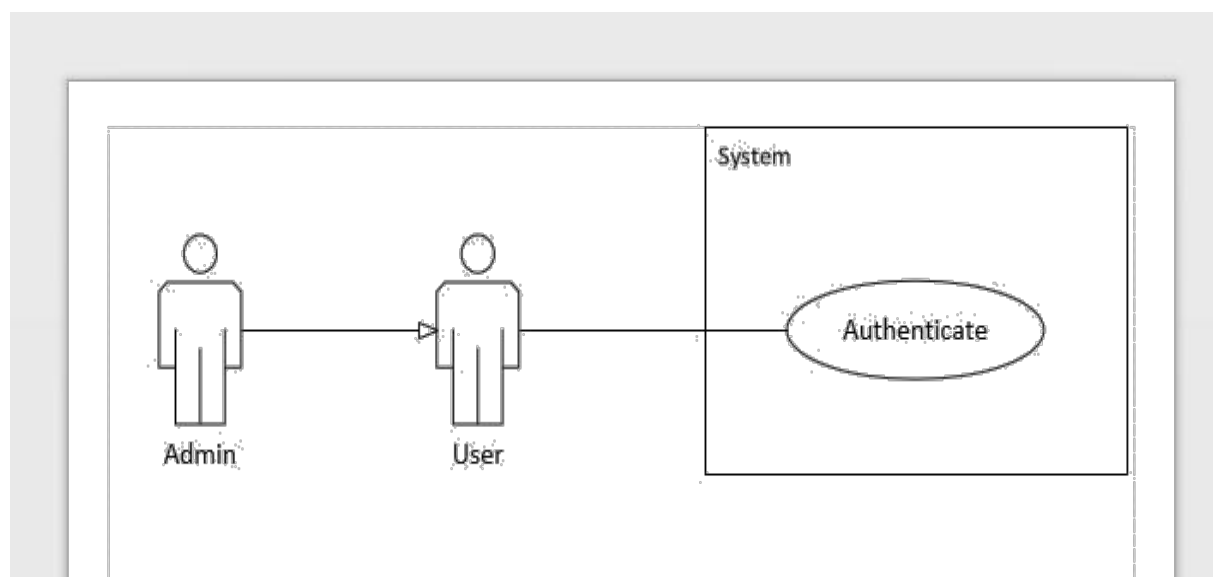


Fig 10: ADMIN & USER MODULE

9. APPLICATIONS OF DATA LEAKAGE

- It helps in detecting whether the distributor's sensitive data has been leaked by the trustworthy or authorized agents.
- It helps to identify the agents who leaked the data.
- Reduces cybercrime.
- Copy prevention & control.
- Source tracking.

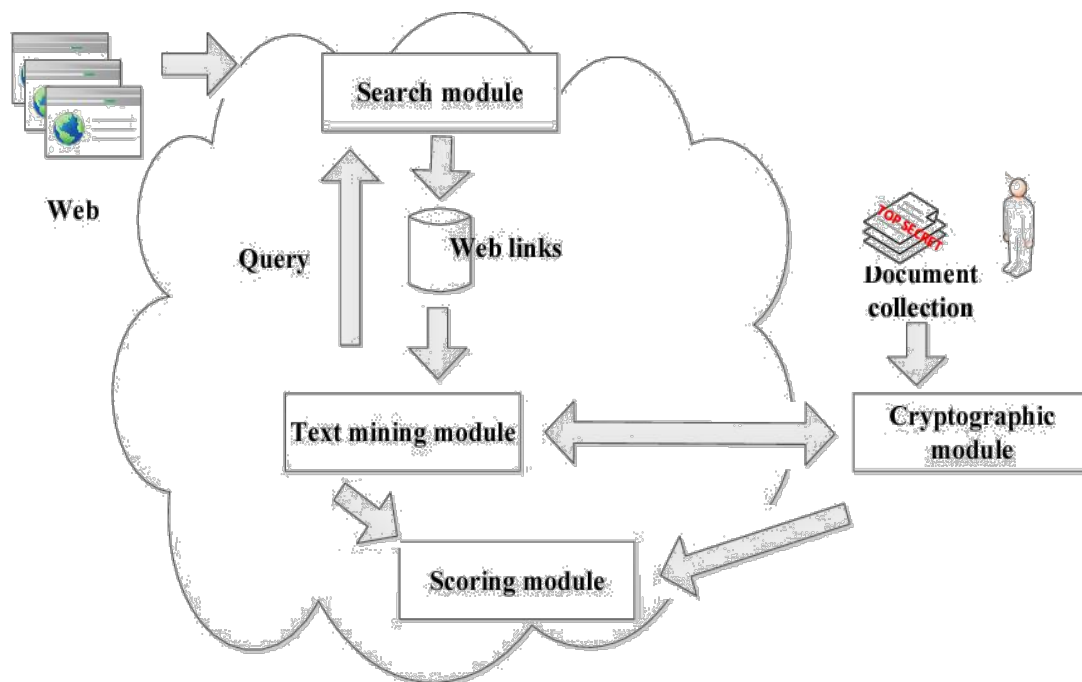


Fig 11: APPLICATION OF DATA LEAKAGE

10.DATA LOSS PREVENTION

10.1 WHAT IS DATA LOSS PREVENTION ?

- ✓ Data loss prevention is a data security technology that detects potential data breach incidents in timely manner and prevents them by monitoring data in-use (end points), in-motion (network traffic) and at-rest (data storage) in an organization's network.

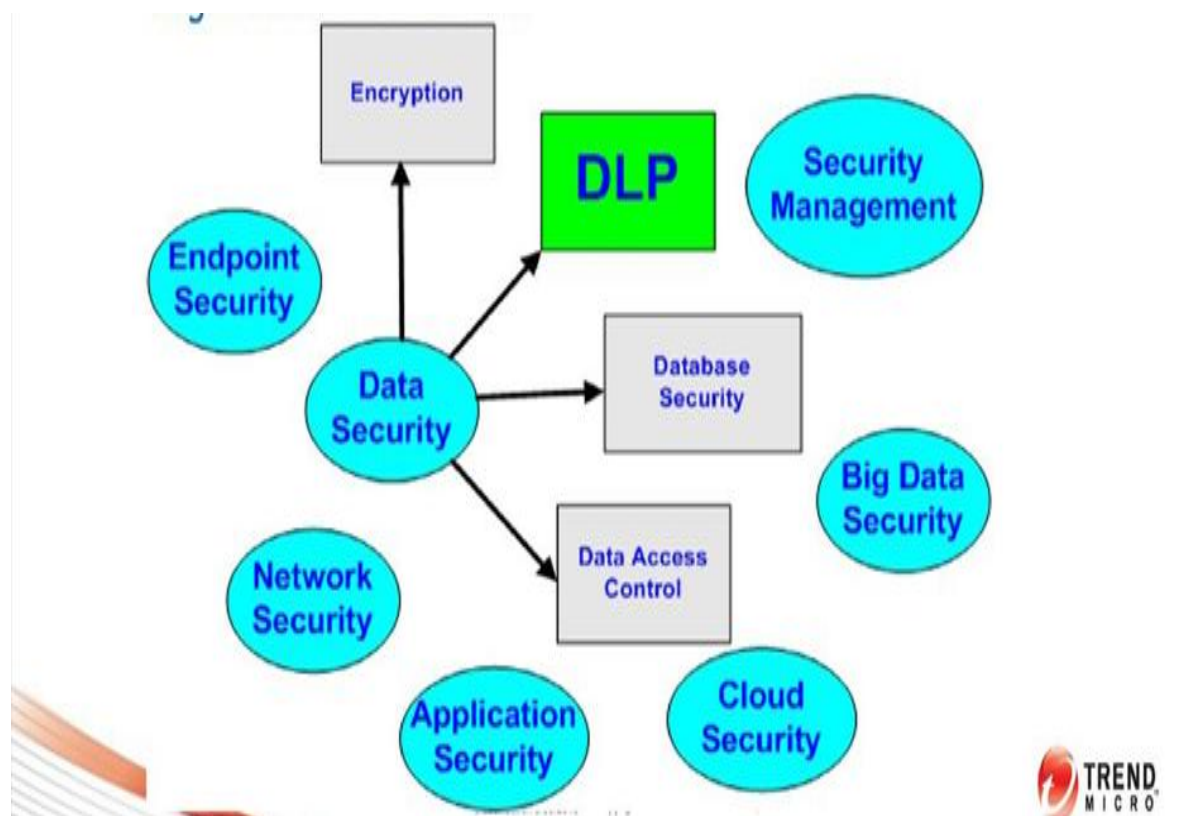


Fig 12: DATA LOSS PREVENTION

- What drives DLP Development?
 - ✓ Regulatory Compliances Such as PCI, SOX,HIPAA,GLBA,SB1382 and etc.
 - ✓ Confidential Information Protection.
 - ✓ Intellectual Property Protection.
- What Data Loss Incidents Does aDLP System Handle?
 - ✓ Incautious Data Leak By An Internal Worker.
 - ✓ Intentional Data Theft By An Unskillful Worker.
 - ✓ Determined Data Theft By A Highly Technical Worker.
 - ✓ Determined Data Theft By External Hackers Or Advanced Malwares Or APT.

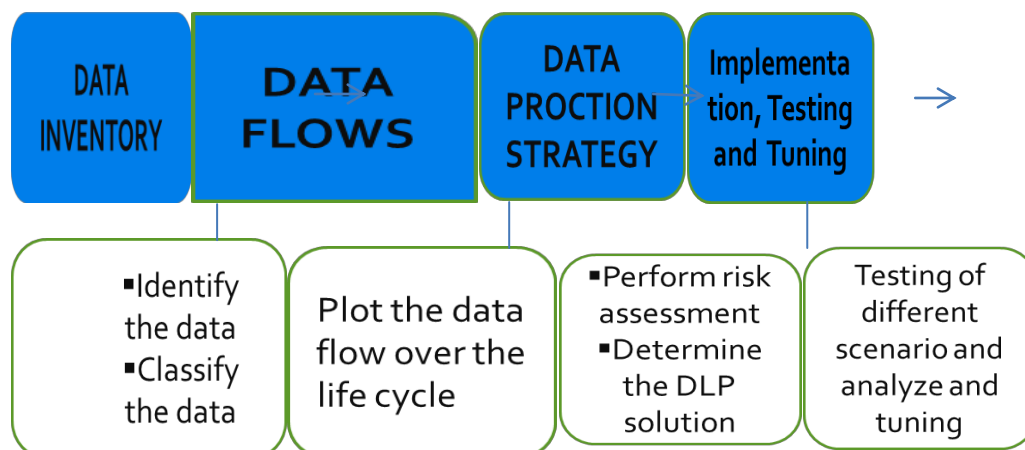
- ❖ Data loss prevention(DLP): a set of tools and processes used to ensure that sensitive data is not lost, misused or accessed by unauthorized users. The goal is to stop information such as intellectual property, financial data and employee or customer details from being sent, either accidentally or intentionally, outside the corporate network.

- PERSONAL INFORMATION PROTECTION /COMPLIANCE :

If your organization collect and store *PERSONALLY IDENTIFIABLE INFORMATION (PII)*, *PROTECTED HEALTH INFORMATION (PHI)* , or *PAYMENT CARD INFORMATION(PCI)* etc.

If so, you are more than likely subject to compliance regulations, such as HIPAA (for PHI) and GDPR (for personal data of EU residents), that require you to protect your customers' sensitive data.

Data Approaches :



10.2 DIFFERENT STATES OF DATA IN DLP:

❖ Data in-use (end points)

- E mail
- Network Accessing
- Wireless Systems

❖ Data in-motion (network traffic)

- Portable Media(USB)
- Removable Media(USB)
- Authorized Abuse

❖ Data at-rest (data storage)

- File Sharing
- Web Uploads
- 1M

10.3 TYPES OF DLP:

➤ NETWORK DLP (applies to data in-motion):-

- ✓ Network DLP protects the information's you send over your network or the internet depending on how it is designed. This protects the user when he/she sends sensitive information like credit card numbers, SSN etc.

○ DRAWBACK OF NETWORK DLP:

- ✓ It will not protect data on devices that are not on the organization network
- ✓ Does not have capability to decrypt encrypted tunnels
- ✓ High cost organizations to deploy only at network check points instead of throughout the network

➤ END POINT DLP (applies to data in-use and data in rest):-

- ✓ Protects the data on the user's laptop
- ✓ An agent is installed an end-system
- ✓ Allows more degree of protection than NDLP

○ DRAWBACK OF END POINT DLP:

- ✓ Complexity
- ✓ Agent management

➤ HYBRID DLP (deploy both End point DLP and Network DLP):-

- ✓ Costly and most complex approach
- ✓ Offers the best coverage and protection

10.4 NECESSARY STEPS IN DLP:

- To protect against confidential data theft and loss, a multi-layered security foundation is needed-
- ✓ Control/limit access to the data - firewalls, remote access controls, network access controls, physical security controls
- ✓ Secure information from threats - protect perimeter and endpoints from malware, botnets, viruses, DOS, etc. with security technology
- ✓ Control use of sensitive data once access is granted—policy-based content inspection, acceptable use, encryption
- Cisco 's Solution or Data Loss Prevention-
- ✓ Build a secure foundation with a Self-Defending Network
- ✓ Integrate DLP controls into security devices to protect data and increase visibility while decreasing the complexity and total cost of ownership of DLP deployments



Fig 13: PROTECTION OF USER DATA

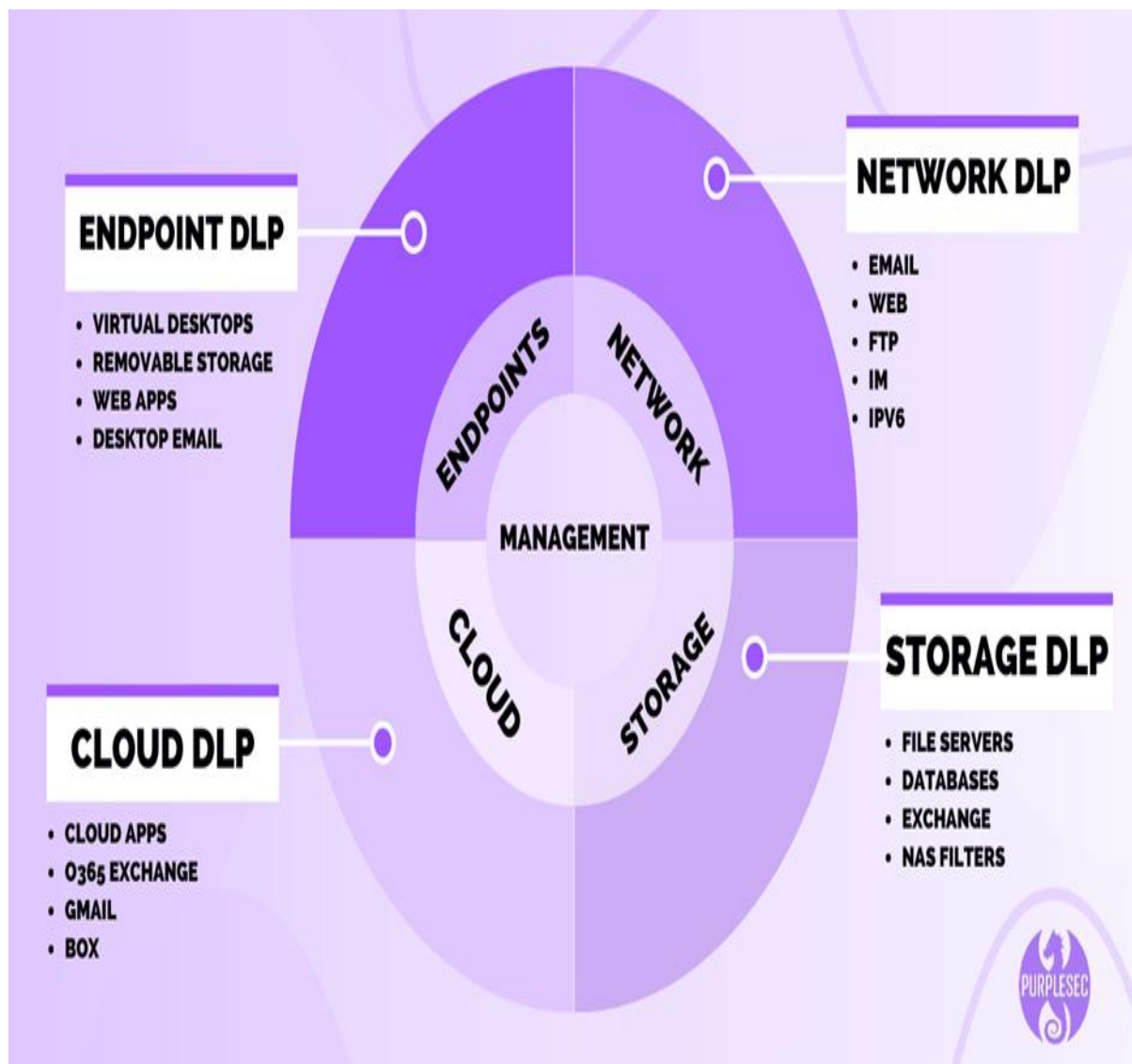


Fig 14: CLASSIFICATION OF DLP

10.5 APPLICATIONS OF DLP:-

- It helps in detecting whether the distributor's sensitive data has been leaked by the trustworthy or authorized agents.
- It helps to identify the agents who leaked the data
- Reduces cybercrime
- It helps to detect and prevent data breaches, exfiltration, or unwanted destruction of sensitive data etc.



Fig 15: APPLICATION OF DLP

11. CLOUD DATA LOSS PREVENTION

11.1 WHAT IS CLOUD DLP?

- Cloud Data Loss Prevention (CDLP) helps keep on organization's sensitive or critical information safe from cyber attacks, insider threats and accidental exposure.
- Cloud DLP solution provide visibility and protection for sensitive data in SaaS and IaaS applications.



Fig 16: Cloud DLP

11.2 CHARACTERISTICS OF CLOUD DLP:-

- Take charge of your data on or off cloud
- Gain visibility into sensitive data risk across your entire organization
- Reduce data risk with obfuscation and de-identification methods like masking and tokenization
- Seamlessly inspect and transform structured and unstructured data etc.

11.3 FEATURES OF CLOUD DLP (CDLP):-

- ✓ Automatic discovery, inspection, classification
- ✓ Simple and powerful redaction
- ✓ Serverless
- ✓ Detailed finding with on-demand inspection
- ✓ Secure data handling
- ✓ Pay as you go pricing
- ✓ Easy workload integration
- ✓ Custom rules

11.4 IMAGES OF CLOUD ARCHITECTURE:-

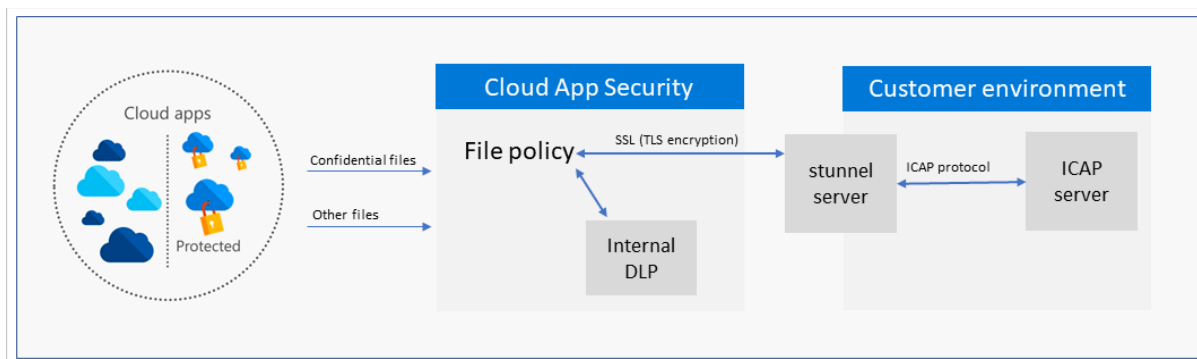
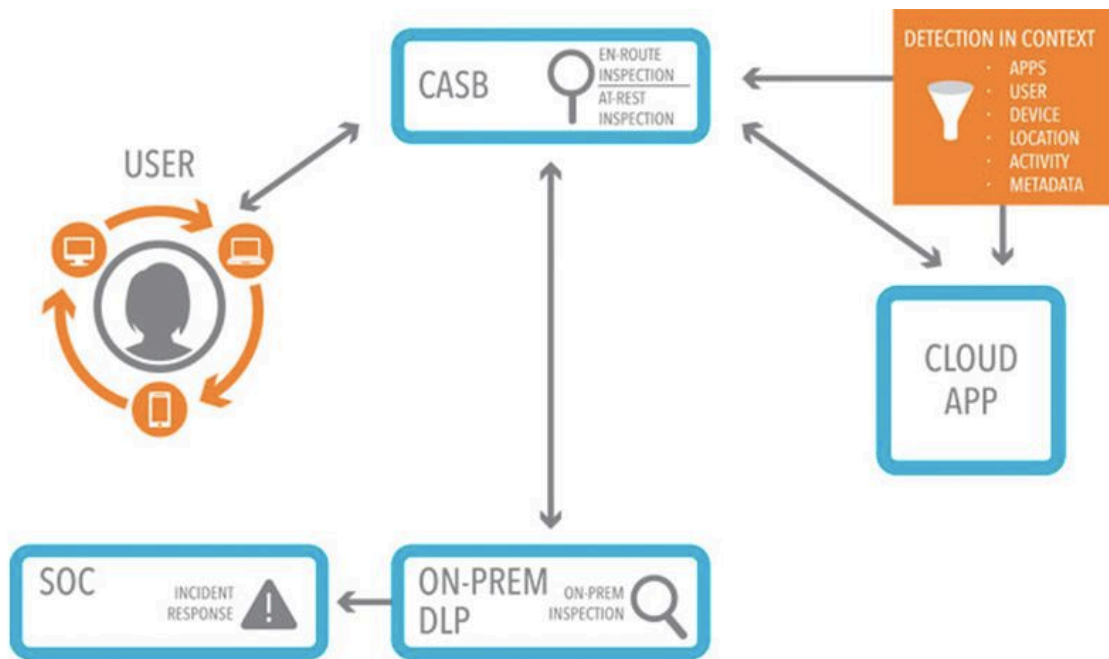


Fig 17: ARCHITECTURE OF CLOUD DLP

11.5 SERVICES OF CLOUD DLP:-

- Gain visibility into the data you store and process-
 - Create dashboards and audit reports. Automate tagging, remediation, or policy based on findings. Connect DLP results into Security Command Center, Data Catalog, or export to your own SIEM or governance tool.

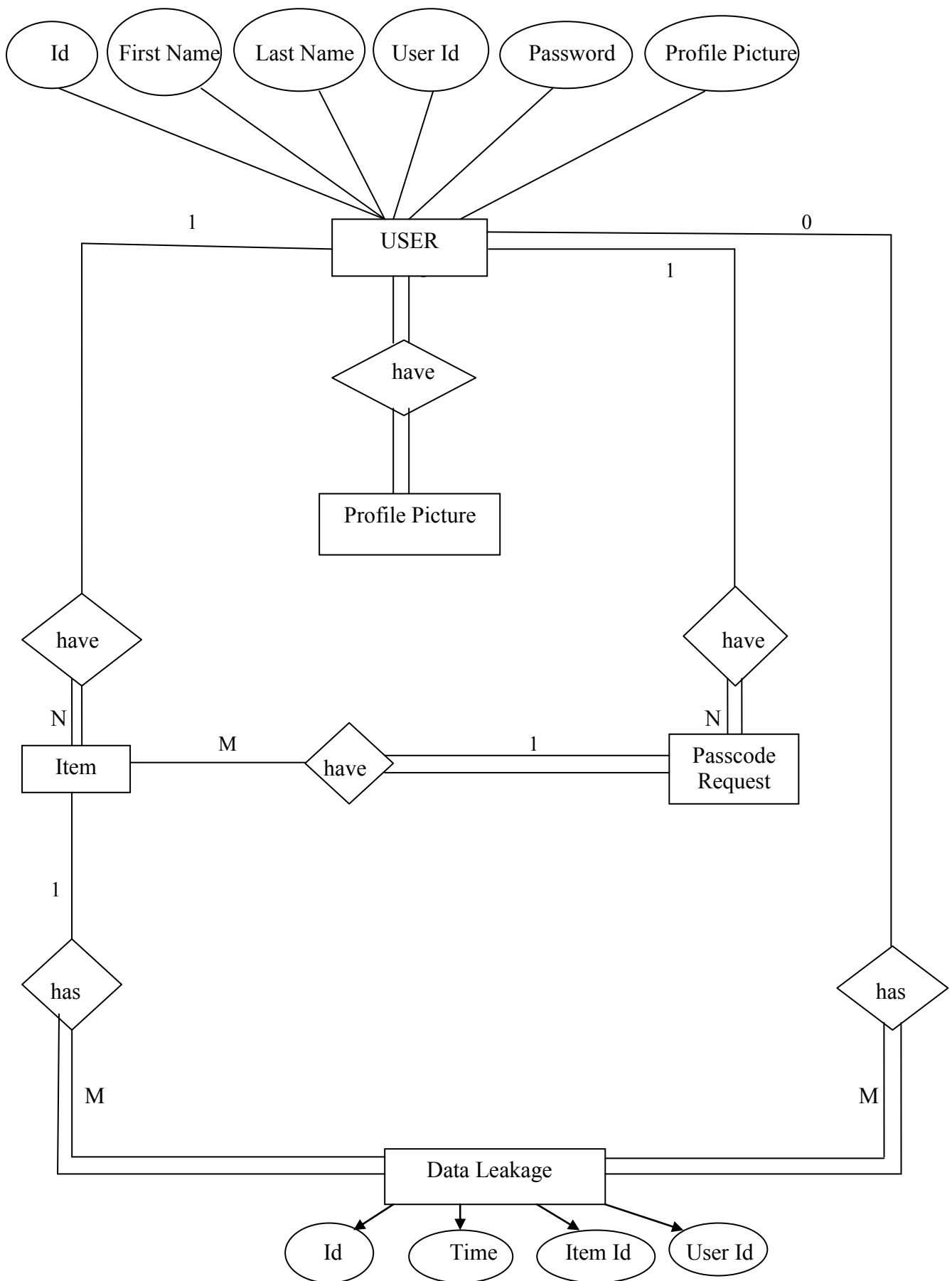
- Configure data inspection and monitoring with ease-
 - Enable DLP across your entire BigQuery footprint to automatically discover, inspect, and classify your data. DLP runs continuously, picking up new data tables as they are added, so you can focus on analysis.

- Reduce risk to unlock more data for your business-
 - Protection of sensitive data, like personally identifiable information (PII), is critical to your business. Deploy de-identification in migrations, data workloads, and real-time data collection and processing.

11.6 CLOUD DLP IMPLEMENTATION:-

- ❖ Automatically mask your data to safely unlock more of the cloud-
- ✓ Cloud DLP provides tools to classify, mask, tokenize, and transform sensitive elements to help you better manage the data that you collect, store, or use for business or analytics. With support for structured and unstructured data, Cloud DLP can help you preserve the utility of your data for joining, analytics, and AI while protecting the raw sensitive identifiers.
- ❖ Measure re-identification risk in structured data-
- ✓ Enhance your understanding of data privacy risk. Quasi-identifiers are partially identifying elements or combinations of data that may link to a single person or a very small group. Cloud DLP allows you to measure statistical properties such as k-anonymity and l-diversity, expanding your ability to understand and protect data privacy.
- ❖ Automated sensitive data discovery for your data warehouse-
- ✓ Discover sensitive data by profiling every BigQuery table and column across your entire organization, select organization folders, or individual projects. Configure directly in the Cloud Console UI and let DLP handle the rest. Use table and column profiles to inform your security and privacy posture.
- ❖ Use Cloud DLP from virtually anywhere, on or off Cloud-
- ✓ With over 150 built-in infoTypes, Cloud DLP gives you the power to scan, discover, classify, and report on data from virtually anywhere. Cloud DLP has built-in support for scanning and classifying sensitive data in Cloud Storage, BigQuery, and Datastore, and a streaming content API to enable support for additional data sources, custom workloads, and applications.

12. ER DIAGRAM



Step 1: Identify The Entities

- User
- Profile Picture
- Item
- Passcode Request
- Data Leakage

Step 2: Identify Attributes of Entities**i) User**

- Id
- First name
- Last name
- User Id
- Password
- Profile Picture

ii) Profile Picture

- Id
- Img no
- Img
- User id

iii) Item

- Id
- Name
- Description
- Path
- User id
- Passcode

iv) Passcode Request

- Id
- Item id
- User id
- Valid

v) Data Leakage

- Id

- Time
- Item id
- User id

Step 3: Identify Relationships Between Entities

- User has profile picture
- User has item
- Passcode request have a item
- User has/have request a passcode
- A user has Data Leakage
- Data Leakage has Item

Step 4: Analyze Cardinality of Relationships

- User has profile picture : A user multiple profile picture → 1:N
- User has item: A user has multiple item → 1:N
- Passcode request have a item → A item have a passcode request → M:1
- User have request a passcode request → one user can have request multiple passcode → 1:N
- user has data leakage → A user have may be multiple data leakage: 1:N
- data leakage has item → item leaked multiple item: 1:N

Step 5: Identify Participation Types

- User has Profile Picture → both total
- User has item → User: Partial, Item: Total
- Item have passcode Request → Item: Partial, Passcode Request: total
- A user has passcode Request → User: Partial, Passcode Request: Total
- A user has data Leakage → Item: Partial, data Leakage: Total

12. DASHBOARD AND OUTPUT

The screenshot shows the Ms.Kundu dashboard with a blue sidebar navigation menu. The main content area features four summary cards at the top: 'Item' (10), 'My Item' (6), 'View Score' (0), and 'Acknowledge ment slip' (5). Below these are two data tables: 'New Item' and 'New My Item'. Both tables have columns for Id, Item Name, Upload By, and Option. The data rows are as follows:

Id	Item Name	Upload By	Option
10	test 5	MAHASWATA KUNDU	
9	test 3	MAHASWATA KUNDU	
8	test 3	MAHASWATA KUNDU	
7	confidential 1	MAHASWATA KUNDU	

Fig 18: DASHBOARD (NEW ITEM, NEW MY ITEM)

This is a picture of **Dashboard** in the system. Shows interface of the system.

The screenshot shows the Ms.Kundu dashboard with a focus on the 'New Request Pascode' section. The sidebar is partially visible. The main content area displays two data tables. The top table shows a list of items with columns for Id, Item Name, and Upload By. The bottom table, titled 'New Request Pascode', has columns for Item Id, Item Name, User Id, Request By, and Option. The data rows are as follows:

Item Id	Item Name	User Id	Request By	Option
10	test 5	MAHASWATA KUNDU		
8	test 3	MAHASWATA KUNDU		
7	confidential 1	MAHASWATA KUNDU		
2	test1	MAHASWATA KUNDU		

Fig 19: DASHBOARD (NEW REQUEST PASSCODE)

This is a picture of **Dashboard** in the system. Shows new item and my item in interface of the system.

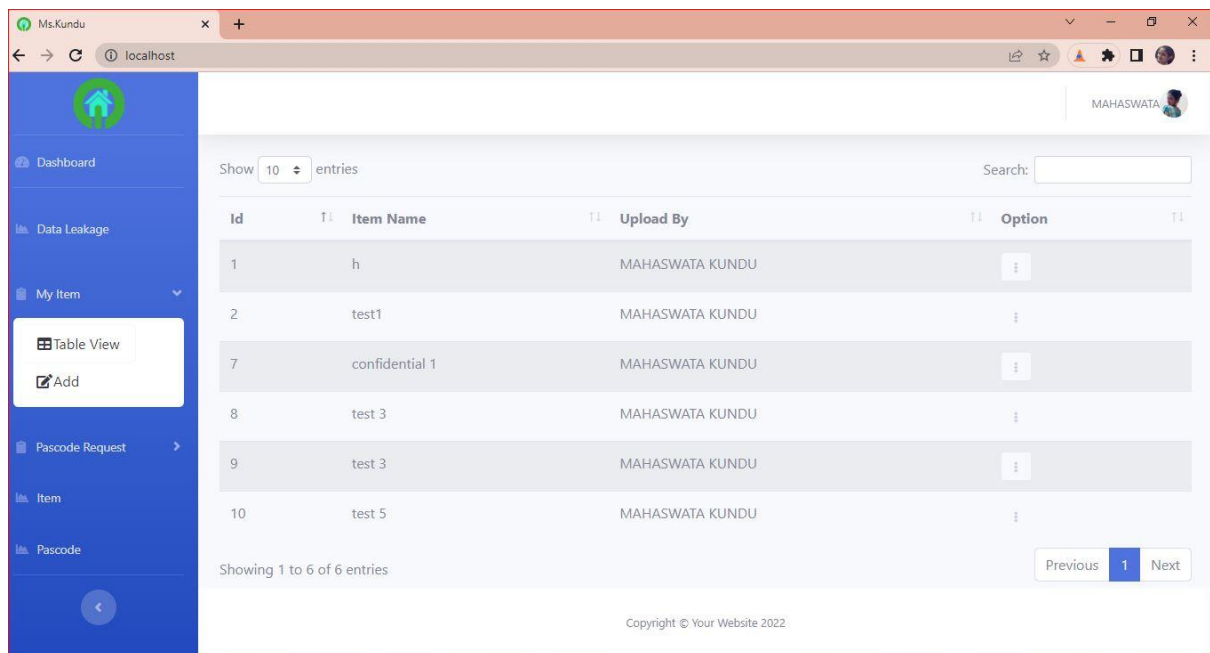


Fig 20: MY ITEM → TABLE VIEW

It is the picture of My Item section Table View. It is viewed as Table form. New requested passcode.

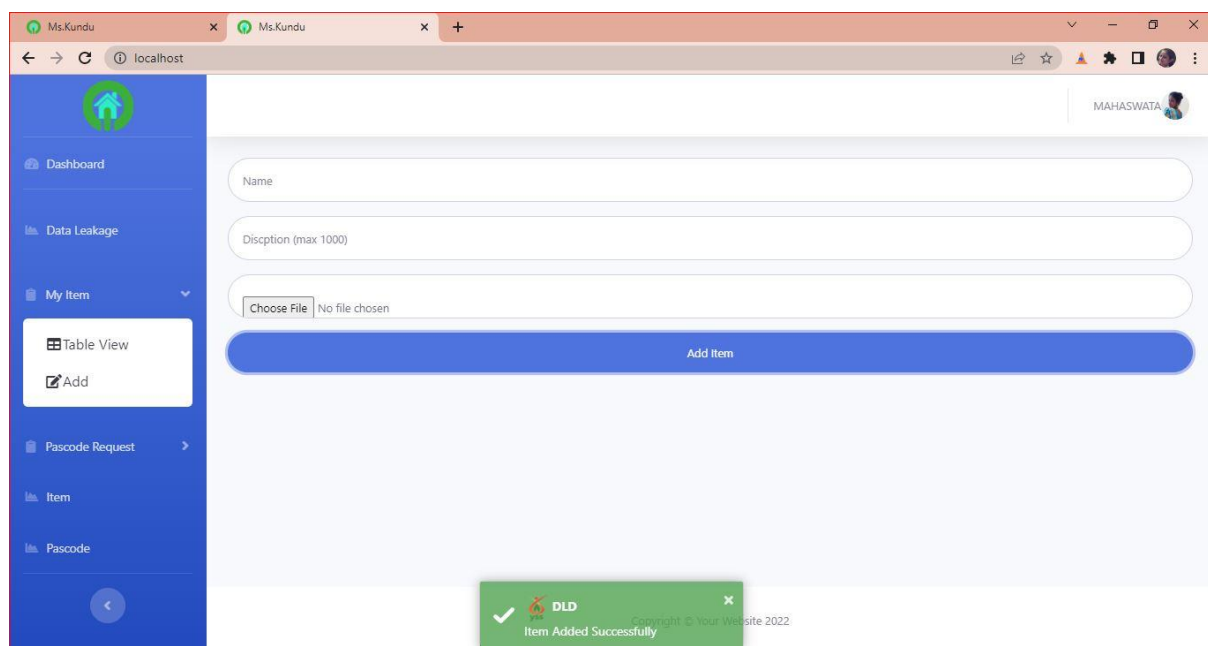


Fig 21: MY ITEM → ADD VIEW (ITEM ADDED SUCCESSFULLY.)

This is the picture of **My Item** section. It is the Add View in My Item section.

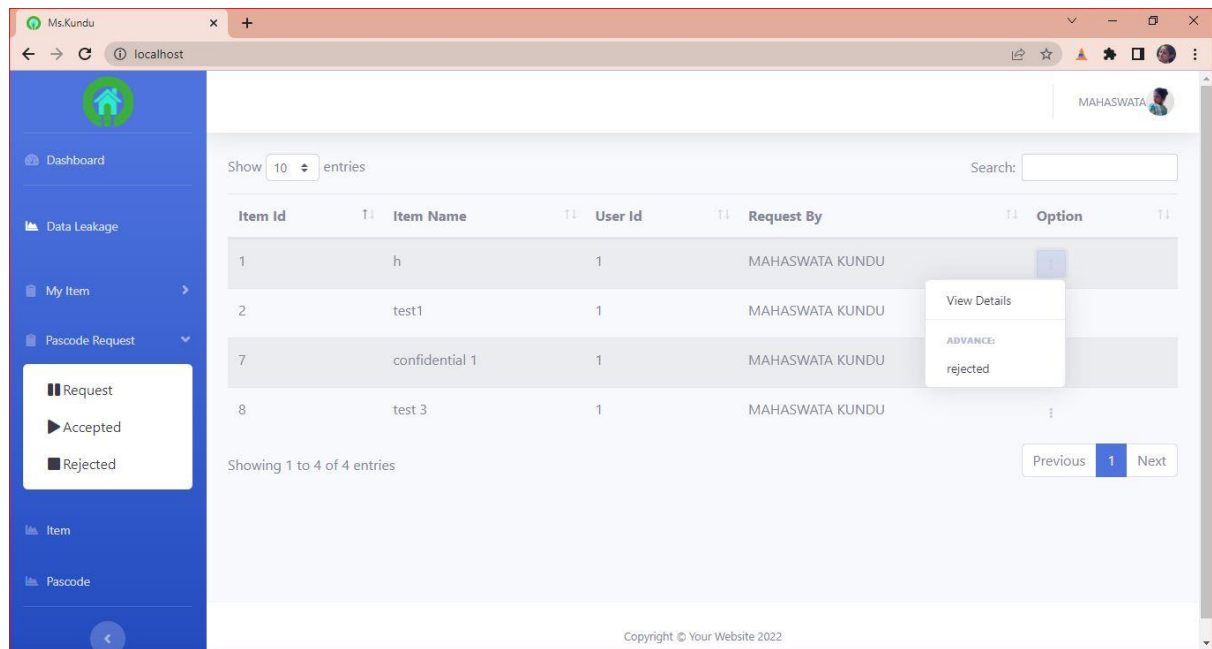


Fig 22: PASSCODE REQUEST

Here you can request for **Passcode**.

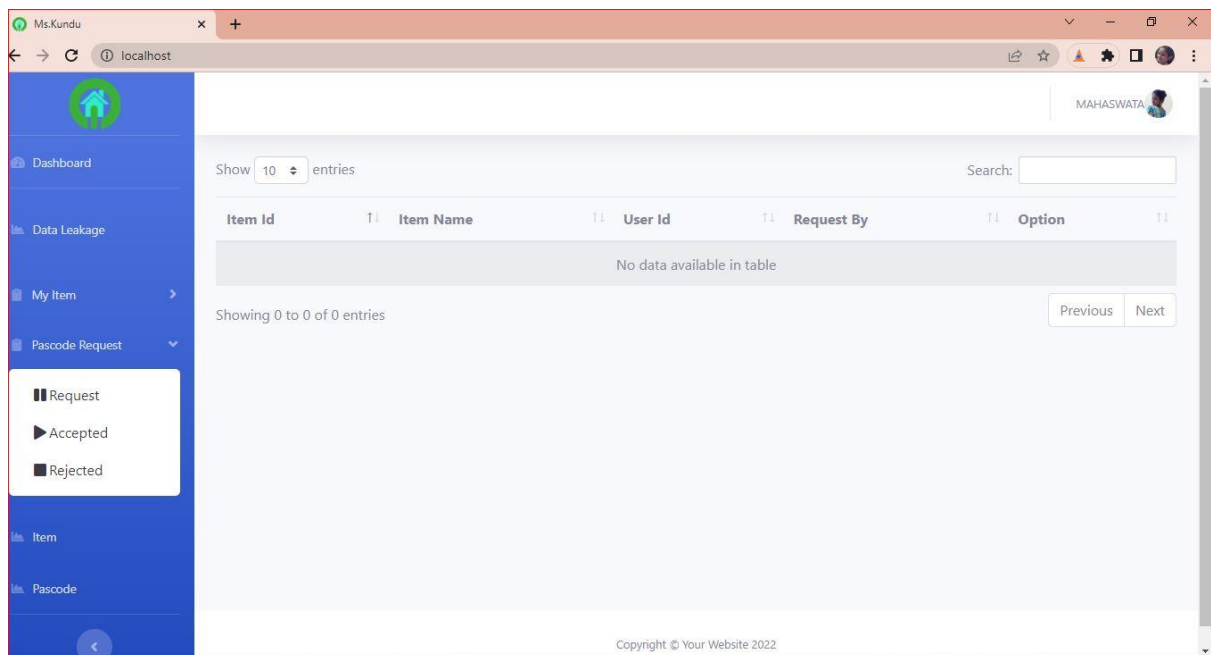


Fig 23: PASSCODE REQUEST

This is a output of **Passcode Request** by a user.

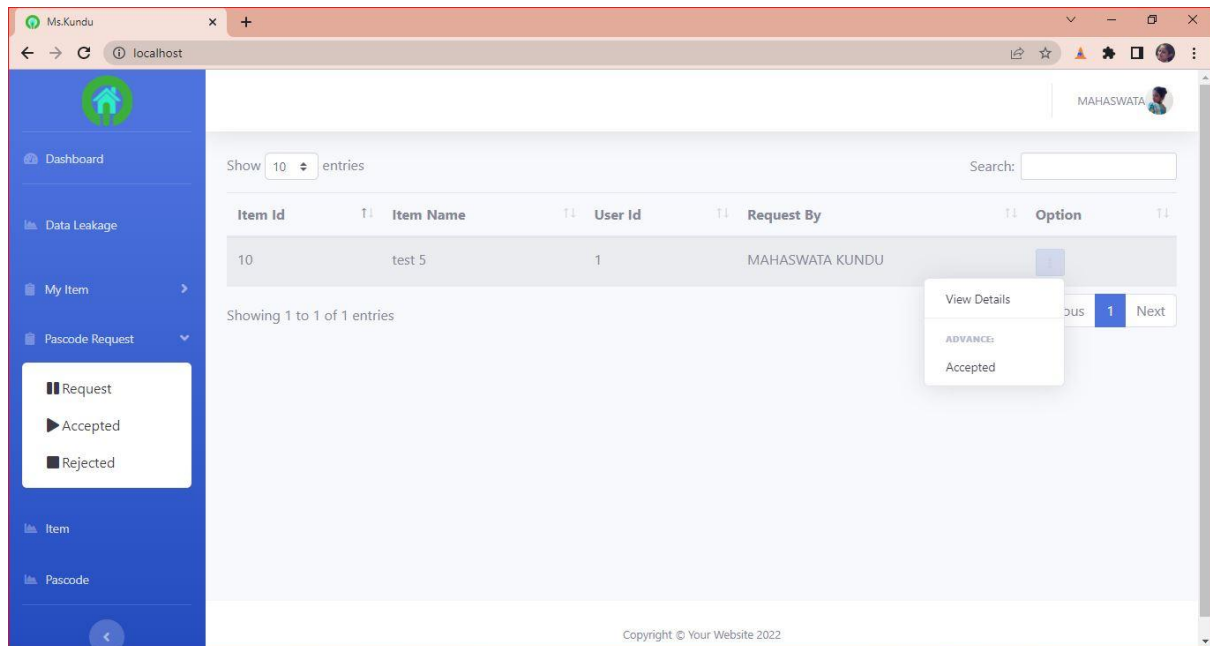


Fig 24: REQUESTED ITEM CAN BE ACCEPTED

In this section, REQUESTED ITEM by a user can be Accepted in the Option field.

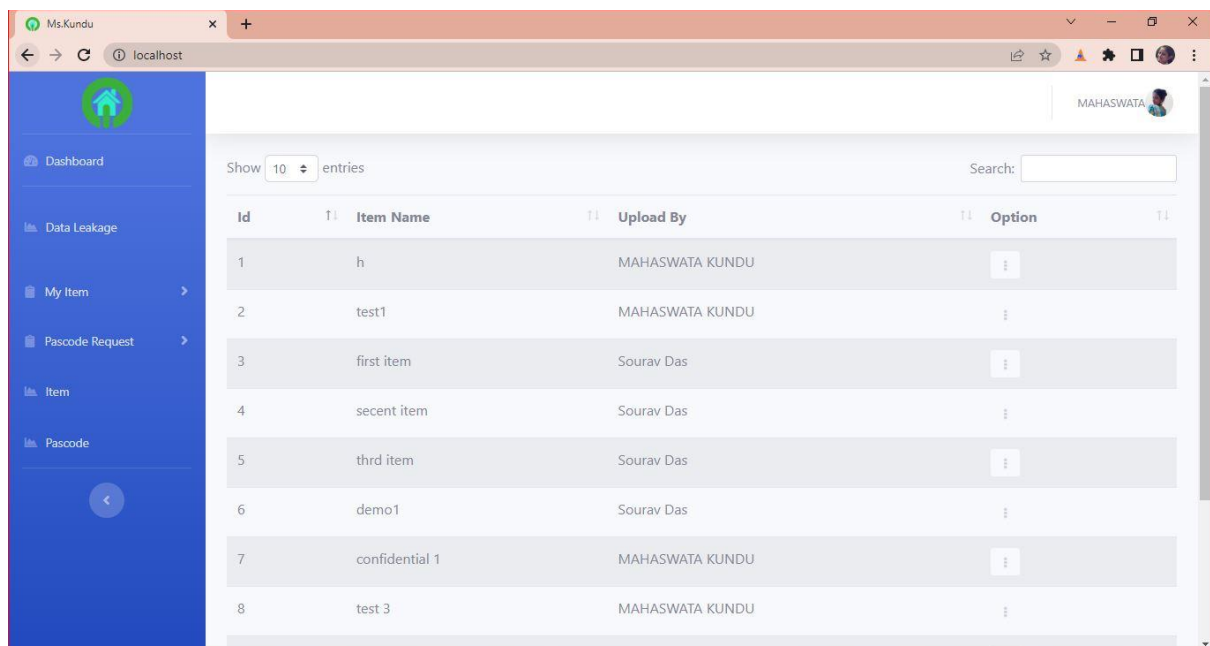


Fig 25: ITEM UPLOADED BY ALL USERS

This is the output of Item uploaded by all users.

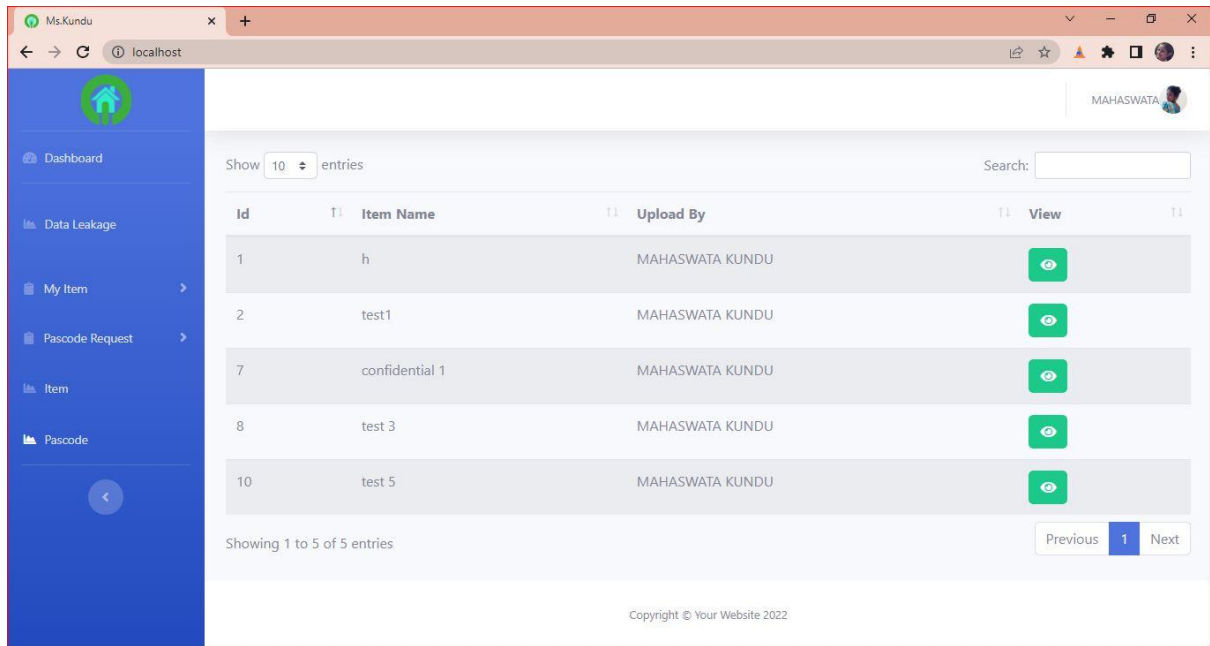


Fig 26: PASSCODE

This is the picture of **Passcode** of item uploaded by user.

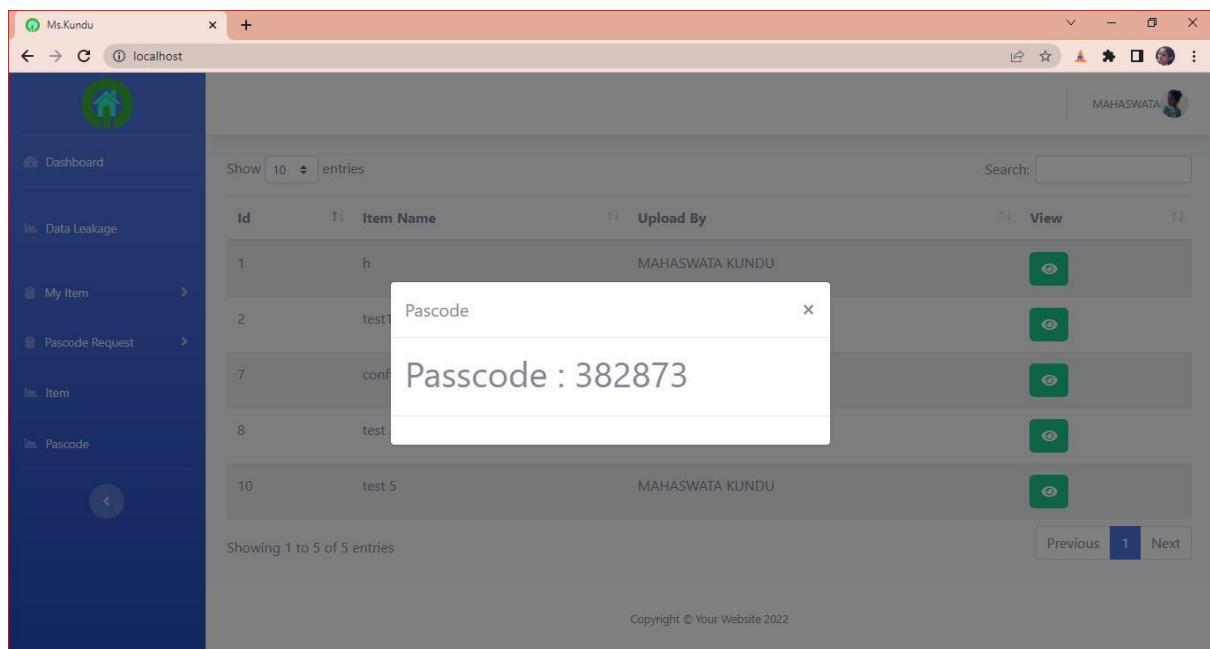


Fig 27: ITEM PASSCODE

This is the picture of Request passcode in view option.

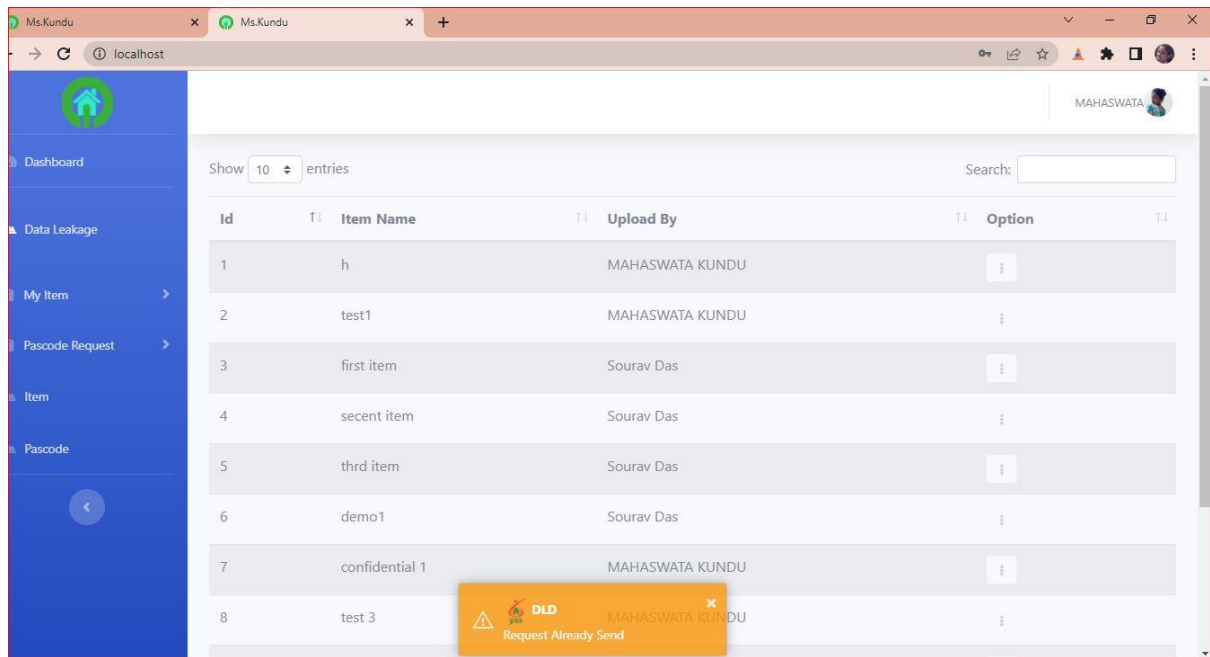


Fig 28: REQUEST SEND

This is the figure of sending request for permission to download an item.

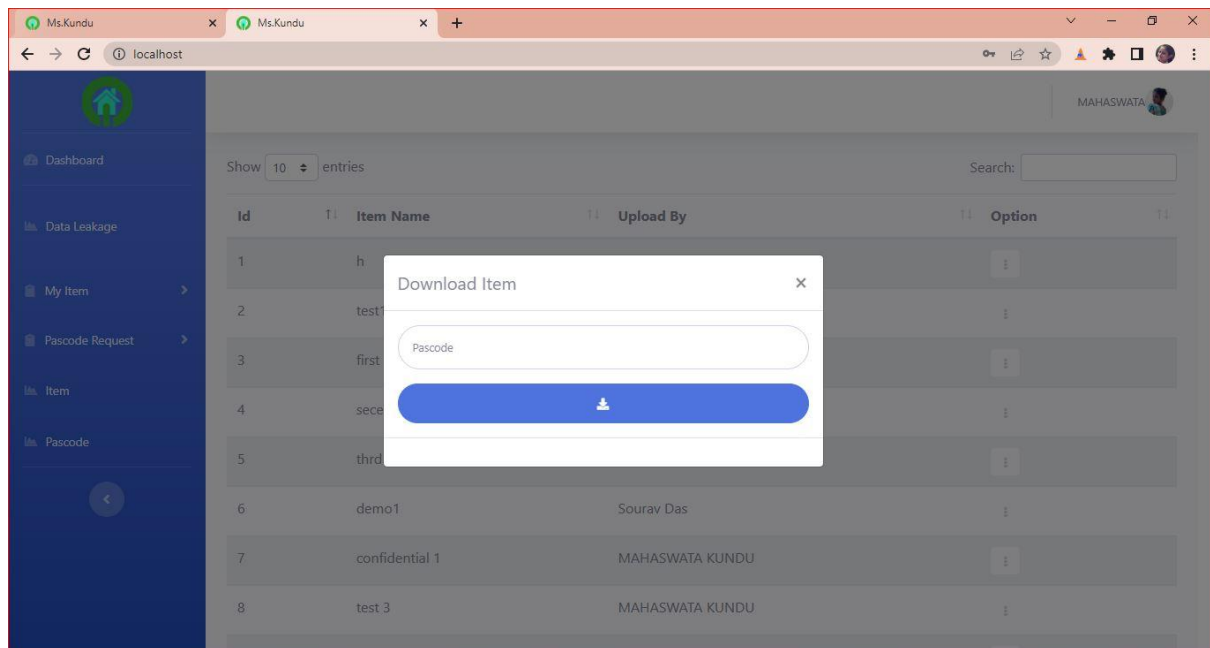


Fig 29: ITEM DOWNLOAD

It's a figure of Item Download where we have to give a passcode.

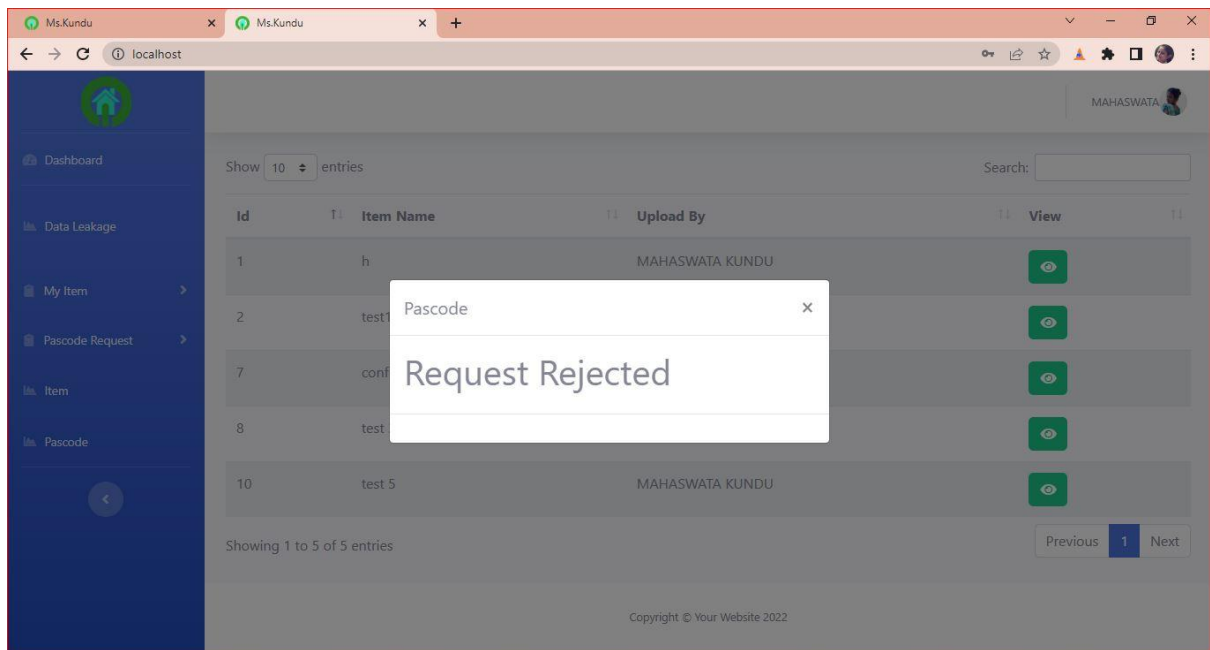


Fig 30: PASSCODE REQUEST REJECTED

This figure shows that the **Passcode Request rejection**.

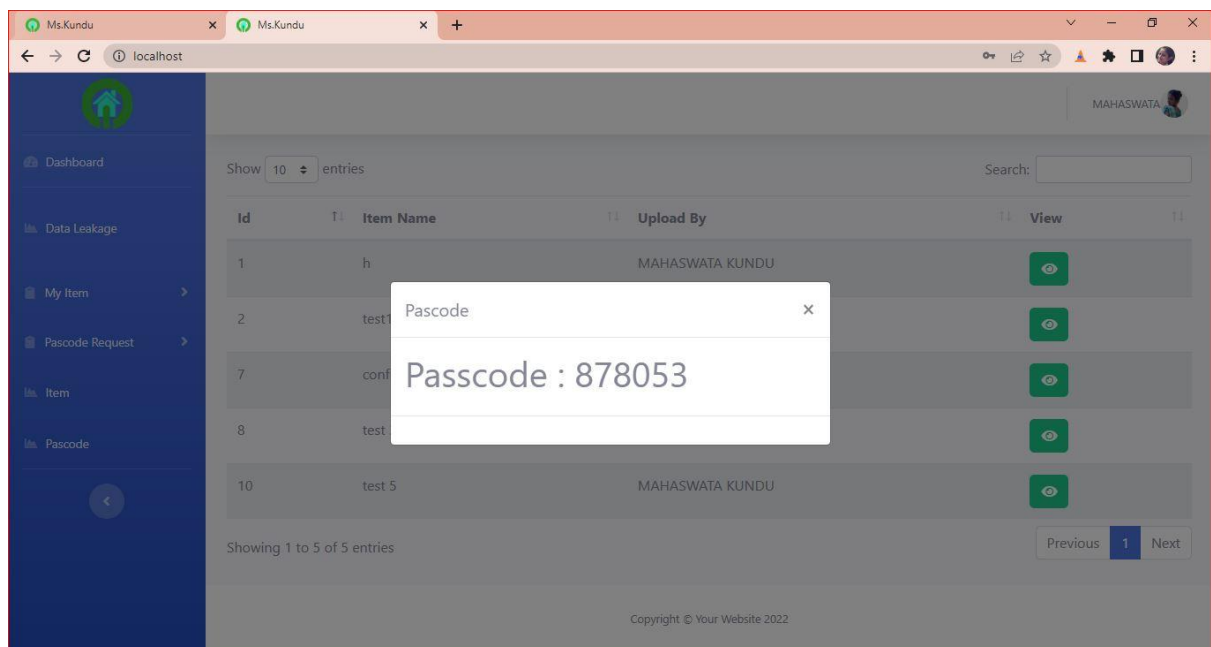


Fig 31: PASSCODE

This is the output of Request passcode in view option.

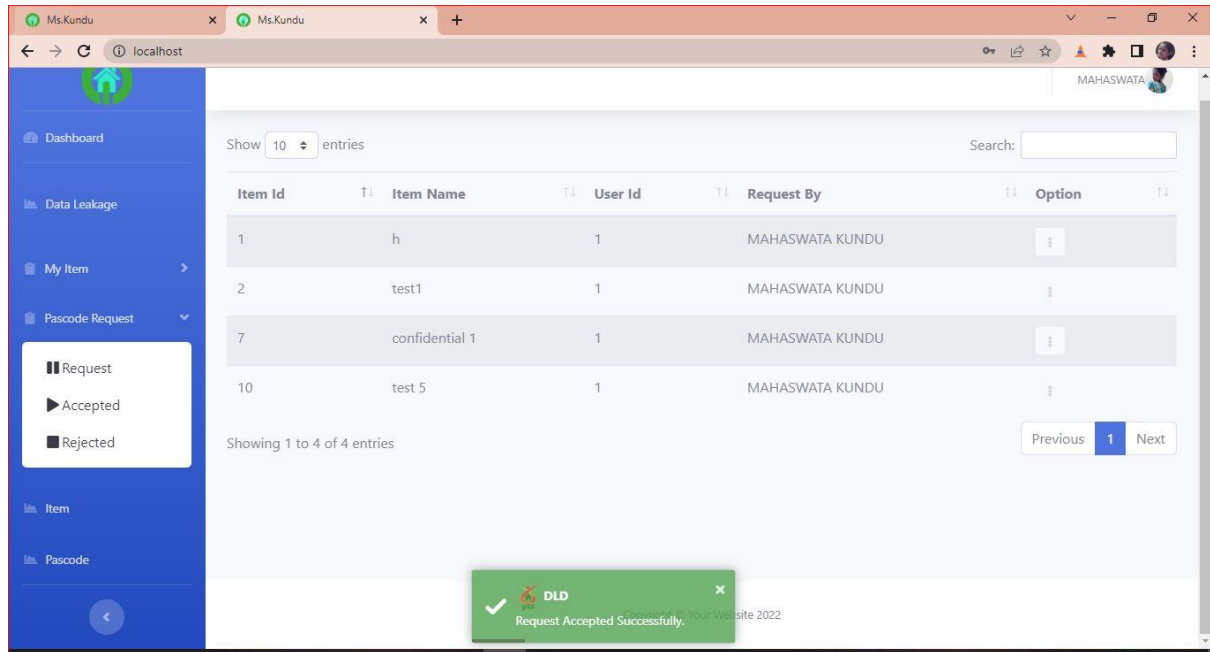


Fig 32: PASSCODE REQUEST ACCEPTED SUCCESSFULLY

This is the figure of **Successfully Accepted Password.**

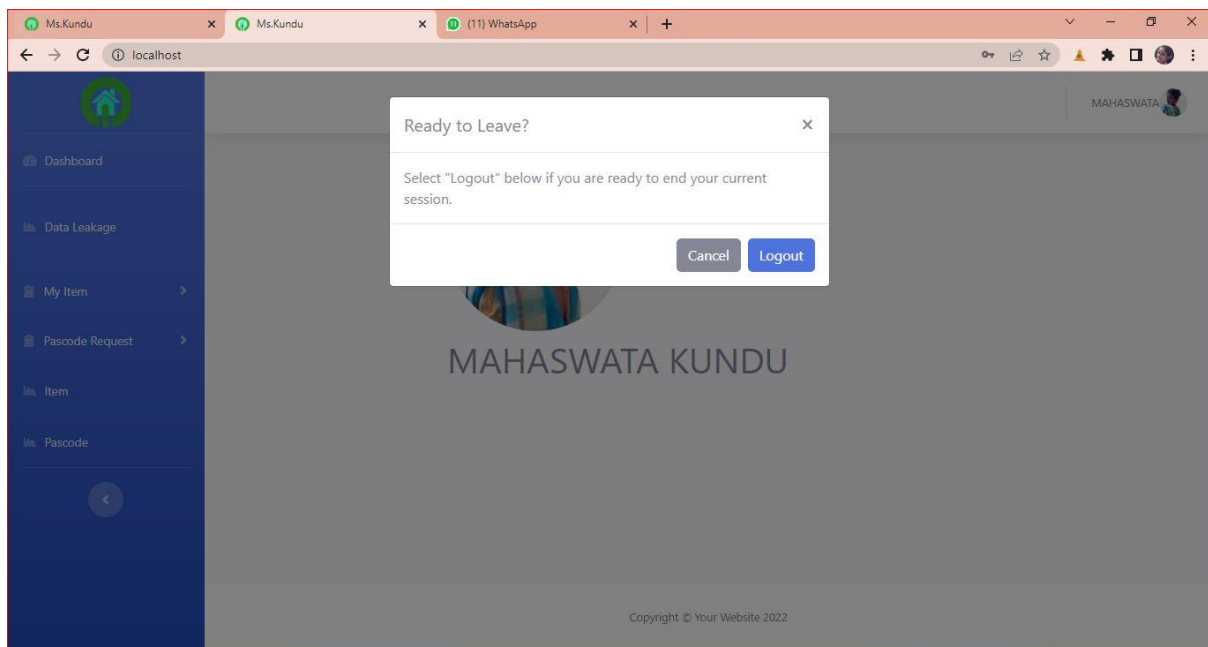
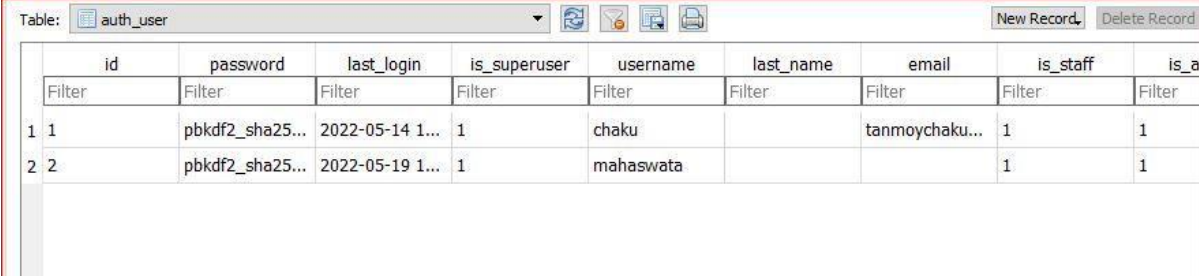


Fig 33: LOGOUT (READY TO LEAVE?)

This is the figure of Logout section which users have logged in, this picture shows its details.

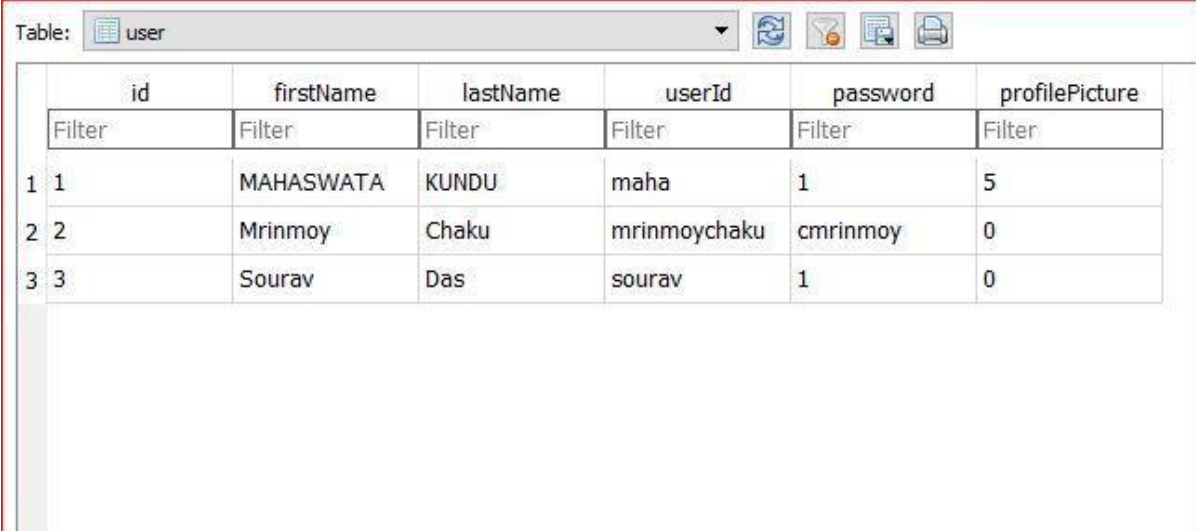
13. DESCRIPTION OF DATABASE



	id	password	last_login	is_superuser	username	last_name	email	is_staff	is_a
1	1	pbkdf2_sha25...	2022-05-14 1...	1	chaku		tanmoychaku...	1	1
2	2	pbkdf2_sha25...	2022-05-19 1...	1	mahaswata			1	1

Fig 34: AUTHORIZED TABLE

Authorization Table means **a table containing information of persons authorized to perform certain functions under this Agreement.**



	id	firstName	lastName	userId	password	profilePicture
1	1	MAHASWATA	KUNDU	maha	1	5
2	2	Mrinmoy	Chaku	mrinmoychaku	cmrinmoy	0
3	3	Sourav	Das	sourav	1	0

Fig 35: USER TABLE

This is a picture of which users have been added to the table.

Table: profilePicture

	id	imgNo	img	userId_id
	Filter	Filter	Filter	Filter
1	1	0	images/pp.jpg	1
2	2	1	images/pp_EeZb5ou.jpg	1
3	3	2	images/pp_yoHMX7f.jpg	1
4	4	3	images/pp_uW6HywF.jpg	1
5	5	4	images/pp_eNM3R8s.jpg	1
6	6	0	images/pp_c2W65af.jpg	3
7	7	5	images/pp_KjUFBfl.jpg	1

Fig 36: PROFILE PICTURE TABLE

This is a picture of which profile pictures have been added to the table.

Table: item

	id	name	discription	path	userId_id	has
	Filter	Filter	Filter	Filter	Filter	Filter
1	1	h		item/1609740...	1	382873
2	2	test1	no descption	item/fig1.psd	1	181371
3	3	first item	normal doco...	item/1609740...	3	591271
4	4	secent item		item/baba.png	3	889347
5	5	thrd item		item/ayan.png	3	363475
6	6	demo1		item/image_2...	3	114774
7	7	confidential 1		item/Name.docx	1	600789
8	8	test 3		item/DS.docx	1	878053
9	9	test 3		item/DS_sCCv...	1	973013
10	10	test 5		item/Name_Pj...	1	418020
11	11	Hilbert Space	Confidential	item/Clusterin...	1	993935

Fig 37: ITEM TABLE

This is a picture of which items have been added to the table.

Table: pascodeRequest				
	id	itemId	userId	valid
	Filter	Filter	Filter	Filter
1	1	1	1	3
2	2	2	1	3
3	3	7	1	1
4	4	6	1	0
5	5	3	1	0
6	6	4	1	0
7	7	8	1	1
8	8	10	1	3

Fig 38: PASSCODE REQUEST TABLE

This is a table of where Passcode Request have been generated.

	id	time	itemId	userId
	Filter	Filter	Filter	Filter
1	1	2022-05-16 13:01:32.262033	6	1

Fig 39: DATA LEAKAGE TABLE

This is a table of where Data Leakage has been detected.

14. TECHNOLOGY USED

- **Single Page Application:** A single-page application is a web application or website that interacts with the user by dynamically rewriting the current web page with new data from the web server, instead of the default method of a web browser loading entire new pages.
- **Language And Framework:**
Python (django), SQL (mySQL), JS (Jquery)
- **Markup Language:** HTML, CSS , Bootstrap
- **Tools:** Pycharm, Visual Studio, MySQL Workbench
- **Browser:** Google Chrome(Developer tools – Network Tab, Console Tab)

15. FUTURE WORK

- Our future work includes the investigation of agent guilt models that capture the leakage scenarios that are not yet considered.
- The extension of our allocation strategies so that they can handle agent requests in an online fashion (the presented strategies assume that there is a fixed set of agents with requests known in advance). Any application does not end with a single version. It can be improved to include new features. Our application is no different from this. The future enhancements that can be made to Data Leakage Detection are:
 - Providing support for other file formats.
 - Creation of a web based GUI for execution of the application.
 - Improving the detection process based on user requirements.
 - Provision of quality or accuracy variance parameter for the user to set.
- We need to check if anyone can access it from another machine or not.
- If someone accesses data from another machine without permission of admin, a mobile notification will be sent to admin.

16. CONCLUSION

From this study we conclude that the data leakage detection system model is very useful as compare to the existing watermarking model. We can provide security to our data during its distribution or transmission and even we can detect if that gets leaked. Thus, using this model security as well as tracking system is developed. Watermarking can just provide security using various algorithms through encryption, whereas this model provides security plus detection technique. Our model is relatively simple, but we believe that it captures the essential trade-offs. The algorithms we have presented implement a variety of data distribution strategies that can improve the distributor's chances of identifying a leaker. We have shown that distributing objects judiciously can make a significant difference in identifying guilty agents, especially in cases where there is large overlap in the data that agents must receive. Our future work includes the investigation of agent guilt models that capture leakage scenarios.

16. REFERENCES

- https://www.researchgate.net/publication/224146568_Data_Leakage_Detection
- <https://www.ijser.org/researchpaper/Data-Leakage-Detection-Using-Cloud-Computing.pdf>
- <https://www.eajournals.org/wp-content/uploads/DATA-LEAKAGE-DETECTION.pdf>
- <http://www.iosrjournals.org/iosr-ice/papers/vol1-issue6/G0163235.pdf>
- https://link.springer.com/chapter/10.1007/978-981-15-1884-3_19

TCP PERFORMANCE ANALYSIS FOR DEVICE TO DEVICE COMMUNICATION

A PROJECT REPORT

Submitted by

DEBDOOT SEN (GCECTB-R16-2012)

BISHWAYAN SAHA (GCECTB-R16-2008)

BUMBA KAR (GCECTB-R16-2009)

*in partial fulfillment for the award of the degree
of*

**BACHELOR OF TECHNOLOGY
IN
INFORMATION TECHNOLOGY**

2019-2020



**GOVERNMENT COLLEGE OF ENGINEERING & CERAMIC
TECHNOLOGY**

73, Abinash Chandra Bannerjee Lane, Kolkata-700010

**TCP PERFORMANCE ANALYSIS FOR
DEVICE TO DEVICE COMMUNICATION**

A PROJECT REPORT

Submitted by

**DEBDOOT SEN (GCECTB-R16-2012)
BISHWAYAN SAHA (GCECTB-R16-2008)
BUMBA KAR (GCECTB-R16-2009)**

in partial fulfillment for the award of the degree

of

BACHELOR OF TECHNOLOGY

IN

INFORMATION TECHNOLOGY

2019-2020



**GOVERNMENT COLLEGE OF ENGINEERING & CERAMIC
TECHNOLOGY**

73, Abinash Chandra Bannerjee Lane, Kolkata - 700010

BONAFIDE CERTIFICATE

Certified that this project report “TCP PERFORMANCE ANALYSIS FOR DEVICE TO DEVICE COMMUNICATION” is a bonafide work of DEBDOOT SEN, BISHWAYAN SAHA and BUMBA KAR who carried out the project work under my supervision.


SIGNATURE

DR. MAUSUMI MAITRA

HEAD OF THE DEPARTMENT

INFORMATION TECHNOLOGY

Government College of Engineering
and Ceramic Technology


SIGNATURE

RITWIK MONDAL

SUPERVISOR

INFORMATION TECHNOLOGY

Government College of Engineering
and Ceramic Technology


SIGNATURE

External Examiner:

ACKNOWLEDGEMENT

We take this opportunity to express our profound gratitude and deep regards to our supervisor RITWIK MONDAL & Head Of the Department (Information Technology) Dr. MOUSUMI MAITRA for their exemplary guidance, monitoring and constant encouragement throughout the course of this project. The blessing, help and guidance given by them time to time, carry us a long way in the journey of life on which we are about to embark.

We are obliged to our project team members & well wishers for the valuable information provided by them in their respective fields. We are grateful for their cooperation during the period of our work.

With gratitude,

Debdoot Sen

DEBDOOT SEN

(Roll No: GCECTB-R16-2012, Reg. No: 161130110050 OF 2016-2017)

Bishwayan Saha

BISHWAYAN SAHA

(Roll No: GCECTB-R16-2008, Reg. No: 161130110046 OF 2016-2017)

Bumba Kar

BUMBA KAR

(Roll No: GCECTB-R16-2009, Reg. No: 161130110047 OF 2016-2017)

TABLE OF CONTENTS

CHAPTER NO.	TITLE	PAGE NO
	ABSTRACT	1
	LIST OF FIGURES	2
	LIST OF SYMBOLS	3
1.	INTRODUCTION	4
2.	LITERATURE REVIEW	6
3.	BACKGROUND	8 - 17
	3.1 EVOLUTION OF GENERATION (G)	8 - 9
	3.2 LONG TERM EVOLUTION (LTE)	9 - 10
	3.3 DEVICE TO DEVICE COMMUNICATION	10 - 12
	3.4 LTE FOR D2D COMMUNICATION	12 - 13
	3.4 MODE SWITCHING	13 - 14
	3.5 TRANSPORT LAYER PROTOCOL (TCP)	15 - 16
	3.6 PERFORANCE OF TCP	16 - 17
4.	METHODOLOGY	18 - 20
5.	EXPERIMENTAL SETUP	21
6.	RESULT & DISCUSSION	22 - 37
7.	CONCLUSION	38
	REFERENCE	39 - 41

ABSTRACT

Device-to-Device (D2D) communication is defined as direct communication between two mobile users without connecting the Base Station (BS) or core network. D2D communication is generally non-transparent to the cellular network and it can occur on the cellular frequencies or on unlicensed spectrum. Direct (or D2D) communications are being investigated in the framework of LTE (Long Term Evolution) network. They allow one to one communications between two end points, under the control of eNodeB, which allocates resources for D2D flow, but does not act as a relay for its traffic. This D2D link can also be used for applications running on TCP. We prepare a simulation of Device to Device communication using OMNeT++ & SimuLTE. Here, we are interested to evaluate the performance of TCP in several scenarios. We show & explain non-intuitive results which arise from TCP protocol mechanisms & compare the existing TCP versions in a dynamic environment, where mode switches can occur.

LIST OF FIGURES

Fig 1: D2D Architecture

Fig 2: Device To Device Communication Classification

Fig 3: Mode switching for single-pair devices

Fig 4: Mode switching for multi-pair device

Fig 5: SingleCell_D2D network

Fig 6: MultiCell_D2D network

Fig 7: Simulation for D2D communication for sending 10 KB

Fig 8: Transmitter Side information for 10KB data sending

Fig 9: Receiver Side information for 10KB data sending

Fig 10: Simulation for D2D communication for sending 10 MB

Fig 11: Transmitter Side information for 10MB data sending

Fig 12: Receiver Side information for 10MB data sending

Fig 13: Simulation model for 10 MB data transmission with reduced window size

Fig 14: Transmitter Side information for 10MB data sending with reduced window size

Fig 15: Receiver Side information for 10MB data sending with reduced window size

Fig 16: Simulation model for one to two D2D communications

Fig 17: Simulation for one to many D2D communications

Fig 18: Fig 18: Flow of events in mode switching

LIST OF SYMBOLS

D2D: Device to Device

LTE: Long Term Evaluation

LTE-A: Long Term Evaluation – Advanced

eNodeB: E-UTRAN Node B / Evolved Node B

UE: User Equipment

BS: Base Station

TCP: Transmission Control Protocol

RTT: Round Trip Time

SYN: Synchronization

ACK: Acknowledgement

OMNeT++: Objective Modular Network Testbed in C++

SimuLTE: Simulator for LTE networks

CQI: Channel Quality Index

DM: Direct Mode

IM: Infrastructure Mode

INTRODUCTION

As telecom operators are struggling to accommodate the existing demand of mobile users, new data intensive applications are emerging in the daily routines of mobile users (e.g., proximity-aware services). Moreover, 4G cellular technologies (LTE-A), which have extremely efficient physical and MAC layer performance, are still lagging behind mobile users' booming data demand. Therefore, researchers are seeking for new paradigms to revolutionize the traditional communication methods of cellular networks. Device- to-Device (D2D) communication is one of such paradigms that appear to be a promising component in next generation cellular technologies.

Device-to-Device (D2D) communication was initially proposed in cellular networks as a new paradigm to enhance network performance. The emergence of new high data rate services such as huge multimedia file distributions, video sharing, gaming, proximity aware social networking introduced new use-cases for D2D communication in cellular networks. In these cases, the users could potentially be in the range for D2D communications which greatly increase the spectral efficiency of the network & reduced communication delay.

Device-to-device (D2D) communication is expected to play a significant role in upcoming cellular networks as it promises ultra-low latency for communication among users. This new mode may operate in licensed or unlicensed spectrum. It is a novel addition to the traditional cellular communication paradigm. Its benefits are, however, accompanied by many technical and business issues that must be resolved before integrating it into the cellular ecosystem.

It may appear that there is nothing new about device-to-device communication as WiFi and Bluetooth have supported short-range wireless communication of this sort for many years. However, these technologies have shortcomings that would undermine their ability to support mass market deployment of proximity-based services. WiFi and Bluetooth rely on manual pairing of devices to enable communication, which would be a serious stumbling block for autonomous services. Also, the security features of WiFi and Bluetooth are much less robust than those used in public cellular systems. Integrating D2D into the LTE-Advanced system offers the prospect of a spectrum-efficient, energy-efficient and secure solution for proximity discovery and device-to-device communication, which would benefit from the LTE ecosystem of spectrum, mobile devices and network equipment.

In D2D communication, the data is transferred between transmitter and receiver using Transport Layer Protocol. Generally, TCP is used in place of UDP because TCP provides flow control, congestion control & sequenced delivery of data stream. Practically, different types of TCP (based upon their congestion control mechanism) are in use in real world. As various types of TCP have different congestion control technique, performance parameter values also changes for same sized data segment delivery.

In any communication system, how much time it takes to transmit a packet of certain size through a certain medium defines the efficiency of that system. During transmission, different parameters play its role like link capacity of the medium, window size of the transmitter, channel quality and amount of noise present in it, occurrence of interference etc. These parameters can affect the round trip time (time taken from sending the message to receiving the message and time taken to receive the corresponding acknowledgement by sender) positively or negatively. We want to observe those changes so that we can do performance analysis of TCP on D2D communication.

LITERATURE SURVEY

Device-to-device (D2D) communication is expected to play a significant role in upcoming cellular networks as it promises ultra-low latency for communication among users. As discussed in “*An overview of device-to-device communication in cellular networks*” Udit NarayanaKar, Debarshi KumarSanyal^[1]. It is a novel addition to the traditional cellular communication paradigm. Its benefits are, however, accompanied by many technical and business issues that must be resolved before integrating it into the cellular ecosystem. The use of D2D communications has the capability of increasing the throughput of wireless video networks by orders of magnitude. When the transmission of the most popular files can be offloaded to D2D, which has high frequency reuse and thus high area spectral efficiency, the BS is freed up for providing rarely requested video files as well as non-video data(*Base-Station Assisted Device-to-Device Communications for High-Throughput Wireless Video Networks*, Negin GolrezaeiParisa MansourifardAndreas F. Molisch)^[2].

Now ensuring a seamless connection when users are moving across radio cells is essential to guarantee a high communication quality. So the performance of TCP during the handover in a Long Term Evolution (LTE) network is very crucial(*Improving TCP Performance During the Intra LTE Handover*, D. Pacifico, M. Pacifico, C. Fischione, H. Hjalrmasson, K. H. Johansson)^[3].

Also D2D communication can be set up between two UE’s within certain vicinity. But if those moving users are out of the range then for maintaining the connection they have to rely on the existing cellular network & thus mode switching takes place. The research paper “*Effect of Mode Switching on TCP Short flows During D2D Communication in LTE-A Networks*” by Abhijan Bhattacharyya, Bhaskar Sardar, Debashis Saha^[4] helped a lot regarding the mode switching scenarios in the communication domain and how it is connected with TCP parameters. Following this, in our work we want to analyze those performance parameters for different environmental setup. Although we are mainly interested in the time taken to receive a whole data segment as speedy delivery is the main reason behind D2D communication’s idea.

As stated in *“Performance evaluation of TCP-based traffic over direct communications in LTE-Advanced”* by Giovanni Nardini, Giovanni Stea, Antonio Virdis^[5], RTT is affected by protocol mechanisms within the LTE-A stack, like RAC and bandwidth stealing. Simulation results showed that D2D communication allows moderate reduction of the RTT. Surprisingly traditional infrastructure communications may even achieve better performance when the sending rate of the TCP flow is high.

Following our project goal, we first have to set up the simulation environment for D2D communication in LTE network and measure the TCP parameters. We got a very clear idea about the software to be used in the research papers *“Simulating device to device communication s in OMNeT++ with SimuLTE: scenarios and configurations ”* by Giovanni Nardini, Antonio Vardis & Giovanni Stea^[6] & *“Simulating LTE/LTE-Advanced networks with SimuLTE ”* by Giovanni Nardini, Antonio Vardis & Giovanni Stea^[7]. These papers gives us the idea how SimuLTE enables system level simulations off LTE networks within OMNeT++ & how SimuLTE can be employed to simulate both one-to-one & one-to-many D2D communications, so that the latter can be exploited as a new communication opportunity in several research fields.

Besides the aforesaid mentioned research papers, this project also involves the study of other reliable and informative research papers as mentioned hereunder:

- “Architecture and Protocols for LTE-based Device to Device Communication”.Balaji Raghothaman, Eric Deng, Ravikumar Pragada, Gregory Sternberg, Tao Deng, Kiran Vanganuru
- “A Survey on Device-to- Device Communication in Cellular Networks”Arash Asadi, Student Member, IEEE, Qing Wang, Student Member, IEEE, and Vincenzo Mancuso, Member, IEEE
- “Opportunities and threats from LTE Device-to-Device (D2D) communication”, Alastair Brydon, 28 february 2014

BACKGROUND

Wireless communication technology inside cell/mobile phones and other mobile devices has evolved over several decades. Starting with the then revolutionary 1G (referred to as the earliest form of voice only network) all the way to the 4G of today and the 5G of the near future.

The word Wireless in dictionary is defined as “having no wires”. In networking terminology, wireless is the term used to describe any computer network where there is no physical wired connection between sender and receiver, but rather the network is connected by radio waves and or microwaves to maintain communication.

Mobile phones generally use a wireless telecommunication system which was first released in the 1980's. Since then there has been a development of Telecom Generations (G) to the present day 4G and upcoming 5G in development progress.

Evolution of Generation (G) in wireless communication:

- **1G Technology:** The Mobile Wireless communication was possible only by the introduction of 1G Technology. It basically was a network with only voice call capabilities and only got the name 1G after 2G was put to use. Even after being the first wireless telecommunication technology, 1G technology wasn't fully digital. Data transmissions were done in analog form at 150 Mhz and above frequency of radio waves. This was the biggest drawback of 1G technology.
- **2G Technology:** 2G or second generation of wireless technology utilised digital signals for voice transmission. Fundamental concentrate of this technology was on digital signals and gave services to convey content and provide picture messages at low speed (in kbps).
- **3G Technology:** 3G networks were introduced in 1998 and stand for the next generation in this series; the third-generation. This was a big

revolution in terms of technological advancement for network and data transmission. 3G had its speed capabilities of up to 2 mbps. It enabled mobile devices to provide faster communication, send/receive large emails and texts, provide fast web browsing, video streaming and more security amongst others. 3G utilises packet switching data transmission rather than circuit switching. Data is broken down into small pieces or packets and then sent to the destination. Using this method of transmission greatly increases the speed, allowing one to send data through multiple channels in parallel rather than one channel in series.

- **4G Technology:** With evolving technology, speed of 3G became insufficient. The next generation came around 2010 in two categories: 4G & 4G LTE (referred to as just LTE). This generation drastically improved data transfer speeds. The 4G standard sets several requirements for mobile networks including mandating the use of Internet Protocol (IP) for data traffic and minimum data rates of 100 Mbps which was a huge jump from the 2 mbps for 3G.

4G LTE is a light version of 4G network. It is a major technical improvement over 3G but not technically 4G. Most cellular carriers now advertise their networks as 4G LTE. Though average customer can't tell difference between 4G and 4G LTE because download and upload speeds are almost same.

LONG TERM EVALUATION (LTE):

- Long Time Evolution (LTE) is a standard for 4G wireless broadband technology that offers increased network capacity & speed to mobile devices users.
- In 2004, a reputed network operator in Japan viz. NTT DoCoMo, proposed making LTE as the next international standard for wireless broadband. Two years later, it was commercially tested as a live demonstration.
- LTE offers high peak data transfer rates- up to 100MBPS as download speed & 30MBPS as upload speed. As a result, users can enjoy improved

streaming, downloads & even uploads. Though globally, the average LTE download speed is 13-15 MBPS.

- It also provides reduced latency, scalable bandwidth. Further developments could yield peak throughput on the order of 300MBPS.
- LTE also connects customers with services in real time. Users can talk to others without experiencing any lag or stutters.

There is another version of LTE called LTE Advanced (LTE-A) which improves the current standard by providing upload & download speed 3 times faster than standard LTE. The main new functionalities introduced in LTE-Advanced are Carrier Aggregation (CA) & Multi Antenna Techniques (using MIMO technology).

CA allows mobile operators to combine two or more LTE carriers into single data channel to increase the capacity of the network and the data rates by exploiting fragmented spectrum allocations.

Multi-input Multi-output (MIMO) technology is the use of multiple receive and transmit antennas to establish a communications link between two, or more, communications systems with greater throughput than would be possible with a single antenna system.

DEVICE TO DEVICE (D2D) COMMUNICATION:

Device-to-Device (D2D) communication in cellular networks is defined as direct communication between two mobile users without traversing the Base Station (BS) or core network. D2D communication is generally non-transparent to the cellular network.

As newer and more demanding applications arise and subscriber base increases exponentially, there is an urgent requirement for more novel techniques to boost data rates and reduce latency. *D2D communication* is a new paradigm in cellular networks. It allows user equipments (UEs) in close proximity to communicate using a direct link rather than having their radio signal travel all the way through the base station (BS) or the core network. One of its main benefits is the ultra-low latency in communication due to a shorter signal traversal path. Various short-range wireless technologies like LTE can be

used to enable D2D communication. D2D connectivity will make operators more flexible in terms of offloading traffic from the core network, increase spectral efficiency and reduce the energy and the cost per bit.

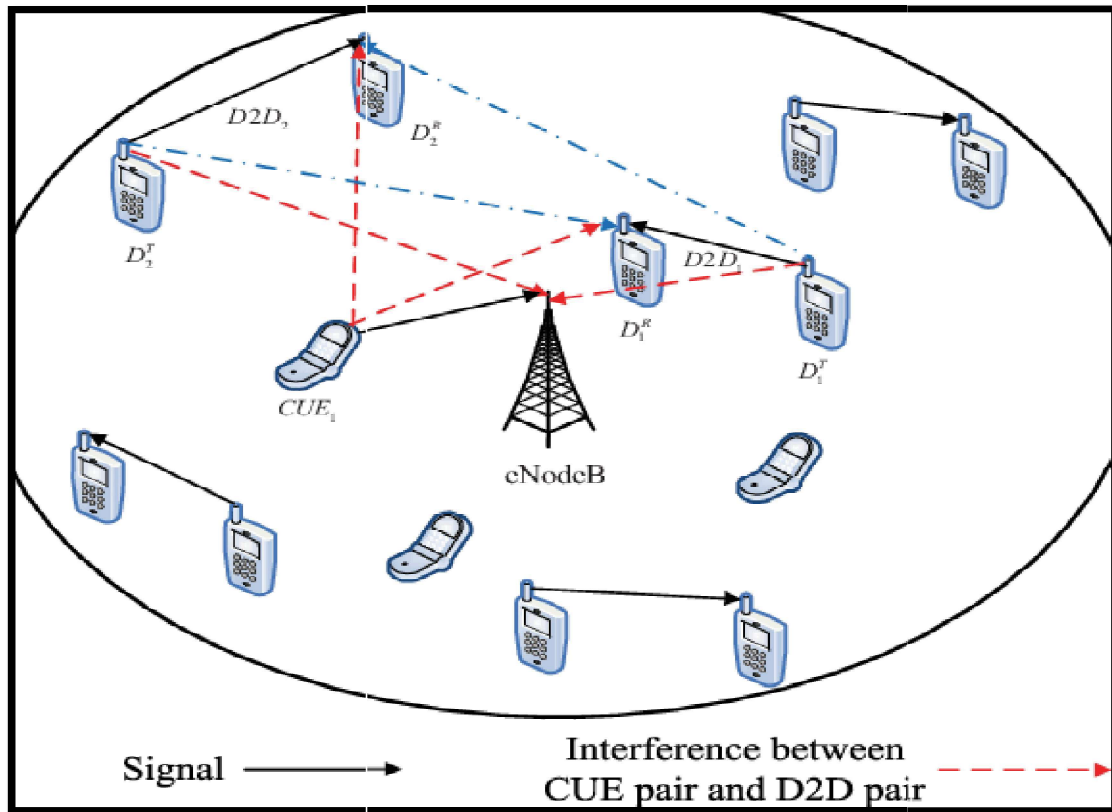


Fig 1 : D2D Architecture

Nevertheless, the advantages of D2D communications are not only limited to low latency. In addition, D2D communications can potentially improve throughput, enhance spectral efficiency, energy efficiency, delay, and fairness.

Taxonomy:

In this section, we categorize the available literature on D2D communication in cellular networks based on the spectrum in which D2D communication occurs. In the following subsection we provide a formal definition for each category and sub- category.

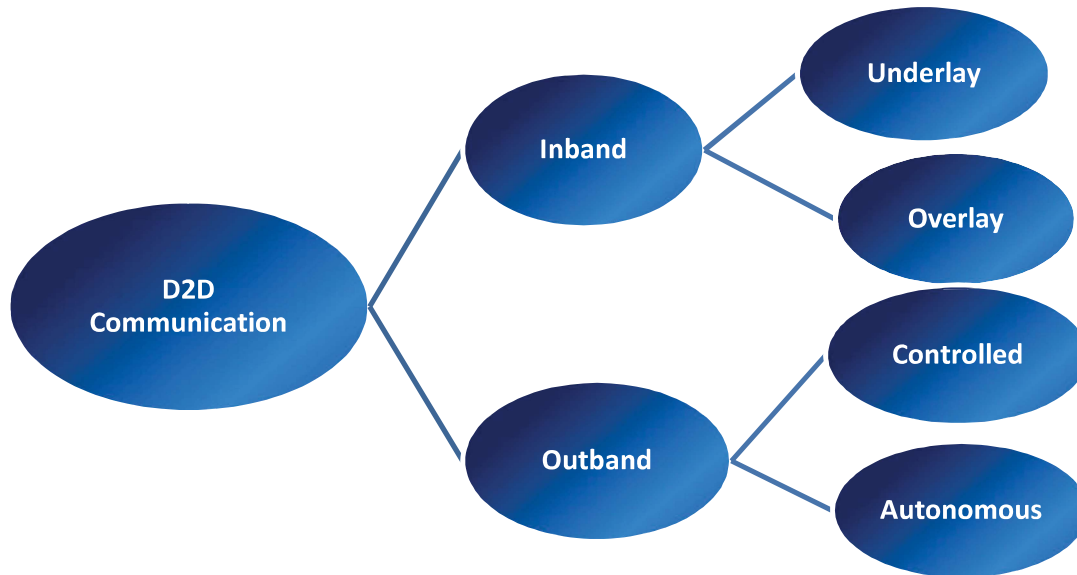


Fig 2: Device To Device Communication Classification

Inband D2D: The motivation for choosing inband communication is usually the high control over cellular (i.e., licensed) spectrum. Inband communication can be further divided into underlay and overlay categories. In underlay D2D communication, cellular and D2D communications share the same radio resources. In contrast, D2D links in overlay communication are given dedicated cellular resources. Inband D2D can improve the spectrum efficiency of cellular networks by reusing spectrum resources (i.e., underlay) or allocating dedicated cellular resources to D2D users that accommodates direct connection between the transmitter and the receiver (i.e., overlay).

Outband D2D: Here the D2D links exploit unlicensed spectrum. The motivation behind using outband D2D communication is to eliminate the interference issue between D2D and cellular link. Using unlicensed spectrum requires an extra interface and usually adopts other wireless technologies such as WiFi Direct or Bluetooth. Some of the work on outband D2D to give the control of the second interface/technology to the cellular network (i.e., controlled). In contrast, others propose to keep cellular communications controlled and leave the D2D communications to the users (i.e., autonomous).

LTE for D2D Communication:

There are various short range wireless technologies such as Bluetooth, Wi-Fi direct, LTE (defined by 3GPP) which can be used to enable D2D

communication. Though among them, LTE provides the best data rate and range.

- Integrating D2D into the LTE-Advanced system offers the prospect of a spectrum-efficient, energy-efficient and secure solution for proximity discovery and device-to-device communication.

- Also it provides the opportunity to achieve energy-efficient device discovery, for example by avoiding the need to scan for other wireless technologies, by synchronizing the transmission and reception of discovery signals to minimize their duty cycle and by waking application software only when relevant devices are found in the local area.

- D2D can take advantage of the key generation and distribution mechanisms already available in LTE, to achieve high levels of security.

That's why LTE is the main cellular system that is expected to adopt the D2D communication. Currently a lot of effort is being made by 3GPP Internet introducing D2D communication in the next amendments of the LTE system.

MODE SWITCHING:

Device-to-device (D2D) communication enables nearby user equipments (UEs) to communicate directly without passing it through a base station (BS). When UEs wish to communicate over direct link it is required to know the channel condition of its D2D link and its cellular link to select a link providing the best quality of service, so called mode selection. UEs participating D2D communication need to conduct measurement over its UE-UE link and its eNB-UE link as well, and BS makes decision on mode switching based on the measurement report of UE.

Three modes of communication:

- DIRECT MODE
- CELLULAR MODE
- RELAY MODE

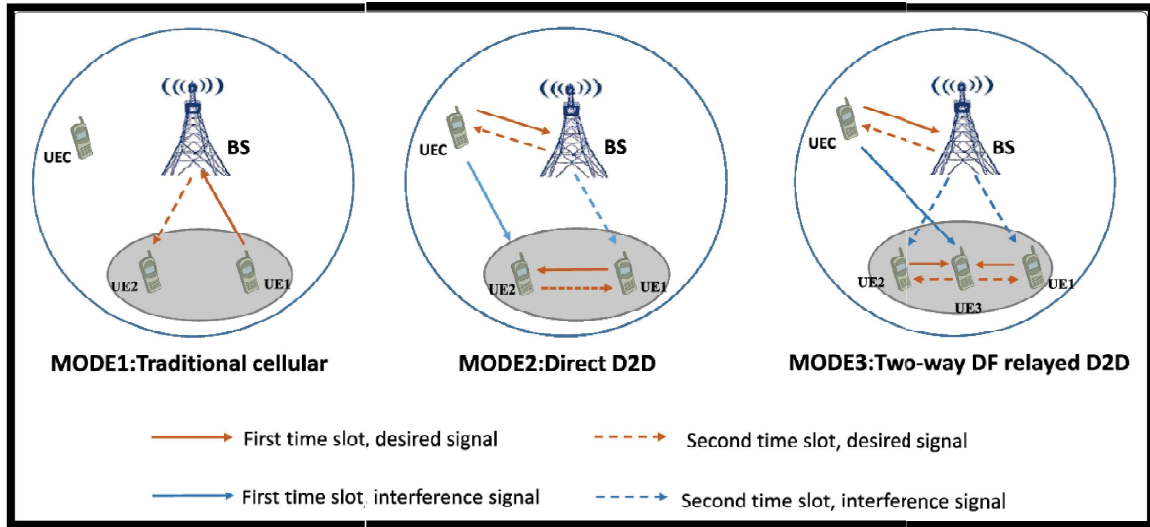


Fig 3: Mode switching for single-pair devices

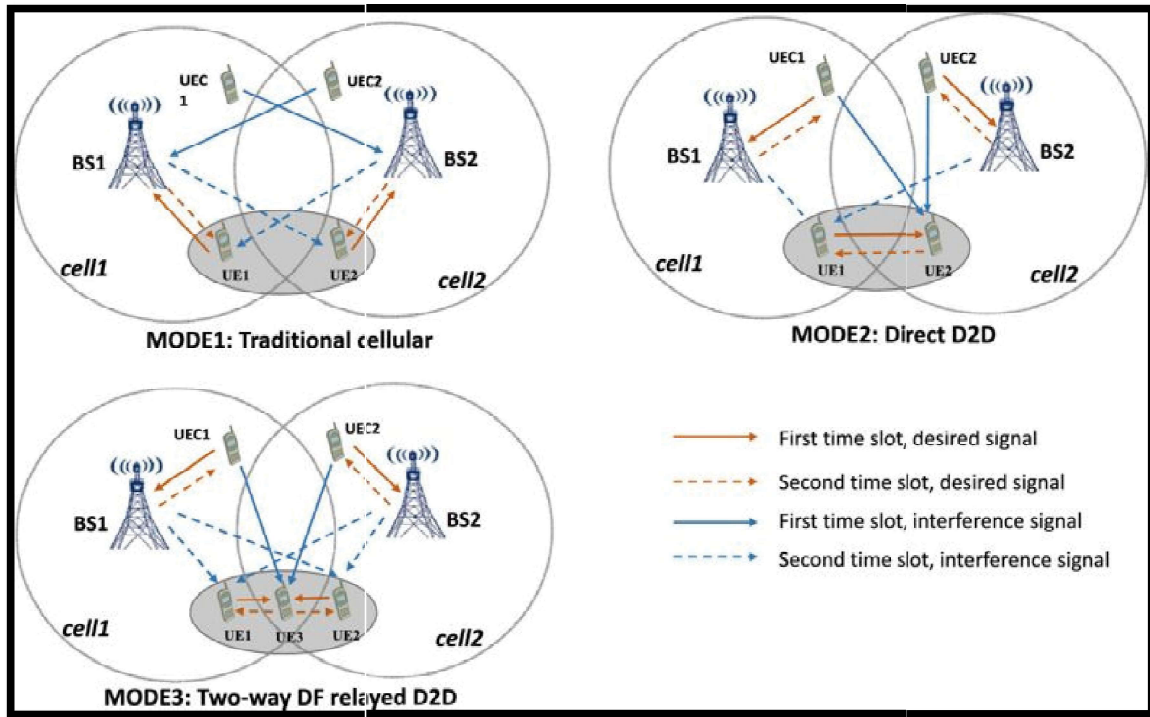


Fig 4: Mode Switching for multi-pair device

TRANSPORT LAYER PROTOCOL:

Transmission Control Protocol is a connection-oriented, reliable protocol. TCP explicitly defines connection establishment, data transfer & connection tear down phases to provide a connection oriented service. To achieve this goal, TCP provides error detection, retransmission of lost or corrupted packets, cumulative & selective acknowledgements & timers. TCP is the most common transport layer protocol in the Internet.

TCP provides following services:

- Process to Process Communication
- Stream Delivery Service
- Sequencing using segment number
- Full-Duplex Communication

TCP can be classified on the basis of how it handles congestion in the channel specifically when it comes to receiving of 3 duplicate acknowledgements.

1. **TAHO TCP** : It uses two different algorithms in their congestion policy: slow start & congestion avoidance. It treats time out & 3 ACKs(causes of congestion) in the same way. When connection is established, TCP starts slow start algorithm & sets threshold value to a pre-assigned value. Each time an ACK arrives, the congestion window is incremented by 1. If congestion is detected, it immediately interrupts & restarts a new slow start algorithm by limiting the threshold value & setting congestion window to 1.
2. **RENO TCP** : This type of TCP treats time out & 3 ACKs differently. If a time out occurs, TCP moves to slow start state. On the other hand, if 3 duplicate ACKs arrive, TCP moves to fast recovery state. The fast recovery state is somewhere between Slow start & congestion-avoidance states.
3. **NEW RENO TCP** : A later version of TCP, called NEW RENO TCP, made an extra optimization on the RENO TCP. In this version, TCP checks if more than one segment is lost in the current window when three duplicate

ACKs arrives. When it receives 3 duplicate ACKs , it retransmits the lost segment until the new ACK arrives.

4. **VEGAS TCP** : TCP Vegas detects congestion at an incipient stage based on increasing Round-Trip Time (RTT) values of the packets in the connection unlike other flavours such as Reno, New Reno, etc., which detect congestion only after it has actually happened via packet loss. The algorithm depends heavily on accurate calculation of the Base RTT value. If it is too small then throughput of the connection will be less than the bandwidth available while if the value is too large then it will overrun the connection.
5. **CUBIC TCP** : Cubic TCP is an implementation with an optimized congestion control algorithm for high bandwidth networks with high latency. The window is a cubic function of time since the last congestion event. Cubic doesn't rely on the receipt of ACK's to increase the window size. It is dependent only on the last congestion event. Cubic allows for more fairness between flows since the window growth is independent of RTT.

PERFORMANCE OF TCP:

The performance of TCP will be measured in terms of some factors :

1. **Round Trip Time (RTT)** is the length of time it takes for a signal to be sent plus the length of time it takes for an acknowledgement of that signal to be received. This time therefore consists of the propagation times between the two points of signal.

RTT depends upon following factors:

- Data rate transfer of source's internet connection.
- The nature of transmission medium.
- The physical distance & no. of nodes between source & destination.
- The amount of traffic on the LAN to which end user is connected.

RTT determines how fast TCP connection (3 way handshaking) is established between client & server. So low RTT denotes fast transmission of

data whereas high RTT value means there is delay in the network and stream delivery is also slow.

2. **The short duration of connection** gives TCP limited opportunity to probe the network & adapt its congestion control parameters to that network.
3. **Transmitter and receiver window size** also determines the speed of segment delivery. Different TCP implements different functions to increase window size for speedy delivery and congestion control.
4. **The quality of channel** through which transmission of data occurs determines the speed. Some channels can be noisy and may interfere with the segments and corrupt them while in some channels connection is established in no time and data is transferred without any occurrence of error. The Channel Quality Index (CQI) generally defines the quality of channel.

METHODOLOGY

Our main objective is to prepare a simulation for Device To Device communication to see the performance analysis of TCP. We arrange all the software for this project work listed below:

- OMNeT++
- INET Framework
- SimuLTE

OMNeT++ (*Objective Modular Network Testbed in C++*) is an object-oriented, modular, discrete event network simulation framework. It has a generic architecture, so it can be (and has been) used in various problem domains:

- Modelling of wired and wireless communication networks
- Protocol modelling
- Modelling of queuing networks
- Modelling of multiprocessors and other distributed hardware systems
- Validating of hardware architectures
- Evaluating performance aspects of complex software systems
- In general, modelling and simulation of any system where the discrete event approach is suitable, and can be conveniently mapped into entities communicating by exchanging messages.

OMNeT++ itself is not a simulator of anything concrete, but rather provides infrastructure and tools for writing simulations. One of the fundamental ingredients of this infrastructure is component architecture for simulation models. Models are assembled from reusable components termed modules. Well-written modules are truly reusable, and can be combined in various ways.

INET Framework is an open-source model library for the OMNeT++ simulation environment. It provides protocols, agents and other models for researchers and students working with communication networks. INET is especially useful when designing and validating new protocols, or exploring new or exotic scenarios.

INET supports a wide class of communication networks, including wired, wireless, mobile, ad hoc and sensor networks. It contains models for the Internet stack (TCP, UDP, IPv4, IPv6, OSPF, BGP, etc.), link layer protocols (Ethernet, PPP, IEEE 802.11, various sensor MAC protocols, etc) and many other protocols and components. It also provides support for node mobility, advanced visualization, network emulation and more.

SimuLTE is an innovative simulation tool enabling complex system level performance-evaluation of LTE and LTE Advanced networks. SimuLTE is an open source project building on top of OMNeT++ and INET Framework.

SimuLTE can be used on any system compatible with OMNeT++ (Windows, Linux, or Mac OS X). SimuLTE requires:

- OMNeT++ v5.0
- INET-Framework v3.4

OMNeT++ uses NED files to define components and to assemble them into larger units like networks. We start implementing our model by adding a NED file. Once created, the file can be edited in the *Editor area* of the OMNeT++ IDE. The OMNeT++ IDE's NED editor has two modes, Design and Source; In Design mode, the topology can be edited graphically, using the mouse and the palette on the right. In Source mode, the NED source code can be directly edited as text. Changes done in one mode will be immediately reflected in the other.

To be able to run the simulation, we need to create an omnetpp.ini file. omnetpp.ini tells the simulation program which network we want to simulate (as NED files may contain several networks), we can pass parameters to the model, explicitly specify seeds for the random number

generators, etc. parameters to the model, explicitly specify seeds for the random number generators, etc. A new omnetpp.ini file will open in an Inifile Editor. As the NED Editor, the Inifile Editor also has two modes, Form and Source, which edit the same content. The former is more suitable for configuring the simulation kernel, and the latter for entering module parameters.

As our project is on performance analysis, our main focus will be on the parameters that can affect the TCP performances. These parameters could be different data segment size, distance between two UE's, speed of the network, quality of the transmission medium, window frame size etc. Our main concern is the time taken to deliver the segments in different environment as data delivery speed is the prime reason to implement D2D communication.

After setting the network, we perform a test run for our network model & perform our pre-planned programs in omnetpp.ini file.

EXPERIMENTAL SETUP

Here we describe how we install & configure OMNeT++ for our project work.

OMNeT++ is available for following environments

- Windows 7 & above(32 bit or 64 bit)
- Mac OS
- Linux based OS(32 bit or 64 bit)

We choose Ubuntu 16.04 as our OS environment & describe the installation process for Linux only.

OMNeT++ requires several packages to be installed on the computer. These packages include the C++ compiler (gcc or clang), several other libraries and programs. Generally, we need superuser permissions to install packages. Not all packages are available from software repositories; some (optional) ones need to be downloaded separately from their web sites, and installed manually.

Now we need to import the INET framework and SimuLTE (already downloaded in the user's computer).

After that we create a new project and create an omnet.ini file. Next, in that file, according to our simulation requirement, we import network (.ned) files defined in the INET framework. Finally, the required source code is written and it is run.

RESULT & DISCUSSION

In performance analysis, we consider the mobility pattern for user equipments to be linear. Though later, we can opt for different mobility pattern for having a practical approach. But here in our project, mobility pattern is not a big concern. We want to see how much time is taken for a data segment of varying size to be sent to the receiver within a pre specified time period with pre defined CQI. For this analysis, we precede with best CQI value i.e. 7.

The network upon which we build our simulation is already defined in the imported INET framework. There are a lot of network files corresponding to different simulation situations. e.g. SingelCell_D2D.ned, Multicell_D2D.ned etc

In a single cell network, only one base station is present and within its range, all the devices will be communicating to each other and base station will supervise the whole communication scenario if D2D mode is selected. Whereas in multi cell network scenario, any device can be present within the range of any base station or it may be the case that a device is in the coverage area of more than one base stations & it may connect to any of them, depending upon the quality control value of the network and other environmental factors.

This .ned files are imported in the omnetpp.ini files to be used in the simulations. The source code written for a certain simulation will make use of the parameters and modules of those .ned files. The figure defining the architecture of SingleCell & MultiCell network is given below.

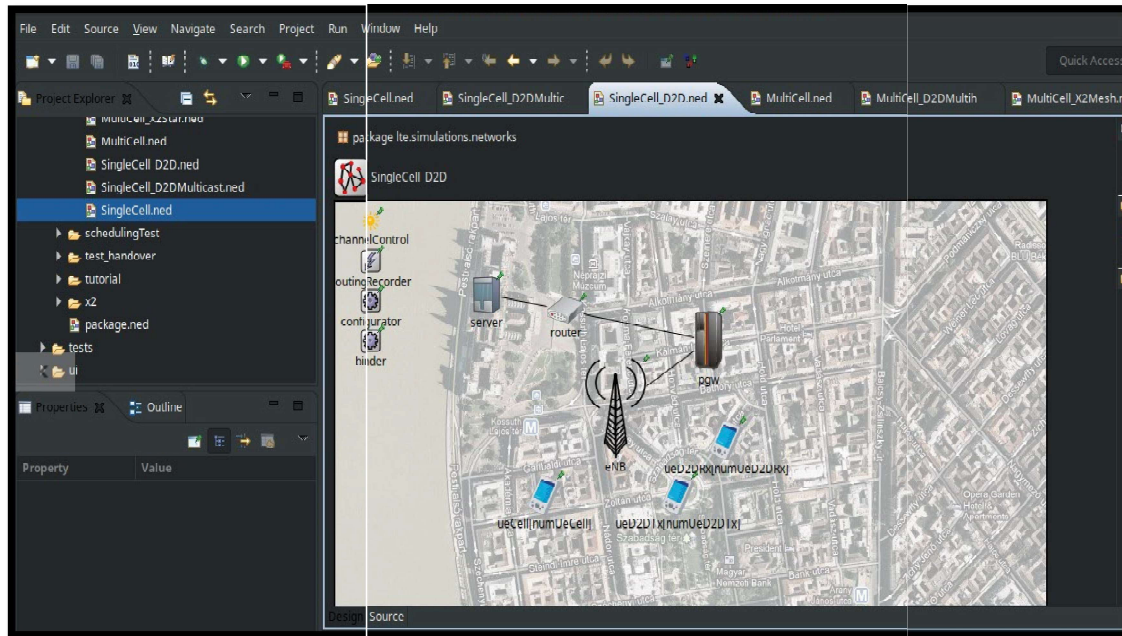


Fig 5: SingleCell_D2D network

In Fig 5, the only base station is represented as eNB and the three user devices are represented as ueD2D Tx[] or ueD2DRx[] depending upon whether it is a transmitting device or receiving device.

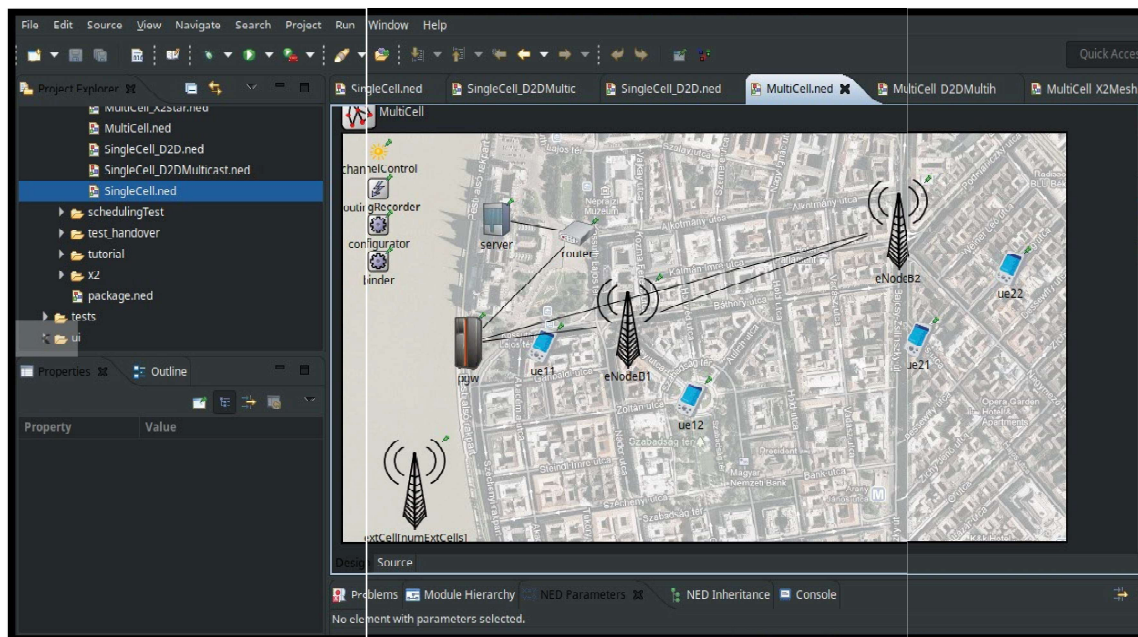


Fig 6: MultiCell_D2D network

In Fig 6, the three base station are represented as eNodeB1, eNodeB2, eNodeB3 respectively & four user devices are placed there viz. ue11 & ue12 (which is under the coverage area of eNodeB1) & ue21 & ue22 (which is under the coverage area of eNodeB2).

Before coming to actual experiments, we provide some information hereunder, about the simulation output window to better understand what different packet names signifies, how connections are established, at what time the transmitter completes sending bytes and receiver accepts all the transmitted bytes etc.

Event Log Information: Here we can observe how the connection is setup for data transmission and acknowledgement is sent as a feedback using some predefined packets. The different types of predefined packets are describes below:

1. **Air Frame Packet :** This packet format is used to send a packet from the physical layer to the channel. All other physical layers that can 'hear' this packet can evaluate noise, interference etc. from the information contained in this packet (especially the signal). When a host transmits an AirFrame, it will send a copy to every other host within interference range. Each host individually evaluates the physical layer model, and decides (based on the signal-noise ratio) whether the frame is receivable. If not, the AirFrame is discarded. Then the frame gets decapsulated from the AirFrame, and the 16-byte MAC address is checked. If the MAC address doesn't match (and it's not broadcast etc), the frame is discarded. Otherwise the IPDatagram gets decapsulated from it and sent up to the IP layer.

2. **H-ARQ Feedback Packet :** D2D communications are acknowledged at the MAC layer, i.e., the receiver sends H-ARQ feedbacks (ACKs/NACKs) upon reception of MAC header & payload. While there is no standard prescription on how to do this, our understanding is that ACKs/NACKs are needed at both the transmitting endpoint (another UE) and the scheduling entity (the eNB), since both need to take action according to the feedback.

In the 'Event Log' of the simulation output we have the detailed scene of how the packet is sent from sender to receiver. Under the heads '**Src/Dist**' and '**Packet Name**', we see some messages which defines how the connection is established.

- '**ueD2DTx [0] → eNodeB**' with corresponding message '**feedback_pkt**' means the transmitter trying to set up a connection with the base station by exchanging feedback packet.

- When '**ueD2DTx [0] → ueD2DRx [0]**' appears under '**Src/Dist**' with message '**Air Frame_pkt**', it means the packet has transferred from the transmitter to the receiver under the supervision of eNodeB.

- '**ueD2DRx [0] → ueD2DTx [0]**' under the head '**Src/Dist**' with message '**H-ARQ Feedback_pkt**' under '**Packet Name**' head states that receiver sends the feedback message back to transmitter telling that previous packet has successfully been received and it is waiting for the next packet to be sent.

After data transmission:

From transmitter side ‘bytesSent’ = 10240

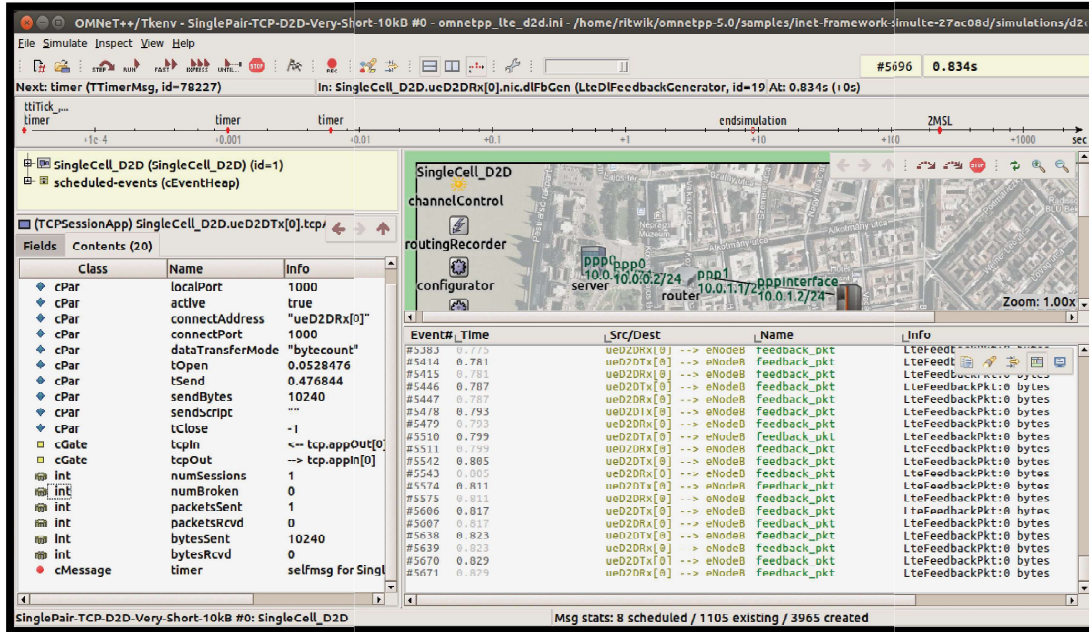


Fig 8: Transmitter Side information for 10KB data sending

From Receiver Side bytesRcvd = 10240

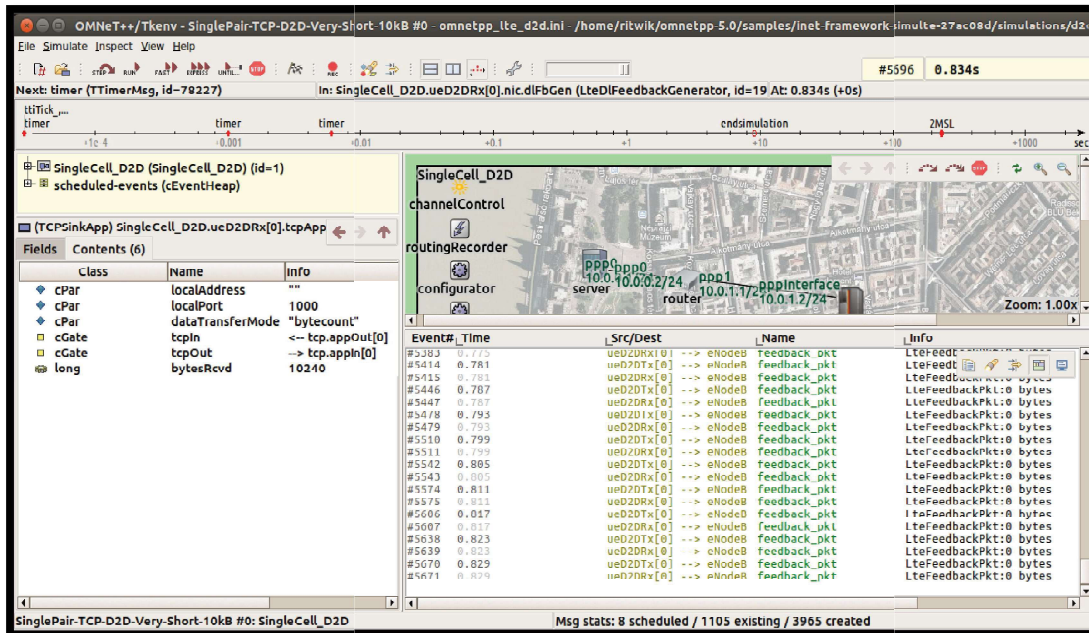


Fig 9: Receiver Side information for 10KB data sending

Observation & Inference: In the omnetpp.ini file for this particular program we adjust the simulation time as 10 seconds. Though in the simulation output time taken between two UE's to complete transmission is 0.834 seconds.

It is interesting to note that the 10 KB data is not sent to receiver as a whole rather it is fragmented into segments and sent. Hence, we can observe in the event log that Air-Frame packet and feedback packets were exchanged between them several times until the whole 10KB data is sent.

Experiment 2:

SinglePair-TCP-D2D-Short-10MB

Before commencement of simulation:

Window size: 100 x 536 bytes

CQI value = 7

Distance between two UEs: 25m

Data Size = 10MB

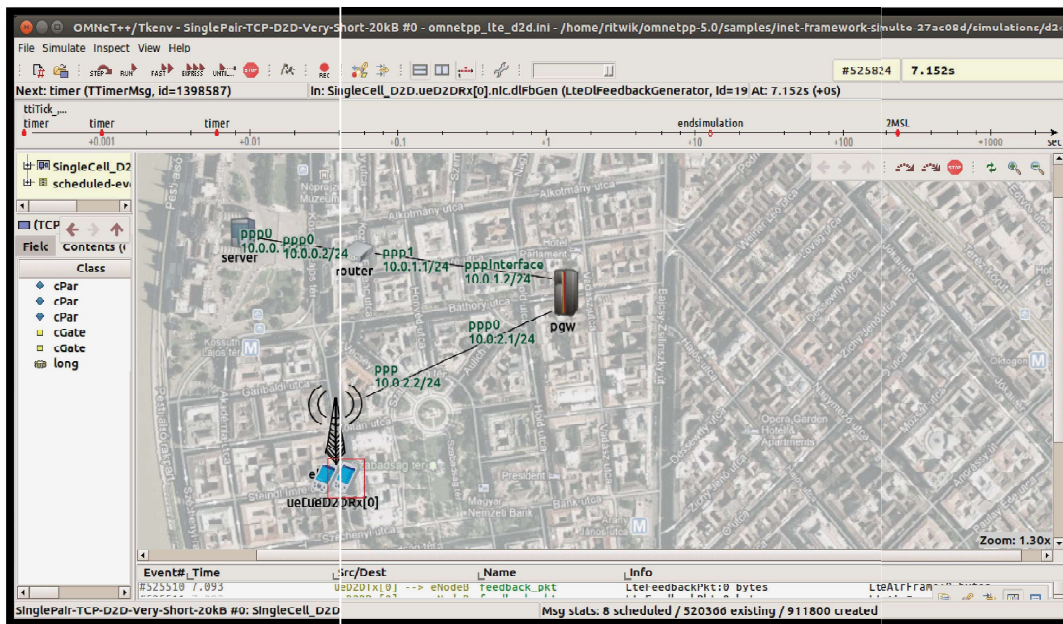


Fig 10: Simulation for D2D communication for sending 10 MB

After data transmission:

From transmitter side ‘bytesSent’ = 10485760

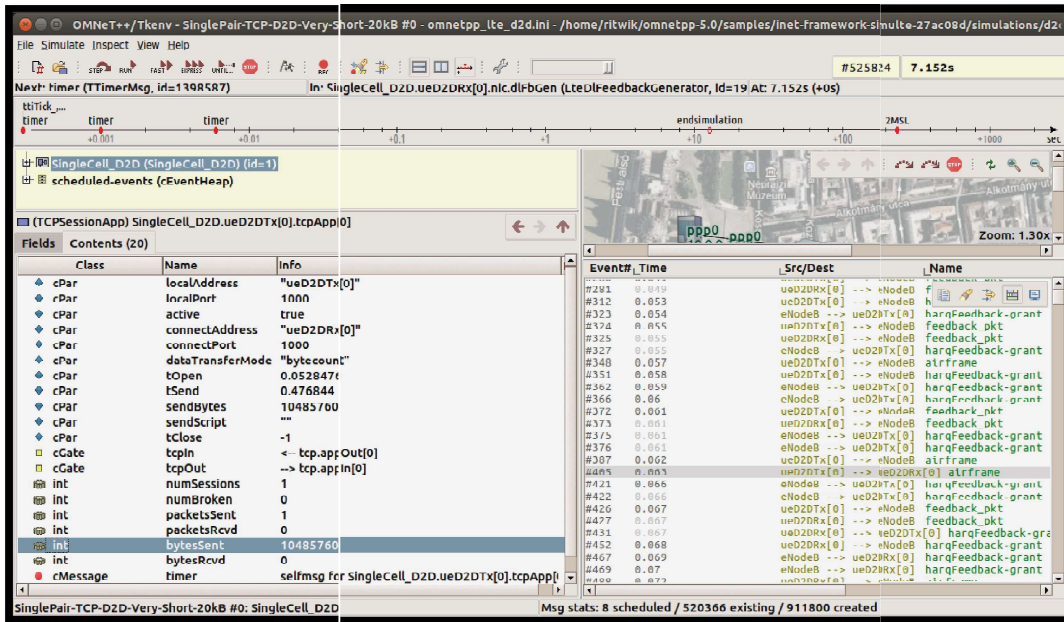


Fig 11: Transmitter Side information for 10MB data sending

From receiver side ‘bytesRcvd’ = 10485760

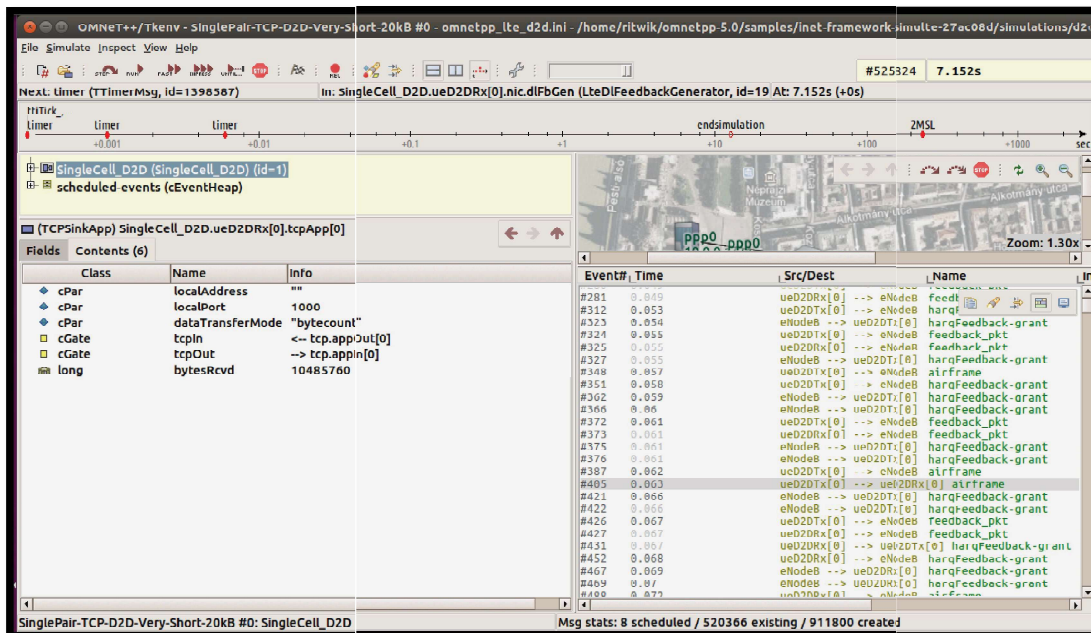


Fig 12: Receiver Side information for 10MB data sending

Observation & Inference: The simulation time for sending 10 MB of data was adjusted at 10 seconds, though the two UE’s completed transitions between 7.152 seconds.

Experiment 3:

SinglePair-TCP-D2D-ReducedWindowFrameSize-Short-10MB

As of now we observe the effect of size of data on time with a constant window frame size (100x536 bytes). But we want to observe how the time changes with varying window size. Hence, keeping all the other parameters same, we reduce the default window size to 100x128 bytes & sent similar 10 MB of data.

Before commencement of simulation:

Window size = 128 bytes

CQI value = 7

Distance between two UEs = 55m

Data Size = 10MB

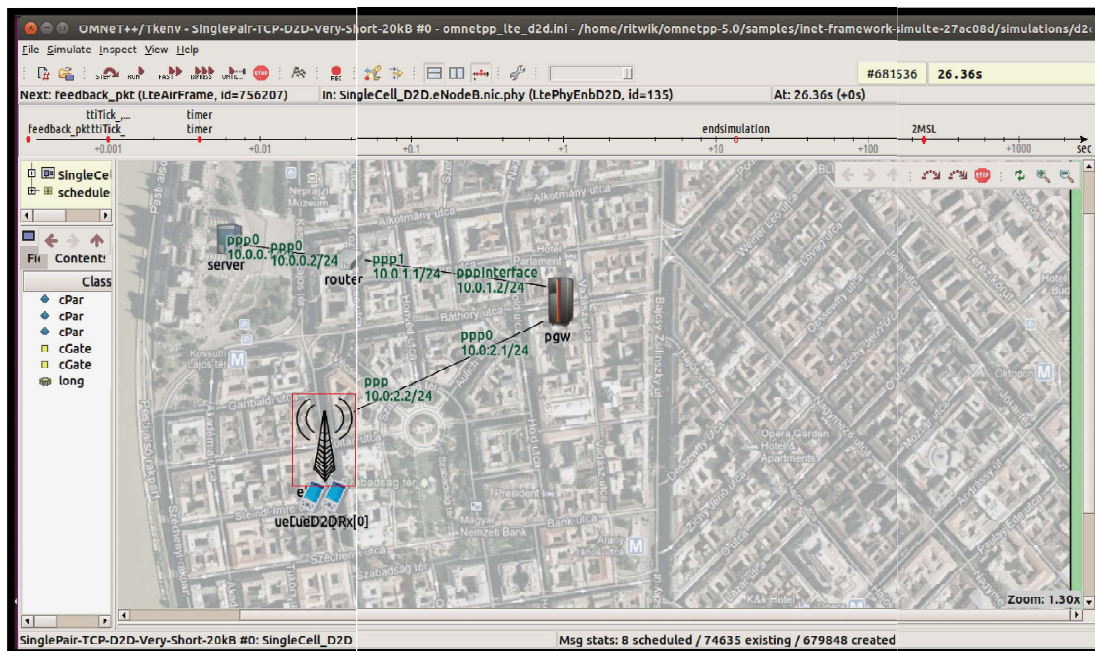


Fig 13: Simulation model for 10 MB data transmission with reduced window size

After data transmission:

From transmitter side bytesSent: 10485760

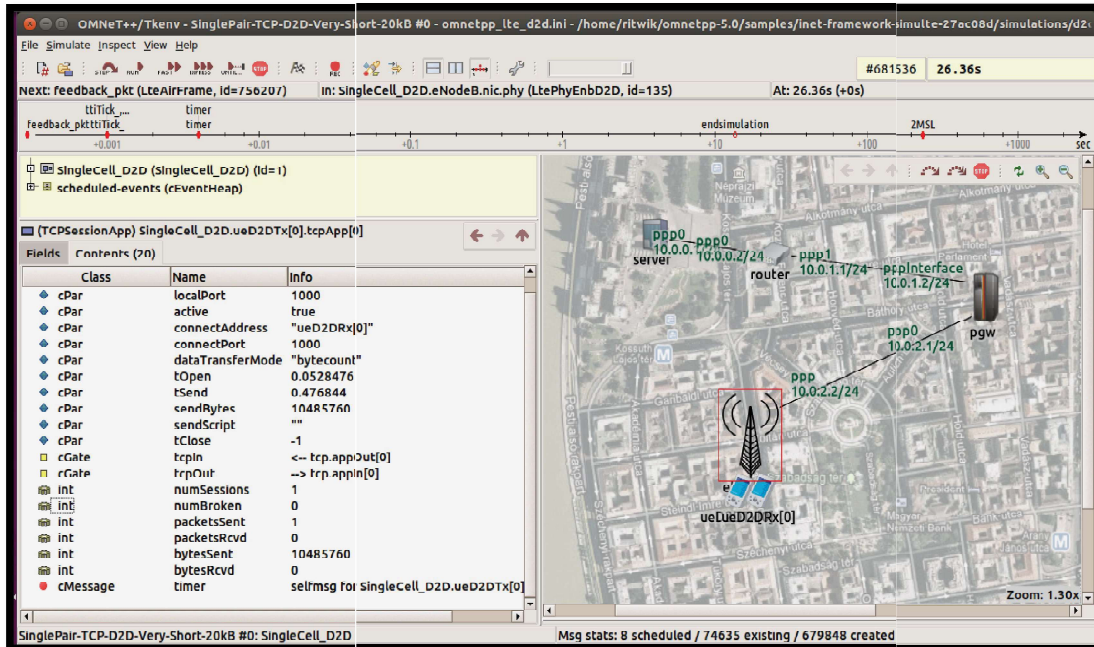


Fig 14 : Transmitter Side information for 10MB data sending with reduced window size

From Receiver side bytesRcvd: 10485760

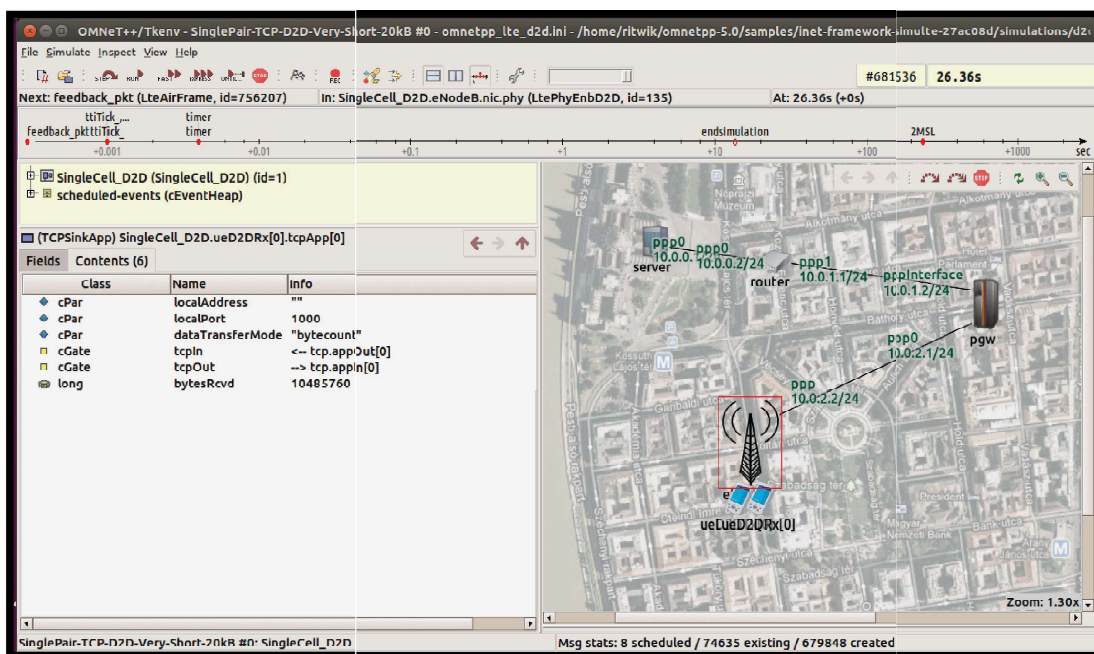


Fig 15: Receiver Side information for 10MB data sending with reduced window size

Observation & Inference: Previously, we saw that the time taken to send 10 MB of data with window size of (536 bytes) is 7.152 seconds & we observe here that it takes 26.36 seconds for transmitting same 10 MB data but with reduced window size of (128 bytes). In both the cases the channel quality index was set to 7.

Though in practical scenarios, it may take more than the experimented time since CQI value is not constant. CQI will vary over time. Also, here we are able to maintain a constant window size but there can be sudden congestion in the actual network & window size may have to be varied according to the situation. Thus, the time to receive the whole data segment will eventually increase. We set the simulation time for this program for 30 seconds.

Experiment 4:

DualPair-TCP-D2D-Short-10MB

Before commencement of simulation:

Window Size = 536 bytes

CQI value = 7

Distance between 'ueD2DTx [0]' & 'ueD2DRx [1]' = 230m

Distance between 'ueD2DTx [0]' & 'ueD2DRx [1]' = 330m

Data Size = 10MB

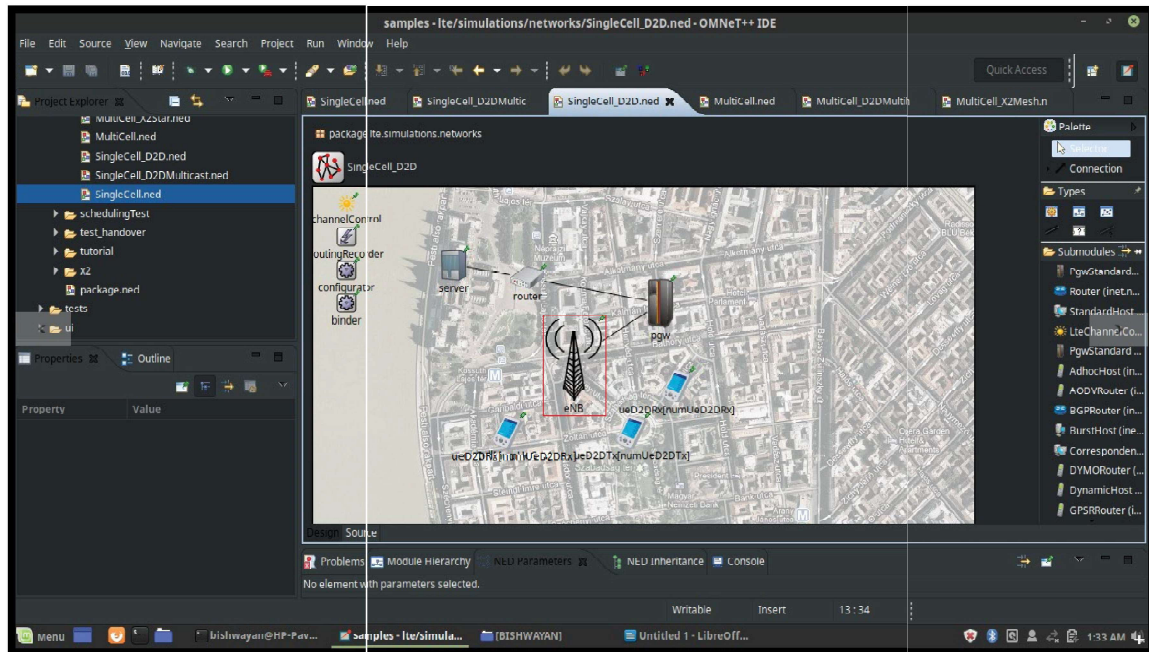


Fig 16: Simulation model for one to two D2D communications

Experiment 5:
MultiPair-TCP-D2D-Short-10MB

Before commencement of simulation:

Window size = 100 x 536 bytes

CQI value = 7

Data Size = 10MB

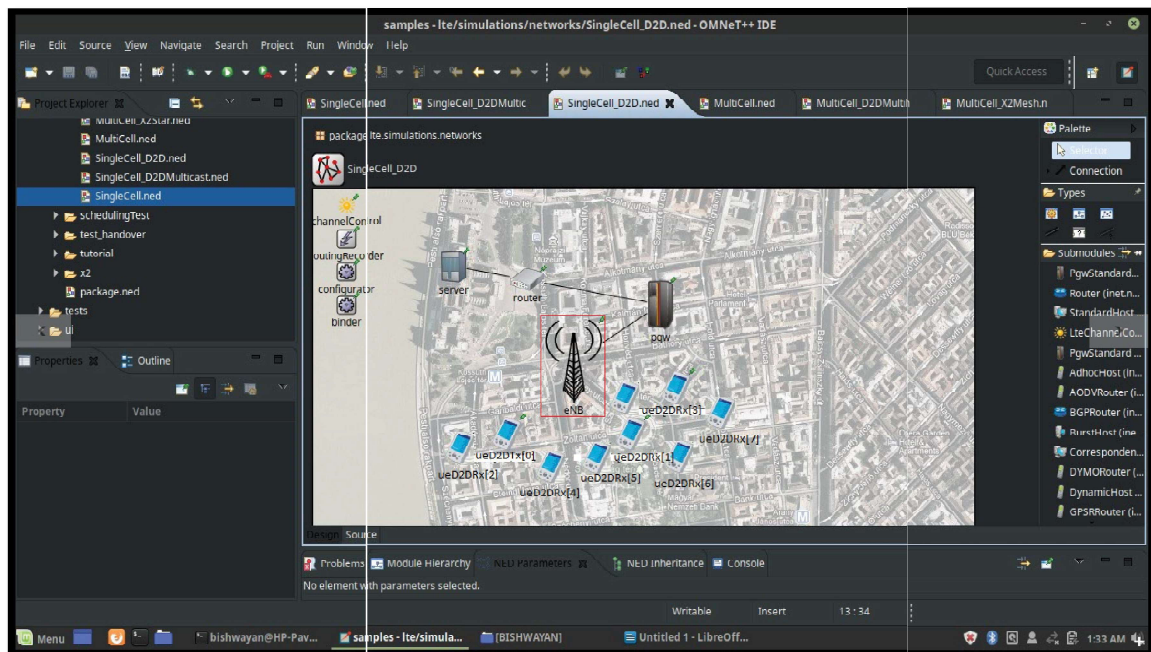


Fig 17: Simulation for one to many D2D communications

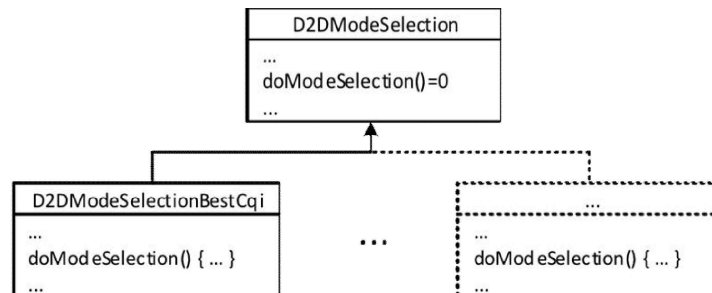
Experiment 6:

SinglePair-ModeSwitching-TCP-D2D-Short-10MB

The communication mode between two D2D-capable UEs may be changed during the simulation, from D2D mode to the traditional infrastructure mode.

To this aim, we endow the LTE NIC at the eNB with a module called *d2dModeSelection*. It is implemented as an abstract class that periodically invokes the *doModeSelection()* function. The latter runs an algorithm that, for each D2D-capable UEs, selects which mode has to be used in the next period to communicate with each of its possible receivers, i.e. those in the *d2dPeerAddresses* list. Since *doModeSelection()* is a pure virtual function, it must be re-implemented by derived classes.

The *d2dModeSelectionBestCqi* module implements a simple algorithm that chooses either D2D or infrastructure mode based on the best CQI between the UL and the SL. This architecture allows one to realize its own mode selection policy by extending the base module and implementing the *doModeSelection()* function. When the selection has been made for each possible D2D pair, a control message is sent to both the endpoints to command the switch to the new communication mode.



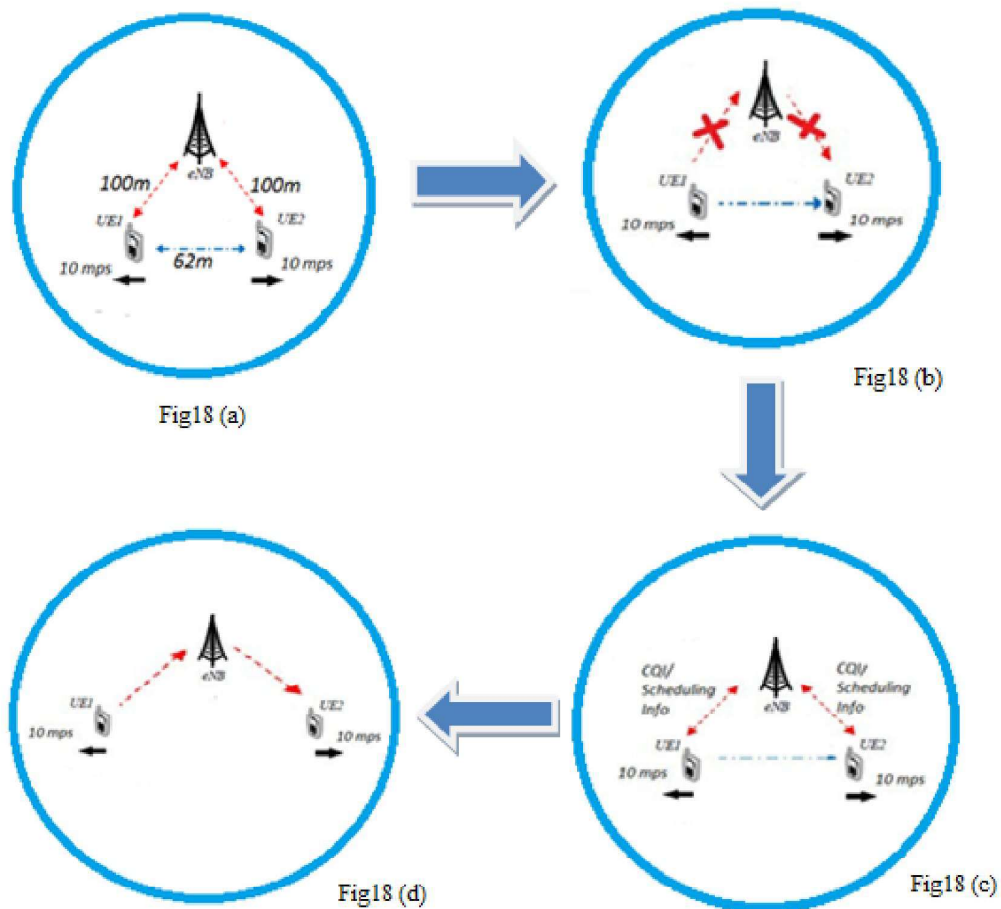


Fig 18: Flow of events in mode switching

Observation & Inference:

- Initially, we place the UEs 100 meters away each from the eNB they are 62 meters away from each other (Fig 18 (a)).
- UE1 & UE2 are close to each other & meanwhile eNB schedules the communication in D2D mode (Fig 18 (b)).
- Two UEs moved a bit from each other. Aerial distance from eNB is unchanged & eNB sense CQI value suitable for D2D (Fig 18 (c))
- eNB schedules the UEs in infrastructure mode (IM) i.e. cellular mode. The communication which started with DM finishes with IM (Fig 18 (d)).

CONCLUSIONS

In this work, we presented OMNeT++, INET framework & SimuLTE as a simulation tool for D2D communication in LTE networks. We have shown the different working areas of SimuLTE based on OMNeT++. In particular, we provided how to configure simulation parameters to assess the impact of different factors on D2D systems.

The simulations built, can be compared with the existing cellular network based on the time. The amount of time (more precisely Round Trip Time) is the most important factor because it defines how fast the communication can be built & how fast data (text, audio or video) is transferred from one place to other.

D2D communication system can be an alternative approach to the cellular network and can also be present side by side to the cellular network. There can be a possibility that in a certain area base station cannot provide the connectivity. In that case two devices, if they are within certain vicinity, can communicate using D2D system.

REFERENCES

- [1] Udit NarayanaKar, Debarshi KumarSanyal “An overview of device-to-device communication in cellular networks,” DOI 10.1109/COMST.2014.2319555, IEEE Communications Surveys & Tutorials
- [2] Negin Golrezaei, Parisa Mansourifard, Andreas F. Molisch “Base-Station Assisted Device-to-Device Communications for High-Throughput Wireless Video Networks,” IEEE Transactions On Wireless Communications, Vol. 13, No. 7, July 2014
- [3] D. Pacifico, M. Pacifico, C. Fischione, H. Hjalrmasson, K. H. Johansson “Improving TCP Performance During the Intra LTE Handover,” School of Electrical Engineering KTH Royal Institute of Technology, Stockholm, Sweden.
- [4] Abhijan Bhattacharyya, Bhaskar Sardar, Debashis Saha “Effect of Mode Switching on TCP Short flows During D2D Communication in LTE-A Networks,” pp1-6
- [5] Giovanni Nardini, Giovanni Stea, Antonio Virdis “Performance evaluation of TCP-based traffic over direct communications in LTE-Advanced,” IEEE VTC, Spring 2016.
- [6] Giovanni Nardini, Antonio Vardis & Giovanni Stea “Simulating device to device communication s in OMNeT++ with SimuLTE:scenarios and configurations.,” IEEE VTC Spring 2016, Nanjing, PRC, 15-18 May 2016.
- [7] Giovanni Nardini, Antonio Vardis & Giovanni Stea “Simulating LTE / LTE-Advanced networks with SimuLTE ,” DOI 10.1007/978-3-319-26470-7_5, in: Advances in Intelligent Systems and Computing, Vol. 402, pp. 83-105, Springer, 15 January 2016.
- [8] Arash Asadi, Student Member, IEEE, Qing Wang, Student Member, IEEE, and Vincenzo Mancuso, Member, IEEE “A Survey on Device-to-Device Communication in Cellular Networks,” IEEE Comm. Surveys and Tutorials, vol.16, no.4, pp.1801-1819, Fourth quarter 2014.

- [9] Balaji Raghothaman, Eric Deng, Ravikumar Pragada, Gregory Sternberg, Tao Deng, Kiran Vanganuru “Architecture and Protocols for LTE-based Device to Device Communication.
- [10] H. Balakrishnan, V.N. Padmanabhan, S. Seshan, M. Stemm, R.H. Katz, “TCP Behavior of a Busy Internet Server: Analysis and Improvements”, in Proc. of IEEE Infocomm ’98, CA, USA, March 1998.
- [11] Farquan Jameel, Zara Hamid, Farhana Jabeen “A Survey of Device-to-Device Communications: Research Issues and Challenges”. Article in IEEE Communications Surveys & Tutorials PP(99) · April 2018 DOI: 10.1109/COMST.2018.2828120
Link:https://www.researchgate.net/publication/324536927_A_Survey_of_Devi ce-to-Device_Communications_Research_Issues_and_Challenges
- [12] F Xin and A Jamalipour, “TCP throughput and fairness performance in presence of delay spikes in wireless networks”, Int. J. Commun Syst, vol. 18, no. 4, pp. 395–407, 2005.
- [13] Negin GolrezaeiParisa MansourifardAndreas F. MolischAlexandros G. DimakisBase “Station Assisted Device-to-Device Communications for High-Throughput Wireless Video Networks
- [14] K. C. Leung, V. O. K. Li, “Transmission Control Protocol (TCP) in wireless networks: issues, approaches, and challenges”, IEEE Communications Surveys, Vol. 8.No. 4, 2006
- [15] Barakat C., Altman E. (2000) Performance of Short TCP Transfers. In: Pujolle G., Perros H., Fdida S., Körner U., Stavrakakis I. (eds) Networking 2000 Broadband Communications, High Performance Networking, and Performance of Communication Networks. NETWORKING 2000. Lecture Notes in Computer Science, vol 1815.Springer, Berlin, Heidelberg
- [16] K. Bogineni, R. Ludwig, P. Mogensen, V. Nandlall, V. Vucetic, B. Yi, and Z. Zvonar, “LTE Part I: Core network,” Communications Magazine, IEEE, vol. 47, no. 2, pp. 40–43, February 2009.
- [17] OMNeT++ Simulation Manual
(Link: https://doc.omnetpp.org/omnetpp/manual/#toc_11)
- [18] SimuLTE – LTE User Plane Simulator for OMNeT++ and INET
(Link: <http://simulte.com>)

- [19] X. Lin, J. G. Andrews, and A. Ghosh, “A comprehensive framework for device-to-device communications in cellular networks,” *arXiv preprint arXiv:1305.4219*, 2013.
- [20] C. Joo, “On random access scheduling for multimedia traffic in multihop wireless networks with fading channels,” *IEEE Transactions on Mobile Computing*, vol. 12, no. 4, pp. 647–656, 2013.
- [21] Z. Liu, T. Peng, H. Chen, and W. Wang, “Optimal D2D user allocation over multi-bands under heterogeneous networks.” in *Proceedings of IEEE GLOBECOM*, 2012, pp. 1339–1344.

GOVERNMENT COLLEGE OF ENGINEERING & CERAMIC TECHNOLOGY



PROJECT REPORT ON

Development of Bauxite based Fly Ash Wear Resistant Ceramics

SUBMITTED BY

DEEPTAYAN BANERJEE

GCECTB-R15-1010

151130110087 of 2015-16

SUCHETAN DEBNATH

GCECTB-R15-1031

151130110108 of 2015-16

SHIBAM GHOSH

GCECTB-R15-1025

151130110102 of 2015-16

UNDER THE GUIDANCE OF

PROF. RAM CHANDRA DAS

ASSOCIATE PROFESSOR, CERAMIC TECHNOLOGY
GCECT, KOLKATA

Govt. College of Engineering & Ceramic Technology

(Formerly College of Ceramic Technology)

Government of West Bengal

73, Abinash Chandra Banerjee Lane, Kolkata-700010

Tele/Fax- 2370 1264, E- mail - gcctwb@gmail.com

Website: www.gcct.ac.in



May 02, 2019

CERTIFICATE

This is to certify that *Sri Deeptayan Banerjee (Roll No. GCECTB-R15-1010)*, *Sri Suchetan Debnath (Roll No. GCECTB-R15-1031)* & *Sri Shibam Ghosh (Roll No. GCECTB-R15-1025)*, final year B.Tech. students of Ceramic Technology, Government College of Engineering of Ceramic Technology, Kolkata (an autonomous college) under Moulana Abul Kalam Azad University of Technology, have carried out project work entitled, “ **Development of Bauxite - Fly Ash based Wear Resistant Ceramics**” under my supervision.

(Ram Chandra Das)

Associate Professor,

Dept of Ceramic Technology,

Kolkata-700010

DECLARATION

It is hereby declared that the work embodied in the report entitled "Development of Bauxite based Fly Ash Wear Resistant Ceramics" is original and was carried out by us in Ceramic Technology Department, GCECT Kolkata under the supervision of Prof. Ram Chandra Das, Associate Professor, Ceramic Technology Department, GCECT, Kolkata.

Deeptayan Banerjee

DEEPTAYAN BANERJEE

GOVT. COLLEGE OF ENGINEERING AND CERAMIC TECHNOLOGY
KOLKATA

Suchetan Debnath

SUCHETAN DEBNATH

GOVT. COLLEGE OF ENGINEERING AND CERAMIC TECHNOLOGY
KOLKATA

Shibam Ghosh.

SHIBAM GHOSH

GOVT. COLLEGE OF ENGINEERING AND CERAMIC TECHNOLOGY
KOLKATA

(Signature) 02/05/2019

PROF. RAM CHANDRA DAS

ASSOCIATE PROFESSOR

GOVT. COLLEGE OF ENGINEERING AND CERAMIC TECHNOLOGY, KOLKATA

ACKNOWLEDGEMENT

We would like to convey our gratitude to Prof. Ram Chandra Das, Associate Professor, Dept. of Ceramic Technology, Government College of Engineering & Ceramic Technology for his constant supports guidance and follow up actions throughout the project period.

We would like to extend our sincere thanks to Dr. Krishnendu Chakrabarty, Principal; Prof. Dr. Rituparno Sen, HOD, Dept. of Ceramic Technology and Dr, Barun Kumar Sanfui Government College of Engineering & Ceramic Technology, Kolkata for their all sorts of supports and departmental facilities needed to carry out this project work.

We would like to thank Mr. Asiruddin Seikh, JRF for supporting us guiding us with help whenever needed to carry out this project.

Last but not the least, we want to extend our sincere thanks to other supporting staff of the college for their helps and testing agencies outside the college for extending their help.

Content

TOPICS	PAGE NO.
1. INTRODUCTION	6
1.1 ABRASION RESISTANT CERAMICS	7
1.2 ABRASION (WEAR)	7
1.3 WEAR MECHANISMS	8
1.4 USE OF FLY ASH IN ABRASION RESISTANT CERAMICS	8
2. LITERATURE REVIEW	9
3. OBJECTIVE OF WORK	16
4. METHODOLOGY	17
4.1 PLAN OF WORK	18
5. EXPERIMENTAL PROCEDURE	20
5.1 ABRASION RESISTANT CERAMICS PREPARATION	20
5.1.1 CHEMICAL ANALYSIS OF RAW MATERIAL	20
5.1.2 BATCH PREPARATION	21
5.1.3 MIXING, SCREENING, PRESSING & DRYING	21
5.1.4 FIRING	22
5.1.5 SAMPLE SPECIMEN	23
5.2 CHARACTERISATION	24
5.2.1 STRUCTURAL PROPERTIES	24
5.2.1.1 SCANNING ELECTRON MICROSCOPE	24
5.2.1.2 X-RAY DEFRACTION	25
6. RESULTS AND ANALYSIS	27
6.1 MICROHARDNESS AND FRACTURE TOUGHNESS	27

6.2 FIRING SHRINKAGE	28
6.3 ABRASION RESISTANCE	29
6.4 APPARENT POROSITY	30
6.5 BULK DENSITY	33
7. CONCLUSIONS	36
8. REFERENCES	37

1. INTRODUCTION:

Coal-based thermal power plants generate fly ash as by-product. An enormous quantity of fly ash generated at coal based thermal power plant. It pollutes the air, water, and soil. However, fly ash could be a very useful resource material for various products. Pulverized coal is burnt to generate heat, but process generates residue, which contains 80% fly ash and 20% bottom ash. The ash carried away by flue gas collected at various points like economizer, air pre-heater and ESP hoppers. Ash collected in the water-impounded hopper below the boiler is called bottom ash.

It is estimated that the global energy demand is supposed to increase by 50% approximately in the period 2016 to 2040. Most of this growth will continue to be in the developing world, primarily China and India, as industrialization, population growth and the unprecedented expansion of the middle class will propel the need for energy in general and coal, in particular. The Indian coal is of low grade with high ash content of the order of 30 - 45% producing large quantity of fly ash at coal/lignite based thermal power stations in the country. The fly ash management has been troublesome in view of its disposal because of its potential of causing pollution of air and water. In the last decade, there has been enormous increase in thermal power plants based on coals/lignite. At present, India produces around 180 million-tons of fly ash. The disposal of such huge quantity of ash is a serious concern.

Since, coal being abundantly available worldwide, therefore, has been major source of energy and expected to remain so in future too. In order to produce energy, pulverized coal is burned. In the combustion process, the volatile matter and carbon is burn off and the coal impurities such as clays, shale, quartz, feldspar etc. mostly fuse and remain in suspension. These fused particles are escaped along with flue gas. As the flue gas temperature decreases, the fused substances coagulate to form mainly spherical particles, which are called fly ash. The remaining parts that agglomerate and settle down at the bottom of furnace are called bottom ash. The distribution of bottom ash and ESP ash is approximately 20% and 80% respectively.

1.1. Abrasion Resistant Ceramics:

Abrasion ceramics can refer to two things: Products that resist abrasion because they are hard (more correctly, these are actually abrasion-resistant ceramics) and products that abrade other materials because they are harder. Of course, even every-day porcelain surfaces are very durable. Some examples are shown in figure 1 & 2 respectively.



Fig. 1. Abrasion resistant pipe



Fig. 2: Abrasion resistant coating

1.2 Abrasion (wear):

1. The process of wearing down or rubbing away by means of friction.
2. A. A scraped or worn area.
B. A scraped area on the skin or on a mucous membrane, resulting from injury or irritation.
3. Plastic deformation at the interface often leads to wear, i.e., deformation induced wear.

4. Chemicals also cause wear.

There are many different kinds of wear mechanisms. We have to analyze these wear mechanisms using mechanics, thermodynamics etc.

Abrasion resistance is the ability of a material to resist surface wear caused by flat rubbing contact with another material. Hardness is one of the major parameters to correlate abrasion resistant. Generally, Hardness \uparrow = Abrasion resistant \uparrow .

1.3 WEAR MECHANISMS:

Wear mechanisms are shown in Table 1.

Classification	Wear Mechanisms	Wear coefficient K (range)
Wear dominated by mechanical Behavior of Materials	<ol style="list-style-type: none">1. Asperity deformation and removal2. Wear caused by plowing3. Delamination wear4. Adhesive wear5. Abrasive wear6. Freting wear7. Wear by solid particle impingement	10^{-4} 10^{-4} 10^{-4} 10^{-4} 10^{-2} to 10^{-1} 10^{-6} to 10^{-4}
Wear dominated by chemical behavior of wear materials	<ol style="list-style-type: none">1. Solution wear2. Oxidation wear3. Diffusion wear4. Wear by melting of the surface layer5. Adhesive wear at high temperatures	

Table.1: Different Wear Mechanisms

1.4 USE OF FLY ASH IN ABRASION RESISTANT CERAMICS:

Fly ash is being utilized extensively as admixture to cement and concrete, the pond ash being relatively coarse do not find enough use except in landfills. On the other hand the coarser particle size of the pond ash is expected to give rise to a better abrasion resistance in case the particles are bonded together to form a solid mass with a specific geometric shape. Therefore, the "Pond Ash" has been chosen as the primary raw material for the current study. However, the problem has been the identification of a suitable sintering aid.

James M.Skiboa, Tamara C. Buttsmf, Michael BrianSchifferb [1] this study explores experimentally the relationship between pottery surface treatments (texture, slip/polish, resin, smooth, and smudge) and abrasion resistance. The surface treatments were applied to low-fired ceramic spheres and then abrasion resistance was measured by weight loss as the specimens were abraded in lapidary tumblers. In terms of total weight loss, slip/polished and textured spheres had the poorest abrasion resistance overall whereas smudged and resin-coated surface treatments provided the best. These results have implications for pottery performance in use, use-wear analysis, and the environmental degradation of pottery. Of particular note is that a resin coating, which is the best surface treatment in terms of abrasion resistance as well as several other performance characteristics, is often applied to pots investigated ethnographically, but it rarely observed on prehistoric ceramics because of biodegradation.

MICHAEL B. SCHIFFER JAMES M. SKIBO [2], it attention to ceramic abrasion as a class of traces that can be employed by the archeologist in a variety of behavioral studies. Basic principles of ceramic abrasion are set forth, built upon the engineering literature and on experiments undertaken in the Laboratory of Traditional Technology. Abrasion mechanisms are discussed, but the limitations of current knowledge are underscored. The major factors pertaining to ceramic, abrader, and contact situations that influence the rate and nature of abrasion are identified.

J Zhu, H Yan [3] A porous mullite ceramic, which was obtained via replica method using coal fly ash as the main starting material, was used as reinforcement preform to fabricate an A356/fly-ash-mullite interpenetrating composites by a three-stage schedule squeeze casting method. Different squeezing pressures (0, 40, 80 and 120 MPa) were applied during the fabricating processes. The optimal composite was obtained at 80 MPa with sound interfacial bonding and interpenetrating structure. Compared to the base A356 alloy, the optimal composite demonstrated increased wear resistance in the pin-on-disc wear tests. The wear rate of the optimal composite was less than half of the one of A356 alloy. In addition, steadier and larger friction coefficient was also achieved by the composite comparable to the A356 alloy. The composite has good potential for use as a wear-resistant braking material.

Harikishor Kumar, R.Prasad, A.Srivastava M.Vashista M.Z.Khan [4] Fly ash (FA), the solid waste resulting from combustion of coal in thermal power plants is a by-product produced in massive quantities across the world. It is considered as an environmental pollutant. Owing to its bad effects on the environment, research is being conducted all over the world for the utilisation of FA. The present work emphasizes the utilization of FA as reinforcement in copper-based surface composite fabricated by friction

stir processing (FSP). The properties of fabricated composite and its environmental impact through leaching test have also been reported in the present study. A groove of known dimension was machined at the center of the plate (6 mm thickness) for compaction of the high amount of FA (almost 18 vol %), processed by FSP. The microstructural features of the fabricated composite were observed by optical and scanning electron microscope revealed equiaxed and fine grain structure with no concentration gradient, agglomeration and segregation along the grain boundary. The stir zone (SZ) was engulfed with particulate along with clean interface and excellent bonding. The XRD pattern revealed no intermetallic or in situ products except copper and particulate. Vickers micro hardness tester machine adjudged significant improvement in hardness. The composite showed higher tensile strength and lower ductility as compared to copper. Enhancement in oxidation and corrosion resistance was also observed whereas electrical conductivity decreased as evaluated by four-probe method. The pin on plate unidirectional dry sliding wear test was performed to evaluate the wear loss. The wear resistance of the fabricated composite improved substantially. The worn surface was observed by scanning electron microscope to have a detailed understanding of wear mechanism. Further through leaching test, it was observed that concentration of leached out metals was far below as specified in Indian legislation.

Saransa Sahoo , Chitra Shijagurumayum Chitra Shijagurumayum [5] as fly ash consist of more fine particles and amorphous in nature, it shows pozzolanic behavior and sometimes-self cementitious character. Depending on the proportion of its porosity and its chemical constituents, its density ranges between 1.3g/cm³ and 4.8g/cm³. To-date cement and concrete industry uses around half of fly ash. Concrete tiles can be another substitution to the costly traditional tiles. Traditional tiles also have low operating life. Here full size tiles for different compositions of fly ash are picked for the abrasion resistance test. The test samples were of size 70.6mm×70.6mm i.e. their surface area is 5000mm².

[6] In our planet, coal is the most abundant fossil fuel (Fig.3). It is a relatively cheap one. Some of the largest deposits in the regions that are China, India and the United States. In last half century, a dominant player in energy generation worldwide is coal and will continue to be so in decades to come.

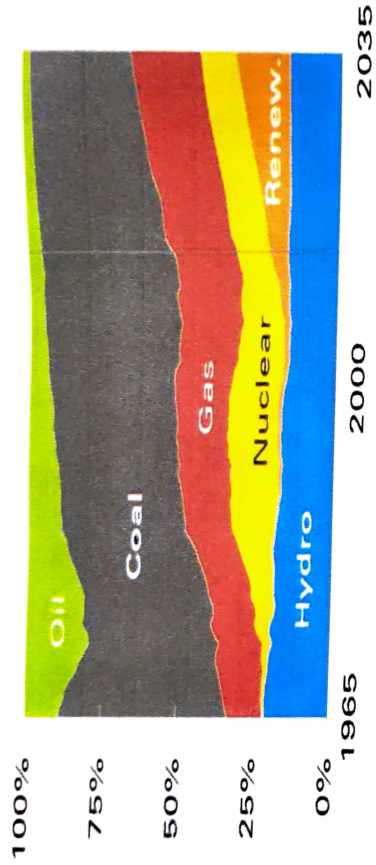


Fig.3 : Fuel-mix in global generation of energy

China is and will remain in future the world's largest coal consumer consuming almost half of global coal supplies in 2035 (Fig.4). India has shown the largest growth in coal consumption (435 M ton), ahead of US to become the world's second biggest consumer of coal. More than two-thirds of India has increased coal demand feeds into the power sector.

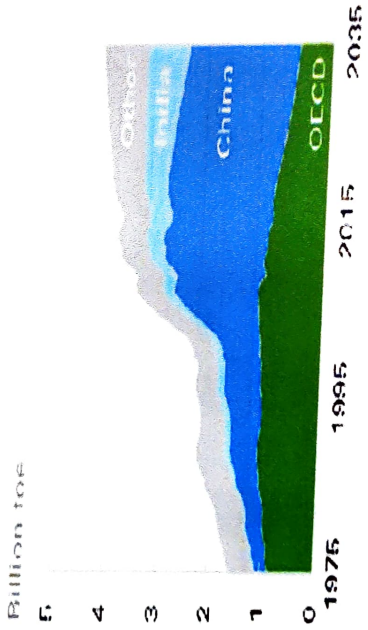


Figure 4: Regional break-up of Coal consumption

In India, thermal power plants consume about 536.64 million tons of coal and about 145044.80 MW power is being generated. Approximately 176.74 million tons of fly ash is generated. Out of which only 63.97% is being utilized for production of cement, construction of embankments and roads, mine filling, agriculture, making bricks, tiles and building materials etc. (Central electricity Authority, 2015-16). Worldwide, a major problem faced by many industries is the handling and disposal of fly ash that is generated in unmanageable volume.

For any country, energy is the backbone for the sustainable development and growth of their industries. For economic development of a nation, energy plays a vital role. A best fitted proverb in this context "*Power is the key to the prosperity and development of a nation*". Today, energy is being needed by each sectors- agriculture, industry, transport, domestic purposes and commercial. No matter the country is both developed or developing countries require a continuous source of energy for their growth and development. India being a developing country, energy plays a vital role in its economy. Like developing countries, India is still dependent on the natural reserves for the generation of energy. India have enough reserves of both coal and nuclear. Even though India is enriched with Thorium and Uranium but still we have very few nuclear power plants. Still, India is lacking in utilization, handling and of nuclear resources as a source of energy. Today even in the 21st century, coal is the first choice as a fuel, both in India and China for the electricity generation. For more than 100 years, coal is being used for the production of electricity at coal-fired thermal power plants worldwide. For electricity generation, India depends mostly (70-75%) on coal-based thermal power plants which annually generates 235 MTs fly ash (2016) and is projected to exceed 1000 million ton by 2031-32.

As an essential ingredient for growth and development, energy has become the driving force of the modern economy. Since the 1970s, traditional fossil fuels have been the dominant energy source (Fig. 5). Oil, the leading energy source in 1970, made up 43% of total energy demand, while the shares of coal and natural gas were at 27% and 15%, respectively. By 2016, however, these figures had shifted somewhat. The share of natural gas had increased to 22%, while that of oil had dropped to 32%. However, Coal's share remained roughly dominant over the period.

Global energy mix by fuel type, 1970–2040

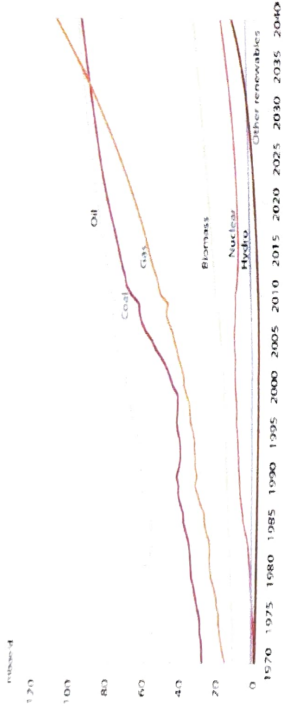


Fig.5: Global Energy mix by fuel type,

1970- 2040 Coal consumption and percentage ash content during 2010-11 to 2016-17 [7] is shown in Table 2.

Descriptions	2010-2011	2011-2012	2012-2013	2013-2014	2014-2015	2015-16	2016-17
TPPs	88	124	138	143	145	151	155
installed capacity (MW)	80458	105925.3	20312.30	33381.30	38915.80	45044.8	45044.8
Coal consumed (MTs)	407.61	437.41	482.97	523.52	549.72	536.4	536.4
Average ash Content (%)	32.16	33.24	33.87	33.02	33.50	32.94	33.22

Table 2: Coal consumption in years

Fly ash, production, utilization in India during the period of year 1998-99 to 2016-17 [7] is shown in Table-3

Descriptions	2010- 11	2011-12	2012-2013	2013-2014	2014-2015	2015-16	2016-17
Fly ash production	131.09	145.42	163.56	172.87	184.14	176.74	169.25
Fly ash utilization	73.13	85.05	100.37	99.62	102.54	107.77	107.10
% Utilization	55.79	58.48	61.37	57.37	55.69	60.97	63.28

Table 3: Fly ash production and usage in years

A large amount of coal ash (both fly ash and bottom ash) emerges as a by-product from the coal combustion in thermal power plants in India annually. The large quantity of coal ash not only occupies valuable land resources but also poses a threat to ground water, so it is of great significance to utilize the industrial waste efficiently to decrease environmental pollution and produce high value-added products. Although extensive researches carried out in recent years for finding applications of coal ash have led to the development of hollow blocks, glass ceramics, silicon carbide, β -cordierite etc., only a small quantity of the total coal ash generated is utilized. Abrasion resistant ceramic has potential in some advanced applications as a structural ceramic, due to its good mechanical strength, high melting point, excellent thermal shock, high creep resistance and low thermal conductivity. A lot of efforts have been made to synthesize Abrasion

resistant ceramic materials from various alumina precursors, such as γ -Al₂O₃, α -Al₂O₃, aluminum fluoride, aluminum hydroxide, and silica precursors including pure natural quartz, amorphous silica etc. These methods involve very high-cost starting materials and powder processing, thus are consequently not appropriate for large-scale production. In this paper, low-cost Abrasion resistant (mullite based) ceramics was prepared from the mixture of coal ash (both fly ash and bottom ash) as silica precursors, calcined bauxite (CB) as alumina precursor for mullitization and china clay (BC) as agglomerate. The effects of sintering temperature on the phase development, microstructure, densification behavior and flexural strength were studied.

3. OBJECTIVE OF WORK:

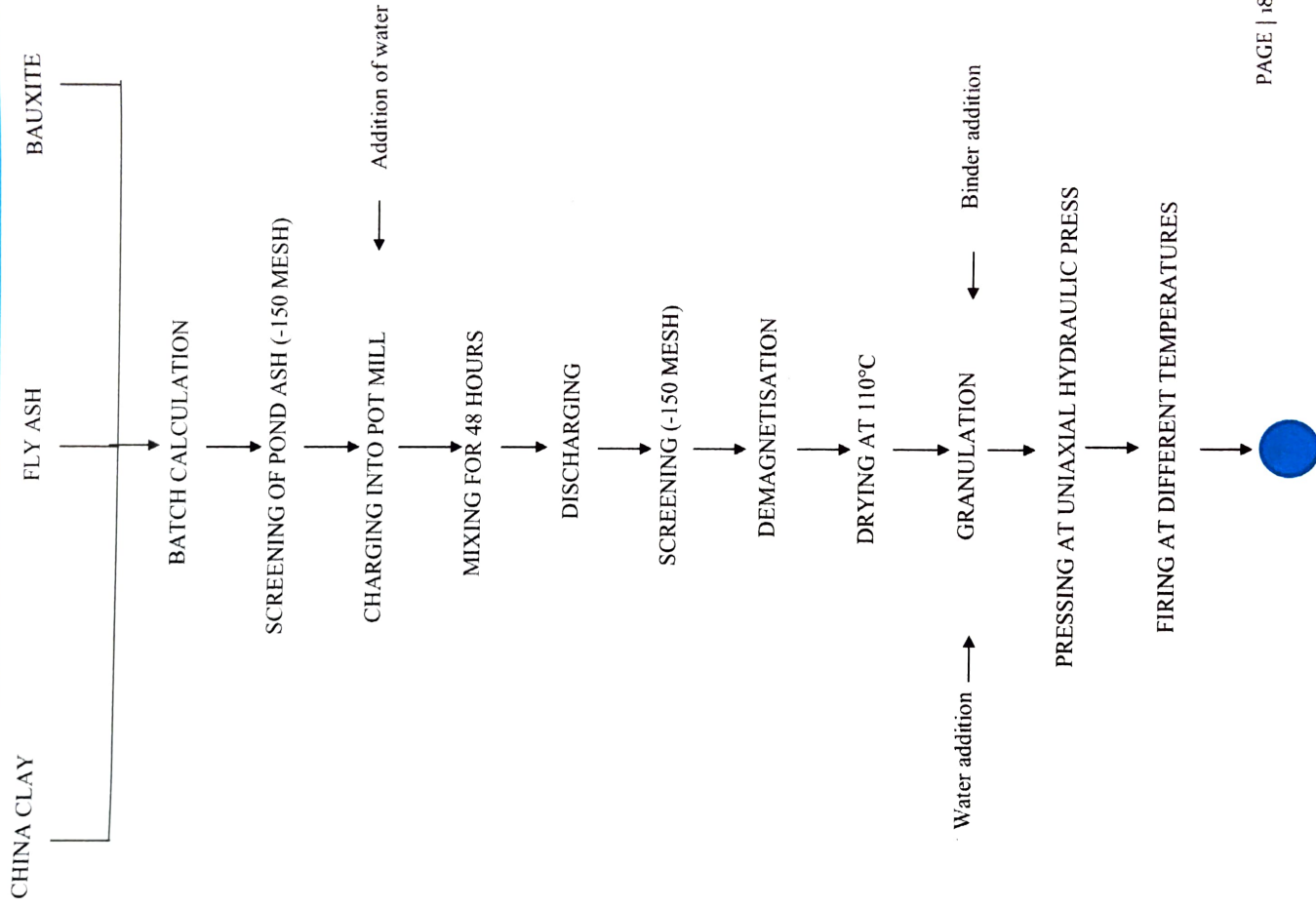
- Development of a low cost high performance abrasion resistant ceramics using coal ash as major raw material suitable for applications in petrochemical, fertilizer and steel plants.
- Development of low cost high performance insulating refractory bodies (both shaped and unshaped) suitable for applications in kilns, pipes, furnaces, incinerators, chimneys etc., using coal ash as a major raw material.
- Correlation of the process parameters with the performance of the developed materials.

4. METHODOLOGY

The project will involve both experimental and analytical work. The project will consist of the following steps

1. Collection of coal ash samples from different power plants across India
2. Detailed characterization of the as received ash samples by measuring their chemical composition, phase composition, morphology, etc.
3. Processing of the ash samples by sieving, drying, characterization of the processed ash samples as mentioned.
4. Mixing of the ash samples with other auxiliary materials, like, bauxite and china clay in different proportions to produce different batches and fabrication of blocks from these batches by hydraulic pressing followed by drying and firing at different.
5. Characterization of the fired masses by measuring their sintering behaviors like bulk density, apparent porosity, linear firing shrinkage, micro hardness, XRD, abrasion resistance, SEM & fracture toughness.
6. Mixing of the ash samples with bauxite, clay in different proportions and pressing of the batches to prepare batches for wear resistant ceramics, which will be heat treated at different elevated temperatures like 1400 °C, 1425 °C, 1450 °C, 1475 °C, 1500 °C, 1550 °C & 1600 °C for 90 mins. Soaking periods and measurement of the abrasion resistant, bulk density, apparent porosity, linear firing shrinkage, hardness etc.

4.1 PLAN OF WORK





CHARACTERISATION

(A.P. / B.D. / SHRINKAGE / MICROHARDNESS / XRD / ABRASION RESISTANCE /
FRACTURE TOUGHNESS)

5. EXPERIMENTAL PROCEDURE:

5.1 Abrasion Resistant Ceramics Preparation:

5.1.1 CHEMICAL ANALYSIS OF RAW MATERIAL:

According to test method IS: 1527-1972, Chemical analysis of some important raw materials was carried out at R.V. Briggs & Co. Pvt. Ltd., Kolkata, and West Bengal, India.

Sl. No.	Sample	Composition	
		Test Item	Observed Value (%)
1.	Bauxite Powder	Al ₂ O ₃	80.98
		Fe ₂ O ₃	11.07
		CaO	Traces
		TiO ₂	2.94
2.	China Clay	Al ₂ O ₃	80.12
		Fe ₂ O ₃	02.36
		Al ₂ O ₃	21.84
		SiO ₂	68.78
		Fe ₂ O ₃	0.53
		TiO ₂	0.12
3.	Alumina powder	CaO	0.17
		MgO	0.59
		Alkali	0.17
		Al ₂ O ₃	96.40
		SiO ₂	02.40
		Fe ₂ O ₃	0.27
4.	Fly Ash	Na ₂ O	0.19
		Sp. Gravity	2.48
		Bulk density (gm/cc)	1.05
		Al ₂ O ₃	28.91
		SiO ₂	56.51
		Fe ₂ O ₃	05.28
		TiO ₂	0.36
		CaO	03.13
		MgO	0.39
		K ₂ O	0.79
Na ₂ O	0.44		
SO ₃	0.08		
P ₂ O ₃			

	LOI	0.19
	Undetermined	3.63
		0.29

5.1.2 BATCH PREPARATION:

After batch, calculation batches are prepared by adding bauxite with fly ash (FB) and alumina with fly ash (FA). These are shown in table 4 and table 5 respectively.

Batch no	Total batch weight(gm)	Bauxite required(gm)	China clay required(gm)	Fly ash required(gm)	Water required(ml)
FB1	800	640(80%)	80(10%)	80(10%)	1000
FB2	800	560(70%)	80(10%)	160(20%)	1000
FB3	800	480(60%)	80(10%)	240(30%)	1000
FB4	800	400(50%)	80(10%)	320(40%)	1000
FB5	800	320(40%)	80(10%)	400(50%)	1000

Table. 4: Batch calculation of Bauxite with Fly Ash

Batch no	Total batch weight(gm)	Alumina required(gm)	China clay required(gm)	Fly ash required(gm)	Water required(ml)
FA1	400	320(80%)	40(10%)	40(10%)	500
FA2	400	280(70%)	40(10%)	80(20%)	500
FA3	500	300(60%)	50(10%)	150(30%)	500
FA4	400	200(50%)	40(10%)	160(40%)	500
FA5	400	160(40%)	40(10%)	200(50%)	500

Table. 5: Batch calculation of Alumina with Fly Ash

5.1.3 MIXING, SCREENING, PRESSING & DRYING

Impurity such as iron can create low melting phase. To avoid this, both the coal ash samples were passed through magnetic separation and then different batches are prepared.

After adding water with the batch as shown in the table the batches are mixed individually and then kept for 24 hrs. This is followed by milling these batches in the ball mill individually for 48 hrs. After milling, the batches are taken out and is separated by magnetic separation. A magnet is pressed like an iron over the milled material to remove iron. The iron impurity cracks the material while firing.

Due to non-plastic nature of both raw materials, Polyvinyl alcohol (5 wt. %) was used as binder. Samples were wet mixed in a pot mill and pressed steel die to form tablets around 25mm in diameter and ~20mm in height applying a pressure of ~ 1038 kg/cm² by using a hydraulic press. After magnetic separation, the batches are dried at 110°C. This is followed by screening with different size sieves. Now mixing binder PVA is added to the sieved mix. After this, the mix is put in mould and pressed for getting the green body. This is shown in table 6.

Batch no	Screening before mixing binder	Screening after mixing binder (PVA 5 wt. %)	pressing
FB1	150 um	355um	110KN
FB2	150um	355um	110KN
FB3	150um	355um	110KN
FB4	150um	355um	110KN
FB5	150um	355um	110KN
FA1	150 um	355um	50KN
FA2	150um	355um	50KN
FA3	150um	355um	50KN
FA4	150um	355um	50KN
FA5	150um	355um	50KN

Table. 6: Screening and Pressing requirement of FB and FA bricks.

After the green body is prepared, they are dried at 110oc for 24 hours before firing.

5.1.4 FIRING:

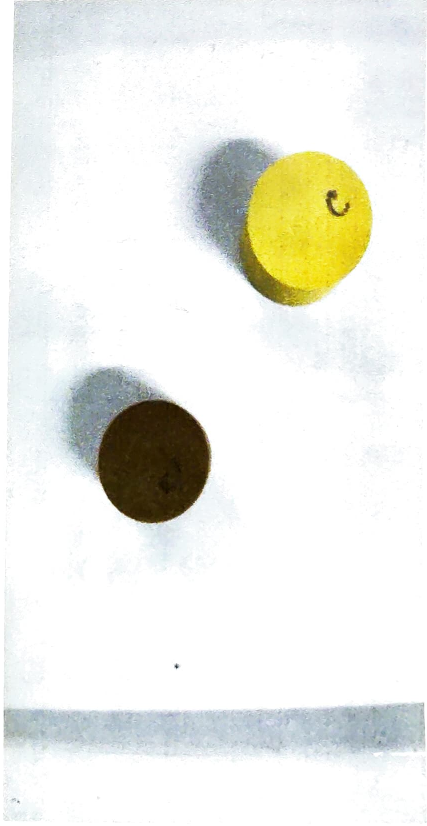
Dried samples were fired at different temperatures ranging from 1400°C to 1600°C for two hrs. To study temperature dependence. Firing is done flowingly as shown in table 6.

Batch no	Firing tem (°C)	Heating Rate (deg/min)	Soaking Temp (hr.)	Furnace started at	Temp reached at	Ammeter Reading (amp)
FB1,FB2, FB3,FB4,FB5	1425	10	2	10:30 a.m	1:00p.m	30-35
FB1,FB2 FB3,FB4,FB5	1475	10	2	8:45 a.m.	11:50 a.m.	30-35
FB1,FB2,FB3	1500	10	2	10:30a.m	1:32p.m	30-35
FB3	1465	10	1.5	10:10a.m	1:15 p.m.	30-35
FB4	1450	10	2	10:2.am	1:24p.m	30-35
FB4	1525	10	2	10:28a.m	1:36p.m	30-35

FB5	1425	10	2	1:00p.m	3:53p.m	30-35
Fb5	1475	10	2	10:00a.m	1:00p.m	30-35
FB5	1420	10	1.5	10:40a.m	1:35p.m	30-35
FA1,FA2, FA3,FA4,FA5	1400	10	2	10.25	1.32	30-35
FA1,FA2, FA3,FA4,FA5	1450	10	2	10.30	1.30	30-35
FA1,FA2, FA3,FA4,FA5	1500	10	2	10.30	1.30	30-35
FA1,FA2, FA3,FA4,FA5	1550	10	2	10.15	1.40	30-36
FA1,FA2, FA3,FA4,FA5	1600	10	2	10.30	1.50	30-36

Table.7: Detailed Firing Schedule

5.1.5 SAMPLE SPECIMEN





5.2 CHARACTERIZATION:

5.2.1 STRUCTURAL PROPERTIES:

5.2.1.1 Scanning Electron Microscopy:

SEM was carried out at Central Mechanical Engineering Research Institute, Durgapur, and West Bengal. The following are the few micrographs of the tested samples:

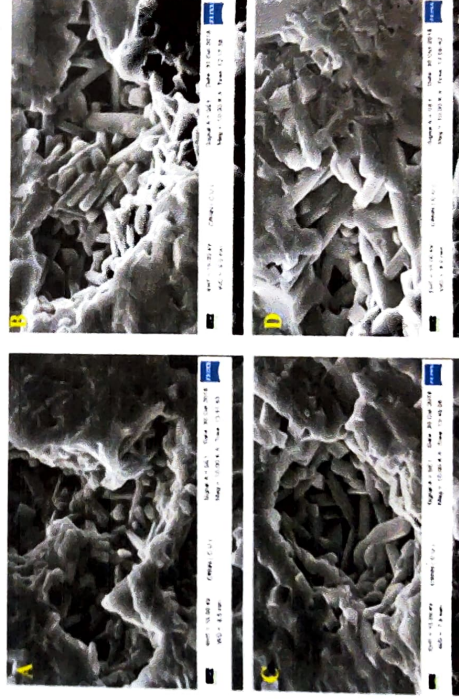


Fig 6: Images of fabricated wear resistant ceramics
Sintered at (A) 1425C B-5 (B) 1450C B-4 (C) 1475C B-3 (D) 1500C B-1

5.2.1.2 X-RAY DEFRACTION:

XRD peaks shows presence of mullite & corundum as major crystalline phases along with glassy phases. This is shown in figure 7.

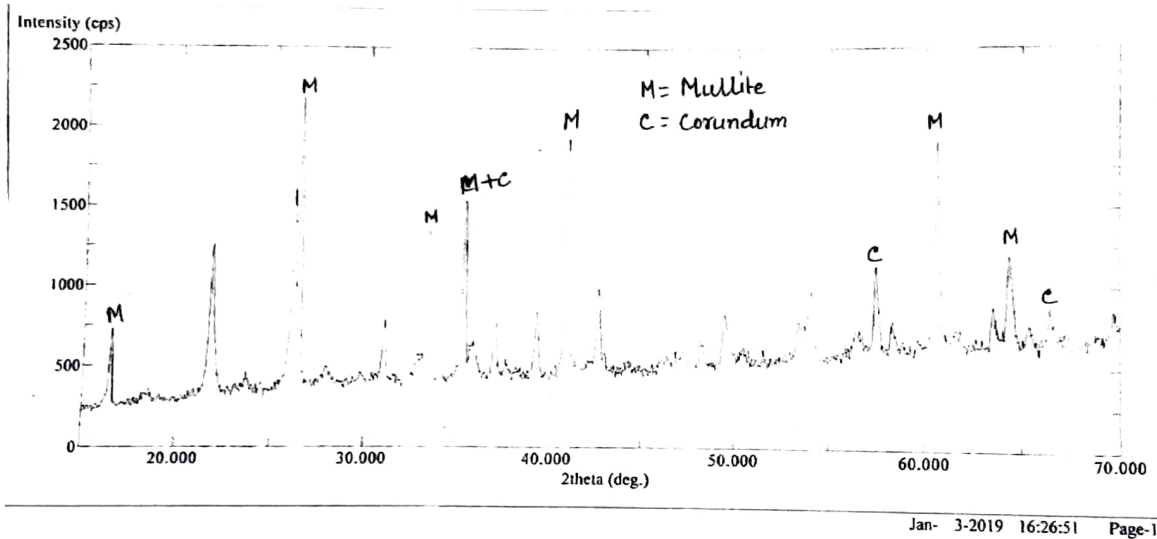


FIG. 7(a)

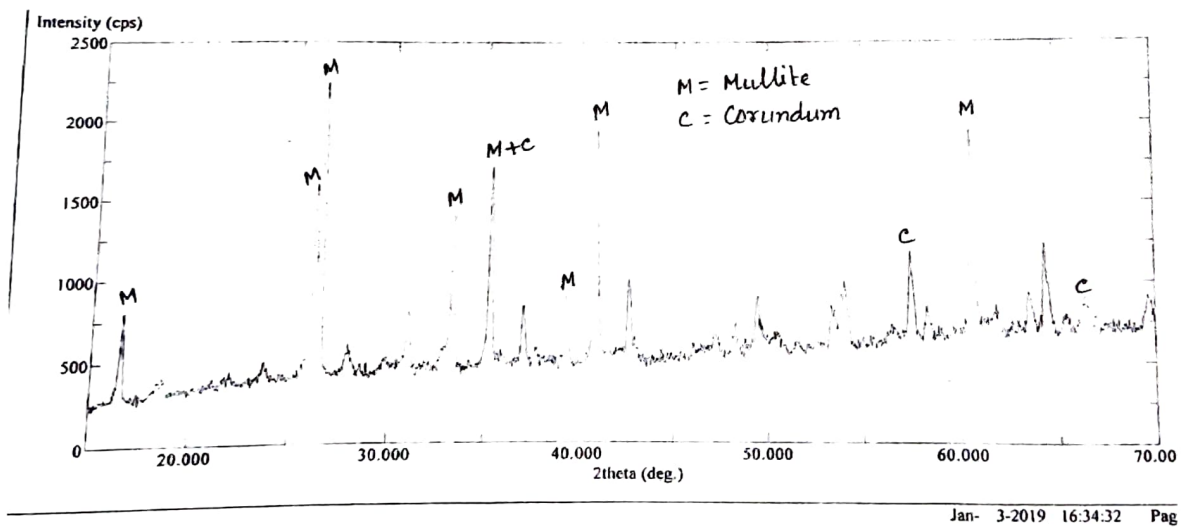


Fig. 7(b)

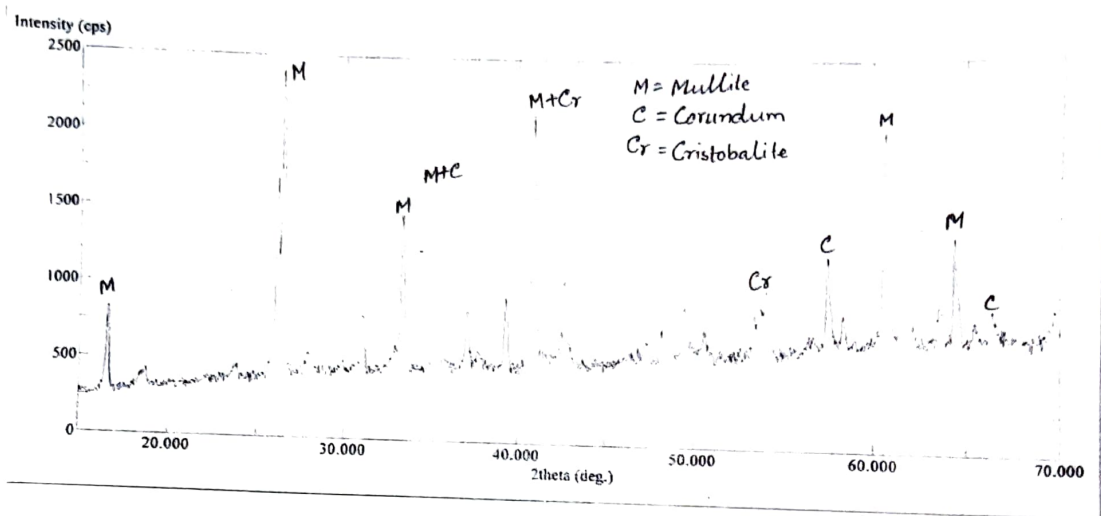


Fig. 7(c)

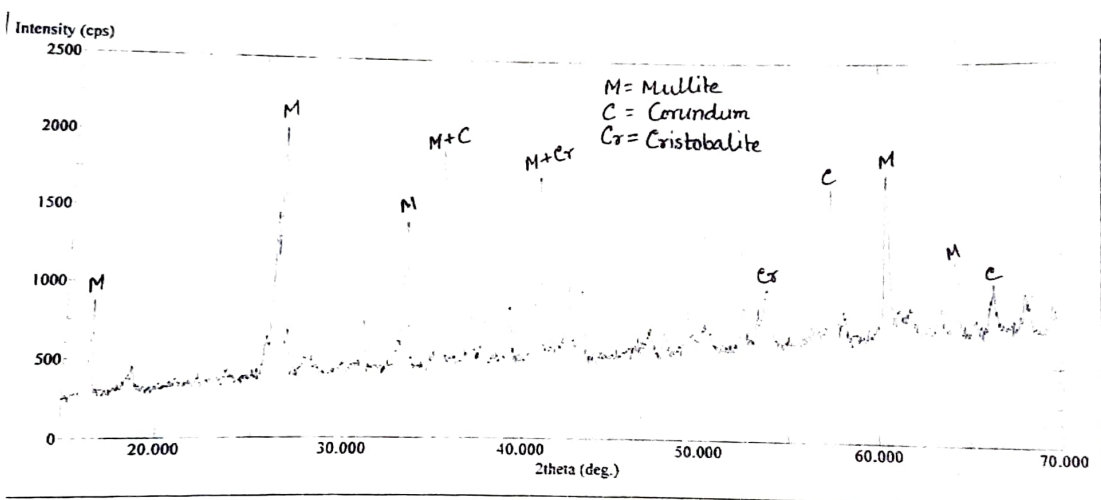


Fig. 7(d)

Fig. 7: XRD of the samples

6. RESULTS AND ANALYSIS:

6.1 MICROHARDNESS AND FRACTURE TOUGHNESS:

Micro hardness tests are used in mechanical engineering to determine the hardness of a material to deformation. Several such tests exist, wherein the examined material is indented until an impression is formed; these tests can be performed on a macroscopic or microscopic scale.

In materials science, fracture toughness is a property which describes the ability of a material containing a crack to resist fracture, and is one of the most important properties of any material for many design applications. The linear-elastic fracture toughness of a material is determined from the stress intensity factor at which a thin crack in the material begins to grow.

This is calculated in two ways

Vickers Hardness (HV): $1.8544 * F/d^2$ (F: Load in Newton; d: average length of diagonal)

Fracture toughness: $K_{ic} = 0.16 (C/A)^{-3/2} * H\sqrt{a}$ (C: crack length; a = half of length of diagonal)

The fracture toughness and micro hardness is shown in table 7 below.

Batch	Firing temp(°C)	Micro hardness(hv) (GPa)	Fracture toughness(MPa√m)
FB1	1470	10.852	2.959
FB2	1470	10.802	3.352
FB3	1465	9.353	2.109
FB4	1145	9.688	2.323
FB5	1420	8.49	2.535

Table. 8: Micro-hardness and Fracture Toughness of the bricks

Micro hardness change with fly ash percentage is shown in figure 8

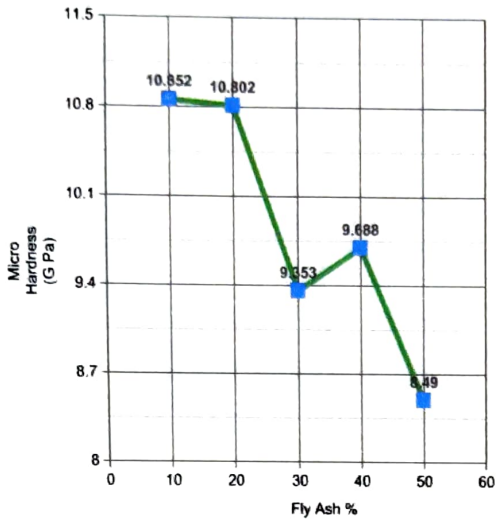


Fig. 8: Micro Hardness vs Fly Ash Percentage

Fracture toughness change with change in fly ash percentage is shown in figure 9

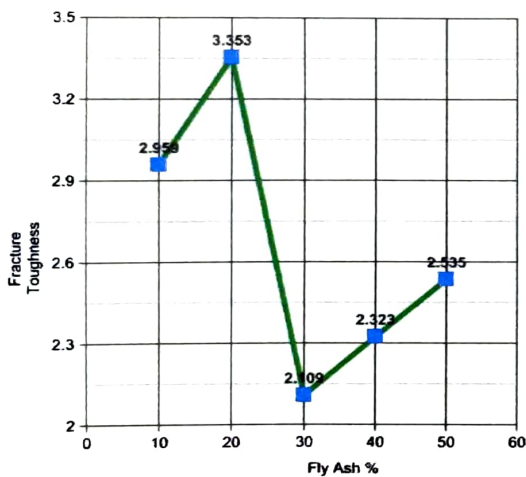


Fig. 9: Fracture Toughness vs Fly Ash Percentage

6.2 Firing Shrinkage:

Fired shrinkage (shrinkage from dry to fire) is a thus comparative indicator of the degree of vitrification. As a clay is fired higher, it shrinks more and more to a point of maximum shrinkage (after which swelling occurs as a precursor to melting).

Firing shrinkage was not done for all the samples. Fly ash bauxite samples of set 4 and 5 (FB4, FB5) which are shown in table 9 .

Batch no	Dried length(mm)	Fired length(mm)	Firing shrinkage (%)
4.A	82	73.37	10.52
4.B	82	72.56	11.51
4.C	55	48.56	11.71
4.D	55	49.15	10.64
4.E	82	72.44	11.64
4.F	82	73.02	10.95
4.G	55	48.92	11.05
4.H	55	49.04	10.84
5.A	82	73.24	10.68
5.B	55	49.32	10.32
5.C	55	49.78	9.49
5.D	82	73.19	10.82

Table. 9: Detailed Firing Shrinkage of Fly Ash bauxite bricks

Fly ash alumina samples of set 8,9,10 (FA8, FA9, FA10) shrinkage are shown in table 10

Batch no	Initial length (mm)	Final fired length (mm)	Avg diam of sample	Firing shrinkage (%)
8A	25.342	24.56	24.83	2.02
8B	25.342	25.13		
8C	25.342	24.95		
8D	25.342	24.69		
9A	25.342	24.34	24.40	3.72
9B	25.342	24.40		
9C	25.342	24.49		
9D	25.342	24.38		
10A	25.342	23.04	22.78	10.11
10B	25.342	22.64		
10C	25.342	22.43		
10D	25.342	23.01		

Table. 10: Detailed Firing Shrinkage of Fly Ash Alumina bricks

6. 3. Abrasion Resistance:

Batches are placed into sand blast cabinet and a spinning wheel pours sand onto the batch continuously for 1 hr. under a constant load.

In Our sand blast cabinet load was 4.3 kg, mesh size of the sand was 212 micrometer, speed 205 rpm, and revolution of wheel was- 4000

Batch no.	Wt. of sample before testing(gm)	Wt. of sample after testing(gm)	Wt. loss (gm)
1. (Fly Ash 10%)	43.220	43.220	0
2. (Fly Ash 20%)	42.990	42.990	0
3. (Fly Ash 30%)	43.493	43.440	0.053
4. (Fly Ash 40%)	43.395	43.350	0.045
5. (Fly Ash 50%)	44.8109	44.786	0.033

Table. 11: Determination of Abrasion Resistance by recording weight loss

Standard weight loss is 0.027 gm. Therefore, the result is nearly satisfaction.

Abrasion resistance with different percentage of fly ash is shown in figure 10.

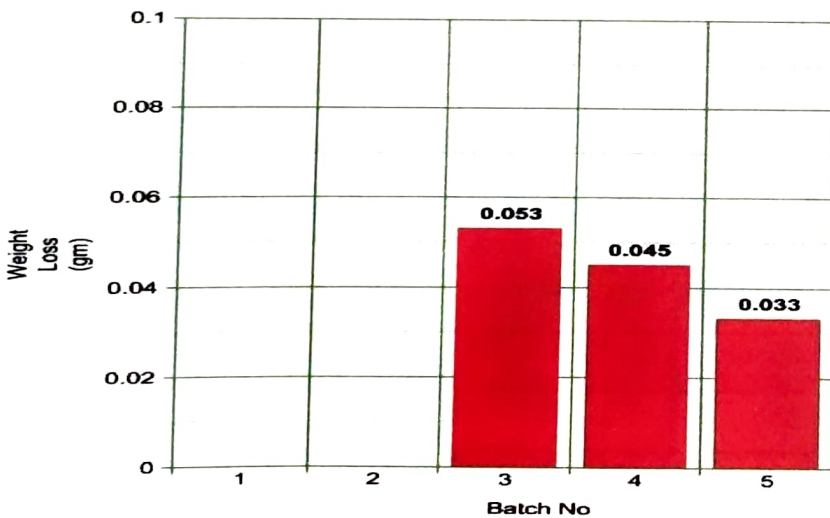


Fig. 10 : Abrasion Resistance vs Fly Ash Percentage

6.4 Apparent Porosity:

An apparent Porosity is defined as the quantity of void (or pores) present in a volume of sediment or porous solid. Generally, the value of porosity is measured as a fraction or percentage.

A.P: $E = [(S - W) / (S - I)] \times 100$ Where,

S = Weight of Piece Soaked

W = Weight of Dry Piece

I = Weight of the Piece Soaked and Immersed

E = Apparent porosity

Variation of apparent porosity with increasing sintering temperatures are presented in figure 11-12. In general, Apparent porosity decreases with increasing sintering temperature. Except for the temperature of 1500°C (set-1, Batch-3) for which the Apparent porosity increases with increasing sintering temperature.

Specific Apparent porosity values of all the samples are presented in the following table (Table 12-13)

Sintering temperature (°C)	Apparent Porosity of Batches (%)				
	Batch-1	Batch-2	Batch-3	Batch-4	Batch-5
1400	23.79	26.42	19.31	4.89	0.57
1425	14.56	19.00	5.59	0.41	0.30
1450	0.86	3.74	0.17	0.09	-
1475	0.06	0.07	0.05	0.04	1.16
1500	0.06	0.03	0.27	-	-

Table. 12: Apparent Porosity of different batches of Fly Ash Bauxite bricks at different sintering temperatures.

Sintering temperature (°C)	Apparent Porosity of Batches (%)				
	Batch-6	Batch-7	Batch-8	Batch-9	Batch-10
1400	42.27	42.28	42.43	40.27	37.40
1450	42.74	43.37	44.19	42.27	38.60

1500				43.65	39.30
1550				40.89	32.81
1600			37.29	33.09	16.30

Table. 13: Apparent Porosity of different batches of Fly Ash Alumina bricks at different sintering temperatures

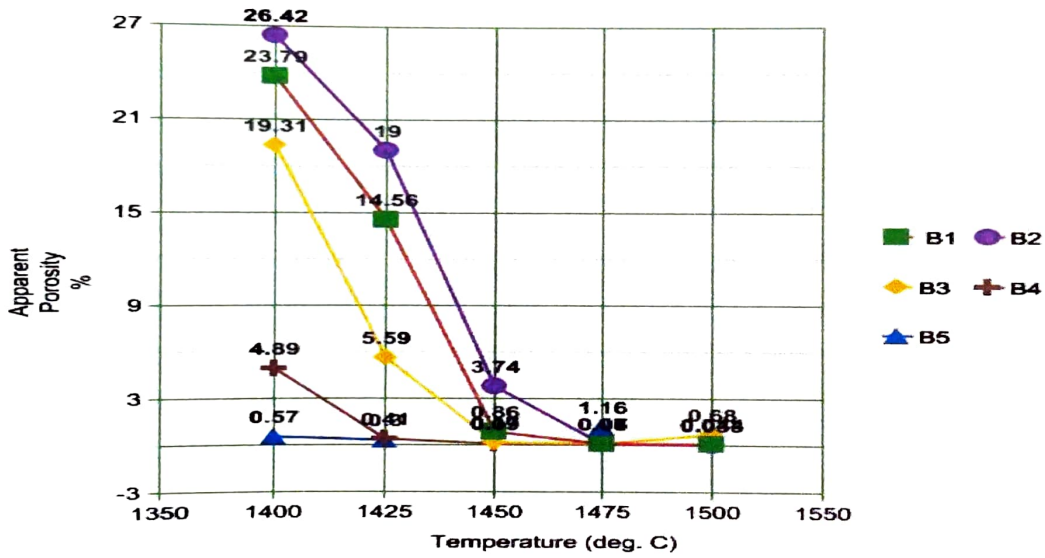


Fig.11: Apparent Porosity of Batches of Bauxite Fly Ash vs Sintering Temperature

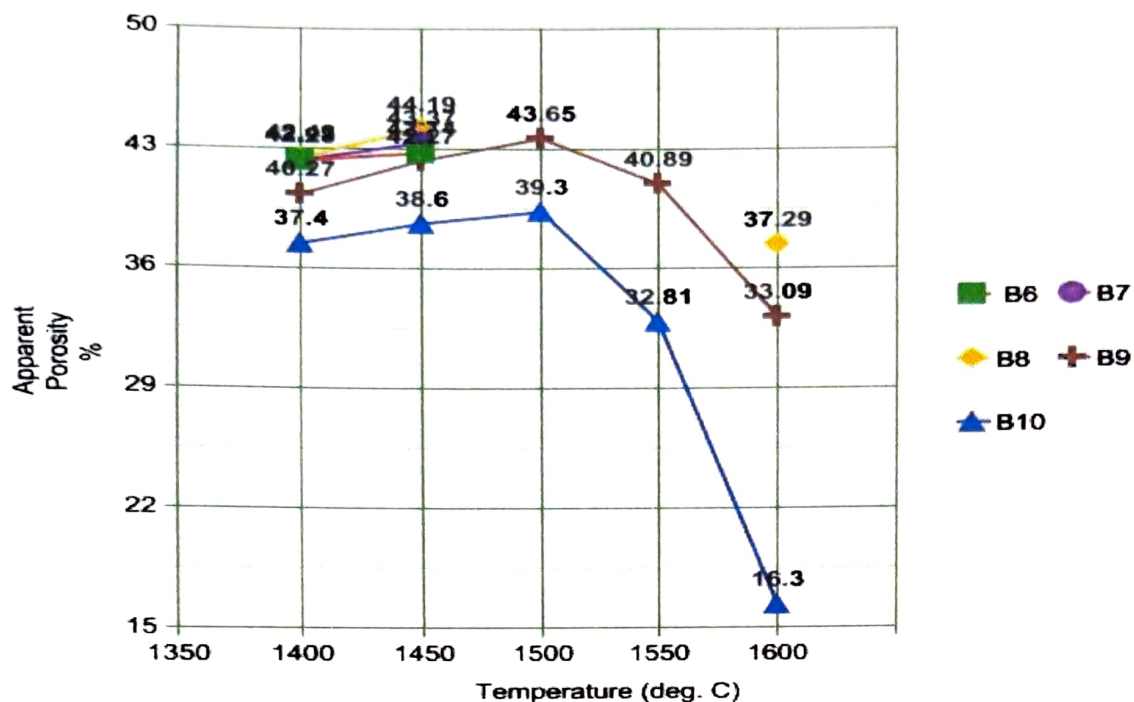


Fig. 12: Apparent Porosity of Batches of Fly Ash Alumina bricks vs Sintering Temperature

6.5 Bulk Density:

Bulk density (BD) is an inverse property of apparent porosity and therefore varies with sintering temperature as shown in figure 13-14. In general, BD increases with increasing sintering temperature except for the temperature of 1500°C (set-1 and set-3) for which the BD decreases with increasing sintering temperature. Lowering of BD at higher temperature is once again due to “bloating” effect.

Specific BD values of all the samples are presented in the following table (Table 14-15)

Sintering temperature (°C)	Bulk Density of Batch composition (g/cc)				
	Batch-1	Batch-2	Batch-3	Batch-4	Batch-5
1400	2.42	2.28	2.42	2.63	2.61
1425	2.71	2.55	2.76	2.80	2.66
1450	3.04	2.88	2.92	2.83	-
1475	3.13	3.04	2.93	2.80	2.47
1500	3.11	3.01	2.85		

Table.14: Bulk Density of different batches of Fly Ash Bauxite bricks at different sintering temperatures

Sintering temperature (°C)	Bulk Density of Batch composition (g/cc)				
	Batch-6	Batch-7	Batch-8	Batch-9	Batch-10
1400	2.03	1.93	1.84	1.83	1.83
1450	2.01	1.89	1.78	1.76	1.81
1500				1.72	1.79
1550				1.80	1.97
1600			2.00	2.03	2.40

Table. 15: Bulk Density of different batches of Fly Ash Alumina bricks at different sintering temperatures

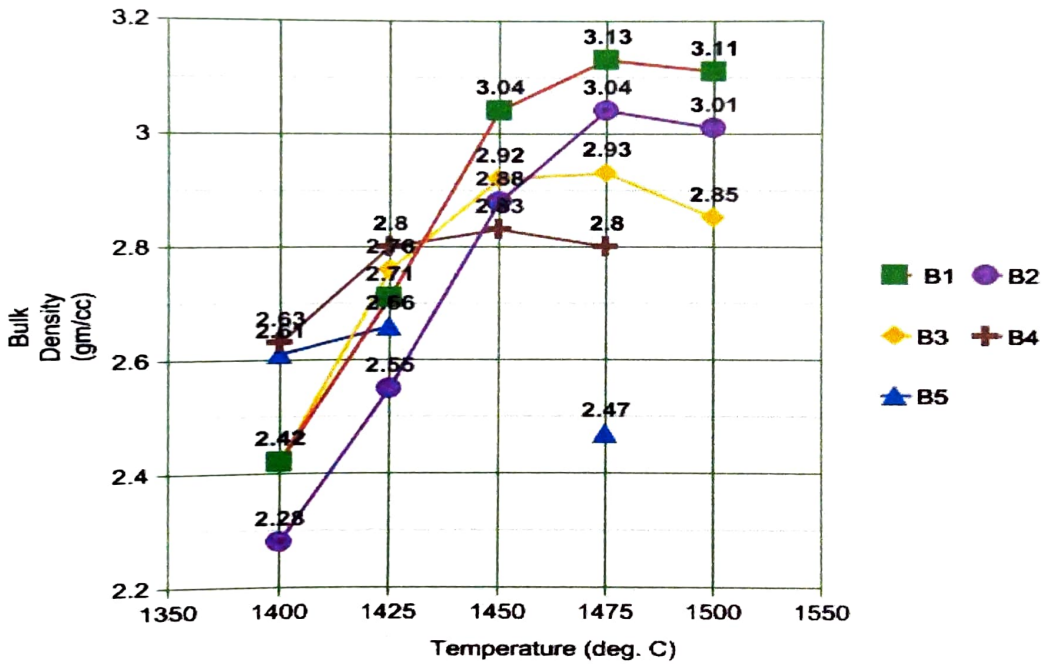


Fig. 13: Bulk Density of Batches of Fly Ash Bauxite bricks vs Sintering Temperature

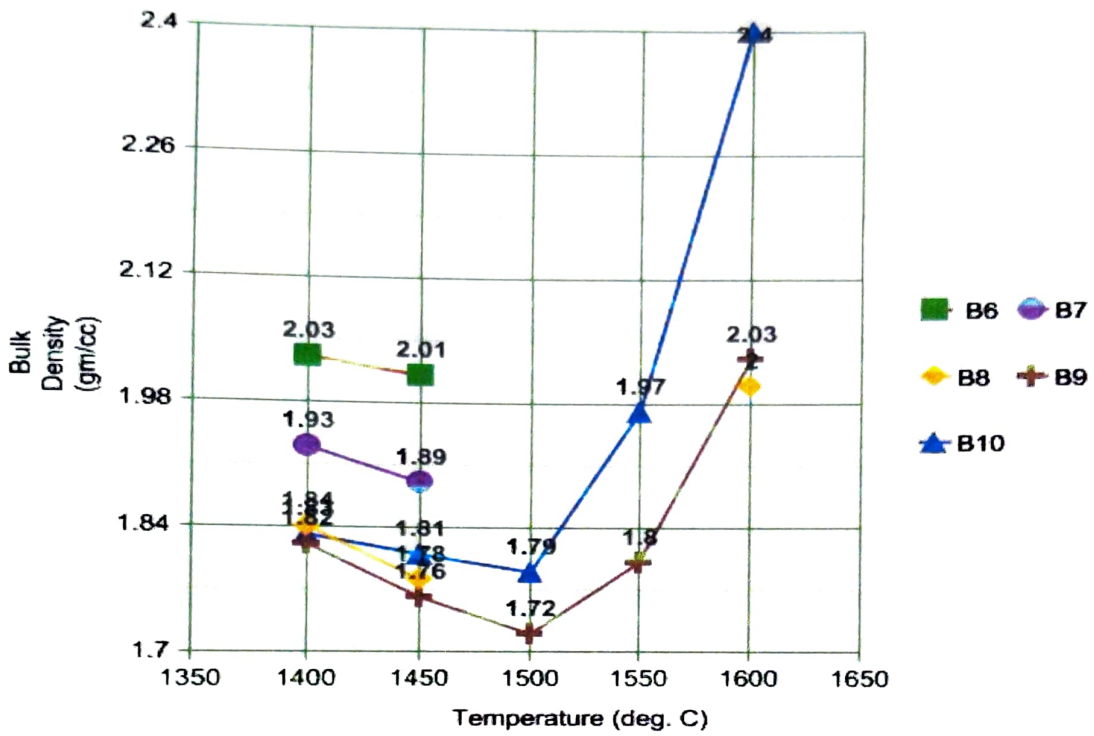


Fig.14: Bulk Density of Fly Ash Alumina bricks vs Sintering Temperature

7. CONCLUSIONS:

1. It has been observed that as fly ash addition increases, maturing temperature decreases from 1500°C for batch 1&2 to 1425°C for batch 5. Maturing temperatures for batches 3 & 4 lies in between.
2. Highest micro hardness achieved at 10% addition of for fly ash.
3. Fracture toughness is highest at 20% fly ash addition.
4. XRD peaks shows presence of mullite, corundum & cristobalite as major crystalline phases along with glassy phases.
5. Erosion test is to be done at CPRI, Bangalore for which quotation has been received.
6. One paper on “Development of Wear Resistant Ceramics using coal ash “ was presented at annual session of Indian Ceramic Society which was to be held at Jamshedpur from 09-10 January, 2019.
7. Sintering temperature is considerably reduced from the range of 1600°C-1650°C to 1425°C~1550°C, which is much lesser than the commercial products we get in market. Therefore, the production cost is reduced.

8. REFERENCES:

1. James M.Skiboa, Tamara C. Buttsbf, Michael BrianSchifferb **Ceramic Surface Treatment and Abrasion Resistance: An Experimental Study.** Journal of Archaeological Science; Volume 24, Issue 4, April 1997, Pages 311-317.
2. MICHAEL B. SCHIFFER JAMES M. SKIBO **A Provisional Theory of Ceramic Abrasion.** Published 1997
3. J Zhu, H Yan **Fabrication of an A356/fly-ash-mullite interpenetrating composite and its wear properties.** Ceramics International, Volume 43, Issue 15, 15 October 2017, Pages 12996-13003.
4. Harikishor Kumar, R.Prasad, A.Srivastava M.Vashista M.Z.Khan. **Utilisation of industrial waste (Fly ash) in synthesis of copper based surface composite through friction stir processing route for wear applications.** Journal of Cleaner Production. Volume 196, 20 September 2018, Pages 460-468.
5. Saransa Sahoo , Chitra Shijagurumayum Chitra Shijagurumayum. **Fly Ash Tiles and Its Resistance to Wear.** GRD Journals- Global Research and Development Journal for Engineering | Volume 2 | Issue 4 | March 2017. ISSN: 2455-5703
6. Fly ash in India: Generation vis-à-vis Utilization and Global perspective, GOI.
7. WIKIPEDIA